Preparation and Characterization of Clathrates in the Systems Ba – Ge, Ba – Ni – Ge, and Ba – Ni – Si

D I S S E R T A T I O N

zur Erlangung des akademischen Grades

Doctor rerum naturalium

(Dr. rer. nat.)

vorgelegt
der Fakultät Mathematik und Naturwissenschaften
der Technischen Universität Dresden
von

M.S. Umut Aydemir

geboren am 15.11.1981 in Erzincan, Türkei

Eingereicht am: 30.01.2012

Die Dissertation wurde in der Zeit von Juli / 2006 bis Dezember / 2011 im Max-Planck-Institut für Chemische Physik fester Stoffe angefertigt.

Tag der Verteidigung: **04.06.2012**

Gutachter: **Prof. Juri Grin**

Prof. Dr. Michael Ruck

Dedicated to my mother and Ebrum. . .

Acknowledgements

Introducing me to the field of clathrates as well as the handling of the diverse difficulties addressed here could not be possible without providing inspiration and constant support of an advisor and cooperation and discussion with huge numbers of coworkers from different competence groups at MPI-CPfS and other institutions.

First and foremost, I would like to express my gratitude to Prof. Juri Grin as my advisor for giving me the opportunity to join his research group. His profound knowledge and invaluable supervision have always inspired me. During my studies, he provided me essential and important concepts which constitute the solid ground of this thesis.

I would like to thank Prof. Dr. Michael Ruck for examining this work as a co-referee.

My profound thanks go to Dr. Horst Borrmann for his excellent guidance, suggestions, helping me for interpretations of the results, and patiently explaining me many aspects of X-ray crystallography.

I would like to express my sincere appreciate to Prof. Dr. Silke Bühler-Paschen, Prof. Dr. Wolf Aßmus and Prof. Dr. Cécile Hébert for their collaborations within the CMA network. It was a great opportunity for me to work with these outstanding scientists whom are among leading experts in their fields.

I would like to thank Dr. Michael Baitinger for his continuous support and many discussions on every step of my Ph.D. work. Until now we have close cooperation for the last nine years, starting from summer internships during my undergraduate studies, continued with M.S. studies and finally with this Ph.D. work. Our discussions extended my experimental skills and broadened my knowledge not only on clathrates but also on many issues related to the solid state chemistry.

I am deeply indebted to Dr. Alim Örmeci for all the theoretical calculations he made and discussions on the results. He was my physics instructor at Koç University. I was fortunate to work with him as a coworker in the institute but more than that to discuss not only about scientific issues but also whole aspects of daily life during the time we spent together.

The work at MPI-CPfS is based on a close collaboration between chemists and physicists. In this regard, I am especially grateful to Dr. Christophe Candolfi from the research group of Prof. Dr. Frank Steglich for putting a lot of efforts on the characterization of physical properties of clathrates and valuable discussions we made.

My sincere thanks go to Dr. Ulrich Burkhardt for the time-consuming XAS measurements and discussions on EDXS and WDXS results.I thank all my colleagues in our group: Dr. Lien Thi Kim Nguyen, Dr. Bodo Böhme, Dr. Igor Veremchuk, Dr. Ying

Liang, and Ms. Duong Nguyen, the group members in Wien: Prof. Dr. Ernst Bauer, Dr. Jeroen Custers, Mr. Rudolf Höfler, Mr. Matthias Ikeda, the group members in Frankfurt: Dr. Amir Haghighirad, Dr. Frank Ritter, Dr. Saskia Gottlieb-Schönmeyer, Mr. Klaus-Dieter Luther, and Mr. Stefan Brühne and the group members in Lausanne: Dr. Barbora Bartova and Dr. Marco Cantoni, for their support and cooperation.

I would like to thank Dr. Yurii Prots, Dr. Raul Cardoso-Gil, and Mr. Steffan Hückmann for X-ray diffraction measurements and many fruitful discussions we made during our group meetings.

I must thank to Dr. Lev Akselrud for the Rietveld refinements. Thanks to him, we could solve the crystal structure of $BaGe_5$ and many other compounds.

I would like to thank Prof. Dr. Frank Haarmann for the NMR measurements and discussions about the results.

I gratefully acknowledge Dr. Walter Schnelle, Dr. Niels Oeschler, Mr. Ralf Koban, and Ms. Renate Hempel-Weber for the physical property measurements.

I sincerely thank to Mr. Yiğit Öztan for SEM measurements. Our journey at MPI-CPfS has started in 2002 with the summer internship and continued until today. I wish him all the best for his studies.

I am thankful to Ms. Petra Scheppan, Ms. Monika Eckert, Mr. Thorsten Vogel, and Ms. Sylvia Kostmann for the metallographic preparations as well as EDXS and WDXS measurements.

Thanks to Dr. Steffan Hoffmann, Ms. Susan Scharsach, and Mr. Philipp Marasas for the thermal analysis measurements.

I sincerely thank to Dr. Wilder Carrillo-Cabrera and Dr. Paul Simon for carrying out the TEM investigations and for the valuable discussions.

I am also very grateful to Dr. Marcus Schmidt for helping me about the thermal transport experiments on chalcopyrites and for growing single crystals with Bridgman technique.

My sincere thanks go to the administration department at MPI-CPfS especially to Ms. Katrin Demian, Ms. Claudia Strochbach, and Ms. Monika Lintz for helping me about the administrative works during my stay at the institute. I would like to thank Ms. Margot Pester and Ms. Suzanne Zücker for their unconditional support related to travel and administrative works. Also thanks to Ina Werner for providing me many references during my Ph.D. thesis work.

I would like to express my sincere appreciate to Prof. Dr. Mehmet Somer for his constant support through my B.S., M.S. and current studies.

Many thanks go to Mr. Bürgehan Terlan, Ms. Cevriye Koz, Ms. Marija Borna, Dr. Bambar Davaasuren, Ms. Burcu Uslu, Ms. Ece Örmeci and other colleagues from MPI-CPfS and Koç University for their support and pleasant times we spent together.

I am deeply indebted to my parents and sisters for their unconditional support and encouragement to pursue my studies.

I would like to thank my love (and my chance) Ebru especially for her patience and understanding. Without her persistent confidence, I would never have completed my present work.

Additional thanks go to all whose direct and indirect support helped me completing my thesis as well as expressing my apology that I could not mention personally one by one.

I gratefully acknowledge the financial support of the Deutsche Forschungsgemeinschaft (SPP 1178) and the Max Planck Society.

Contents

Symbols viii
Abbreviations x

Chapter 1: Introduction 1

Chapter 2: Literature Review on Clathrates 4
2.1 History of clathrates 4
2.2 Classification of clathrate structures 5
2.3 Electronic structure of clathrates based on the Zintl concept 12
2.4 Clathrates as promising thermoelectric materials 14

Chapter 3: Experimental Methods and Theoretical Concepts 17
3.1 Materials and chemicals used, sources, and purity 17
3.2 Sample preparation techniques 18
3.3 Materials characterization techniques 19
3.4 Physical properties measurements 23
3.5 Quantum chemical calculations 30

Chapter 4: Preparation and Characterization of $Ba_8Ge_{43}\square_3$ 31
4.1 Phase diagram of the Ba – Ge system between 66.67 and 100 at.% Ge 31
4.2 Preparation 34
4.3 Crystal structure 39
4.4 Chemical bonding and electronic structure 46
4.5 Physical properties 49
4.6 Conclusions 55

Chapter 5: A New Type of Intermetallic Clathrate: $BaGe_5$ 57
5.1 Preparation 57
5.2 Thermal behavior 59
5.3 Microstructure 61
5.4 Crystal structure 66
5.5 Electronic band structure and chemical bonding 72
5.6 Physical properties 74
5.7 Conclusions 82

Chapter 6: Type-I Clathrate in the System Ba – Ni – Ge 84
6.1 Preparation 84
6.2 Phase analysis 86
6.3 Thermal behavior 90
6.4 Stability of $Ba_8Ni_4Ge_{42}$ under ambient conditions 92
6.5 Crystal structure 95
6.5.1 Crystal structure investigation for clathrate with superstructure 95
6.5.2 Total energy calculations on $Ba_8NiGe_{42}\square_3$ and $Ba_8NiGe_{43}\square_2$ 97
6.5.3 Crystal structure of single crystalline $Ba_8Ni_{3.5}Ge_{42.1}\square_{0.4}$ 99
6.6 Physical properties 101
6.7 Conclusions 112

Chapter 7: Type-I Clathrate in the System Ba – Ni – Si 114
7.1 Sample preparation 115
7.2 Estimation of primary crystallization field of the clathrate-I phase 117
7.3 Isothermal section of the system $BaSi_2$ – NiSi – α-Si at 1000 °C 119
7.4 Metastable compositions 121
7.5 Heat of formation and phase stability 122
7.6 Crystal structure 124
7.7 X-ray absorption spectroscopy 126
7.8 Chemical bonding 128
7.9 Electronic structure and physical properties 129
7.10 Conclusions 150

Chapter 8: The Metallic Zintl Phase Ba_3Si_4 151
8.1 Preparation and characterization 151
8.2 Phase relations 154
8.3 Crystal structure 156
8.4 Electronic structure 159
8.5 Physical properties 162
8.6 ^{29}Si NMR investigations 164
8.7 Oxidation of Ba_3Si_4 with gaseous HCl 168
8.8 Conclusions 169

Chapter 9: Preparation of Chalcopyrites for Charge Density Analysis 170
9.1 Chalcopyrites for charge density analysis 171
9.2 Preparation and characterization 173
9.2.1 Preparation of polycrystalline and single crystalline $ZnSiP_2$ 173
9.2.2 Preparation of polycrystalline and single crystalline $CuAlS_2$ 182
9.3 Preparation of $ZnSiP_2$ single crystals for static charge density analysis and analysis under external electric field 184
9.4 Crystal structure 186
9.5 NMR investigation of $ZnSiP_2$ 193
9.6 Conclusions 196

Chapter 10: Summary and Outlook 197

Chapter 11: Appendix 201
11.1 Figures 201
11.2 Tables 228

References 254
Curriculum Vitae 267
Publications 268
Oral and Poster Presentations 271
Schools and Workshops Attended 274
Versicherung 275

Symbols

a	:	Crystallographic axis, lattice constant
A	:	Cross-sectional area
b	:	Crystallographic axis, lattice constant
B	:	Magnetic field
c	:	Crystallographic axis, lattice constant
C	:	Thermal conductance
C_p	:	Specific heat at constant pressure
C_{ph}	:	Lattice contribution to the specific heat
C_v	:	Specific heat at constant volume
C_D	:	Debye contribution to the specific heat
C_{Ei}	:	Einstein contribution to the specific heat
d	:	Thermal diffusivity
e	:	Elementary charge
E_F	:	Fermi energy level
E_g	:	Band gap energy
F	:	Structure factor
F_o	:	Observed structure factor
F_c	:	Calculated structure factor
$F(000)$	:	Number of electrons in the unit cell
h	:	Planck constant
H	:	Magnetic field
I	:	Applied current
K_{iso}	:	Knight shift
k_B	:	Boltzmann constant
l	:	Distance
L	:	Lorentz number
M	:	Magnetization
$M(H)$	:	Isothermal magnetization
n	:	Multiplicity
$N(E_F)$	:	Density of states at Fermi energy level
N	:	Number of atoms per formula unit
N_{Ei}	:	Number of Einstein oscillators
N_A	:	Avagadro number
P	:	Electrical power

R^*	:	Gas constant
R, $R1$	:	Residual factor
R_{int}, R_σ	:	Merging residual values
R_i	:	Bragg R-factor
R_p	:	Profile R-factor
R_{wp}	:	Weighted profile R-factor
R_H	:	Hall constant
T	:	Temperature
T_c	:	Critical temperature for superconductivity
T_1	:	Spin-lattice relaxation times
U_{iso}	:	Isotropic displacement parameter
U_{ij}	:	Anisotropic displacement parameter
U_{eq}	:	Equivalent isotropic displacement parameter
V	:	Voltage
V_H	:	Transverse voltage
$wR2$	:	Weighted R-factor
Z	:	Number of formula units
ZT	:	Dimensionless thermoelectric figure of merit
α	:	Seebeck coefficient or thermopower
β	:	Phononic term
χ	:	Magnetic susceptibility
χ_{Pauli}	:	Pauli contribution to the magnetic susceptibility
Δ	:	Anisotropy parameter
η	:	Asymmetry parameter
γ	:	Electronic Sommerfeld term
Υ	:	ELI isosurface value
κ	:	Total thermal conductivity
κ_l	:	Lattice thermal conductivity
κ_e	:	Electronic thermal conductivity
λ	:	Wavelength; Coupling constant.
$\lambda_{e\text{-}ph}$	:	Electron-phonon coupling constant
μ	:	Absorption coefficient
μ_H	:	Hall mobility
μ^*	:	Effective electron-electron repulsion
ρ	:	Electrical resistivity
ρ_0	:	Resistivity at a reference temperature

ρ_H : Hall resistivity
ρ_V : Density of material
σ : Electrical conductivity
θ_D : Debye temperature
θ_{Ei} : Einstein temperature
ω : Oscillation frequency

Abbreviations

ADP : Atomic displacement parameters
CVT : Chemical vapor transport
DOS : Density of states
DSC : Differential scanning calorimetry
DTA : Differential thermal analysis
ED : Electron density
EDXS : Energy dispersive X-ray spectroscopy
ELF : Electron localization function
ELI : Electron localizability indicator
FPLO : All-electron full-potential local orbital minimal basis method
HRTEM: High resolution transmission electron microscopy
IF : Induction furnace
LDA : Local density approximation
MAS : Magic angle spinning
NMR : Nuclear magnetic resonance
PPMS : Physical property measurement system
PXRD : Powder X-ray diffraction
SAED : Selected area electron diffraction
SEM : Scanning electron microscope
TB-LMTO-ASA: Tight-binding linear muffin-tin orbital atomic-sphere approximation
TEM : Transmission electron microscopy
VCD : Valence charge density
WDXS: Wavelength dispersive X-ray spectroscopy
□ : Schottky-symbol for framework vacancies

Chapter 1

Introduction

The history of intermetallic clathrate investigations dates back to 1950s so that the knowledge in this field has been built up on a long standing research interest. I have been involved in clathrate research since 2002, when I joined the group of Prof. Juri Grin at the MPI-CPfS for summer internship. Hence, the results presented in this thesis regarding to clathrates could be indeed obtained thanks to the experience of the last nine years.

Intermetallic clathrates have attracted renewed attention because of their intriguing properties such as high thermoelectric efficiency, glass-like characteristic of heat transport, magnetic ordering and superconductivity in sp^3-framework.[1-6] But most of the research activities have been promoted in particular due to their promising thermoelectric properties and the growing demand for thermoelectric materials. The possibility to finely tune the electronic properties from metallic to semiconducting behavior coupled with a cage-like crystal structure efficiently disrupting the harmonic modes of the lattice are key ingredients to achieve attractive thermoelectric properties.[1, 2, 4, 7] The thermoelectric efficiency is expressed in the so called dimensionless figure of merit $ZT = \alpha^2 T / \rho\kappa$, where α is the thermopower or Seebeck coefficient, ρ is the electrical resistivity, κ is the thermal conductivity and T is the absolute temperature. High ZT values were generally obtained for either Ge-based type-I clathrates such as $Ba_8Ga_{16}Ge_{30}$ ($ZT \approx 1.35$ at 900 K),[8] $Ba_8Ni_{0.31}Zn_{0.52}Ga_{13.06}Ge_{32.2}$ ($ZT \approx 1.2$ at 1000 K),[9] and $Ba_8Au_{5.3}Ge_{40.7}$ ($ZT \approx 0.9$ at 680 K),[10] or Si-based type-I clathrates like $Ba_8Ga_{16}Si_{30}$ ($ZT \approx 0.9$ at 870 K).[11] While it was widely confirmed that the thermoelectric properties can be tuned by changing the composition, it turned out that the structure-property relations in clathrates are rather complex. It was realized that measured physical properties on bulk samples can differ substantially from the intrinsic properties of homogeneous samples with specific composition. In particular, the role of vacancies in the clathrate frameworks is generally overlooked in the interpretation of X-ray diffraction results. Depending on the vacancy content, compounds of otherwise similar composition can show metallic or semiconducting properties and even *n*- or *p*-type conduction. In addition, different superstructures are formed by vacancy ordering

exhibiting complex physical properties. Hence, to elucidate complex structure-property relations along with the applicability as a thermoelectric material, a reliable knowledge about all these properties is necessary. The thorough characterization of clathrates developed into a joint field of cross-disciplinary research at our institute and in the European Network of Excellence - Complex Metallic Alloys (NoE CMA). The clathrate-I phase in the system Ba – Ni – Ge was selected as model substance within the NoE CMA since 2006. The research motivations were described as fundamental understanding of the guest-host interactions, bonding situation and structure-property relationships in clathrates of this system.

The main focus of this work is the preparation, chemical and structural characterization along with the investigation of physical properties of intermetallic clathrates. Starting from the history of clathrate research, classification of clathrate types, their structural properties and possible application areas are evaluated in *chapter 2*. The methodologies of sample preparation and materials characterization as well as quantum chemical calculations are discussed in *chapter 3*.

The complete characterization of $Ba_8Ge_{43}\square_3$ (□ is a Schottky-symbol standing for vacancies),[12-14] which is a parent compound for the variety of ternary variants, is the subject of *chapter 4*. $Ba_8Ge_{43}\square_3$ is a high temperature phase,[12] which was prepared for the first time as single phase bulk material in this work.[15, 16] In this way, the intrinsic transport properties could be investigated without influence of grain boundary and impurity effects. The transport behavior is analyzed at low and high temperatures and referred to the former results. In addition, crystal structure and vacancy ordering in terms of the reaction conditions are discussed. Chemical bonding in $Ba_8Ge_{43}\square_3$ is investigated by topological analysis of the electron localizability indicator and the electron density.

Chapter 5 deals with the preparation, phase analysis, crystal structure and physical properties of $BaGe_5$, which constitutes a new clathrate type *oP*60.[17, 18] So far, two clathrate types were known in the binary system Ba – Ge, namely the clathrate *cP*124 Ba_6Ge_{25},[19-21] and the clathrate-I $Ba_8Ge_{43}\square_3$. Originally, $BaGe_5$ was detected by optical and scanning electron microscopy within the grains of $Ba_8Ge_{43}\square_3$.[12] Once the preparation of phase-pure $Ba_8Ge_{43}\square_3$ was achieved, it became possible to make detailed investigations of its decomposition along with the formation of $BaGe_5$. A detailed theoretical and experimental analysis on the relation between crystal structure and physical properties of $BaGe_5$ is presented.

In *chapter 6*, a thorough structural characterization and the physical properties of clathrates in the system Ba – Ni – Ge is presented based on the subtle relation between the crystal structure containing vacancies and the thermoelectric properties. During the investigations in this system, a large single crystal was grown by Nguyen *et al.* [22, 23] from the melt with the composition $Ba_8Ni_{3.5}Ge_{42.1}\square_{0.4}$. A systematic reinvestigation of the phase relations in this system was performed and the influence of different Ni content to the crystal structure and physical properties is evaluated.

The Si-based ternary clathrate with composition $Ba_{8-\delta}Ni_x\square_ySi_{46-x-y}$ is the subject of *chapter 7*. The phase relations and the homogeneity range are established. The crystal structure taking into account vacancies in the framework is discussed. Physical properties of bulk pieces are analyzed and the results are related to the sample composition. In addition, first-principles electronic structure calculations are carried out to assess variations in the electronic band structure, phase stability and chemical bonding.[24]

Chapter 8 reports on the intermetallic compound Ba_3Si_4,[25, 26] which was encountered during the investigations on the Ba – Ni – Si phase diagram. The discussion covers issues related to preparation, crystal structure, phase diagram analysis, electrical and magnetic properties, NMR measurements, quantum mechanical calculations and oxidation to nanoporous silicon with gaseous HCl.

Besides my contributions to the NoE CMA, I studied under the Priority Program 1178 of Deutsche Forschungsgemeinschaft "*Experimental electron density as the key for understanding chemical interactions*" with the project of "*Charge distribution changes by external electric fields: investigations of bond selective redistributions of valence electron densities*". *Chapter 9* deals with the preparation of chalcopyrites $ZnSiP_2$ and $CuAlS_2$ for experimental charge density analysis. Both phases show semiconducting properties and have non-centrosymmetric structures with high space group symmetry as needed to investigate the structural changes induced by external electric field. In this chapter, I describe the preparation and the crystal structure analyses of $ZnSiP_2$ and $CuAlS_2$ including issues related to the data collection as well as the results of NMR investigation.

Chapter 2

Literature Review on Clathrates

2.1 History of clathrates

Clathrates are inclusion compounds having a three-dimensional framework of 'host' structure which encapsulate in cavities 'guest' molecules, atoms or ions.[27] The term was introduced by Powell in 1948 to describe organic inclusion compounds of β-quinol, $3C_6H_4(OH)_2M$, formed with *e.g.* M = SO_2, HCN, HCl, CH_3OH, *etc.*[28] The term originates from Latin word *clathratus* meaning 'enclosed or protected by cross bars of a grating.'

The first report on clathrates dates back to the discovery of gas hydrates by H. Davy in 1811.[29] During the experiments, he passed chlorine gas through water cooled down to 275 K. The nominal composition of the resulting chlorine-ice compound could not be identified, even thought to be crystalline chlorine. In 1823, Faraday proposed the chemical formula of this gas hydrate as $Cl_2(H_2O)_{10}$.[30] The composition $(Cl_2)(H_2O)_{5.75}$ was determined around 1950s by X-ray diffraction.[31-33] The crystal structure of this chlorine hydrate was described as a three-dimensional framework of water molecules linked by hydrogen bonds. Each oxygen atom is surrounded tetrahedrally by hydrogen atoms forming polyhedral cavities which encapsulate chlorine molecules. In the crystal structure of chlorine hydrate, two cavities of different sizes have been identified as 20-atom pentagonal dodecahedron $[5^{12}]$ ($[5^{12}]$ refers to a polyhedron with 12 pentagonal faces) and 24-atom tetrakaidacahedron $[5^{12}6^2]$ ($[5^{12}6^2]$ refers to a polyhedron with 12 pentagonal and 2 hexagonal faces), formed by 46 water molecules per formula unit. Considering all the cages are completely occupied by Cl_2 molecule, an idealized composition of $(Cl_2)_8(H_2O)_{46}$ is obtained. In the mean time, large number of clathrate hydrates of other gases, inorganic and organic compounds were obtained with *e.g.*, Ar, Kr, Xe, N_2, O_2, H_2S, CO_2, CH_4, CH_3Cl, C_2H_6, CH_3NO_2, *etc.*[34]

In 1965, Cross and coworkers synthesized first representatives of a new class of compounds namely "intermetallic clathrates" with the compositions Na_8Si_{46} and Na_xSi_{136} ($3 < x < 11$).[35, 36] These two compounds have crystal structures of so called "type-I" and "type-II" gas hydrates: the guest species in the new clathrates are Na atoms and the host framework is formed by Si atoms. The discovery of the silicon clathrates enabled the synthesis of other intermetallic clathrates with group 14 elements (E14 = Si, Ge, Sn, and Pb). The first type-I germanium clathrates, $K_{7.4}Ge_{45}$ [37] and K_8Ge_{46},[38] and tin clathrates, K_8Sn_{46},[38] were synthesized by solid state reaction from elements. Later on, experimental

and theoretical works have been performed to investigate the intermetallic clathrates of *E*14 elements with alkali metals, alkaline earth metals and rare earth metals.

In addition to clathrate hydrates, more than 150 compounds crystallizing in different clathrate structures are reported so far which are referred to in literature mostly as "intermetallic clathrates" or "semiconducting clathrates" (Fig. 2.1). I will use in the rest of the discussion the general term *clathrates* to refer *all* clathrates but *clathrate hydrates*.

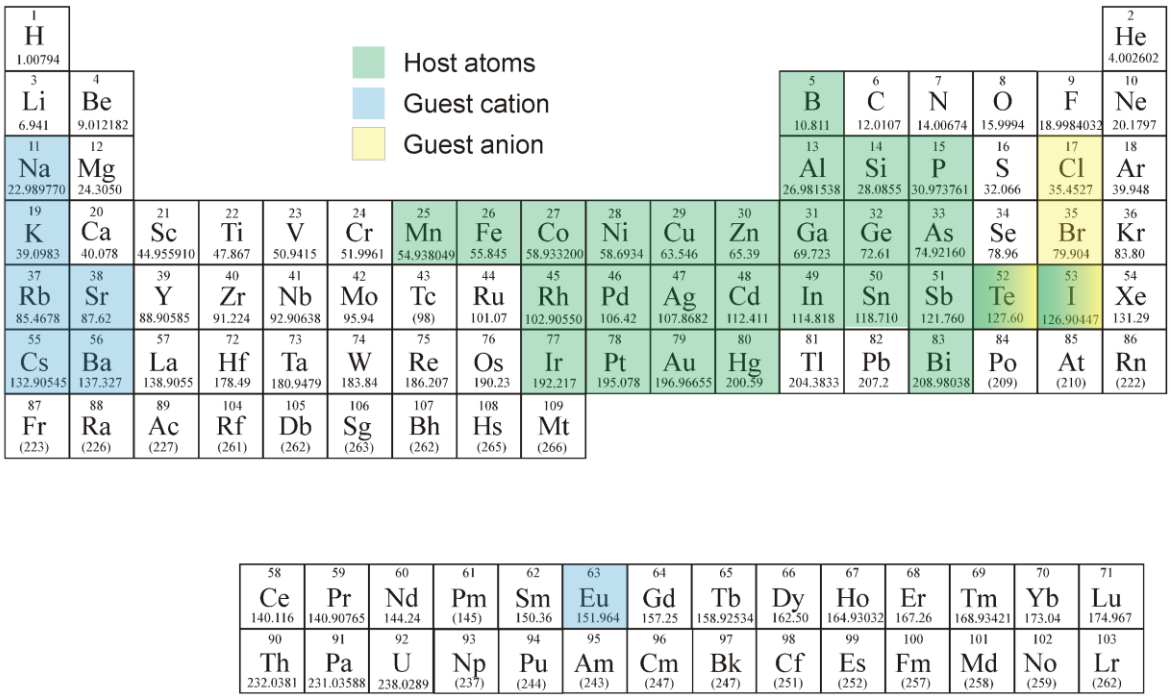

Figure 2.1: Elements forming clathrate structures.

2.2 Classification of clathrate structures

The crystal structures of clathrate hydrates can be classified with respect to packing of different building polyhedra.[39, 40] In another word, the stability of a clathrate depends on the cavity volumes and the size of the guest atoms or molecules. The chemical nature of the guest molecules may not be much decisive for the formation of the crystal structure.[34] Originally clathrate hydrate structure types were labeled with Roman numerals as type-I, type-II, …, type-VII. Later, two clathrate types as type VIII and type IV were also reported which have no corresponding clathrate hydrate structure. In literature, another labeling type is also used for clathrates as clathrate-I, clathrate-II, *etc.* In this thesis, both of these labeling types are used.

Another criterion to classify clathrates is the formal charge of the framework.[34, 41, 42] If the framework bears a negative charge and the guest atoms are cations, then the resulting structure is considered as a polyanionic clathrate. On the other hand, if the framework bears

a positive charge and the guest atoms are anions *e.g.*, Te, Cl, Br, I, *etc.*, then polycationic clathrates form.[43-46]

The major building units of the crystal structures of clathrates are large cavities formed by polyhedra with $n \geq 20$ vertices with pentagonal and hexagonal faces.[27, 41, 47] A common structural unit of all clathrate structures is the pentagonal dodecahedron consisting of 20 vertices and 12 pentagons [5^{12}] (Fig. 2.2a). Except for type-I clathrates, pentagonal dodecahedra are condensed via common faces in other structure types. Since it is not possible to fill the space with only pentagonal dodecahedra without gaps and distortions, it is required to combine pentagonal dodecahedra with other types of polyhedra which contain *e.g.* additional hexagonal faces. In this case, larger cages form namely tetrakaidecahedron [$5^{12}6^2$] (Fig. 2.2b), pentakaidecahedron [$5^{12}6^3$] (Fig. 2.2c), and hexakaidecahedron [$5^{12}6^4$] (Fig. 2.2d).

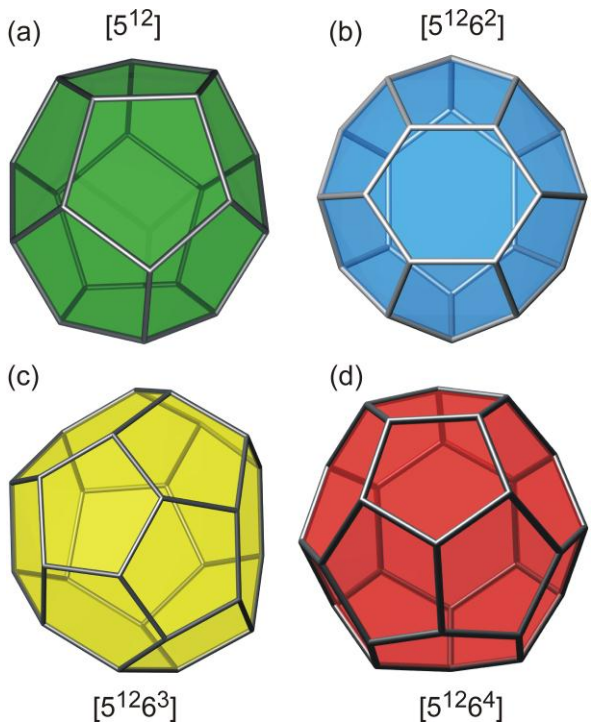

Figure 2.2: Polyhedral cavities in the crystal structure of clathrates: (**a**) pentagonal dodecahedron, (**b**) tetrakaidecahedron, (**c**) pentakaidecahedron and (**d**) hexakaidecahedron.

Type-I clathrates crystallize in the cubic space group $Pm\bar{3}n$ (no. 223) and comprise 2 pentagonal dodecahedra and 6 tetrakaidecahedra per unit cell (Fig. 2.3). The polyhedra are arranged in a space filling stacking nature. The tetrakaidecahedra are arranged in a three-dimensional mutually perpendicular system of non-intersecting columns along <100> by sharing common hexagonal faces (Fig. 2.4). The pentagonal dodecahedra are enclosed and thereby isolated from each other by these columns. Guest atoms, *G*, are entrapped in these

polyhedra corresponding to an idealized chemical composition $G'_2G''_6E_{46}$ (G' and G'' stand for guest species found in pentagonal dodecahedra and tetrakaidecahedra, respectively). In the structure of type-I clathrates, while the framework atoms occupy the Wyckoff sites 6*c* (¼, 0, ½), 16*i* (*x*, *x*, *x*), 24*k* (0, *y*, *z*), the guest atoms are found in sites 2*a* (0, 0, 0) and 6*d* (¼, ½, 0) in standard setting of the space group $Pm\bar{3}n$. Based on the X-ray and neutron diffraction results, the guest atoms encapsulated especially inside the large polyhedra (6*d* site) show large displacement parameters, stemming probably from the absence of rigid bonds between the guest atoms and the framework,[34] which may reflect the "rattling" of the guest atoms in tetrakaidecahedra.[48-51] Even a site splitting was proposed in some studies for the atoms found at this site with a higher multiplicity and lower occupancy *e.g.* to 24*k* or 24*j* with 25 % occupancy each or to 12*h* with 50 % occupancy. [22, 52-55]

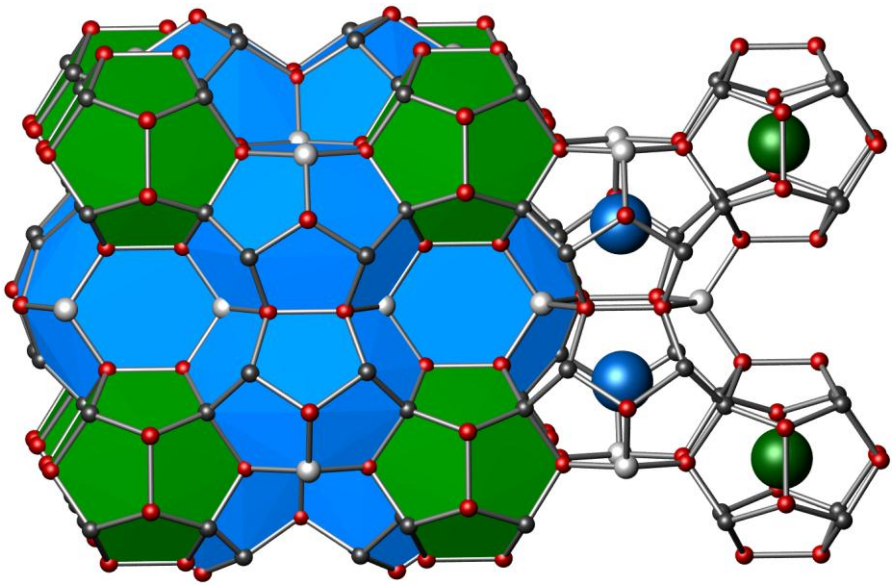

Figure 2.3: The type-I clathrate structure: Guest atoms G' (2*a*) and G'' (6*d*) are shown in green and blue colors and the framework atoms are shown in white (6*c*), grey (16*i*) and red (24*k*) colors.

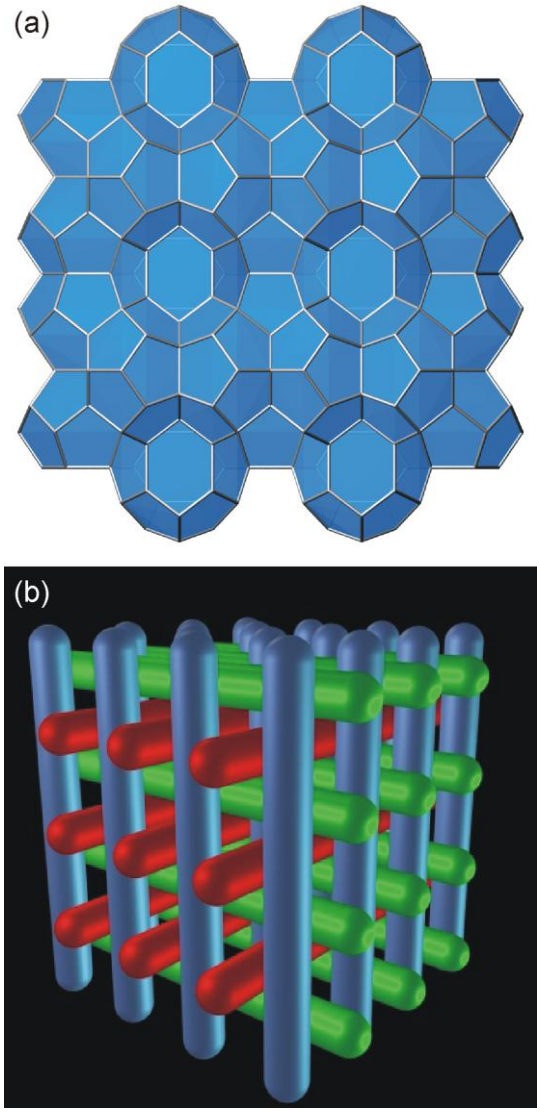

Figure 2.4: (**a**) Tetrakaidecahedra in the type-I clathrate structure share pentagonal and hexagonal faces and (**b**) assemble in three mutually perpendicular columns.

Contrary to what is often stated, not all of the framework atoms in type-I clathrate structure have an ideal tetrahedral environment. In fact, the 120° angles of the planar hexagons formed by 6*c* and 24*k* sites are unfavorable for four-bonded framework atoms. This explains formation of vacancies which was observed at this site, except for boron atoms in $K_7B_7Si_{39}$.[56] Vacancies in some type-I clathrate compounds like in $K_8Ge_{44}\square_2$ [57, 58] were reported to be either randomly distributed or ordered in the clathrate framework resulting in formation of a 2 × 2 × 2 supercell with space group $Ia\bar{3}d$ (no. 230) as observed for $Ba_8Ge_{43}\square_3$, [12-14] or for $G_8Sn_{44}\square_2$ (*G* = Rb, Cs).[59, 60] In addition, the framework atoms can be replaced at this site by transition metals such as Ni, Pd, Pt, Cu, Ag, Au, *etc*.[61]

Type-II clathrates crystallize in the space group $Fd\bar{3}m$ in which the framework is contain 16 pentagonal dodecahedral and 8 hexakaidecahedral cavities per unit cell leading the composition $G'_{16}G''_{8}E_{136}$ (Fig. 2.5). The dodecahedra are form layers with their common faces alternating in the order [ABC] similar to cubic close packing. Hexakaidecahedra are linked by common hexagonal faces and form diamond-like framework. They are enclosed between the layers formed by pentagon dodecahedra. Due to the large size difference between the cavities in the framework, type-II clathrates generally occur with two guest atoms with very different sizes *e.g.* $Cs_8Na_{16}Si_{136}$.[62] In type-II clathrates, one type or both types of cavities can be free of guest atoms as observed for $Ba_{16}\square_8Ga_{32}Sn_{104}$,[63] Si_{136},[64, 65] or Ge_{136}.[66] On the other hand, a complete occupancy of the both cavities with the same atom is reported for $Na_{24}Si_{136}$.[67]

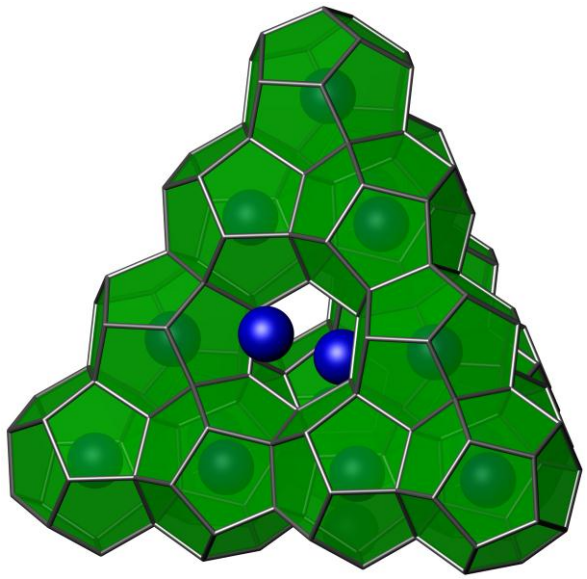

Figure 2.5: The type-II clathrate structure formed by 16 pentagonal dodecahedra and 8 hexakaidecahedra per unit cell.

Only very few compounds are known up to date which crystallize in type-III clathrate structure as *e.g.*, $Cs_{30}[Na_{2.5}Sn_{162.6}]$,[68] $Cs_{13.8}Rb_{16.2}[Na_{2.8}Sn_{162.3}]$,[68] and $[Si_{130}P_{42}]Te_{21.2}\square_8$.[69] The prototype structures of type-III clathrates are *e.g.*, bromine hydrate $(Br_2)_{20}\square_{10}[(H_2O)_{172}]$ or dimethyl ether hydrate $(CH_3OCH_3)_{20}\square_{10}[(H_2O)_{172}]$.[70] The crystal structure consists of three different types of polyhedra, pentagon dodecahedra, tetrakaidekahedra and pentakaidekahedra (Fig. 2.6). The ratio of the building polyhedra is 10 : 16 : 4, respectively. The three dimensional framework consists of 172 atoms per unit cell. The ideal chemical formula of type III clathrates without vacancies is $G'_{10}G''_{16}G'''_{4}E_{172}$. However, certain amount of vacancies is also found in the framework which can be a reason for the formation of this clathrate structure.[68]

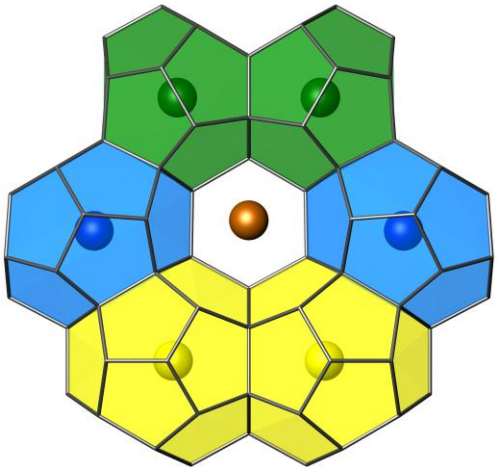

Figure 2.6: The type-III clathrate structure formed by pentagon dodecahedra (green), tetrakaidecahedra (blue) and pentakaidekahedra (yellow).

Two examples are known crystallizing in clathrate *cI*54 (in literature sometimes called as type-VIII clathrate) crystal structure: α-$Ba_8[Ga_{16}Sn_{30}]$,[71, 72] and α-$Eu_8[Ga_{16}Ge_{30}]$.[52, 73] The compounds with this structure type crystallize in non-centrosymmetric space group $I\bar{4}3m$ and transform at high temperatures to type-I clathrate modification. The clathrate *cI*54 contains exclusively four-coordinated framework atoms and it has the same chemical composition as the type-I clathrates, G_8E_{46}. However, this crystal structure unlike the type-I case consists of only one type of polyhedral cavity (Fig. 2.7). These cavities have a form of distorted pentagonal dodecahedra E_{20+3}. Due to the fact that the complete space cannot be filled exclusively by this type of polyhedra, the structure additionally contains small eight-vertex cavities remaining free of guest species.

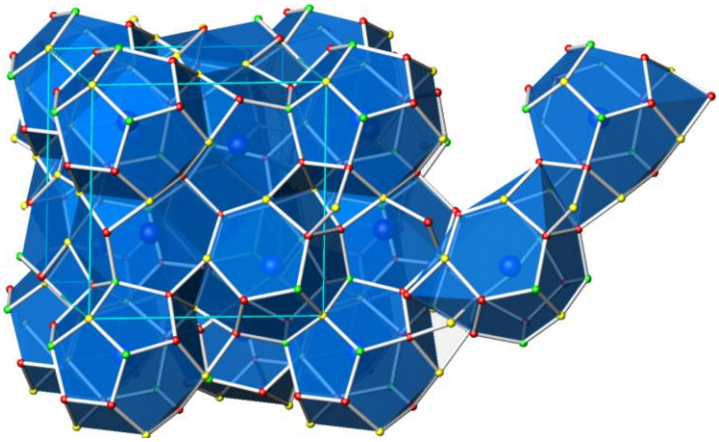

Figure 2.7: The crystal structure of clathrate *cI*54. The polyhedral cavities in the crystal structure are described as distorted pentagonal dodecahedra (blue) shown more clearly right side of the figure.

Clathrate *cP*124 (in literature sometimes called as type-III or type-IX clathrate) crystallizes in the non-centrosymmetric chiral space group $P4_132$. The crystal structure comprises 3D network of condensed pentagonal dodecahedra with the chemical formula $G_{24}E_{100}$ per unit cell (Z = 4, Fig. 2.8). The pentagonal dodecahedra share common pentagonal faces and form helixes around each 4_1 axis. The pentagonal dodecahedra arrange in a zeolite-like non space-filling manner providing additional cavities which enclose electropositive atoms. In the structure 32 out of 100 framework atoms are 3-bonded (3b)E^{-}. Some compounds crystallizing in this space group are $Ba_6In_4Ge_{21}$,[74] Ba_6Ge_{25},[19-21, 75] Ba_6Si_{25},[76] K_6Sn_{25},[77] *etc.*

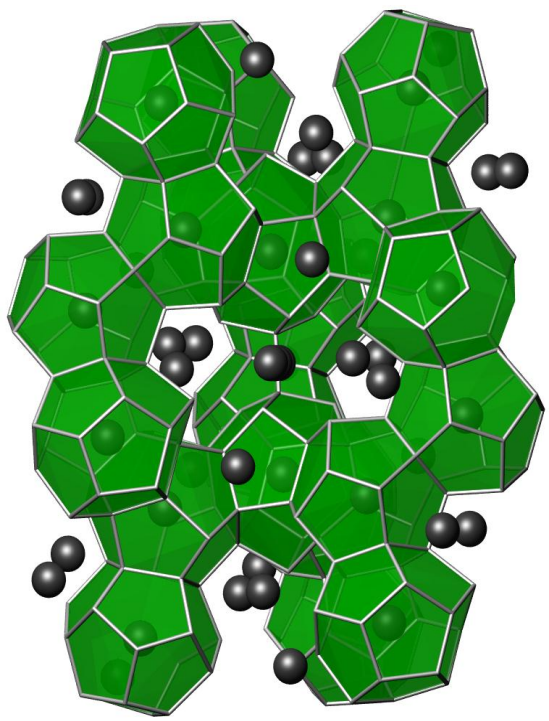

Figure 2.8: The crystal structure of clathrate *cP*124. The guest atoms are found both in the cages of pentagon dodecahedron and in channels.

A different perspective for the description of the several clathrate types was proposed by Kasper [78] and O'Keeffe [79] considering *duality* between the four-connected clathrate structures and some of the tetrahedrally close-packed intermetallic structures. The duality is due to: (**a**) correspondence of metal atom sites in intermetallics and the centers of the polyhedra in the clathrate structure, (**b**) occupation of the framework atoms in the clathrate structure to the tetrahedral holes of the original intermetallic structure. For a type-I clathrate of $G'_2G''_6E_{46}$, G' occupy the vertices, G'' the faces and the framework atoms E all tetrahedral voids of the cubic unit cell. The positions of the centers of the polyhedra in type-I clathrates correspond to the vertices and faces of the Cr_3Si structure, and the

positions of framework atoms correspond to the tetrahedral holes in the structure of Cr_3Si. Therefore, Cr_3Si and type-I clathrates are considered to be dual structures (Fig. 2.9). In the same way, type-II clathrate structure is the dual of the $MgCu_2$ crystal structure.

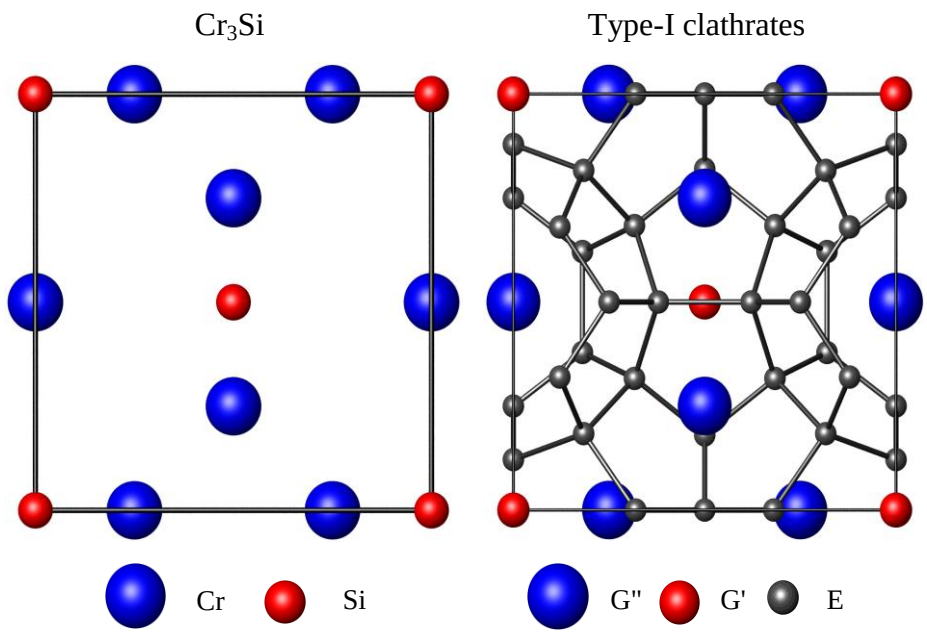

Figure 2.9: Dual crystal structures of the type-I clathrates and Cr_3Si.

Besides known clathrate structures, several clathrate-like structures were also reported as $A_3Na_{10}Sn_{23}$ (A = Cs, Rb, K),[80] $Cs_2BaCu_8Te_{10}$,[81, 82] $Ba_{16}Na_{204}Sn_{310}$,[83] and $Te_{9.5}Si_{17.5}$.[84] The common feature of these compounds is that the major polyhedron found in their crystal structures is the pentagonal dodecahedron.

2.3 Electronic structure of clathrates based on the Zintl concept

The formal electronic structure of intermetallic clathrates can be often explained by the Zintl concept.[42, 85-88] In a Zintl compound, each constituent atom achieves a closed valence shell by combining a formal charge transfer with covalent bonds. The more electropositive atoms formally donate their valence electrons to the more electronegative atoms such that the latter complete their valence requirement, or octet rule, and build a covalently bonded structure. The more electropositive atoms make only ionic bonds to the more electronegative atoms. Zintl formalism thus provides a relationship between stoichiometry (number of valence electrons) and crystal structure (connections between the atoms).[26, 86]

Considering clathrates as Zintl compounds, host-guest interaction of ionic nature implies transfer of valence electrons from guest atoms towards the framework. By partial substitution of E14 with three-valent atoms like Ga, the additional electrons may be accommodated by formation of four-bonded Zintl-anions [(4b)Ga^-]. This results in ideal

compositions like $K_8Ga_8Si_{38}$ [89] or $Ba_8Ga_{16}Ge_{30}$ [71, 90-92] with following electronic balances $[K^+]_8[Ga^-]_8[Si^0]_{38}$ and $[Ba^{2+}]_8[Ga^-]_{16}[Ge^0]_{30}$, respectively. However, charge balance is not always fully achieved this way. In particular clathrates with homoatomic framework of four-bonded *E*14 atoms do not require any additional electrons if following the 8-*N* rule. Such compounds containing excess electrons are often observed for silicon clathrates. In the metallic type-I clathrate silicides like Na_8Si_{46} [93] or $Cs_{8-x}Si_{46}$,[94] the electrons transferred from the guest atoms fill up antibonding conduction bands of the corresponding empty Si_{46} clathrate. Clathrates of the heavier homologues Ge and Sn may accommodate excess electrons also by the formation of vacancies. It was shown by *von Schnering* from single crystal X-ray diffraction data that the binary clathrates 'K_8Ge_{46}' and 'Cs_8Sn_{46}' actually exist at the compositions $K_8Ge_{44}\square_2$,[57, 95] and $Cs_8Sn_{44}\square_2$,[96] respectively. If a single atom is removed from a four-connected Ge network, the resulting vacancy □ is surrounded by four unsaturated three-bonded Ge atoms. The unsaturated Ge atoms can reach close shell configuration $[(3b)Ge^-]$ each by additional electrons transferred from the electropositive guest atoms to the framework (Fig. 2.10). Therefore, by the formation of vacancies, the electrons transferred to the host framework occupy non-bonding instead of antibonding states. In case of $K_8Ge_{44}\square_2$, two vacancies □ per unit cell are surrounded by 8 three-bonded Ge anions reaching closed shell configuration with the valence electrons from 8 K atoms. The electronic balance $[K^+]_8[(3b)Ge^-)_4]_2[(4b)Ge^0]_{36}$ is achieved, which may explain the semiconducting-like behavior observed for $K_8Ge_{44}\square_2$.[97]

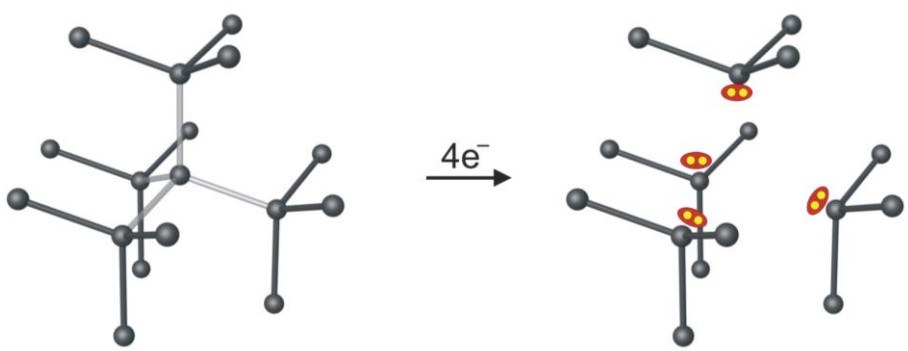

Figure 2.10: Electronic configuration when a vacancy forms in the clathrate framework**.**

Type-I clathrates Ba_8M_{46-x} (*M* = Si or Ge) can be further stabilized with substituting Si or Ge atoms by transition metals *TM* = *E*7, *E*9 – *E*12.[10, 61, 98-110] However, latest studies also showed the presence of vacancies especially for the Ge frameworks.[22, 107] Therefore, the formation of these phases can be explained by Zintl concept only with detailed information about the vacancy concentration.[111] A relationship between the vacancy formation and the Zintl concept was formulated by Nesper,[112] and von Schnering.[113] For a compound of main

group elements $A_aX_x\square_d$ (A = cation, X = anion), the total number of the valence electrons per formula unit, e, can be found by:

$$e = (8 - b) \times (a + x) + b^* \times d \tag{2.1}$$

where b refers to average bond order of the structure and b^* is the average number of broken two center two electron bonds per vacancy.[42] If we consider only the polyanionic framework, then Eq.2.1 reduces to:

$$e = (8 - b_X) \times x + b^*_X \times d \tag{2.2}$$

By using Eq. 2.2, it is possible to correlate valence electron concentration, crystal structure, and prototypical structure types.

2.4 Clathrates as promising thermoelectric materials

Intermetallic clathrates have received increasing attention over the last decades because of their intriguing properties such as superconductivity in $Na_2Ba_6Si_{46}$,[114] or Ba_8Si_{46},[115] ferromagnetism in $Eu_8Ga_{16}Ge_{30}$,[116] glass-like characteristic of heat transport in $Sr_8Ga_{16}Ge_{30}$,[117] and high thermoelectric efficiency in $Ba_8Ga_{16}Ge_{30}$.[8] Among these, clathrates have attracted attention for their thermoelectric properties.[118]

The thermoelectric effect refers to the direct conversion of temperature differences to electric potential or conversely moving of heat by applying electric current. T*he efficiency of a thermoelectric material* is captured by the dimensionless thermoelectric figure of merit, *ZT:*

$$ZT = \frac{\alpha^2 T}{\rho\kappa} = \frac{\alpha^2 \sigma\, T}{\kappa} \tag{2.3}$$

where α, $\rho(\sigma)$ and κ are standing for the Seebeck coefficient or thermopower, electrical resistivity (conductivity) and thermal conductivity, respectively.[1] The electrical conductivity is generally high for metals, but it is very low for semiconductors or even lower for insulators. The electrical conductivity increases with the charge carrier concentration, whereas the Seebeck coefficient or thermopower decreases. Hence, the electrical power factor, $\alpha^2\sigma$, is maximized at a carrier concentration of around $10^{19} - 10^{20}$ cm^{-3} (Fig. 2.11).[1] The electronic contribution to the thermal conductivity κ_e increases with carrier concentration too. Therefore, the ZT is maximized at carrier concentrations which

correspond to heavily doped semiconductors. That is why semiconducting clathrates have been intensively investigated for thermoelectric applications.

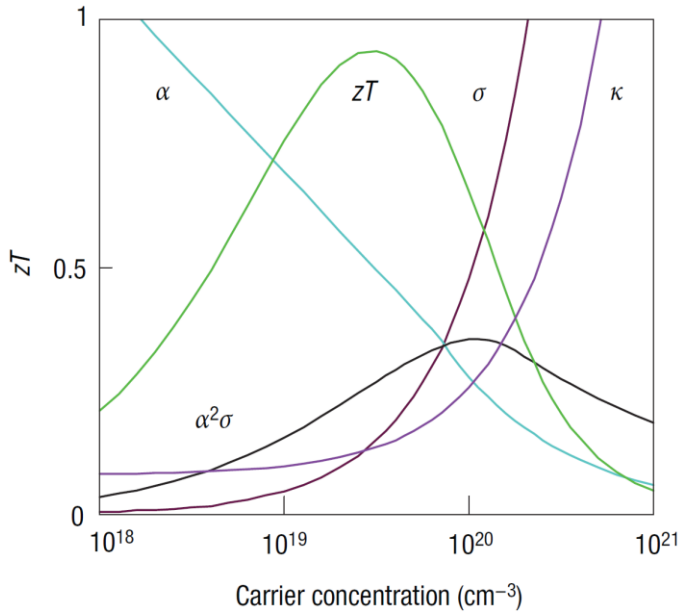

Figure 2.11: Dependence of thermopower, electrical conductivity, power factor, and thermal conductivity on carrier concentration.[3]

Considering thermoelectric properties, clathrates are discussed in the context of a phonon glass and an electron single crystal (PGEC) concept.[119] These classes of materials posses lattice thermal conductivities similar to amorphous materials but have electronic structures of crystalline solids. Hence, solids having structures with large and weakly bounded ions that can 'rattle' inside oversized cages of the host network independently of its own phonon modes are candidates as PGECs. Interest in clathrates as thermoelectric materials is due to the fact that electronic and thermal transport properties can be tuned by optimizing chemical composition. Clathrates generally show low lattice thermal conductivity values (Fig. 2.12) as an intrinsic property of their crystal structure which is attributed to the interaction of the heat-carrying phonons with local vibration modes of guest atoms in the polyhedral cages.[120] On the other hand, relatively high charge-carrier mobility of clathrates indicates that the guest-host interactions do not substantially degrade the electronic properties.[121] Hence, it is possible to finely tune the electronic properties of clathrate from metallic-like to semiconducting-like behavior by adjusting the chemical composition as well as by vacancy formation. The charge carrier concentrations of clathrates can be adjusted via controlling the concentration of guest atoms in the cages as well as substitution of the framework atoms. In addition, vacancies in the crystal structures play an important role in altering an *n*-type conductor to a *p*-type conductor and thus change the thermoelectric properties.[120, 122, 123]

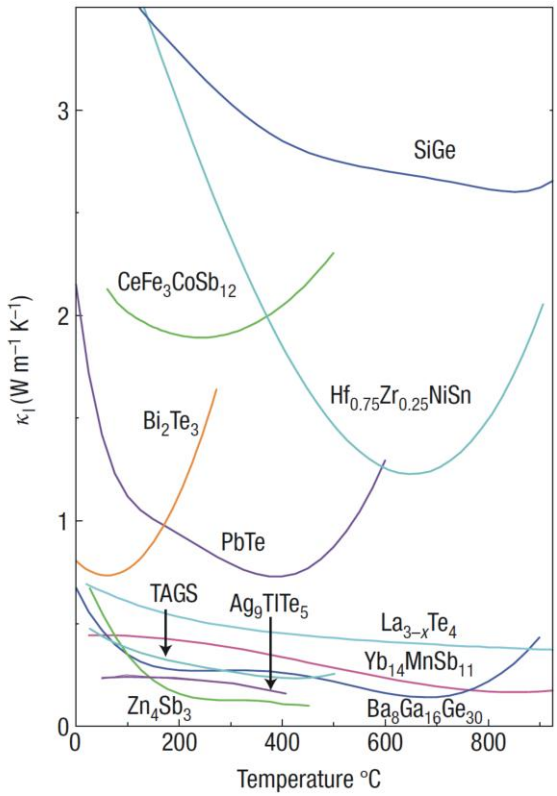

Figure 2.12: Lattice thermal conductivity of state-of-the-art thermoelectric alloys and comlex material systems (clathrates, skutterudides, *etc.*).[3]

A widespread use of thermoelectric generators based on clathrate compounds necessitates both *n*- and *p*-type materials of almost equal thermoelectric potential and compatible in terms of thermal expansion to minimize stress effects. Even though mostly *n*-type behavior was observed for most of clathrates, several clathrates have been discovered to exhibit either a *p*-type electrical conduction such as in $Ba_8Ga_{16}Ge_{30}$,[91, 123-125] $Ba_8Ga_{16}Zn_xGe_{30-x}$,[126] and $Ba_8Ga_{16}Al_xGe_{30-x}$,[127] or a transition from *n*- to *p*-type conduction in $Ba_8Au_xGe_{46-x-y}\square_y$,[128] and $Ba_8Ni_xGe_{46-x-y}\square_y$.[100]

In considering the thermoelectric efficiency, the highest reported *ZT* for a clathrate is about 1.35 at 900 K for *n*-type $Ba_8Ga_xGe_{46-x}$ (Ga/Ge stoichiometry near x = 15.3) and extrapolated maximum of 1.63 was predicted at 1100 K.[8] However this result was found to be not reproducible and the maximum *ZT* value of 0.8 at around 1050 K was achieved with subsequent investigation on the same system.[129] A *ZT* value of 1.2 was obtained at 1000 K for *n*-type $Ba_8Ni_{0.31}Zn_{0.52}Ga_{13.06}Ge_{32.2}$,[9] and recently another *n*-type single crystalline clathrate with the composition $Ba_8Ga_{15.967}Cu_{0.033}Sn_{30}$ was synthesized having a *ZT* value 1.35 at 540 K.[130] For a *p*-type material, a relatively high *ZT* value of 0.61 was observed for $Ba_8Ga_{16}Al_3Ge_{27}$ at around 763 K.[127]

Chapter 3

Experimental Methods and Theoretical Concepts

Since some of the starting elements as well as reaction products are air and/or moisture sensitive, all sample manipulations, syntheses and storage were carried out in inert atmosphere of argon filled dry glove box (MBraun). The gas atmosphere in the glove box was controlled by monitoring the oxygen and water level in parts per million with the minimum threshold set at less than 1 ppm. All containers, preparatory apparatus, *etc.* were dried in an oven at 50 °C for several hours prior to transferring into the glove box.

3.1 Materials and chemicals used, sources, and purity

Table 3.1 gives an overview of the chemicals utilized in this work. The elements were used as starting materials without further purification. For NMR experiments, 99.8 % enriched ^{29}Si was bought from Isoflex. Tantalum tubes (∅ = 6 – 12 mm, PLANSEE) and glassy carbon crucibles (∅ = 2 – 12 mm, SIGDADUR) were preferred as container materials. When annealing of samples was required, the container material was sealed in a quartz tube (∅ = 8 – 24 mm, QSIL) under vacuum or argon atmosphere (Fig. 3.1).

Table 3.1: Chemicals used and their specifications.

Chemicals	Weight	MP, BP (°C)	Physical State	Company	Purity (%, metals basis)
Ba	137.327	727	Dentritic Solid	Alfa Aesar	99.9
Ni	58.6934	1455	Powder (≤149μ)	ChemPur	99.99
Si	28.0855	1410	Lump	ABCR	99.9999
Ge	72.61	938	Lump	ChemPur	99.9999
Cu	63.546	1085	Powder (≤149μ)	Alfa Aesar	99.999
Al	26.981538	660	Powder (≤44μ)	Alfa Aesar	99.97
S	32.066	115, 445	Pieces (≤7mm)	ChemPur	99.999
Zn	65.39	420, 907	Powder (≤74μ)	ChemPur	99.9999
P (red)	30.973762	416 (subl.)	Pieces	ChemPur	99.999
Sn	118.710	232, 2602	Granule (2-4mm)	ChemPur	99.999
I_2	253.81	183 (subl.)	Crystals (resublimed)	ChemPur	99.999
$ZnCl_2$	136.28	290, 732	Powder	Alfa Aesar	99.999

Figure 3.1: Ta container sealed in Ar-filled quartz tube.

3.2 Sample preparation techniques

Arc melting. Arc melting furnace is used both for the synthesis of compounds by direct reaction of the elements and sealing metal crucibles. It is placed inside the glove box equipped with the cooling system, copper hearts of various sizes and tungsten electrode. The furnace chamber can be evacuated or filled with Ar during the operation. The operating temperature may reach up to 3500 °C.

High-frequency induction furnace. A high-frequency induction furnace (IF, TIG 5/300 by Hüttinger) is mainly used for pre-reacting (melting) the elements in container crucibles. The furnace has a copper coil with girth-diameter of 40 mm, 6 spiral turns and a height of 30 mm. To obtain a homogeneous temperature distribution under an inert atmosphere, the furnace was integrated inside the glove box providing optimal reaction conditions. The *in-situ* temperature measurement was accomplished at the surface of the crucibles via using an IR pyrometer (Maurer, Dr. George Maurer GmbH Optoelectronic) with a detectable temperature range 600 – 1600 °C.

Steel-quenching technique. A fast cooling technique was developed by striking a molten sample onto a cold stainless-steel plate and subsequently sandwiching the sample by another stainless-steel plate to room temperature (Fig. 3.2). By this method, samples which decompose by applying lower cooling rates, *e.g.* Ar or water quenching, were successfully synthesized with high purities. Considering a total mass of 2.0 g of sample, solidified cylindrical pieces are typically obtained with ~ 10 – 15 mm in diameter and ~ 1 – 2 mm in thickness. The resultant bulk pieces are suitable for the physical properties measurements. Samples with a desired geometry can easily be obtained by cutting these pieces.

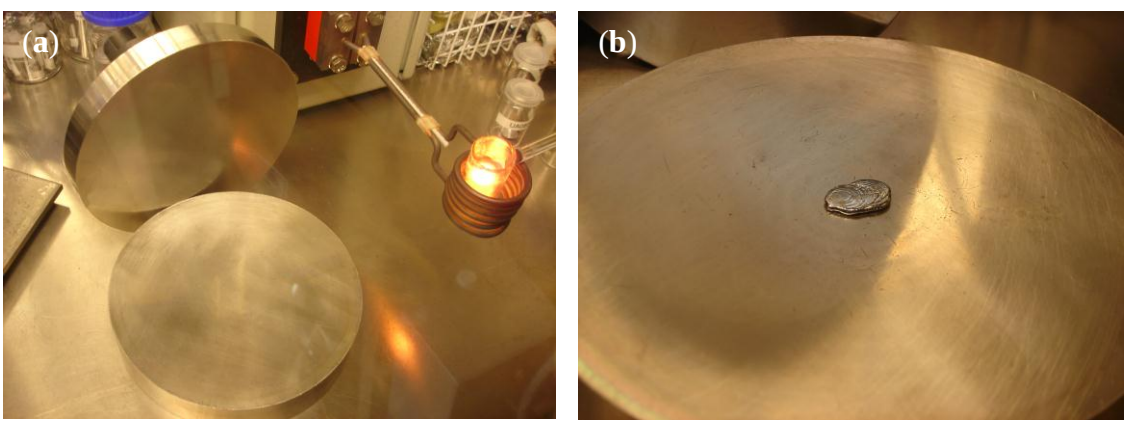

Figure 3.2: (**a**) Melting of educts in container crucible by IF and (**b**) the resultant bulk piece by subsequent quenching of melt between steel plates.

Bridgman technique. The Bridgman technique is suitable for growing single crystal ingots from congruently melting polycrystalline materials. This technique is based on heating the polycrystalline materials until a complete melt is obtained and cooling it subsequently very slowly so that single crystal progressively grows along the length of the container material. The process can be performed in a horizontal or vertical alignment. In our crystal growth experiments, a vertical Bridgman method was applied with a graphite crucible (∅ = 8 mm, l = 75 mm) under Ar atmosphere. To allow a temperature gradient within the ingot, the crucible was mounted directly on the water-cooled pulling rod which is necessary for stable directional crystallization.

Diamond wire cutting. A diamond wire saw was used for two main purposes: (**a**) to cut single crystals close to cubic shape (a ~ 50 μm) for single crystal X-ray diffraction experiments, (**b**) to cut bulk pieces in desired geometries for physical properties measurements. Diamond wire cutting is the process of using diamond wires as well as an abrasive material, which is mixed with a lubricant to cut through any material softer than diamond itself. In our case, either silicon carbide or boron carbide powders were used as abrasive materials which are then mixed with glycerol served as a lubricant. The diameter of the diamond wire is around 50 μm.

3.3 Materials characterization techniques

X-ray diffraction techniques. Powder X-ray diffraction experiments were performed on samples ground to fine powders to avoid any preferred orientation of the crystals. The powder was then spread on either a Polyimide (Kapton®, Chemplex) film for air and moisture sensitive case or a Mylar® film (Chemplex) for measurements at ambient conditions. To fix particles during the measurement, a thin layer of vacuum grease (Lithelen, Leybold) was smeared on the bottom film. The second protecting film was placed on top of the first one and they were stretched and fixed by an aluminum ring. PXRD data were collected with X-ray Guinier diffraction technique in transmission mode (Huber G670 camera, graphite monochromator, $5° \leq 2\theta \leq 100°$, $\Delta 2\theta = 0.005°$). Various X-ray sources were available as Cu-$K\alpha_1$ (λ = 1.540598 Å), Co-$K\alpha_1$ (λ = 1.788965 Å) and Cr-$K\alpha_1$ (λ = 2.289700 Å). All X-ray powder diagrams were analyzed by STOE WinXPOW software.[131] Most of the phase analyses were performed by using crystallographic data from ICSD database.[132] The positions of the reflections were determined by profile deconvolution of the powder pattern and corrected with LaB_6 standard (a = 4.15683(9) Å at 295(2) K), which was added for the measurement in small amounts. The unit cell parameters were then calculated by a least-squares refinement using WinCSD program

package.[133] The data for Rietveld refinements [134] were collected with a STOE STADI P diffractometer (Ge (111) monochromator, Cu-$K\alpha_1$ radiation, zero-background holder, Bragg-Brentano geometry) and the calculations were performed with WinCSD. The drawings of structure figures were prepared with the program ATOMS.[135]

For single crystal X-ray analyses, suitably sized single crystals were picked and mounted properly on top of the sharpened end of glass capillaries. For air and moisture sensitive samples, single crystals were selected inside a glove box and sealed inside Mark-tubes (borosilicate glass, ∅ = 0.2 mm, d = 0.01 mm, Hilgenberg). The structure data at room temperature were collected either with Rigaku AFC7 diffractometer (Mercury CCD detector, graphite monochromator, Mo-$K\alpha$ radiation, λ = 0.71073 Å) or by a RIGAKU Spider diffractometer (rotating anode, Varimax optics, Ag-$K\alpha$ radiation, λ = 1.54185 Å). Using a silver source is particularly needed to obtain high-resolution data sets and to deal with absorption as well as extinction problems. Low temperature single crystal measurements were performed with the STOE IPDS automatic diffractometer equipped with an open nitrogen gas stream as coolant. Absorption correction was performed with a multi-scan procedure. The structure solutions and refinements were performed either by using SHELXS-97 and SHELXL-97 programs,[136] integrated in WinGX software package,[137] or with WinCSD software package.

Synchrotron powder X-ray diffraction. Room-temperature synchrotron powder X-ray diffraction data were collected at the high-resolution beamline ID31 of European Synchrotron Radiation Facility (ESRF) in Grenoble: a multianalyzer stage with nine detectors each preceded by a Si 111 crystal, Debye-Scherrer geometry, λ = 0.35415 Å, scan step of 0.002° for the 2θ range from 0° to 40°. To obtain a homogenous powder, samples were ground with a pestle on an agate mortar, sieved to particle size less than 32 µm and subsequently filled in quartz capillaries (∅ = 0.5 mm).

X-ray absorption spectroscopy (XAS). The X-ray absorption spectra of the clathrate phase in the system Ba – Ni – Si have been determined close to the Ni K-edge (8333 eV). For the measurements, ≈ 20 mg of samples were ground into fine powders and mixed with B_4C and paraffin wax. Samples were then placed on Kapton foils with an area of 1 cm^2. Wavelength selection was realized by means of Si (111) double crystal monochromator. The energy range 8150 eV < E < 9600 eV was scanned with an EXAFS program starting with constant energy step size ΔE = 0.2 eV / (integration time t = 1 sec) in the XANES region close to the Ni K-edge and a constant step size in reciprocal space with $\Delta k = \sqrt{(E-E_{Ni})} = 7 \times 10^{-3}$ Å^{-1} in the EXAFS region. In total, 660 points and an increasing integration time up to 5 sec at 9600 eV led to totals of 30 min per scan. The absorption

$\mu(E) = -\ln(I_1/I_0)$ was calculated from the measured intensities at ionization chambers C_1 and C_0 which were arranged behind and in front of the sample. For spectra evaluations, two successively measured spectra were averaged. The energy values were calibrated by means of the first inflection point of the simultaneously measured reference spectrum of Ni foil (E_{Ni} = 8333 eV). EXAFS data analyses were carried out using IFEFFIT program package.[138-140] Normalization of the absorption spectra $\mu(E)$ and the extraction of the EXAFS interference function $\chi(k)$ was performed with a standard procedure including pre- and post-edge background removal. The applied cut-off value of R = 1.17 Å corresponds roughly to half of the shortest distances in the crystal structure of the clathrate phase. To enhance the features at higher k values, the EXAFS oscillations were multiplied by a scaling factor k^2.

X-ray fluorescence techniques and elemental analysis. The bulk samples for energy dispersive X-ray spectroscopy (EDXS) and wavelength dispersive X-ray spectroscopy (WDXS) analyses were prepared by grinding them with silicon carbide papers in different grit sizes together with either alcohol including lubricant or water. Following that, the surface was polished in steps by using slurry with different micron sized diamond powders (6, 3, ¼ µm) in paraffin. To perform EDXS analyses on powder materials, they were spread carefully on a conductive carbon tapes fixed on an Al-sample holder. In cases where better conductivity was required, the surfaces of the powder materials were coated with gold for couple of minutes by Cressington 108 Auto Sputtercoater. Handling of all air sensitive materials was made in an Ar-filled glove box.

The microstructure of the samples was investigated with a Philips XL 30 Scanning Electron Microscope (SEM, LaB_6 cathode). EDXS was performed with an attached EDAX Si(Li) detector for determination of chemical compositions. The data handling and the standardless quantification (ZAF) were carried out by EDAX software package. The chemical compositions were determined additionally by WDXS (Cameca SX 100) as well as by chemical analyses with inductively coupled plasma optical emission spectrometry (ICP-OES, Varian, Vista RL). As a standard for WDXS analysis, either elements or their binaries with precisely determined compositions were selected. The quantitative analysis and imaging were performed by Cameca Peak Sight software package. The optical microscope images were obtained by Light Optical Polarization Microscope (Zeiss Axio Plan 2).

Transmission electron microscopy (TEM). TEM experiments were performed by using a Technai 10 electron microscope (FEI). For the experiments, fine powder of the sample was deposited on a holey-carbon film supported by a copper grid. Selected area electron

diffraction (SAED) patterns in different crystallographic directions were collected and used for the space group determination.

Nuclear magnetic resonance (NMR) spectroscopy. For NMR measurements, fine-powdered samples were diluted in the volume ratio of about 1:5 with dry GeO_2 (Chempur, 99.999%) to avoid a skin effect of the electric-conducting material and eddy currents during magic angle spinning (MAS) experiments. The mixture was enclosed under Ar into a ZrO_2 rotor (∅ = 4 mm). The spectra were recorded using a Bruker AVANCE 500 WB spectrometer (B_0 = 11.74 T, ν = 99.364 MHz and 202.389 MHz for ^{29}Si and ^{31}P, respectively). MAS and static wide line experiments were performed with a 4 mm standard triple resonance probe (Bruker). The spectral parameters of the MAS signals were determined by a single pulse sequence with 1.5 μs pulse duration for Ba_3Si_4 and 0.8 μs pulse duration for $ZnSiP_2$. A Hahn-echo pulse sequence with 1.5 μs and 3.0 μs pulse duration and an inter-pulse delay of ν = 60 μs was used for the static measurement for Ba_3Si_4. A cycle delay of 100 s and 10 s was applied to the ^{29}Si and ^{31}P experiments for $ZnSiP_2$. A saturation recovery pulse sequence was used for spin-lattice relaxation (T_1) experiments applying a sample rotation frequency of 7.5 kHz. 30 relaxation delays equally spaced on logarithmic time scale were measured to determine T_1 for each of seven measurement temperatures from 170 K to 298 K. All experiments were performed by eight-fold phase cycling of the pulse sequences. The spectral parameters of the signals were determined from the line shapes by least-squares analysis with the program SIMPSON.[141] The definitions from Bak *et al.* are used for the isotropic signal shift, the anisotropic signal shift and the asymmetry parameter.[141] The ^{29}Si and ^{31}P signal shifts are referred to tetramethylsilane (TMS) and H_3PO_4, respectively.

Thermal analysis. Heat-flux differential scanning calorimetry, (DSC, Netzsch DSC 404C, thermocouple E), differential thermal analysis, (DTA, Netzsch DTA 404), as well as simultaneous thermogravimetry and differential thermal analysis, (TG-DTA, NETZSCH STA 409C/CD), were performed to obtain the temperatures of the invariant reactions and / or corresponding weight loss. Investigation of phase transitions at low temperatures was performed with Netzsch DSC 204 automatic calorimeter. The measurements were conducted over a temperature range from –150 °C to 150 °C at heating / cooling rate of 5 or 20 °C/min. Data were analyzed with the software program Netzsch Proteus-Thermal Analysis-Version 4.8.3. The maximum temperature limit of the DSC and TG-DSC instruments is around 1300 °C. If heating to very high temperatures was needed, Netzsch DTA 404 was used in which the temperatures around 2000 °C are accessible. All

measurements were carried out with various dynamic or isothermal heat treatments and by applying different heating / cooling rates from 0.1 °C/min to 20 °C/min.

During the measurements it was observed that metal crucibles react rapidly with most of the silicon and germanium containing melts. To prevent any contact with the metal surface, around 30 mg of samples were weighed in glassy carbon crucibles (∅ 4 mm, l = 6 mm) and then sealed in Nb ampoules (∅ = 5 mm, 600 mg). For precise determination of temperatures of peritectoid transformations, 30 mg of samples were transferred in a corundum crucible placed in a Pt crucible with a lid. For materials stable at ambient conditions, either Al_2O_3 or Y_2O_3 crucible was preferred for the measurements. After the heat treatments, the samples were analyzed by PXRD and EDXS to determine the types of products formed.

3.4 Physical properties measurements

Magnetic properties. Measurements of the magnetic susceptibility, χ, were carried out with a SQUID magnetometer (MPMS XL – 7, Quantum Design). The air and moisture sensitive polycrystalline samples were sealed inside a pre-calibrated thin walled quartz tube under a He-pressure of 400 mbar. When the samples are stable in ambient conditions, they were fixed inside a plastic straw. The contribution of the sample holders was accurately determined and then subtracted from total susceptibilities as background signal. The magnetic susceptibilities were measured in a ^{4}He cryostat in magnetic fields 2 mT – 7 T. Isothermal magnetization curves, $M(H)$, were also measured under fields of 0 – 5 T to probe for possible ferromagnetic and paramagnetic contributions stemming from impurity phases. The measurements were performed in a temperature range from 1.8 to 400 K.

Electrical resistivity. The electrical resistivity, ρ, of samples was measured with a 4-contact method and calculated based on the following formula:

$$\rho = \frac{\Delta V}{I}\frac{A}{l} \tag{3.1}$$

where I is the applied current, l is the distance between the two points at which the created voltage, ΔV, is measured and A is the cross-sectional area perpendicular to the direction of the current.

Although electrical resistivity of metals increases by increasing temperature, electrical resistivity of semiconductors decreases exponentially due to increasing concentrations of

charge carriers as electrons in conduction band (*n*-type) and holes in the valence band (*p*-type) according to:

$$\rho(T) \propto \exp\,(E_g / k_B T) \tag{3.2}$$

in which E_g is the band gap energy, k_B is the Boltzmann constant, and T is the temperature.

For the high-temperature data, resistivity for semiconductors can be written as:

$$\rho = \rho_0 e^{\frac{E_g}{2k_B T}} \tag{3.3}$$

where ρ_0 is the resistivity at a reference temperature *e.g.* 300K. By using Eq. 3.3, a plot of $\ln(\rho/\rho_0)$ versus $1/T$ gives a linear relation so that energy band gap E_g can be determined for a semiconductor.

The resistivity measurements of the compacted samples were performed by standard four-point dc method with cryostat in an Ar-filled glove box. The samples were ground with a tungsten carbide mortar and then pressed under 0.5 GPa pressure to a prism-shaped specimen (*e.g.* 6.0 × 1.5 × 1.0 mm^3). The contacts were made by silver-filled epoxy glue with using either wires of 30 μm in diameter Pt or 50 μm in diameter Cu. The pellets with the attached probes were then mounted on the top of a chip, which was then connected to the multimeter with the help of four coaxial wires. The resistivity measurements of pressed pellets were performed at temperatures in the range of 3.8 – 320 K.

For both low and high temperature resistivity measurements on bulk pieces, parallelepiped shaped samples were cut from as-cast samples with a diamond wire saw to typical dimensions of 2 × 2 × 8 mm^3. The low temperature resistivity measurements of these samples were performed by standard four-point dc method with a Physical Property Measurement System (PPMS, Quantum Design) in the 2 – 350 K temperature range. Copper wires of 200 μm in diameter were contacted onto the samples using a tiny amount of silver paste. The bar-shaped samples were then mounted on the PPMS puck (Fig. 3.3). In addition to electrical resistivity, thermopower and thermal conductivity measurements at low temperatures can be performed on the same setup. Electrical resistivity of samples at high temperatures (300 – 673 K) was measured by a standard method using a ZEM 3 (Ulvac-Riko) system.

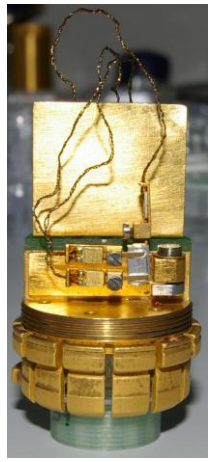

Figure 3.3: Experimental cell for electrical resistivity, thermal conductivity and thermopower measurements at low temperatures.

Thermal conductivity and thermopower. Unlike electrical conduction, considered due to the movement of electrons, thermal conduction results from contributions of both electrons and phonons. Hence, the total thermal conductivity, κ , can be written as:

$$\kappa = \kappa_{\mathrm{e}} + \kappa_l \tag{3.4}$$

where κ_{e} and κ_{l} are the electronic and lattice (phononic) contributions to the thermal conductivity, respectively.[142] The electronic contribution of thermal conductivity is related to electrical resistivity of a material by the Wiedemann-Franz law:

$$\kappa_{\mathrm{e}} = \frac{LT}{\rho} \tag{3.5}$$

where L is referred as the Lorenz number, $L = 2.44 \times 10^{-8}$ WΩ/K^2.

The thermal conductivity and thermopower measurements were performed on the same setup (Fig. 3.3). One end of the sample was maintained at a fixed temperature by use of a heat sink and the other end was in good thermal contact with a resistive furnace. In this way, a thermal gradient and a one-dimensional heat flow were introduced through the sample. The temperature difference ΔT was determined by two thermocouples which are connected to the central part of the sample and separated by a distance l. κ can be calculated by:

$$\kappa = C\frac{l}{A} = \frac{P}{\Delta T}\frac{l}{A} \tag{3.6}$$

where C is the thermal conductance of the sample and P is the electrical power.

In addition, a thermoelectric voltage ΔV is created due to the formation of the temperature gradient. Resulting thermopower, α, is then given by:

$$\alpha = \alpha_{\text{wires}} - \frac{\Delta V}{\Delta T} \tag{3.7}$$

where α_{wires} represents the thermopower of wires measuring the voltage.

For semiconducting materials, from the maximum thermopower value $\alpha_{\max}$ and the temperature at which this maximum occurs $T_{\max}$, the band gap energy E_g can be estimated using:

$$E_g = 2e\alpha_{\max} T_{\max} \tag{3.8}$$

The thermal conductivity and thermopower measurements were performed simultaneously with PPMS over the temperature range 2 – 350 K. The typical dimensions of a parallelepiped sample were 2 × 2 × 8 mm^3. To minimize the uncertainty in the geometry factor, involved in the measurement of electrical resistivity and thermal conductivity, particular attention was given to obtain perfectly parallel sides of the bulk pieces. High temperature thermopower was measured in the 300 – 673 K temperature range by a standard method using a ZEM 3 (Ulvac-Riko) system.

Hall effect. When a magnetic field, B, is applied to a sample in which an electric current is flowing, the trajectories of the charge carriers are deflected to the sides due to resulting transverse force. In this way, a transverse voltage, V_{H}, is created which is known as the Hall effect. The Hall constant R_{H} is then calculated by:

$$R_{\text{H}} = \frac{V_{\text{H}} A}{IdB} = \frac{\rho_{\text{H}}}{B} \qquad R_{\text{H}} = -\frac{1}{ne} \text{ (electron)} \qquad R_{\text{H}} = \frac{1}{pe} \text{ (hole)} \tag{3.9}$$

where I is the current, d is the transverse dimension of the sample, ρ_{H} is the Hall resistivity, n (p) is the electron (hole) concentration and e is the elementary charge. Hall coefficient is obtained from the slope of the $\rho_{\text{H}}(B)$ curves.

The Hall mobility, μ_{H}, of the charge carriers can be derived via the relation:

$$\mu_{\text{H}} = R_{\text{H}} / \rho \tag{3.10}$$

Hall effect is very useful in measuring the charge carrier concentration as well as determining the type of charge carriers as negative (electrons) or positive (holes).

The Hall effect measurements were performed using PPMS between 5 and 350 K. Fig. 3.4 shows the sample holder used for the measurement of electrical resistivity and Hall effect. The cryostat is equipped with a superconducting coil to generate a magnetic field from –7 to 7 T. The measurements were made with an alternating current. The samples were the same as those used for measurements of electrical and thermal transport at low temperatures.

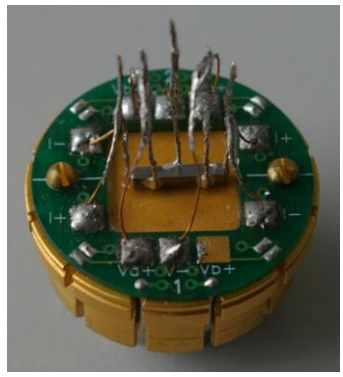

Figure 3.4 Sample holder used for electrical resistivity and Hall effect measurements.

Specific heat. Classical statistical thermodynamics states that specific heat is constant and proportional to:

$$C_v = 3N_A k_B = 24.94 \text{ Jmol}^{-1}\text{K}^{-1} \tag{3.11}$$

where N_A is the Avogadro number ($6.02\,214 \times 10^{23}$ mol^{-1}). This is the classical value of the specific heat predicted by the Dulong-Petit law,[143] which is valid only at high temperatures because specific heat varies as the temperature changes.

The lattice (phononic) contribution to the specific heat, C_{ph}, can be written as:

$$C_{ph} = \left[\frac{\partial Q}{\partial T}\right]_V = 9Nk_B\left(\frac{T}{\theta_D}\right)^3 \int_0^{\frac{\theta_D}{T}} \frac{x^4 e^x}{\left(e^x - 1\right)^2} \mathrm{d}x \tag{3.12}$$

in which $x = \hbar\omega / k_B T$ (ω is the frequency), $\hbar = h / 2\pi$ (h is the Planck constant) and $\theta_D = \hbar\omega_D / k_B$ known as Debye temperature (ω_D is the frequency above which the oscillators behave classically). At low temperatures, the Eq. 3.12 turns to:

$$C_{\mathrm{ph}} = \frac{12\pi^4}{5} N_0 k_{\mathrm{B}} (\frac{T}{\theta_{\mathrm{D}}})^3 \tag{3.13}$$

giving the experimentally observed T^3 dependence of the specific heat at low temperatures. In the same way the electronic contribution to the specific heat can be found as:

$$C_e = \left[\frac{\partial Q}{\partial T}\right]_V = \frac{\pi^2 k_B{}^2 N(E_{\mathrm{F}})T}{3} = \gamma T \tag{3.14}$$

in which $N(E_{\mathrm{F}})$ is the density of states at the Fermi energy and γ is the Sommerfeld coefficient.

At temperatures much below Debye temperature, the total specific heat of non-magnetic materials can be written as the sum of electronic and phononic contributions:

$$C_{\mathrm{p}} = C_{\mathrm{e}} + C_{\mathrm{ph}} = \gamma T + \beta T^3 \tag{3.15}$$

where β is the Debye T^3 lattice term (phononic term). A plot of C_{p} / T versus T^2 usually yields a straight line with an intercept γ and a slope of β. The β coefficient is related to the Debye temperature, θ_{D}, via the relation,

$$\theta_{\mathrm{D}} = ((12\pi^4 NR^*) / (5\beta))^{1/3} \tag{3.16}$$

where N is the number of atoms per formula unit and R^* is the gas constant.

For clathrates, the specific heat is usually treated as a sum of a background vibrations spectrum originating from the cage-like structure *i.e.* a Debye contribution and an Einstein contribution arising from the localized vibrational modes of the guest atoms and quantified through characteristic Einstein temperatures, θ_{E_i} . The specific heat can be thus written as:

$$C_{\mathrm{p}} = C_{\mathrm{e}} + C_{\mathrm{ph}} = C_{\mathrm{e}} + C_{\mathrm{D}} + \sum C_{\mathrm{Ei}} = \gamma T + \frac{12\pi^4 N_{\mathrm{D}} k_{\mathrm{B}}}{5} \int \frac{x^4 e^x dx}{(e^x - 1)^2} + \sum_i p_i N_{\mathrm{Ei}} R^* \left(\frac{\theta_{\mathrm{Ei}}}{T}\right)^2 \frac{e^{\theta_{\mathrm{Ei}}/T}}{(e^{\theta_{\mathrm{Ei}}/T} - 1)^2} \tag{3.17}$$

where C_{D}, and C_{Ei} is Debye contribution to the specific heat and an Einstein contribution of the ith vibrational mode of the rattling atoms, respectively, N_{D} is the number of Debye oscillators per formula unit and p_i, N_{Ei} and θ_{Ei} are the degrees of freedom, the number of Einstein oscillators, and the Einstein temperature related to the ith vibrational mode,

respectively.

The relaxation method is a commonly applied technique to measure the specific heat of samples with small masses down to very low temperatures. To perform this type of measurement, the sample is mounted on a platform at the center of the sample holder (Fig. 3.5) with Apiezon N grease which enables good thermal contact. Low-temperature specific heat measurements were performed on irregular crystalline pieces ($m \approx 30$ mg) in the temperature range 1.8 – 320 K with a relaxation-type calorimeter setup (PPMS, Quantum Design). High-temperature C_p measurements were performed in the temperature range the 300 – 773 K on a Netzsch Pegasus differential scanning calorimetry (DSC).

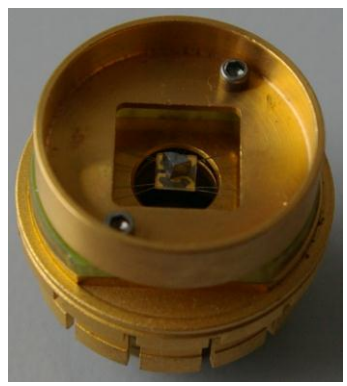

Figure 3.5 Sample holder used for specific heat measurements.

Thermal diffusivity. The thermal conductivity at high temperatures can be calculated indirectly through measuring the thermal diffusivity, *d*, by:

$$\kappa = d(T)\rho_V(T)C_p(T) \tag{3.18}$$

where $\rho_V(T)$ is the density of material being investigated.

The measurement of thermal diffusivity was carried out on a $6 \times 6 \times 1$ mm^3 square prism shape sample by a laser flash technique (Netzsch LFA 427) in an argon atmosphere from room temperature up to 800 K.

3.5 Quantum chemical calculations

Electronic structure calculations were carried out by two methods namely the all-electron full-potential local orbital minimal basis method, FPLO,[144, 145] or tight-binding linear muffin-tin orbital atomic-sphere approximation, TB-LMTO-ASA.[146] In FPLO, the atomic orbital-like basis functions are obtained by solving an Schrödinger equation applying a spherically averaged crystal potential and a confining potential.[144] The confining potential forces the basis functions to be more localized than the genuine atomic orbitals. FPLO calculations were performed within the density functional theory [147] in the local density approximation (LDA).[148] The Perdew-Wang parameterization [149] was chosen for the exchange-correlation potential. For TB-LMTO-ASA, the Barth-Hedin exchange potential was employed for the LDA calculations.[150] The radial scalar-relativistic Dirac equation was solved to get the partial waves. The calculation within the atomic sphere approximation (ASA) includes corrections for the neglect of interstitial regions and partial waves of higher order.[151] The atomic parameters from single-crystal diffraction data or Rietveld refinements were used in the calculations.

The electron localizability indicator (ELI, Υ) [152-156] and at the earlier stage the electron localization function (ELF) [152, 157] were calculated using dedicated modules in TB-LMTO-ASA or the FPLO program packages.[158] ELI was evaluated in the ELI-D representation.[159] ELI-D and electron density were analyzed using the program Basin [160] with consecutive integration of the electron density in basins, which are bound by zero-flux surfaces in the ELI-D or electron density gradient field. Such treatment of ELI-D is similar to the procedure proposed by Bader for the electron density.[161]

Chapter 4

Preparation and Characterization of $Ba_8Ge_{43}\square_3$

In the earlier investigations, the crystal structure of $Ba_8Ge_{43}\square_3$ was described by clathrate-I structure comprising three framework vacancies per unit cell ($a \approx 10.66$ Å, space group $Pm\bar{3}n$).[162, 163] Although super structure reflections were detected by electron diffraction patterns of $Ba_8Ge_{43}\square_3$, no ordered crystal structure model was suggested.[164] By collecting accurate single crystal as well as synchrotron powder X-ray diffraction data, the crystal structure of $Ba_8Ge_{43}\square_3$ was redetermined revealing an ordered vacancy arrangement with a 2 × 2 × 2 supercell in the space group $Ia\bar{3}d$.[12-15] $Ba_8Ge_{43}\square_3$ was originally predicted to show metallic behavior according to the 8–*N* rule,[12] because only 12 of the 16 valence electrons related to the Ba atoms are necessary to satisfy electronic requirements of 12 Ge anions surrounding the three vacancies. Experimentally, it was found that the compound shows semiconducting behavior.[13, 164] The apparent discrepancy to the simple valence rules has been tentatively ascribed to an ordering of the framework vacancies resulting in modifications of the electronic band structure near the Fermi level.[13]

4.1 Phase diagram of the Ba – Ge system between 66.67 and 100 at.% Ge

The binary phase diagram Ba – Ge has been thoroughly investigated.[12, 165, 166] In the Ge-rich part of the phase diagram (Fig. 4.1), $BaGe_2$ forms congruently from the melt at 1105 °C. Ba_6Ge_{25} decomposes peritectically at 815 °C to $BaGe_2$ and the corresponding melt. $Ba_8Ge_{43}\square_3$ forms at 810 °C by a peritectic reaction from α-Ge and melt and crystallizes in an eutectic mixture with Ba_6Ge_{25} at 808 °C. $Ba_8Ge_{43}\square_3$ is a high-temperature phase stable in the temperature range 770 °C – 810 °C.[12] Between 770 °C and 535 °C, $Ba_8Ge_{43}\square_3$ decomposes to Ba_6Ge_{25} and α-Ge and below 535 °C to α-Ge and another clathrate phase $BaGe_5$, which is discussed in detail in Chapter 5.[17]

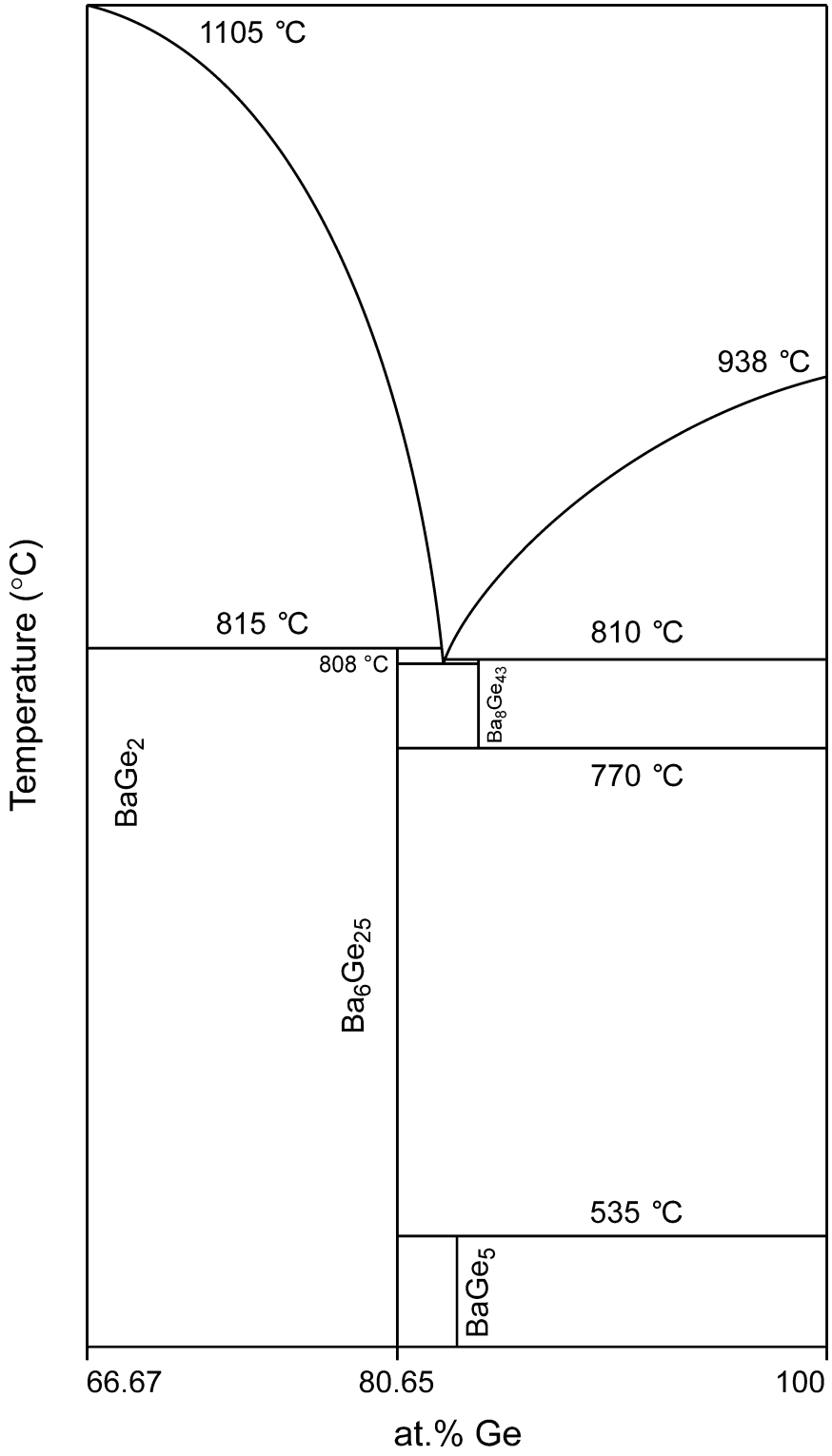

Figure 4.1: Phase diagram of the Ba – Ge system in the germanium-rich region.

DSC measurements were performed on single-phase samples of $Ba_8Ge_{43}\square_3$ (Fig. 4.2). Further steps concerning the optimization of the preparation conditions of $Ba_8Ge_{43}\square_3$ and annealing experiments were conducted taking into account the results of these thermal analyses.

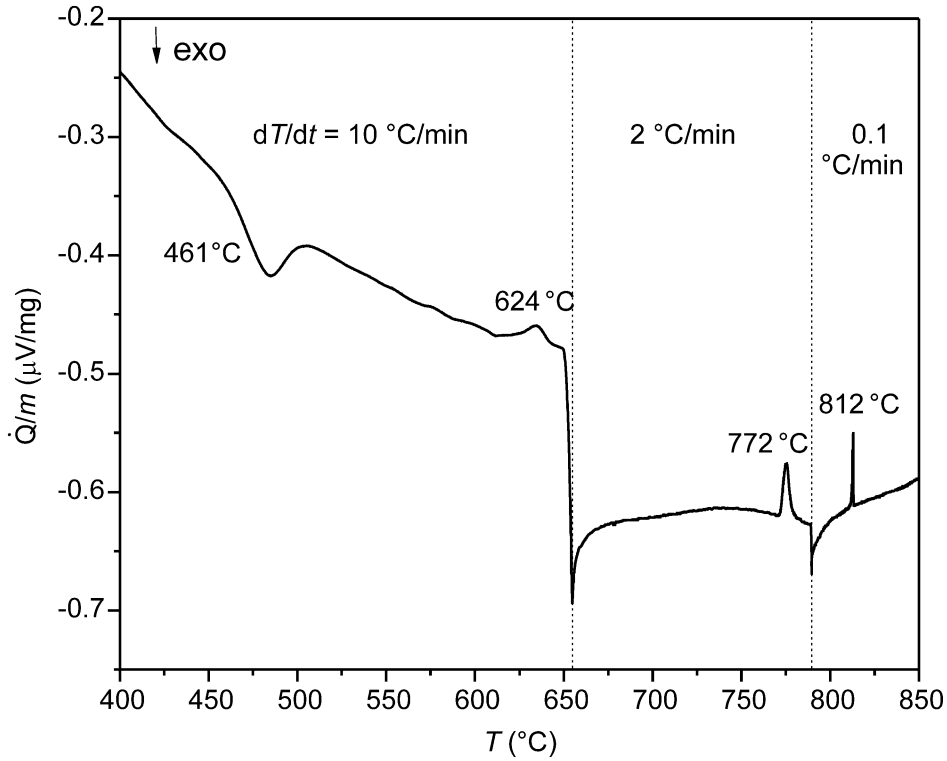

Figure 4.2: Thermal behavior of $Ba_8Ge_{43}\square_3$ from DSC. Measurements with different heating rates and onset temperatures are shown.

The exothermic peak with an onset temperature of 461 °C represents the formation of $BaGe_5$ presumably according to $Ba_8Ge_{43} \rightarrow 8BaGe_5 + 3\alpha\text{-Ge}$. Peritectoid transformation of $BaGe_5$ into Ba_6Ge_{25} and α-Ge takes place at 624 °C at this heating rate. Depending on the heating rate, the thermal effect of the slow solid-solid transformation is shifted towards higher temperatures: 590 °C for 0.3 °C/min, 605 °C for 5 °C/min and 620 °C for 10 °C/min.[17] The actual transition temperature of ≈ 535 °C which was shown on the Fig. 4.1 was determined from long time annealing experiments. The endothermic peak at 772 °C reveals the formation of Clathrate-I Ba_8Ge_{43} by reaction of Ba_6Ge_{25} with α-Ge. Peritectic transformation of $Ba_8Ge_{43}\square_3$ to α-Ge and the respective melt takes place at 812 °C. After the DSC measurement, the final product consists of Ba_6Ge_{25} and α-Ge according to PXRD analysis (Fig. 4.3).

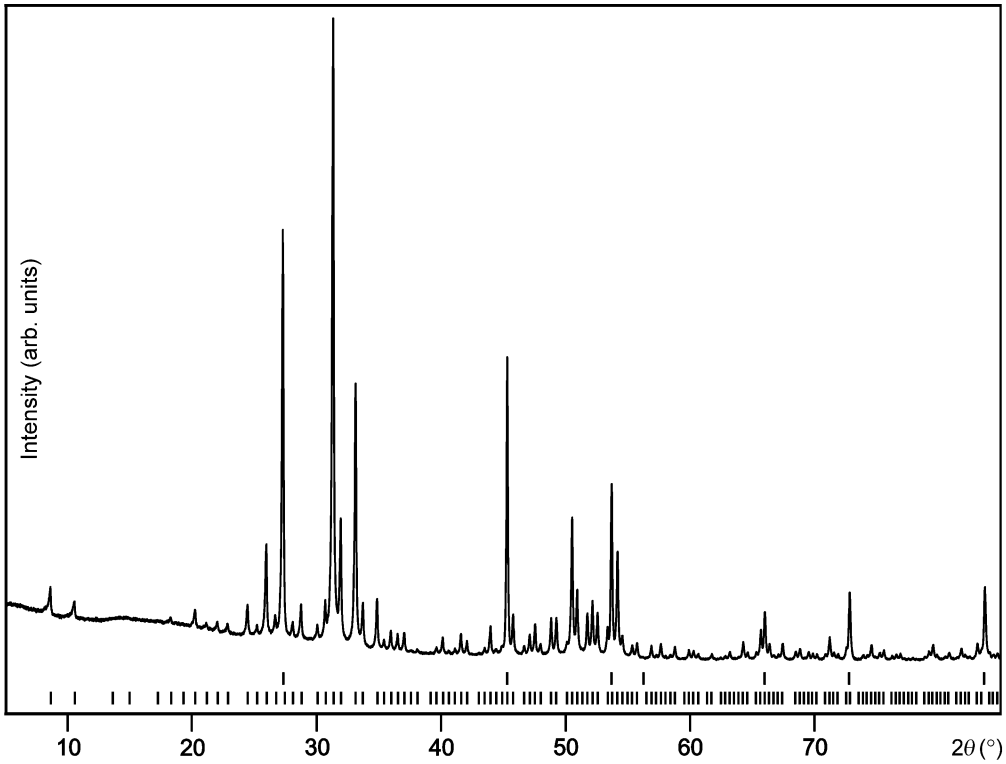

Figure 4.3: PXRD pattern of a $Ba_8Ge_{43}\square_3$ sample after thermal analysis with DSC (Cu-$K\alpha_1$ radiation). Upper and lower ticks mark the calculated reflection positions of α-Ge and Ba_6Ge_{25}, respectively.

4.2 Preparation

Preparation of single phase $Ba_8Ge_{43}\square_3$ has turned to be challenging due to its narrow stability region between 770 °C and 810 °C. Either after cooling from the melt or after annealing experiments, conventional quenching techniques *e.g.* quenching in Ar atmosphere (meaning that removing the reaction crucible from induction coil after having complete melt inside the glove box, Fig. 4.4 top) or water quenching (Fig. 4.4 middle), is insufficient to suppress the partial decomposition of $Ba_8Ge_{43}\square_3$ to Ba_6Ge_{25}, α-Ge, and / or $BaGe_5$. Therefore, we applied a technique enabling very fast cooling of stoichiometric melt to room temperature. Single phase $Ba_8Ge_{43}\square_3$ was prepared by quenching of melt with the composition $Ba_{15.69}Ge_{84.31}$ ('$Ba_8Ge_{43}\square_3$') between *steel plates*.[15, 16] Stoichiometric mixtures of Ba and Ge pieces were put in a glassy carbon crucible (∅ 12 mm, l = 12 mm) and heated slowly with an induction furnace until the reactants were completely molten. The melt was then poured onto a polished stainless-steel plate and immediately sandwiched with the second one. The cooling rate obtained this way was higher than 10^3 K/sec. Hence, with this cooling rate, the high-temperature phase is quenched without further decomposition. The final products are stable on air as well as in dilute acids and bases and did not show any impurity phase in PXRD (Fig. 4.5).

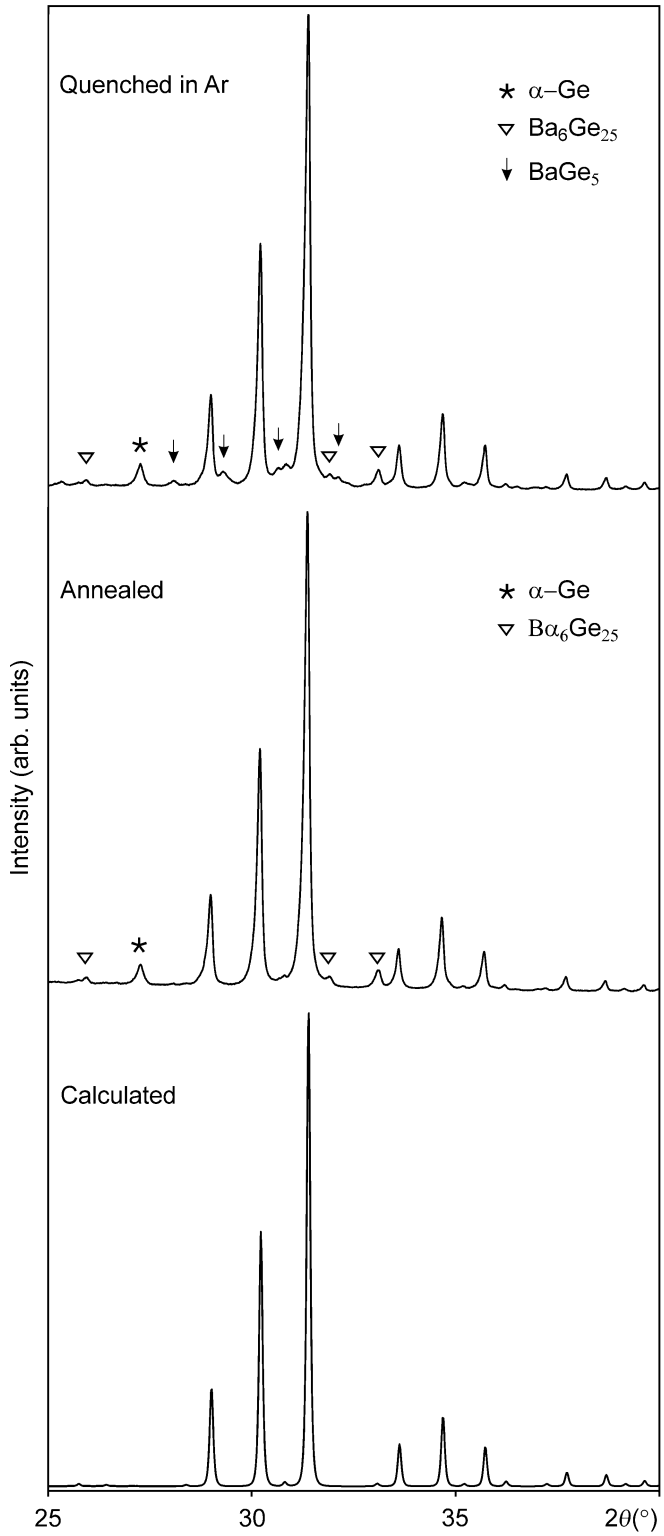

Figure 4.4: PXRD patterns after quenching $Ba_{15.69}Ge_{84.31}$ (Ba_8Ge_{43}) sample in Ar atmosphere (**top**), after annealing at 790 °C for 1 month followed by water-quenching (**middle**) and the calculated powder pattern for $Ba_8Ge_{43}\square_3$ (**bottom**) (Cu-$K\alpha_1$ radiation). Besides $Ba_8Ge_{43}\square_3$, samples contain small amounts of α-Ge, Ba_6Ge_{25} and/or $BaGe_5$ as by-products due to partial decomposition during quenching processes.

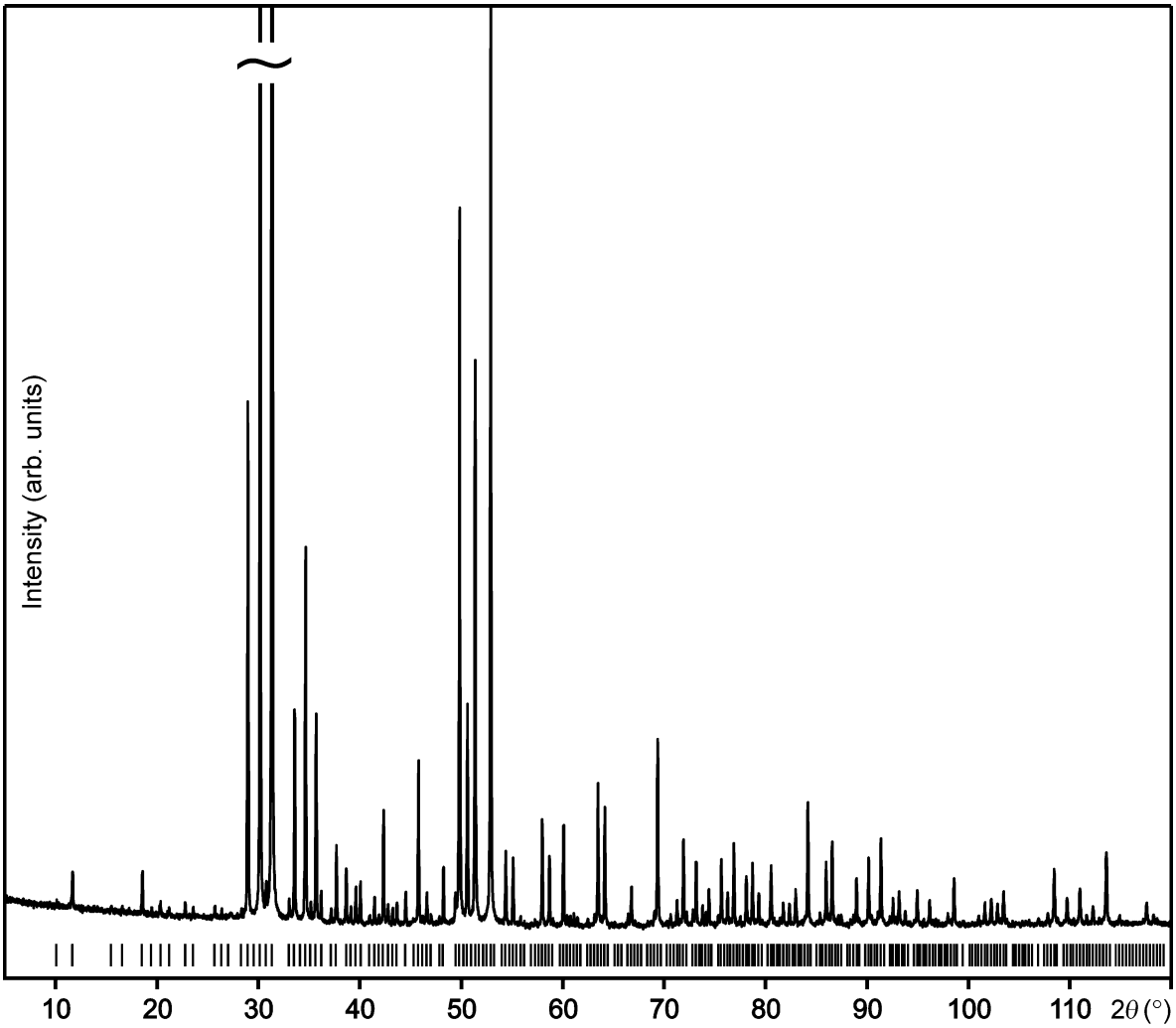

Figure 4.5: PXRD pattern of the $Ba_{15.69}Ge_{84.31}$ (Ba_8Ge_{43}) sample obtained after steel-quenching corroborates the single phase character (Cu-$K\alpha_1$ radiation). The ticks mark the calculated reflection positions of clathrate-I phase.

For annealing experiments, single-phase bulk pieces of $Ba_8Ge_{43}\square_3$ were placed into glassy carbon crucibles, sealed in Ta tubes and in turn jacketed in argon-filled quartz ampoules. At the end of the annealing process, the ampoule was quenched in water. When an isothermal heat treatment is applied between 550 °C and 770 °C, a complete decomposition to Ba_6Ge_{25} and α-Ge was observed as expected from the phase diagram. After annealing for 30 d at 790 °C followed by water quenching, a partial decomposition to α-Ge and Ba_6Ge_{25} was observed due probably to lower cooling rate (Fig. 4.4 middle).

The single-phase character of the steel-quenched samples was confirmed by metallographic analysis as well (Fig. 4.6 top). The partial decomposition of $Ba_8Ge_{43}\square_3$ after quenching in Ar atmosphere as well as after annealing experiments is shown in Fig. 4.6 middle and bottom. The clathrate composition $Ba_8Ge_{43.0(1)}$ determined from WDXS as

well as the lattice parameter $a \approx 21.307(1)$ Å did not change significantly on annealing (Table 4.1). A homogeneity range was not found within the detection limit of PXRD and WDXS analyses. This is in agreement with the constant lattice parameter obtained for $Ba_8Ge_{43}\square_3$ in samples with different starting compositions. Steel quenching of samples with off-stoichiometric nominal compositions, *e.g.* $Ba_{16}Ge_{84}$ ("$Ba_8Ge_{42}\square_4$") and $Ba_{15.38}Ge_{84.62}$ ("$Ba_8Ge_{44}\square_2$"), resulted in formation of $Ba_8Ge_{43}\square_3$ and secondary phases *e.g.* α-Ge or Ba_6Ge_{25} according to PXRD and optical microscope images (Fig. 4.7).

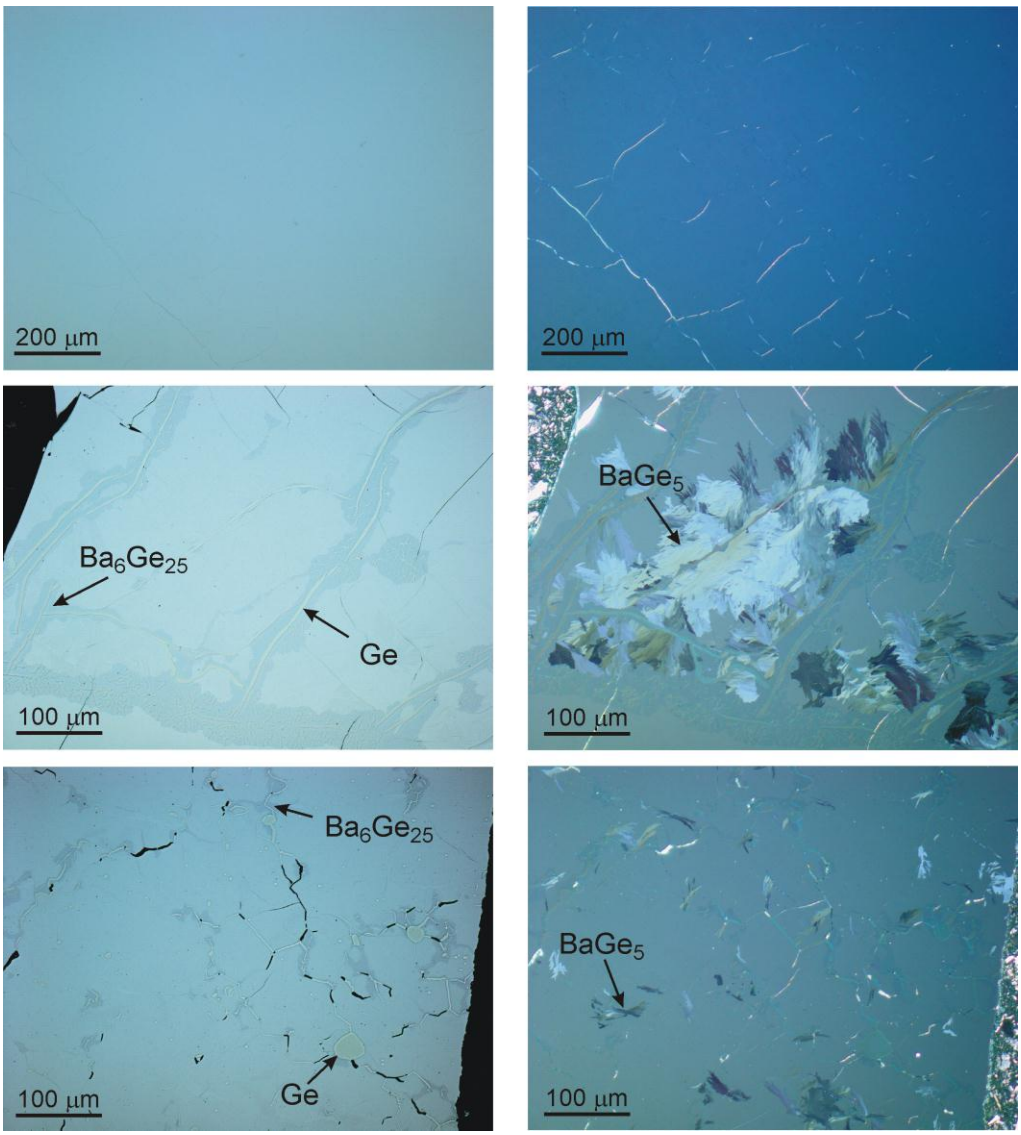

Figure 4.6: Microstructure of $Ba_{15.69}Ge_{84.31}$ samples after steel-quenching (**top**), after quenching in Ar atmosphere (**middle**) and after annealing $Ba_8Ge_{43}\square_3$ at 790 °C for 1 month followed by water quenching (**bottom**). On the left and right sides are the bright-field and polarized-light images, respectively.

Table 4.1: Lattice parameter and chemical composition of clathrate samples.

Starting material	Preparation route	*a* (Å)	Composition (WDXS)	Reference
$Ba_{15.69}Ge_{84.31}$ (Ba_8Ge_{43})	steel-quenched	21.3079(2)	$Ba_8Ge_{42.9(1)}$	This work
	steel-quenched	21.3062(2)	$Ba_8Ge_{43.0(1)}$	This work
	ann. at 790 °C for 1 m then water-quenched	21.3069(3)	$Ba_8Ge_{43.0(1)}$	This work
	Cooled in Ar, as-cast	21.3123(6)	$Ba_8Ge_{42.9(1)}$	[12]
	ann. at 795 °C for 42 d, then water-quenched	21.3123(5)	$Ba_8Ge_{42.9(1)}$	[12]
	ann. at 790 °C for 12 h, then oil-quenched	21.2748(2)	-	[14]
$Ba_{16}Ge_{84}$ (Ba_8Ge_{42})	steel-quenched	21.3085(2)	$Ba_8Ge_{43.0(1)}$	This work
$Ba_{15.38}Ge_{84.62}$ (Ba_8Ge_{44})	steel-quenched	21.3066(2)	$Ba_8Ge_{43.0(1)}$	This work

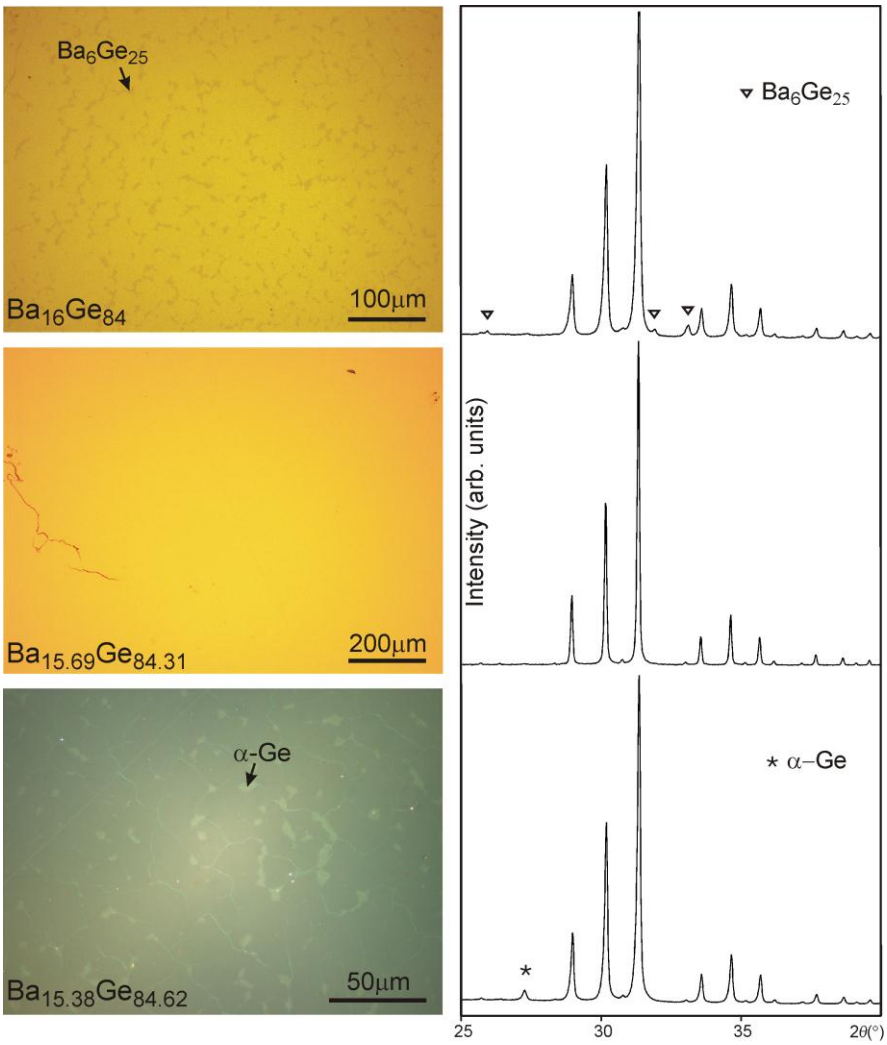

Figure 4.7: Microstructure (Bright-field images, **left**) and PXRD patterns (Cu-$K\alpha_1$ radiation) (**right**) of steel-quenched samples with different starting compositions. The sample with stoichiometric composition is a single-phase $Ba_8Ge_{43}\square_3$. For the other compositions, the detected impurity phases are marked.

4.3 Crystal structure

All reflections of the PXRD pattern of $Ba_8Ge_{43}\square_3$ were indexed with the space group $Ia\bar{3}d$ (no. 230) (Fig. 4.8). The reflection intensities are in good agreement with the structure model derived from our single crystal diffraction data (see following sections). The unit cell parameters were calculated to be in the range of a = 21.3062(2) Å – 21.3079(1) Å (112 reflections indexed, $2\theta_{max}$ = 100 º; Table 4.1). The calculated lattice parameter for $Ba_8Ge_{43}\square_3$ (a = 21.3062 Å – 21.3085 Å) in our investigation is slightly smaller than that reported by Carrillo-Cabrera *et al.*,[12] a = 21.3123 Å, and considerably larger than the reported value of, a = 21.2748 Å by Okamoto *et. al.*[14]

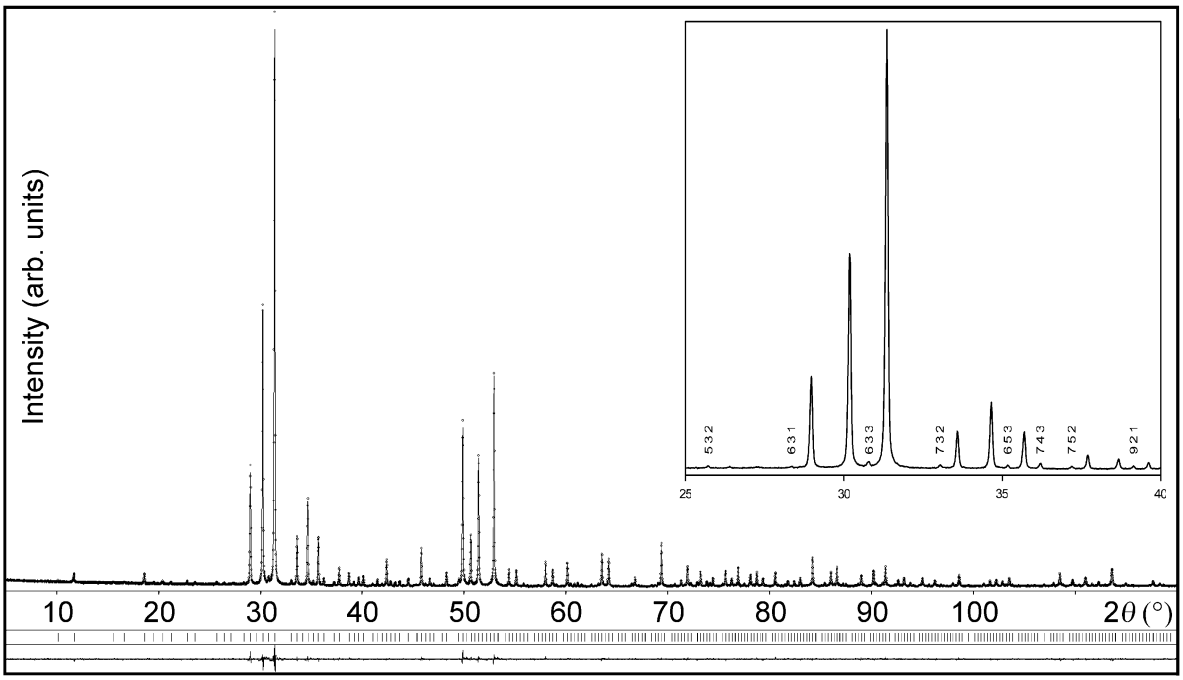

Figure 4.8: PXRD pattern of $Ba_8Ge_{43}\square_3$ (Cu-$K\alpha_1$ radiation). All reflections can be indexed with the cubic lattice parameter a = 21.3079(2) Å. The baseline corresponds to the residuals of a Rietveld refinement based on a single crystal data of steel quenched sample. Inset figure shows the most intense superstructure reflections in the 2θ range of 25 º and 40 º.

Single crystals from steel-quenched as well as annealed samples for X-ray diffraction experiments were selected and mounted as described in section 3.3. High resolution data sets for structure analyses were collected at room temperature with a RIGAKU Spider diffractometer (rotating anode, Varimax optics, Ag-$K\alpha$ radiation). The structure refinements were performed with WinCSD software package. Details concerning the data collection and structure refinement are given in Table 11.1.

Similar to the diamond structure of α-Ge, a hypothetical clathrate-I germanium "Ge_{46}"

consists of four-connected Ge atoms. In contrast to the puckered hexagons in α-Ge, the Ge atoms in the clathrate-I allotrope form pentagons and planar hexagons. The crystal structure in the space group $Pm\bar{3}n$ (no. 223) for a hypothetical compound "Ba_8Ge_{46}" represents a space-filling stacking of pentagon dodecahedron Ge_{20} $[5^{12}]$ and tetrakaidecahedron Ge_{24} $[5^{12}6^2]$, with the Ge sites 6*c* (Ge1), 16*i* (Ge2) and 24*k* (Ge3) (Fig. 4.9). Both polyhedral cages host Ba atoms at the sites 2*a* (Ba1@Ge_{20}) and 6*d* (Ba2@Ge_{24}), respectively.

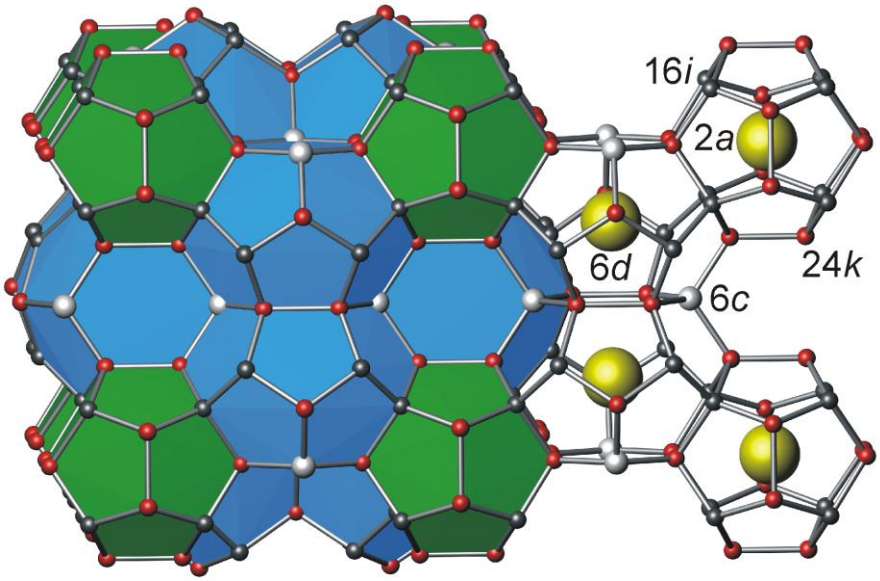

Figure 4.9: The crystal structure of type-I clathrate for a hypothetical compound "Ba_8Ge_{46}" in the space group $Pm\bar{3}n$. 20-atom polyhedra and 24-atom polyhedra are centered by Ba atoms at sites 2*a* (Ba1) and 6*d* (Ba2), respectively. The Ge atoms at the sites 6*c* (Ge1), 16*i* (Ge2), 24*k* (Ge3) sites are shown in white, grey, and red, respectively.

An allotrope Ge (*cP*46) with empty clathrate-I structure is predicted to be a semiconductor with a band gap larger than that of α-Ge.[167, 168] Filled clathrates with homoatomic frameworks were originally expected to show metallic behavior. However, if a single Ge atom would be removed from the 4-connected germanium framework, a vacancy is formed and surrounded by four unsaturated three bonded Ge atoms, $(3b)Ge^-$. If four additional electrons are available, the unsaturated Ge atoms can reach the stable closed shell configuration of a Ge^- anion (see Fig. 2.10). The valence electrons transferred from guest atoms to the framework occupy nonbonding states of Ge^- anions instead of antibonding states.

If Ba atoms are placed into the ideal germanium framework of "Ge_{46}", the composition "Ba_8Ge_{46}" formally results. A full electron transfer from Ba atoms to the Ge framework

would lead to 16 excess electrons according to following electron count $[Ba^{2+}]_8[(4b)Ge^0]_{46} \cdot 16e^-$. In this case, the occupation of antibonding states would be prevented by 4 vacancies per unit cell and the composition "$Ba_8Ge_{42}\square_4$" is expected. In fact, the composition $Ba_8Ge_{43}\square_3$ was confirmed in several investigations.[12, 14, 15, 162] According to the 8–*N* rule, 4 excess electrons per formula unit are left and $Ba_8Ge_{43}\square_3$ should exhibit metallic behavior (Table 4.2). But surprisingly, the compound was measured to be a semiconductor.[13] Therefore, neither the composition nor the physical behavior could be explained by applying simple valence rules.

Table 4.2: Electron count for clathrates according to the 8–*N* rule. Compositions with bold characters are experimentally obtained.

Composition	Electron count	Num. of excess e^-
$\mathbf{K_8Ge_{44}\square_2}$	$(K^+)_8(Ge^-)_8(Ge^0)_{36}$	0
'K_8Ge_{46}'	$(K^+)_8(Ge^0)_{46}$	8
'$Ba_8Ge_{42}\square_4$'	$(Ba^{2+})_8(Ge^-)_{16}(Ge^0)_{26}$	0
$\mathbf{Ba_8Ge_{43}\square_3}$	$(Ba^{2+})_8(Ge^-)_{12}(Ge^0)_{31}$	4
'Ba_8Ge_{46}'	$(Ba^{2+})_8(Ge^0)_{46}$	16

To understand, why the composition $Ba_8Ge_{43}\square_3$ is formed rather than '$Ba_8Ge_{42}\square_4$', some peculiar features of the clathrate-I structure must be considered. First of all, not all of the framework atoms in clathrate-I structure have an ideal tetrahedral environment. In fact, the ~120° angles of the planar hexagons formed by Ge1 and Ge3 atoms are unfavorable for (4b)Ge atoms. The bond angles of Ge1 atoms joining two such hexagons are especially unfavorable and consequently, vacancies in clathrate-I compounds are usually formed at this position. The hexagons are connected via common Ge1 atoms to infinite chains (spiro-hexagon chains) along the <100> direction, in which every second hexagon is rotated by 90° (Fig. 4.10 and 4.11a). The formation of vacancies at the Ge1 site may also lead to a release of tension, which is expressed by the relaxation of the neighboring Ge3 atoms. This induces a splitting of Ge3 sites into Ge31 and Ge32. The determination of that small difference in distance along with the vacancy concentration is so far achieved most accurately by single crystal X-ray diffraction data. Assuming that the vacancies are only present at Ge1 site (6*c*), then the following occupancy relations hold (Fig. 4.10):

$$Occ.\ \text{Ge 31 } (24k) + Occ.\ \text{Ge32 } (24k) = 1.0$$
$$Occ.\ \text{Ge1 } (6c) = Occ.\ \text{Ge31 } (24k)$$
$$Occ.\ \text{Ge1 } (6c) = 1 - Occ.\ \text{Ge32 } (24k)$$

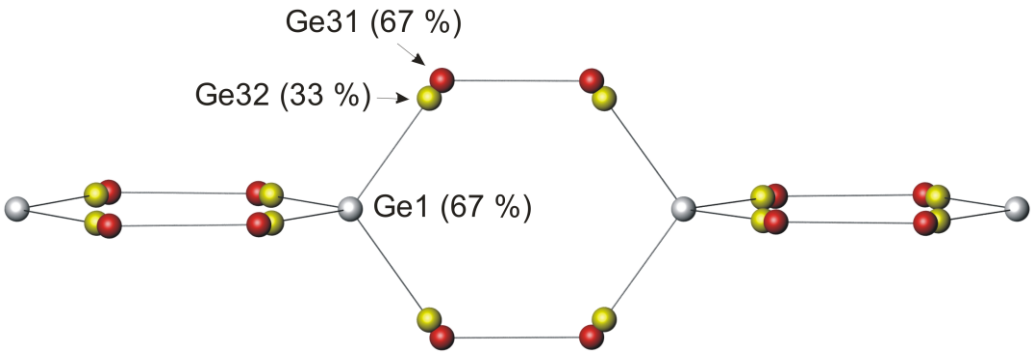

Figure 4.10: Correlation of the split sites Ge31 and Ge32 and the occupation of the vacancy position Ge1 in the clathrate-I structure (space group $Pm\bar{3}n$).

These relationships are especially important for ternary systems in which different kinds of atoms as well as vacancies are found at the 6*c* site. In this case, the relationship between the observed electron number in 6*c* position and composition is not straightforward. By taking into account the occupancies of Ge31 and Ge32 positions with afore-mentioned relations, one can estimate the vacancy concentration.

The presence of two vacancies in the same 6-ring is not expected, because a full relaxation of neighboring Ge3 atoms would lead to a large elongation of Ge3–Ge3 bonds as well as direct contact of [(3b)Ge^-] anions (Fig. 4.11b). Thus, the Ge1 site at 6*c* should not be empty more than 50 %, which may explain, why the composition $Ba_8Ge_{43}\square_3$ with four excess electrons is formed instead of '$Ba_8Ge_{42}\square_4$' with complete electronic balance.

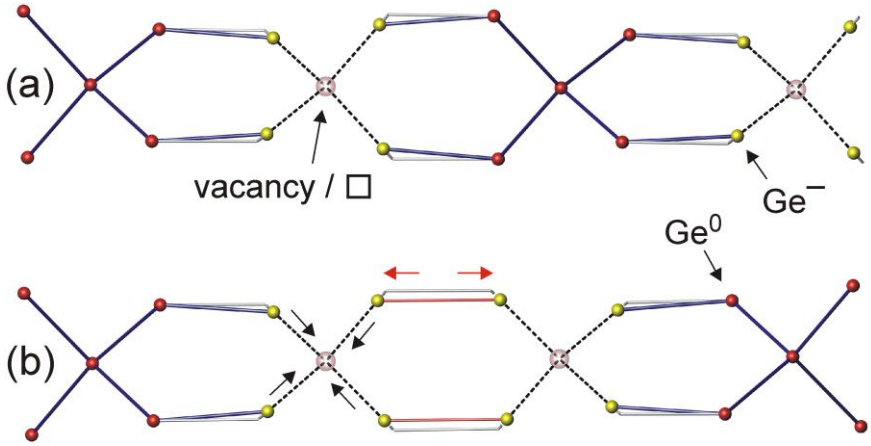

Figure 4.11: Atomic arrangements and chemical bonding within the spiro-hexagon chains along [100] in the crystal structure of $Ba_8Ge_{43}\square_3$: (**a**) vacancy-alternating and (**b**) vacancy-cumulating arrangement. The grey lines represent the bonds of an undistorted hexagon.

As discussed previously, $Ba_8Ge_{43}\square_3$ has been first obtained with apparently statistical vacancy distribution (space group $Pm\bar{3}n$). Later on, superstructure in the space group $Ia\bar{3}d$ has been identified with partially-ordered vacancy arrangement after fast cooling and almost fully-ordered vacancy arrangement after annealing at 795 °C. Compared with the ideal crystal structure of type-I clathrates with space group $Pm\bar{3}n$ and the cubic cell parameter a_0, in the observed superstructure with a 2 × 2 × 2 unit cell and the direct subgroup $Ia\bar{3}d$, a Ge site splitting is observed as illustrated in Fig. 4.12.

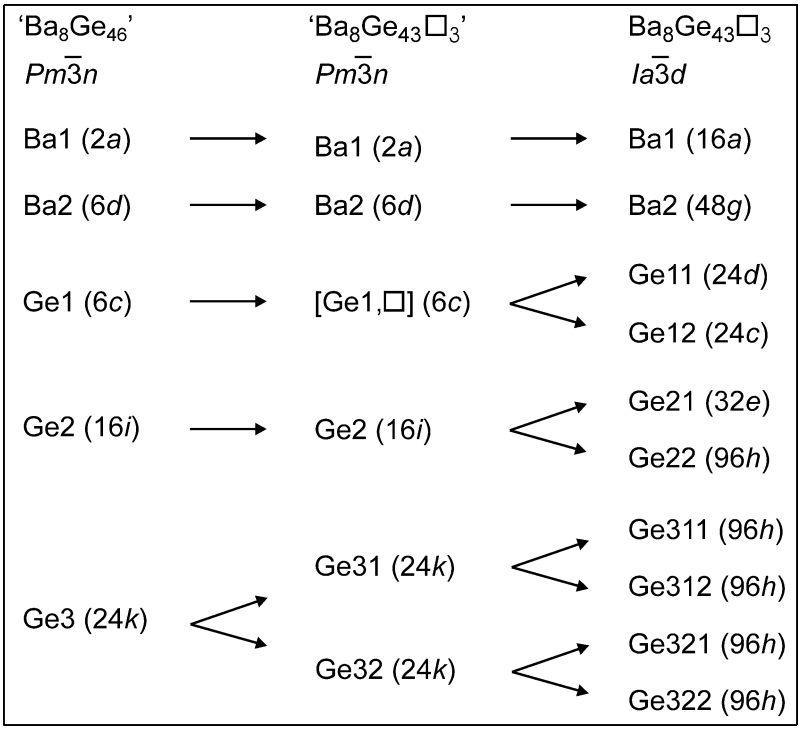

Figure 4.12: Relation of Wyckoff sites between a clathrate free of vacancies ($Pm\bar{3}n$, **left**), with statistically distributed vacancies ($Pm\bar{3}n$, **middle**) and ordered vacancy arrangement ($Ia\bar{3}d$, **right**).

To investigate the effect of temperature treatment on vacancy ordering, structure determinations were performed on two single crystals obtained from steel quenching without and with subsequent annealing. For a fully-ordered structure in the space group $Ia\bar{3}d$ either the site Ge11 or Ge12 should be empty, for partially-ordered vacancies both sites are differently occupied. For both crystals, it was found out that the occupancy of site Ge11 is larger than 90 % and larger than the occupancy of site Ge12 which is less than 10 % (Tables 11.2-11.3). The disorder in the annealed sample is even slightly higher. Thus, both preparation techniques yield close to complete ordering of the vacancies in the framework. Refinement of the occupancy factors for all partially occupied sites in

$Ba_8Ge_{43}\square_3$ gave the same composition $Ba_8Ge_{43.0(1)}$ for crystals of both quenched and annealed samples. Hence, the chemical composition does not depend on the thermal treatment and is in agreement with previous reports.

From the experimental results a question arises: why does the superstructure of $Ba_8Ge_{43}\square_3$ form even after rapid quenching? The preferred vacancy ordering in $Ba_8Ge_{43}\square_3$ is assumed to be related to the local distortion of the framework. In a type-I clathrate compound without framework vacancies in the space group $Pm\overline{3}n$, the spiro-hexagon chains along [100] consists of the sites Ge1 and Ge3 (Fig. 4.13a). A vacancy on a position of the Ge1 site induces a distinct shift of the neighboring Ge3 atoms as discussed above. As long as the vacancies are statistically distributed over the Ge1 site, the crystal structure still belongs to space group $Pm\overline{3}n$ (Fig. 4.13b), however, an ordered arrangement of vacancies lead the formation of superstructure in the space group $Ia\overline{3}d$ (Fig. 4.13c).

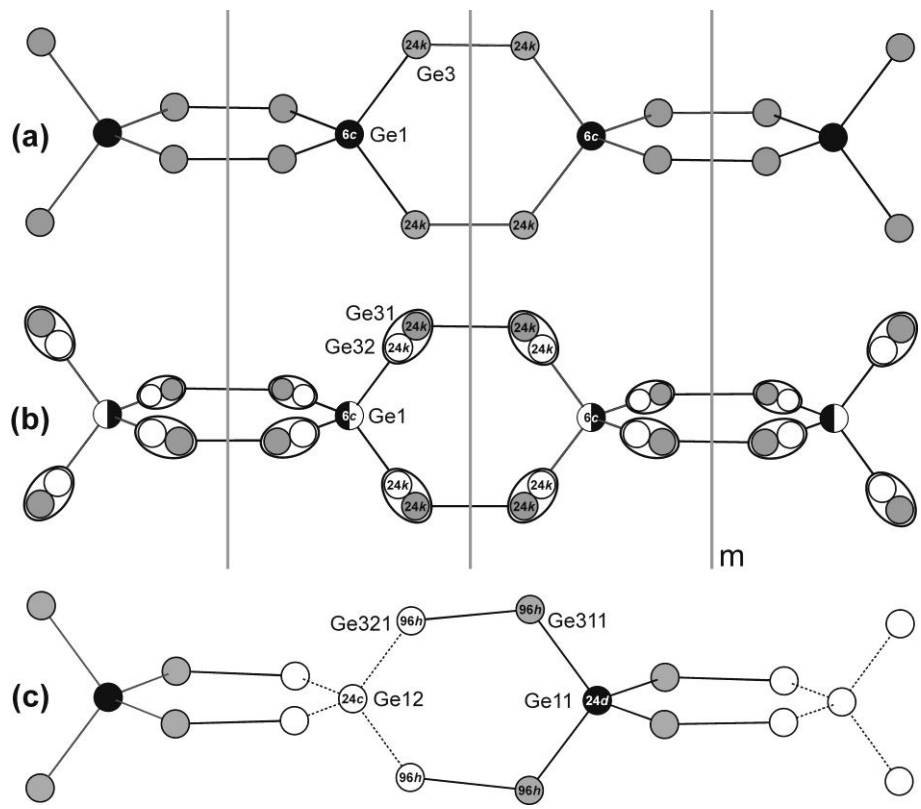

Figure 4.13: Description of the vacancies within the spiro-hexagon chains in the space groups $Pm\overline{3}n$ and $Ia\overline{3}d$. (**a**) vacancy free arrangement in $Pm\overline{3}n$, (**b**) split atom model of a clathrate with vacancies in $Pm\overline{3}n$, (**c**) ordered vacancy arrangement in space group $Ia\overline{3}d$.

According to the crystal structure refinement on annealed and quenched samples the site Ge311 with the local symmetry $\bar{4}$ is occupied by ~ 90 % whereas the site Ge321 with the local symmetry 222 by ~10 % (Tables 11.2-11.3) The partial occupancy of both sites may at first imply the presence of cumulated vacancies within the same hexagon, which would contradict the suggested boundary condition. However, the partial occupancy of the sites Ge11 and Ge12 (as well as Ge311, Ge312, Ge321 and Ge322) can be also a consequence of the positional disorder between neighboring spiro-hexagon chains. A partial structure of these chains constitutes a 3D rod packing (Fig. 4.14). If, *e.g.*, one out of twelve rods is shifted so that atoms, formerly located at site Ge11, superimpose positions of site Ge12, a partial occupancy of 0.92 for Ge11, Ge311 and Ge321 and a partial occupancy of 0.08 for Ge12, Ge312 and Ge322 would result, which is quite close to the experimental occupancies. The breaking of the translational symmetry is in such case so weak that it would be hardly detected from diffraction data.

The partial occupancies obtained from the structure refinement may be an effect of mosaicity too. Different domains might show occupation of either Ge11 or Ge12 sites. This effect would be averaged in the recorded reflection intensities. The presence of anti-phase boundaries in $Ba_8Ge_{43}\square_3$ has been reported by high resolution transmission electron microscopy.[13]

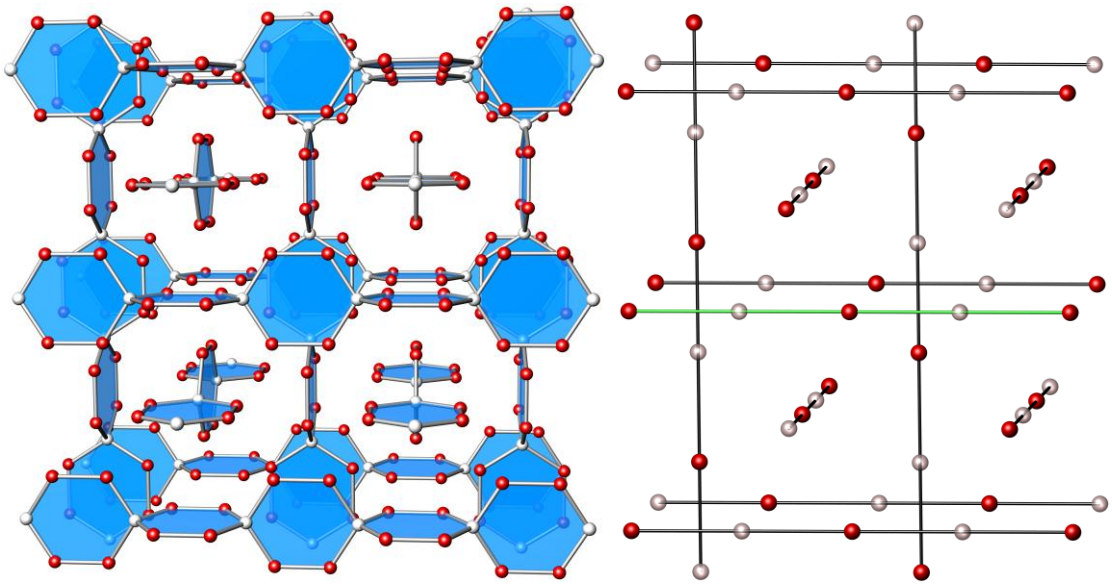

Figure 4.14: (**Left**) Spatial arrangement of the spiro-hexagon chains in the crystal structure of $Ba_8Ge_{43}\square_3$ (Ge1 (white) and Ge3 (red)). (**Right**) Possible arrangements of the vacancies (transparent violet spheres) within the partially ordering chains. The shift of one rod (green) out of twelve yields the occupancy of ≈ 8% for the Ge12 site as it is similarly observed in the crystal structure refinement.

The interatomic distances between Ge atoms in the crystal structure of quenched and annealed samples of $Ba_8Ge_{43}\square_3$ vary in the range *d*(Ge – Ge) ≈ 2.42 Å – 2.64 Å (Table 11.4, Fig. 4.15). The distance between Ge and the vacancy position is around *d*(Ge – □) ≈ 2.18 Å. The interatomic distances between Ba2 and its surrounding cage atoms in tetrakaidekahedra (3.43 Å – 4.09 Å) are generally longer than those between Ba1 and its surrounding cage atoms in pentagonal dodecahedron (3.38 Å – 3.87(3) Å). This might reveal that the interaction between Ba2 atoms and its surrounding cage atoms in tetrakaidekahedra are relatively weaker than that of Ba1 and Ge atoms forming pentagonal dodecahedra. Correspondingly the Ba2 atoms vibrate more significantly than Ba1 atoms which can be deducted also from the value of atomic displacement parameters (Tables 11.2-11.3). Some angles in the Ge framework significantly deviate from the ideal tetrahedral bond angle of 109.5° with the extreme one on the planar hexagon of tetrakaidecahedra □ (Ge11 – Ge312 – Ge322) = 132.1(5) º (Table 11.5).

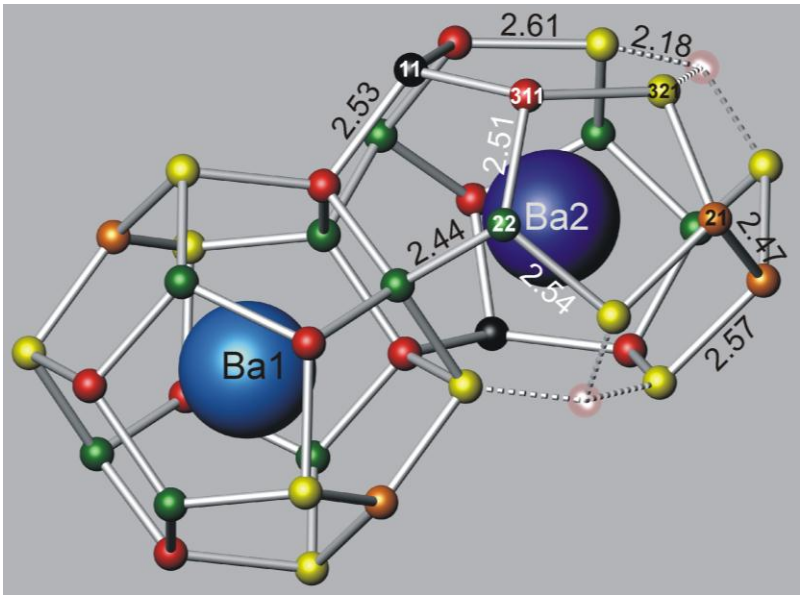

Figure 4.15: Some Ge–Ge and Ge–□ distances (Å) in the crystal structure of steel-quenched $Ba_8Ge_{43}\square_3$.

4.4 Chemical bonding and electronic structure

ELI was evaluated in the ELI-D representation by using the TB-LMTO-ASA program package. The atomic coordinates for a structure model with fully ordered vacancies were used: space group $Ia\bar{3}d$, *a* = 21.3074(5) Å, Ba1 in 16*a* (0 0 0); Ba2 in 48*g* (*x* ¼ +*x* 1/8; *x* = 0.2528); Ge11 in 24*d* (0 ¼ 3/8); Ge21 in 32*e* (*x x x*; *x* = 0.09144); Ge22 in 96*h* (*x y z*; *x* = 0.08999, *y* = 0.40513, *z* = 0.09097); Ge321 in 96*h* (*x y z*; *x* = 0.49942, *y* = 0.15332, *z* = 0.05629); Ge322 in 96*h* (*x y z*; *x* = 0.00111, *y* = 0.16667, *z* = 0.06549).[12] The calculation

within the atomic sphere approximation (ASA) includes corrections to neglect the interstitial regions and the partial waves of higher order. Nevertheless, the addition of empty spheres E was necessary at the positions of the framework vacancies and within the large cage around Ba2. The following radii of the atomic spheres were applied for the calculations: *r*(Ba1) = 2.451 Å, *r*(Ba2) = 2.419 Å, *r*(Ge11) = 1.470 Å, *r*(Ge21) = 1.436 Å, *r*(Ge22) = 1.415 Å, *r*(Ge321) = 1.460 Å, *r*(Ge322) = 1.519 Å, *r*(E1) = 1.021 Å, *r*(E2) = 1.018 Å, *r*(E3) = 1.019 Å, *r*(E4) = 0.957 Å. A basis set containing Ba(6*s*, 5*d*) and Ge(4*s*, 4*p*) orbitals was employed for a self-consistent calculation with Ba(6*p*, 4*f*) and Ge(4*d*) functions being downfolded.

The formation of electron pairs, either in $2e^-$ bonds or lone pairs, is the key element of the models for chemical bonding in clathrates. This opens a possibility to discover and visualize the chemical bonding using quantum chemical functions or functionals related to the correlated motion of electrons and electron pair density. The maxima of ELI in the valence region or/and structuring of the outer core shell provide signatures for directed covalent bonding. Analysis of the distributiom of ELI in vicinity of the vacancies in the hexagons for $Ba_8Ge_{43}\square_3$ (Fig. 4.16) reveals maxima close to the mid points of Ge–Ge contacts within the framework. For both types of the Ge–Ge bonds, (3b)Ge–(4b)Ge and (4b)Ge–(4b)Ge, the topology of ELI reveals two-centre interactions. In addition, the maxima of ELI were found close to the (3b)Ge atom toward the vacancy position in the framework. They represent the ‘lone’ pairs. Integration of electron density yields 1.8 – 2.1 electrons within the basins of the bonding attractors and 1.8 – 2.0 electrons for the ‘lone-pair’ attractors. Thus, the ELI picture fits completely the expectations from the electron counting scheme described in the previous sections.

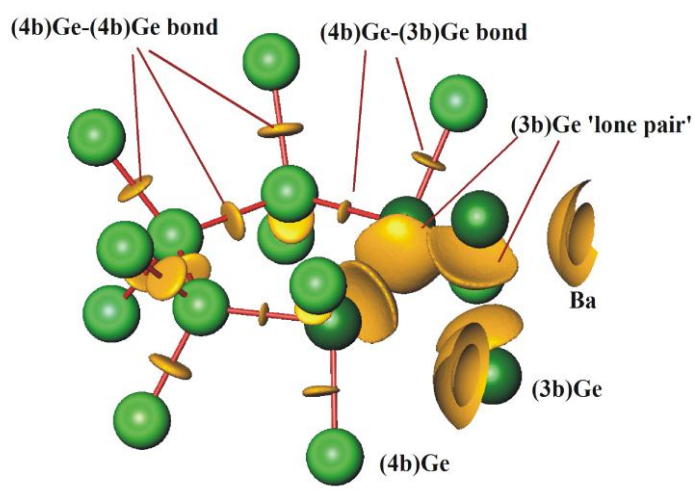

Figure 4.16: Distribution of the electron localizability indicator in vicinity of the vacancy and the adjacent part of the chain. The positions of the ELI maxima reflecting the Ge–Ge bonds and the ‘lone pairs’ are visualized by the isosurfaces with $\Upsilon = 1.3$. The part of the outer core shells of the Ba atoms is shown on the right side.

Electronic structure calculations were carried out using the TB-LMTO-ASA program package. The calculation of the electronic DOS for a fully ordered model of the crystal structure of $Ba_8Ge_{43}\square_3$ reveals a general picture in agreement with the electron counting above (Fig. 4.17 top): the bonding states at low energies are completely occupied (–12 eV < E < –0.8 eV). In addition, a part of the antibonding states (–0.5 eV < $E \leq E_F$) is filled by the excess electrons. A more detailed analysis of the Fermi level region of the electronic DOS reveals the position of the Fermi level on the steep shoulder (∂DOS/∂E < 0) of a spike (Fig. 4.17 middle). Such a picture resembles the electronic DOS for the strongly correlated systems, whereas the height of the spike in the DOS for $Ba_8Ge_{43}\square_3$ is much smaller than usually observed for strongly correlated systems. The influence of temperature on the electronic structure is modeled roughly by using larger volumes. With an enlarged volume by 6 %, Fermi level falls on top of a local maxima (not shown) while at 15 % increased volume Fermi level shifts to the other side of the spike in a positive gradient region of the DOS (∂DOS/∂E > 0, Fig. 4.17 bottom). Therefore, the spiky details in the electronic band structure near the Fermi level are observed to change with increased volume in such ways that the gradient of the DOS can switch signs at the Fermi energy from negative to positive. This sign change found in first-principles calculations may have implications regarding the temperature dependence of the sign of charge carriers.

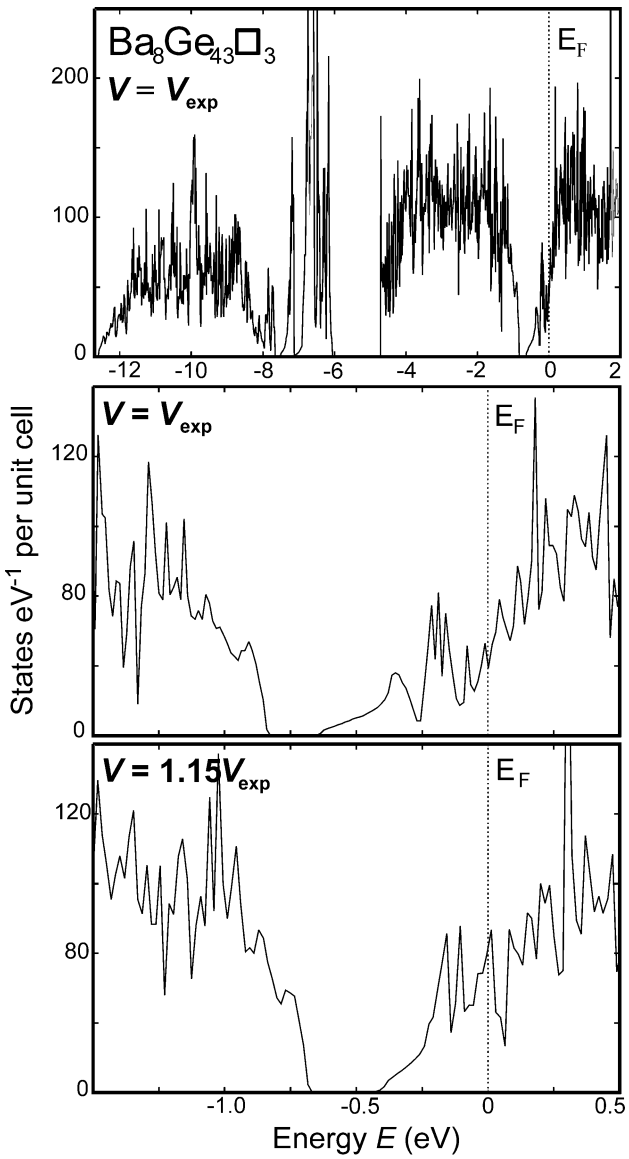

Figure 4.17: Electronic density of states for an ordered model of $Ba_8Ge_{43}\square_3$ (cf. calculation procedure): (**top**) general view confirming occupancy of the antibonding states by excess electrons; (**middle**) energy region around the Fermi level as calculated for the experimentally observed unit cell volume; (**bottom**) energy region around the Fermi level as calculated for a larger volume to model the temperature influence on the DOS.

4.5 Physical properties

Measurements of physical properties were performed on single phase bulk polycrystalline materials of steel-quenched samples.

The temperature dependence of the magnetic susceptibility, χ , of $Ba_8Ge_{43}\square_3$ revealed a temperature-dependent diamagnetism of the bulk phase reaching the value of $\chi \approx -4200 \times 10^{-6}$ emu.mol^{-1} at room temperature (Fig. 4.18). With the diamagnetic increments of Ba^{2+} cations [169] and Ge atoms in α-Ge,[170] only a value of about 995×10^{-6} emu.mol^{-1} is expected. This discrepancy signifies the presence of an extra source of diamagnetism in $Ba_8Ge_{43}\square_3$ which cannot be attributed to the presence of secondary phases. The higher experimental value might be due to the contribution of the Ge^- anions, for which no increments have been reported yet. However, the exact underlying mechanism is still not clear. It was suggested that molecular-ring currents, induced by the Lorentz force under an applied magnetic field and responsible for the magnetic properties of carbon allotropes and aromatic molecules, might also play a role in clathrates. [97, 164, 171, 172] To validate this mechanism, further theoretical and experimental studies need to be performed.

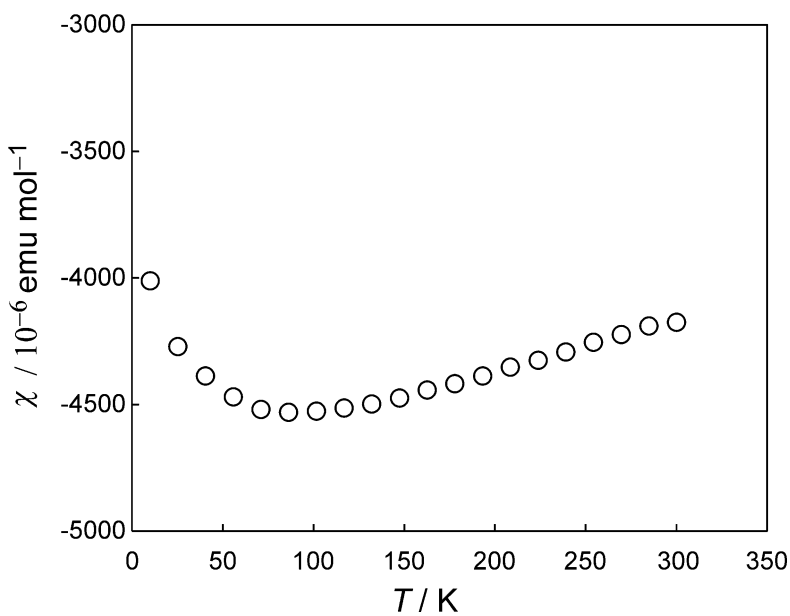

Figure 4.18: Magnetic susceptibility $\chi(T)$ of $Ba_8Ge_{43}\square_3$ at low temperatures

The electrical resistivity was investigated in the temperature range 2 – 673 K (Fig. 4.19). The measured values are one order of magnitude lower than those previously reported,[13] indicating the high quality of the present polycrystalline sample. At low temperatures the electrical resistivity displays a 'bad metal' behavior ($\partial\rho / \partial T > 0$). Above room temperature, the resistivity turns into a semiconducting-like regime of conduction ($\partial\rho / \partial T < 0$). A gap of ≈ 60 meV might be obtained from an Arrhenius plot of the

electrical resistivity in the 400 – 673 K temperature range. The high-temperature semiconducting-like behavior is in agreement with the observations of Okamoto *et al.*[13]

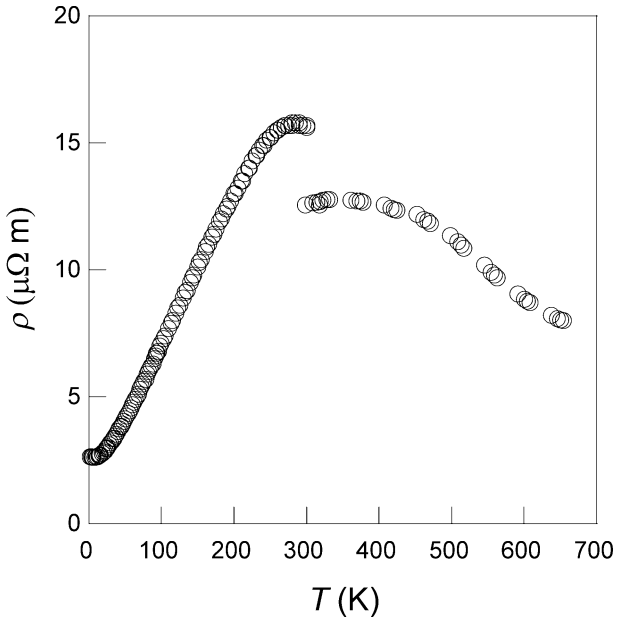

Figure 4.19: Temperature dependence of the electrical resistivity of $Ba_8Ge_{43}\square_3$ in the temperature range 2 – 673 K. The shift at room temperature is caused by differences in the measurement setups for the low- and high-temperature ranges

Overall temperature dependence of $\alpha(T)$ constitutes a striking and peculiar feature of the carrier transport in this compound (Fig. 4.20): A low-temperature *n*-type conduction turning into *p*-type behavior near 90 K that switches over to *n*-type conduction near room temperature and finally followed by a semiconductor-like behavior up to 673K. While below 300 K the thermopower values are of the order of several μV K^{-1}, the absolute value of thermopower linearly increases above this temperature to reach ≈ –40 μV K^{-1} at 673 K. The change in sign of $\alpha(T)$ occurs at the temperature of the maximum in the electrical resistivity.

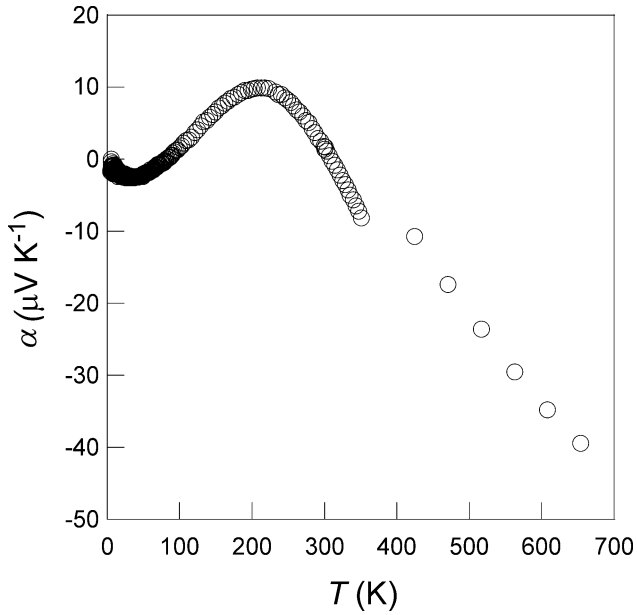

Figure 4.20: Temperature dependence of the thermopower of $Ba_8Ge_{43}\square_3$.

In non-magnetic materials, the thermopower mainly originates from the thermal diffusion of charge carriers. At low temperatures, an additional contribution may arise from phonon drag that leads to a maximum between $\theta_D/10$ and $\theta_D/3$, where $\theta_D \approx 235$ K is the Debye temperature. In the present case, a phonon-drag contribution may therefore manifest itself in the ≈ 25 – 75 K temperature range and account for the observed low-temperature maximum in $|\alpha|$ near 40 K (Fig. 4.20). However, the lack of coincidence of this last temperature with that of the maximum of the lattice thermal conductivity (see following sections) rather suggests an electronic origin. As it is shown from the band structure, the Fermi level is positioned in a region where strong variations of the density of states occur. As the temperature increases, a slight shift of the Fermi level may result in sign change of the energy derivative of the density of states, then leading to a crossover from *n*-type to *p*-type conduction. Thus, the two observed thermopower crossovers might reflect variations of the density of states near the Fermi level, as it is shown above for the calculated electronic DOS. Alternatively to this scenario, such complex behavior may signify the breakdown of a single-band model that usually holds in ordinary metals, thus suggesting multi-band conduction with differing temperature-dependent mobilities of holes and electrons. In this regard, the results of recently performed Hall effect experiments support that multi-band conduction mechanism thus signifying that both types of carriers play a role in the electrical conduction of $Ba_8Ge_{43}\square_3$.[173]

Fig. 4.21 shows the temperature dependence of the specific heat in the temperature range 2 – 300 K. At room temperature, the specific heat values are slightly larger than those expected from the Dulong-Petit law (Eq. 3.11). Inset of Fig. 4.21 illustrates the low-

temperature dependence of the specific heat plotted as C_p/T vs T^2. A fit between 2 and 4 K of the data with the Eq. 3.15 gives γ = 24.8 mJ mol^{-1} K^{-2} and β = 0.79 mJ mol^{-1} K^{-4}. The low but finite value of the Sommerfeld coefficient (γ/51 = 0.5 mJ mol^{-1} K^{-2} atom^{-1}) confirms the existence of a Fermi surface, which appears consistent with both our low temperature measurements and band structure calculations. Assuming validity of the simple relation in the non-interacting limit:

$$\gamma = 0.173\, N(E_F) \tag{4.1}$$

where γ and $N(E_F)$ are expressed in mJ mol^{-1} K^{-2} and states Ry^{-1}, respectively, the above-mentioned value leads to $N(E_F) \approx 143$ states Ry^{-1} *i.e.* 10.5 states eV^{-1} per formula unit, in agreement with our calculations (see section 4.4).[174] Previous theoretical studies on the hypothetic compound "Ba_8Ge_{46}" and on $Ba_8Ge_{43}\square_3$ within a model considering a vacancy sublattice without superstructure have led to $N(E_F)$ values of ≈ 45 states eV^{-1} and ≈ 20 states eV^{-1}, respectively.[175] Both, these and our theoretical results show that the presence of vacancies strongly reduces $N(E_F)$, which may be a reason for the absence of superconductivity in $Ba_8Ge_{43}\square_3$ with respect to the Si-based counterpart.[115, 176] This also underlines the importance of the superstructure for the transport properties in the present case. The β coefficient corresponds to an initial Debye temperature of θ_D ~232 K, in agreement with the values observed for several $Ba_8Ge_{43}\square_3$ - related compounds.[100, 103]

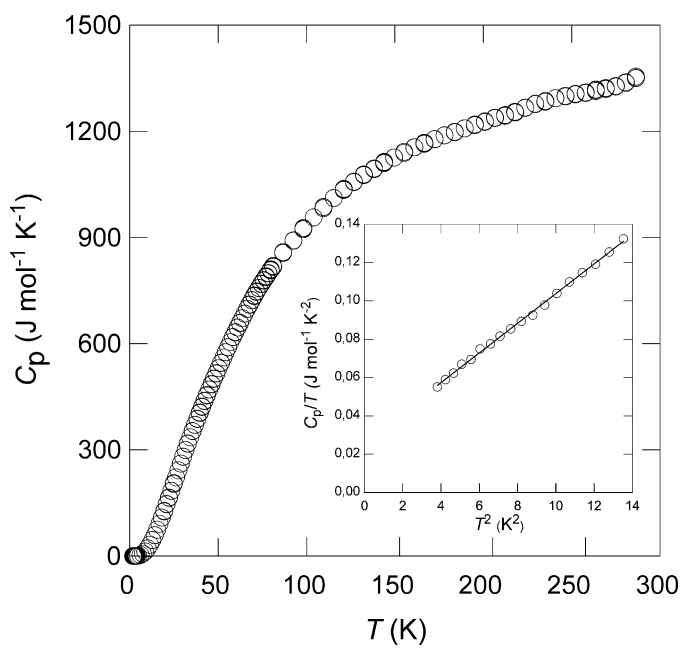

Figure 4.21: Low-temperature dependence of the specific heat C_p. In the inset figure, C_p / T plotted as a function of T^2 in the 2 – 3.5 K temperature range in which the solid line stands for the best fit to the data according to Eq. 3.15.

A conventional description of the low temperature specific heat only applies in a narrow temperature window suggesting a complex phonon spectrum. This picture is reinforced by the overall temperature dependence of the lattice specific heat that cannot be solely described within the Debye theory in any extended temperature range. To have a deeper insight into the lattice dynamics of clathrate compounds, C_{ph}/T^3 as a function of T is plotted after subtracting the electronic contribution (Fig. 4.22).

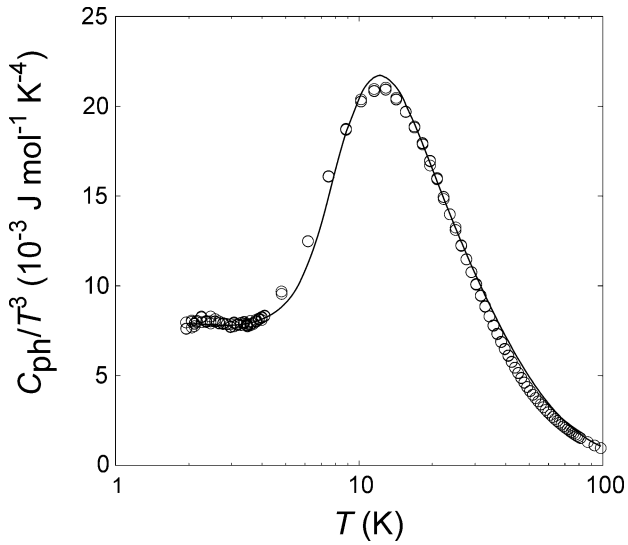

Figure 4.22: Lattice contribution to the specific heat C_{ph} plotted as C_{ph}/T^3 vs T on a logarithmic scale, the solid line represents the best fit to the data.

The contribution of the localized vibrations then appears as a pronounced peak over a Debye background centered at ~ 10 K. To analyze further these localized modes, a model that takes into account the essential crystallographic characteristics of these compounds was used.[177, 178] Several X-ray and neutron diffraction studies have shown that the Ba2 atoms display large atomic displacement parameters (ADP) while the ADP values observed for the Ba1 atoms are similar to those of the framework atoms.[103] Thus, only the Ba2 atoms can be considered to behave as Einstein-like oscillators. In addition, these atoms display anisotropic vibrations which require two vibrational modes to describe the two-dimensional in-plane (parallel to two hexagons, $\theta_{E2}^{\square}$) and one-dimensional out-of-plane ($\theta_{E2}^{\perp}$) motions. The degrees of freedom and the numbers of oscillators are then constrained and equal to $p_2^{\square}N_{E2}^{\square} = 2 \times 6$ and $p_2^{\perp}N_{E2}^{\perp} = 1 \times 6$. The best fit to the data according to lattice part of the specific heat in the Eq. 3.15 is shown in Fig. 4.22 and results in $\theta_D \approx 225$K, $\theta_{E2}^{\square} \approx 57$ K and $\theta_{E2}^{\perp} \approx 72$ K being consistent with the larger in-plane vibrational amplitude which implies a lower Einstein temperature. The obtained values are also in good agreement with those

obtained from the temperature dependence of the ADP values in several systems based on $Ba_8Ge_{43}\square_3$.[100, 103] As can be appreciated in Fig. 4.22, this model provides a satisfying theoretical background to account for the low-temperature lattice specific heat of $Ba_8Ge_{43}\square_3$. A Raman experiment revealed peaks of low wavenumbers at 39 cm^{-1}, 46 cm^{-1} and 68 cm^{-1} which were attributed to the motion of Ba atoms.[179] Though the specific heat analysis is not sensitive enough to probe fine details of the phonon spectrum as compared to Raman spectroscopy or inelastic neutron scattering, the above-mentioned values are in good agreement with those obtained from the Raman experiments (57 and 72 K results in 39 and 50 cm^{-1}, respectively).

Fig. 4.23a and 4.23b show the temperature dependence of the total thermal conductivity at low and high temperatures, respectively. Note that due to radiation losses inherent to the method used at low temperatures, the thermal conductivity has only been investigated up to 150 K. The measured values are coherent with those reported for the ternary $Ba_8TM_xGe_{46-x-y}\square_y$ compounds.[100, 103] Using the measured thermal conductivity and electrical resistivity values and the Wiedemann-Franz law (Eq. 3.5) the lattice and electronic contributions may be separated from the total thermal conductivity (Fig. 4.23b). At low temperatures, the electronic contribution only amounts to ≈ 1 % of the total thermal conductivity, which is therefore dominated by the lattice contribution. At high temperatures, the increase in κ is intimately related to the increase in the electrical resistivity. In the whole temperature range investigated, the lattice thermal conductivity values are small and in line with the data previously reported for Ge-based type-I clathrate compounds.[100, 103] An essential outcome of these measurements lies in the sharp dielectric maximum characteristic for crystalline lattices which contrasts with the glass-like behavior observed, *e.g.*, in *p*-type $Ba_8Ga_{16}Ge_{30}$, in $Eu_8Ga_{16}Ge_{30}$ or in $Sr_8Ga_{16}Ge_{30}$.[117, 123, 177, 180] This result also seems to contradict the behavior observed in the $Ba_8TM_xGe_{46-x-y}\square_y$ compounds for which a marked decrease of the sharp maximum occurs when x decreases *i.e.* when the vacancy concentration increases suggesting that phonon scattering on vacancies is the most prominent scattering mechanism at play.[103]

Based on the electrical resistivity, thermopower and thermal conductivity values, the maximum value of $ZT \approx 0.035$ at 673 K remains very low, as expected from the observed small thermopower values.

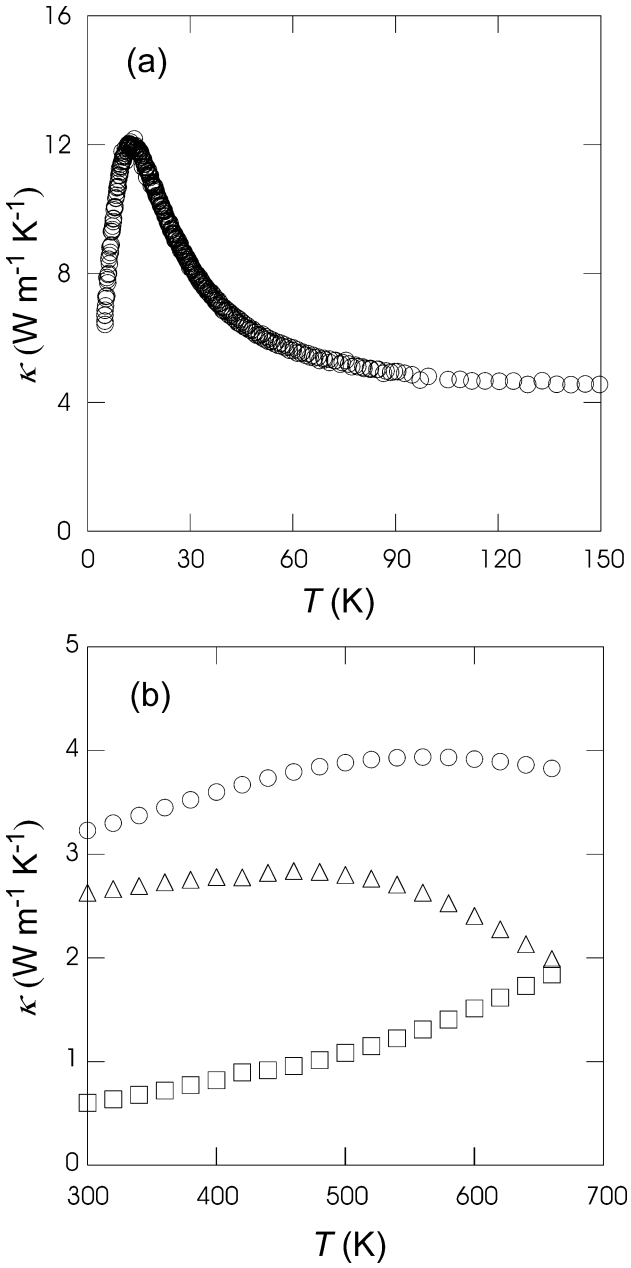

Figure 4.23: Thermal conductivity of $Ba_8Ge_{43}\square_3$: (**a**) temperature dependence of the total thermal conductivity in the low temperature range of 5 – 150 K. (**b**) high-temperature dependence of the total (°), electronic (□) and lattice (Δ) thermal conductivity.

4.6 Conclusions

Polycrystalline samples as well as single crystals of $Ba_8Ge_{43}\square_3$ have been prepared by steel-quenching technique and annealing at 790 °C for 1 month and carefully investigated to identify the vacancy ordering and the relationship between the composition, the crystal structure and the physical properties. A single phase sample of $Ba_8Ge_{43}\square_3$ could be only obtained after steel-quenching of the stoichiometric melt. Other preparation routes always

led to partial decomposition to by-products. $Ba_8Ge_{43}\square_3$ was found to be stable only in the temperature range 770 – 810 °C in agreement with the previous reports. It decomposes to Ba_6Ge_{25} and α-Ge between 770 – 535 °C and at even lower temperatures to $BaGe_5$ and α-Ge. Single crystal X-ray diffraction experiments enabled a thorough study of the crystal structure of this compound and, within some basic crystallographic considerations, a model of the vacancy ordering is proposed and provides a possible explanation for the presence of three vacancies per formula unit in this compound. Transport properties including electrical resistivity, thermopower, thermal conductivity and specific heat have been measured in the 2 – 673 K temperature range. The electrical properties reflect a metallic-like regime of conduction turning into a semiconductor-like behavior near room temperature. Two crossovers from electron-like to hole-like transport characterize the complex temperature dependence of the thermopower. Thermal transport measurements reveal a crystal-like behavior of the lattice thermal conductivity that exhibits low values up to high temperatures. Additional valuable information on the phonon spectrum of this material is provided by a detailed analysis of the temperature dependence of the specific heat within the framework of the Debye model including Einstein-like modes. The values obtained from the characteristic Einstein temperatures associated to the motion of Ba2 atoms are in good agreement with the low-energy phonon modes experimentally observed by Raman spectroscopy.

Chapter 5

A New Type of Intermetallic Clathrate: $BaGe_5$

In the Ge-rich part of the binary system Ba – Ge, Ba_6Ge_{25} and $Ba_8Ge_{43}\square_3$ were considered to be the only clathrate phases in thermal equilibrium with α-Ge.[12] No other phases were proposed to be thermodynamically stable between Ba_6Ge_{25} and α-Ge below 770 °C. On the other hand, a phase with composition $BaGe_5$ was found by optical and scanning electron microscopy within grains of $Ba_8Ge_{43}\square_3$. From thermal analyses, $BaGe_5$ was concluded to be metastable.[12] The lattice parameters indexed from PXRD data, a = 10.723(2) Å, b = 9.283(1) Å and c = 14.784(2) Å, as well as possible space group of *Pmna* from selected area electron diffraction analysis were already reported.[181] However, the crystal structure could not be resolved until the present investigation.

5.1 Preparation

All preparation steps of $BaGe_5$ were carried out under inert atmosphere of an argon-filled dry glove box. High purity Ba and Ge pieces were used (see Table 3.1). A melt with composition $Ba_{16.67}Ge_{83.33}$ ($BaGe_5$) was steel-quenched which resulted in Ba_6Ge_{25} along with $Ba_8Ge_{43}\square_3$ (Fig. 11.1 bottom). By slow cooling the melt within several hours to room temperature, a mixture of Ba_6Ge_{25} and α-Ge was obtained (Fig. 11.1 top). All attempts to react Ba_6Ge_{25} with α-Ge to $BaGe_5$ at temperatures below 770 °C failed. Only after solidifying the melt within 2-3 minutes, $BaGe_5$ could be identified besides $Ba_8Ge_{43}\square_3$, Ba_6Ge_{25} and α-Ge (Fig. 11.2). Obviously, $BaGe_5$ forms via decomposition of $Ba_8Ge_{43}\square_3$, but at low temperatures only. The preparation of single phase $Ba_8Ge_{43}\square_3$ (see section 4.2) allowed for detailed investigation of its decomposition along with the formation of $BaGe_5$. $BaGe_5$ was obtained in high yield by decomposition of bulk pieces of $Ba_8Ge_{43}\square_3$. For this case, $Ba_8Ge_{43}\square_3$ pieces were placed in glassy carbon crucibles which were then sealed in Ta tubes and jacketed in argon-filled quartz ampoules (Fig. 5.1). The annealing experiments were performed at the temperatures between 350 °C and 600 °C for the time periods from 1 h to 7 weeks followed by quenching in water. Phase analysis based on PXRD data shows that annealing of $Ba_8Ge_{43}\square_3$ at 350 °C for 40 d resulted in the complete disproportionation of $Ba_8Ge_{43}\square_3$ into $BaGe_5$ and α-Ge (≈5 wt.%). At 400 °C, the conversion of $Ba_8Ge_{43}\square_3$ was already complete within 12 h (Fig. 5.2), at 520 °C within 1 h. No decomposition of $BaGe_5$ was detected after further annealing for 7 weeks at 520 °C. A direct reaction of $BaGe_2$ or Ba_6Ge_{25} with α-Ge, which should yield $BaGe_5$, was not observed and is probably kinetically hindered below this temperature. The conversion

of $Ba_8Ge_{43}\square_3$ into $BaGe_5$ and α-Ge is reversible. $Ba_8Ge_{43}\square_3$ was retrieved after annealing $BaGe_5$ and α-Ge at 790 °C for 2 weeks. $BaGe_5$ is stable in air as well as in dilute acids and bases.

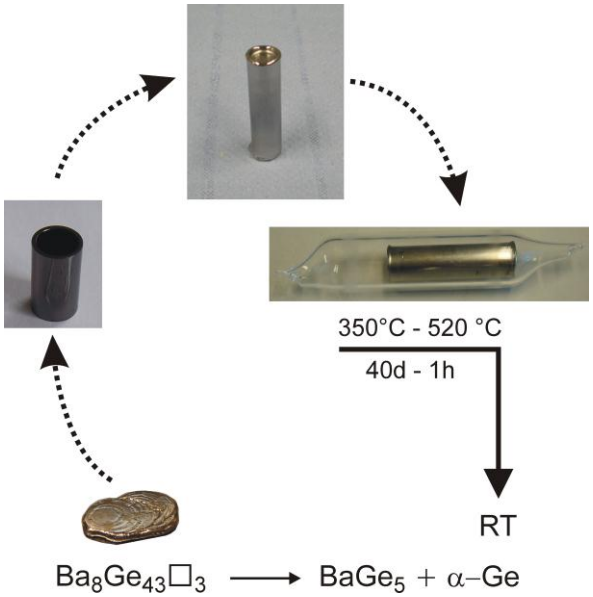

Figure 5.1: Preparation of $BaGe_5$ via decomposition of $Ba_8Ge_{43}\square_3$ at different temperatures and annealing times.

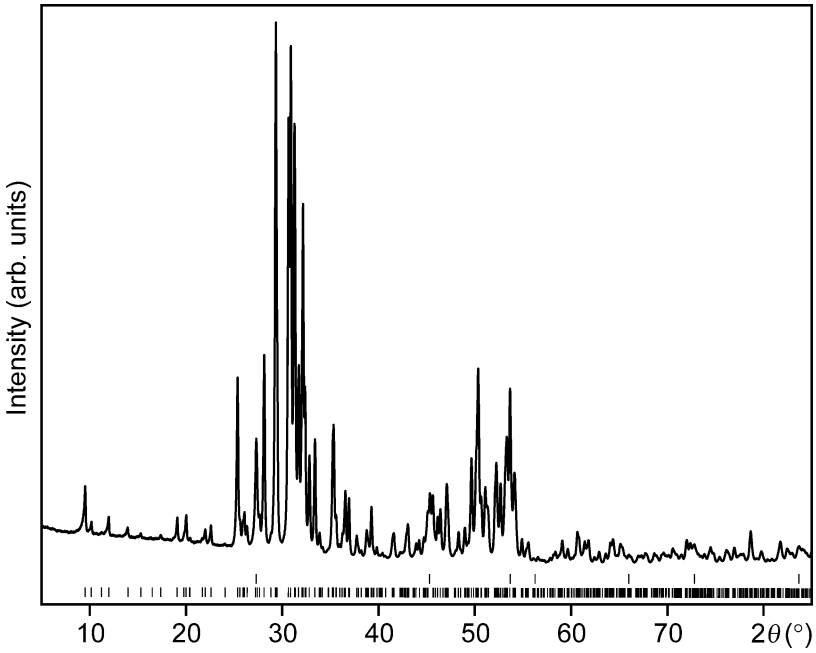

Figure 5.2: PXRD pattern of the sample after annealing $Ba_8Ge_{43}\square_3$ at 400 ºC for 12 h (Cu-$K\alpha_1$ radiation). Upper and lower ticks mark the calculated reflection positions of α-Ge and $BaGe_5$, respectively. $BaGe_5$ was obtained in high yield together with ca. 5 wt.% α-Ge as byproduct.

5.2 Thermal behavior

DSC experiments were carried out with different heating and cooling rates from 0.3 °C/min to 10 °C/min (Fig. 5.3). On heating, a broad endothermic peak was observed in the temperature range 590 °C – 620 °C which is assigned to the peritectoid decomposition of $BaGe_5$ into Ba_6Ge_{25} and α-Ge. Depending on the heating rate, the thermal effect of the slow solid-solid transformation is shifted towards higher temperatures: 590 °C for 0.3 °C/min, 605 °C for 5 °C/min and 620 °C for 10 °C/min. Clathrate-I $Ba_8Ge_{43}\square_3$ forms by the reaction of Ba_6Ge_{25} with α-Ge at around 773 °C. Peritectic transformation of $Ba_8Ge_{43}\square_3$ to α-Ge and the respective melt occurs at around 813 °C. Due to the precipitation of α-Ge within the $BaGe_5$ grains and at the grain boundaries, the melting of α-Ge is hardly visible for this heating rate.

For final determination of the peritectoid transformation temperature of $BaGe_5$, long-time annealing experiments were performed. Heat treatment of $BaGe_5$ phase (the sample contains ca. 5 wt.% α-Ge) for 7 weeks at 520 °C showed identical PXRD pattern as before heat treatment. However, at a slightly higher temperature of 535 °C, the sample completely decomposed to Ba_6Ge_{25} and α-Ge in 45 d. $BaGe_5$ was partially decomposed into Ba_6Ge_{25} and α-Ge at 550 °C in 1 week and at 575 °C, a complete decomposition was observed within 1 week (Fig. 11.3). Hence, the results of DSC, PXRD and microstructure analyses reveal the peritectoid phase transformation of $BaGe_5$ into Ba_6Ge_{25} and α-Ge at around 535 °C (see Fig. 4.1 also):

$$6\ BaGe_5 \leftrightarrow Ba_6Ge_{25} + 5\ Ge.$$

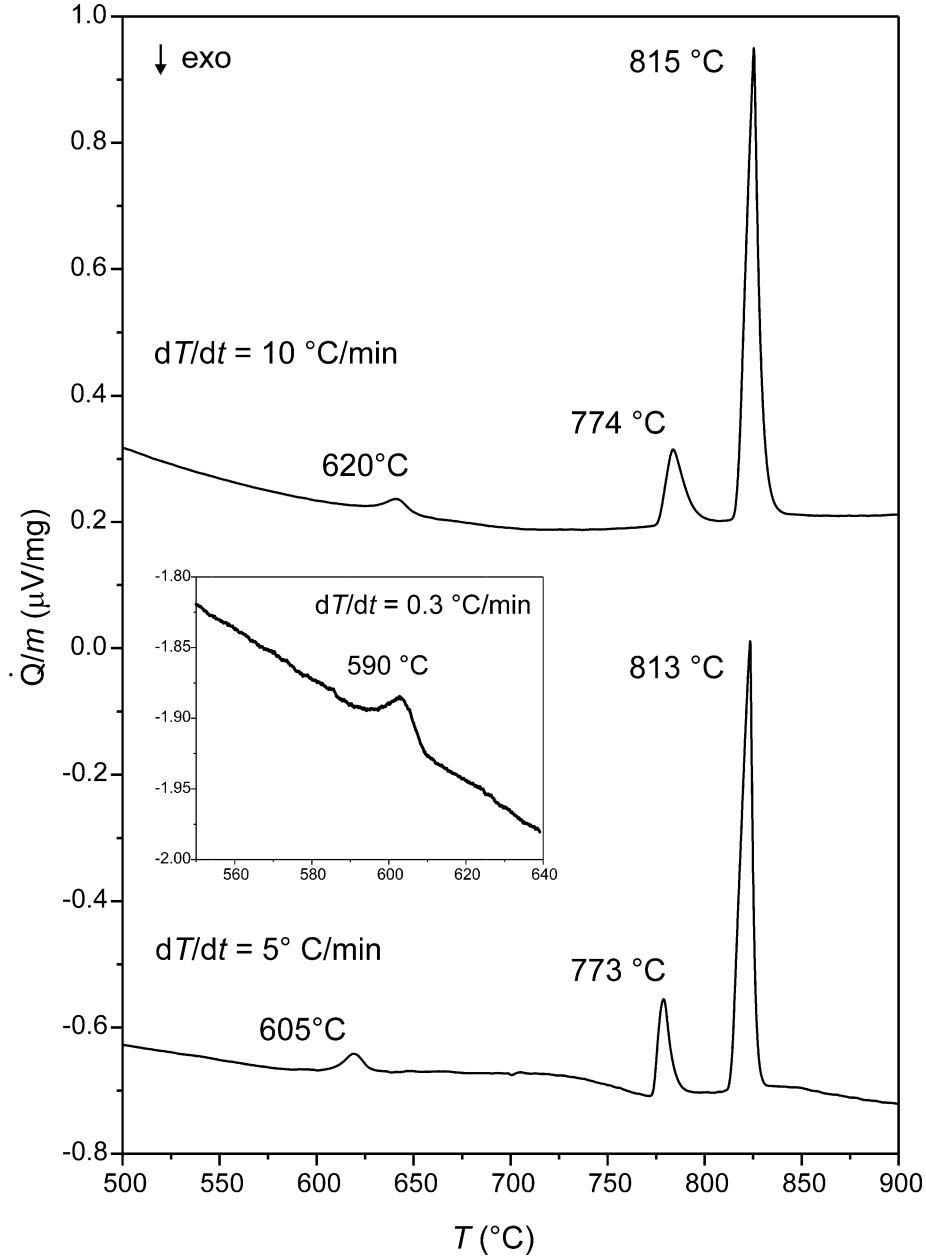

Figure 5.3: Thermal behavior of $BaGe_5$. Heat-flux DSC measurements with different heating rates are shown. The onset temperature regarding the decomposition of $BaGe_5$ into Ba_6Ge_{25} and α-Ge shifts to lower temperatures by decreasing the heating rate. On the other hand temperatures regarding the formation and decomposition of $Ba_8Ge_{43}\square_3$ are confirmed within the accuracy of measurements.

5.3 Microstructure

The compositions along with the existence of a homogeneity range were analyzed based on WDXS and PXRD. For WDXS analyses, Ba_6Ge_{25} ($Ba_{19.35}Ge_{80.65}$) was used as a standard material for Ba and Ge source. The samples obtained from stoichiometric composition $Ba_{16.67}Ge_{83.33}$ ($BaGe_5$) as well as from decomposition of $Ba_8Ge_{43}\square_3$ were investigated. After fast cooling of the molten $Ba_{16.67}Ge_{83.33}$ by steel plates, the reaction product was found to be $Ba_8Ge_{43}\square_3$ with inclusions of Ba_6Ge_{25}. After the annealing experiments performed on this end product between 400 ºC and 520 ºC for 4 d, $BaGe_5$ was formed together with Ba_6Ge_{25} and α-Ge (Fig. 5.4). When starting with the stoichiometric melt, Ba_6Ge_{25} always formed during solidification and remained unreacted during decomposition process. After the decomposition of phase pure $Ba_8Ge_{43}\square_3$ between 400 ºC and 520 ºC, $BaGe_5$ was obtained in high yield even in several hours.

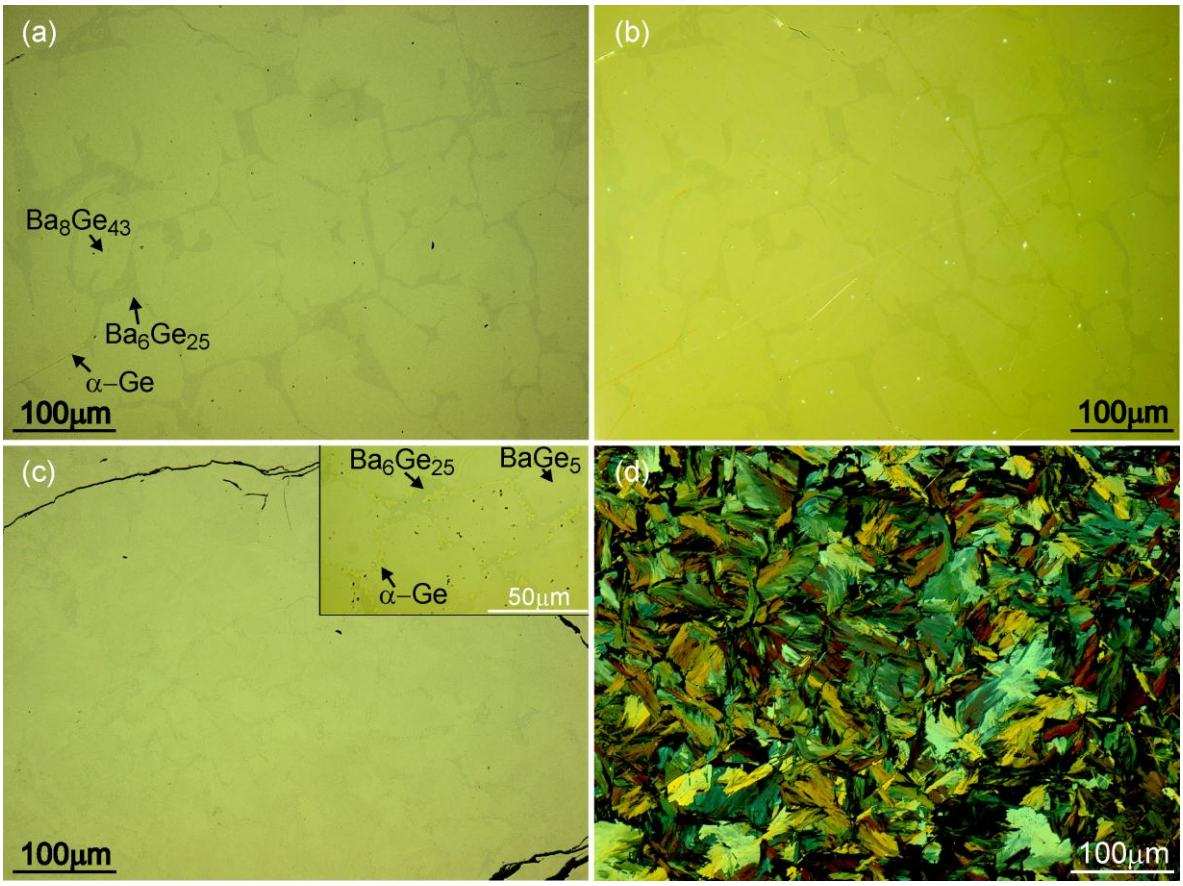

Figure 5.4: Optical microscope images (bright-field (**a**) and polarized light (**b**)) of a sample obtained after steel-quenching of the molten $Ba_{16.67}Ge_{83.33}$ by steel plates. (**c**) Bright-field optical microscopy image of a sample after annealing the steel-quenched specimens at 520 ºC for 4 d. Inset figure shows the inclusions of Ba_6Ge_{25} and α-Ge at the grain boundaries of $BaGe_5$. (**d**) Polarized light optical microscopy image of the same sample (c) shows the structuring of different $BaGe_5$ domains with respect to each other.

The time-temperature dependence of the transformation behavior of $Ba_8Ge_{43}\square_3$ into $BaGe_5$ and α-Ge was investigated by means of light and electron microscopy as well as PXRD analyses. The orthorhombic $BaGe_5$ phase shows a very anisotropic reflectivity in polarized light and is easy to distinguish from the cubic phases α-Ge, $Ba_8Ge_{43}\square_3$ and Ba_6Ge_{25} with vanishing orientation contrast. Microstructure and PXRD pattern after annealing of $Ba_8Ge_{43}\square_3$ at 400 °C reveal that diffusion controlled decomposition of $Ba_8Ge_{43}\square_3$ can be observed even after 1.5 h leading significant contribution of $BaGe_5$ phase and α-Ge. Nearly 50 % of $Ba_8Ge_{43}\square_3$ is transformed after 3 h and completely transformed microstructure occurs after heat treatment of 12 h (Fig. 5.5) at this temperature. The transformation process is accompanied by the precipitation of α-Ge at the grain boundaries of the primary $Ba_8Ge_{43}\square_3$ grains and – due to the reduced diffusion mobility in the solid state – by fine dispersive α-Ge precipitates with point- or needle/plate-like morphology inside the $BaGe_5$ grains or at grain boundaries (Fig. 5.6). Small dimensions of these α-Ge precipitates do not allow accurate quantitative analyses but their darker shade in BSE images agrees with the very reduced Ba content of the EDX analyses. Annealing at higher temperatures leads to a rounding of the α-Ge needles/plates and an almost spherical morphology of these particles was observed at 520 ºC. This is more obvious for a sample annealed at 550 ºC for 1 week (Fig. 11.5). For this sample, only round α-Ge domains are found within the grains of $BaGe_5$ and no needle-like α-Ge precipitates are observed. Further annealing for a longer time period (30 d – 40 d) results in elongation of the $BaGe_5$ grains reaching up to 500 µm (Fig. 5.6 and 11.6). Except for grain sizes, the microstructures of long time annealed samples show similar features to those annealed for 4 d or 10 d.

A characteristic feature of the $BaGe_5$ domains in the microstructure is their multi-faceted appearance in polarized light microscopy (Fig. 11.7). After long term annealing, *e.g.* at 520 °C for 30 d, the completely transformed microstructure containing the main phase $BaGe_5$ and α-Ge appears in polarized light microscopy like paint brush painting.

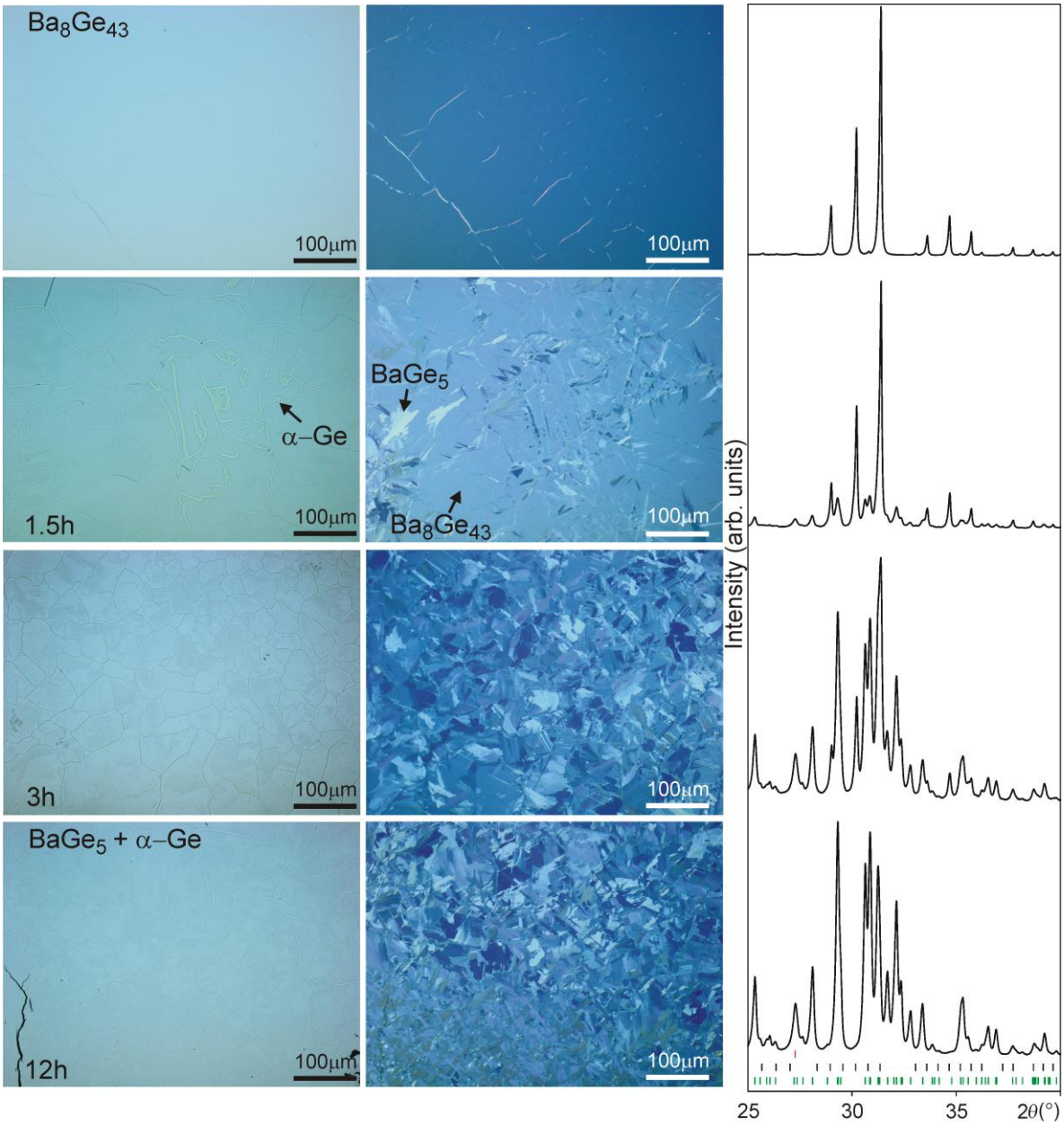

Figure 5.5: Optical microscopy images (bright field (**left**), polarized light (**middle**)) and PXRD pattern (**right,** Cu-$K\alpha_1$ radiation) of samples obtained via decomposition of $Ba_8Ge_{43}\square_3$ at 400 °C for different periods of time demonstrate the formation of $BaGe_5$ starts even after 1.5 h and is complete in 12 h. The ticks at the bottom of PXRD patterns mark the calculated reflection positions of $BaGe_5$ (green), $Ba_8Ge_{43}\square_3$ (black), and α-Ge (red).

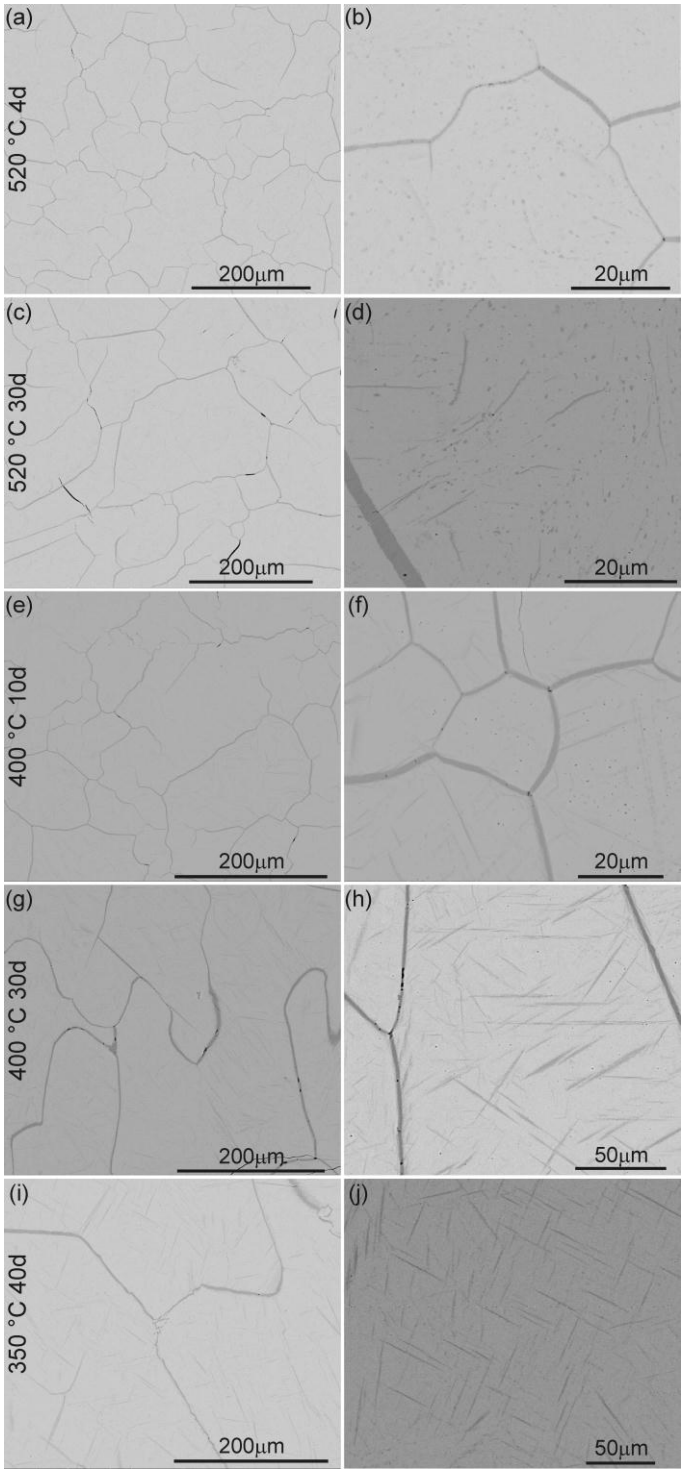

Figure 5.6: SEM images (BSE contrast) of samples obtained via decomposition of $Ba_8Ge_{43}\square_3$ at 520 °C in 4 d (**a**, **b**) and 30 d (**c**, **d**), at 400 °C in 10 d (**e**, **f**) and 30 d (**g**, **h**) and at 350 °C in 40 d (**i**, **j**). The images show formation of large $BaGe_5$ grains and the precipitation of α-Ge within and at the boundaries of $BaGe_5$ grains. $BaGe_5$ and α-Ge are shown as light and dark grey areas, respectively.

$BaGe_5$ domains are composed of fiber-like elongated sub-domains with variable color impression and brightness. Sub-domains with similar elongation and orientation form areas which are terminated often by α-Ge precipitates at the primary $Ba_8Ge_{43}\square_3$ grains. The arrangement and intergrowth of these almost uniformly oriented areas indicate that nucleation occurs at these grain boundaries. A significant degree of disorder is indicated by the fine textured microstructure. Needle/plate-like α-Ge precipitates are located at the boundaries of the elongated $BaGe_5$ sub-domains due to the diffusion controlled transformation process (Fig. 11.8). The fine dispersive α-Ge dots are not clearly correlated with the sub-domain boundaries. Microstructures of short term annealed $Ba_8Ge_{43}\square_3$ samples contain partially transformed phase mixtures and give indications on basic nucleation and grain growth processes of the $BaGe_5$ phase. After annealing at 400 °C for 1.5 h, $BaGe_5$ grain growth starts at the surfaces of α-Ge precipitates (Fig. 11.9). Additionally, plate-like $BaGe_5$ grains are formed in primary $Ba_8Ge_{43}\square_3$ without α-Ge precipitations. When $BaGe_5$ was further annealed at 790 °C for 3 d, microstructures show partially transformed phase mixtures and give indications on basic nucleation of $BaGe_5$ phase and grain growth process of the $Ba_8Ge_{43}\square_3$ phase (Fig. 11.10a-b). In the microstructure, nucleation of $BaGe_5$ is accompanied with α-Ge precipitates surrounded by Ge-depleted regions with composition close to Ba_6Ge_{25} phase. $BaGe_5$ has common interfaces with these Ge-depleted regions. After further annealing at 790 °C for 2 weeks, $Ba_8Ge_{43}\square_3$ phase was obtained without detectable secondary phases as $BaGe_5$, Ba_6Ge_{25} or α-Ge (Fig. 11.10c).

Preparation conditions of $BaGe_5$ samples, the measured compositions and the lattice parameters are tabulated in Table 5.1. The compositions and the lattice parameters are found to be almost identical within the accuracy of measurements regardless of the starting preparation conditions. Therefore, a homogeneity range for $BaGe_5$ could not be resolved by means of PXRD and WDXS analyses.

Table 5.1: Chemical composition and lattice parameters of $BaGe_5$ samples.

Starting composition	Preparation route Temperature (°C)	Time (d)	*a, b, c* (Å)	Composition (WDXS)
$Ba_{16.67}Ge_{83.33}$ ('$BaGe_5$')	520	4	10.723(1), 9.2874(9), 14.792(1)	$Ba_{0.98(1)}Ge_{5.02(1)}$
$Ba_{15.69}Ge_{84.31}$ (Ba_8Ge_{43})	520	4	10.7224(7), 9.2841(7), 14.794(1)	$Ba_{1.00(2)}Ge_{5.00(2)}$
		10	10.7246(9), 9.2860(8), 14.797(1)	$Ba_{0.98(1)}Ge_{5.02(1)}$
		30	10.7252(7), 9.2867(6), 14.795(1)	$Ba_{0.99(1)}Ge_{5.01(1)}$
	460	10	10.7255(9), 9.2871(8), 14.797(1)	$Ba_{0.99(1)}Ge_{5.01(1)}$
	400	4	10.7273(7), 9.2855(6), 14.792(1)	$Ba_{0.98(1)}Ge_{5.02(1)}$
		10	10.7265(8), 9.2839(5), 14.791(1)	$Ba_{0.99(1)}Ge_{5.01(1)}$
		30	10.7261(7), 9.2848(7), 14.794(1)	$Ba_{0.99(1)}Ge_{5.01(1)}$
	350	40	10.7267(9), 9.2851(8), 14.798(1)	$Ba_{1.00(1)}Ge_{5.00(1)}$

5.4 Crystal structure

It was not possible to obtain single crystals of $BaGe_5$ suitable for X-ray single crystal analysis because of the microstructure with very small grain size. Hence, high-resolution synchrotron powder X-ray diffraction data (see section 3.3) were collected on two samples obtained from the decomposition of $Ba_8Ge_{43}\square_3$ at 400 °C and at 520 °C in 10d. Besides the reflections of α-Ge, all reflections were indexed in a primitive, orthorhombic unit cell in agreement with the previous results (Fig. 5.7, Table 5.1).[181] The crystal structure was solved *ab initio* from synchrotron X-ray powder diffraction data using WinCSD program package. Structure solution succeeded in space group *Pmna* (no. 53) in agreement with the selected area electron diffraction (SAED) results (Table 11.6, Fig. 5.8).[181] The Rietveld refinements resulted in the chemical composition $BaGe_5$ (Z = 10) which is in good agreement with the wavelength dispersive X-ray spectroscopy results (see Table 5.1).

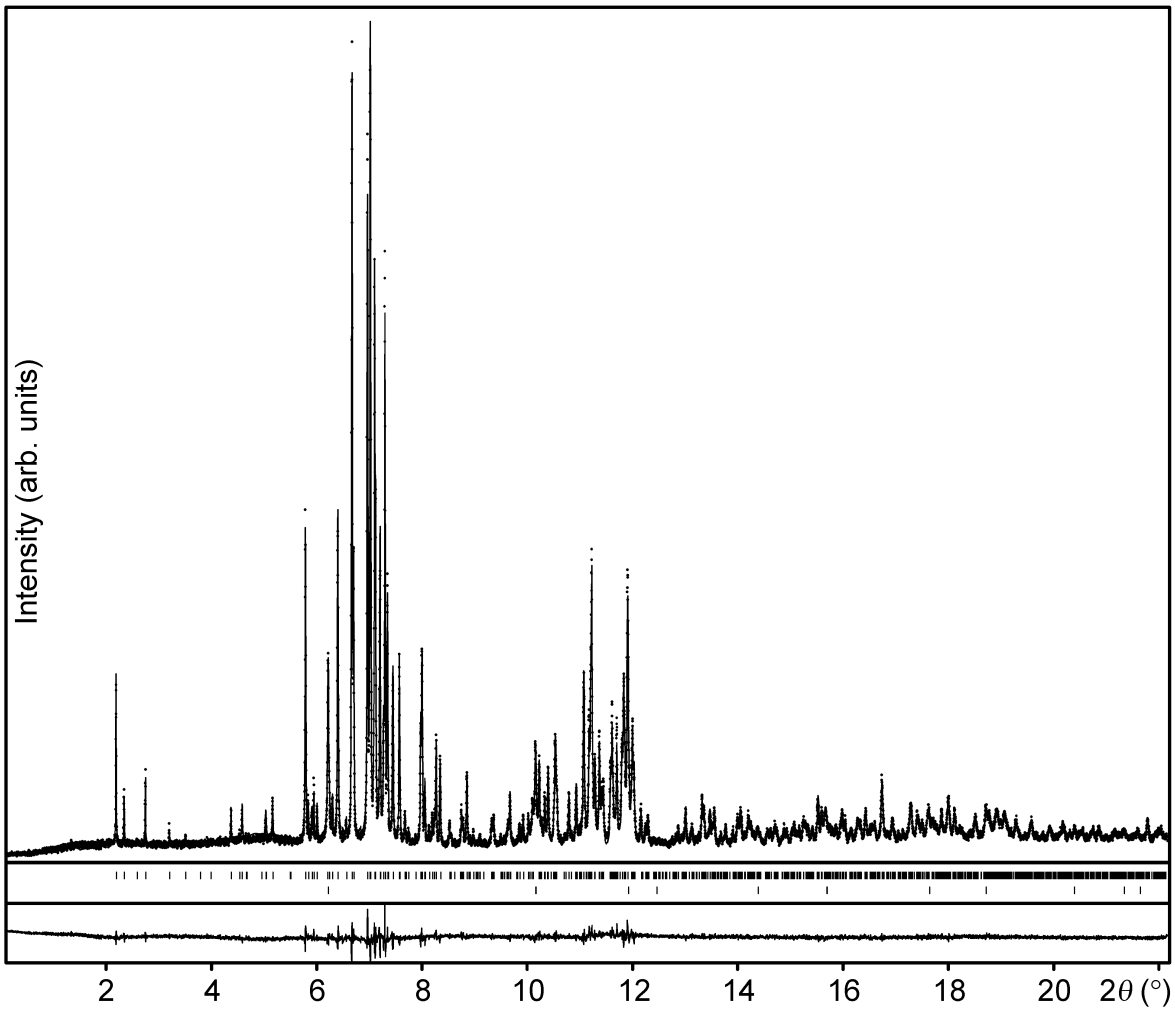

Figure 5.7: Synchrotron powder X-ray diffraction pattern of a sample obtained at 400 ºC in 10 d (λ = 0.35415 Å, dotted line). The calculated profile after Rietveld refinement (solid line) and difference curve (below) are shown. Upper and lower ticks mark the calculated reflection positions of $BaGe_5$ and α-Ge, respectively.

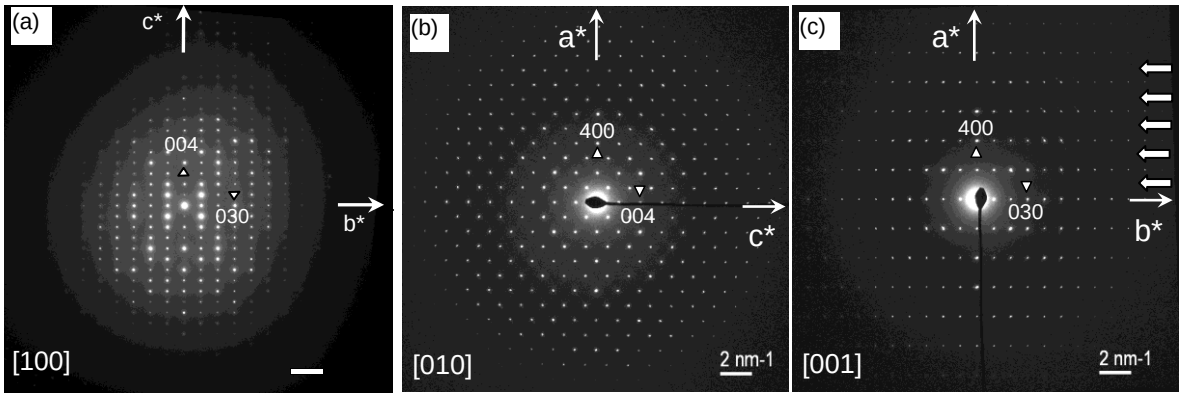

Figure 5.8: SAED patterns of $BaGe_5$. The reflection conditions are in agreement with the space group *Pmna*. The white arrows in (c) indicate no reflection lines for $h + l = 2n + 1$.[181]

The crystal structure of $BaGe_5$ is characterized by clathrate-like layers perpendicular to [010], consisting of Ge_{20} dodecahedra connected by pentagons and hexagons (Fig. 5.9). The layers are interconnected via (3b)Ge^- anions. Similar 2D infinite layers, but fully separated by the cations and cluster anions, have been observed in the crystal structure of $A_3Na_{10}Sn_{23}$ (A = Cs, Rb, K; Fig. 5.10).[80] In $BaGe_5$, the anions linking the Ge layers partially occupy two crystallographic sites (*Occ*. = 50 %)(Table 11.7, Fig. 5.9b). An ordered arrangement of the (3b)Ge^- anions in an isomorphic subgroup such as $Pmn2_1$ or *Pma*2 could not be verified by Rietveld refinements (Fig. 5.11). In the crystal structure of $BaGe_5$, the Ba atoms occupy three crystallographic sites with distinctly different local environments. Ba1 atoms are enclosed within pentagon dodecahedra arranged on a B-centered orthorhombic lattice. Ba2 atoms are located in infinite channels running along [100] and Ba3 atoms are situated along the infinite channels in open cages formed by Ge_5-pentagons and Ge_6-hexagon. As Ba2 and Ba3 atoms are arranged in between the layers, their local environment depends strongly on the actual position of the (3b)Ge^- anions Ge4 and Ge5 (Fig. 5.12).

The crystal structure of $BaGe_5$ may be described as intermediate between $Ba_8Ge_{43}\square_3$ (clathrate-I, Fig. 5.9c) and Ba_6Ge_{25} (clathrate *cP*124, Fig. 5.9d). In analogy to Ba_6Ge_{25}, $BaGe_5$ contains only one type of polyhedral cages, Ge_{20} dodecahedra, centered by Ba1 atoms and Ba2 atoms are assembled in channels. Ba3 atoms are located in cavities resembling the Ge_{24} polyhedra of $Ba_8Ge_{43}\square_3$. In the crystal structure of $BaGe_5$, 20 Ge atoms per unit cell are three-bonded, leading to the electronic balance $[Ba^{2+}]_{10}[(3b)Ge^-]_{20}[(4b)Ge^0]_{30}$. Hence, $BaGe_5$ can be considered as a Zintl phase.

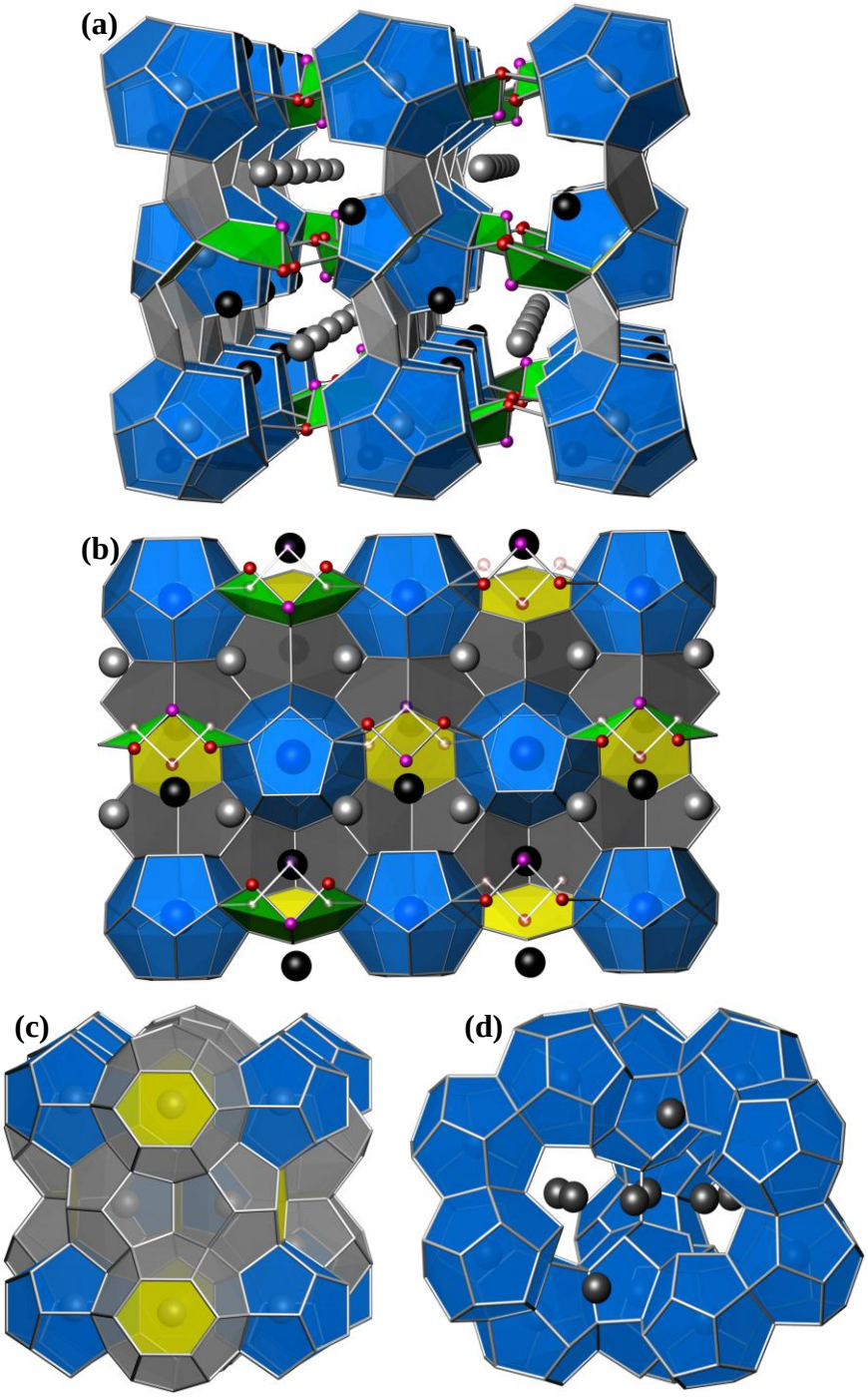

Figure 5.9: (a) Crystal structure of $BaGe_5$ with channels and covalently bonded layers along [100]. **(b)** View along [010]. Ba1 atoms are situated inside blue dodecahedra, Ba2 and Ba3 atoms are shown in gray and black, respectively. Alternatively occupied Ge sites are represented in colors (Ge4 in purple and Ge5 in red) and transparent ones. Respective features in clathrate-I **(c)** and clathrate *cP*124 **(d)**.

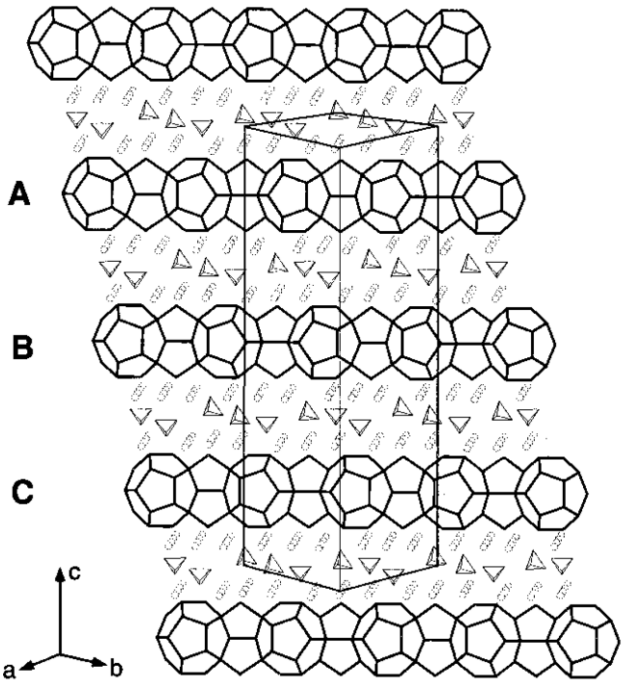

Figure 5.10: Crystal structure of $A_3Na_{10}Sn_{23}$ (A = Cs, Rb, K). Layers of tin pentagon dodecahedra are arranged in ABC order along the c axis. These layers were isolated by tin tetrahedra and alkali metal cations (open circles).[80]

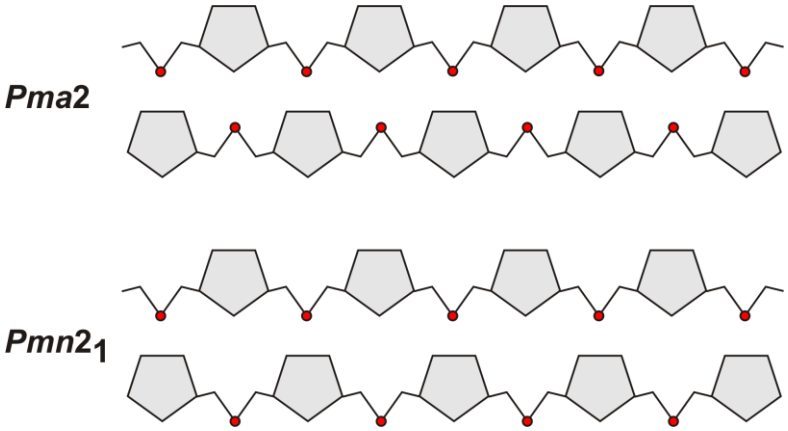

Figure 5.11: Ordered connection patterns of (3b)Ge^- anions Ge4 and Ge5 (shown in red) in the direct subgroups of the space group *Pmna*.

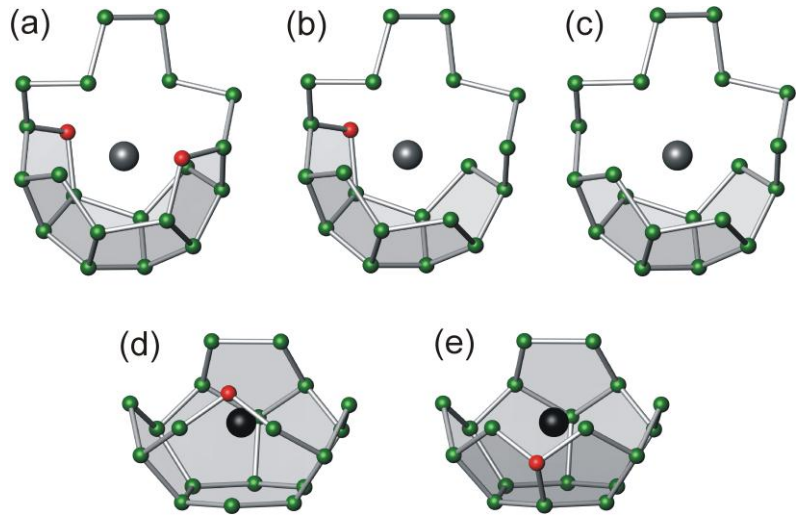

Figure 5.12: Local environment of Ba2 (**a-c**) and Ba3 (**d-e**) atoms depending on the actual position of Ge4 and Ge5 atoms shown in red.

The interatomic distances between Ge atoms in the crystal structure of $BaGe_5$ vary in the range *d*(Ge–Ge) ≈ 2.38 Å – 2.57 Å (Table 11.8). Ge1, Ge4, Ge5 and Ge7 atoms are three-bonded. Ge2 atom is either three- or four-bonded depending on whether the neighboring Ge-4 position is occupied or not. Other Ge atoms are four-bonded. The short interatomic distance of 2 Å between half-occupied Ge4 and Ge5 sites is very short considering the typical Ge–Ge bond of ≈ 2.45 Å in α-Ge. The possible connection patterns with plausible Ge–Ge interatomic distances of ≈ 2.50 Å are shown in Fig. 5.13. Barium atoms located in pentagon dodecahedron as well as in open cavities have quite long interatomic distances with Ge atoms ranging *d*(Ba–Ge) ≈ 3.11 Å – 3.90 Å. The isotropic displacement parameters for the Ba atoms increase as the cavity size or interatomic distances with the framework atoms increase. This is in agreement with what is observed in structurally related clathrate compounds $Ba_8Ge_{43}\square_3$ and Ba_6Ge_{25}.

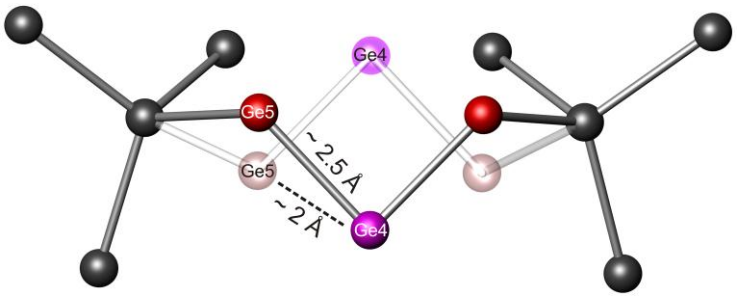

Figure 5.13: Alternative connection pattern of Ge4 and Ge5 split atoms. Two connection patterns are possible as shown by grey and transparent grey bonds, respectively.

5.5 Electronic structure and chemical bonding

FPLO was used to investigate the electronic structure and chemical bonding in $BaGe_5$ (see section 3.5). The basis set consisted of Ba: 5s, 5p / 6s, 6p, 5d; Ge: 3p, 3d / 4s, 4p, 4d corresponding to semicore / valence states, respectively. The lower-lying states were treated in a fully-relativistic way, while scalar-relativistic treatment was applied to the basis sets. Chemical bonding analysis was performed by applying ELI in combination ED.

Due to the presence of two Ge positions with half occupancy in the crystal structure of $BaGe_5$, ordered models are necessary to deal with this implied disorder in the electronic structure calculations. Since the original unit cell is already large with 60 atoms, subgroups of the original space group *Pmna* are considered only in the same unit cell. Three possible space groups with relatively high symmetry allow half-occupied positions to be split into two positions with equal multiplicities: $Pmn2_1$ (no. 31), *Pma*2 (no. 28) and *P*2/*m* (no. 10). However, one of the half-occupied positions (Ge5 at 8*i*) actually contains sites with unphysically short interatomic distances of *d*(Ge5–Ge5) ≈ 0.9 Å. Such contacts can be avoided within the first two space groups and therefore the *P*2/*m* option was not considered. In either of the $Pmn2_1$ or *Pma*2 subgroups, an ordered model can be obtained in two different ways. A first possibility results in Ge4–Ge5 interatomic distances of around 2 Å which are much shorter than typical Ge–Ge distances in α-Ge. In addition, this model leads to very high total energies and an electronic band structure characteristic of a metal which clearly contradicts the experimental findings (see following sections). The second possibility results in reasonable nearest-neighbor Ge–Ge distances together with a band gap of 0.24 eV and 0.22 eV in the space groups $Pmn2_1$ and *Pma*2, respectively. These calculations are thus consistent with the semiconducting nature of this compound. The total energies of these two semiconducting structural models are comparable and may explain the absence of a superstructure or failure of any attempt to refine the crystal structure within an ordered model in various subgroups. The electronic DOS obtained using the ordered models in the two space groups are shown in Fig. 5.14. As can be seen, both models lead to very similar electronic structures. The region between –12.3 and –7 eV mainly originates from Ge 4*s* states. In the –7 and –5.3 eV energy range, the contribution of Ge 4*p* states is comparable to that of 4*s* states and then becomes dominant between –4.2 and 0 eV. In the occupied bands, Ba 5*d* contributions are important mainly in the top region. As stated earlier, $BaGe_5$ can be considered as a semiconducting Zintl phase with a narrow band gap.

Chemical bonding analysis based on the ELI/ED concept further corroborates the expectation about total number of three- and four-bonded atoms (Fig. 5.15). The ELI attractors in the valence region of Ge are found to be of dysnaptic and monosynaptic type.

The former corresponds to two-centered Ge–Ge bonds with an electron counts of ~ 2 while the latter is related to lone-pair-like features.

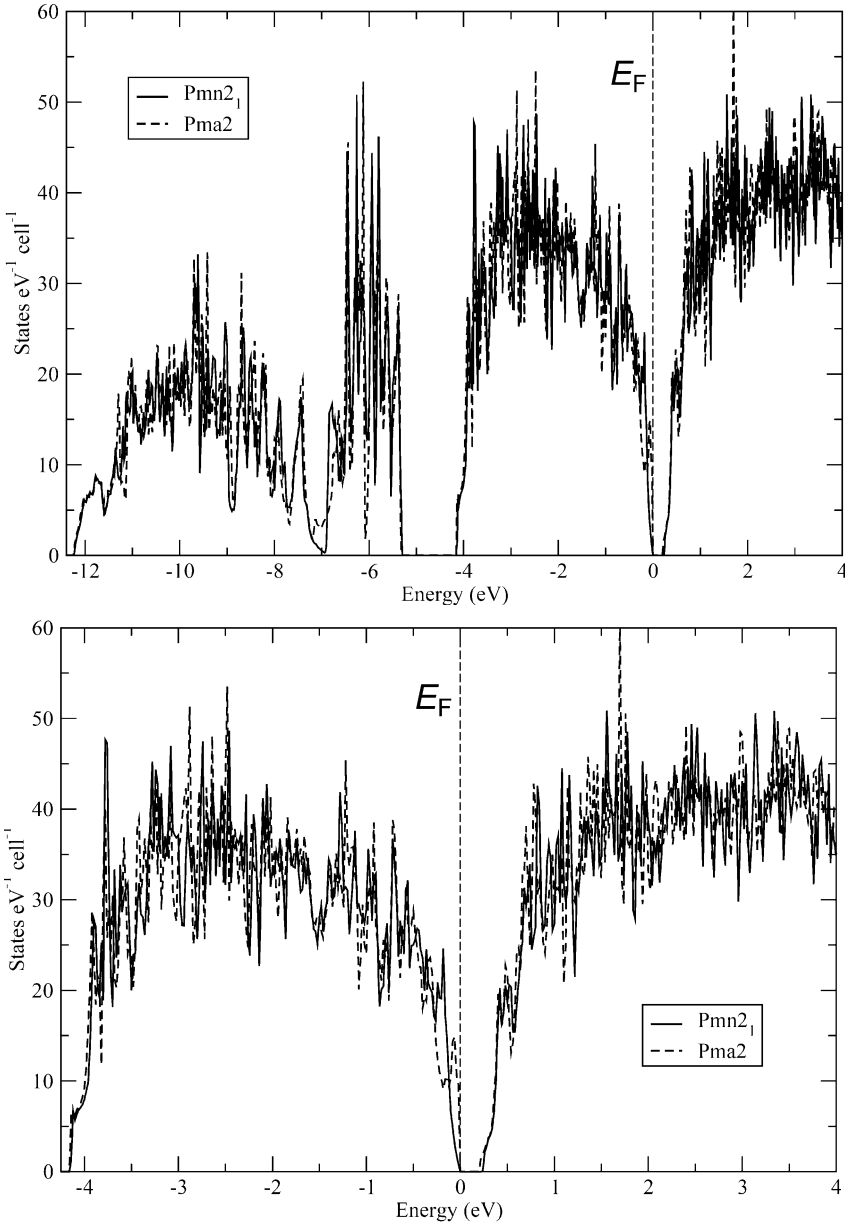

Figure 5.14: (Top) Total electronic density of states of $BaGe_5$ calculated for the space groups *Pmn*2_1 and *Pma*2. (**Bottom**) A more focused region of total DOS around Fermi level between –4 eV and 4 eV.

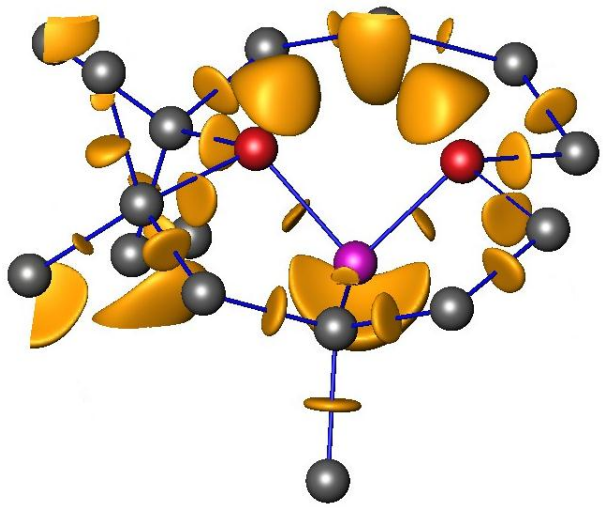

Figure 5.15: The ELI isosurface with isosurface value Υ = 1.256 depicted in the vicinity of the half-occupied sites. The purple and red spheres denote the three-bonded Ge4 and Ge5 atoms, respectively, while the gray spheres represent the Ge atoms at the fully-occupied sites. The lone pairs of Ge4 and Ge5 are clearly seen.

5.6 Physical properties

Low temperature measurements were initially performed on samples obtained by annealing at 350 ºC, 400 ºC and 520 ºC for 40 d, 10 d and 4 d, respectively (Fig. 5.16a-c). In terms of the transport properties, preparation conditions of $BaGe_5$ do not affect the temperature dependences but result in slight variations in the absolute values. The thermopower decreases in absolute values with increasing annealing temperature to reach values ranging between –150 and –180 μVK^{-1} at 300 K. While the thermal conductivity values remain similar regardless of the annealing temperature, the electrical resistivity is strongly influenced, the values exhibiting a steeper rise towards low temperatures as the annealing temperature is decreased. These small changes in transport properties can be related to composition of the clathrate phase, crystal structure as well as microstructure. Within the experimental accuracy, compositions of clathrate phase based on WDXS analyses, lattice parameters together with Rietveld refinements could not uncover variations in the composition and crystal structure in relation to the synthesis conditions. However, the variations in transport properties may be still an effect of mosaicity. Different $BaGe_5$ domains might show slight differences regarding the occupancies and orientations of alternatively occupied Ge positions (Ge4 and Ge5). This effect would be averaged in the recorded reflection intensities for the powdered particles and hence averaged lattice parameters as well as structure model would be obtained from the refinements.

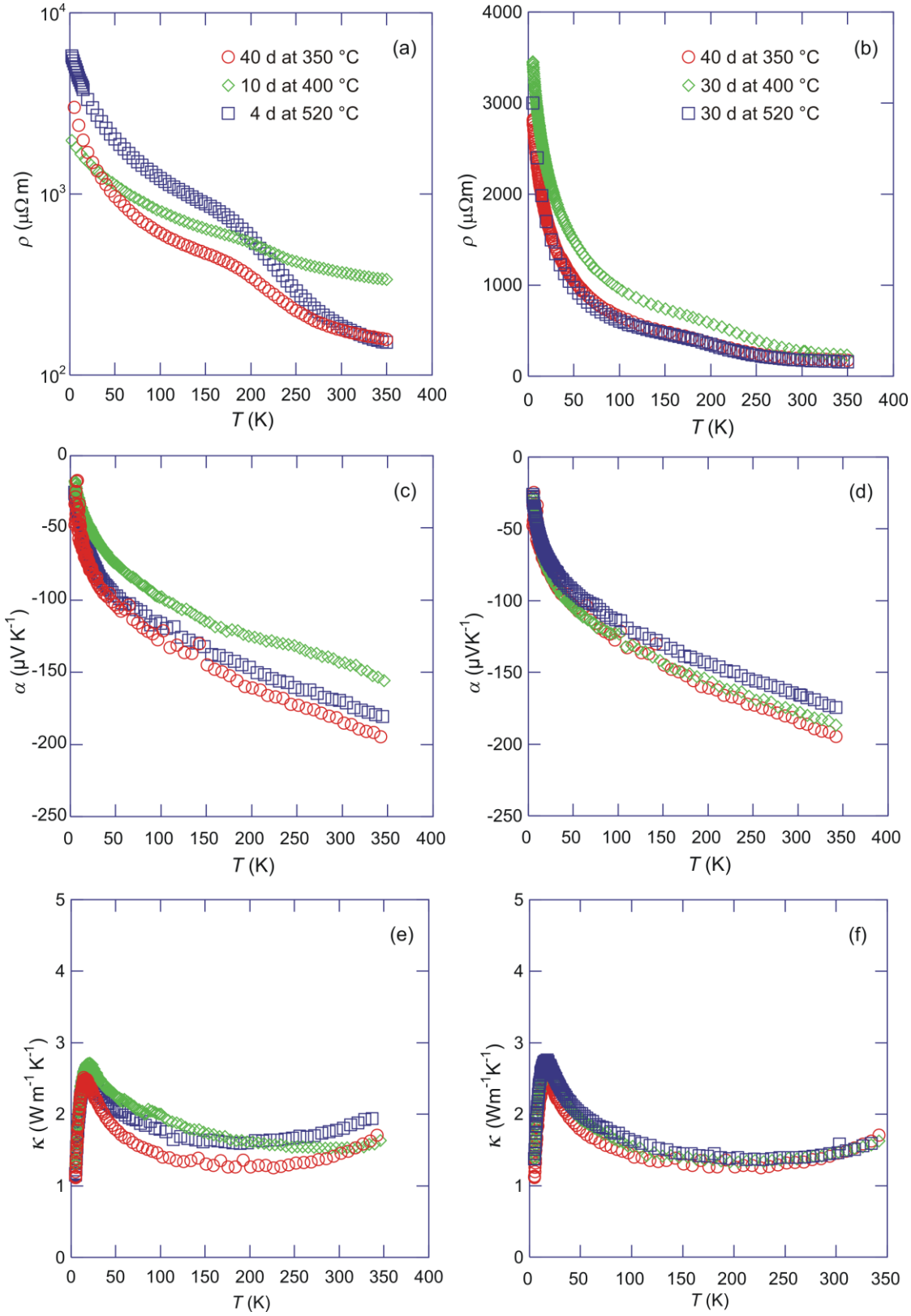

Figure 5.16: Temperature dependence of the electrical resistivity (**a**, **d**), thermopower (**b, e**) and total thermal conductivity (**c, f**) of samples annealed at 350 ºC (○), 400 ºC (□) and 520 ºC (◊). The preparation conditions of the samples are the same for the same column.

Besides crystal structure and chemical composition, several aspects revealed by our microstructure investigations as shown in section 5.3 may stand for underlying mechanisms of the observed differences in transport properties. A first essential point is related to the grain size of the samples, a longer annealing time results in larger $BaGe_5$ grains. In addition, the HRTEM investigations have revealed the presence of planar defects within the $BaGe_5$ grains even after long time heat treatment. Hence these microstructural properties along with the presence of α-Ge within and at the boundaries of $BaGe_5$ grains likely influence the electrical transport thereby explaining significant variations in the ρ values. The strong disorder inherent to the microstructure of these materials may also explain the quasi-insensitivity of the thermal conductivity to the synthesis conditions.

To further shed light on these possibilities, samples previously annealed for 10 d at 400 ºC and for 4 d at 520 ºC were further annealed at these temperatures up to 30 d. This long time annealing treatment leads to similar absolute values and temperature dependences of transport properties of these samples in the whole temperature range (Fig. 5.16d-f). The slightly different electrical resistivity values distinguishable among the long time annealed samples may still originate from differences in the microstructure of these compounds. The thermopower values, however, do not merge into a single curve suggesting that some differences survive in the samples even after a long-time annealing treatment. Considering that the role played by the microstructure on the thermopower should be of minor importance, this might indicate the existence of variations in the crystal structure.

Since the transport properties of long time annealed samples are very similar, the rest of the section deals with the transport properties of a sample annealed at 400 ºC for 30 d.

The temperature dependence of the magnetic susceptibility, χ, is shown in Fig. 5.17. An estimation of the core diamagnetic contribution, χ_{dia}, using tabulated diamagnetic increments of Ba and Ge,[169, 170] yielded -110×10^{-6} emumol^{-1} which is considerably lower in absolute value than the experimental value -210×10^{-6} emumol^{-1} at 300 K. The magnetic susceptibility of samples annealed for a longer period (30 – 40 d) is significantly smaller in absolute values. At room temperature, χ amounts to -135×10^{-6} emumol^{-1} which is in good agreement with the calculated value. These results thus show that the magnetic properties of all samples develop similarly with annealing time. Further, chemical characterizations have not only shown similar compositions regardless of the annealing temperature within our experimental accuracy but have also indicated the presence of α-Ge as the only secondary phase. It seems therefore unlikely that such large variations originate from small differences in the microstructure of these samples. An alternative explanation might therefore be related to the increments of Ba^{2+} and α-Ge used for the above-mentioned estimation,[169, 170] the difference arising from the high content of Ge^{-} anions in

$BaGe_5$ which may lead to variations in the diamagnetic contributions of the Ge atoms with the annealing time. Our crystallographic investigations revealed an inherent disorder on the Ge4 and Ge5 sites preventing a superstructure to be observed. As discussed above, the three-bonded Ge anions are arranged in a disordered manner in the crystal structure. As atoms with lone pairs have in general a strong influence on the diamagnetic behavior, the actual arrangement of these atoms in the crystal structure might be a reason for the different χ values observed after annealing. The fact that a longer annealing time leads to a closer agreement between the experimental and theoretical values may be interpreted as a lower amount of vacancies in the crystal structure with annealing time. In this regard, whether longer annealing times may result in a fully ordered crystal structure remains an interesting and open question which requires further investigations.

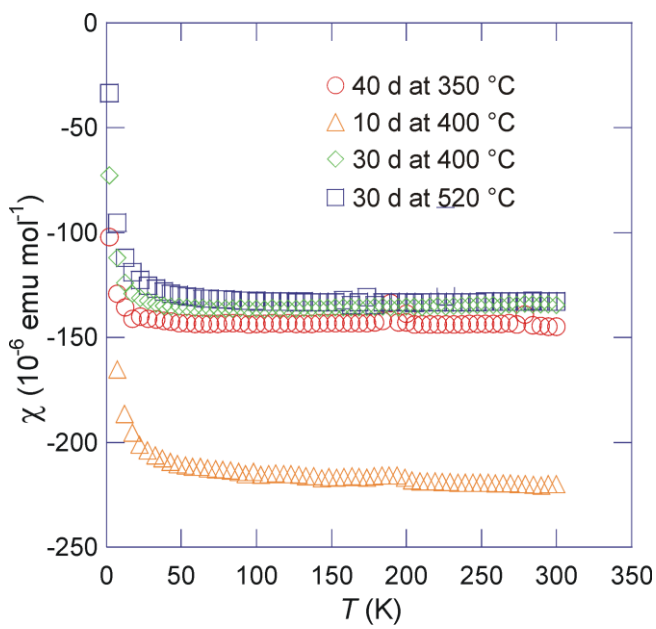

Figure 5.17: Temperature dependence of the magnetic susceptibility of the $BaGe_5$ samples obtained at different preparation conditions.

The magnetic field dependence of Hall resistivity ρ_H for selected temperatures of the sample annealed at 400 °C for 30 d is depicted in Fig. 5.18a. To dismiss any magnetoresistive contribution and thus, to reliably extract the charge carrier concentration, the antisymmetric part of the transverse resistivity under magnetic field reversal was determined via the relation:

$$(\rho_{xy}(+\mu_0 H) - \rho_{xy}(-\mu_0 H))/2 \tag{5.1}$$

Regardless of the annealing temperature, this results in linear variations of the $\rho_H(\mu_0 H)$ curves characterized by a negative slope in the whole temperature range indicating a dominant electron-like response. Within a single-band model, the electron concentration, n, can be then derived from Eq. 3.9. For all samples, n is observed to show similar temperature dependence indicative of an activated behavior consistent with the semiconducting nature of $BaGe_5$ (Fig. 5.19b). However, varying the annealing temperature leads to slight variations in n which ranges between 7.1×10^{19} and 1.2×10^{20} cm^{-3} at 275 K. These variations are consistent with the slight differences observed in the thermopower data (see Fig. 5.16e) and point to subtle changes of the crystal structure depending on the annealing temperature. Hall effect measurements therefore provide further evidence showing possible variations in the crystal structure as a function of the annealing temperature. The Hall mobility, μ_H, of the charge carriers, derived from Eq. 3.10 is low for all samples and on the order of a few $cm^2V^{-1}s^{-1}$ in the whole temperature range.

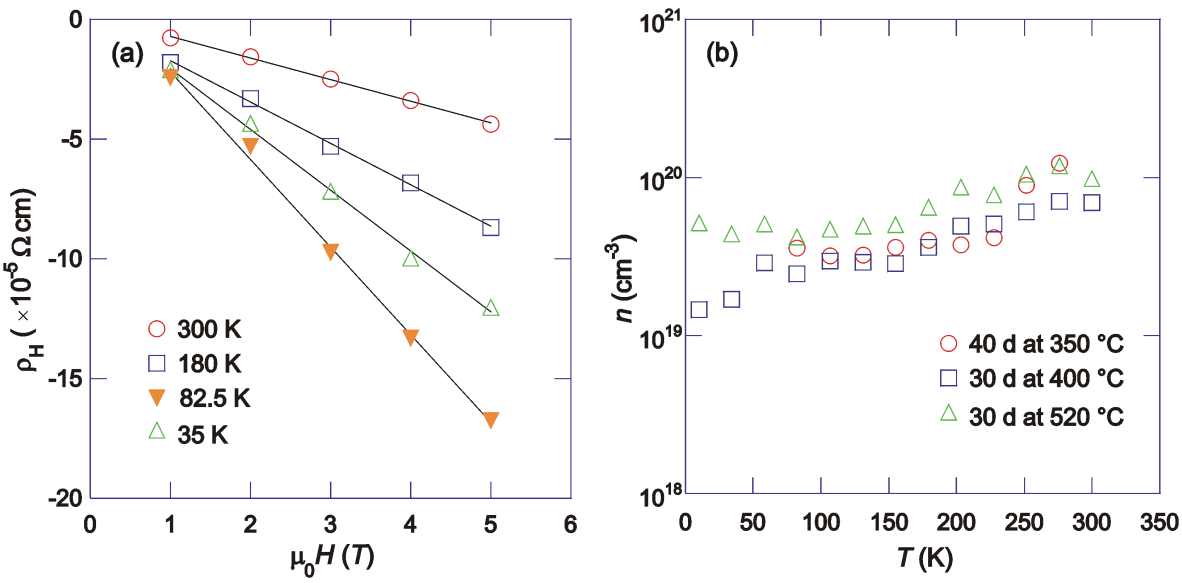

Figure 5.18: (**a**) Hall resistivity, ρ_H, as a function of the magnetic field measured at various temperatures for the illustrative sample annealed at 400 °C for 30 d. (**b**) Temperature dependence of the carrier concentration inferred from the Hall effect data for the samples annealed at different temperatures.

Fig. 5.19a shows the temperature dependence of the specific heat, $C_p(T)$, in the temperature range 1.9 – 550 K. Varying the annealing temperature does not lead to variations in C_p within the experimental accuracy. Above room temperature, the C_p values increase with increasing temperature reflecting the anharmonicity of the lattice contribution. The observed values, however, are very close to those expected from the Dulong-Petit value (Eq. 3. 11). To probe the electronic ground state of these materials, the

low temperature data have been plotted as C_p / T versus T^2 (Fig. 5.19b). A fit based on the conventional free-electron formula in Eq. 3.15 in the 4 – 20 T^2 range yields a γ value indistinguishable from zero within the experimental error and thus, indicates a semiconducting ground state. The β coefficient is related to the Debye temperature, θ_D, via Eq. 3.16. Using β = 1.85 $mJmol^{-1}K^{-4}$ and 6 atoms per formula unit as determined from the crystal structure, $\theta_D \approx 233$ K was obtained. This value is in line with the Debye temperature of various Ge-based type-I clathrates and corresponds to that of $Ba_8Ge_{43}\square_3$ inferred from specific heat analyses ($\theta_D \approx 232$ K).[15, 100, 103] In clathrates, the thermal motion of the entrapped cations leads to an additional contribution to the specific heat that dominates the low temperature variations of C_p and appears as a pronounced peak centered near 15 K. To determine whether or not this contribution survives the collapse of the tetrakaidecahedra, C_p / T^3 was plotted as a function of T in Fig. 5.19c. As can be observed, a peaked structure is resolved near 15 K in $BaGe_5$ indicating the presence of low-energy modes that usually cannot be captured by a single θ_D parameter within the Debye theory.

X-ray and neutron diffraction studies carried out on various type-I clathrates have shown that the Ba atoms located in the pentagonal dodecahedra behave as the framework atoms in terms of atomic vibrations. A similar conclusion can be drawn for $BaGe_5$ as revealed by our crystal structure analyses. Thus these low energy modes are most probably associated to the motions of Ba2 and Ba3 atoms. Even though modeling the dynamics of the Ba atoms in type-I clathrates through Debye and Einstein terms was found to satisfactorily describe the low temperature specific heat, any attempt to apply this model in the present case failed. This points to a more complex lattice dynamics in $BaGe_5$ with respect to type-I clathrates. In this regard, it would be of interest to probe these low-energy modes with more sensitive techniques such as inelastic neutron scattering or Raman spectroscopy.

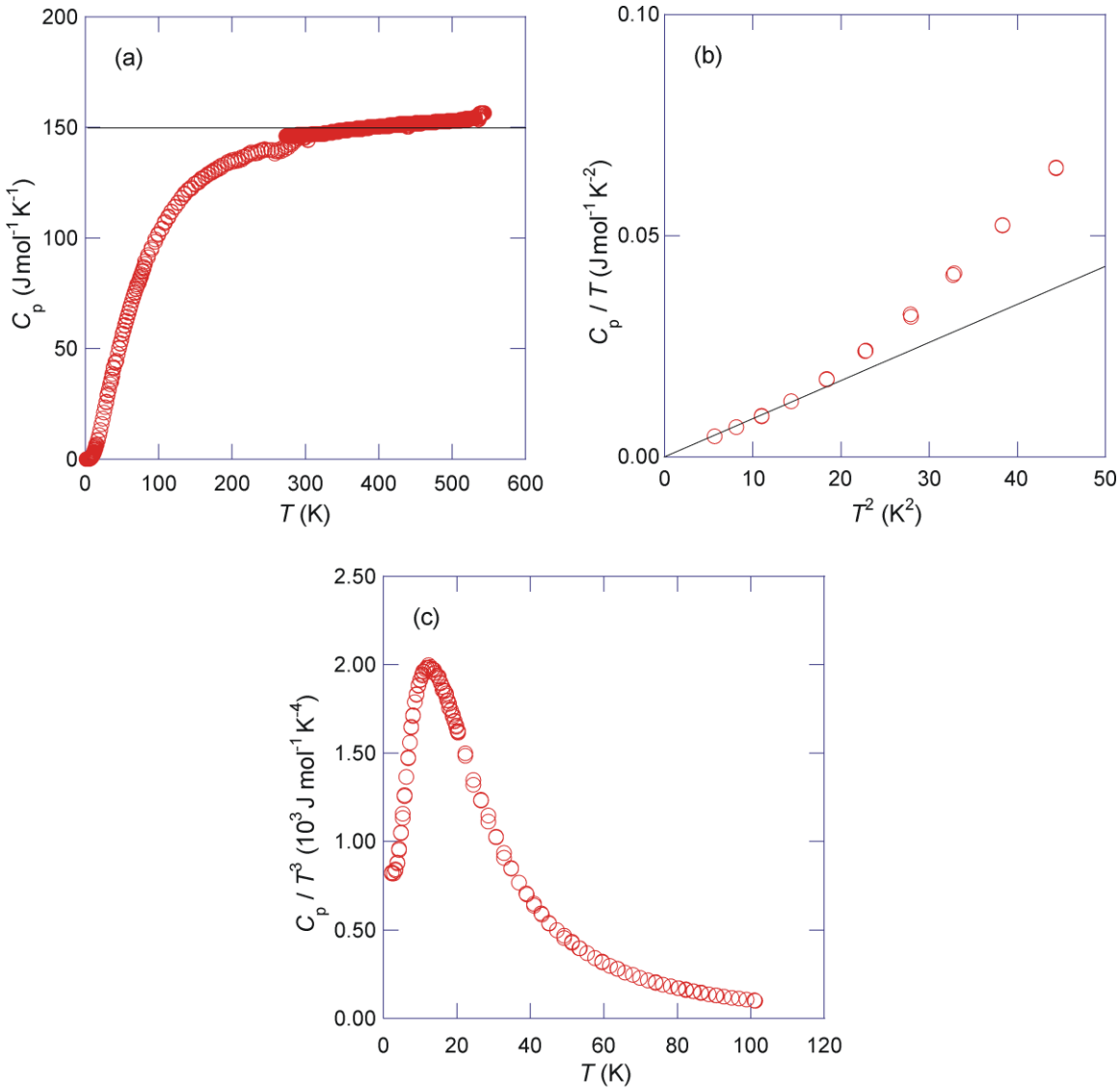

Figure 5.19: (**a**) Specific heat, C_p, as a function of the temperature. The horizontal solid line stands for the Dulong-Petit value. (**b**) C_p / T as a function of T^2. The solid line is a guide to the eye to underline the narrow temperature window where a linear dependence is observed. (**c**) C_p / T^3 as a function of T to highlight the low temperature peak possibly related to thermal motion of Ba2 and Ba3 atoms.

Fig. 5.20a shows the temperature dependence of the electrical resistivity of the sample annealed at 400 ºC in the temperature range 5 – 773 K. The negative electrical resistivity coefficient $\partial\rho / \partial T$ reflects the semiconducting nature of this material and is thus consistent with the low temperature specific heat data. In addition, an anomaly centered near 180 K can be observed. The measurements performed on different samples always led to the presence of this anomaly ruling out an extrinsic origin of this feature. This anomaly does not lead to a hysteresis effect as the electrical resistivity curves on cooling and heating are strictly similar. Even though it is not obviously correlated with any features in

magnetization, specific heat or transport properties, a possible transition to an ordered crystal structure cannot be strictly ruled out. In this regard, further crystallographic investigations at low temperatures should help discern the origin of this anomaly. A downturn occurring near 550 K characterizing the high temperature behavior of $BaGe_5$ and, as shown by the thermopower data, can be attributed to the thermal activation of the minority carriers across the band gap.

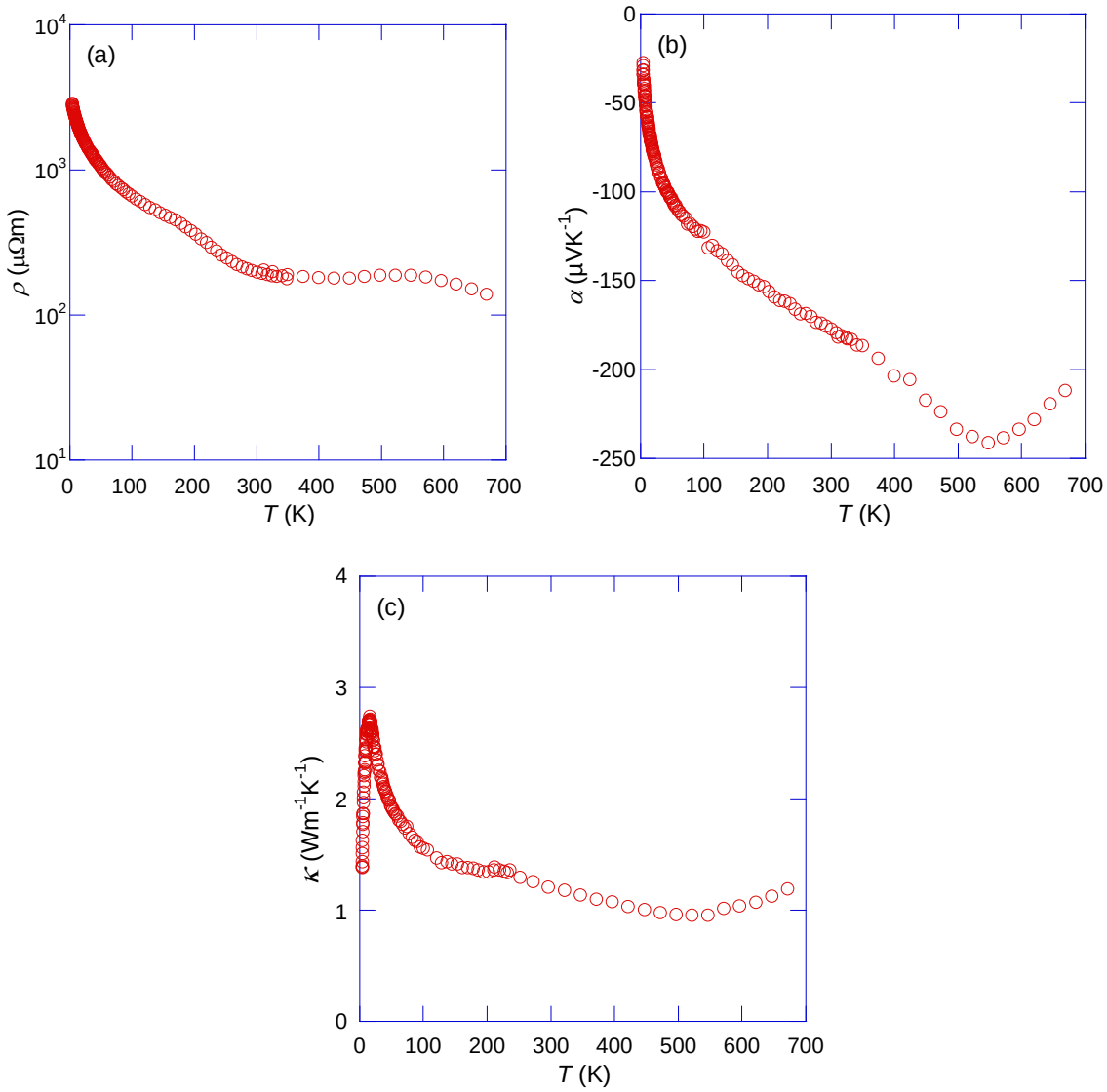

Figure 5.20: Temperature dependence of the electrical resistivity (**a**), the thermopower (**b**) and total thermal conductivity (**c**) of $BaGe_5$ obtained at 400 °C in 30 d.

The temperature dependence of the thermopower is depicted in Fig. 5.20b and shows that $BaGe_5$ exhibits negative values in the whole temperature range indicative of electrons as the prominent charge carriers. The high thermopower values together with the low temperature behavior are consistent with the semiconducting character of this compound.

Above 550 K, $|\alpha|$ decreases with increasing temperature suggesting that this sample experiences minority carrier effect. From the temperature at which this maximum occurs, an estimation of the band gap E_g can be obtained using Eq. 3.8. With T_{max} = 550 K and $|\alpha_{max}|$ = 230 μVK^{-1}, a band gap of 236 meV is obtained, which is in very good agreement with our band structure calculations.

Fig. 5.20c shows the temperature dependence of the total thermal conductivity. $BaGe_5$ exhibits a temperature dependence characteristic of crystalline insulators which feature a dielectric maximum at low temperatures followed by an exponential decrease originating from Umklapp scattering processes. Thus, the higher degree of complexity of the crystal structure of $BaGe_5$ with respect to $Ba_8Ge_{43}\square_3$ does not result in marked differences in the thermal conductivity nor does it lead to glass-like thermal transport as observed in some type-I clathrate compounds. Since the semiconducting character of $BaGe_5$ yields in large electrical resistivity values, the measured κ values almost entirely reflect the lattice contribution, the electronic contribution amounting to ~ 2.5 % at 300 K calculated by using the Wiedemann-Franz law (Eq. 3.5). Above 550 K, the thermal conductivity increases due to the thermal activation of minority carriers leading to an additional ambipolar contribution in agreement with the electrical resistivity and thermopower data.

Due to high electrical resistivity, high *ZT* values were not achieved for $BaGe_5$. A maximum *ZT* of ~ 0.2 is reached at 550 K. Further investigations aiming at tuning the carrier concentration through a partial substitution of Ge may be an interesting undertaking to enhance the thermoelectric properties of $BaGe_5$.

5.7 Conclusions

$BaGe_5$ was synthesized via diffusion controlled decomposition of $Ba_8Ge_{43}\square_3$ at temperatures between 350 ºC and 520 ºC. $Ba_8Ge_{43}\square_3$ completely transforms into $BaGe_5$ and α-Ge at 520 ºC in 1 h and at 400 ºC in 12 h. Towards lower temperatures, the transformation takes place in longer time period *e.g.* at 350 ºC in 40 d. Compositions based on the WDXS analysis, lattice parameters and also Rietveld refinements indicate no substantial differences for different heat treated $BaGe_5$ samples. The metallographic analyses demonstrate that various microstructure modifications can be obtained using different heat treatments. DSC results indicate that $BaGe_5$ is a stable phase and decomposes at a peritectoid temperature of 535 ºC to Ba_6Ge_{25} and α-Ge. $BaGe_5$ crystallizes with a new clathrate type, clathrate *oP*60. The crystal structure of $BaGe_5$ consists of characteristic layers of Ge20 pentagon dodecahedra which are interconnected by alternatively occupied (3b)Ge^- anions. $BaGe_5$ is a semiconducting Zintl phase. Physical properties of $BaGe_5$ obtained after various decomposition processes has been investigated. Differences in the

transport properties arise after short-time annealing treatments at different temperatures. These differences disappear by applying longer annealing times regardless of the annealing temperature. Transport property measurements have indicated a semiconducting nature in agreement with electronic band structure calculations. Even though a low thermal conductivity emerges from the complex crystal structure, the high electrical resistivity values prevent to achieve high ZT values ($ZT_{max} \approx 0.2$ at 550 K).

Chapter 6

Type-I Clathrate in the System Ba – Ni – Ge

A large variety of type-I clathrates were obtained by substituting the *E*14 elements with different transition metals *TM* = *E*7 – *E*12.[10, 61, 98-110, 182] Complex crystal structures emerge after this substitution as *TM* and *E*14 atoms as well as vacancies may all be present on the clathrate-I framework. In the system Ba – Ni – Ge, a clathrate-I phase was originally reported with nominal composition $Ba_8Ni_6Ge_{40}$, which was synthesized by slow heating and subsequent cooling from the melt.[61] The crystal structure was determined based on single crystal X-ray diffraction data. The low temperature transport properties for this nominal composition were recently investigated.[101] Samples in a narrow composition range with the nominal compositions $Ba_8Ni_{6-x}Ge_{40+x}$ ($0 \leq x \leq 0.6$) were also prepared.[100, 182] Sample preparations were carried out by reaction of stoichiometric amounts of Ba_6Ge_{25}, Ni, and Ge but no phase analysis was reported for the resulting compositions. Physical properties of the samples showed that a metal-to-insulator transition takes place depending on the Ni content along with a *p*- to *n*- type conduction.[100] While type-I clathrates generally crystallize in primitive cubic cell (space group $Pm\bar{3}n$), ordering of the vacancies in the clathrate framework may result in a 2 × 2 × 2 superstructure with space group $Ia\bar{3}d$ as in the case of $Ba_8Ge_{43}\square_3$.[12, 13, 15] Formation of superstructures due to the ordering of vacancies was not investigated so far for transition metal doped type-I clathrates.

Within the NoE CMA, cooperation was established among the groups of Prof. Juri Grin at the MPI-CPfS, Prof. Dr. Wolf Aßmus at the Goethe-Universität Frankfurt, and Prof. Dr. Silke Bühler-Paschen at the TU Wien to investigate the structure-property relations of the clathrates in the system Ba – Ni – Ge. During the project, polycrystalline samples were provided by our group to grow single crystalline $Ba_8Ni_{3.5}Ge_{42.1}\square_{0.4}$ by the Bridgman technique in Frankfurt and the transport properties of the single crystal were investigated in Vienna.[22, 23, 183] In the present work, type-I clathrate phase in the system Ba – Ni – Ge was reinvestigated by focusing on the influence of different Ni and vacancy contents on the phase formation, the crystal structure and the physical properties.

6.1 Preparation

Polycrystalline samples were prepared from elemental Ba, Ni powder and Ge pieces (see Table 3.1). In the early stages of sample preparations, Ta ampoules were used as crucible materials. After melting starting elements inside the ampoules followed by annealing at 700 °C for 4 d, it was observed from SEM investigations that $TaGe_2$ was formed as

secondary phase (Fig. 6.1). Since loss of Ge eventually changes the stoichiometry of compositions, Ta ampoules were not preferred for the later preparations. On the other hand, glassy carbon crucibles were observed to be relatively inert against molten samples and were used as container materials.

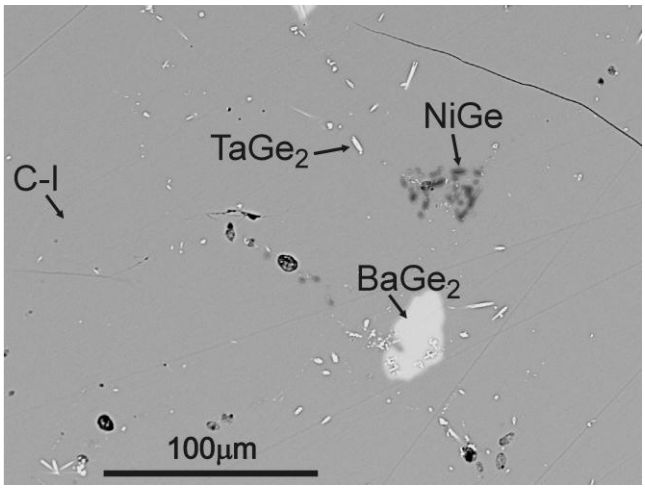

Figure 6.1: The SEM figure (BSE contrast) of a sample with nominal composition $Ba_8Ni_4Ge_{42}$ annealed in a Ta ampoule. Formed phases are shown by arrows (C-I = clathrate-I).

For the sample preparations, stoichiometric mixtures of the elements were weighed in glassy carbon crucibles (∅ = 12 mm, *l* = 12 mm) and heated with an induction furnace in an argon-filled glove box. An exothermic reaction takes place at around the melting point of Ba (~ 727 ºC) stemming probably from the reaction of Ba melt with Ge. Therefore, the samples were slowly heated within several minutes close to 727 ºC and kept at this temperature until the exothermic reaction was observed. After further heating to 1000 ºC, a complete melt was obtained. For homogenization, weak vibrations were applied to the reactor at this temperature. After melting in IF, the melt was fast-cooled in between two polished stainless-steel plates. Some part of the as-cast material was used for PXRD and microstructure analysis to identify the formed phases. Further annealing of the bulk pieces was performed at temperatures varying between 500 and 820 °C in glassy carbon crucibles sealed in Ta ampoules and followed by water quenching. Single crystals with composition $Ba_8Ni_{3.5}Ge_{42.1}\square_{0.4}$ were grown with Bridgman method by Nguyen *et al.*[22, 23, 183] using polycrystalline $Ba_8Ni_4Ge_{42}$ as precursor. Polycrystalline as well as single crystalline materials were observed to be stable in ambient conditions.

6.2 Phase analysis

Clathrate-I samples $Ba_8Ni_x\square_yGe_{46-x-y}$ obtained by steel-quenching with lowest nominal Ni content, $0.2 \leq x \leq 1$; $2 \leq y \leq 3$, contain clathrate-I phase crystallizing in the space group $Ia\bar{3}d$ (no. 230). In addition small amounts of α-Ge and/or Ba_6Ge_{25} were found (Fig 11.11, Table 6.1). Samples with compositions $1.5 \leq x \leq 3.5$, contains clathrate-I phase crystallizing in the space group $Pm\bar{3}n$ (no. 223) sometimes with traces of α-Ge and/or Ba_6Ge_{25} (Fig 11.12, Table 6.2). Quasi single phase samples with higher Ni content up to x ≈ 4.2 ($Ba_{8.00(2)}Ni_{4.22(1)}Ge_{41.29(7)}$) were obtained by annealing at 700 °C for 4 d. Samples prepared with nominal Ni content $x \geq 4.5$, after annealing at 700 °C for 4 d, showed increasing amount of NiGe and $BaGe_2$ as by-products besides clathrate-I phase (Fig. 11.13, Table 6.3).

Table 6.1: The compositions of the clathrate-I phase (C-I) with low Ni content obtained after steel-quenching together with observed products and the determined lattice parameters.

Nominal composition	Products (PXRD & EDXS)	Composition (WDXS)	*a* (Å)
Ba_8Ge_{43}	C-I (100 %)	$Ba_{8.00(1)}Ge_{42.99(4)}$	21.3079(2)
$Ba_8Ni_{0.2}Ge_{42.8}$	C-I (> 97 %), α-Ge (< 3 %)	$Ba_{8.00(2)}Ni_{0.19(2)}Ge_{42.89(3)}$	21.3085(3)
$Ba_8Ni_{0.5}Ge_{42.5}$	C-I (> 99 %), α-Ge (< 1 %)	$Ba_{8.0(1)}Ni_{0.6(2)}Ge_{42.7(2)}$	21.3140(2)
$Ba_8Ni_{0.8}Ge_{42.2}$	C-I (> 99 %), α-Ge (< 1 %)	$Ba_{8.0(1)}Ni_{0.9(2)}Ge_{42.5(2)}$	21.3151(2)
$Ba_8Ni_1Ge_{42}$	C-I (> 97 %), Ba_6Ge_{25} (< 3 %)	$Ba_{8.0(1)}Ni_{1.0(2)}Ge_{43.1(3)}$	21.3166(2)
$Ba_8Ni_{0.2}Ge_{43}$	C-I (> 98 %), α-Ge (< 2 %)	$Ba_{8.0(2)}Ni_{0.20(4)}Ge_{43.4(2)}$	21.3071(2)
$Ba_8Ni_{0.5}Ge_{43}$	C-I (> 98 %), α-Ge (< 2 %)	$Ba_{8.00(2)}Ni_{0.6(1)}Ge_{43.1(1)}$	21.3108(2)
$Ba_8Ni_1Ge_{43}$	C-I (> 98 %), α-Ge (< 2 %)	$Ba_{8.0(1)}Ni_{1.0(2)}Ge_{42.7(2)}$	21.3189(2)

Table 6.2: The clathrate-I phase(C-I) with higher Ni content ($x \geq 1.5$) obtained after steel-quenching with observed products (estimated amounts) as well as determined compositions and lattice parameters.

Nominal composition	Products (PXRD & EDXS)	Composition (WDXS)	*a* (Å)
$Ba_8Ni_{1.5}Ge_{44.5}$	C-I (> 95 %), α-Ge (< 5 %)	$Ba_{8.00(3)}Ni_{1.90(1)}Ge_{42.6(1)}$	10.6617(1)
$Ba_8Ni_2Ge_{40}$	C-I (> 98 %), α-Ge (< 1 %), Ba_6Ge_{25} (< 1 %)		10.6649(1)
$Ba_8Ni_2Ge_{41}$	C-I (> 98 %), Ba_6Ge_{25} (< 2 %)		10.6659(1)
$Ba_8Ni_2Ge_{42}$	C-I (> 99 %), Ba_6Ge_{25} (< 1 %)	$Ba_{8.0(1)}Ni_{2.4(1)}Ge_{42.9(1)}$	10.6662(1)
$Ba_8Ni_2Ge_{43}$	C-I (> 97 %), α-Ge (< 3 %)		10.6660(2)
$Ba_8Ni_2Ge_{44}$	C-I (> 95 %), α-Ge (< 5 %)	$Ba_{8.00(4)}Ni_{2.3(1)}Ge_{42.6(1)}$	10.6662(1)
$Ba_8Ni_{2.5}Ge_{43.5}$	C-I (> 97 %), α-Ge (< 3 %)	$Ba_{8.00(3)}Ni_{2.69(6)}Ge_{42.96(4)}$	10.6701(1)
$Ba_8Ni_3Ge_{40}$	C-I (> 98 %), α-Ge (< 1 %), Ba_6Ge_{25} (< 1 %)		10.6778(2)
$Ba_8Ni_3Ge_{41}$	C-I (100 %)		10.6767(1)
$Ba_8Ni_3Ge_{42}$	C-I (100 %)	$Ba_{8.00(4)}Ni_{3.01(9)}Ge_{42.15(8)}$	10.6766(1)
$Ba_8Ni_3Ge_{43}$	C-I (> 98 %), α-Ge (< 2 %)	$Ba_{8.00(4)}Ni_{2.98(3)}Ge_{42.07(2)}$	10.6762(1)
$Ba_8Ni_{3.5}Ge_{42}$	C-I (100 %)	$Ba_{8.00(2)}Ni_{3.49(5)}Ge_{42.34(5)}$	10.6803(1)
$Ba_8Ni_{3.5}Ge_{42.5}$	C-I (> 99 %), α-Ge (< 1 %)	$Ba_{8.00(3)}Ni_{3.41(4)}Ge_{42.40(4)}$	10.6797(1)
$Ba_8Ni_{3.8}Ge_{42}$	C-I (> 99 %), NiGe (< 1 %)	$Ba_{8.00(2)}Ni_{3.42(6)}Ge_{42.23(5)}$	10.6781(1)
$Ba_8Ni_4Ge_{40}$	C-I (100 %)		10.6779(1)
$Ba_8Ni_4Ge_{41}$	C-I (> 98 %), NiGe (< 1 %), $BaGe_2$ (< 1 %)		10.6773(1)
$Ba_8Ni_4Ge_{42}$	C-I (> 99 %), NiGe (< 1 %)	$Ba_{8.00(2)}Ni_{3.59(5)}Ge_{42.17(4)}$	10.6787(1)
$Ba_8Ni_{4.2}Ge_{41.8}$	C-I (> 99 %), NiGe (< 1 %)	$Ba_{8.00(2)}Ni_{3.7(1)}Ge_{42.21(9)}$	10.6767(1)
$Ba_8Ni_5Ge_{40}$	C-I (> 95 %), NiGe (< 3 %), $BaGe_2$ (< 2 %)		10.6771(1)
$Ba_8Ni_5Ge_{41}$	C-I (> 95 %), NiGe (< 3 %), $BaGe_2$ (< 2 %)		10.6769(1)
$Ba_8Ni_6Ge_{40}$	C-I (> 90 %), NiGe (< 6 %), $BaGe_2$ (< 4 %)	$Ba_{8.00(5)}Ni_{4.0(2)}Ge_{42.4(2)}$	10.6769(1)
$Ba_8Ni_{10}Ge_{36}$	C-I (> 70 %), NiGe (< 15 %), $BaGe_2$ (< 15 %)		10.6770(4)

Table 6.3: The reaction products of the samples annealed at 700 °C together with observed products (estimated amounts), determined compositions and lattice parameters (C-I = clathrate-I).

Nominal composition	Products (PXRD & EDXS)	Composition (WDXS)	*a* (Å)
$Ba_8Ni_2Ge_{42}$	C-I (> 95 %), α-Ge (< 5 %)	$Ba_{8.00(2)}Ni_{2.11(1)}Ge_{42.72(1)}$	10.6672(1)
$Ba_8Ni_2Ge_{44}$	C-I (> 95 %), α-Ge (< 5 %)	$Ba_{8.00(3)}Ni_{2.01(1)}Ge_{42.65(4)}$	10.6667(1)
$Ba_8Ni_3Ge_{42}$	C-I (> 99 %), α-Ge (< 1 %)	-	10.6767(1)
$Ba_8Ni_3Ge_{43}$	C-I (> 95 %), α-Ge (< 5 %)	$Ba_{8.00(4)}Ni_{3.06(1)}Ge_{42.32(5)}$	10.6769(1)
$Ba_8Ni_{3.5}Ge_{42}$	C-I (> 97 %), α-Ge (< 3 %)	$Ba_{8.00(2)}Ni_{3.65(1)}Ge_{42.40(2)}$	10.6781(2)
$Ba_8Ni_{3.8}Ge_{42}$	C-I (> 97 %), α-Ge (< 3 %)	$Ba_{8.00(3)}Ni_{3.90(1)}Ge_{42.03(4)}$	10.6787(1)
$Ba_8Ni_4Ge_{42}$	C-I (> 99 %), NiGe (< 1 %)	$Ba_{8.0(1)}Ni_{4.0(2)}Ge_{42.0(1)}$	10.6780(1)
$Ba_8Ni_{4.2}Ge_{41.8}$	C-I (> 99 %), NiGe (< 1 %)	$Ba_{8.00(3)}Ni_{4.08(1)}Ge_{41.87(3)}$	10.6771(1)
$Ba_8Ni_6Ge_{40}$	C-I (> 90 %), NiGe (< 6 %), $BaGe_2$ (< 4 %)	$Ba_{8.00(2)}Ni_{4.22(1)}Ge_{41.29(7)}$	10.6765(1)

The determination of the lattice parameter reflected unambiguously the variations in clathrate compositions. Generally, the change in lattice parameter can be associated to the occupancy of the Ba atoms, as well as Ni and the vacancy content. Partial occupancy of Ba sites is neglected as single crystal structure analysis revealed that the Ba atoms fully occupy the center of cages in the clathrate-I framework within the investigated composition range (see section 6.5). Based on the PXRD analysis, two fields of clathrate-I phase were characterized in the system Ba – Ni – Ge. The first one is characterized as the solid solution of Ni into the binary $Ba_8Ge_{43}\square_3$ for $0.2 \leq x \leq 1$ (Table 6.1). Here, vacancies can be filled up by additional Ni atoms ($Ba_8Ni_xGe_{43}\square_{3-x}$), Ni atoms can substitute Ge atoms ($Ba_8Ni_xGe_{43-x}\square_3$) or both of them can take place at the same time ($Ba_8Ni_xGe_{43-y}\square_z$). The lattice parameter in each case increases as the Ni content increases (Fig. 6.2). The second field of clathrate-I phase is derived from an idealized Zintl phase with composition "$Ba_8Ge_{42}\square_4$" (see section 4.3) in which the framework vacancies can be successively filled by Ni atoms for $1 < x \leq 4$ (Table 6.2). While introducing more Ni atoms to the framework, the lattice parameter increases until a maximum is reached for $x = 3.5$ (Fig. 6.2). The value of lattice parameter for polycrystalline sample is in good agreement with that of a = 10.6798(2) Å for $Ba_8Ni_{3.5}Ge_{42.1}\square_{0.4}$ single crystal,[22] and is significantly larger than the reported ones for even higher Ni content. [61, 100, 101, 182] For higher nominal Ni content $3.5 < x \leq 4.2$, the lattice parameter decreases slightly to a = 10.6767(1) Å for $x = 4.2$ and remains constant for $x > 4.2$ (Fig. 6.2). This may indicate that for these compositions Ni substitute Ge atoms. Based on these results, Ni compositions above $x = 4.2$ may not be accessible.

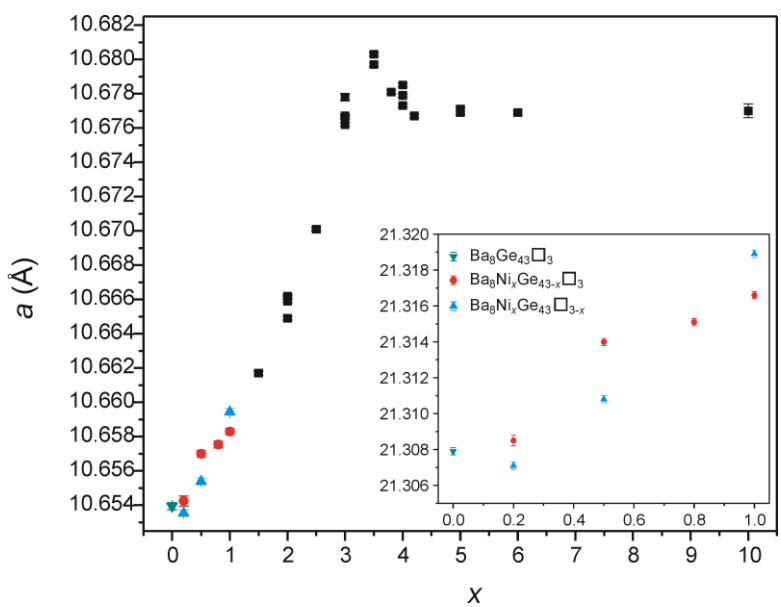

Figure 6.2: An overall trend of the lattice parameters regarding the nominal Ni content x for clathrate compounds extracted by considering half of the lattice parameter of the compounds from the first field of clathrate-I phase with superstructure (**inset,** $Ba_8Ge_{43}\square_3$ (green), $Ba_8Ni_xGe_{43-x}\square_3$ (red), $Ba_8Ni_xGe_{43}\square_{3-x}$ (blue)), and without superstructure (black).

There is a correlation between the number of vacancies and the Ni content for the second field of clathrate-I phase approved by a series of syntheses with systematic variation of the nominal composition (Table 6.2). For clathrates obtained with certain amount of Ni, the lattice parameter depends only on the nominal Ni content. Excess Ge in the nominal composition leads always to the formation of α-Ge without affecting the lattice parameter (Fig. 6.3). Therefore, the vacancies in the framework cannot be further filled up by adding Ge atoms. When the framework is saturated with Ni atoms, NiGe is formed together with $BaGe_2$.

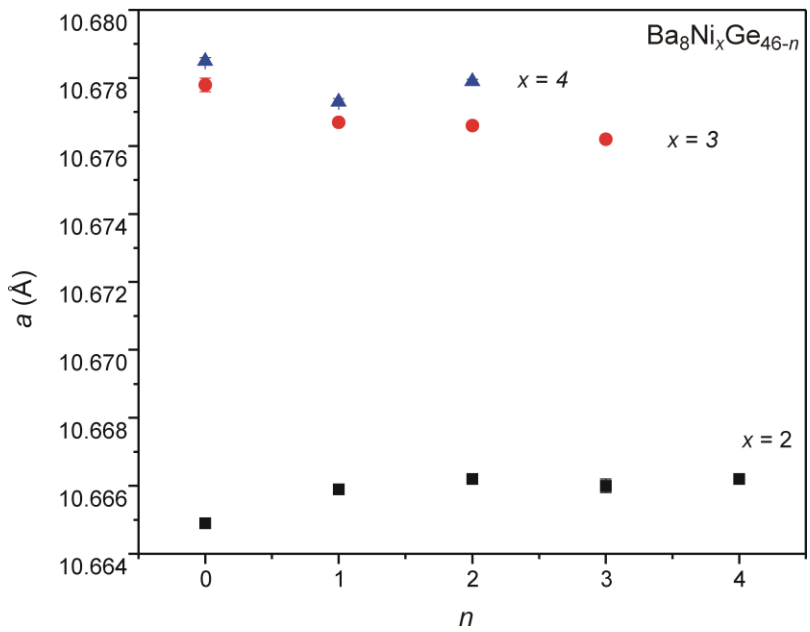

Figure 6.3: Lattice parameter of clathrate-I phase without superstructure with respect to changes in Ge content *n*. The lattice parameter is almost independent of the changes in Ge content.

Considering the two fields of clathrate-I phase, there are two possibilities: (1) They may indicate two phases in which the first one is the solution of Ni in $Ba_8Ge_{43}\square_3$ superstructure (space group $Ia\bar{3}d$) and the second one derives from "$Ba_8Ge_{42}\square_4$" crystallizing in the space group $Pm\bar{3}n$. (2) There may be only one phase in which the vacancies are filled by Ni and the superstructure becomes invisible by PXRD due to low scattering contrast between Ni and Ge. As two different phases were not observed together for none of the prepared samples, so far, the second model seems to be more probable. Detailed investigation in isothermal sections of the phase diagram may elucidate the problem in future.

Chemical compositions suggested by the trend of the lattice parameters are confirmed by WDXS analyses (Tables 6.1-6.3, Fig. 6.4). For the data evaluation, the Ba content for all samples is considered to be 8 atoms per formula unit as determined from the single crystal structure analyses. However, this way the experimental error in the Ba determination is expressed by the values of the other elements (Ni and Ge) with an additional inaccuracy. Assuming in a first approximation the same accuracy for all elements the determination of Ge results in the largest uncertainty due to high Ge content in the unit cell. Therefore, the actual number of vacancies per unit cell $n_{vac} = 46 - (n_{Ni} + n_{Ge})$ cannot be deduced from metallographic investigations but obtained by crystal structure analysis.

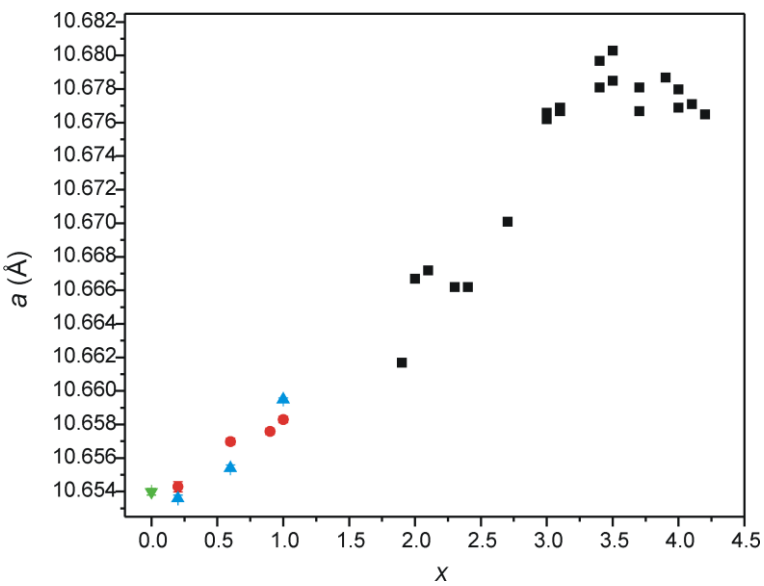

Figure 6.4: An overall trend of the lattice parameter with respect to Ni content x as determined by WDXS for clathrate-I phase with superstructure ($Ba_8Ge_{43}\square_3$ (green), $Ba_8Ni_xGe_{43-x}\square_3$ (red), $Ba_8Ni_xGe_{43}\square_{3-x}$ (blue)), and without superstructure (black).

6.3 Thermal behavior

Thermal behavior of clathrate samples was investigated by DSC experiments (see section 3.3). An almost single-phase sample with nominal composition $Ba_8Ni_{0.5}Ge_{42.5}$ was heated with 10 °C/min to 795 °C, subsequently with 5 °C/min to 1000 °C and finally cooled down to room temperature with 10 °C/min (Fig. 6.5). On heating, a broad exothermic effect was observed at around 550 °C which is attributed to the decomposition of the clathrate-I phase to $BaGe_5$, NiGe and α-Ge. On further heating, an endothermic peak appears at around 585 °C due to the decomposition of $BaGe_5$ into Ba_6Ge_{25} and α-Ge. The clathrate phase forms at around 750 ºC and is stable up to 815 ºC. This gives a hint that the thermal stability range of Ni doped clathrates is extended compared to $Ba_8Ge_{43}\square_3$. The PXRD pattern of the end

product show the reflections of clathrate-I phase without superstructure, Ba_6Ge_{25}, α-Ge and $BaGe_5$ (Fig. 11.14).

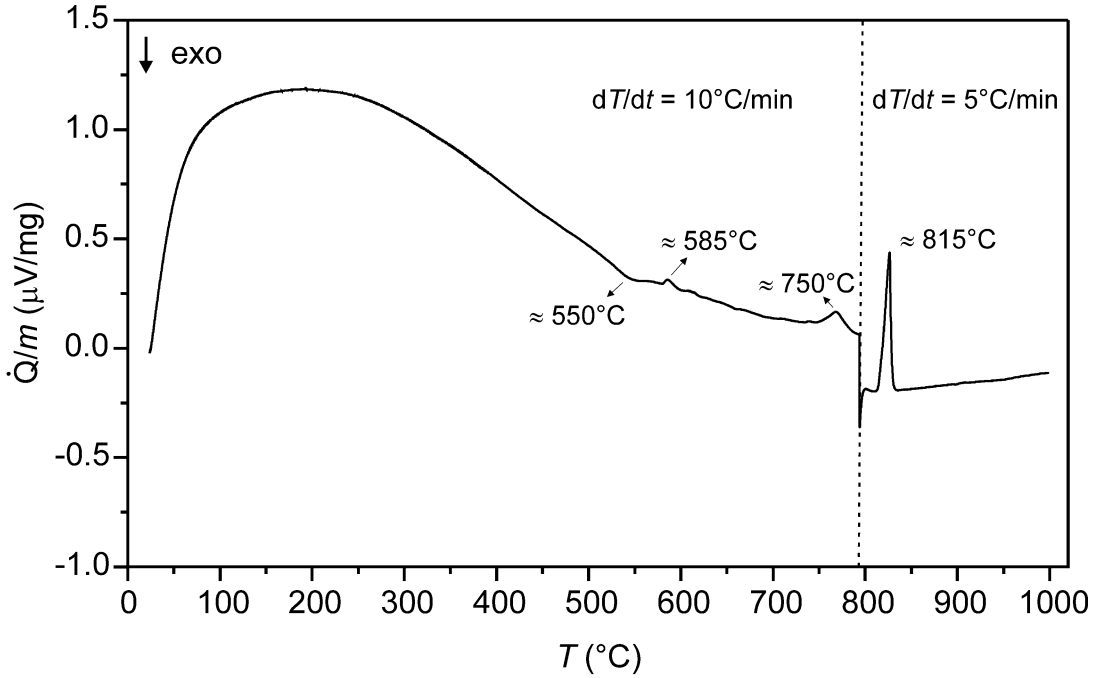

Figure 6.5: Thermal behavior of the sample with nominal composition $Ba_8Ni_{0.5}Ge_{42.5}$ from DSC. Heating rates used and the temperatures associated to different thermal effects are shown. Except for 815 ºC which is the onset temperature, the temperatures indicate peak maxima.

The thermal behavior of the single phase clathrate-I sample with nominal composition $Ba_8Ni_{3.5}Ge_{42}$ was investigated by heating the sample up to 1000 °C with 10 °C/min and then subsequently cooling down to room temperature with the same rate (Fig. 6.6). For heating and cooling steps, an endothermic and an exothermic effect were observed with onset temperatures of 840 °C and 770 °C, respectively. These thermal effects may be assigned to the temperatures of formation and decomposition, respectively. The end product shows almost single phase clathrate-I without superstructure (Fig. 11.15).

Further analysis of the thermal behavior of clathrate phase was carried out by annealing experiments between 500 °C and 820 °C. A sample with nominal composition $Ba_8Ni_{0.5}Ge_{45.5}$ was annealed for 1 w at 790 °C, 700 °C and 500 °C. After annealing at 790 °C, the sample was observed to be stable and the superstructure reflections are still clearly visible (Fig. 11.16). At 700 °C, the sample was widely decomposed to Ba_6Ge_{25}, α-Ge and a clathrate phase with smaller lattice parameter ($a \approx 10.66$ Å, Fig. 11.17). At even lower temperature as 500 °C, the clathrate phase $BaGe_5$ forms together with Ba_6Ge_{25}, α-Ge and NiGe (Fig. 11.18).

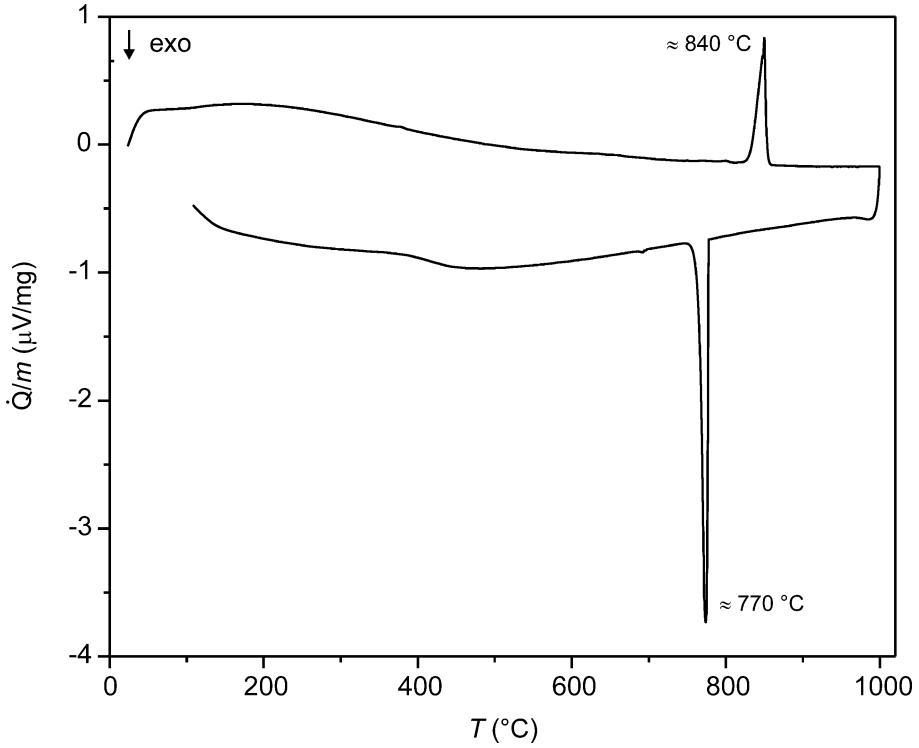

Figure 6.6: Thermal behavior of a sample with nominal composition $Ba_8Ni_{3.5}Ge_{42}$ from differential scanning calorimetry (heating/cooling rate = 10 °C/min). The onset temperatures concerning the melting and crystallization of the phase are given.

Considering the thermal behavior of clathrate phase without superstructure, the sample with nominal composition $Ba_8Ni_2Ge_{42}$ partially decomposed after annealing for one week at 720 °C to Ba_6Ge_{25} and α-Ge (Fig. 11.19). At lower temperatures of 600 °C and 500 °C, the amount of secondary phases Ba_6Ge_{25} and α-Ge increases. No $BaGe_5$ phase could be observed at 500 °C after one week annealing. Clathrate samples with higher Ni content, $x >$ 2.5, were found to be stable at all annealing temperatures lower than their melting points at least for one week. Hence, the annealing experiments together with DSC results indicate that the stability range of clathrates with respect to temperature increases with Ni content. Similar results were found for Mn and Co substituted compounds.[98]

6.4 Stability of $Ba_8Ni_4Ge_{42}$ under ambient conditions

To investigate the stability against oxidation on air, the type-I clathrate with nominal composition $Ba_8Ni_4Ge_{42}$ has been either crushed into powder and sieved to less than 63 µm or used as bulk pieces. The oxidation reactions were performed in alumina crucibles at different temperatures varying from 200 ºC to 800 ºC and for different time periods from 3 h to 72 h. The oxidized samples have been investigated initially by PXRD. $Ba_8Ni_4Ge_{42}$ was observed to be stable at 400 °C up to 72 h (Fig. 6.7). From 500 °C on, the sample started to be oxidized even after 1 h. At 800 °C after 3 h, almost no clathrate phase could

be observed. To understand the oxidation process, the products oxidized at 400 °C and 500 °C were further analyzed by SEM and TEM in collaboration with Prof. Cécile Hébert at the EPFL, Lausanne.[184] The samples were embedded in resin and cut with an ultramicrotome and the resulting clean surfaces were imaged by SEM.

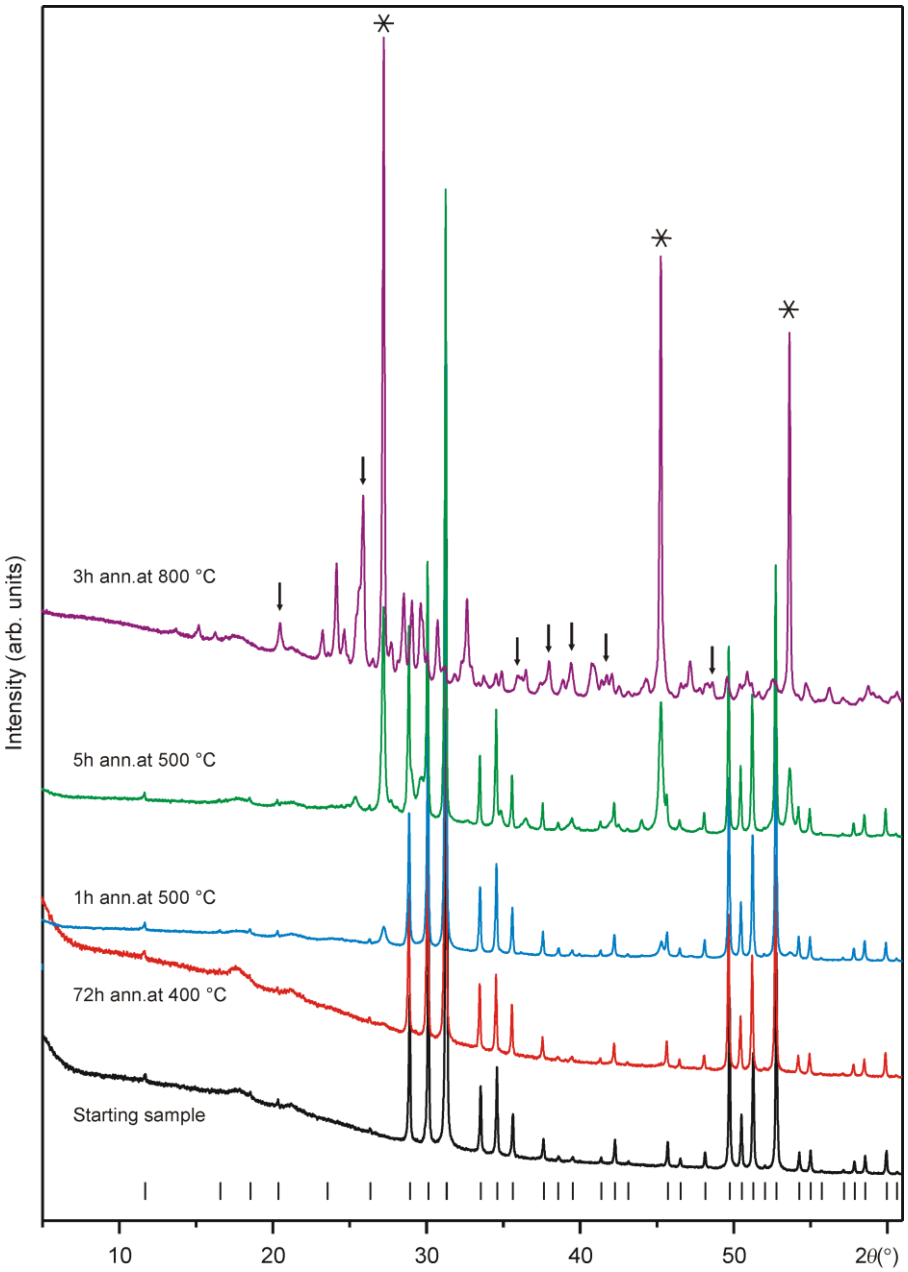

Figure 6.7: PXRD patterns of samples after oxidation of $Ba_8Ni_4Ge_{42}$ (black) on air for 72h at 400 ºC (red), 1 h at 500 ºC (blue), 5 h at 500 ºC (green) and 3 h at 800 ºC (purple) (Cu-$K\alpha_1$ radiation). Single phase $Ba_8Ni_4Ge_{42}$ sample is stable at 400 ºC for at least 72 h. At higher temperatures sample starts to be oxidized. The ticks mark the calculated position of clathrate-I phase, the arrows point to some intense reflections of alpha-quartz type GeO_2 and asterisks show the reflections of α-Ge.

From the SEM study on samples oxidized at 400 °C, a layer covering the surface was observed in which the thickness increases with the oxidation time as shown in Fig. 6.8a. The mean values presented in this figure represent average of 10 measurements. The oxide layer for shorter times of annealing was hardly detectable, whereas it could be analyzed for samples annealed for 24 h and longer time periods. Typical microstructure of the oxide layer is shown in Fig. 6.8b.

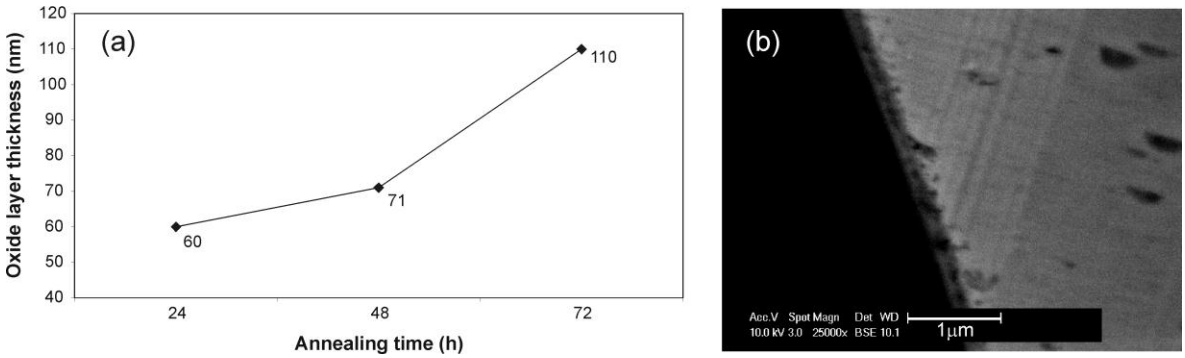

Figure 6.8: (**a**) Thickness of the amorphous layer as a function of oxidation time at 400 °C. (**b**) Typical SEM image of the amorphous layer.[184]

One grain of the sample after oxidation for 72 h has been prepared for TEM investigation using a focused ion beam. 100–200 nm thick amorphous layer of GeO_x was observed with small crystalline inclusions of Ni-rich phases (most probably NiO) at the interface with the clathrate phase (Fig. 6.9). The composition of the external layer of the amorphous phase is close to GeO_2. The part at the interface with the clathrate has the composition close to GeO. The Ba concentration was found to be very homogenous in the amorphous phase, and the atomic ratio of Ba to Ge is similar to the one of the original phase suggesting very little or no Ba diffusion.

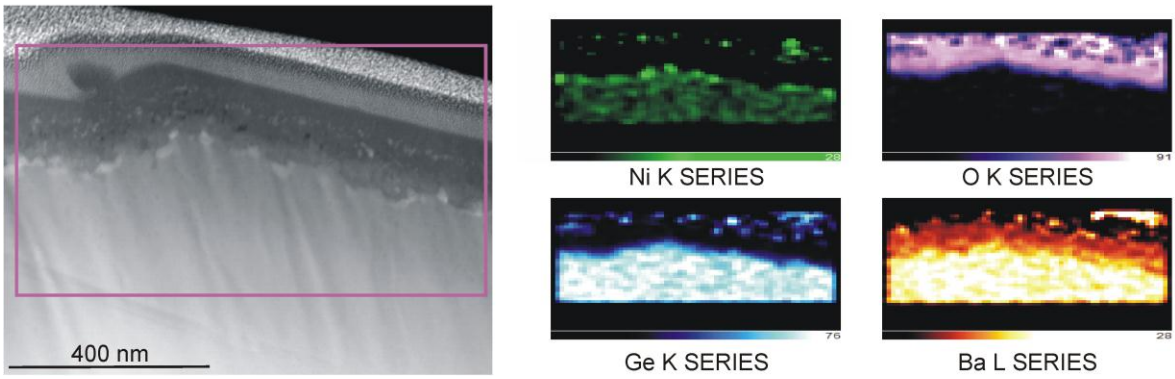

Figure 6.9: Dark scanning transmission electron microscopy (STEM) image of the FIB lamella and EDXS chemical map of the squared region (left image) showing the oxidized layer and the Ni segregation at the interface between the amorphous layer and the clathrate phase.[184]

As observed from PXRD (see Fig. 6.7), the oxidation process at 500 °C is much faster than at 400 °C. The structure of the oxide layer is quite different and constitutes higher amounts of pores as can be seen from Fig. 6.10. The increase in oxidation rate with time may indicate that the Ni segregation plays a key role in the oxidation process.

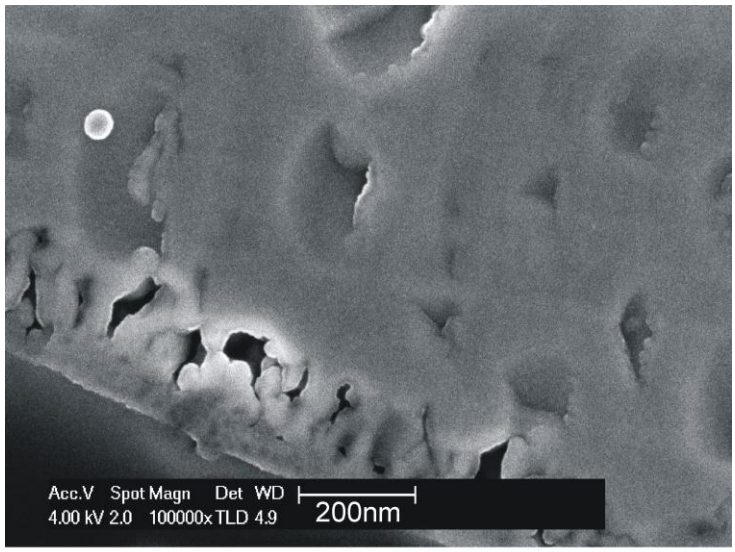

Figure 6.10: SEM image of the sample oxidized at 500 °C for 1 h showing the porous layer on the surface of the clathrate phase.[184]

6.5 Crystal structure

6.5.1 Crystal structure investigation for clathrate with superstructure

In the system Ba – Ni – Ge, compounds with very low Ni content ($x \leq 1$) form a solution with $Ba_8Ge_{43}\square_3$. $Ba_8Ge_{43}\square_3$ crystallizes in the direct subgroup $Ia\bar{3}d$ in which the lattice parameter is doubled to 2*a*. In the crystal structure of $Ba_8Ge_{43}\square_3$, a Ge site splitting is observed as discussed in chapter 4 (see Fig. 4.12) in which the structure contains in total 2 Ba (16*a*, 48*g*) and 4 Ge sites (24*d*, 24*c*, 32*e*, 96*h*). The 6*c* site (Ge1) in $Pm\bar{3}n$ splits into two sites in $Ia\bar{3}d$ as 24*d* (Ge11) and 24*c* (Ge12). From the crystal structure refinements on $Ba_8Ge_{43}\square_3$, the occupancy of Ge11 position is found to be larger than 90% and the occupancy of Ge12 position is less than 10% (see Tables 11.2-11.3). A difficulty arises for refinement of crystal structure data when Ni atoms are introduced to the Ge framework. Since X-ray scattering power of Ni and Ge atoms is very similar, it is not possible to distinguish the position of Ni atoms in the crystal structure reliably.

For the crystal structure investigation of compounds crystallizing with superstructure, a crystal was picked from the sample with nominal composition $Ba_8Ni_{0.5}Ge_{42.5}$ (a = 21.3140(2) Å) (see Table 6.1). The chemical composition was determined by WDXS to be $Ba_{8.0(1)}Ni_{0.6(2)}Ge_{42.7(2)}$ which is an average value of 10 measurement points on the bulk material. The refinement of the crystal structure was performed with the WinCSD program

package (see Table 11.9). In the first stage of the refinement, only Ba and Ge atoms are considered. For the same crystallographic positions as $Ba_8Ge_{43}\square_3$, the Ba positions are found to be fully occupied (Table 11.10). The Ge positions Ge11 and Ge12 are partially occupied as observed in $Ba_8Ge_{43}\square_3$ with occupancies around 85% and 18% Ge. Ge21 and Ge22 positions are fully occupied, while a site splitting model was introduced for Ge31 and Ge32 positions. Since all other sites except for 24*c* and 24*d* are fully occupied when refining only with Ge atoms, the possibility of Ni atoms at these sites was avoided. As the transition metal atoms are mostly found at the 6*c* site of the primitive cell, Ni atoms in superstructure model are considered to occupy 24*c* or 24*d* sites or simultaneously both of them. The partial occupancy of Ge atoms, Ni atoms, and vacancies in the same site complicates the structure analysis. For example, if the 24*d* site is regarded as fully occupied by Ni and Ge atoms, the refinement gives 0.15 Ge and 0.85 Ni occupancy meaning that 0.45 Ge and 2.55 Ni atoms per formula unit which is by far different from the WDXS result. If the Ni content at 24*d* site is fixed with the WDXS value, then the refinement gives the composition $Ba_8Ni_{0.6}Ge_{42.6}$ which is almost the same as the composition obtained from WDXS. Now, if 0.6 Ni atoms per formula unit are placed in 24*c* then only 0.05 Ge atoms remain at this site. In this case, the composition was found to be $Ba_8Ni_{0.6}Ge_{42.6}$ which is the same as considering all Ni atoms are placed in 24*c* site. The residual value R_F was refined to be around 0.028 and remains the same for both cases. Hence, it is not possible to decide the Ni position solely from the single crystal refinement. Additional information was obtained from the calculated powder patterns for the cases $Ba_8Ge_{43}Ni_x\square_{3-x}$ and $Ba_8Ni_xGe_{43-x}\square_3$ (Fig. 6.11). For the calculated powder patterns, the occupancies of the split positions Ge311, Ge312, Ge321 and Ge322 are kept constant according to our single crystal refinement result. When the Ni atoms fill the vacancy site 24*c*, the superstructure reflections gradually disappear but they are still visible for $x = 3$. The intensity of superstructure reflections is almost preserved when leaving the 24*c* site completely unoccupied (Ge atoms are replaced by Ni atoms in 24*d* site). This can be understood with the ordered arrangement of the vacancies as in the framework of $Ba_8Ge_{43}\square_3$. An important point is that the superstructure reflections at around 36.2 º and 40.1 º are quite sensitive to the occupancies of split positions Ge311, Ge312, Ge321 and Ge322. As they are fixed for the calculated powder patterns, the intensity of these reflections remains almost constant. In terms of experimental data, the intensity of all superstructure reflections becomes weaker towards high Ni contents irrespective if Ni atoms substitute Ge atoms or they fill the vacancies. Therefore, there is a more complicated arrangement of Ni and Ge atoms as well as vacancies in the framework of clathrates. The physical properties measurements on samples with the compositions $Ba_8Ge_{43}Ni_x\square_{3-x}$ and $Ba_8Ni_xGe_{43-x}\square_3$ indicate very similar results thereby not enabling us to make a clear differentiation (see section 6.6).

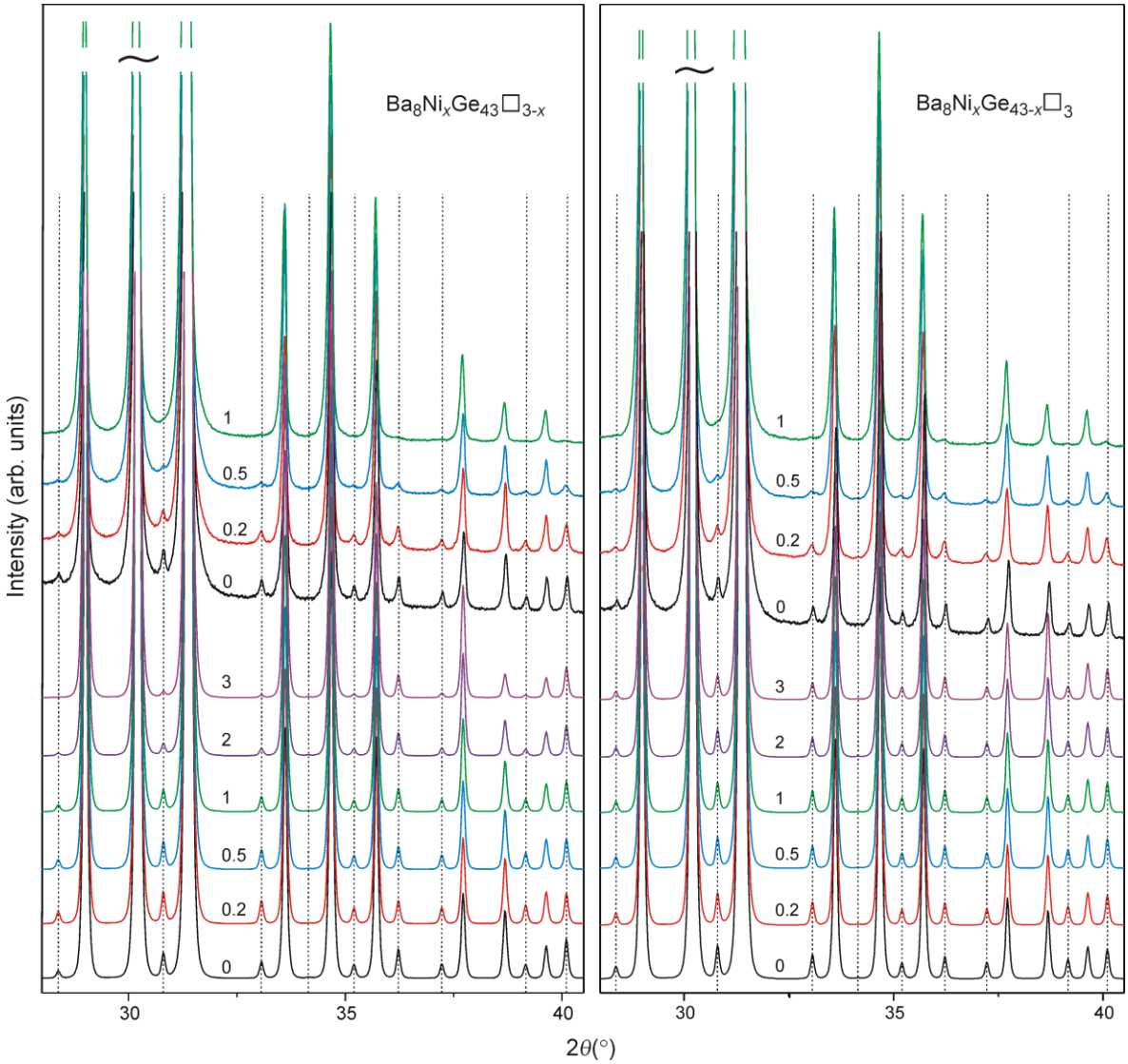

Figure 6.11: PXRD patterns calculated for the compositions $Ba_8Ge_{43}Ni_x\square_{3-x}$ (**left**) and $Ba_8Ni_xGe_{43-x}\square_3$ (**right**) with $0 \leq x \leq 3$ (**bottom**) (Cu-$K\alpha_1$ radiation). The experimental patterns are shown on top of the calculated ones for $0 \leq x \leq 1$. The dashed lines point to the positions of superstructure reflections.

6.5.2 Total energy calculations on $Ba_8NiGe_{42}\square_3$ and $Ba_8NiGe_{43}\square_2$

Since crystal structure analysis as well as physical properties measurements do not give a clear hint for a reasonable model for compounds with superstructure, the clathrates in this phase range are also investigated by first-principles total energy calculations for two compositions $Ba_8NiGe_{42}\square_3$ and $Ba_8NiGe_{43}\square_2$. The aim of the total energy calculations is to understand which configuration is energetically more favorable if one Ni atom is introduced for the framework of clathrate-I with superstructure. To deal with the partial occupancy of the 24*c* and 24*d* Wyckoff positions of the space group $Ia\bar{3}d$, the most suitable subgroup of $I4_1/acd$ (no. 142) was chosen. In this subgroup the 24*c* site splits into

16*e* and 8*b*, and 24*d* site into 16*e* and 8*a* positions. Total energies of all possible configurations within this space group for 1 Ni, 2 Ge, 3 □ and 1 Ni, 3 Ge, 2 □ per formula unit occupying the 24*c*- and 24*d*-derived sites are computed by employing FPLO method.

For the clathrates with low Ni content, a convenient starting point for analysis is the binary $Ba_8Ge_{43}\square_3$ clathrate. Experimentally, Ge occupancy of the 24*d* and 24*c* sites are about 90% and 10%, respectively as discussed in Chapter 4. According to our first-principles calculations the model with all 24*d* sites occupied with Ge has a lower energy than the model with all 24*c* sites occupied with Ge by an amount 1.6 meV per atom. Hence, both experimental and theoretical findings imply that in $Ba_8Ge_{43}\square_3$ having most of the 24*c* sites empty is energetically more favorable. Now, $Ba_8NiGe_{42}\square_3$ can be considered as one Ni atom replacing one Ge atom leaving the vacancy number unchanged with respect to $Ba_8Ge_{43}\square_3$. The lowest total energy is obtained for the configuration where Ni and Ge atoms fully occupy the 24*d*-derived sites so that all 24*c*-derived sites remain empty. However, the case with Ge at the 16*e* split from 24*d* and Ni at 8*b* (split from 24*c*) is also a very close contender: it is higher in energy by only 0.26 meV per atom, an energy difference below the accuracy level of ~ 0.5 meV per atom. This result means that as long as Ge atoms occupy most of the 24*d* sites, energetically it does not matter much whether the Ni atoms are located at 24*d*- or 24*c*-derived sites. Hence, the experimental difficulties in determining the Ni location and occupancy seem to have a total-energy related dimension, as well. $Ba_8NiGe_{43}\square_2$, on the other hand, can be considered as one Ni atom occupying an empty site leaving the number of Ge atoms unchanged. For this clathrate the lowest-energy configuration is the one where all 24*d*-derived sites are occupied by Ge, and Ni atoms go to the 8*b* Wyckoff position. This configuration is not contested by the other configurations: the second best case (with 52 meV per atom higher energy) is obtained when Ni replaces Ge at the 8*a* position (split from 24*d*) and the replaced Ge atoms occupy the 8*b* sites. The highest energy occurs when all 24*c* sites are occupied by Ge atoms (154 meV per atom higher). Now the discussion can be made on which reaction path is energetically more favorable if one Ni atom is added per formula unit to the binary $Ba_8Ge_{43}\square_3$:

$$Ba_8Ge_{43}\square_3 + Ni \rightarrow Ba_8NiGe_{43}\square_2 + \Delta E_1 \tag{6.1}$$

$$Ba_8Ge_{43}\square_3 + Ni \rightarrow Ba_8NiGe_{42}\square_3 + Ge + \Delta E_2 \tag{6.2}$$

The elemental solid energies are computed for ferromagnetic fcc Ni and Ge in the diamond structure. The formation energies ΔE_1 and ΔE_2 are 807 and 15 meV per formula unit, respectively. Although the former value is a solid number, the latter is within the overall

error bar of 0.5 meV per atom. Thus, formation of $Ba_8NiGe_{43}\square_2$ is clearly favored, while that of $Ba_8NiGe_{42}\square_3$ is not so clear as far as total electronic energies are concerned. Another way of comparing these two clathrates is to consider the following equation:

$$Ba_8NiGe_{42}\square_3 + Ge \rightarrow Ba_8NiGe_{43}\square_2 + \Delta E \qquad (6.3)$$

The above values give ΔE = 0.79 eV per formula unit which means that $Ba_8NiGe_{43}\square_2$ is energetically more favorable than $Ba_8NiGe_{42}\square_3$. Hence although X-ray diffraction analyses and physical properties do not give any hint for the differentiation of compositions discussed above, total energy studies suggest that Ni atoms preferentially occupy the empty sites of $Ba_8Ge_{43}\square_3$ rather than substituting Ge atoms.

6.5.3 Crystal structure of single crystalline $Ba_8Ni_{3.5}Ge_{42.1}\square_{0.4}$

All reflections of the PXRD pattern of $Ba_8Ni_{3.5}Ge_{42.1}\square_{0.4}$ were indexed with the space group $Pm\bar{3}n$ (no. 223, a = 10.6798(2) Å). No super-cell reflections were observed as in the case of $Ba_8Ge_{43}\square_3$. In the first step of the structure refinement, the structure model of Cordier and Woll was applied in which all (six) Ni atoms was assigned to the site 6*c* with the overall composition "$Ba_8Ni_6Ge_{40}$".[61] After refinement of the anisotropic displacement parameters, U_{aniso}, a relatively low residual value (on F^2) of 0.026 was obtained for 1409 independent reflections. The large U_{aniso} value of the Ba2 atoms at site 6*d* can be alternatively described by split positions at 24*k*. The full occupancy of 6*c* site by Ni atoms cannot be *a priory* excluded from the occupancy refinement of this site. The distance between Ni and Ge atoms *d*(Ni–Ge) ≈ 2.39 Å compares well to those of binary compounds (*e.g.*, NiGe [185]) and is too short for a Ge–Ge distance of typically ≈ 2.5 Å. On the other hand, a sizable anisotropy was observed in the displacement parameter of the Ge atoms at 24*k* (Fig. 6.12). Similar case has previously been observed for the binary clathrate-I $Cs_8Sn_{44}\square_2$,[96] and the transition metal substituted type-I clathrates $Ba_8TM_xGe_{46-x-y}\square_y$ (*TM* = Cu,[104] Zn,[107, 108] Pd,[102] Pt,[103] *etc.*). The value of U_{aniso} at 24*k* was correlated to the amount of vacancies at the 6*c* site. U_{aniso} of 24*k* for $Ba_8Ni_{3.5}Ge_{42.1}\square_{0.4}$ can be described by a superposition of distances Ge(6*c*)–Ge(24*k*), Ni(6*c*)–Ge(24*k*), and □ (6*c*)–Ge(24*k*).

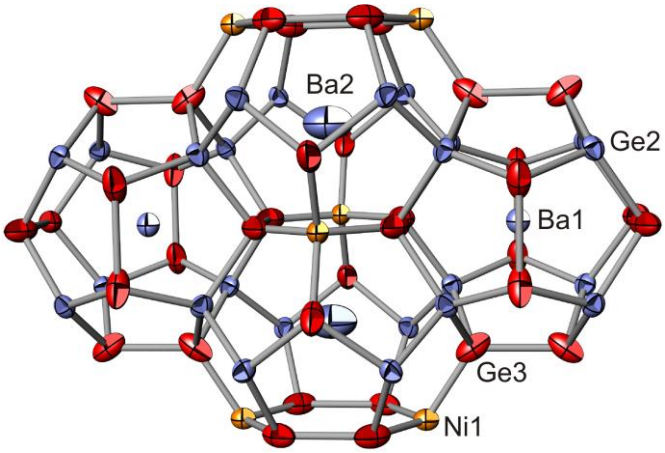

Figure 6.12: Atomic displacement ellipsoids of $Ba_8Ni_{3.5}Ge_{42.1}\square_{0.4}$ for a structure model of Cordier and Woll.[61] Considering full occupancy by Ni atoms (light/orange) at the 6*c* site, the composition "$Ba_8Ni_6Ge_{40}$" is obtained in which Ge2 and Ge3 positions are shown by smaller ellipsoids/blue and larger ellipsoids/red, respectively.[22, 183]

As discussed above, the mixed occupancy of 6*c* with Ge atoms, Ni atoms, and vacancies complicates the structure analysis, in particular due to the similar atomic scattering factors of Ni and Ge. Therefore, in the next step of the structure refinement the number of Ni atoms per unit cell was fixed to the value obtained from WDXS analysis. All Ni atoms were assumed to be located at the site 6*c* (Tables 11.11-11.12). Equal displacement parameters were considered for Ni1 and Ge1 positions. The number of Ge1 atoms was refined to be 2.1 at the position 6*c* so that 0.4 vacancies (~7 %) remain at 6*c*. To explicitly account for the mixed occupancy at 6*c*, the mean electron density around 24*k* site was described by three Ge positions Ge31 (if 2.1 Ge at 6*c*), Ge32 (if 3.5 Ni at 6*c*), and Ge33 (if 0.4 □ at 6*c*). To obtain a self-consistent data set, the atomic coordinates, displacement parameters, and the occupancies (except for Ni and Ba) were repeatedly refined until good agreement between the structure model and the experimental data was obtained. The distances of approximately 2.2 Å, 2.3 Å, and 2.5 Å were found for Ge33–□, Ge32–Ni, and Ge31–Ge which are in good agreement with the distance Ge–□ in $Ba_8Ge_{43}\square_3$ (2.13 – 2.18 Å),[15] the Ge–Ni distances in NiGe (2.32 Å, 2.39 Å, and 2.48 Å),[185] and the Ge–Ge distance in α-Ge (2.45 Å)[186] (Fig. 6.13, Table 11.13).

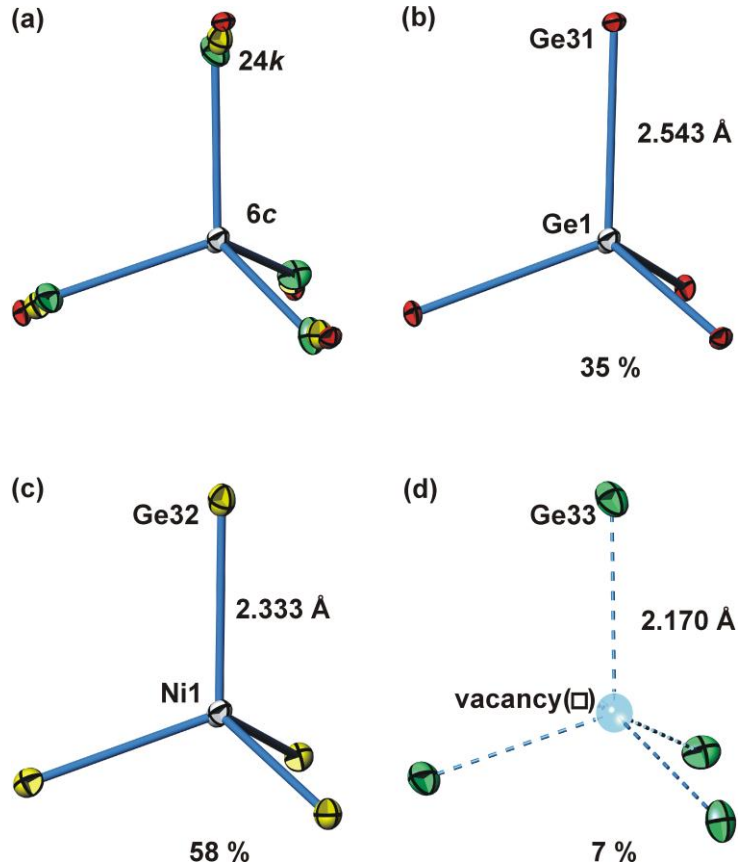

Figure 6.13: Local atomic arrangements in $Ba_8Ni_{3.5}Ge_{42.1}\square_{0.4}$ for vacancy (□), Ni or Ge at site 6*c*.[22, 183] The underlying refinement procedure is described in the text.

6.6 Physical properties

Physical properties of polycrystalline samples and single crystalline $Ba_8Ni_{3.5}Ge_{42.1}\square_{0.4}$ wete determined. As polycrystalline materials, steel-quenched samples (up to $x \leq 3.5$) and samples annealed at 700 °C (x > 3.5) were used. On each figure, the nominal compositions of the samples are provided (see Tables 6.1-6.3).

Fig. 6.14 shows the temperature dependence of the magnetic susceptibility χ for selected samples. Regardless of the composition, the χ values are negative indicative of diamagnetic behavior as usually encountered in type-I clathrates. Towards low temperatures, the susceptibility rises slightly leading to positive values at 2 K for $Ba_8Ge_{43}\square_3$. These upturns are most likely due to very small amounts of paramagnetic impurities which are present in all samples.

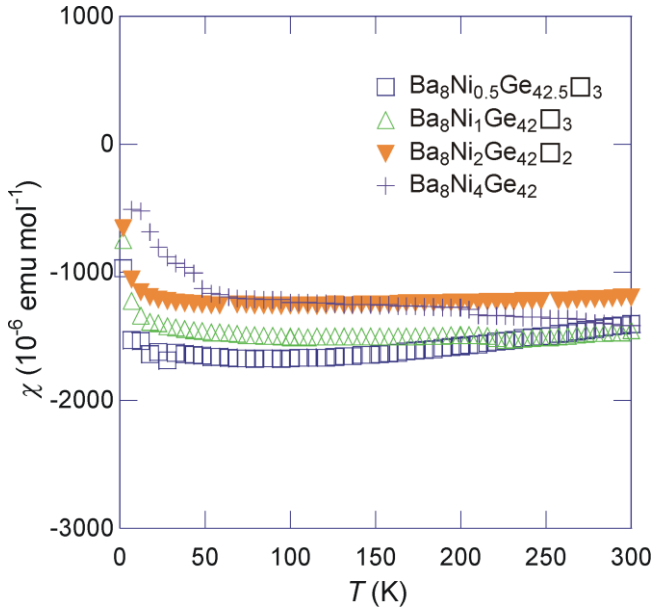

Figure 6.14: Temperature dependence of χ of $Ba_8Ni_x\square_yGe_{46-x-y}$.

As observed for the other clathrate compounds, the measured χ values are significantly higher in absolute values than those calculated from diamagnetic increments. For example for $Ba_8Ni_1Ge_{42}\square_3$, a distinctly lower susceptibility of $\chi_{calc} \approx -927 \times 10^{-6}$ emumol^{-1} ($\chi_{meas} \approx -1400 \times 10^{-6}$ emumol^{-1} at 300 K) is calculated based on the diamagnetic increments of Ba^{2+} (-32×10^{-6} emumol^{-1}), Ni^{2+} (-12×10^{-6} emumol^{-1}) and Ge atoms (-15.7×10^{-6} emumol^{-1}).[169, 170] One possible explanation could be the contribution of Ge^- anions for which no data were reported. Another contribution to experimental susceptibilities can be due to so called "Landau diamagnetism" which arises from free electrons. An estimation of the diamagnetic values, χ_{dia}, can be obtained via Pauli susceptibility contribution, χ_{Pauli}, which can be found as:

$$\chi_{\text{Pauli}} = 2.376 \times 10^{-6} \times N(E_{\text{F}}) \tag{6.4}$$

where χ_{Pauli} and $N(E_F)$ are expressed in emu mol^{-1} and states Ry^{-1} per formula unit, respectively. Using the calculated $N(E_F)$ value of 61.90 states Ry^{-1}per formula unit for $Ba_8Ni_1Ge_{42}\square_3$, the χ_{Pauli} value can be obtained to be around 147×10^{-6} emu.mol^{-1}. Diamagnetic contribution due to free electrons is then calculated by:[187]

$$\chi_{\text{dia}} = -\frac{\chi_{\text{Pauli}}}{3} \tag{6.5}$$

which gives the value around -49×10^{-6} emu.mol^{-1} still a nonnegligible correction but far

away from explaining the apparent difference between expected and calculated values of diamagnetism in investigated clathrates. Other contributions to the experimental diamagnetism values would be diamagnetic impurities present in the samples or molecular-ring currents as discussed in section 4.5.

The temperature dependence of the electrical resistivity ρ is shown in Fig. 6.15. The ρ values first decrease with the addition of Ni up to x = 0.5. The values measured in the samples with x = 0.8 and 1 are similar but slightly higher. This behavior shows that increasing the Ni content first drives the system to a more metallic state up to x = 1 where a continuous increase of the ρ values with x occurs. The peculiar temperature dependence together with the high ρ values observed in the parent compound $Ba_8Ge_{43}\square_3$ was attributed to the contribution of both holes and electrons to the electrical conduction. Upon substituting Ge by Ni, the maximum in $Ba_8Ge_{43}\square_3$ centered near 250 K is strongly suppressed although still discernable in the temperature dependence of the samples with x = 0.2, 0.5, 0.8 and 1. This behavior is therefore consistent with the idea that holes and electrons are still involved in the electrical conduction of these compounds. At higher Ni contents (x > 1), a linear temperature dependence can be observed indicative of a metallic character (x = 3). For x = 3.5, the metallic-like behavior turns into a semiconducting-like dependence below 100 K and shows that the system is approaching a semiconducting state which occurs for the sample with x = 4.2. The single crystalline $Ba_8Ni_{3.5}Ge_{42.1}\square_{0.4}$ shows similar resistivity behavior compared to the polycrystalline material with x = 3.5.[22, 183] The values are slightly smaller in single crystal due probably to absence of grain boundaries and the semiconducting transition takes place at a lower temperature of 10 K.

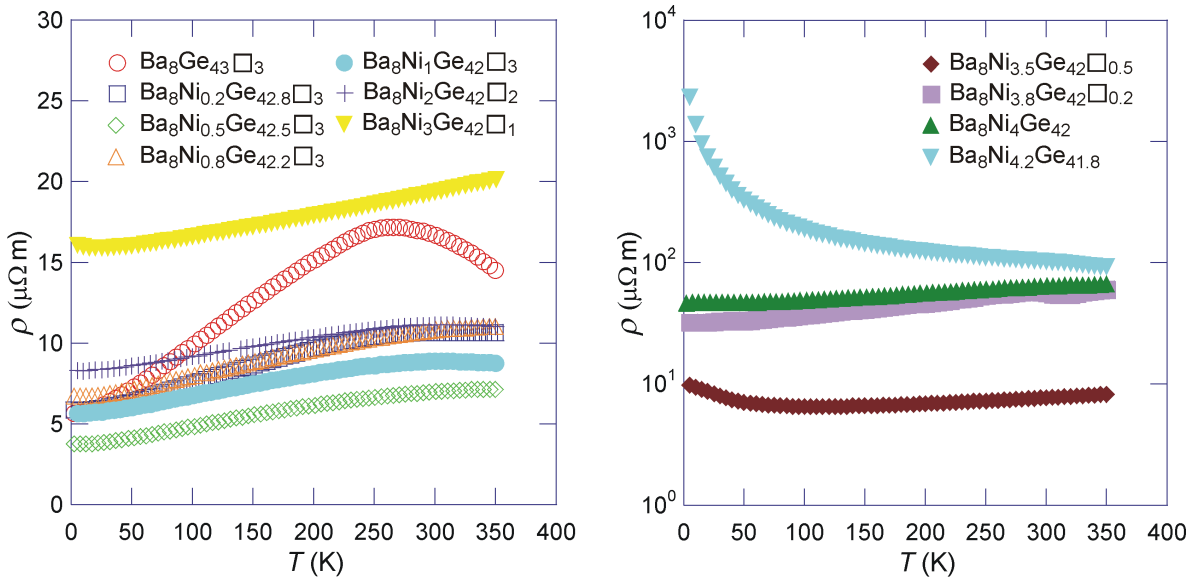

Figure 6.15: Temperature dependence of the electrical resistivity ρ of $Ba_8Ni_x\square_yGe_{46-x-y}$ at low temperatures.

Fig. 6.16 compiles the high-temperature electrical resistivity data. At low Ni contents ($x < 2$), ρ decreases with increasing temperature resembling a semiconducting behavior. These dependences contrast with those observed at low temperature indicating a typical metallic-like behavior. In $Ba_8Ge_{43}\square_3$, this resembling metal-insulator transition is related to the contribution of both holes and electrons to the electrical conduction. As revealed by the thermopower data, the simultaneous presence of both types of carriers extends over a large window of Ni concentration thereby explaining the behavior of ρ. At higher Ni contents ($x > 3$), a metallic-like behavior can be observed. A decrease of the ρ values, occurring above 600 K for the samples with x = 3.5, 3.8 and 4, is most likely due to minority carrier effects as can be seen in the thermopower and thermal conductivity data (see Fig. 6.19 and 6.25). The sample with x = 4.2 displays a semiconducting behavior typified by a decrease of ρ in the whole temperature range consistent with the high thermopower values measured.

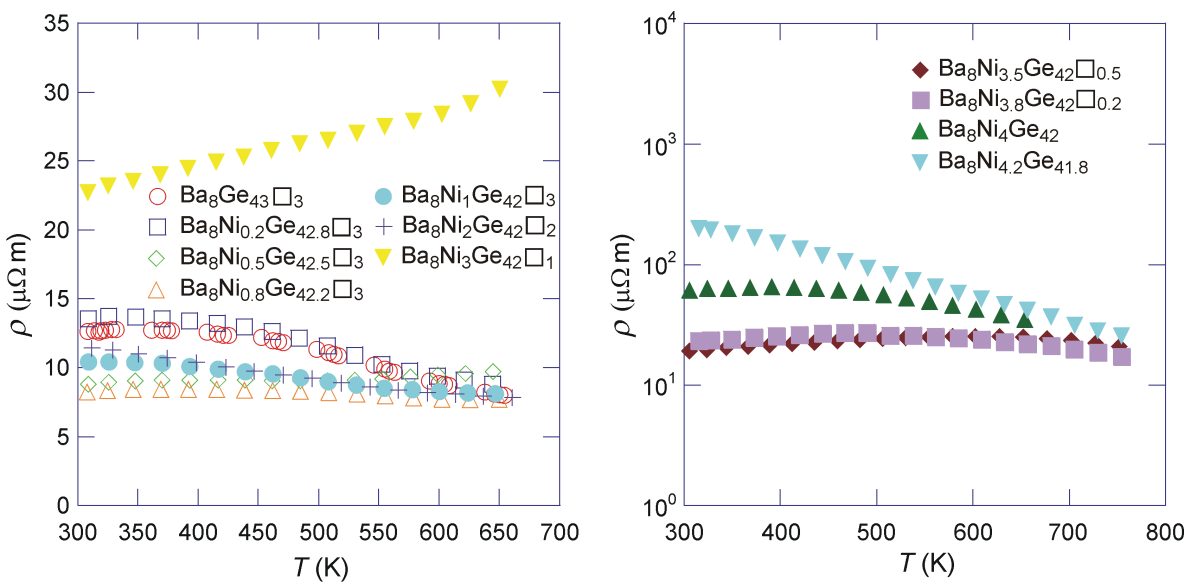

Figure 6.16: Temperature dependence of ρ of $Ba_8Ni_x\square_yGe_{46-x-y}$ at high temperatures.

The temperature dependence of the thermopower α at low Ni concentrations ($x < 0.8$) resembles that of the parent $Ba_8Ge_{43}\square_3$ characterized by two crossovers from n- to p-type conduction (Fig. 6.17). This complex temperature dependence which originates from the simultaneous presence of holes and electrons is preserved upon alloying with Ni up to x = 0.5. However, a smooth evolution towards pure n-type conduction occurs as x increases. For samples with x = 0.2 and x = 0.5, the low-temperature maximum in $|\alpha|$ is washed out while the maximum centered around 225 K still exists. A crossover from p- to n-type conduction then occurs near room temperature in both compounds. Upon introducing more

Ni, this maximum is shifted to lower temperatures (x = 0.5) and disappears for x = 0.8. For samples with x = 0.8 and x = 1.0, the thermopower values remain negative in the whole temperature range and are close to zero below 150 K promoting the idea of a compensation of the hole and electron contributions to the thermopower. The increase in the $|\alpha|$ values with increasing Ni content above x = 1 is consistent with a smooth evolution from a metallic state to a semiconducting behavior reached at sample with x = 4. At high Ni contents (x > 3), the thermopower exhibits a linear temperature dependence indicative of a purely diffusive nature. A slight increase in the Ni concentration from x = 4 to x = 4.2 drives the system to a p-type conduction characterized by positive thermopower values. The low-temperature curvature observed for x = 4.2 is consistent with the semiconducting-like nature of this compound. Band gap energy E_g can be estimated using Eq. 3.8 for the sample with x = 4.2 which results in a value of ≈ 65 meV.

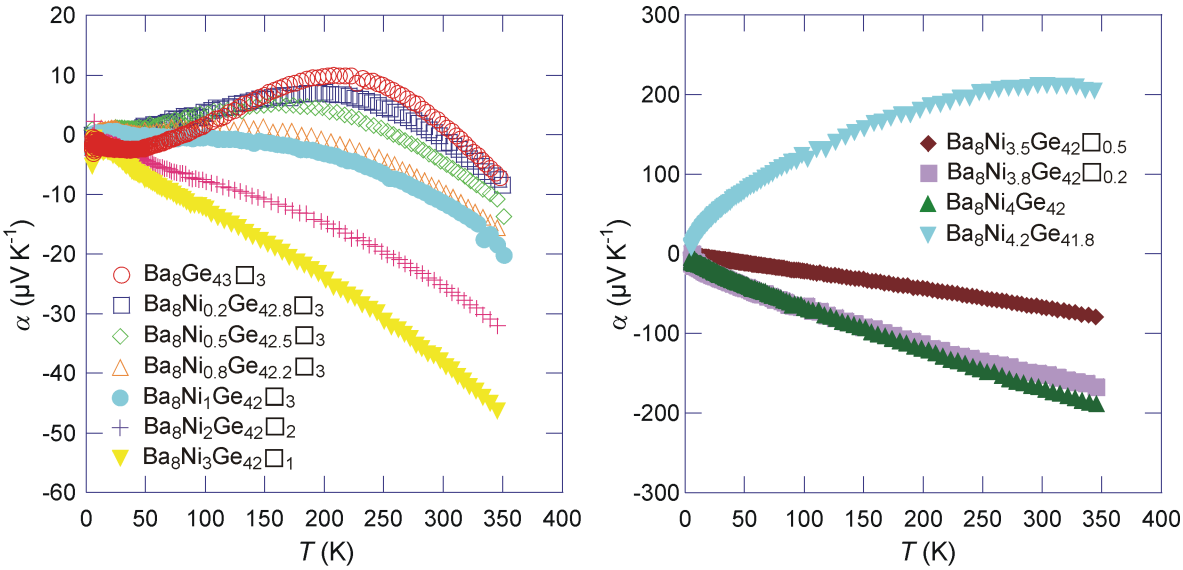

Figure 6.17: Temperature dependence of α of $Ba_8Ni_x\square_yGe_{46-x-y}$ at low temperatures.

As mentioned in preceding sections, our structural and chemical characterizations did not allow us to determine whether Ni fills vacancies or solely substitutes Ge at low Ni contents. The thermopower strongly depends on the details of the electronic band structure and therefore offers a sensitive probe to further shed light on this issue. Fig. 6.18 shows $\alpha(T)$ for two series of samples with x = 0.5 and x = 1.0. As can be observed, both compositions lead to similar temperature dependences and values within our experimental accuracy.

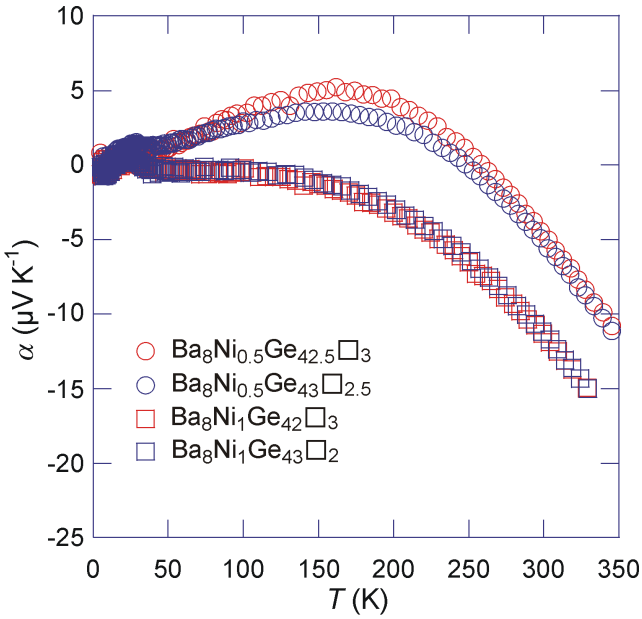

Figure 6.18: Comparison of temperature dependence of α for samples prepared with the compositions $Ba_8Ni_xGe_{43-x}\square_3$ and $Ba_8Ni_xGe_{43}\square_{3-x}$.

At high temperatures, $|\alpha|$ increases linearly up to 650 K for samples with $0.2 \leq x \leq 3$ regardless of the composition (Fig. 6.19). The measured values increase with the Ni content as expected from a decrease of the carrier concentration. No signature of minority carrier activation can be observed which is consistent with the metallic state of these samples. This does not hold true however for Ni contents higher than $x = 3.5$ for which a decrease in $|\alpha|$ with increasing temperature occurs. Compared to the single crystalline $Ba_8Ni_{3.5}Ge_{42.1}\square_{0.4}$ in which $|\alpha| \approx 120\ \mu VK^{-1}$ at 650 K,[22, 183] polycrystalline material with $x = 3.5$ had slightly lower maximum value of $|\alpha| \approx 100\ \mu VK^{-1}$ at the same temperature. This might be due to very small difference in the composition of the clathrate phase which could not be identified within the resolution of WDXS analysis. Furthermore, the large values observed for the samples with $x = 3.8$, 4.0 and 4.2 are consistent with a highly-doped semiconducting state.

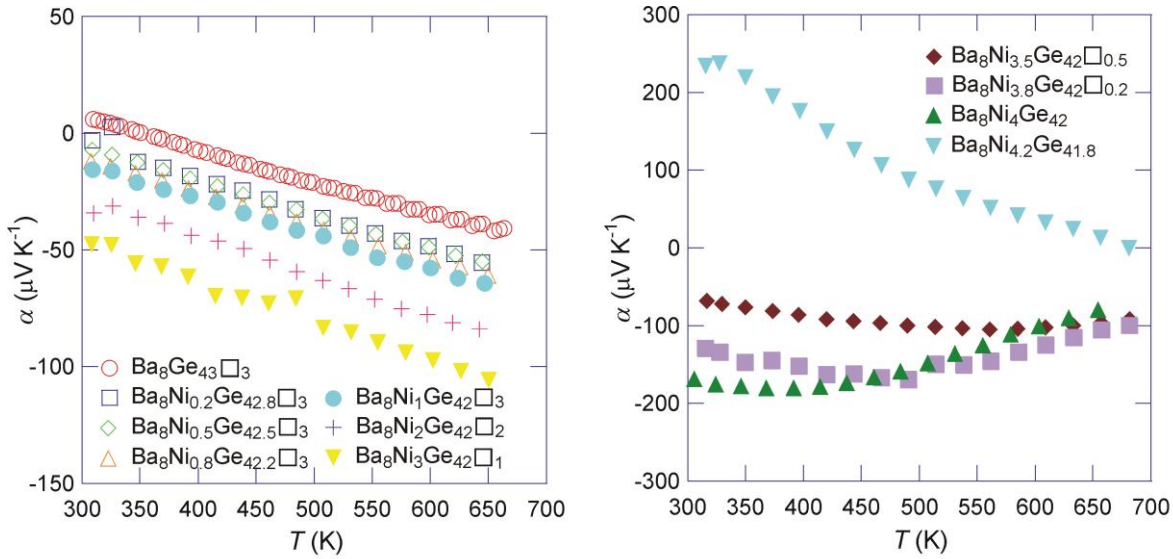

Figure 6.19: Temperature dependence α of $Ba_8Ni_x\square_yGe_{46-x-y}$ at high temperatures.

The temperature dependence of the specific heat, C_p, between 1.9 and 500 K is plotted in Fig. 6.20 for the illustrative sample $Ba_8NiGe_{42}\square_3$. Above 300 K, the C_p values increase with increasing temperature and deviate from the theoretical value according to the Dulong-Petit law (Eq. 3.11). The Sommerfeld coefficient, γ, which enables to probe the variations in the density of states at the Fermi level as a function of the Ni content, was inferred from an analysis of the low temperature specific heat data via Eq. 3.15 (Fig. 6.21). Below x = 1.0, γ varies between ~ 25 up to 42 $mJmol^{-1}K^{-2}$ in a non-linear fashion, the highest value being achieved in the x = 0.8 sample. Above x = 1.0, γ tends to decrease monotonically with increasing the Ni content up to x = 4 where a minimum value of 4 $mJmol^{-1}K^{-2}$ is reached. This behavior is consistent with both the thermopower and electrical resistivity data which show that the system evolves from a metallic state towards a semiconducting state. In the *p*-type region, the γ values then slightly increase with the Ni content reflecting a shift of the Fermi level deeper inside the valence bands.

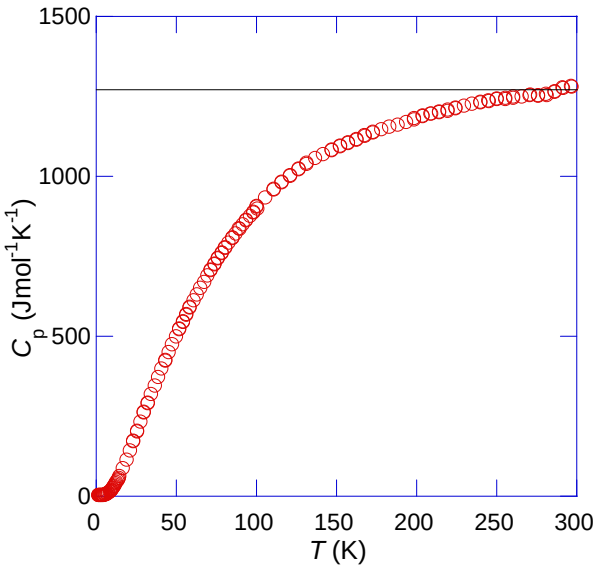

Figure 6.20: Temperature dependence of C_p, of the illustrative sample $Ba_8NiGe_{42}\square_3$. The solid black line stands for the theoretical value following the Dulong-Petit law.

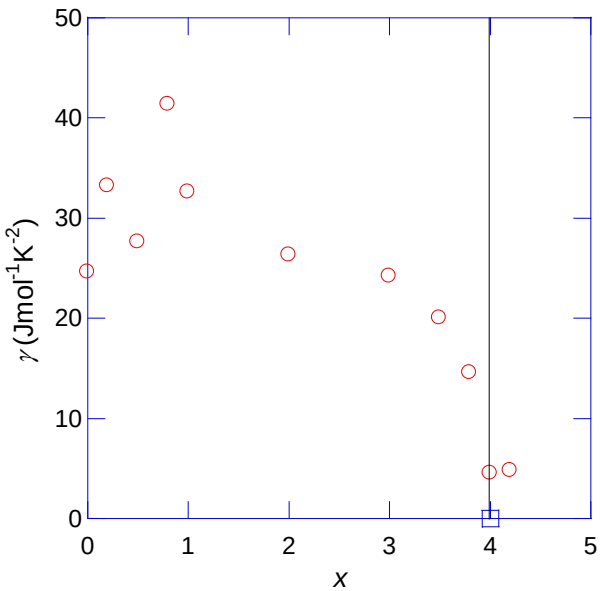

Figure 6.21: Sommerfeld coefficient, γ, of $Ba_8Ni_x\square_yGe_{46-x-y}$ as a function of x. The symbol □ refers to the zero value expected in a semiconducting state.

The β coefficient is related to the Debye temperature, θ_D, via Eq. 3.16. Using the number of atoms derived from WDXS compositions, the θ_D values can be then calculated and are depicted in Fig. 6.22 as a function of the Ni content.

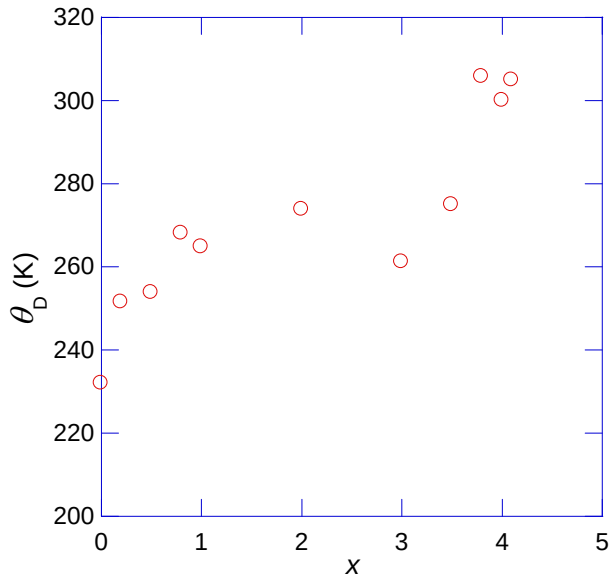

Figure 6.22: Debye temperature θ_D of $Ba_8Ni_x\square_yGe_{46-x-y}$ as a function of x.

As can be observed, the θ_D values increase upon substituting and vary in the 255 – 275 K temperature range for $2 \leq x \leq 3.5$. Above $x = 3.5$, the Debye temperatures inferred become significantly higher reaching ~ 300 K. This intriguing feature might be caused by complex disorder introduced by mixed occupancy of Ni, Ge and vacancies in the crystal structure resulting in variations in the bonding scheme at high Ni contents.

The temperature dependence of the total thermal conductivity κ is shown in Fig. 6.23. The temperature dependence of the binary compound features a pronounced low temperature dielectric maximum followed by a strong decrease typical of crystalline materials. A small addition of Ni then results in a strong drop in the thermal conductivity values which then only slightly vary upon further alloying. The amplitude of the dielectric maximum observed at low temperatures is concomitantly strongly lowered by the presence of Ni. Since the superstructure is preserved up to $x = 1$, these variations may then be related to enhanced disorder and strain effects originating from distortions of the framework when Ge is substituted by Ni. Above $x = 1$, the thermal conductivity further decreases as the crystal structure changes from superstructure to primitive cell. This behavior is a direct consequence of the increase in the electrical resistivity values thereby decreasing the electronic contribution to the thermal conductivity. The values measured in the samples with $x = 2$ and 3 thus almost entirely reflect the lattice thermal conductivity. This is further corroborated by the temperature dependence of the lattice thermal conductivity, κ_l, obtained after subtracting the electronic contribution using the Wiedemann-Franz law (Eq. 3.5, Fig. 6.24). The κ_l values of the Ni-substituted compounds are significantly lower than that of $Ba_8Ge_{43}\square_3$. κ_l remains practically unchanged when the Ni content spans the range $0.2 \leq x \leq 3.0$ and is in line with the values encountered in other type-I clathrates.

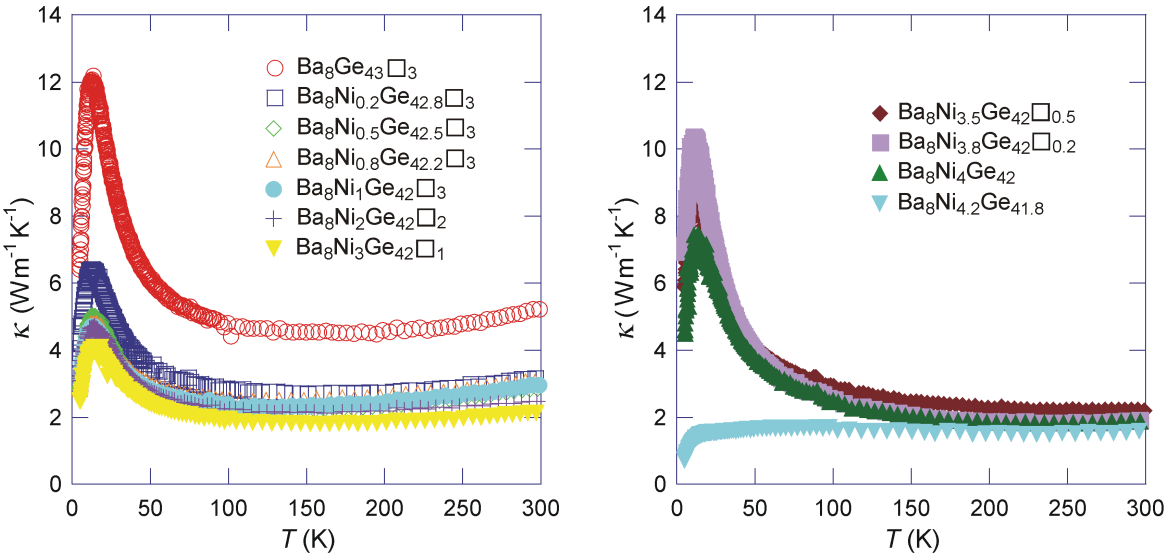

Figure 6.23: Temperature dependence of κ of $Ba_8Ni_x\square_yGe_{46-x-y}$ at low temperatures.

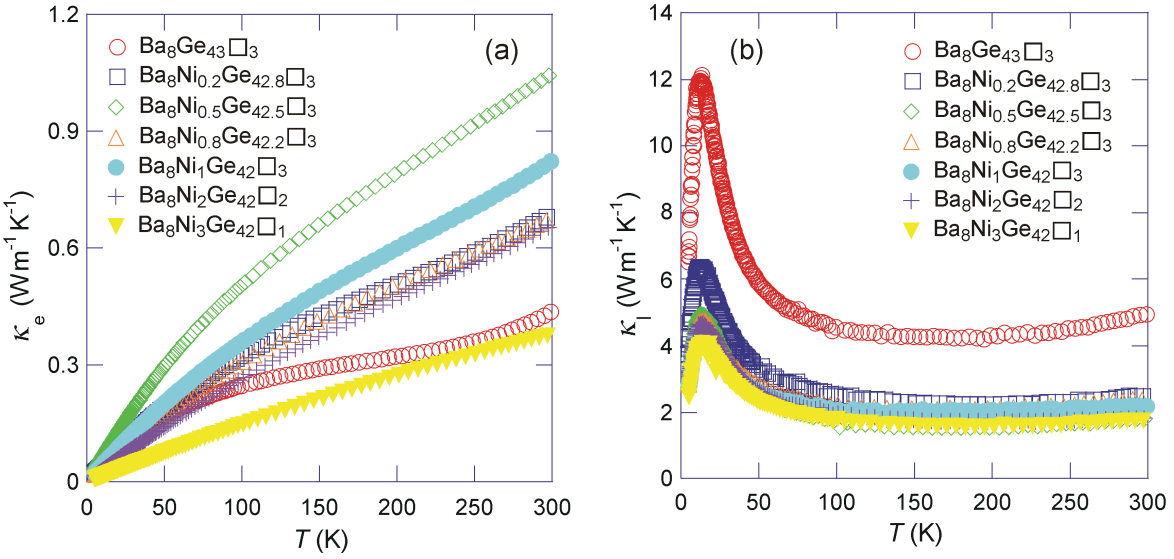

Figure 6.24: Temperature dependence of the electronic (κ_e, **a**) and lattice (κ_l, **b**) thermal conductivity of $Ba_8Ni_x\square_yGe_{46-x-y}$ at low temperatures.

Similar thermal conductivity values are observed in the samples with x = 3.5, 3.8 and 4.0 which feature a more pronounced dielectric maximum than in the samples with x = 2.0 and 3.0. This may be attributed to the annealing treatment which probably increases the crystallinity of the samples and leads to variations in the microstructure (*e.g.* grain size) with respect to the steel-quenched samples. A slight increase in the Ni content from x = 4.0 to x = 4.2 then results in a drastic suppression of the low-temperature maximum. The observed temperature dependence mimics that of glass-like systems and is consistent with prior investigations on *p*-type Ni-substituted clathrates.[182] This disappearance might be related to the presence of secondary phases as revealed by our chemical analyses, the

dielectric maximum being sensitive to the purity as well as the amount of disorder in the sample. Alternatively, this behavior might be also a consequence of the presence of Ni atoms on both the 6*c* and 24*k* sites of the crystal structure. This double occupancy may enhance the disorder in the unit cell giving rise to the suppression of this maximum as already observed in the $Ba_8Au_xSi_{46-x}$ compounds.[188]

Fig. 6.25 shows the temperature dependence of the thermal conductivity obtained form thermal diffusivity measurements by use of Eq. 3.18. At low Ni contents ($x < 3$), κ slightly increases with increasing temperature reflecting the dominant electronic contribution. The increase observed at high Ni contents, however, originates from the thermal activation of the minority carriers across the band gap. The coincidence of the upturn near 450 K with the maximum in the thermopower data further supports this scenario.

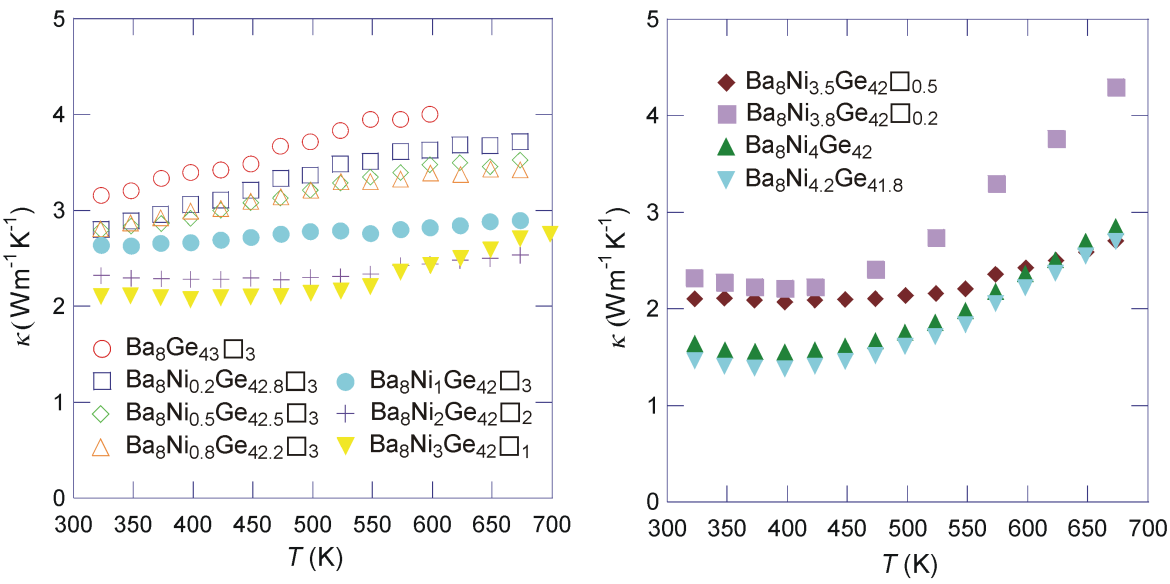

Figure 6.25: Temperature dependence of κ of $Ba_8Ni_x\square_yGe_{46-x-y}$ at high temperatures.

Fig. 6.26 shows the temperature dependence of the dimensionless figure of merit *ZT* for selected samples. The maximum *ZT* values achieved reach ~ 0.2 at 500 and 650 K for the samples with $x = 2$ and 3.8, respectively, which is very close to the value obtained for single crystalline $Ba_8Ni_{3.5}Ge_{42.1}\square_{0.4}$ ($ZT \approx 0.21$ at 680 K).[22, 183] The decrease in the values at high temperatures originates from the decrease in the thermopower due to minority carrier effects. It is interesting to notice that the above-mentioned maximum value is also reached in the sample with $x = 2$ *i.e.* in a composition driving the system away from the semiconducting state. This rather surprising result is a direct consequence of the decrease in the electrical resistivity values at high temperatures.

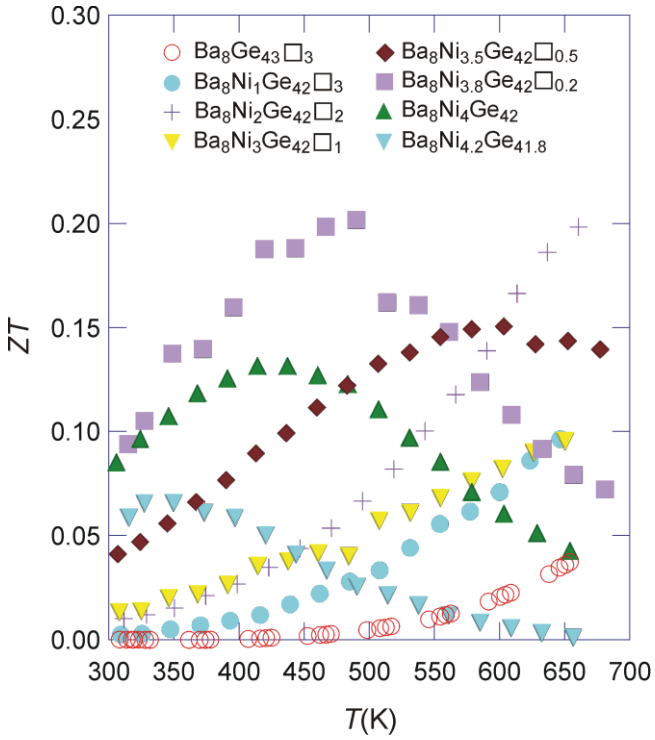

Figure 6.26: Temperature dependence of *ZT* of $Ba_8Ni_x\square_yGe_{46-x-y}$.

6.7 Conclusions

Type-I clathrate phase $Ba_8Ni_x\square_yGe_{46-x-y}$ constitutes two existence fields depending on Ni content: compounds with low Ni content, $0 < x \leq 1$, are considered as solution of Ni in the binary $Ba_8Ge_{43}\square_3$ and compounds with higher Ni content, $1 < x \leq 4.2$, crystallize in the space group $Pm\bar{3}n$ in which the chemical composition derives from a hypothetic compound "$Ba_8Ge_{42}\square_4$". Almost single phase polycrystalline samples were prepared either after steel-quenching or annealing at 700 °C for 4 days. By using polycrystalline $Ba_8Ni_4Ge_{42}$ as precursor material, single crystalline $Ba_8Ni_{3.5}Ge_{42.1}\square_{0.4}$ was grown using the Bridgman method by Nguyen *et al.* in Frankfurt. The increase in lattice parameter of compounds is associated with the change in Ni content determined by microprobe analyses (EDXS, WDXS). Compounds towards lower Ni content are high temperature phases which show a lower stability range ΔT with decreasing Ni content, whereas compounds with high Ni content are stable at temperatures lower than 700 °C. According to single crystal X-ray diffraction results, Ni atoms in $Ba_8Ni_{0.6}Ge_{42.6}\square_{2.8}$ are considered to occupy the 24*c* and/or 24*d* sites in which a decisive assessment is not possible due to similar X-ray scattering power of Ni and Ge atoms. On the other hand, the total energy calculations predict that the case in which Ni atoms filling the vacancies at the 24*c* site is favored. In the crystal structure of $Ba_8Ni_{3.5}Ge_{42.1}\square_{0.4}$, all Ni atoms and framework vacancies are found at the site 6*c*. This leads to a distortion of the framework in which Ge atoms at the site 24*k* move

towards the site 6*c* by different amounts depending on whether a Ni or Ge atom or vacancy is found at that 6*c* position. Magnetic susceptibility measurements showed a temperature independent diamagnetism for all investigated compositions. Polycrystalline samples offer an opportunity to probe the evolution of the peculiar properties of the parent clathrate $Ba_8Ge_{43}\square_3$ upon substituting. These variations were traced by thermopower data revealing a smooth evolution from a nearly-compensated semimetallic state (x = 0) towards a narrow-band-gap semiconducting state (x = 4). Variation from metal- to semiconductor-like as well as a crossover from *n*- to *p*-type behavior is confirmed for the compositions $3.8 \leq x \leq 4.2$. Single crystalline $Ba_8Ni_{3.5}Ge_{42.1}\square_{0.4}$ is an *n*-type metal with estimated $ZT \approx 0.21$ at 680 K which is slightly higher than the polycrystalline material ($ZT \approx 0.14$ at 680 K). The maximum ZT values reach ≈ 0.2 at 500 K and 650 K for the polycrystalline samples with x = 2 and 3.8, respectively. For further enhancement of the ZT values, investigations with the aim at tuning the carrier concentration through a partial substitution of Ni or Ge with other transition metal atoms can be carried out.

Chapter 7

Type-I Clathrate in the System Ba – Ni – Si

The first type-I silicon clathrate, Na_8Si_{46}, was structurally characterized in 1965.[36] In the crystal structure, Si atoms form four-connected, covalently-bonded framework with 20- and 24-atom polyhedral cages filled by Na atoms. Following the Zintl-Klemm concept, the valence electrons of Na are not needed to form the four-bonded silicon framework. Na_8Si_{46} shows metallic behavior,[189] which implies that the excess electrons occupy antibonding (conduction) bands according to $[Na^{1+}]_8[(4b)Si^0]_{46} \cdot 8e^-$. Later, it was shown that the polyhedral cages can also be filled by Ba atoms and clathrates can bear even larger amount of excess electrons as $Na_2Ba_6Si_{46}$ with $[Na^{1+}]_2[Ba^{2+}]_6[(4b)Si^0]_{46} \cdot 14e^-$.[190] This phase attracted considerable attention since it was found to be the first superconductor based on an sp^3-framework with $T_c \approx 4$ K.[114] A higher transition temperature of $T_c \approx 8$ K was found for Ba_8Si_{46}.[115] Ternary superconducting clathrates have been reported as well, in which silicon atoms are partially replaced with other elements, *e.g.*, Ge,[163] Ga,[191] Cu,[175] Ag.[192] However, in all these cases, T_c was found to decrease with increasing content of substitution atoms and superconductivity vanishes after a certain substitution level is reached. Generally, the number of excess electrons in clathrate-I silicides is reduced by the substitution atoms in the framework. In the Zintl phase $Ba_8Ga_{16}Si_{30}$, *e.g.*, Si atoms are substituted by Ga resulting in the charge balance $[Ba^{2+}]_8[(4b)Ga^{1-}]_{16}[(4b)Si^0]_{30}$.[11, 55, 90] When full charge balance is achieved, semiconducting clathrates can be obtained. Such phases are of high interest for thermoelectric properties.[119] As discussed in chapter 2, intermetallic clathrates usually show favorably low lattice thermal conductivity regardless of composition. Hence, clathrates with high thermoelectric efficiency might be achieved by optimizing thermopower and electrical resistivity. In this respect, clathrate systems with an extended homogeneity range are promising candidates, because they allow for tuning the charge carrier concentration through chemical composition. For example, clathrates in the systems Ba – Ni – Ge [100, 182] (see chapter 6) and Ba – Au – Si [188, 193] show either *n*- or *p*-type conduction behavior depending on the content of transition metal. For the system Ba – Ni – Si, a clathrate-I phase was originally reported for only one composition $Ba_8Ni_{1.8}Si_{44.2}$.[61] Crystals of this composition were directly obtained from the melt, whereas the binary $Ba_{8-x}Si_{46}$ has been prepared only under high pressure [115, 163, 194, 195] or, recently, by oxidation of $Li_2Ba_4Si_6$ with gaseous HCl.[196] Remarkably, the reported lattice parameter of $Ba_8Ni_{1.8}Si_{44.2}$ (a = 10.285(5) Å) is significantly smaller than that of Ba_8Si_{46} (a = 10.328(2) Å).[115]

7.1 Sample preparation

Polycrystalline samples were synthesized by reaction of crystalline Ba, Ni powder and ground Si pieces in an argon-filled glove box (see Table 3.1). Stoichiometric amounts of elements with total weight of around 2 g were placed in an open glassy carbon crucible and slowly heated to the melt using an induction furnace. The melts were then cooled down to room temperature by pouring on a steel plate. The resulting specimens contained a mixture of the clathrate-I, α-Si, $BaSi_2$, NiSi, or $NiSi_2$ phases according to metallography and powder X-ray diffraction. For the annealing experiments, specimens were placed in glassy carbon crucibles and welded in tantalum ampoules which were in turn sealed in an argon-filled quartz tube. To avoid any influence from the cooling process, the ampoules were quenched in water. Clathrate phase in high purity was obtained after 1 week of annealing at 1000 °C (Fig. 7.1). Superconducting clathrate samples with low Ni content $Ba_{8-\delta}Ni_xSi_{46-x}$ ($\delta \approx 0.1$; $x \approx 1.4$, 1.6) were obtained by fast cooling of the melt between two steel plates (steel-quenching). Besides the clathrate phase, the reaction products mainly contained $BaSi_2$ and α-Si, which were removed by treatment with 3M HCl for 8 h and afterwards by 1M NaOH for 8 h (Fig. 11.20).

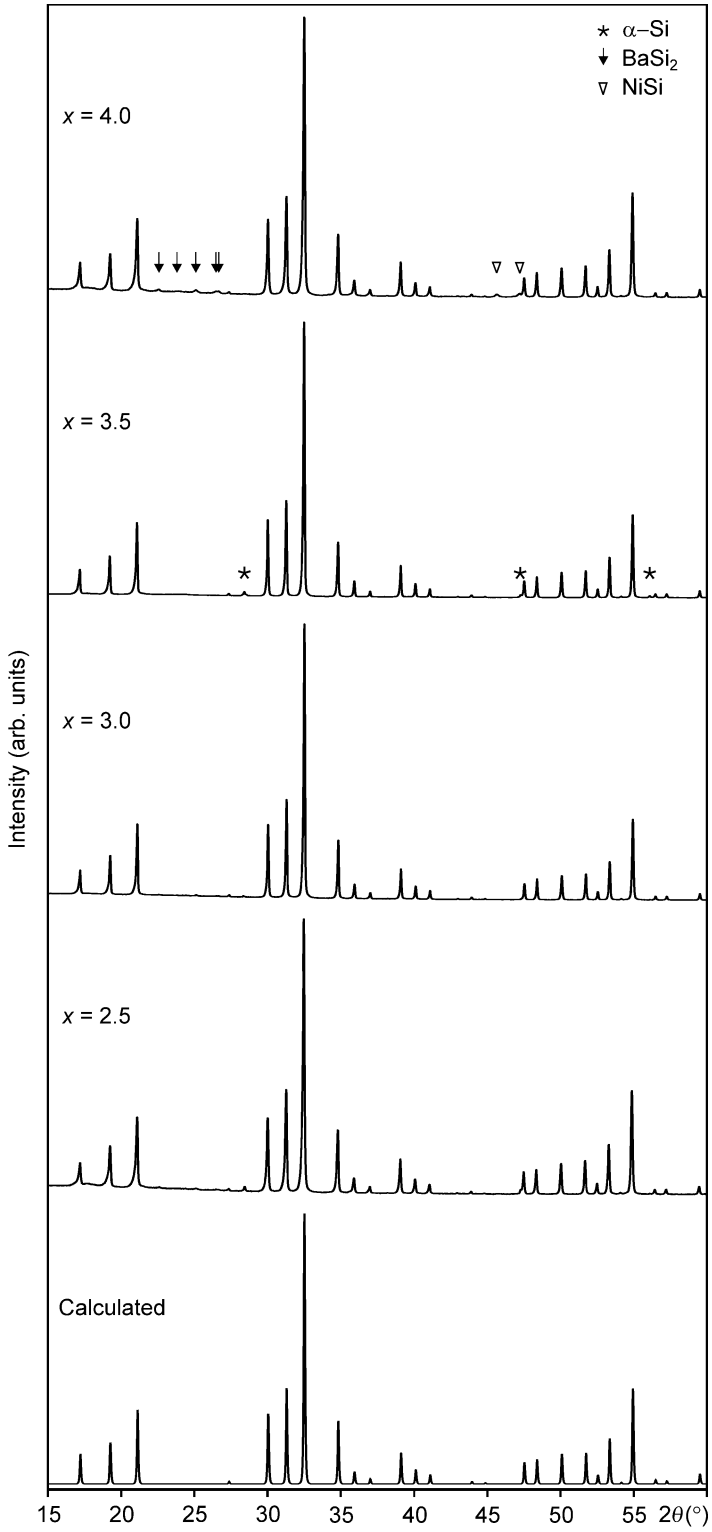

Figure 7.1: PXRD patterns of samples $Ba_8Ni_xSi_{46-x}$ annealed at 1000 °C with nominal compositions x = 2.5, 3.0, 3.5 and 4.0. Calculated profiles are based on single crystal analysis (Cu-$K\alpha_1$ radiation, see section 7.6). The symbols mark the position of the reflections of the secondary phases *e.g.*, α-Si, $BaSi_2$ and NiSi (only shown for x = 3.5 and 4.0 cases).

7.2 Estimation of primary crystallization field of the clathrate-I phase

A clathrate-I phase with composition $Ba_8Ni_{1.8}Si_{44.2}$ was originally synthesized from a sample with nominal composition '$Ba_8Ni_6Si_{40}$'.[61] A polycrystalline product was obtained by heating up the sample in a corundum crucible to the melt, followed by cooling with 100 °C / h to room temperature. The composition was established from single crystal analysis. The homogeneity of the reaction product was not discussed, but due to differing compositions of starting material and clathrate phase, a multiphase product would be expected. For both compositions, a multi-phase clathrate product was obtained by cooling down the melt within several minutes to room temperature. In order to understand the formation of the clathrate phase, the primary crystallization fields of the system $BaSi_2$ – NiSi – α-Si were investigated which constitute a subtriangle of congruently melting phases in the ternary system Ba – Ni – Si (Fig. 7.2).

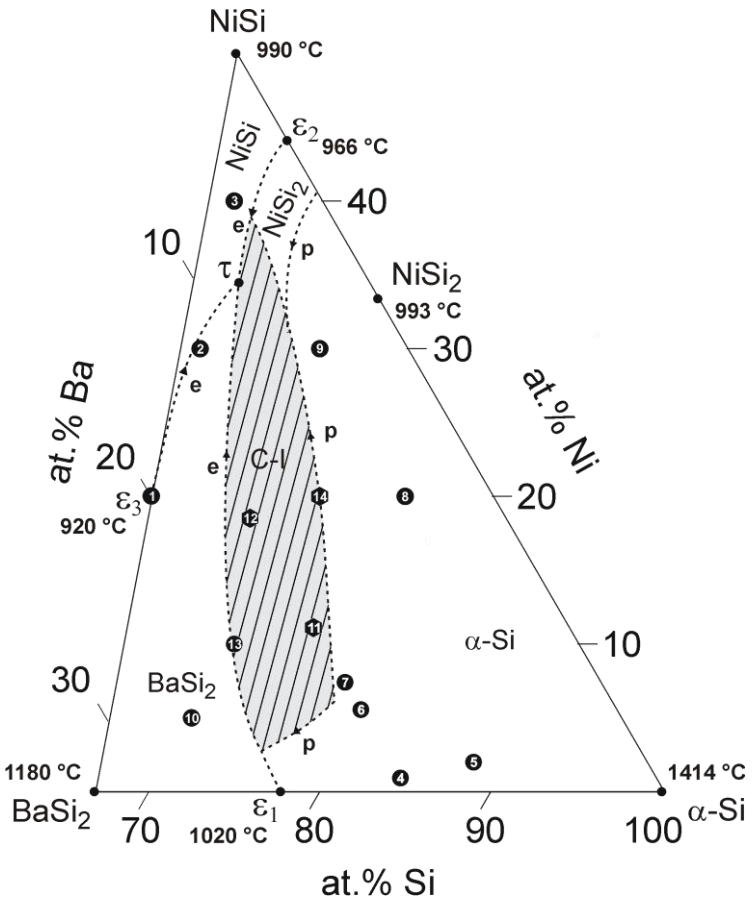

Figure 7.2: Estimated primary crystallization fields in the system $BaSi_2$ – NiSi – α-Si. The investigated compositions are numbered as: $Ba_{20}Ni_{20}Si_{60}$ (**1**), $Ba_{12}Ni_{30}Si_{58}$ (**2**), $Ba_5Ni_{40}Si_{55}$ (**3**), $Ba_8Ni_{0.5}Si_{45.5}$ (**4**), $Ba_{10}Ni_2Si_{88}$ (**5**), $Ba_8Ni_3Si_{43}$ (**6**), $Ba_8Ni_4Si_{42}$ (**7**), $Ba_5Ni_{20}Si_{75}$ (**8**), $Ba_5Ni_{30}Si_{65}$ (**9**), $Ba_{25}Ni_5Si_{70}$ (**10**), $Ba_8Ni_6Si_{40}$ (**11**), $Ba_8Ni_{10}Si_{36}$ (**12**), $Ba_{20}Ni_{10}Si_{70}$ (**13**), and $Ba_{10}Ni_{20}Si_{70}$ (**14**). Binary and ternary eutectics are marked with ε and τ, respectively.

For the binary systems $BaSi_2$ – Si and NiSi – Si, a eutectic composition was reported at 77 at.% Si (Fig. 7.2, point ε_1),[197] and at 56 at.% Si (point ε_2),[198] respectively. The eutectic point ε_3 of the quasi-binary system $BaSi_2$ – NiSi was assigned from sample 1 to be 20 at.% Ba, 20 at.% Ni, 60 at.% Si with a melting temperature at around 920 °C (Fig. 11.21). At this composition, the microstructure contains finely distributed crystallites of $BaSi_2$ and NiSi (Fig. 11.22a). The ternary eutectic point of $BaSi_2$, NiSi and the clathrate phase was roughly estimated by microstructure analysis of samples 2 (Fig. 11.22b) and 3 (Fig. 11.22c) to be 8 at.% Ba, 34 at.% Ni, 58 at.% Si (Fig.7.2, point τ).

The primary crystallization field of α-Si is subdivided into three parts. At low Ni content, it is in contact with the primary crystallization field of $BaSi_2$. Microstructure analysis of sample 4 (Fig. 11.22d) showed large and well-shaped crystallites of the primary phase α-Si. On further cooling, smaller but distinctly-shaped crystallites of $BaSi_2$ and α-Si appear. With increasing Ni content, the peritectic reaction L + α-Si → C-I is observed at 1105 °C. Hence, the microstructure of samples 5–7 contains grains of α-Si, enveloped by the crystallites of the clathrate-I, and remaining $BaSi_2$ (sample 7, Fig. 11.22e). Further increase of Ni content leads to formation of the clathrate-I phase besides α-Si. The microstructure of sample 8 (Fig. 11.22f) and sample 9 (Fig. 11.22g) contains primary grains of α-Si which are almost entirely enveloped by $NiSi_2$ crystallites. Upon crystallization of $NiSi_2$, the crystallization field of the clathrate phase is reached as both phases are formed with well-shaped crystals. At lower temperatures, the eutectic channel between clathrate and NiSi is reached, represented in the microstructure by areas with a finely grained mixture of NiSi and the clathrate phase. The primary crystallization field of $BaSi_2$ is observed in the samples 10 and 2 in which primary grains of $BaSi_2$ are in contact with clathrate-I (Fig. 11.22h) or NiSi crystallites (Fig. 11.22b), respectively. The primary crystallization of NiSi is observed in sample 3 (primary grains of NiSi in contact with $BaSi_2$ crystallites, Fig. 11.22c). The small field of crystallization of $NiSi_2$ may be expected close to the binary system α-Si – NiSi and was not further characterized. The primary crystallization of the clathrate-I phase is observed for the samples 11–14 (region C-I, Fig. 7.2) showing large areas of clathrate-I phase in contact with $BaSi_2$ and NiSi (samples 11–13, Fig. 11.22i) or NiSi and $NiSi_2$ (sample 14), respectively. Almost equal amounts of clathrate-I and $BaSi_2$ phases are observed in sample 13 (Fig. 11.22j) suggesting that the eutectic channel is running close to this concentration point.

7.3 Isothermal section of the system $BaSi_2$ – NiSi – α-Si at 1000 °C

As discussed in the previous section, only multiphase products can be formed on cooling ternary mixtures from the melt. A homogeneous clathrate phase $Ba_8Ni_x\square_ySi_{46-x-y}$ with $2.4 \leq x \leq 3.8$ and $y \leq 0.9$ was obtained after annealing at 1000 °C for one week. In the ternary system $BaSi_2$ – NiSi – α-Si, the melting points of NiSi, $NiSi_2$, the quasi-binary eutectic "$BaNiSi_3$" and the ternary eutectic are below 1000 °C (see Fig. 7.2). Therefore, samples with higher Ni content are either entirely molten or solid phases are in equilibrium with melt (Fig. 7.3a). The three-phase region between clathrate-I + $BaSi_2$ + α-Si is observed in the samples with the nominal compositions $Ba_8Ni_{0.5}Si_{45.5}$ (Fig. 7.3a, sample 1), $Ba_8Ni_2Si_{44}$ (Fig. 7.3a, sample 2), $Ba_{22.5}Ni_{2.5}Si_{75}$ (Fig. 7.3a, sample 3), and $Ba_{10}Ni_2Si_{88}$ (Fig. 7.3a, sample 4). The microstructure of these samples always showed well separated grains of $BaSi_2$, α-Si and clathrate-I phase in the respective amounts (Fig. 11.23a-d). The lower limit of Ni content in the homogeneity range $Ba_8Ni_x\square_ySi_{46-x-y}$ at 1000 °C was determined to be $Ba_{8.00(5)}Ni_{2.36(4)}Si_{43.94(6)}$ from the sample 2 (Table 7.1). Two-phase regions were found at the compositions $Ba_{18}Ni_5Si_{77}$ (Fig. 7.3a, sample 5), containing $BaSi_2$ and clathrate (Fig. 11.23e), and $Ba_{13}Ni_5Si_{82}$ (Fig. 7.3a, sample 6) showing a mixture of α-Si and clathrate (Fig. 11.23f). Samples with the composition $Ba_{25}Ni_5Si_{70}$ (Fig. 7.3a, sample 7) and $Ba_{2.5}Ni_{2.5}Si_{95}$ (Fig. 7.3a, sample 8) belong to three-phase regions $BaSi_2$ + clathrate-I + melt and clathrate-I + α-Si + melt, respectively (Fig. 11.23g-h). For the composition $Ba_8Ni_4Si_{42}$ (Fig. 7.3a, sample 9), the clathrate phase is in equilibrium with the melt. The microstructure of this sample shows large grains of the clathrate phase surrounded by a finely grained mixture formed from the melt after the sample was quenched from 1000 °C to room temperature (Fig. 11.23i). The composition $Ba_{8.00(3)}Ni_{3.82(4)}Si_{41.33(6)}$ determined for the clathrate phase in this sample represents the upper limit of Ni content at 1000 °C, which was also confirmed from samples with higher nominal Ni content (Table 7.1). Analysis of the clathrate-I phase by wavelength dispersive X-ray spectroscopy (WDXS) shows a distinct deviation from the nominal composition $Ba_8Ni_xSi_{46-x}$ (Fig 7.3b, Table 7.1). In particular for higher Ni contents, the ratio of concentrations $(c_{Ni} + c_{Si}) / c_{Ba}$ is influenced by the presence of vacancies in the Ni–Si framework. Full occupancy of the Ba sites as well as the existence of framework vacancies were shown by structure analyses based on single crystal data (see section 7.6).

Clathrate products obtained at 1000 °C were investigated by thermal analysis. For all compositions $2.4 < x < 3.8$, the peritectic decomposition of the clathrate-I phase was indicated by a single, strong endothermic effect close to $T = 1105$ °C, followed by a broad endothermic peak indicating the liquidus (Fig. 11.24). On cooling, several exothermic effects appeared in agreement with the incongruent (peritectic) formation of the clathrate phase.

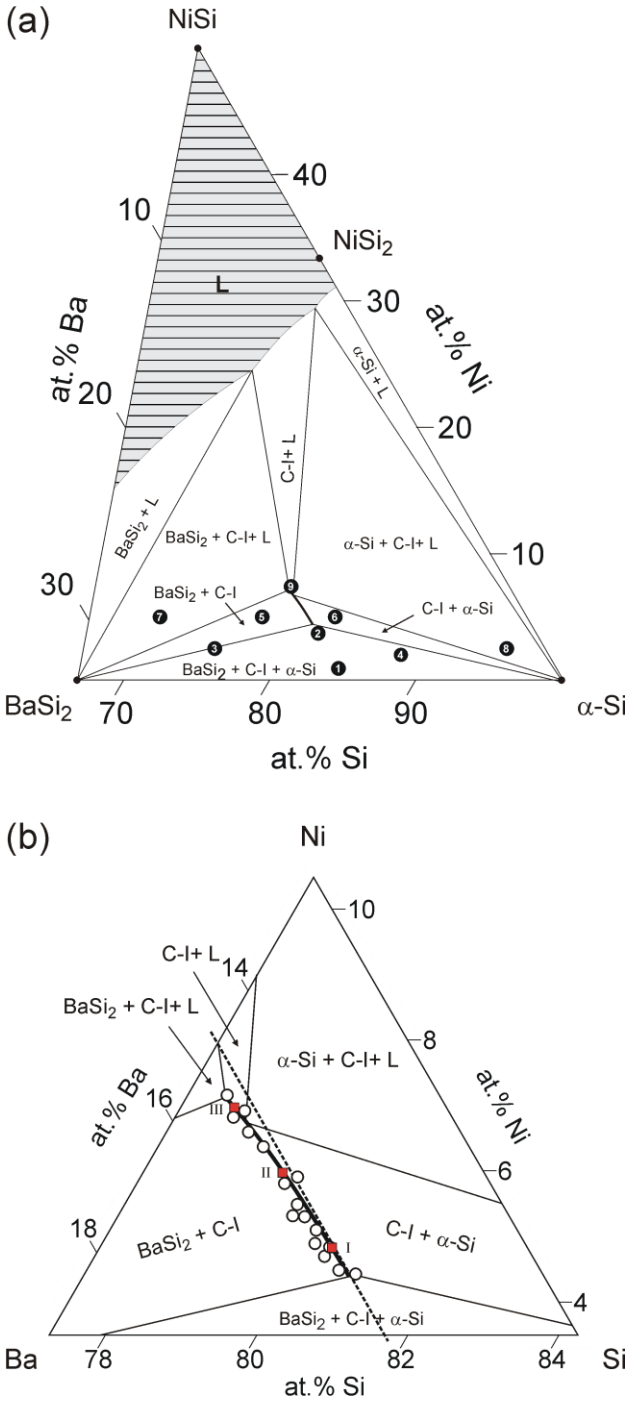

Figure 7.3: (**a**) Isothermal section of the system $BaSi_2$ – NiSi – α-Si at 1000 °C based on the investigated samples: $Ba_8Ni_{0.5}Si_{45.5}$ (**1**), $Ba_8Ni_2Si_{44}$ (**2**), $Ba_{22.5}Ni_{2.5}Si_{75}$ (**3**), $Ba_{10}Ni_2Si_{88}$ (**4**), $Ba_{18}Ni_5Si_{77}$ (**5**), $Ba_{13}Ni_5Si_{82}$ (**6**), $Ba_{25}Ni_5Si_{70}$ (**7**), $Ba_{2.5}Ni_{2.5}Si_{95}$ (**8**), and $Ba_8Ni_4Si_{42}$ (**9**). The part of the phase diagram which should be liquid at 1000 °C is only estimated and shown as hatched grey area. (**b**) The homogeneity range of the clathrate phase based on the WDXS data is shown as thick line. The refined single crystal compositions (**I**, **II**, **III**) are shown with squares. The dashed-line represents the isoconcentrate of 14.81 at.% Ba ($Ba_8Ni_xSi_{46-x}$).

Table 7.1: The lattice parameter and compositions of the samples obtained after annealing at 1000 ºC for one week (C-I = Clathrate-I).

Nominal composition	Products (PXRD & EDXS)	Composition (WDXS)	*a* (Å)
$Ba_8Ni_{0.2}Si_{45.8}$	C-I (< 10 %), $BaSi_2$ (> 40 %), α-Si (> 50 %)	$Ba_{8.0(3)}Ni_{2.5(1)}Si_{42.0(2)}$	10.2994(1)
$Ba_8Ni_{0.5}Si_{45.5}$	C-I (< 20 %), $BaSi_2$ (> 40 %), α-Si (> 40 %)	$Ba_{8.0(3)}Ni_{2.5(1)}Si_{42.3(3)}$	10.2997(1)
$Ba_8Ni_1Si_{45}$	C-I (> 40%), $BaSi_2$ (<30 %), α-Si (< 30 %)	$Ba_{8.00(3)}Ni_{2.43(2)}Si_{43.30(4)}$	10.3007(1)
$Ba_8Ni_2Si_{44}$	C-I (> 80%), $BaSi_2$ (<10 %), α-Si (< 10 %)	$Ba_{8.00(5)}Ni_{2.36(4)}Si_{43.94(6)}$	10.3011(2)
$Ba_8Ni_2Si_{44}$	C-I (> 80%), $BaSi_2$ (<10 %), α-Si (< 10 %)	$Ba_{8.00(3)}Ni_{2.44(2)}Si_{42.81(3)}$	10.3007(1)
$Ba_8Ni_{2.5}Si_{43.5}$	C-I (> 95%), $BaSi_2$ (<3 %), α-Si (< 2 %)	$Ba_{8.00(3)}Ni_{2.62(1)}Si_{42.57(3)}$	10.2982(1)
$Ba_8Ni_{2.5}Si_{43.5}$	C-I (> 95%), $BaSi_2$ (<3 %), α-Si (< 2 %)	$Ba_{8.00(2)}Ni_{2.64(2)}Si_{43.23(4)}$	10.2981(1)
$Ba_8Ni_{2.65}Si_{43.35}$	C-I (> 96%), $BaSi_2$ (<2 %), α-Si (< 2 %)	$Ba_{8.00(5)}Ni_{2.73(1)}Si_{42.89(5)}$	10.2958(1)
$Ba_8Ni_{2.75}Si_{43.25}$	C-I (> 98%), $BaSi_2$ (<1 %), α-Si (< 1 %)	$Ba_{8.00(2)}Ni_{2.81(2)}Si_{42.10(3)}$	10.2951(1)
$Ba_8Ni_{2.75}Si_{43.25}$	C-I (> 98%), $BaSi_2$ (<1 %), α-Si (< 1 %)	$Ba_{8.00(2)}Ni_{2.83(1)}Si_{42.61(1)}$	10.2947(1)
$Ba_8Ni_{2.85}Si_{43.15}$	C-I (> 98%), $BaSi_2$ (<1 %), α-Si (< 1 %)	$Ba_{8.00(1)}Ni_{2.93(1)}Si_{42.50(1)}$	10.2929(1)
$Ba_8Ni_3Si_{43}$	C-I (> 98%), $BaSi_2$ (<1 %), α-Si (< 1 %)	$Ba_{8.00(2)}Ni_{3.11(1)}Si_{42.26(2)}$	10.2923(1)
$Ba_8Ni_3Si_{43}$	C-I (> 98%), $BaSi_2$ (<1 %), α-Si (< 1 %)	$Ba_{8.00(2)}Ni_{3.17(1)}Si_{43.03(2)}$	10.2922(1)
$Ba_8Ni_{3.5}Si_{42.5}$	C-I (> 99%), α-Si (< 1 %)	$Ba_{8.00(7)}Ni_{3.42(3)}Si_{41.99(4)}$	10.2904(1)
$Ba_8Ni_{3.5}Si_{42.5}$	C-I (> 99 %), NiSi (< 1 %)	$Ba_{8.00(3)}Ni_{3.46(4)}Si_{41.56(7)}$	10.2897(1)
$Ba_8Ni_4Si_{42}$	C-I (> 98%), $BaSi_2$, NiSi, $NiSi_2$ (<2 %)	$Ba_{8.00(4)}Ni_{3.72(9)}Si_{41.83(5)}$	10.2906(1)
$Ba_8Ni_4Si_{42}$	C-I (> 98%), $BaSi_2$, NiSi, $NiSi_2$ (<2 %)	$Ba_{8.00(3)}Ni_{3.82(4)}Si_{41.33(6)}$	10.2896(1)
$Ba_8Ni_6Si_{40}$	C-I (> 90%), $BaSi_2$, NiSi, $NiSi_2$ (<10 %)	$Ba_{8.00(1)}Ni_{3.62(3)}Si_{41.16(3)}$	10.2907(1)
$Ba_8Ni_{10}Si_{36}$	C-I (> 70 %), $BaSi_2$, NiSi, $NiSi_2$ (<30 %)	$Ba_{8.00(1)}Ni_{3.71(3)}Si_{42.46(3)}$	-

7.4 Metastable compositions

The clathrate phase with distinctly lower Ni content was obtained by steel-quenching of molten samples. The compositions were determined from Rietveld refinement on PXRD data and qualitatively confirmed by EDXS on pressed-powder after removing $BaSi_2$ and α-Si with dilute HCl and NaOH (Table 7.2). From the starting composition $Ba_8Ni_{0.2}Si_{45.8}$, a clathrate phase with the composition $Ba_{7.9(1)}Ni_{1.4(1)}Si_{44.6(1)}$ (a = 10.3088(1) Å) was formed as a minority product together with $BaSi_2$ and α-Si (see section 7.6). Similarly, $Ba_{7.9(1)}Ni_{1.6(1)}Si_{44.4(1)}$ (a = 10.3078(1) Å) was obtained starting from $Ba_8Ni_{0.5}Si_{45.5}$. In the DSC experiment, $Ba_{7.9(1)}Ni_{1.6(1)}Si_{44.4(1)}$ showed an exothermic effect at ≈ 715 ºC on heating with 10 K/min indicating the decomposition of a metastable phase (Fig. 11.25). Therefore, it is possible that the steel-quenched clathrate products with low Ni content belong to a Ni-stabilized high pressure phase $Ba_{8-\delta}Ni_xSi_{46-x}$.

Table 7.2: The lattice parameter and composition of the clathrate phase (C-I) in the samples obtained by steel-quenching.

Nominal composition	Products (PXRD & EDXS)	Composition (EDXS)	*a* (Å)
$Ba_8Ni_{0.2}Si_{45.8}$	C-I (< 5 %), $BaSi_2$ (> 40 %), α-Si (> 50 %)	$Ba_{7.5}Ni_{1.6}Si_{44.4}$	10.3088(1)
$Ba_8Ni_{0.5}Si_{45.5}$	C-I (< 10 %), $BaSi_2$ (> 40 %), α-Si (> 40 %)	$Ba_{7.5}Ni_{1.8}Si_{44.2}$	10.3078(1)
$Ba_8Ni_3Si_{43}$	C-I (> 60%), $BaSi_2$ (< 20 %), α-Si (< 20 %)	$Ba_8Ni_{3.0}Si_{45.6}$	10.2932(1)
$Ba_8Ni_{3.5}Si_{42.5}$	C-I (> 70%), $BaSi_2$ (< 15 %), α-Si (< 15 %)	$Ba_8Ni_{3.0}Si_{42.3}$	10.2927(1)
$Ba_8Ni_6Si_{40}$	C-I (> 80%), $BaSi_2$ (<15 %), NiSi(< 5 %)	$Ba_8Ni_{3.2}Si_{45.9}$	10.2935(1)

7.5 Heat of formation and phase stability

The heat of formation of $Ba_8Ni_x\square_ySi_{46-x-y}$ was computed based on the total energies obtained from first principles electronic structure calculations by considering the following balance:

$$8Ba_{bcc} + xNi_{fcc;\,FM} + (46-x-y)\ \alpha\text{-Si} = Ba_8Ni_x\square_ySi_{46-x-y} + \Delta H_f\,(x, y) \qquad (7.1)$$

The stability of the clathrate phase with respect to the competing phases $BaSi_2$, NiSi, $NiSi_2$, and α-Si was also explored (see Table 7.1). Since both NiSi and $NiSi_2$ can form by decomposition of the clathrate phase, the two limiting balances were taken into account:

$$Ba_8Ni_x\square_ySi_{46-x-y} = 8\ BaSi_2 + x\ NiSi + (30-2x-y)\ \alpha\text{-Si} + \Delta E_1(x, y) \qquad (7.2)$$

$$Ba_8Ni_x\square_ySi_{46-x-y} = 8\ BaSi_2 + x\ NiSi_2 + (30-3x-y)\ \alpha\text{-Si} + \Delta E_2(x, y) \qquad (7.3)$$

In agreement with the phase diagram, Eq. 7.3 is more realistic because $NiSi_2$ was calculated to be more stable than NiSi + α-Si by 46.6 meV/atom.

The heat of formation ΔH_f of $Ba_8Ni_x\square_ySi_{46-x-y}$ (for $y = 0$) varies linearly with Ni content with two different slopes in the ranges $0 \le x \le 3$ and $3 \le x \le 6$ (Fig. 7.4 inset). The additional energy saved upon forming a clathrate with one more Ni atom per formula unit for x up to 3 is almost twice that for $x > 3$. In this context, it is remarkable that the composition with $x = 3$ was also found to be special as it delineates two regions of different transport behavior (see section 7.9). Examination of Table 7.3 and Fig. 7.4 reveals that: (i) all clathrates with compositions $x \le 4$ are stable according to Eq. 7.2; (ii) the binary clathrate Ba_8Si_{46} and the compositions with $1 < x < 4$ are stable according to Eq. 7.3; (iii) the composition with $x = 3$ is the most stable one; and (iv) compositions with vacancies ($y = 0$) are unstable. ΔE_1 and ΔE_2 having different signs for cases $x = 1$ and $x = 4$ should be considered taking two aspects into account: the ratio of the balances Eq. 7.2 and Eq. 7.3 is

indeterminant and none of the clathrate models was optimized in a supercell. While both aspects may be important for the x = 1 case, only the former one is crucial for the x = 4 case. Furthermore, the presence of vacancies at the 6c site and the associated entropy contributions of phonons to the free energy introduce more uncertainty to the case of x = 4. Since after three Ni atoms, addition of an extra Ni atom saves less energy, the competing phases quickly become more favorable for x > 3. This result reflects the tendency to avoid two Ni atoms to be situated at consecutive 6c positions of the same six-ring. Finally, $Ba_8Ni_6Si_{40}$ (x = 6) is found to be unstable in agreement with the fact that clathrate-I at this composition has not been observed yet.

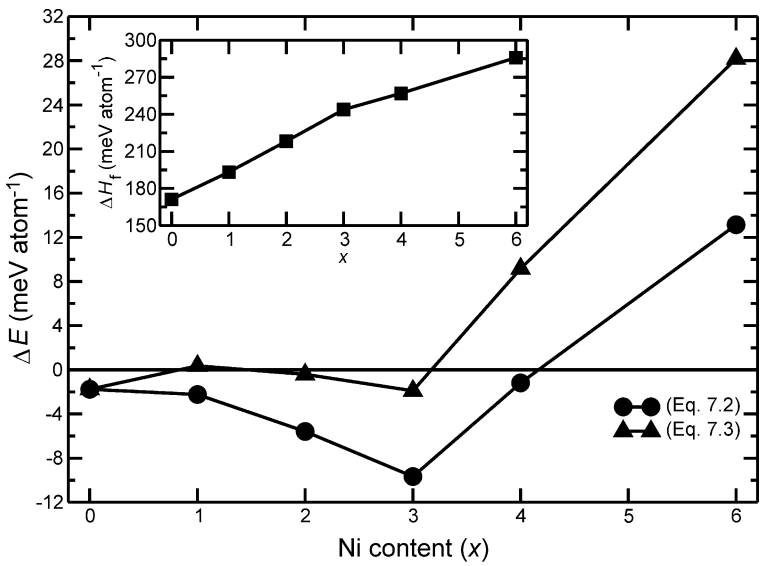

Figure 7.4: Enthalpies ΔE_1 (●), ΔE_2 (▲), and heat of formation (**inset**) as a function of nominal Ni content for vacancy-free compositions.

Table 7.3: ΔH_f (Eq. 7.1), ΔE_1 (Eq. 7.2), and ΔE_2 (Eq. 7.3) in meV atom^{-1} for $Ba_8Ni_x\square_ySi_{46-x-y}$. Negative values of ΔE indicate that the clathrate phase is more stable than the competing phases.

(x, y)	ΔH_f	ΔE_1	ΔE_2
(0, 0)	171.3	–1.8	–1.8
(1, 0)	193.3	–2.2	0.4
(2, 0)	218.2	–5.6	–0.4
(3, 0)	243.9	–9.7	–1.9
(3, 1)	222.0	16.6	24.6
(4, 0)	257.0	–1.2	9.2
(4, 1)	231.3	29.4	39.9
(6, 0)	285.8	13.1	28.2

The effect of vacancy formation on phase stability of clathrates was investigated for compositions with x = 3 and 4 using the following balances:

$$Ba_8Ni_3Si_{43} = Ba_8Ni_3Si_{42}\square_1 + \alpha\text{-Si} + \Delta E_v \quad (7.4)$$

$$Ba_8Ni_4Si_{42} = Ba_8Ni_4Si_{41}\square_1 + \alpha\text{-Si} + \Delta E_v \quad (7.5)$$

The computed vacancy formation energies are –1.4 and –1.6 eV for one vacancy per formula unit for x = 3 and 4, respectively, leading to the conclusion that internal energy contributions alone would favor vacancy-free compositions $Ba_8Ni_3Si_{43}$ and $Ba_8Ni_4Si_{42}$. However, the formation of vacancies, which are observed in the crystal structure (see following section) may be favored by entropy contributions.

7.6 Crystal structure

PXRD patterns of all clathrate-I products in this system could be indexed with a primitive cubic lattice in agreement with the space group $Pm\bar{3}n$ (no. 223). A supercell indicating an ordered arrangement of Ni atoms or vacancies in the clathrate-I framework was not observed. As the reflections in all powder patterns were distinctly narrow, it was assumed that the bulk composition determined by WDXS is also valid for the single crystalline fragments.

Crystal structure determinations were performed on three single crystals selected from samples annealed at 1000° C with compositions $Ba_{8.00(3)}Ni_{2.62(1)}Si_{42.57(3)}$ (**I**), $Ba_{8.00(2)}Ni_{3.17(1)}Si_{43.03(2)}$ (**II**), and $Ba_{8.00(4)}Ni_{3.72(9)}Si_{41.83(5)}$ (**III**) (Table 11.14, Fig. 7.3b). Structure refinement revealed in all cases full occupancy of Ba1 at 2*a* site and Ba2 at 6*d* site. Ba2 in oversized 24-atom cages shows relatively large anisotropic displacement which is usually interpreted as off-centered positioning of the guest atoms.[32, 199] When the Ba2 atoms were refined at the 24*k* site with 0.25 occupancy, the residual values were considerably lowered (*e.g.* R_F for **I** drops from 3.9 % to 3.0 %). In the next step, the Ni to Si ratio of the framework site 6*c* was refined assuming full site occupancy, while sites 16*i* and 24*k* were refined with full Si occupancy. With such distribution of Ni and Si, the number of Ni atoms per formula unit was obtained to be 2.49(6) for **I**, 2.90(5) for **II**, and 3.05(4) for **III** which is distinctly lower than the respective Ni content obtained from WDXS analyses. The discrepancy can be explained by the presence of vacancies at the 6*c* site, which was also indicated by the slightly increasing displacement anisotropy of the Si atoms at the 24*k* site. This sizable anisotropy has been correlated with the amount of vacancies as shown for $Cs_8Sn_{44}\square_2$,[96] $K_8Ge_{44}\square_2$,[58] and for ternary variants $Ba_8TM_x\square_yGe_{46-x-y}$ (*TM* = Ni,[22] Pd,[102] Pt,[103] Zn,[107, 108] *etc.*).

In the next step of the structure refinement, the Ni content was fixed according to WDXS analysis. The final structure refinements yielded the compositions $Ba_8Ni_{2.6}Si_{43.3}\square_{0.1}$ for **I**, $Ba_8Ni_{3.2}Si_{42.4}\square_{0.4}$ for **II** and $Ba_8Ni_{3.7}Si_{41.4}\square_{0.9}$ for **III** (Tables 11.15-18). Due to the mixed occupancy of the 6*c* site by vacancies, Ni, and Si, the atoms in the neighboring 24*k* site may be located at three different positions. In particular, the presence of vacancies at the 6*c* site leads to a shift of the neighboring atoms towards the vacancy position. Due to the small amount of vacancies in crystal **I**, position Si33 could not be resolved. The interatomic distances *d*(Si1–Si31) varying in the range 2.40 Å – 2.46 Å are slightly longer than the Si – Si distance in α-Si (≈ 2.35 Å) but agree well with those observed for other silicon clathrates *e.g.*, $Na_2Ba_6Si_{46}$ (*d*(Si1–Si3) ≈ 2.39,[200] 2.40 Å [201]), Ba_8Si_{46} (*d*(Si1–Si3) ≈ 2.42Å)[115] or $Cs_{7.8}Si_{46}$ (*d*(Si1–Si3) ≈ 2.44 Å).[94] The distances *d*(Ni–Si32) ≈ 2.28 Å – 2.33 Å are in the range with those reported in NiSi as *d*(Ni–Si) ≈ 2.29 – 2.40 Å,[202] or in $NiSi_2$ as *d*(Ni–Si) ≈ 2.34 Å.[203] The shorter distance *d*(Ni–Si) compared to *d*(Si–Si) explains the contraction of the framework with increasing Ni content as revealed by PXRD data (Fig. 7.5). Distances *d*(□–Si33) are found to be ≈ 2.15 Å for **II** and ≈ 2.19 Å for **III**.

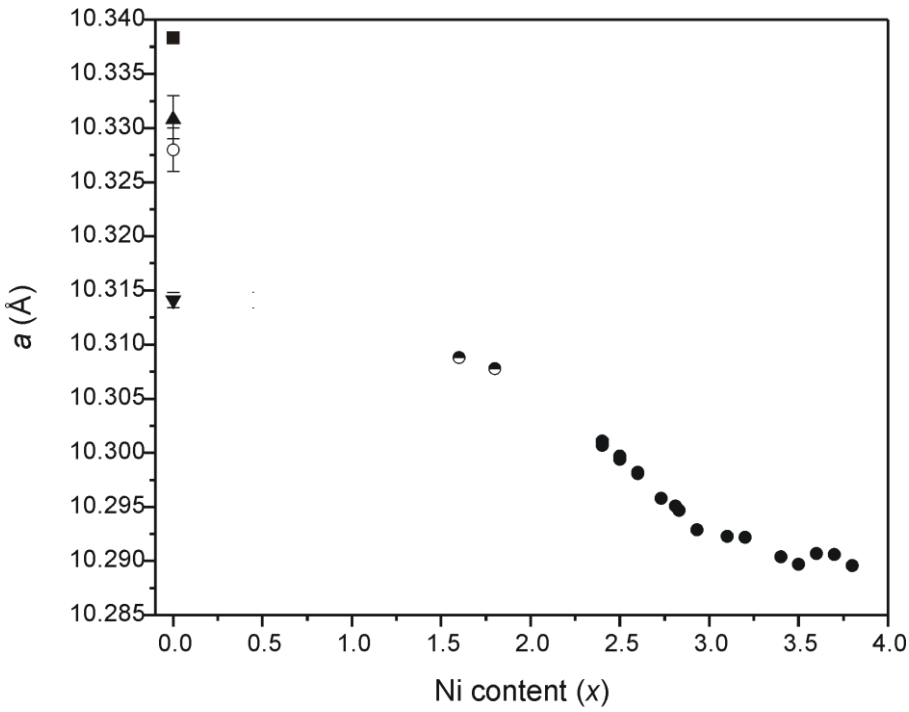

Figure 7.5: Lattice parameter of Ba_8Si_{46} (○),[115] Ba_8Si_{46} (extrapolated based on our data and $Ba_{8-\delta}Si_{46}$ [196]) (■), $Ba_{7.76}Si_{46}$ (▼),[194] $Ba_{7.6}Si_{46}$ (▲),[163] $Ba_{8-\delta}Ni_xSi_{46-x}$ obtained by steel-quenching (◓), and clathrate samples annealed at 1000 °C (●) with respect to determined Ni content. For our samples, the errors of the lattice parameters are smaller than the size of the symbols used.

The crystal structure of the phase $Ba_{8-\delta}Ni_xSi_{46-x}$ obtained by steel-quenching (see section 7.4) was refined from PXRD data for samples with nominal δ=0, x = 0.2 and x = 0.5. In the structure refinement, the site 2*a* was found to be partially occupied by Ba atoms in both samples. However, Ba2 at 6*d* site, the framework sites Ni1/Si1 at 6*c*, Si2 at 16*i* and Si3 at 24*k* were refined with full occupancy (Fig. 11.26-27, Tables 11.19-20). Accordingly, the compositions were determined to be $Ba_{7.9(1)}Ni_{1.4(1)}Si_{44.6(1)}$ and $Ba_{7.9(1)}Ni_{1.6(1)}Si_{44.4(1)}$ for the samples prepared with x = 0.2 and x = 0.5, respectively. To check if Ba deficient samples can be also synthesized for clathrates with higher Ni content, a sample with nominal composition $Ba_8Ni_{3.5}Si_{42.5}$ was steel-quenched. The composition was determined with EDXS analysis as $Ba_{8.0}Ni_{3.0}Si_{42.3}$ (Table 7.2). From the Rietveld analysis, both Ba1 and Ba2 sites were found to be fully occupied but 6*c* site (1/4, 0, 1/2) on the framework shows around 0.4 vacancy per formula unit which is slightly smaller than 0.7, determined from the EDXS analysis.

7.7 X-ray absorption spectroscopy

It was reported by several studies dealing with Ni compounds (*e.g.*, $KNiIO_6$, $LiNiO_2$, NiO; $LaNiO_3$, $LaNi_2O_5$, $LaNiO_2$) that the energy of the X-ray absorption edge correlates well with Ni valency and shifts to higher values as the valency increases.[204, 205] X-ray absorption spectra of $Ba_8Ni_x\square_ySi_{46-x-y}$ were determined close to the Ni *K*-edge (8333 eV) on four samples annealed at 700 °C with determined Ni contents x = 2.6, 3.1, 3.4, and 3.8 (Fig. 7.6a). For comparison, the spectra of Ni foil, NiSi, NiI_2 and NiO were also recorded (Fig. 7.6b). The Ni *K*-edge XANES and EXAFS regions of all clathrate samples show qualitatively identical features. Near the Ni *K*-edge, the spectra exhibit distinct characteristics dominated by the dipole-allowed transition of the Ni-1*s* electron to unoccupied 4*p* states (Fig. 7.6a). The position of the Ni absorption edge was found to be very close to those of Ni foil and NiSi and distinctly separated from those of NiI_2 and NiO. Accordingly, the electronic state of Ni in clathrate $Ba_8Ni_x\square_ySi_{46-x-y}$ is close to that in the element. EXAFS data for all clathrate samples show almost identical features pointing to very similar local environments (Fig. 7.7). The major peak in the Fourier-transformed curves reflects the fourfold coordination of the Ni atoms by Si atoms with d(Ni–Si) ≈ 2.2 Å. The broad peak at around 3.7 Å is associated to Ni – Ba2 contacts.

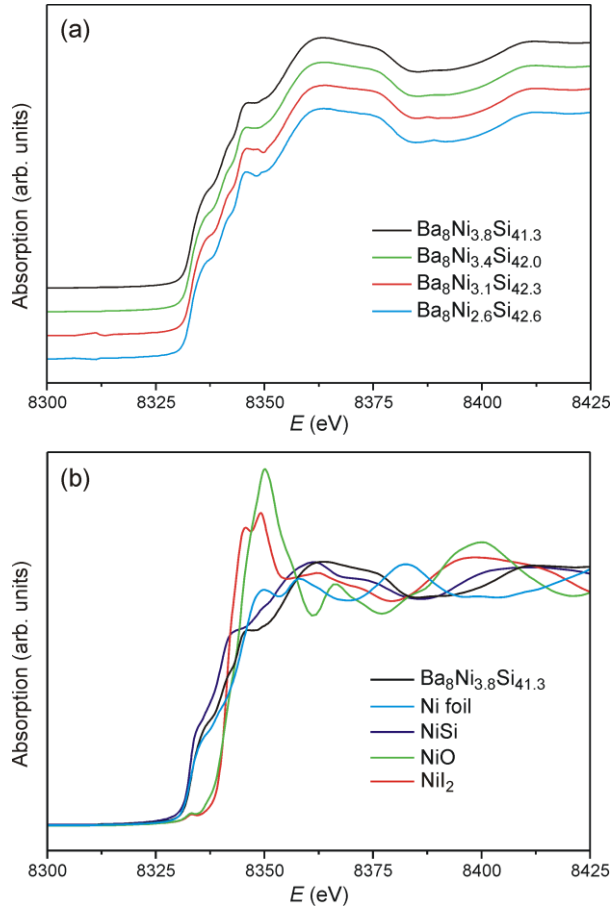

Figure 7.6: Normalized Ni *K*-edge XANES spectra: (**a**) The clathrate $Ba_8Ni_x\square_ySi_{46-x-y}$ with determined compositions $Ba_8Ni_{2.6}Si_{42.6}$, $Ba_8Ni_{3.1}Si_{42.3}$, $Ba_8Ni_{3.4}Si_{42}$, and $Ba_8Ni_{3.8}Si_{41.3}$; (**b**) Ni foil, NiSi, NiO and NiI_2. Spectra are shifted vertically for clarity.

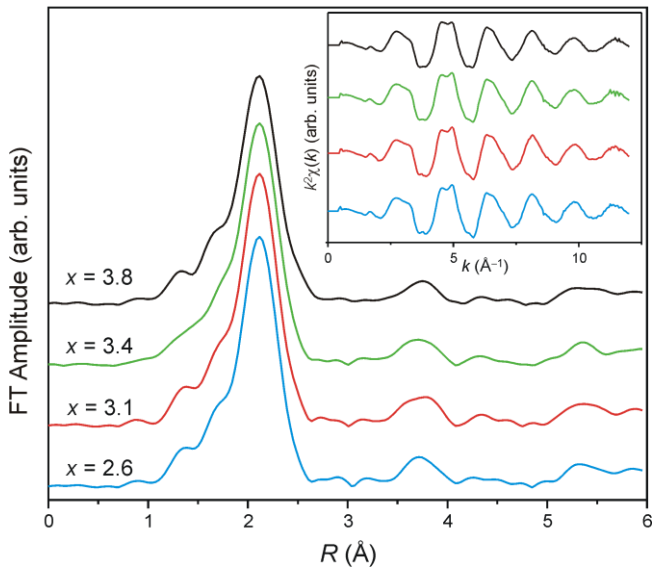

Figure 7.7: k^2-weighted Ni *K*-edge EXAFS (**inset**) and associated Fourier transform for the clathrate $Ba_8Ni_x\square_ySi_{46-x-y}$ with determined compositions $Ba_8Ni_{2.6}Si_{42.6}$, $Ba_8Ni_{3.1}Si_{42.3}$, $Ba_8Ni_{3.4}Si_{42}$, and $Ba_8Ni_{3.8}Si_{41.3}$.

7.8 Chemical bonding

The atomic interactions in the $Ba_8Ni_x\square_ySi_{46-x-y}$ system are studied within the ELI-ED approach for the composition $Ba_8Ni_4Si_{42}$. In $Ba_8Ni_4Si_{42}$, the computed atomic charges are as follows: 54.8 electrons for Ba1, 54.7 for Ba2, 28.4 for Ni, 14.1 for Si1 and 14.2 for Si2. Si3 atoms can be grouped into two according to being nearest neighbors of (**i**) Ni, (**ii**) Si1 atoms. The former group has 14.1 and the latter 14.3 electrons. This analysis shows that Ni atoms get quite a large part (0.4 electrons per atom) of the electrons transferred from Ba atoms to the framework.

Topological analysis of the ELI reveals two-center Si–Si and two-center banana-type Ni–Si bonds. The electron counts inside bond basins can be summarized as follows: Ni–Si3: 2.18, Si1–Si3: 2.09, Si2–Si2: 2.03, Si3–Si3: 1.98. The Si2–Si3 bond charges show a small difference depending on whether the Si3 atom is a neighbor of a (i) Ni or (ii) Si atom: Si2–Si3 (i): 1.97 on average (it varies between 1.94 and 1.99); Si2–Si3 (ii): 2.01. It is observed that the largest valence bond electron populations are obtained for the (6*c*)–Si3 bonds suggesting that excess valence charge tends to accumulate near the 6*c* sites. Hence, isosurfaces of the ELI distribution around a six-ring containing (a) Ni–Ni, (b) Ni–Si pairs at its 6*c* positions are shown in Fig. 7.8. Ba 5d orbitals hybridize with framework orbitals (mainly Si 3p and Ni 3d) and have sizable occupancies (0.8 and 0.6 electrons for Ba1 and Ba2, respectively, for $x = 4$). However, due to large number of framework neighbors (20 and 24 atoms around Ba1 and Ba2, respectively), the structuring in the $n = 5$ shell of the Ba atoms is negligibly small (in our calculations both Ba types are placed at the centers of the cages, 2*a* and 6*d* sites, so that the framework atoms are distributed fairly isotropically). On the other hand, the participation of Ni 3d orbitals in the Ni–Si interactions gives rise to a clearly-observable structuring of the $n = 3$ shell (Fig. 7.8c).

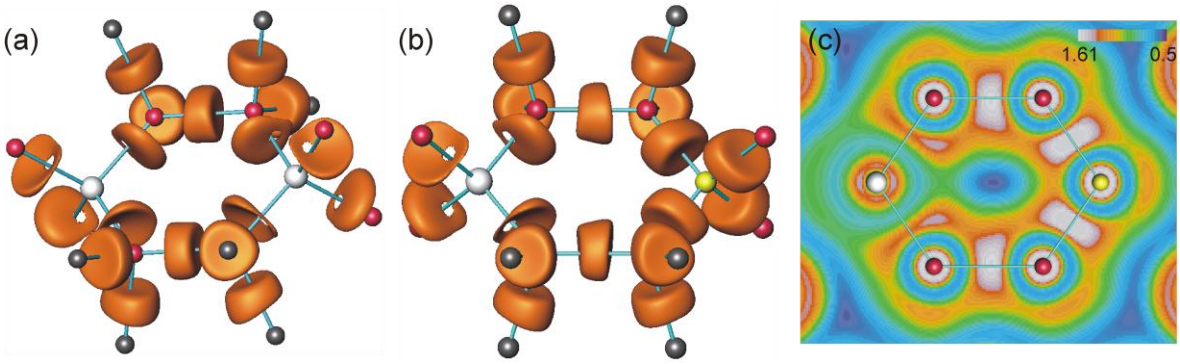

Figure 7.8: Electron localizability indicator, Υ, in $Ba_8Ni_4Si_{42}$: (**a**) ELI isosurface with $\Upsilon = 1.33$ around a six-ring whose 6c sites are occupied by Ni atoms, (**b**) ELI isosurface with $\Upsilon = 1.33$ around a six-ring whose 6c sites are occupied by one Ni and one Si atoms, (**c**) contour plot of the ELI distribution in the plane of a six ring revealing the structuring of the penultimate ($n = 3$) shell of the Ni atom. Ni atoms are denoted by white, Si1 by yellow, Si2 by grey, Si3 by red spheres. Ba atoms are not shown.

7.9 Electronic structure and physical properties

Electronic band structure calculations for $Ba_8Ni_xSi_{46-x}$ (x = 0, 2, 3, 4 and 6) were carried out by the FPLO method. The two end-member compounds, x = 0 and 6, display an ordered crystal structure enabling to use the original space group $Pm\bar{3}n$ (for x = 6, Ni atoms fully occupy the 6c position). However, to treat the chemical disorder which inevitably accompanies a chemical substitution at the 6c position, a supercell approach is required for the other cases (x = 2, 3 and 4). Supercells were chosen by taking into account the group-subgroup relations along with the way the 6c Wyckoff position in $Pm\bar{3}n$ is split in possible subgroups. Consequently, for x = 2 and 4, the space group $P4_122$ (No. 91) with lattice parameters $a \times a \times 2a$ containing two formula units was used, while for x = 3 the calculations were conducted in the space group $Ia\bar{3}d$ (No. 230) with lattice parameters $2a \times 2a \times 2a$ (eight formula units in the primitive cell). In all the present calculations, Ba atoms were assumed to be located at the centers of the cages and the possibility of vacancies at the 6c position was ignored. The good qualitative agreement found between the experimental and theoretical results (see following sections) suggests that the qualitative picture emerging from the first-principles calculations will not change significantly by the introduction of vacancies. Nonetheless, the effects of vacancies on the electronic structure especially for the x = 4 case will not be discussed in this study. Regarding the binary clathrate Ba_8Si_{46}, only the unit cell volume was optimized while keeping the experimental values of the atomic coordinates fixed.[115] Since the x = 6 clathrate does not exist, both the atomic coordinates and the unit cell volume were optimized. In the case of x = 2, 3 and 4, the experimental crystallographic parameters derived from X-ray diffraction data for x = 2.6, 3.2 and 3.7, respectively, were used (Table 7.4).

Table 7.4: Crystallographic data of the x = 2.6, 3.2 and 3.7 compounds derived from single-crystal X-ray diffraction experiments. For the calculations, no site splitting was introduced to the data.

Actual Ni content x	a (Å)	Si in 16i (x, x, x)	Si in 24k (0, y, z)
2.6	10.2982	0.18463	y = 0.31126 z = 0.12137
3.2	10.2922	0.18442	y = 0.31233 z = 0.12178
3.7	10.2906	0.18440	y = 0.31249 z = 0.12165

The use of supercells is required to investigate the electronic structures of the $Ba_8Ni_xSi_{46-x}$ clathrates for x = 2, 3, 4. In the tetragonal space group $P4_122$, suitable for x = 2 and 4, the 6c position of $Pm\bar{3}n$ splits into three Wyckoff positions: two 4a (0, y, 0) positions (one with y = ¼, the other with y = –¼) and the 4c (x, x, ⅜) position (with x = ½). Two distinct models are then possible: the 4a sites can be occupied either by the atoms of (a) the same element or by (b) both Ni and Si. The latter model has a lower total energy, the energy differences amounting to 2.4 and 2.3 meV atom^{-1} for x = 2 and 4, respectively. For x = 3, the 6c position in $Pm\bar{3}n$ splits into 24c (⅛, 0, ¼) and 24d (⅜, 0, ¼) positions in the space group $Ia\bar{3}d$. The total energy difference between the Ni-at-24c and the Ni-at-24d models is quite small, 0.5 meV atom^{-1} in favor of the former. This slight difference may be regarded as a sign of lack of superstructure.

The electronic band structures of $Ba_8Ni_xSi_{46-x}$ for x = 0, 2, 3 and 4 are shown in Fig. 7.9. Note that, except for the binary compound, the Brillouin zones shown are not folded back to that of the original cubic lattice but are those of the supercell lattices. The number of bands crossing the Fermi level amounts to four for x = 0 and 2, then increases to eight for x = 3.0 before decreasing to only three bands for x = 4. This first result highlights the sensitivity of the electronic structure of these compounds to the Ni content and thus indicates a non-rigid like evolution of the band structure with x. The higher degree of complexity of the band structure in the x = 3 compound may also support the possibility of distinct transport properties which may extend over a small concentration range around x = 3.

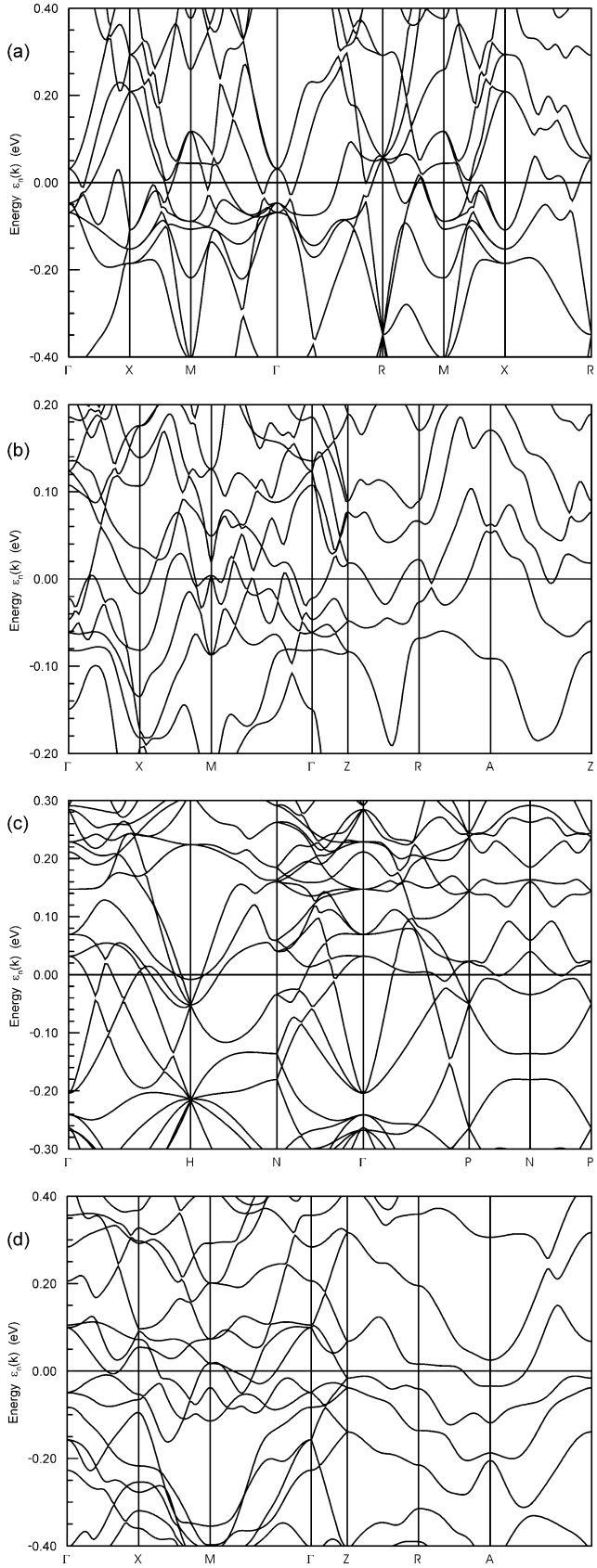

Figure 7.9: Dispersion curves along high symmetry directions near the Fermi level of $Ba_8Ni_xSi_{46-x}$ for x = 0 (**a**), 2.0 (**b**), 3.0 (**c**) and 4.0 (**d**).

The projection of the dispersion curves onto the energy axis results in the energy dependence of the total DOS as shown in Fig. 7.10.

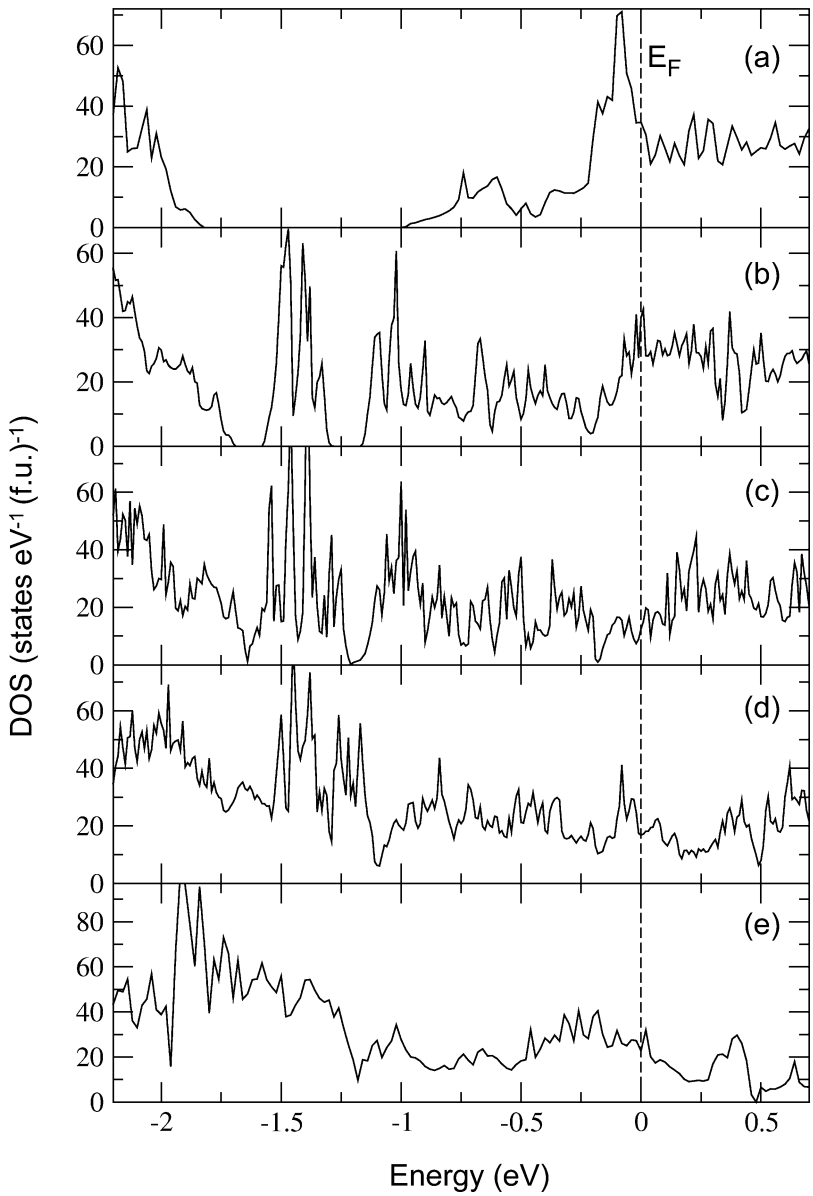

Figure 7.10: Energy dependence of the total density of states near the Fermi level of $Ba_8Ni_xSi_{46-x}$ for x = 0 (**a**), 2 (**b**), 3 (**c**), 4 (**d**) and 6 (**e**). The vertical dashed line at 0 eV stands for the Fermi level.

$Ba_8Ni_xSi_{46-x}$ (x = 0, 2, 3, 4 and 6) shows metallic behavior. The electronic structure of Ba_8Si_{46} (Figure 7.10a) is in good agreement with those reported previously in the literature.[195, 206, 207] A gap between –1.8 and –1.0 eV and a sharp peak located just below the Fermi level arising from the strong hybridization of the Ba 5*d* and Si 3*p* orbitals stand for the two main characteristics of the DOS. The gap is a feature inherited from the

(hypothetical) empty Si_{46} clathrate in which all Si atoms have four Si neighbors as in α-Si. Filling the cages with Ba atoms introduces 16 extra electrons which should occupy the lower parts of the Si_{46} conduction band made up by anti-bonding Si 3*p* states. However, the hybridization of the Ba 5*d* orbitals which become occupied, with the Si 3*p* orbitals makes the situation more complex than this simple picture. Nevertheless, the original gap of the Si_{46} clathrate is preserved, the DOS integrated between –1 eV and the Fermi level giving exactly 16 electrons. The contribution of the Ba 5*d* orbitals to the DOS starts to be important mainly above –1 eV and their occupancies are 0.86 and 0.66 electrons for Ba in the small and large cages, respectively.

The valence bands extend down to –12.6 eV. The region between –12.6 eV and –7.7 eV is dominated by Si 3*s* states. A group of Si 3*s*–3*p* bands of width ~ 2 eV follows a pseudo-gap of ~ 0.2 eV. A gap of ~ 0.5 eV separates this group from a predominantly Si 3*p* band (with small admixtures of Ba 5*d*) covering the energy range –5 eV, –1.8 eV.

The substitution of Si by Ni atoms at the 6*c* position mainly result in three effects: (i) the valence electron count increases by 6 (including 3*d* electrons) for each Si → Ni exchange, (ii) nine orbitals of Ni (4*s*, 4*p*, 3*d*) replace four orbitals of Si, (iii) due to the larger atomic number of Ni, the bandwidth of the valence band region decreases with increasing the Ni content (12.6 eV versus 11.5 eV for 0 and 6 Ni atoms in the formula unit, respectively) which is associated to a Ni–3*d* – Si–3*p* energy difference (charge transfer energy). Because of the second and third effects, a simple rigid band approach breaks down as already suggested by the variations in the dispersion curves. Among the Ni orbitals, the 3*d*'s are the most relevant, and behave very differently in comparison to Si 3*p* orbitals. On one hand, the Ni 3*d* orbitals hybridize mainly with the Si 3*p* orbitals and on the other hand, they display atomic-like behavior giving rise to sharp features in the DOS. In addition, Ni 3*d* states have a narrower bandwidth and lie roughly between –5 and 2 eV. The Ni 3*d* occupation, as calculated from projected DOS, is 8.8 electrons and remains constant with *x*. Likewise, the Ba 5*d* occupations are also fairly constant and only slightly vary between 0.76 and 0.86 and between 0.62 and 0.66 electrons for Ba in small and large cages, respectively. The Ni-content dependence of the total DOS at the Fermi energy, $N(E_F)$, and its atom-resolved components are listed in Table 7.5. $N(E_F)$ is mainly dominated by Si 3*p* states, the Ni contribution exceeding that of Ba only at $x = 4$. It is observed that $N(E_F)$ drops significantly from ~ 35 to ~ 10 states.eV^{-1}.(f.u.)$^{-1}$ when the Ni content is increased from $x = 2$ to $x = 3$. $N(E_F)$ starts to increase for $x > 3$ reaching ~ 17 and ~ 23 states.eV^{-1} (f.u.)$^{-1}$ for $x = 4$ and 6, respectively. The large values of $N(E_F)$ at $x = 0$ and $x = 2$ in combination of a pseudo-gap opening at 0.25 and 0.5eV most probably signal instability towards superconductivity, while the somewhat smaller values at $x = 4$ and 6 may hint at structural instability. Indeed, the latter does not form and the former is found to contain

vacancies as mentioned above. The decrease of $N(E_F)$ with increasing the concentration x of the substituting element was observed in other Si-based ternary type-I clathrates [175, 191, 192] and was correlated to the decrease of the superconducting transition temperature T_c with x.

Table 7.5: Total and atom-resolved densities of states at the Fermi level expressed in states eV^{-1} $(f.u.)^{-1}$

Theoretical Ni content x	**0**	**2.0**	**3.0**	**4.0**	**6.0**
$N(E_F)$	34.66	35.83	9.89	16.81	22.76
Ba	7.79	7.06	1.96	2.28	1.82
Si at 6*c*	4.09	3.61	0.66	0.51	-
Si at 16*i*	7.38	8.04	2.52	3.73	4.42
Si at 24*k*	15.40	16.06	4.12	7.24	11.39
Ni at 6*c*	-	1.06	0.63	3.04	5.13

The partial DOS depicting Ni 3*d* and Si 3*p* contributions for x = 2, 3, 4 are shown in Fig. 7.11. The contributions are referred to the Wyckoff positions in the original cell's space group after evaluating per atom averages in respective supercells. For x = 2, the sharp peaks around –1.5 eV originate from Ni 3*d* states. These states have negligible dispersion with a bandwidth of ~ 0.3 eV. They are located inside the gap (between –1.70 and –1.15 eV) which is narrower by 0.25 eV than the gap observed in the binary Ba_8Si_{46} clathrate and are due to the Ni 3*d* orbitals exhibiting a more atomic-like behaviour.[195, 206, 207] These weakly dispersing Ni 3*d* states are observable also for x = 3 around –1.5 eV with a larger bandwidth of ~0.45 eV. The original gap disappears and two pseudogap-like features develop at –1.65 and –1.20 eV. With a further increase of the Ni content *e.g.* x = 4, no sign of the original gap is observed. Although Ni 3*d* states still display sharp features in the DOS, the corresponding bands (not shown) are actually more dispersive. These modifications in the electronic structure generated by the Ni substitution are qualitatively similar to those observed in the $Ba_8Ga_xSi_{46-x}$, $Ba_8Cu_xSi_{46-x}$ and $Ba_8Ag_xSi_{46-x}$ systems.[30-32]

In conclusion, as the Ni content increases, so does the number of weakly-dispersing Ni *3d* states. Thus, these states start filling the band gap originating from the hypothetical Si_{46} clathrate. Furthermore, these states show increasing hybridization (both Ni–Si and Ni–Ni) with increasing x, so that a transition from the isolated *d* bands (x = 2) to the appearance of pseudo-gaps (x = 3.0), and finally to a gapless band structure (x = 4) occurs.

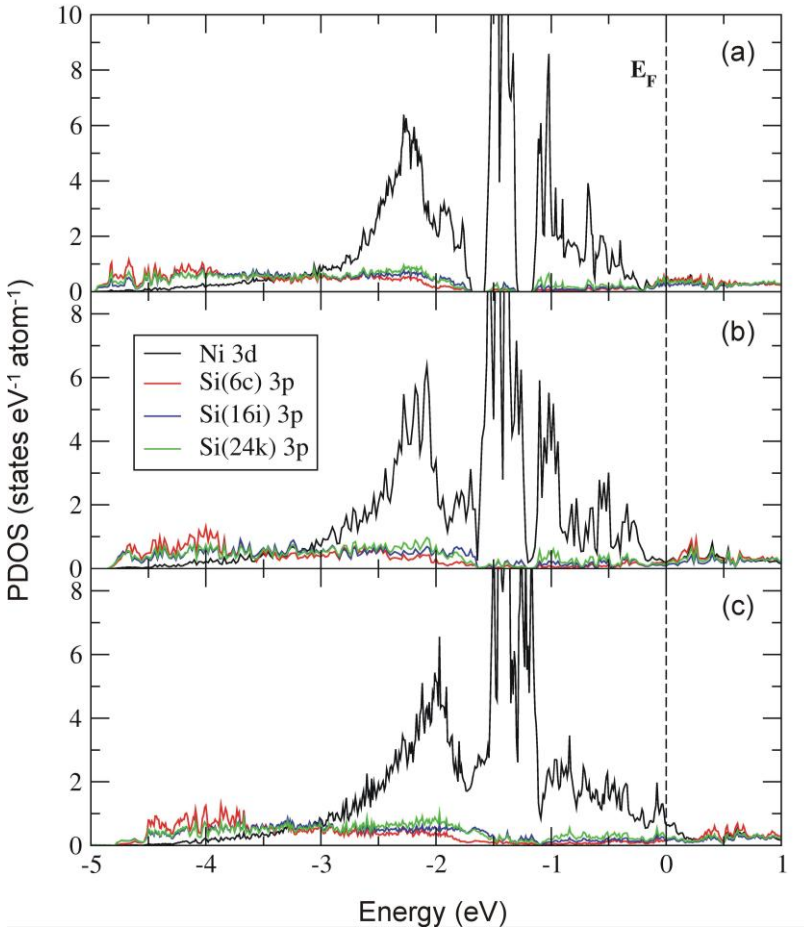

Figure 7.11: Partial density of states of $Ba_8Ni_xSi_{46-x}$ for x = 2.0 (**a**), 3.0 (**b**) and 4.0 (**c**). The vertical dashed line stands for the Fermi level.

Fig. 7.12a shows C_p / T as a function of T^2 in the temperature range 1.9 – 15 K for the illustrative composition with determined x = 3.1 (see Eq. 3.15). While the parent compound Ba_8Si_{46} becomes superconducting below ~ 8 K,[6, 163] no superconducting transition could be observed down to 1.9 K in the Ni-substituted samples for $2.4 \leq x \leq 3.8$. This result is consistent with previous studies revealing that substituting either on the Ba or on the Si site tends to decrease the critical temperature, T_c.[6] Several theoretical studies have indicated that superconductivity is an intrinsic property of the sp^3 network, therefore suggesting that the similarity between Ga or Ge atoms and Si helps maintain superconductivity.[163, 175, 191, 192] This hypothesis seems to be further corroborated by results obtained in the $Ba_8Cu_xSi_{46-x}$ system for which T_c was drastically lowered down to 2.9 K for x = 4.[175] To clarify whether superconductivity survives by the addition of Ni and thus, appears at lower temperatures, further measurements down to 0.4 K using the He^3 option of PPMS were carried out. No superconducting transition could be detected above 0.4 K demonstrating that replacing ~ 6 at.% Si atoms prevents the formation of a superconducting state. Magnetic susceptibility

data have clearly shown that Ni atoms are in a non-magnetic state ruling out magnetic pair-breaking effect *i.e.* interaction of magnetic moments with conduction electrons breaking the time-reversal symmetry of the Cooper pairs and leading to a strong reduction of T_c with x. Thus, the observed variation seems to support the idea of a direct link between the strong decrease of T_c and $N(E_F)$ via the electron-phonon coupling constant, $\lambda_{e\text{-}ph}$, at least above x = 2. Between x = 0 and x = 2, however, our electronic band structure calculations suggest a negligible influence of Ni on $N(E_F)$ which might preserve the existence of a superconducting state. Clearly, further experiments at lower Ni contents are required to pin down the exact variations in T_c across the entire possible Ni concentration range.[34] To further explore if the variations in $N(E_F)$ trace the disappearance of T_c for $0 \leq x \leq 3.8$, the Sommerfeld coefficient, γ, which reflects the renormalized density of states $(1 + \lambda_{e\text{-}ph})$ $N(E_F)$, were extracted from the low temperature regions (1.8 – 6 K) using Eq. 3.15. The inferred γ and β values are listed in Table 7.6.

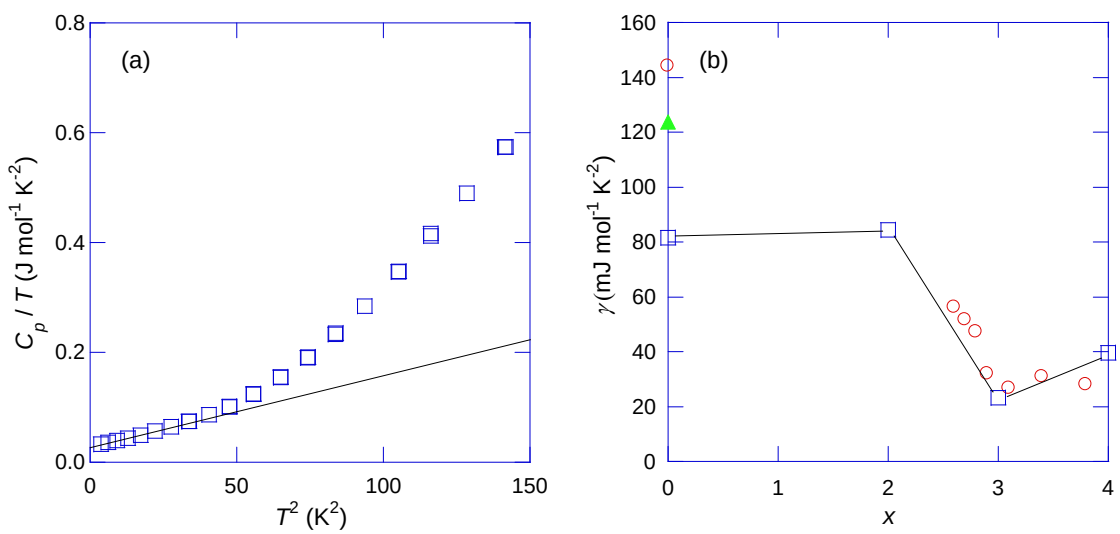

Figure 7.12: (**a**) C_p / T as a function of T^2 for the illustrative sample with determined x = 3.1. All samples studied display a similar temperature dependence. The solid line is a guide to the eye to underline the narrow temperature window where a linear dependence is observed. (**b**) Sommerfeld coefficient, γ, as a function of the Ni content. The symbols (○) refer to the experimental γ values while the symbols (□) stand for the theoretical values inferred from band structure calculations. The symbol (▲) refers to the experimental value of Ba_8Si_{46} obtained from specific heat measurements.[208]

Table 7.6: Values of the γ and β parameters along with the Debye temperature, θ_D, the theoretical values of the Sommerfeld coefficient, γ_{FPLO}, and the electron-phonon coupling constant $\lambda_{\text{e-ph}} = \gamma / \gamma_{\text{FPLO}}$ for $Ba_8Ni_x\square_ySi_{46-x-y}$.

Ni content x (WDXS)	γ (mJmol^{-1}K^{-2})	β (mJmol^{-1}K^{-4})	θ_D (K)	γ_{FPLO} (mJmol^{-1}K^{-2})	$\lambda_{\text{e-ph}}$
2.6	56.1	1.15	450	47.6	0.18
2.7	51.7	1.08	460	41.6	0.24
2.8	47.2	0.98	474	35.2	0.34
2.9	32.0	1.16	448	29.2	0.10
3.1	26.8	1.38	424	24.1	0.11
3.4	30.8	1.32	430	29.0	0.06
3.8	27.9	1.31	431	35.6	-

Within the Debye model, the β coefficient is related to the Debye temperature through Eq. 3.16. With $n = 54$ for all samples, θ_D is obtained in the range ~ 420 – 470 K regardless of the Ni content. These values are slightly higher but coherent with that reported for Ba_8Si_{46} (θ_D ~ 370 K) and suggest that the phonon spectrum is not significantly modified in the presence of Ni atoms.[176]

As suggested by our band structure calculations, the x = 3 composition delineates two regions. Below this value, γ strongly decreases with the Ni content before increasing up to x = 3.8 (Fig. 7.12b). Assuming a linear variation in $N(E_F)$ with different slopes between x = 2 and 3 and x = 3 and 4, an estimation of $\lambda_{\text{e-ph}}$ can be inferred (Table 7.6). The presence of Ni drastically depresses the $\lambda_{\text{e-ph}}$ values from 0.8–1.2 in Ba_8Si_{46} down to 0.1 at x = 2.9 reflecting the decrease in $N(E_F)$.[176, 208] At higher Ni contents, however, the theoretical γ values overestimate the experimental ones. Our detailed structural and chemical characterizations have shown that vacancies are present in the crystal structure at high Ni contents and may be a reason for the observed discrepancy. Further calculations taking into account vacancies may help to determine their influence on the electronic band structure of these compounds. Several studies undertaken on the Ba_8Si_{46} compound and on its ternary derivatives have shown that the thermodynamic properties of the superconducting state can be satisfactorily described within the BCS theory.[6, 176] Assuming that this result can be extended to these Ni substituted compounds, the superconducting transition temperature can be estimated using the $\lambda_{\text{e-ph}}$ values and the McMillan formula:[209]

$$T_c = \frac{\theta_D}{1.45} \exp\left(\frac{-1.04(1+\lambda_{\text{e-ph}})}{\lambda_{\text{e-ph}} - \mu^*(1+0.62\lambda_{\text{e-ph}})} \right) \tag{7.6}$$

where μ^* is the effective electron-electron repulsion. The value of this parameter was estimated to be ~ 0.23 for Ba_8Si_{46} from measurements of the superconducting isotope coefficient.[176] Though this value is higher than those usually assumed in conventional superconductors (~ 0.1 – 0.15) and thus at the border of the BCS theory, it appears to be consistent with the theoretical value ~ 0.24.[210] Assuming that μ^* does not appreciably vary across the Ni concentration range and taking the θ_D values derived from the lattice contribution to the specific heat, the values of $\lambda_{e\text{-}ph}$ obtained are clearly too low to induce a superconducting transition in these samples. In addition, a maximum T_c of 0.4 K in Eq. 7.6 alternatively gives a lower limit of $\mu^* = 0.21$, further supporting a large value of this parameter in Ba_8Si_{46} and its ternary derivatives. This result might hint towards a more complex mechanism involved in the formation of the superconducting condensate such as two-gap superconductivity as recently suggested by tunneling-spectroscopy experiments carried out on Ba_8Si_{46}.[211] In addition, these results complement previous reports indicating that the variations in $N(E_F)$ primarily govern the superconducting transition temperature in Si-based type-I clathrates.[6, 195]

The temperature dependence of the magnetic susceptibility, χ, of $Ba_8Ni_x\square_ySi_{46-x-y}$ is shown in Fig. 7.13.

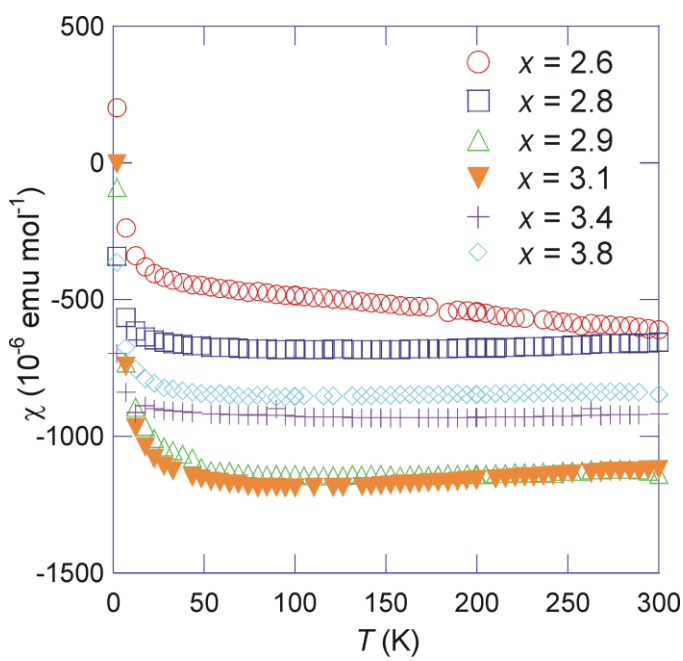

Figure 7.13 Temperature dependence of the magnetic susceptibility of $Ba_8Ni_x\square_ySi_{46-x-y}$.

The measurements of the isothermal magnetization curves, $M(H)$, performed at 5 and 300 K revealed a perfect linearity up to 5 T and thus, the absence of ferromagnetic impurities. Regardless of the Ni content, χ is negative and quasi temperature-independent down to

~ 20 K indicating diamagnetic behavior. These results indicate that Ni assumes $3d^{10}$ electronic configuration and thus possesses a zero-spin state in these compounds. This conclusion is further confirmed by investigations of the local structure surrounding the Ni atoms via XANES measurements described in section 7.7. Traces of Curie-paramagnetic impurities are likely responsible for the upturns towards low temperatures which result in positive values at 2 K in the x = 3.1 and 3.4 samples. At room temperature, the magnetic susceptibility reaches values ranging between –600 and –1200 × 10^{-6} emu mol^{-1}. These values are consistent with that of the parent Ba_8Si_{46} compound estimated to be –1150 ×10^{-6} emu mol^{-1}.[176] An estimation of the core diamagnetic values, χ_{dia}, can be obtained by subtracting the Pauli susceptibility contribution, χ_{Pauli}, which arises from the contribution of magnetically non-polarized charge carriers. The Pauli susceptibility is related to $N(E_F)$ via Eq. 6.4. Using the calculated $N(E_F)$ values (Table 7.5), the χ_{Pauli} values can be inferred and are summarized in Table 7.7. Note that, as a first approximation, the theoretical $N(E_F)$ values for x = 2.6, 2.8, 2.9 and 3.4 were estimated assuming a linear variation of $N(E_F)$ with two different slopes for x varying between 2 and 3 and between 3 and 4, respectively. Within this assumption, the core diamagnetic contributions obtained are roughly similar across the entire Ni concentration range (Table 7.7). Even though none of the samples studied contain any paramagnetic phases, additional diamagnetic contributions originating from secondary phases may also play a role in the observed differences. In addition, these values can be compared to the expected χ_{dia} values estimated using the tabulated diamagnetic contributions of closed-shell cations (Table 7.7).[212] This yields (absolute) values significantly lower than the experimental ones pointing to the presence of an extra source of diamagnetism in these compounds which cannot be attributed to the small amount of secondary phases. This discrepancy is however restricted neither to $Ba_8Ni_xSi_{46-x}$ nor to clathrate structures and several other intermetallic compounds such as $CoSb_3$ or $RuAl_2$ are known to exhibit enhanced diamagnetism.[213, 214] Though the exact underlying mechanism in these materials remains an unsettled issue, it was suggested that molecular-ring currents, induced by the Lorentz force under an applied magnetic field and responsible for the magnetic properties of carbon allotropes and aromatic molecules, might be equally at play in clathrates.[97, 172] However, this mechanism is not firmly established in clathrates and clearly requires further theoretical and experimental studies before drawing any final conclusion.

Table 7.7: Debye temperature, θ_D, the coefficient of the phonon contribution to the electrical resistivity, R, and the residual electrical resistivity, ρ_0, as determined from the best fits to the data according to the Bloch-Grüneisen law (Eq. 7.7) for $Ba_8Ni_x\square_ySi_{46-x-y}$. Note that the ρ_0 values are expressed here in μΩcm.

Ni content x (WDXS)	θ_D (K)	R (μΩcmK^{-1})	ρ_0 (μΩcm)
2.6	343	7.8	244
2.8	243	5.8	218
2.9	206	5.3	270
3.1	578	8.7	297
3.4	404	16.6	355
3.8	287	13.9	288

Low-temperature electrical resistivity $\rho(T)$ of $Ba_{8-\delta}Ni_xSi_{46-x}$ phase with low Ni content shows superconducting behavior (Fig. 7.14). The ρ values of the samples with compositions $Ba_{7.9(1)}Ni_{1.4(1)}Si_{44.6(1)}$ and $Ba_{7.9(1)}Ni_{1.6(1)}Si_{44.4(1)}$ remained quasi-constant down to the superconducting transition with onsets at T_c = 6 K and 5.5 K and zero-resistance temperatures 3.5 K and 3 K, respectively. The broad superconducting transitions of ΔT_c ~ 2.5 K for both compounds may be related to inhomogeneities in the Ni content arising from rapid cooling. Since X-ray diffraction measurements together with the EDXS analyses revealed no detectable impurity phases, this indicates that the superconducting transition observed is an intrinsic property of the clathrate phase at these compositions. The presence of Ni results in a slight decrease of T_c compared to Ba_8Si_{46} where a superconducting state sets in at 8 K. Higher Ni contents ($x \geq 2.4$) resulted in a complete suppression of superconductivity down to 0.4 K as shown by low-temperature electrical resistivity measurements. This sharp decrease in T_c with Ni content reflects the evolution of the density of states at the Fermi level, $N(E_F)$, which shows only slight variation for $0 \leq x \leq 2.0$ before exhibiting a drastic decrease between x = 2.0 and x = 3.0. Thus the decrease in the electron-phonon coupling strength in $Ba_{8-\delta}Ni_x\square_ySi_{46-x-y}$ originates from the Ni-content-dependent variations in the electronic band structure. A decrease in T_c is a feature shared by all ternary type-I clathrates investigated so far showing that both alloying on the Ba or Si site tends to suppress superconductivity. However, the variation in T_c strongly depends on the substituting element as found out in several studies on $Ba_8M_xSi_{46-x}$ for M = Ge,[163] Ga,[191] or Cu.[175] While a superconducting state still develops in the Ge- and Ga-substituted systems up to x = 25 and x = 10, respectively, a lower Cu content of x = 4 is sufficient to drop T_c from 8 K down to 2.9 K. In the present case, Ni has a stronger influence since the superconductivity disappears for $x \geq 2.4$.

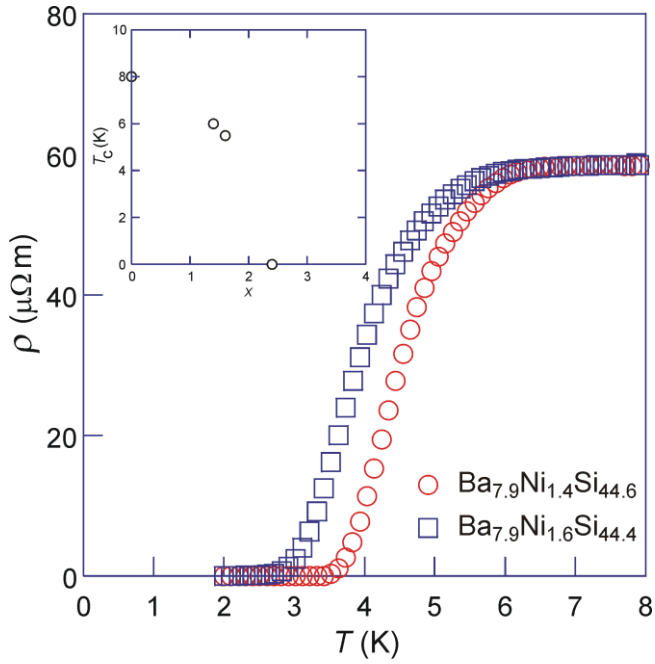

Figure 7.14: Electrical resistivity of the steel-quenched samples as a function of temperature: $Ba_{7.9(1)}Ni_{1.4(1)}Si_{44.6(1)}$ (○) and $Ba_{7.9(1)}Ni_{1.6(1)}Si_{44.4(1)}$ (□), showing the superconducting transition with onsets at 6.0 and 5.5 K, respectively. The inset figure illustrates the evolution of the critical temperature T_c as a function of the Ni content. The T_c value of Ba_8Si_{46} (x = 0) is taken from Yamanaka *et al.*[115]

The temperature dependence of the electrical resistivity of $Ba_8Ni_xSi_{46-x}$ is shown in Fig. 7.15. All the samples studied display a positive electrical resistivity coefficient $d\rho/dT$ indicative of metallic behavior in agreement with our band structure calculations. For x = 2.6, 2.8, 2.9, 3.4 and 3.8, the electrical resistivity exhibits a metallic-like behavior down to ~ 30 K and then slightly levels off at lower temperatures. The electrical resistivity of the x = 3.1 sample assumes quasi-constant values below 50 K to become weakly temperature dependent above this temperature up to 350 K. The $d\rho$ / dT coefficient varies across the Ni concentration range. The temperature dependence of ρ in simple metals and metallic alloys is usually dominated by electron-phonon scattering and is quantitatively expressed through the Bloch-Grüneisen law [215]:

$$\rho(T) = \rho_0 + 4\theta_D R\left(\frac{T}{\theta_D}\right)^5 \int_0^{\theta_D/T} \frac{x^5 dx}{\left(e^x - 1\right)\left(1 - e^{-x}\right)} \tag{7.7}$$

where R is the coefficient of the phonon contribution to the electrical resistivity which mainly controls the $d\rho$ / dT values. The variations in the R values should therefore reflect the variations in the electron-phonon coupling strength. The observed variation in R,

inferred from least-squares fits to the data according to Eq. 7.7 using ρ_0, R and θ_D as free parameters, seems to be in agreement with this picture (Table 7.7). However, even though a discrepancy between the Debye temperatures obtained from the Bloch-Grüneisen law and those extracted from specific heat analyses is usually observed due to the fact that only the longitudinal phonons are taken into account in deriving Eq. 7.7, marked differences appear in the present case. In the absence of electronic and magnetic correlations, such discrepancy may be a sign of a multiband conduction as suggested by our band structure calculations.

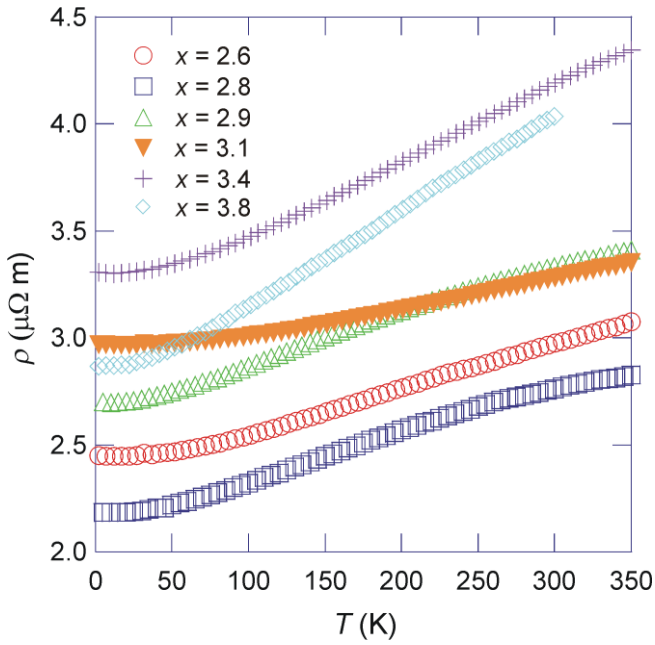

Figure 7.15: Temperature dependence of the electrical resistivity of $Ba_8Ni_x\square_ySi_{46-x-y}$.

In the whole temperature range, the ρ values are only slightly sensitive to the Ni content and range between 2.8 μΩm and 4.5 μΩm at room temperature (Table 7.8). No clear trend towards lower or higher ρ values with Ni substitution can be observed in these data. The theoretical prediction that both holes and electrons are involved in the electrical conduction of these materials may explain this behavior, since the mobilities along with the hole and electron concentrations are intimately related to the Ni content and to the subtleties of the band structure, specifically near the x = 3 composition. However, slight differences in the microstructure and in the amount of secondary phases which vary across this series of samples may potentially mask any real x dependence in the data.

Table 7.8: Room temperature values of the electron concentration (n), Seebeck coefficient (α) and electrical resistivity (ρ) of $Ba_8Ni_x\square_ySi_{46-x-y}$. The total thermal conductivity (κ) values are given at 200 K due to the radiative contribution responsible for the slight upturns above this temperature.

Actual Ni content x	n (10^{21} cm^{-3})	α (μVK^{-1})	ρ (μΩm)	κ (Wm^{-1}K^{-1})
2.6	7.0	– 13.3	3.0	4.4
2.8	5.2	– 11.1	2.8	4.6
2.9	3.5	– 11.4	3.3	4.6
3.1	3.5	– 7.0	3.3	4.3
3.4	4.1	– 17.6	4.5	4.0
3.8	4.5	– 26.1	4.0	4.2

Hall effect experiments, performed in the 10 – 300 K temperature range, provide additional information regarding the effect of the Ni content on the electronic band structure. Fig. 7.16a shows the Hall resistivity, ρ_H, as a function of the magnetic field at selected temperatures for the illustrative clathrate with determined $x = 3.4$. To exclude the longitudinal magnetoresistive contribution coming from misalignment of contacts, the Hall resistivity was derived from the antisymmetric part of the transverse resistivity under magnetic field reversal following the formula:

$$(\rho_{xy}(+\mu_0 H) - \rho_{xy}(-\mu_0 H))/2 \tag{7.8}$$

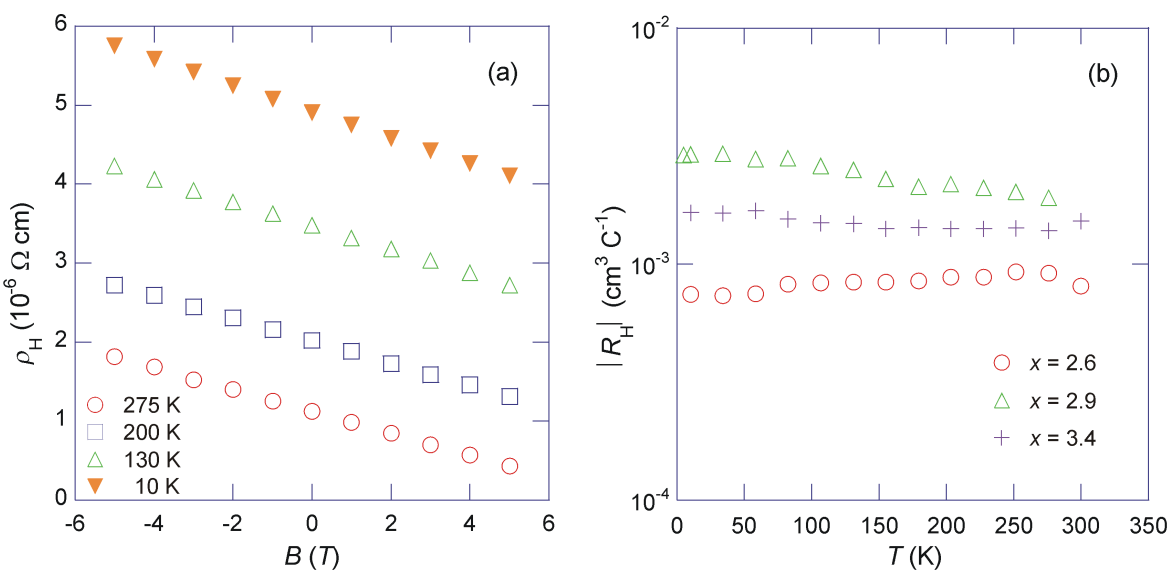

Figure 7.16: (**a**) Field dependence of the Hall resistivity, ρ_H , for the illustrative sample $x = 3.4$ at different temperatures. (**b**) Temperature dependence of the Hall coefficient, $|R_H|$, of $Ba_8Ni_x\square_ySi_{46-x-y}$.

For all samples, $\rho_H(\mu_0 H)$ data are linear with a negative slope in the whole temperature and field ranges investigated indicative of a dominant electron-like signal. No indications of departure from linearity as may be expected from the presence of both types of carrier can be observed in the present data. Assuming that both carriers contribute to the measured Hall signal, this absence of departure may then indicate that holes remain in the low-field limit ($\mu_H B << 1$) in the field range covered by our experiments. The Hall coefficient, R_H, inferred from the slope of the $\rho_H(\mu_0 H)$ curves, is weakly temperature dependent for the x = 2.6 and 3.4 samples and is consistent with the metallic nature of these compounds (Fig. 7.16b). The temperature dependence of the x = 2.9 sample is somewhat stronger, the $|R_H|$ values decreasing with increasing temperature from 2.85×10^{-3} at 10 K to 1.90×10^{-3} cm^3C^{-1} at 275 K. Within a single-band picture, this would correspond to an increase of the electron concentration, n, from 2.15×10^{21} at 10 K up to 3.3×10^{21} cm^{-3} at 275 K using the single-carrier relation (Eq. 3.9). The temperature dependence of the x = 2.9 sample might indicate that both holes and electrons contribute to the Hall signal. Nevertheless, adopting a single-band model to derive n at room temperature (Table 7.8) leads to a decrease of n with increasing x up to x = 3.1 before slightly increasing up to x = 3.8. In any case, the variations in n as a function of the Ni content are consistent with an overall decrease in $N(E_F)$ as previously discussed.

Though direct experimental evidence of the contribution of both types of carriers remains elusive from electrical resistivity and Hall effect data, the temperature and x dependences of the thermopower, shown in Fig. 7.17, provide some hints for the presence of both types of carriers.

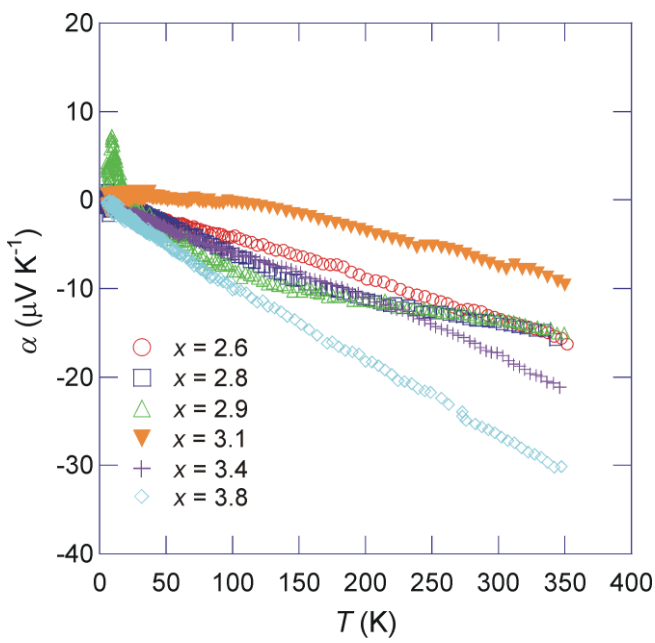

Figure 7.17: Temperature dependence of the thermopower of $Ba_8Ni_x\square_ySi_{46-x-y}$.

Regardless of the Ni content, α increases in absolute value with increasing temperature to reach values ranging between –7 and –26 μVK^{-1} at 300 K (Table 7.8). The negative sign of α suggests that electrons dominate the electrical conduction and is therefore consistent with a dominant electron-like response in the Hall effect measurements. These results also reveal a non-monotonic behavior of the thermopower with x. At low Ni contents, $\alpha(T)$ varies linearly before evolving into a non-linear dependence upon decreasing temperature, the departure from linearity being stronger as the Ni content is slightly increased from x = 2.8 to x = 2.9. Such behavior is not confined to these compounds and qualitatively resembles those of the $Ba_8Pt_xSi_{46-x}$ and $Ba_8Pd_xSi_{46-x}$ systems in which complex variations in $\alpha(T)$ as a function of temperature and substitution level were observed.[216] A transition from negative to positive values occurs below 20 K in the x = 2.9 sample with a maximum of ~ 8 μVK^{-1} at 10 K. A maximum in α at low temperatures is usually related to a phonon or magnon-drag effect. However, the diamagnetic nature of the samples studied and the lack of coincidence of the peak temperature and the temperature of the dielectric maximum in the thermal conductivity suggest a different origin. The observed positive values of α together with the negative slope of the $\rho_H(\mu_0 H)$ curves clearly show that both holes and electrons are involved in the electrical conduction processes. Another conclusive signature is related to the variations in α with x. As evidenced in Table 7.8, at room temperature, α first decreases with increasing x before increasing with further addition of Ni. The concomitant drop in α and in the carrier concentration as shown by Hall effect data is unusual and contrasts with the expectation of an increase of the diffusion part of the thermopower, α_d, with decreasing carrier concentration following the free-electron relation [217]:

$$\alpha_d = \frac{\pi^2 k_B^2 2m_e}{e\hbar^2 (3n\pi^2)^{2/3}} T \tag{7.9}$$

Note that this relation is valid above θ_D where the electron-phonon scattering is expected to be the dominant scattering mechanism. In the present case, thermopower measurements performed at high temperatures have shown that the slope is temperature-independent, enabling to apply this relation at temperatures slightly below θ_D. Attempting to fit the $\alpha(T)$ data in the 250 – 350 K temperature range using Eq. 7.9 then yields an estimation of the charge carrier concentration, n, which amounts to 9.6 × 10^{21}, 2.1 × 10^{22}, 2.6 × 10^{22}, 1.3 × 10^{22}, 5.1 × 10^{21} and 3.8 × 10^{21} cm^{-3} for x = 2.6, 2.8, 2.9, 3.1, 3.4 and 3.8, respectively. At low Ni contents (x < 3.4), these values significantly differ from those derived from Hall effect data. At higher Ni concentrations (x = 3.4 and 3.8), however, a fairly good agreement

is achieved and shows that the thermal diffusion of charge carriers then dominates the temperature dependence of α. A possible explanation of this discrepancy could be related to the effective mass of the charge carriers significantly differing from the bare electron mass. In the present case, the above-mentioned values would imply an effective mass ranging between 0.15 and 0.35 for x = 2.8, 2.9 and 3.1. Even though variations in the effective mass with x cannot be strictly ruled out, the inapplicability of Eq. 7.9 at low substitution levels may rather reflect a hole contribution to the thermopower of increasing importance as the Ni content is approaching x = 3.0 where a quasi-compensation seems to be achieved. The smaller magnitude of α as the carrier concentration decreases may therefore originate from x-dependent hole and electron contributions to the thermopower which, in a two-band system, is expressed as:

$$\alpha = (\sigma_p a_p + \sigma_n a_n) / (\sigma_p + \sigma_n) \tag{7.10}$$

where α_p and α_n stand for the thermopower contributions of holes and electrons, respectively, while σ_p and σ_n are the respective partial electrical conductivities of holes and electrons.

The temperature dependence of the total thermal conductivity is shown in Fig. 7.18a. All the samples exhibit similar temperature dependence typical of simple crystalline insulators: the low temperature region is dominated by a pronounced dielectric maximum followed by an approximately T^{-1} dependence associated to propagating phonons scattered by anharmonic interactions. As expected from such close compositions, the thermal conductivity values remain quasi-constant as the Ni concentration spans the range $2.6 \leq x \leq 3.8$. The observed difference in magnitude of the dielectric maximum values near 25 K may be due to slight differences in the microstructure and to the varying amount of secondary phases present in our collection of samples. Nevertheless, the quasi-independence of the thermal conductivity with respect to x is consistent with the specific heat data suggesting minimal impact of an increase in the Ni content on the thermal properties of these materials. The experimental values of the thermal conductivity and of the electrical resistivity allow the lattice thermal conductivity, κ_l, to be extracted by subtracting the electronic contribution which can be estimated using the Wiedemann-Franz law (Eq. 3.5, Fig. 7.18b, c). All samples exhibit similar low κ_l values in agreement with those observed in various Ge-, Sn- and Si-based type-I clathrates.[4]

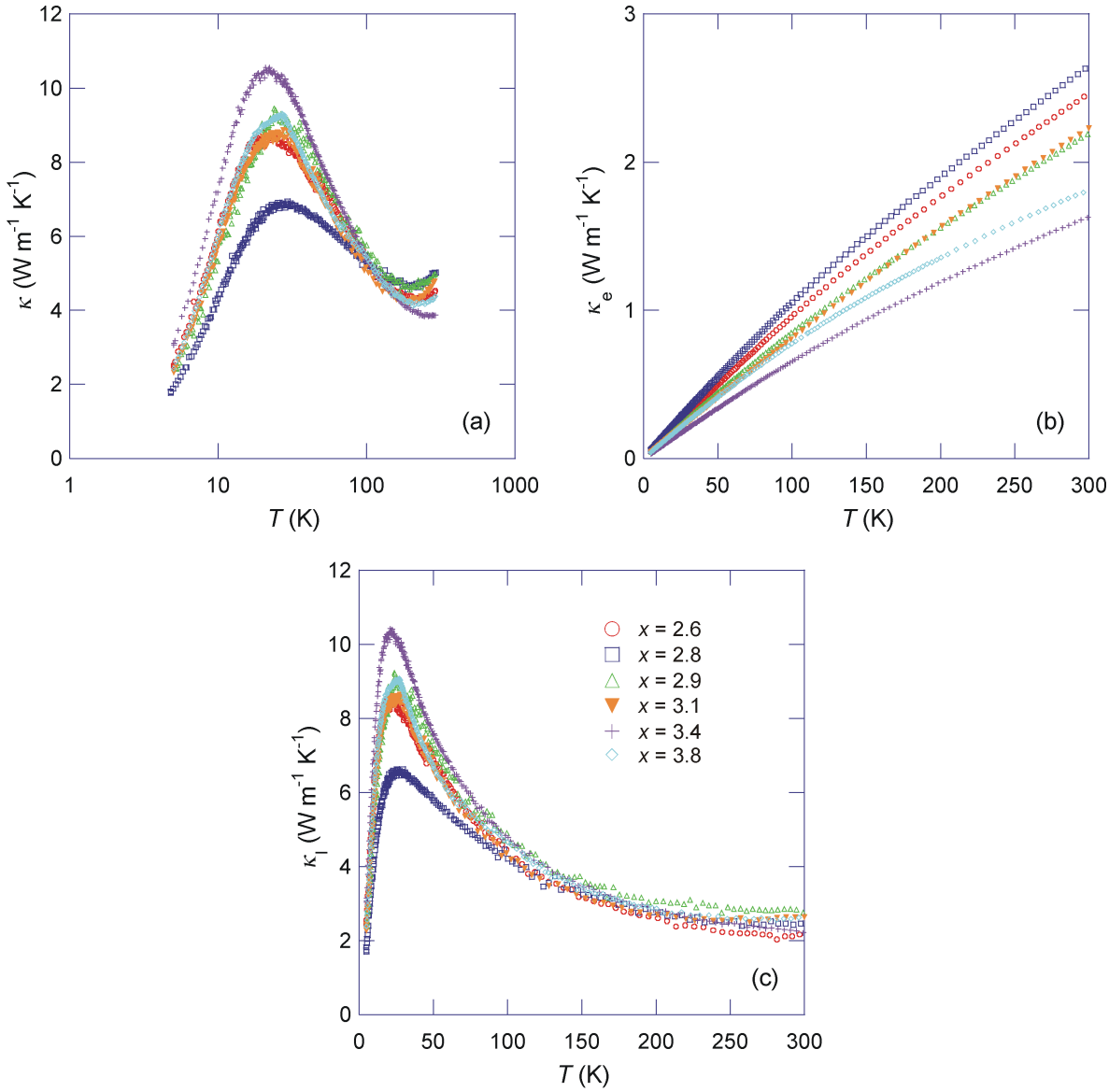

Figure 7.18: Temperature dependence of the total (**a**), electronic (**b**) and lattice (**c**) thermal conductivity of $Ba_8Ni_x\square_ySi_{46-x-y}$.

In addition to the low temperature characterization, the thermoelectric properties of $Ba_8Ni_x\square_ySi_{46-x-y}$ were determined in the temperature range 300 – 773 K (Fig. 7.19). The electrical resistivity of the samples increases linearly with increasing temperature in agreement with the metallic-like behavior observed in the low temperature range, and reaches the values between 3.5 and 5.9 μΩm at 750 K (Fig. 7.19a). The substitution of Si by Ni results in a slight increase of the electrical resistivity. Regardless of the composition, the thermopower values remain negative above room temperature, indicating a dominant contribution from electrons (Fig. 7.19b). The metallic character of these samples results in moderate values of thermopower that increase in absolute values with temperature reaching the values between –30 and –55 μVK^{-1} at 750 K. A clear trend of the thermopower values

as a function of the Ni content was not observed. This behavior can be attributed to a balance between the hole and electron contributions as observed in the low temperature investigation.

For all compositions, the thermal conductivity values are weakly temperature dependent ranging between 4.0 and 6.5 $Wm^{-1}K^{-1}$ at 773 K (Fig 7.19c). The measured values decrease with increasing Ni content up to x = 3.4. The observed behavior against x mainly reflects the variation of the electrical resistivity as evidenced by the temperature dependence of the lattice and electronic thermal conductivity displayed in Fig. 7.19d. To separate these two contributions, the electrical resistivity values were used to estimate the electronic contribution, κ_e, via the Wiedemann-Franz law (Eq. 3.5). The Lorenz number L was assumed as a first approximation to be equal to the value of a degenerate electron gas $L = L_0 = 2.44 \times 10^{-8}\ V^2K^{-2}$. The lattice thermal conductivity values κ_L are in the expected range for Si-based clathrates and decrease with increasing temperature as a result of dominant phonon-phonon interactions. In addition, κ_L decreases slightly as the Ni concentration increases. The combination of the transport properties results in a maximum ZT value of around 0.1 at 700 K for the sample with x = 3.8. The metallic nature of these samples is the main reason for the low ZT values.

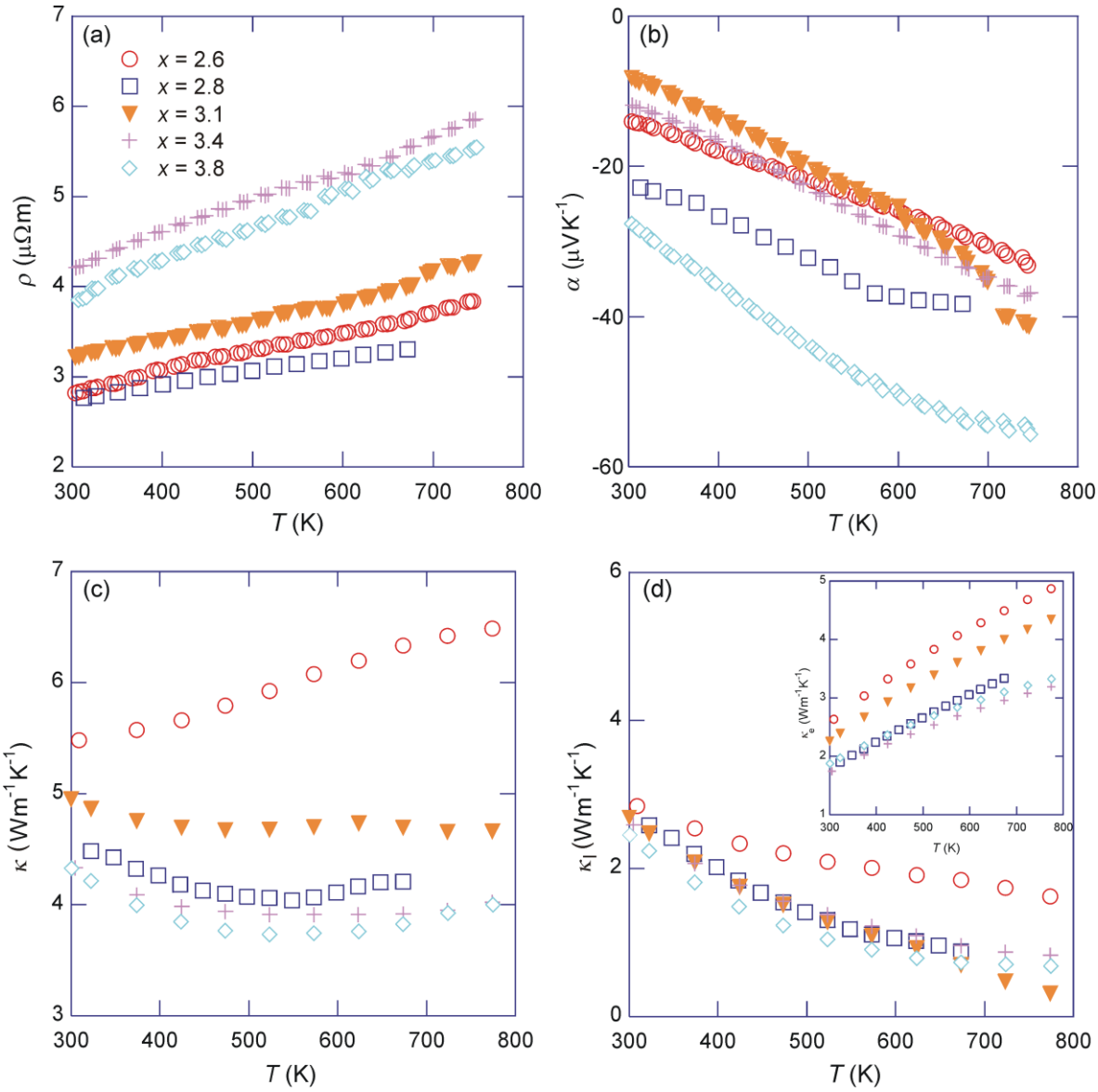

Figure 7.19: Transport properties of the clathrate $Ba_8Ni_x\square_ySi_{46-x-y}$ with determined compositions $Ba_8Ni_{2.6}Si_{42.6}$ (○), $Ba_8Ni_{2.8}Si_{42.1}$ (□), $Ba_8Ni_{3.1}Si_{42.3}$ (▼), $Ba_8Ni_{3.4}Si_{42}$ (+), and $Ba_8Ni_{3.8}Si_{41.3}$ (◊). Temperature dependence of the electrical resistivity (**a**), the thermopower (**b**), the total thermal conductivity (**c**), and the lattice and electronic thermal conductivities (**d**, **inset**) are shown.

7.10 Conclusions

The homogeneity range of the clathrate-I phase $Ba_8Ni_x\square_ySi_{46-x-y}$ was determined to be $2.4 \leq x \leq 3.8$ and $0 \leq y \leq 0.9$ at 1000 °C. The phase crystallizes in the space group $Pm\bar{3}n$. Single-crystal X-ray diffraction investigations together with microprobe analyses reveal the presence of framework vacancies for compositions with higher Ni content. The metastable clathrate phase $Ba_{8-\delta}Ni_xSi_{46-x}$ was prepared by steel-quenching and with $x \approx 1.4$ and 1.6. For $Ba_{8-\delta}Ni_x\square_ySi_{46-x-y}$, the lattice parameter decreases with Ni content starting from a = 10.3088(1) Å for $Ba_{7.9}Ni_{1.6}Si_{44.4}$ to a = 10.2896(1) Å for $Ba_8Ni_{3.8}Si_{41.3}$. Chemical bonding was analyzed based on ELI revealing two-electron two-center type Si–Si and two-center banana-type Ni–Si bonds in the valence region. For all compositions, XANES investigations indicate that the electronic state of the Ni atoms is close to that of the element. Physical properties including magnetic susceptibility, electrical resistivity, Hall effect, thermopower and thermal conductivity were investigated. Magnetic susceptibility data indicate that the Ni atoms have a non-magnetic state in these clathrates in agreement with the XANES results. Low-temperature electrical resistivity measurements show the samples with compositions $Ba_{7.9}Ni_{1.4}Si_{44.6}$ and $Ba_{7.9}Ni_{1.6}Si_{44.4}$ are superconducting with T_c around 6.0 K and 5.5 K, respectively. First-principles calculations have revealed a non-rigid variation in the electronic band structure and strong variations in $N(E_F)$ with x. These theoretical results are in line with experimental findings *viz.*, the variations in the electronic properties with the Ni content *i.e.*, a strongly depressed electron-phonon coupling strength as well as non-monotonic variations in electrical resistivity and thermopower as x increases. The thermopower data indicate that both holes and electrons are involved in the electrical conduction in these materials. All these results highlight the sensitivity of the electronic properties to the Ni content suggesting that these properties may not be confined to the Ni-substitution but may be observed in other ternary Si-based type-I clathrates. The metallic nature of $Ba_8Ni_x\square_ySi_{46-x-y}$ prevents achieving high ZT values ($ZT \approx 0.1$ at 700 K for $x = 3.8$) in the temperature range investigated.

Chapter 8

The Metallic Zintl Phase Ba_3Si_4

The intermetallic compound Ba_3Si_4 was encountered during the investigation of Ba – Ni – Si phase diagram. Intermetallic compounds of alkali metals and earth alkali metals with group 14 elements form crystal structures with a broad variety of polyanions with covalent bonds, which follow the Zintl-Klemm concept.[86] Numerous crystal structures of Zintl phases were determined, but only little is known about their physical properties due to their high reactivity against oxygen and moisture. It is expected that Zintl phases of closed shell cations and polyanions should be in general diamagnetic semiconductors. However, atomic interactions in solid phases influence the electronic structure, which may result in a nonzero DOS at E_F.[42, 218] Therefore, more precise predictions of physical properties need quantum mechanical calculations as demonstrated, *e.g.*, by the unexpected metallic behavior of single phase Ba_3Si_4. Ba_3Si_4 contains quasi-isolated Si_4^{6-} anion, as first reported in 1969 by Eisenmann *et al.*[25] The butterfly shaped anion was explained with the formal charge distribution $[Ba^{2+}]_3[(3b)Si^{1-}]_2[(2b)Si^{2-}]_2$ being in agreement with the Zintl concept.[25, 219] Investigations on the oxidation behavior of the binary alkali metal compounds with the main group elements led to the preparation of new phases with framework structures.[66, 200, 220] These studies were extended to the compounds of alkaline earth metals *e.g.* Ba_3Si_4.

8.1 Preparation and characterization

Ba_3Si_4. 0.7858 g (5.7 mmol) Ba (ChemPur, 99.9%) and 0.2143 g (7.6 mmol) Si (ChemPur, 99.999%) were sealed under argon in a Ta container. The container was further fused under argon in a silica ampoule and placed vertically in a tube furnace. In the first step of the reaction, the sample was heated in 3 h to 1200 °C, annealed for 1 h at this temperature, and then quenched to room temperature. Alternatively, induction heating was used as the first step. The heating was performed slowly enough to prevent the evaporation of Ba. In the second step, the sample was annealed for 3 d at 1000 °C. The reaction product consists of metallic shining, brittle, well-shaped crystals and is a single phase according to PXRD (Fig. 8.1) and SEM (Fig. 8.2). Ba_3Si_4 is very sensitive to air and moisture, therefore, all sample manipulations were carried out in an argon-filled glove box. EDXS analysis on three different pieces revealed the chemical composition $Ba_{3.0(1)}Si_{4.1(1)}$. A reaction under same conditions in open glassy carbon crucibles, welded in tantalum ampoules, lead always to the formation of small amounts of $BaSi_2$ as a by-product.

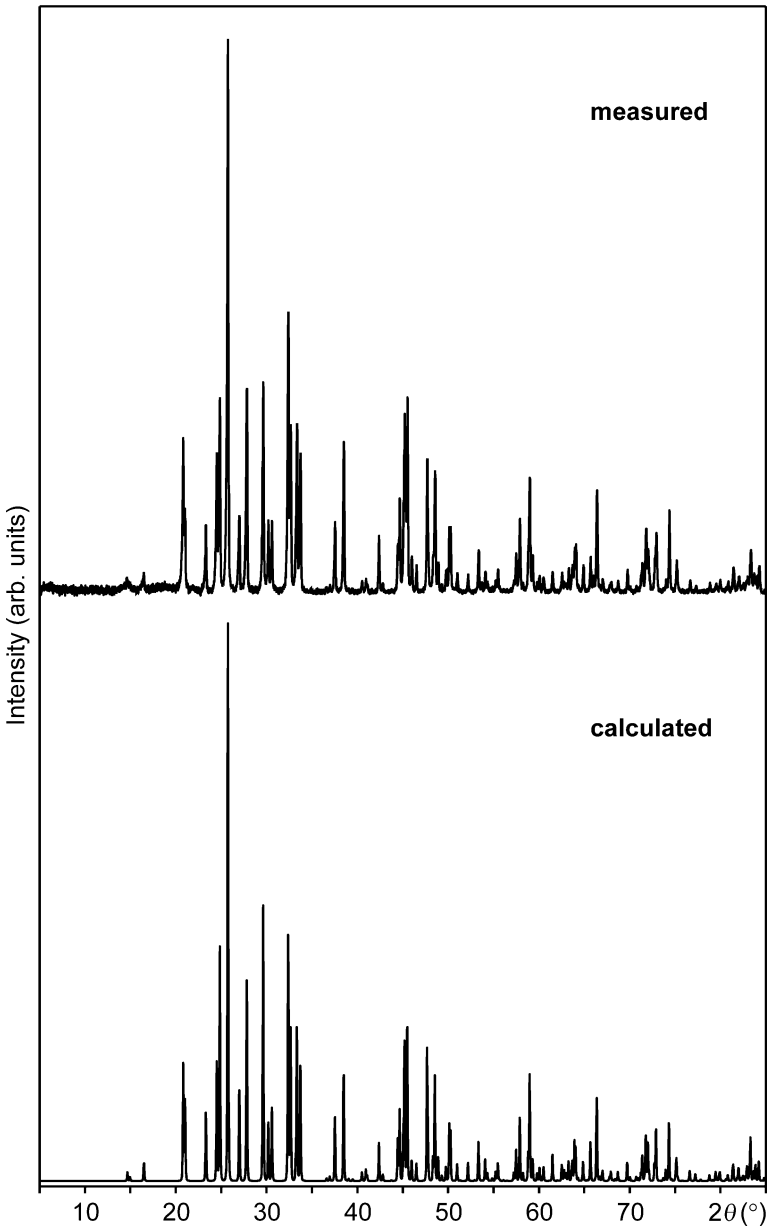

Figure 8.1: Experimental PXRD pattern of Ba_3Si_4 together with calculated pattern based on our single crystal X-ray analysis (Cu-$K\alpha_1$ radiation). Besides Ba_3Si_4, no additional phase was observed.

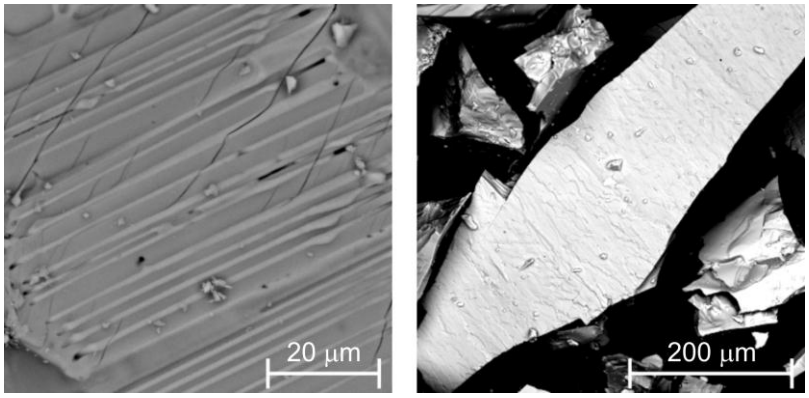

Figure 8.2: SEM images of Ba_3Si_4. The lamellar structure is an indication of the formation from the melt. The sample is homogeneous according to EDXS.

$Ba_3{}^{29}Si_4$. A sample for NMR experiments was synthesized with the same reaction conditions from 98.70 % enriched ^{29}Si. No silicon-containing impurity phases were detected in the ^{29}Si NMR experiment. PXRD shows single phase Ba_3Si_4.

BaSi. 0.8302 g (6.05 mmol) Ba and 0.1698 g (6.05 mmol) Si were sealed under argon in a Ta ampoule. The sample was heated in 24 h to 1200 °C and then annealed for 2 h at this temperature. The ampoule was quenched in water to room temperature and then annealed for 3 d at 800 °C. The reaction product is metallic shining, brittle, and very sensitive to air and moisture. PXRD did not show any by-products.

$BaSi_2$. 0.7097 g (5.17 mmol) Ba and 0.2903 g (10.34 mmol) Si were placed in a glassy carbon crucible. The sample was melted under argon with an induction furnace and cooled down within few minutes to room temperature. No Ba evaporation was observed. The fine crystalline powder is sensitive to air and moisture and did not contain any by-product according to PXRD. Larger crystals were obtained by subsequent annealing at 1000 °C for 2 d.

Nanoporous silicon. Fine powder of Ba_3Si_4 (13 mg, 0.025 mmol) and dry NH_4Cl (40 mg, 0.75 mmol) were placed into separate aluminum oxide crucibles and were sealed together into a quartz ampoule under Ar atmosphere. Subsequently, the ampoule was annealed in a tube furnace at 600 °C for 2.5 h. PXRD of the reaction product shows the reflections of $BaCl_2$. The product was washed with distilled water to dissolve $BaCl_2$. Brownish powder was obtained which is amorphous according to PXRD. All particles which were investigated by EDXS with high-resolution SEM consist only of silicon.

8.2 Phase relations

In the only former report of the binary system Ba – Si,[221] two phases BaSi and $BaSi_2$ were evaluated. Meanwhile, the crystal structures of the phases Ba_2Si,[222, 223] Ba_5Si_3,[224, 225] BaSi,[226, 227] Ba_3Si_4,[25] and $BaSi_2$,[228, 229] are known. Furthermore, Ba_6Si_{25} [230] and $Ba_{8-x}Si_{46}$ [194] have been obtained by high pressure experiments. The region 45 at.% – 66.7 at.% Si is investigated by PXRD, DSC and microstructure analyses.

The compositions of the samples and the phase equilibria are shown in Fig. 8.3, the lattice parameters are listed in Table 8.1. DSC measurements were performed in welded Nb crucibles. However, the metal crucibles react rapidly with all silicon containing melts and, therefore, the liquidus line could only be approximated. To investigate, which phases are formed from the melt, the samples were melted by induction heating in open glassy carbon crucibles under Ar and cooled down within few minutes to room temperature.

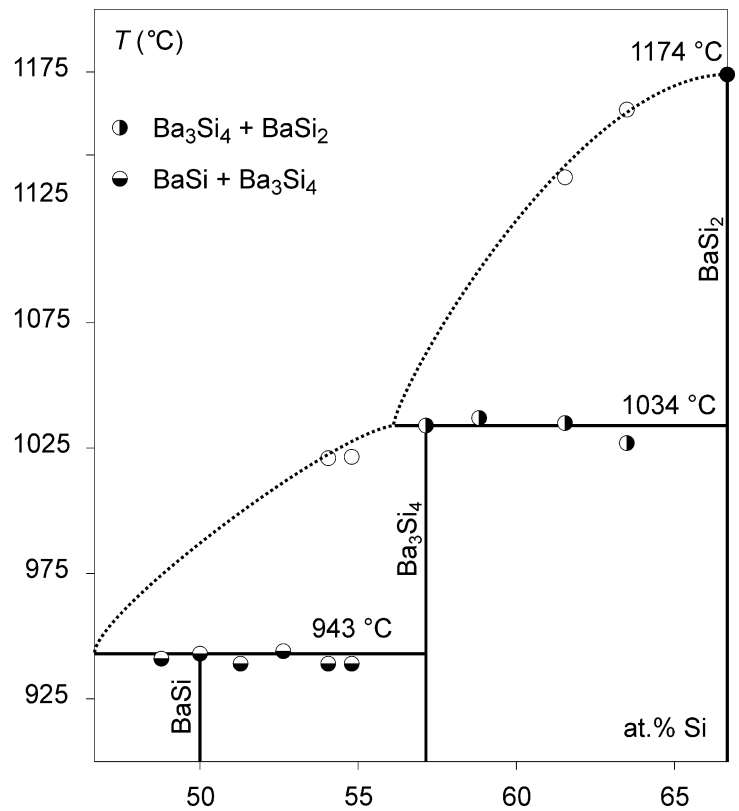

Figure 8.3: Phase diagram of the system Ba/Si in the range of 45 – 67 at.% Si. Grey circles show thermal effects of the liquidus curve. Half-filled circles indicate the phases observed by PXRD (without annealing).

Table 8.1: Lattice parameters of selected phases in the system Ba – Si.

Phases	Space group	Lattice parameters (Å)	Method	Reference
Ba_3Si_4	$P4_2/mnm$	a = 8.5233(3) c = 11.8322(6)	Powder ; Cu-$K\alpha_1$ $2\theta_{max}$ = 100° ; 115 *hkl*; LaB_6 standard	This work
Ba_3Si_4	$P4_2/mnm$	a = 8.5223(4) c = 11.830(1)	Powder ; Cr-$K\alpha_1$ $2\theta_{max}$ = 100° ; 42 *hkl*; LaB_6 standard	This work
Ba_3Si_4	$P4_2/mnm$	a = 8.52(2) c = 11.84(2)	Single crystal, Mo-$K\alpha_1$	[25]
BaSi	*Cmcm*	a = 5.0404(8) b = 11.937(2) c = 4.1389(7)	Powder ; Cu-$K\alpha_1$ $2\theta_{max}$ = 100° ; 51 *hkl*; LaB_6 standard	This work
BaSi	*Cmcm*	a = 5.0430(8) b = 11.933(2) c = 4.1395(8)	Single crystal, Mo-$K\alpha_1$	[227]
$BaSi_2$	*Pnma*	a = 8.9314(3) b = 6.7271(2) c = 11.5345 (3)	Powder ; Cu-$K\alpha_1$ $2\theta_{max}$ = 100° ; 105 *hkl*; LaB_6 standard	This work
$BaSi_2$	*Pnma*	a = 8.92(6) b = 6.75(6) c = 11.57(6)	Single crystal, Mo-$K\alpha_1$	[229]

$BaSi_2$ (66.7 at.% Si) is formed congruently from the melt. The melting point was determined to be 1174(5) °C, which is in accordance with the reported phase diagram.[221] Between 57 and 66.7 at.% Si, a mixture of Ba_3Si_4 (57.1 at.% Si) and $BaSi_2$ is always formed after cooling from the melt, indicating a peritectic formation of Ba_3Si_4. The peritectic temperature of Ba_3Si_4 was determined to be 1034(5) °C.

DSC measurements in Nb ampoules on single phase samples of Ba_3Si_4 can be misleading, because a sufficient amount of Si reacts always with the Nb crucible, which might give the wrong impression of a congruent instead of a peritectic formation of Ba_3Si_4. Nevertheless, SEM pictures of Ba_3Si_4 samples, which were cooled from the melt within few minutes, show that the phase was directly crystallized from the melt and not formed by diffusion in solid state (Fig. 8.2). This might also explain why the synthesis of a single phase was only possible in Ta with short annealing times and not in inert glassy carbon crucibles. In the molten state, a part of Si reacts with the crucible wall and therefore Ba_3Si_4 instead of $BaSi_2$ crystallizes from the melt. Towards higher Ba content, Ba_3Si_4 is in

equilibrium with BaSi, which decomposes peritectically at 943(5) °C to Ba_3Si_4 and a Ba-rich melt. The lattice parameters of single phase Ba_3Si_4 are identical within e.s.d. with all equilibrium samples in the two-phase regions with $BaSi_2$ and BaSi. Thus the compound exists at a constant composition.

8.3 Crystal structure

Single crystal X-ray analysis was performed according to section 3.3. The measurements were performed with a rotating anode diffractometer with Ag-*K*α radiation. The crystal structure refinement was carried out by employing a full-matrix least-squares procedure with SHELXL-97. Details concerning the data collection and structure refinement are given in Table 11.21.

The first structure determination resulted in unexpectedly short and different Si – Si bond lengths of about 2.29 Å (1×) and 2.34 Å (4×) in the Si_4^{6-} polyanion (Weißenberg-film data).[25] Assuming an average oxidation number of 1.5− on the silicon atoms,[219] the average distance $\bar{d}(\mathrm{Si-Si})$ within the polyanion is expected to be between the average distances in $BaSi_2$ (2.40 Å, Si^{1-}) and BaSi (2.50 Å, Si^{2-}). The previously observed average distance $\bar{d}(\mathrm{Si-Si})$ = 2.33 Å is significantly smaller. The present crystal structure data resolve this discrepancy. In agreement with the previous data, Ba_3Si_4 crystallizes in the space group $P4_2/mnm$ (no. 136) with four formula units in the tetragonal unit cell (Table 11.21-23). Silicon atoms in two crystallographically independent positions form quasi-isolated, butterfly-shaped, Si_4^{6-} anions (Fig. 8.4a) with the point symmetry $mm2$ – C_{2v} around the position $4g$ ($x,\bar{x},0$ with x = 0.2505).

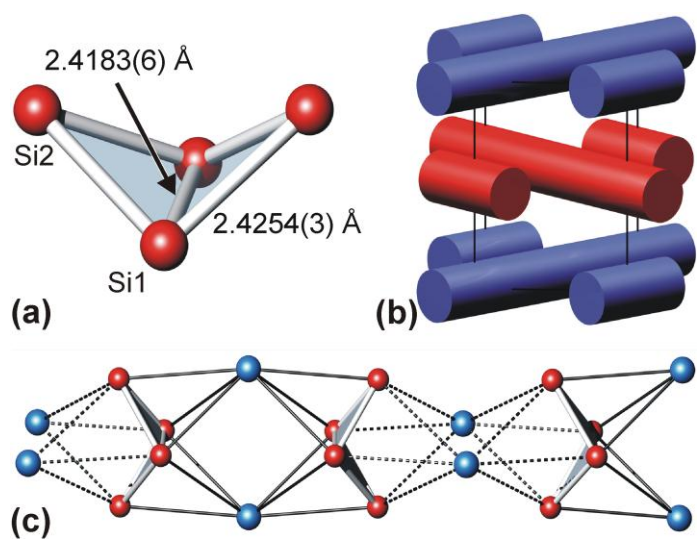

Figure 8.4: The Si_4^{6-} anions (**a**) are condensed via Ba atoms to 1D infinite polymers (red and blue) along [110] resulting in a twofold rod packing (**b**, **c**).

The bond length between the threefold-bonded Si atoms (3b)Si of 2.4183(6) Å is smaller than the distance *d*((3b)Si – (2b)Si) = 2.4254(3) Å. The differences to the previous data can be understood taking in account that the atomic parameters by Eisenmann *et al.*[25] were not least-square refined. Now, as expected from the average oxidation number of the silicon atoms in the polyanion, the average bond length $\bar{d}(\mathrm{Si-Si})$ = 2.424(3) Å in Ba_3Si_4 is smaller than in BaSi and larger than in $BaSi_2$ (Table 8.2). The reduction of the tetrahedranide Si_4^{4-} to the Si_4^{6-} anion results in the break of one bond, so that the (2b)Si atoms are now at a distance of 3.4543(6) Å.

Table 8.2: Average bond lengths and formal charges of the silicon anions.

Compound	Connectivity symbols	Average Si charge	$\bar{d}$ (Si–Si) (Å)	Literature
Ba_5Si_3	$(1b)Si^{3-}$, $(0b)Si^{4-}$	– 3.333	2.437(7) 2.74	[225] [229]
BaSi	$(2b)Si^{2-}$	– 2	2.502(3)	[227]
Ba_3Si_4	$(2b)Si^{2-}$, $(3b)Si^{1-}$	– 1.5	2.424(3)	This work
$BaSi_2$	$(3b)Si^{1-}$	– 1	2.404(2)	[231]
$Na_2Ba_6Si_{46}$	(4b) $Si^{0.3-}$	– 0.304	2.385(3)	[200]
Si	$(4b)Si^0$	0	2.351776(4)	[232]

The Si_4^{6-} anions are surrounded by 12 Ba cations and each Ba cation by four Si_4^{6-} anions: $(Si_4)Ba_{12/4}$. Each Ba atom is eightfold coordinated by Si atoms. The cations act as single bonded ligands or as μ_2-, and μ_3- bridging ligands. Four μ_3 Ba-bridges of Ba1 and Ba2 complete the Si_4 cluster to a distorted tetrahedron star (*stella quadrangula*), similar to those in K_4Si_4 [233] and Na_4Pb_4.[234] The Ba1 and Ba2 atoms act as μ_3 bridging ligands for two Si_4 clusters, which results in infinite one dimensional polymers ${}^{1}_{\infty}[Ba_4Si_8]$ along [110]. The polymers form a simple two-fold rod packing, in which each neighboring layer is turned by 90° (Fig. 8.4b, c).

The shortest distance *d*(Ba1 – Si) = 3.5761(3) Å is much longer than the shortest distances *d*(Ba2 – Si) = 3.2584(3) Å and *d*(Ba3 – Si) = 3.3088(2) Å. This may explain that only the Ba2 and Ba3, but not the Ba1 atoms can be substituted by Sr atoms ($Ba_{3-x}Sr_xSi_4$, $0 \leq x \leq 2$),[235] and that Sr_3Si_4 does not exist (Fig. 8.5).

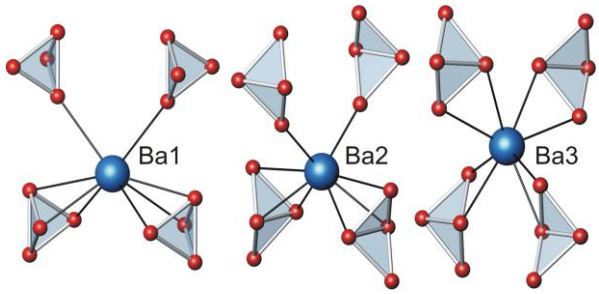

Figure 8.5: Coordination of the Ba atoms in Ba_3Si_4 (Si: red spheres).

The centers of the $[Si_4]$ clusters at positions $x\bar{x}0$ (x = 1/4) form the non-characteristic Wyckoff position $I4/mmm$ $(2a, 2b)$ [236] in the reduced cell $a' = a\sqrt{2}/2$, $c' = c$ and $c'/a' = 1.963$. This leads directly to the Al_3Ti structure-type and to the structures of a series of complex fluorides like $Na_3[UF_7]$, which are hierarchical replacement derivatives of the Al_3Ti type (c/a = 2.01 – 2.23 for the Al_3Ti members; c/a = 1.97 – 2.00 for the $Na_3[UF_7]$ members).[237] Fig. 8.6 shows the structures of Al_3Ti and Ba_3Si_4 with the replacement of Ti (and $[UF_7]$) by the Si_4^{6-} cluster anion. Due to the local $mm2$ symmetry of Si_4^{6-}, the Ba cations show small shifts from the ideal Al (or Na) positions.

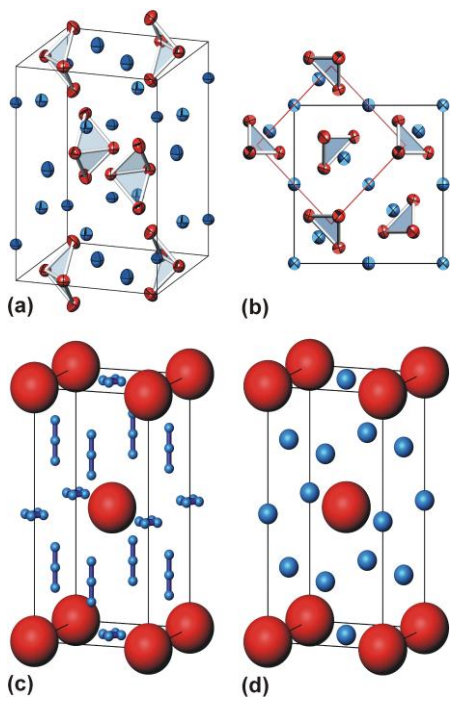

Figure 8.6: (**a**, **b**): Unit cell of Ba_3Si_4 with displacement ellipsoids at 99% probability (Si: red; Ba: blue). The relation to the Al_3Ti structure type is indicated in (**b**) by the smaller red cell in the projection along the c-axis. (**c**): Averaged Ba_3Si_4 crystal structure, resulting from the shifts of all equivalent atomic positions into a smaller Al_3Ti segments shown in (**b**). The centers of the Si_4^{6-} anions are represented by large red spheres. (**d**): Unit cell of the Al_3Ti structure (Al: blue; Ti: red; $a' = a\sqrt{2}/2$).

8.4 Electronic structure

FPLO was used to calculate the electronic structure of Ba_3Si_4 as explained in section 3.5. The basis sets for Si and Ba consisted of 2*s*, 2*p* / 3*s*, 3*p*, 3*d* and 5*s*, 5*p* / 6*s*, 6*p*, 5*d*, respectively. Convergence with respect to k point number was carefully checked. The atomic parameters from single-crystal diffraction data (Table 11.22) were used in the calculations. ELF was calculated using a module implemented in the FPLO method.

The validity of the Zintl-Klemm concept is sometimes associated with physical property measurements, and especially the metallic state is then believed to be in conflict with the concept. In fact, Zintl phases can be expected to show a low electrical conductivity but they may show metal-like temperature dependence of the conductivity as well. The Zintl-Klemm concept implies an electron transfer to the atoms with the highest electronegativity and this way the covalent bonds of the Zintl anions are derived. The real charges are reduced with ion-to-ion interactions (*e.g.*, ±0.75 – ±0.80 in NaCl[238]), but this does not change the count for the covalent bonds. Applying the concept of 'polar covalency' of Sanderson,[239] the effective charges in an isolated Ba_3Si_4 molecule are estimated to be q(Ba) = +1/2 and q(Si) = –3/8. However, detailed predictions for the physical properties can only be obtained from quantum mechanical methods.

DOS reveals metallic behavior for Ba_3Si_4 with $N(E_F)$ = 4.8 states eV^{-1} per cell at Fermi energy (Fig. 8.7). The states between –3.6 eV and Fermi energy are made up of mainly Si 3*p* and Ba 5*d* basis functions. The occupancies of the Ba 5*d* states (1.22 – 1.36 e^-) are much larger than those of the 6*s* states (0.30 – 0.44 e^-) and 6*p* states (0.26 – 0.53 e^-) and the strong Si 3*p* – Ba 5*d* hybridization is responsible for the non-zero DOS at the Fermi level.

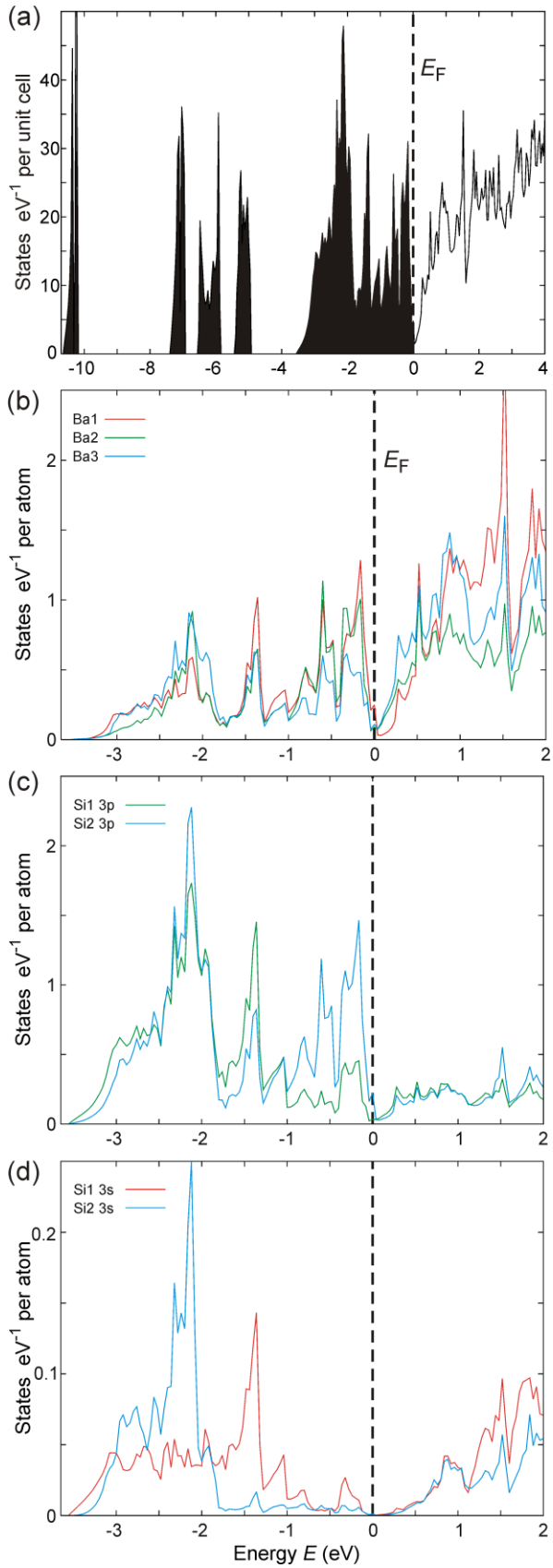

Figure 8.7: Total (**a**) and atom resolved (**b**) electronic density of states for Ba_3Si_4.

The states forming the Fermi surface can be analyzed from the band structure (Fig. 8.8). Starting from the Γ - X line, there is one band (red colored) occupied at Γ but unoccupied at X with a large upward dispersion (bandwidth of 0.7 eV). Along the M - Γ line, this band crosses the Fermi energy near Γ , along Γ and Z it becomes unoccupied again close to Z. This band is largely made up of Si(1) p_x, p_y, Ba(2) $d_{x^2-y^2}$ and Ba(3) $d_{z^2-r^2}$ orbitals. A doubly degenerated band (blue colored) along the Γ - X line is barely unoccupied at Γ with a downward dispersion towards X (bandwidth of ≈ 0.3 eV). This band crosses the Fermi energy between M and Γ close to Γ. Between Γ and Z it stays unoccupied, flat and doubly degenerate and gets occupied again between Z and R close to Z. Major contributors to this band are Si(2) p_z and Ba(1) d_{xz}, d_{yz} orbitals, together with a very weak Ba(3) $d_{z^2-r^2}$ orbital participation. The topology of the Fermi surface shows no pronounced anisotropy for the metallic conductivity.

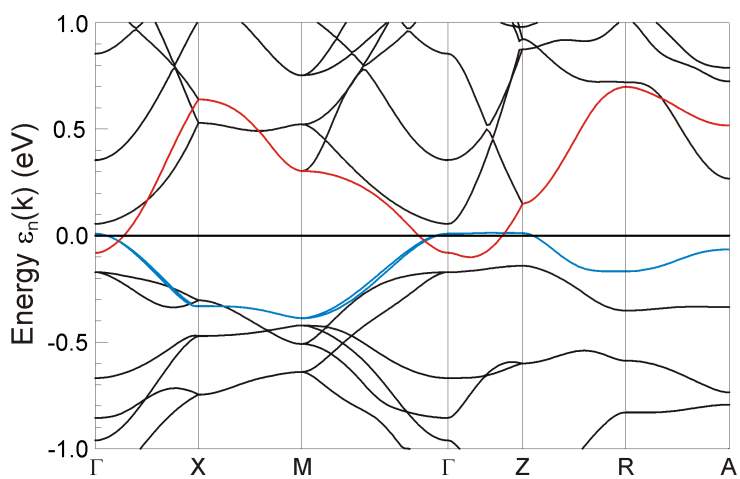

Figure 8.8: The electronic band structure of Ba_3Si_4 between –1 and 1 eV. For colors see text.

A topological analysis of the electron density calculated by FPLO shows that only 3.4 instead of 6 electrons are transferred from the three Ba atoms to the butterfly. Therefore the difference between the total atomic basin charges of the (3b)Si1 atoms (14.7 electrons; $Si^{0.7-}$) and the (2b)Si2 atoms (15 electrons; Si^{1-}) is smaller than expected. Bond distances in Zintl anions are usually related to the charge of the atoms (Table 8.2) as for the Si_4^{6-} anion *d*(Si1–Si1) is smaller than *d*(Si1–Si2). The atomic charges for the Ba atoms with different site symmetries are similar (~54.9 electrons; Ba^{1+}).

Topological analysis of the ELF yields two bond attractors (Si1 – Si1, Si1 – Si2) and three lone-pair attractors (one for Si1 and two for Si2) in the valence region (Fig. 8.9). Both bond attractors, Si1 – Si1 and Si1 – Si2, are off the direct connection line between the Si

atoms. With bent Si – Si bonds, the bond angles of the Si atoms become closer to tetrahedral angles, as shown *e.g.* for carbosilanes.[240] The electron counts in the basins of the Si1 – Si1 and Si1 – Si2 bonds are 1.0 and 1.6, respectively. The basin of the lone-pair attractor at Si1 contains 2.5 electrons, while the lone pairs at Si2 contain 1.9 and 2.0 electrons. The total electron count of the $(Si1)_2$ fragment is therefore in agreement with the expected value of six electrons, but the distribution between the bond and the lone-pairs is different from the expected one (similar examples were reported by Chestnut[241]).

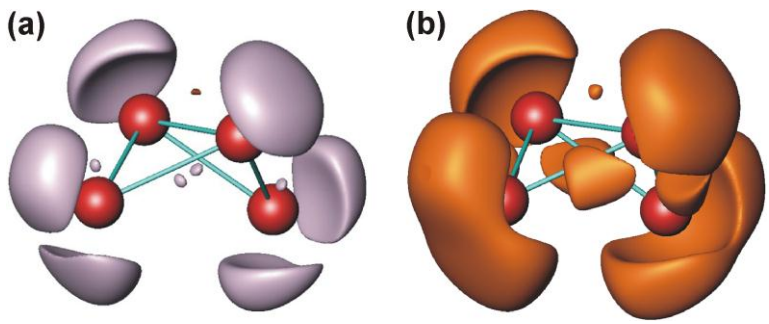

Figure 8.9: ELF isosurfaces for the isolated Si_4^{6-} anion in Ba_3Si_4. The ELF values are 0.82 for the silver (**a**), and 0.76 for the golden (**b**) isosurfaces.

According to the topological analysis of the ELF in the core region, the average of the electron counts in the Ba and Si core basins is 54.4 and 10.1 electrons, respectively. Generally, the individual core shell occupancies as calculated by ELF analysis are never exactly equal to the integer values as required by the *Aufbau* principle, but the total ELF for free atoms are usually within ≈ 0.1 electrons of the corresponding integer value.[242] In Ba_3Si_4, the large deviation of the Ba ELF core basin populations from the expected value of 54.0 is due to the influence of Ba 5*d* orbitals. In the crystalline environment of Ba_3Si_4, the Ba *5d* energy levels go down significantly in energy and become occupied. They contribute to the charge density in the core region, thereby increasing the total ELF core basin population by amounts up to almost half-an-electron.

8.5 Physical properties

Magnetization measurements revealed a weakly temperature-dependent diamagnetism of the bulk phase at elevated temperatures with the susceptibility $\chi \approx -50(20) \times 10^{-6}$ cm^3 mol^{-1} (cgs system) (Fig. 8.10). With the diamagnetic increments of Ba^{2+} and silicon atoms, [169] a distinctly lower susceptibility of about $\chi_{calc} \approx -120 \times 10^{-6}$ cm^3 mol^{-1} is expected (the value would be even lower for anionic silicon increments). The difference between the measured and calculated values indicates the presence of Pauli paramagnetism. In a free electron model,[243] the difference of about 70×10^{-6} cm^3 mol^{-1} would correspond to a density of

states of $N(E_F) \approx 8$ states eV^{-1} per cell, which is on the order of magnitude as the calculated DOS value $N(E_F) = 4.8$ states eV^{-1} per cell. Below 50 K, the susceptibility rises slightly, but the sample remains diamagnetic. In terms of paramagnetic impurities this increase would be equivalent to 0.1 % of S = 1/2 species. No superconductivity was found above 1.8 K in fields as low as $\mu_0 H = 2$ mT.

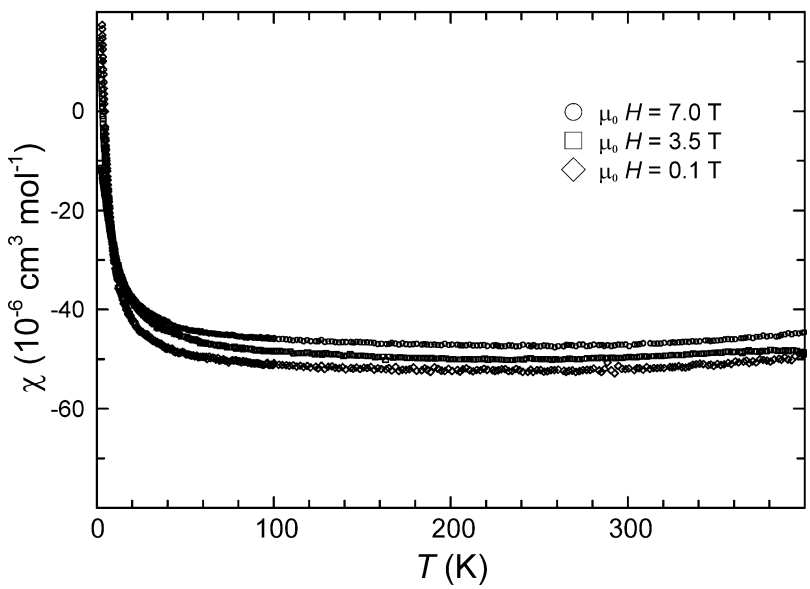

Figure 8.10: Magnetic susceptibility of Ba_3Si_4 between 1.8 and 400 K at $\mu_0 H = 0.1$, 3.5 and 7 T.

The temperature-dependent resistivity measurement (Fig. 8.11) on a polycrystalline bulk sample of Ba_3Si_4 (ca. $3.5 \times 2.1 \times 1.7$ mm^3) revealed a high resistivity at room temperature but a typical metal-like increase of the resistivity with the temperature (ρ(300 K) $\approx 1.2 \times 10^{-3}$ Ωm; $\rho_0 \approx 0.4 \times 10^{-3}$ Ωm). Ba_3Si_4 is therefore a bad metal with low charge carrier concentration, in agreement with the result of the band structure calculation. A small upturn below 20 K may indicate a metal-to-semiconductor transition.

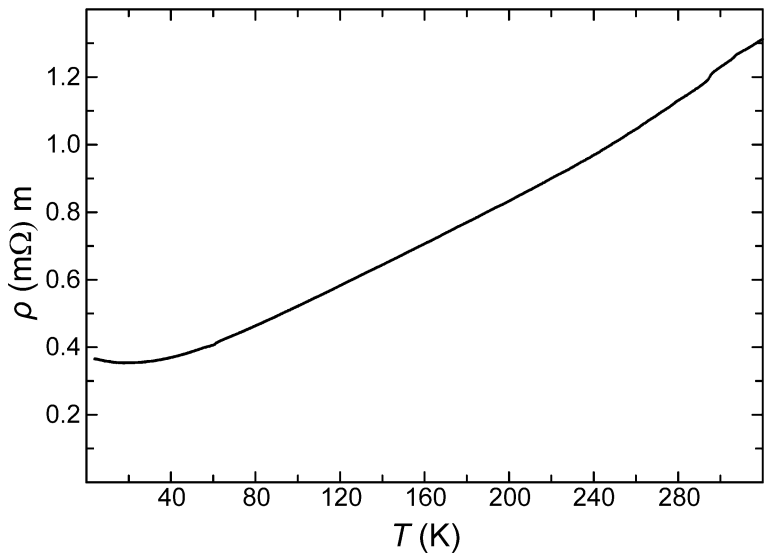

Figure 8.11: Electrical resistivity of Ba_3Si_4 between 3.8 and 320 K.

8.6 ^{29}Si NMR investigations

NMR measurements on fine powder of Ba_3Si_4 were performed according to section 3.3. The static ^{29}Si NMR experiment on an isotope-enriched Ba_3Si_4 sample showed a broad signal, indicating a superposition of different signal contributions (Fig. 8.12). MAS at a low frequency of 2.65 kHz already allowed the separation of two signal contributions (Fig. 8.12), which is in accordance with two crystallographic sites for the Si atoms (Table 11.22). The spectral parameters (Table 8.3) were determined by a least-squares fit. The isotropic shift positions K_{iso} were confirmed in a series of MAS experiments at different rotation frequencies. The isotropic shift of both ^{29}Si signals is positive and outside of the expected range of -350 ppm $\leq \delta \leq 50$ ppm for diamagnetic, non-metallic materials.[244] The large positive signal shift indicates an interaction of the nuclear spins with the electron spins of conduction electrons (*e.g.* Knight shift).[245, 246] For metallic conductors, the isotropic shift of a signal is related to the s-orbital contribution of an atom to the density of states at the Fermi energy. Assuming metallic conductivity for Ba_3Si_4, Si1 (0.0005 states eV^{-1} per atom) is assigned to the signal with the lower isotropic shift and and Si2 (0.001 states eV^{-1} per atom) to the signal with the higher isotropic shift.

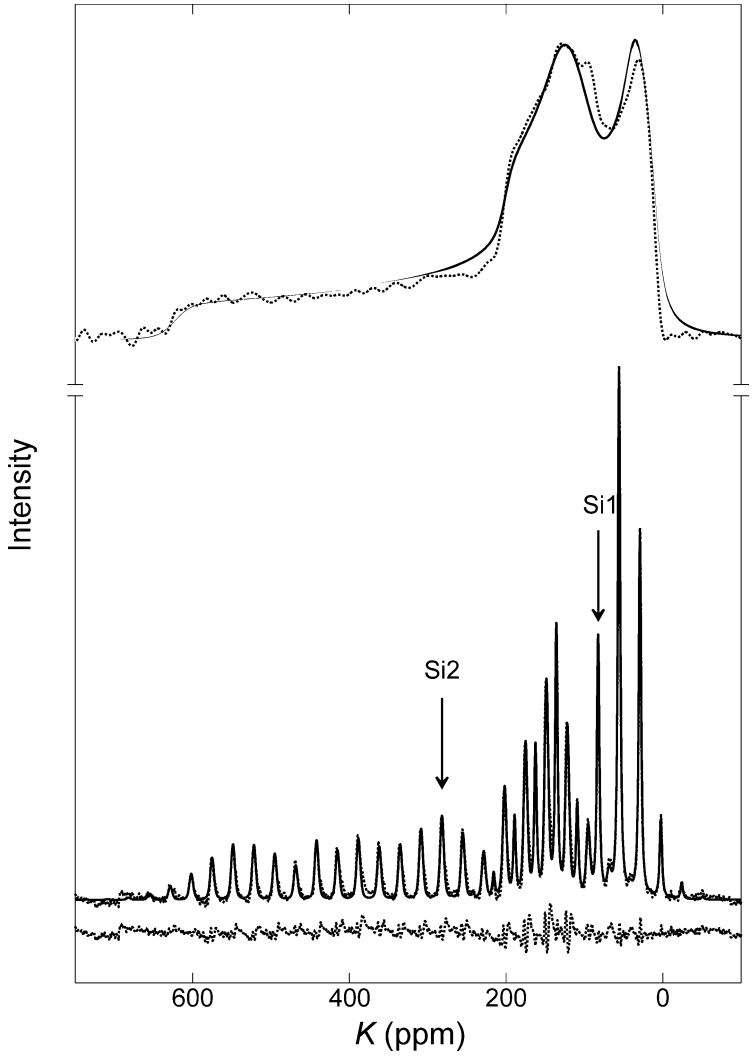

Figure 8.12: ^{29}Si NMR signals of Ba_3Si_4. (**Top**) Static experiment; experimental data are represented by a black dashed line. Grey lines represent simulated signal contributions, the black line the sum of the calculated signal contributions. The simulations are based on the spectral parameters obtained by least-squares fitting of the MAS signals. (**Bottom**) Magic angle spinning (MAS) at 2.45 KHz. Full lines represent the sum of the simulated signal contributions, dashed lines the experimental results. The difference between the simulated and experimental signals is shown at the bottom. The simulations of the signals are based on the parameters from Table 8.3. Isotropic shift positions of the MAS signals are marked by arrows.

Table 8.3: Spectral parameters of the ^{29}Si NMR signals of enriched Ba_3Si_4 determined by least-squares analysis.[141] K_{iso} corresponds to the isotropic Knight shift, Δ to the anisotropy parameter and η to the asymmetry parameter.

Atoms	K_{iso} / ppm	Δ / ppm	η
Si1	82.4(1)	120.1(3)	0.22(5)
Si2	281.8(1)	348.3(1)	0.10(5)

The electrical transport properties of Ba_3Si_4 were investigated with respect to the temperature dependence of the isotropic signal shift (Fig. 8.13) and of the spin-lattice relaxation times (T_1). The isotropic shift for Si2 is temperature independent, as it is expected for a metal, but the isotropic shift of Si1 slightly increases with temperature, which is frequently observed for semiconductors. A semi logarithmic plot of $K_{iso}/T^{1/2}$ versus T^{-1} shows a positive gradient, which is clear evidence that Ba_3Si_4 is not a semiconductor (Fig. 8.14). For semiconductors, a negative gradient is expected.[247]

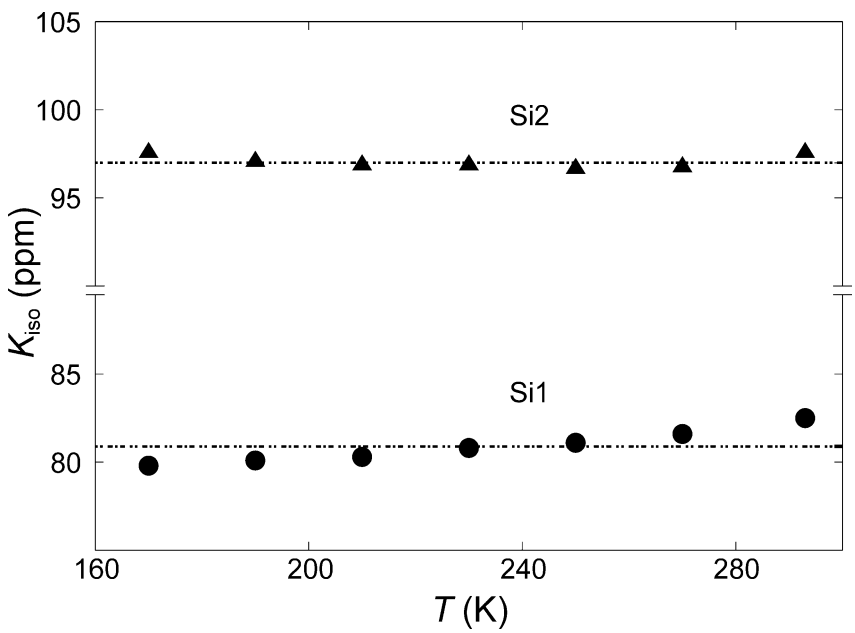

Figure 8.13: Isotropic shift of ^{29}Si NMR signals of Ba_3Si_4 at various temperatures: Si1 (circles), Si2 (triangles), least-squares fit (dotted lines).

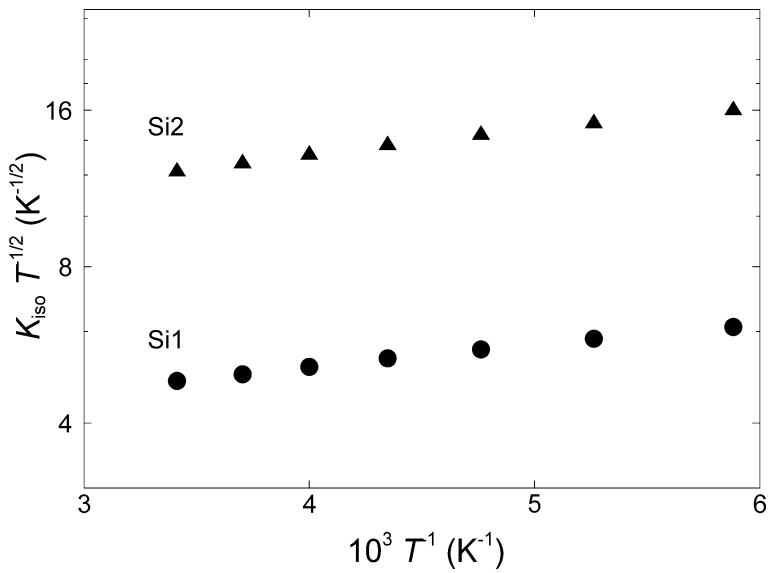

Figure 8.14: Semi-logarithmic representation of the ^{29}Si NMR isotropic signal shift $K_{iso}T^{-1/2}$ of Ba_3Si_4 as a function of T^{-1} (Si1 (circles), Si2 (triangles)).

The spin-lattice relaxation times T_1 differ for both signals. At ambient temperature, the values for Si1 (1.1 s) and Si2 (10.9 s) are large in comparison with well conducting metals, but they are at least two orders of magnitude shorter than observed for the semiconducting alkali metal monosilicides M_4Si_4 (M = Na, K, Rb, Cs).[231] For semiconductors, a positive gradient of the plot $\log(1/(T_1\ T^2))\ /\ T^{-1}$ is expected,[247] which is not observed for Ba_3Si_4. In general, T_1 for metals decreases linearly with increasing temperature,[245, 246] as it is observed for Si1. T_1 for Si2 shows a non-linear temperature dependence (Fig. 8.15), indicating another relaxation mechanism, which becomes more relevant at higher temperatures. The reason might be that the charge distribution around Si2 with 2 lone pairs is more anisotropic than for Si1 with 1 lone pair. The higher anisotropy leads to an enhanced spin lattice relaxation, which is due to the interaction of the fluctuating electric field induced by phonons with the charge distribution around the atoms.

The line shape of the signals results from the charge distribution in the vicinity of the Si atoms. The large anisotropy parameter Δ of the signals is due to the chemical shielding, which is caused by orbital contributions of localized electrons. It is about 3 times larger for Si2 than for Si1 (Table 8.3). The anisotropy parameter of Si1 is similar to those observed for the (3b)Si^{1-} anions in M_4Si_4 (M = Na, K, Rb, Cs).[231, 248] The asymmetry parameter η of the Si2 signal is smaller than that of Si1 (Table 8.3) and they are similar to those observed for Si atoms in M_4Si_4 (M = Na, K, Rb, Cs).[231, 248] An asymmetry parameter different from zero indicates that the symmetry of the charge distribution is reduced compared to an ideal

tetrahedranide anion. The charge distribution around the E14 atoms is less distorted for the silicides M_4Si_4 (M = Na, K, Rb, Cs) than for the monostannides M_4Sn_4 ($0.26 \leq \eta \leq 0.45$).[249]

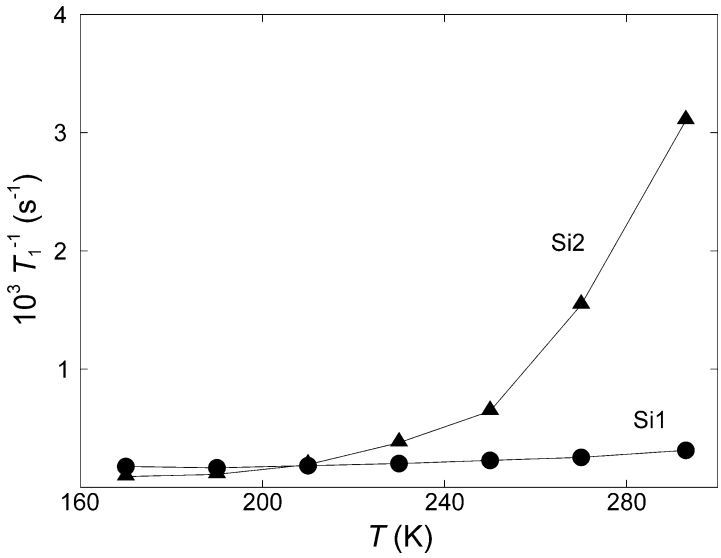

Figure 8.15: Spin lattice relaxation times (T_1) of the ^{29}Si NMR signals of Ba_3Si_4 for various temperatures (Si1 (circles), Si2 (triangles)).

8.7 Oxidation of Ba_3Si_4 with gaseous HCl

A new application for reactive intermetallic phases has arisen from their oxidation behavior as it was demonstrated by the oxidation of Na_4Ge_4 or $Na_{12}Ge_{17}$ to a new element modification of Ge (*cF*136),[66] or the oxidation of Mg_2Ge to mesoporous Ge.[250] In this work, nanoporous silicon was obtained from the oxidation of Ba_3Si_4 with HCl. Gaseous HCl was evolved from the quantitative dissociation of NH_4Cl into NH_3, N_2, H_2 and HCl at 600 °C. [251, 252] Ba_3Si_4 reacted to a fine, brown powder, which is a mixture of nanoporous Si and $BaCl_2$. The reaction is driven by the formation of solid $BaCl_2$. The evolution of gaseous H_2 might suppress the formation of crystalline α-Si and promote the formation of nanoporous Si. The product is stable on air and $BaCl_2$ was removed by water. Similar techniques were previously applied for the syntheses of $Na_{6.2}Si_{46}$,[220] K_7Si_{46},[220] and $Na_2Ba_6Si_{46}$.[200]

HRTEM (see section 3.3) of the washed sample reveals a porous structure, resembling a sponge, which is amorphous according to the SAED pattern. On average, the cavities have a diameter of about 9 nm and they are not ordered (Fig. 8.16). Only less than 1 wt.% Ba content was found with EDXS of the bulk sample, while all single particles, which were investigated by high resolution environmental scanning electron microscope show only the presence of silicon and a small content of oxygen. Similar reactions were reported with the oxidation of NaSi by NH_4Br to nanocrystalline or amorphous Si particles.[253, 254] Amorphous silicon is currently used for solar cells, which are easier to manufacture, but less efficient than solar cells based on crystalline silicon.

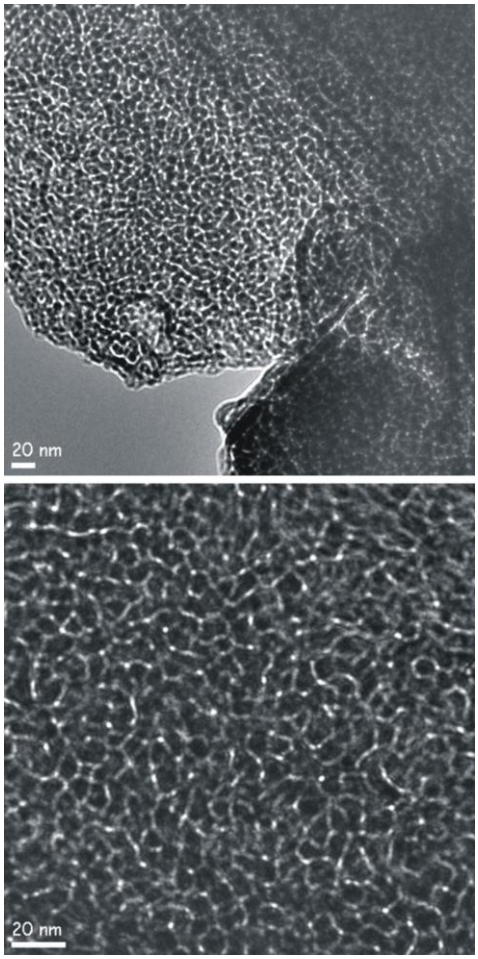

Figure 8.16: HRTEM images of nanoporous Si obtained by oxidation of Ba_3Si_4 with HCl.

8.9 Conclusions

The Zintl phase Ba_3Si_4 has been synthesized from the elements at 1000 °C as a single phase. No homogeneity range has been found. The compound decomposes peritectically at 1034(5) °C to $BaSi_2$ and melt. The butterfly-shaped Si_4^{6-} Zintl anion in the crystal structure of Ba_3Si_4 (Pearson symbol *tP*28, space group $P4_2/mnm$, a = 8.5233(3) Å, c = 11.8322(6) Å) shows only slightly different Si–Si bond lengths of d(Si–Si) = 2.4183(6) Å (1×) and 2.4254(3) Å (4×). The compound is diamagnetic with $\chi \approx -50 \times 10^{-6}$ cm^3 mol^{-1}. DC resistivity measurements show a high electrical resistivity (ρ(300 K) $\approx 1.2 \times 10^{-3}$ Ω m) with positive temperature gradient dρ/dT. The temperature dependence of the isotropic signal shift and the spin-lattice relaxation times in ^{29}Si NMR confirms the metallic behavior. The experimental results are in accordance with the calculated electronic band structure, which indicates a metal with a low density of states at the Fermi level. ELF reveals two bond attractor for Si1–Si1 and Si1–Si2 and three lone pairs, one for Si1 and two for Si2 in the valence region. The reaction of solid Ba_3Si_4 with gaseous HCl leads to the oxidation of the Si_4^{6-} Zintl anion and yields nanoporous silicon.

Chapter 9

Preparation of Chalcopyrites for Analysis of Static Charge Density and Charge Distribution Changes Induced by External Electric Field

Experimental and theoretical charge density analyses have been applied to a broad range of crystals including non-linear materials, metallo-organic complexes and inorganic compounds due to chemical and physical interests.[255-258] The charge density is a physically observable quantity which can be obtained experimentally from X-ray diffraction data. To account for the density deformations due to chemical bonding, various approaches have been developed based on nucleus-centered finite multipole expansion of electron density. In the commonly used formalism of Hansen and Coppens,[259] the individual atomic densities are described with spherical core, valence densities as well as valence deformations (expansion or contraction of valence shell). The topology of the charge density, which provides information about chemical bonding, molecular structure, and molecular stability, is described in Bader's quantum theory of atoms in molecules.[161] In Bader's theory, the presence of a critical point, a point in space at which the first derivatives of the density is zero, is regarded as a necessary and sufficient condition for chemical bonding. The Laplacian as second derivative of the electron density provides information about both structural and reactive properties of a molecule. The region of the outer shell of an atom in which the Laplacian is greater than zero is called the valence shell charge concentration. In case of chemical bonding, valence shell charge concentration is distorted and extrema are formed.[258]

The valence charge density (VCD) is a ground state property and subsequently an important quantity for determination and prediction of chemical bonds and physical properties of crystals.[260-262] Experimentally the VCD can be determined by applying X-ray crystal structure analysis as mentioned above. Important structural parameters as the atomic positions, thermal vibration tensor and the deformation of the electron shells of atoms can be extracted from multipole analysis of experimental structure amplitudes. For the refinement of multipole and structural parameters based on measured diffraction intensities, the program packages *e.g.*, MOLLY,[263] XD,[264] WinCSD,[133] *etc.*, can be used. In addition to the Bader topological analysis, it is a powerful tool to predict the strength of chemical bonding. However, the multipole refinement face with difficulties mainly related to the phase problem in X-ray crystallography and incorrect treatment of the secondary extinction. For a crystal without the centre of inversion, the undetermined phases of the measured structure factors lead to the uncertainties of odd order multipole populations.[265]

The model diffraction intensities of low-order reflections, which are the most important ones for VCD determination, can be significantly distorted by incorrect treatment of extinction. The multipole refinement of the VCD in crystals comprising heavy elements is also difficult because of higher absorption and extinction reducing the precision of measured diffraction data.

Dynamical structure analysis based on the measurement of the X-ray diffraction intensities under the influence of an external high electric field is a recently established method. This new approach provides the opportunity to measure the site selective response of chemical bond to the disturbed electrostatic equilibrium within the crystal. Such an investigation is carried out by measuring the intensities of selected Bragg reflections with and without applied electric field along with recording the relative intensity variations induced by electric field. For the measurements, a crystal platelet is covered with thin metal films with the aim of providing contacts to an external high voltage supply. For specimens exhibiting high electrical resistivity behavior, field strengths up to 10 kV/mm can be applied. Generally, field-induced variations of the Bragg intensities are around 1% and can be measured with precision of 0.1%.[266]

9.1 Chalcopyrites for charge density analysis

To investigate the structural changes induced by external electric field, certain aspects should be satisfied for a material being investigated like non-metallic properties along with preferentially non-centrosymmetric structures with high space group symmetry. Along this line, the ternary II–IV–V_2 and I–III–VI_2 compounds having chalcopyrite ($CuFeS_2$) structure are considered to be candidates for the investigation of charge distribution changes by external electric field. These compounds are semiconductors, E_g changes from 0.16 eV for $CuFeSe_2$ to 3.35eV for $CuAlS_2$,[267] crystallizing in non-centrosymmetric space group $I\bar{4}2d$ in which the constituent atoms are all tetrahedrally coordinated.

The first synthesis of compounds crystallizing in chalcopyrite structure dates back to early 1950s. Hahn *et al.* synthesized some I–III–VI_2 compounds already in 1953.[268] Goodman proposed in 1957 that by cross-substitution of Group II and IV atoms for the Group III atoms in III–V compounds, new semiconducting II–IV–V_2 compounds could be obtained.[269] In the following years, the synthesis of the chalcopyrite compounds has been subject of several investigations.[267, 270-272] The synthesis of polycrystalline materials as well as growing of the single crystals of chalcopyrites could be achieved mainly by applying four principal techniques [272]:

(**1**) Direct synthesis by slow heating of the stoichiometric mixtures of the elements until a complete melt is obtained followed by gradual cooling until the material becomes solidified. Since the vapor pressure of some constituent elements like P and S are relatively

large, a special care has to be taken during heating (the heating rates should be minimized) to avoid any explosion to occur. Big single crystals can be grown in this way from the melt by use of *e.g.* Bridgman technique. (**2**) Direct synthesis by using relevant binary compounds as starting materials. This method lowers the equilibrium vapor pressure inside the reaction ampoule during heating process and hence minimizes the risk of explosion. Steps (**1**) and (**2**) may be followed by annealing below the melting points of the target compounds from hours to days to get more homogenous materials. (**3**) Chemical vapor transport (CVT) of the constituent elements. CVT is described as a reversible chemical reaction of a solid or liquid with a gaseous transport medium and defined by Schäfer as "solubility of the solid in the gas phase".[273] A small amount of transport agent *e.g.*, I_2, Cl_2, $ZnCl_2$, $CdCl_2$, *etc.*, is used to form volatile compounds of the constituent elements to promote transport and vapor phase mixing for subsequent condensation of crystals. For CVT, the transport agent behaves like a catalyst and is released after the condensation of gaseous species. CVT reactions are generally carried out in evacuated and sealed ampoules in which two ends are held at different temperatures. In this way, the driving force for the transport of material between the dissolution and the precipitation side can be achieved by resulting chemical potential gradient.[274] The reaction conditions can be optimized with respect to total amount of sample to be transported by the type and the amount of the transport agent, volume of the container material and temperature of the system along with the partial pressures of the gaseous species present during the vapor transport reaction. (**4**) Solution or flux growth by use of molten metals *e.g.*, Sn, In, Pb, Al, Ga, *etc.*, as media for the synthesis. For this case, several requirements must be satisfied for a metal to be suitable flux for reaction chemistry.[275] First of all, the metal should form a flux at relatively low temperatures provided that normal heating equipments and containers can be used. The difference between the melting point and the boiling point of the metal should be high. After the reaction is completed, it should be possible to separate the metal from the reaction product by *e.g.* chemical dissolution. Last but not least, the metal flux should not react with any of the educts to form stable compounds.

Considering above mentioned issues, we decided to synthesize single crystals of $ZnSiP_2$ as representative of II–IV–V_2 compounds as well as $CuAlS_2$ as representative of I–III–VI_2 compound for experimental charge density analysis. Various preparation routes for $ZnSiP_2$[267, 270, 272, 276-282] and $CuAlS_2$[267, 271, 272, 283-287] have been reported and also reviewed which are based on one or combination of above mentioned techniques. Main goals of this project were to grow (a) µm-size crystals for static charge density analyses, (b) mm-size crystals for measurements in external electric field and (c) as-grown crystals should satisfy the criteria that despite differences in size, no significant differences should emerge in terms of quality of the grown single crystals. This was a joint project between our group

and the group of Prof. Dr. Ulrich Pietsch at Universität Siegen. Prof. Pietsch was interested in chalcopyrites to investigate the charge distribution changes by external electric fields.

9.2 Preparation and characterization

All the sample preparation steps were carried out in an Ar-filled glove box. The synthesis of polycrystalline as well as single crystalline samples was performed in sealed quartz ampoules ($\varnothing_{outer}$ = 14 or 20 mm, wall thickness of 1.5 mm). The quartz ampoules should be clean and free from water for the synthesis of pure materials, for this reason, the ampoules were rinsed several times with ethanol following that treated with hydrogen-oxygen flame around 30 min under 10^{-4} mbar of vacuum. The end products were observed to be stable under ambient conditions.

9.2.1 Preparation of polycrystalline and single crystalline $ZnSiP_2$

First experiments for preparation of polycrystalline materials were carried out starting from stoichiometric amount of constituent elements (see Table 3.1). The educts were placed in a glassy carbon crucible before inserting in quartz ampoules to prevent any side reactions of the reactants with the ampoules. In total 3 g of samples were sealed in a dried quartz ampoule ($\varnothing$ = 20 mm, l = 13mm) and various thermal treatments were applied. It was observed that if heating of the reaction medium is too fast then red phosphorus does not have sufficient time to react with other elements which give rise to a high vapor pressure and cause an explosion of the quartz ampoule. Considering this fact, the reaction ampoules were slowly heated even sometimes applying several annealing steps at lower temperatures (Table 9.1). The reaction products were analyzed by PXRD and found out that besides $ZnSiP_2$, samples contain large amounts of secondary phases *e.g.*, Zn_3P_2, ZnP_2 or α-Si.

Table 9.1: Heat treated polycrystalline samples of $ZnSiP_2$ together with reaction products in sequence of amounts determined based on PXRD analyses (left to right the amounts decrease).

Heat treatment	Reaction products
RT $\xrightarrow{1d}$ 800 ºC, 5d ann., $\xrightarrow{1d}$ RT	Zn_3P_2, ZnP_2, α-Si, $ZnSiP_2$
RT $\xrightarrow{1d}$ 900 ºC, 5d ann., $\xrightarrow{1d}$ RT	Zn_3P_2, ZnP_2, α-Si, $ZnSiP_2$
RT $\xrightarrow{12h}$ 300 ºC, 1d ann., $\xrightarrow{12h}$ 500ºC, 1d ann., $\xrightarrow{12h}$ 700 ºC, 1d ann., $\xrightarrow{12h}$ 900ºC, 2d ann., $\xrightarrow{12h}$ RT	$ZnSiP_2$, ZnP_2, α-Si
RT $\xrightarrow{12h}$ 400 ºC, 1d ann., $\xrightarrow{12h}$ 600ºC, 1d ann., $\xrightarrow{12h}$ 800 ºC, 1d ann., $\xrightarrow{12h}$ 1000ºC, 2d ann., $\xrightarrow{12h}$ RT	$ZnSiP_2$, ZnP_2, α-Si, Zn_3P_2

As single phase polycrystalline materials could not be prepared by direct reaction of the elements, using a carrier gas as transporting agent has been considered to help obtaining $ZnSiP_2$ in high yield. Around 4 mg/cm^3 $ZnCl_2$ was added to the reaction media while preserving the correct stoichiometric amount of Zn in the starting material. The sample was heated in 40 °C/h to 900 °C. Annealing 3 d at this temperature and subsequent cooling with 80 °C/h to room temperature resulted in a red single phase polycrystalline powder of $ZnSiP_2$ (Fig. 9.1). The composition of this polycrystalline powder was determined from the chemical analysis as $Zn_{1.03(1)}Si_{0.98(1)}P_{2.03(1)}$ (see section 3.3). The thermal analysis performed on polycrystalline material of $ZnSiP_2$ revealed that the material melts at around 1340 ºC (peak maximum, Fig. 9.2) which is close to the reported temperature of 1370 ºC.[272] A thermal effect which may indicate a phase transition was not observed differently than reported for some other chalcopyrite compounds *e.g.* $CuTlSe_2$,[288] and $AgInS_2$.[268]

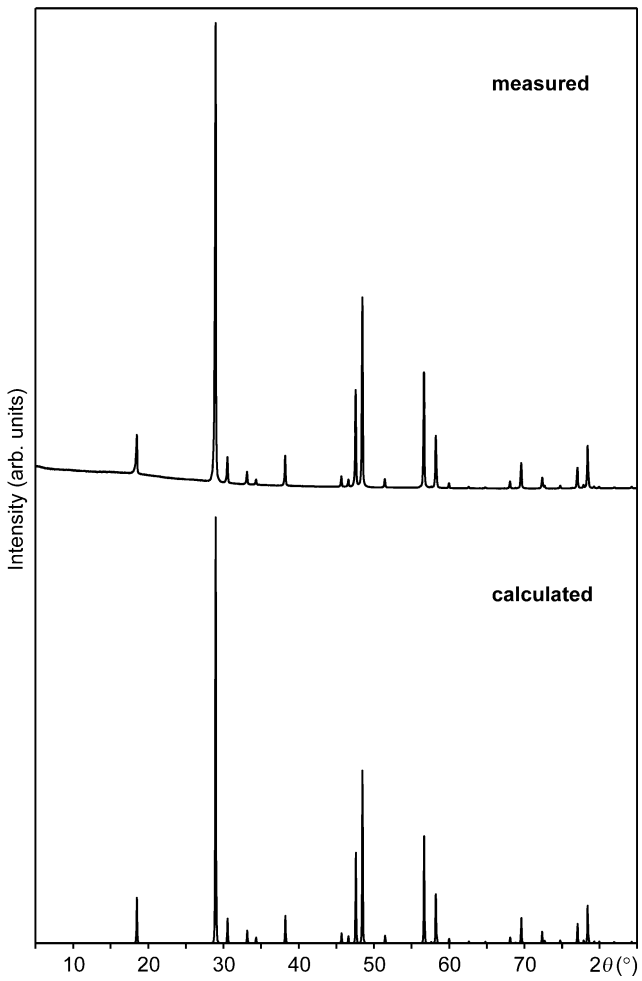

Figure 9.1: PXRD pattern of polycrystalline $ZnSiP_2$ together with the calculated one based on our single crystal X-ray analysis (Cu-$K\alpha_1$ radiation). The reflection intensities are in agreement with the structure model derived from the single crystal diffraction data (see section 9.4). No additional phase was observed.

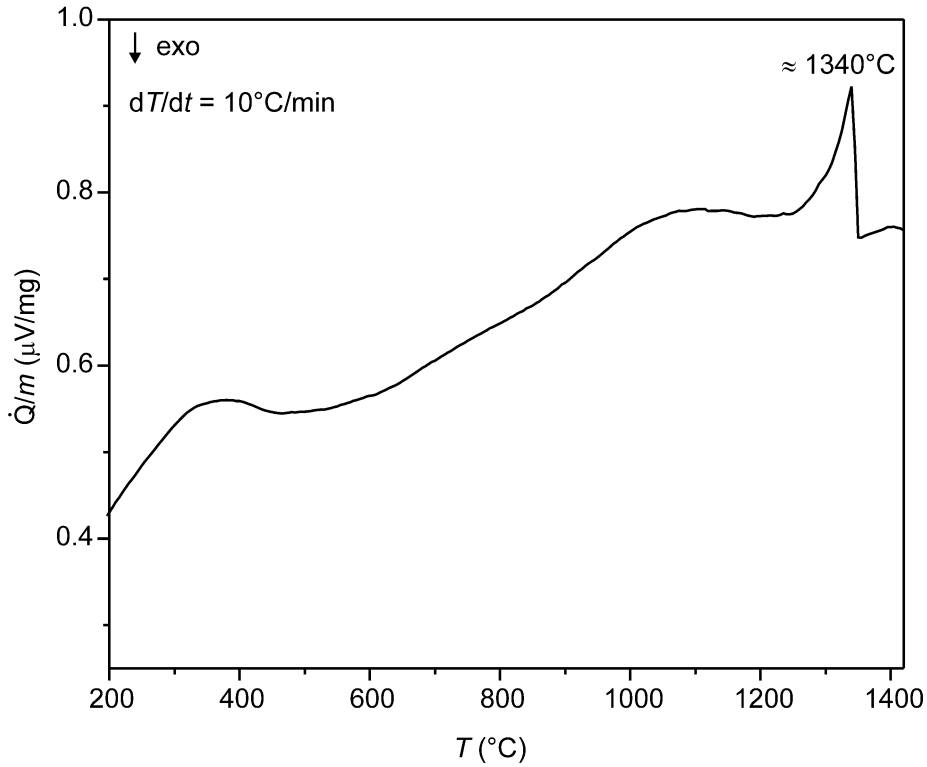

Figure 9.2: Thermal behavior of single phase polycrystalline $ZnSiP_2$ based on heat flux DSC experiment. While heating, an endothermic effect at around 1340 ºC (peak maximum) was observed and attributed to the melting of $ZnSiP_2$. The wide humps observed below that temperature effect probably stem from problems in the baseline correction.

A polycrystalline sample for NMR experiments was synthesized with the same reaction conditions mentioned above from 98.70 % enriched ^{29}Si (Isoflex). PXRD shows formation of single phase $ZnSiP_2$.

For the synthesis of single crystalline $ZnSiP_2$ via CVT reactions, it is required to know all condensed phases and all gaseous species present in the system and their thermodynamic characteristics to determine optimal transport conditions. First thermodynamical model calculations for describing the solid-phase and gaseous-phase equilibria, the composition of the gaseous phases as well as the temperature dependent partial pressure courses were carried out with the program package TRAGMIN,[289] in collaboration with Dr. Marcus Schmidt at MPI-CPfS. The minimization of the free enthalpy of the system according to Eriksson's method constitutes the basis of the above-mentioned thermodynamic calculations.[290] The calculations were performed considering the CVT reactions of $ZnSiP_2$ with $ZnCl_2$ as transport agent in the temperature range from 1050 K to 1300 K. The decision of the temperature range was made based on the previous reports on crystal growth of $ZnSiP_2$ by CVT.[272] The calculated gaseous phases with their partial pressures as well as their calculated transport efficiency are shown in Fig. 9.3. The dominating gaseous species, besides $ZnCl_2$, were calculated to be Zn, P_2 and $SiCl_4$ (Fig.

9.3a) which have highest transport efficiencies (Fig. 9.3b). Based on these results, a possible transport equation towards the formation of $ZnSiP_2$ single crystals may be written as:

$$ZnSiP_2(s) + 2ZnCl_2(g) \rightleftharpoons 3Zn(g) + SiCl_4(g) + P_2(g) \tag{9.1}$$

By using available thermodynamic data,[291] reaction enthalpy, reaction entropy and Gibbs free energy could be calculated as $\Delta H_{R,\ 1300K} \approx 571$ kj/mol, $\Delta S_{R,\ 1300K} \approx 375$j/mol K, and $\Delta G_{R,\ 1300K} \approx 83$ kj/mol, respectively. A positive reaction enthalpy indicates the endothermic transport behavior of this system.

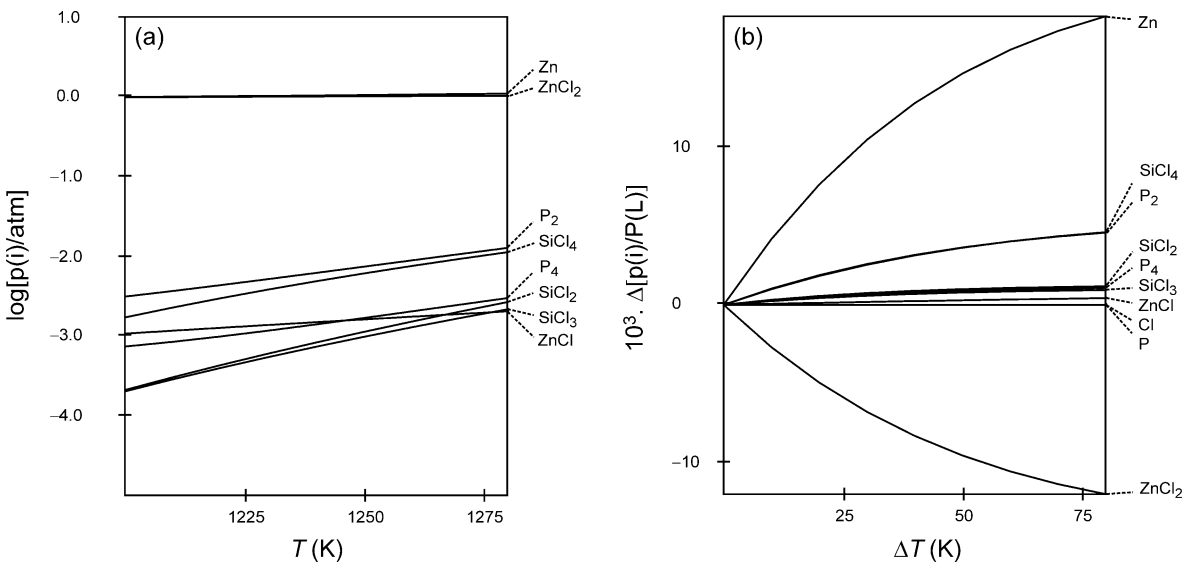

Figure 9.3: (**a**) Gaseous phase composition of $ZnSiP_2$ with $ZnCl_2$ for the range of possible reaction temperatures. (**b**) Calculated transport efficiency of the gaseous phase species for the chemical transport of $ZnSiP_2$ with $ZnCl_2$.

mm-size single crystals were grown with CVT reactions of pre-reacted $ZnSiP_2$ as a starting material (Fig. 9.4). Small amounts of $ZnCl_2$, *e.g.* 25 – 60 mg, as transport agent were filled in a quartz capillary and loaded inside a quartz ampoule (Table 9.2). The reaction ampoule was then placed in a two-zone furnace which provides transport of pre-reacted powder from hot side to the cold end of the ampoule.

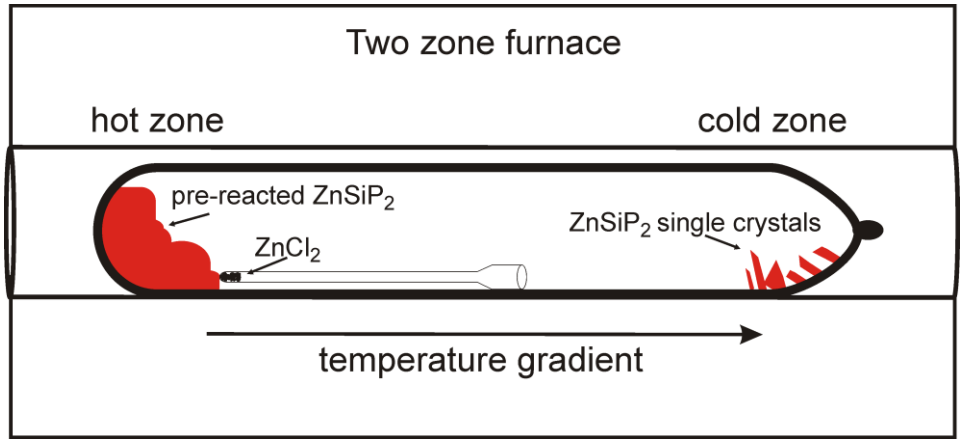

Figure 9.4: Schematic representation of a loaded ampoule for growing single crystals of $ZnSiP_2$ via chemical vapor transport with $ZnCl_2$ placed in a quartz capillary. The pre-reacted powder of $ZnSiP_2$ was placed in hot zone and the single crystals were grown at the cold side of the ampoule.

A temperature gradient was applied to the ampoule as mentioned in Table 9.2. Most relevant parameters, *e.g.*, absolute temperatures, temperature gradient, amounts of starting materials and transport agent, and volume of reaction ampoule have been widely changed. After several days, the starting materials were transported to give red transparent single crystals of $ZnSiP_2$ (Fig. 9.5). Some single crystals obtained via CVT reactions showed noticeable differences in their particular color which was considered as a hint towards small inhomogeneity within individual crystals. Accordingly, the experimental conditions of the transport reactions were altered in various ways, but without leading any obvious change in terms of small inhomogeneities present in single crystals. EDXS analysis performed on a single crystal from sample UA_MG02 revealed the composition of $Zn_{0.96}Si_{1.12}P_{1.92}$ which is slightly Zn and P deficient and Si excess compared to the ideal composition.

Table 9.2: Selected vapor transport experiments to grow $ZnSiP_2$ single crystals from pre-reacted powder.

Sample name	Preparation conditions	Lattice parameters (Å)
UA_MG02	1080 °C → 980 °C, 7 d 1 g $ZnSiP_2$, 40 mg $ZnCl_2$ ∅ =14 mm, *l* = 13cm	5.3995(1) 10.4386(3)
UA_MG72	1040 °C → 980 °C, 4 d 1 g $ZnSiP_2$, 40 mg $ZnCl_2$ ∅ =14 mm, *l* = 13cm	5.3992(1) 10.4373(3)
UA_MG45	1040 °C → 930 °C, 4 d 1.5 g $ZnSiP_2$, 40 mg $ZnCl_2$ ∅ =20 mm, *l* = 13cm	5.3991(1) 10.4379(3)
UA_MG62	1040 °C → 930 °C, 4 d 1.5 g $ZnSiP_2$, 60 mg $ZnCl_2$ ∅ =14 mm, *l* = 13cm	5.3993(2) 10.4383(5)
UA_MG71	1040 °C → 930 °C, 4 d, 1 g $ZnSiP_2$, 40 mg $ZnCl_2$ ∅ =14 mm, *l* = 13cm	5.3992(1) 10.4382(3)
UA_MG60	1000 °C → 925 °C, 3 d, 1.5 g $ZnSiP_2$, 60 mg $ZnCl_2$ ∅ =20 mm, *l* = 13cm	5.3988(2) 10.4378(4)
UA_MG80	990 °C → 910 °C, 4 d, 1 g $ZnSiP_2$, 25 mg $ZnCl_2$ ∅ =14 mm, *l* = 10cm	5.4001(2) 10.4366(4)
UA_MG77	990 °C → 940 °C, 4 d, 1.5 g $ZnSiP_2$, 40 mg $ZnCl_2$ ∅ =14 mm, *l* = 13cm	No transport
UA_MG89	990 °C → 910°C, 4 d, 1.5 g $ZnSiP_2$, 25 mg $ZnCl_2$ ∅ =14 mm, *l* = 10cm	5.3996(1) 10.4386(4)

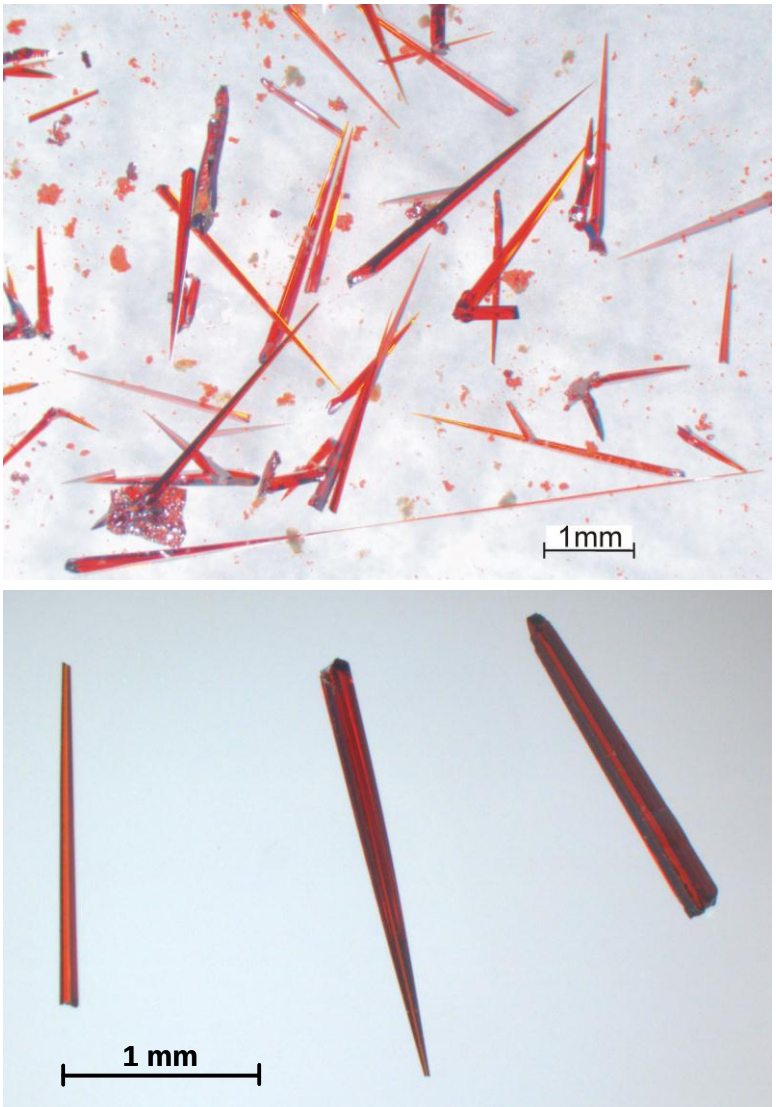

Figure 9.5: mm-size single crystals of $ZnSiP_2$ (UA_MG80) obtained by chemical vapor transport.

Considering the solid state synthesis, the reactions are generally too slow to cause sufficient diffusion at low temperatures. To achieve enhanced diffusion of elements, molten solids are used as solvents. Hence, in addition to CVT, $ZnSiP_2$ crystals were grown by using Sn as a flux material. For the synthesis, the elements or pre-reacted samples together with Sn have been placed in a quartz ampoule in different molar concentrations and experimental conditions were applied as shown in Table 9.3. In some cases, a continuous vibration is applied to obtain a homogenous melt. Frequently, Sn melt was tapped off from $ZnSiP_2$ to the other end of the ampoule. At the end of the reaction, the mixture of $ZnSiP_2$ and Sn was treated with warm concentrated HCl (at around 50 ºC) to dissolve Sn residue. It was observed that $ZnSiP_2$ crystals were not attacked by hydrochloric

acid. Certain parts of crystals which were grown in Sn flux show very homogenous red color (Fig. 9.6). However, most crystals exhibit cavities, and in few cases, even Sn droplets were observed on the openings of such cavities. This resembles findings in systems like Sn – In – S,[292] or in $M\mathrm{In}_7X_9$ (M = Rb, Cs; X = S, Se).[293] One reason for this kind of behavior may be gradients in the activities of various components during the growth process. Along this line, experiments which included rocking or rotation of the reaction ampoule during the growth process considerably reduced the formation of cavities in the crystals. However, the application of vibration was found to increase the number of Sn inclusions which could not be totally removed from crystals. EDXS analysis performed on a single crystal from the sample UA_MG95 revealed the composition of $Zn_{0.94}Si_{1.13}P_{1.92}$ which is similar to the composition obtained from CVT experiment.

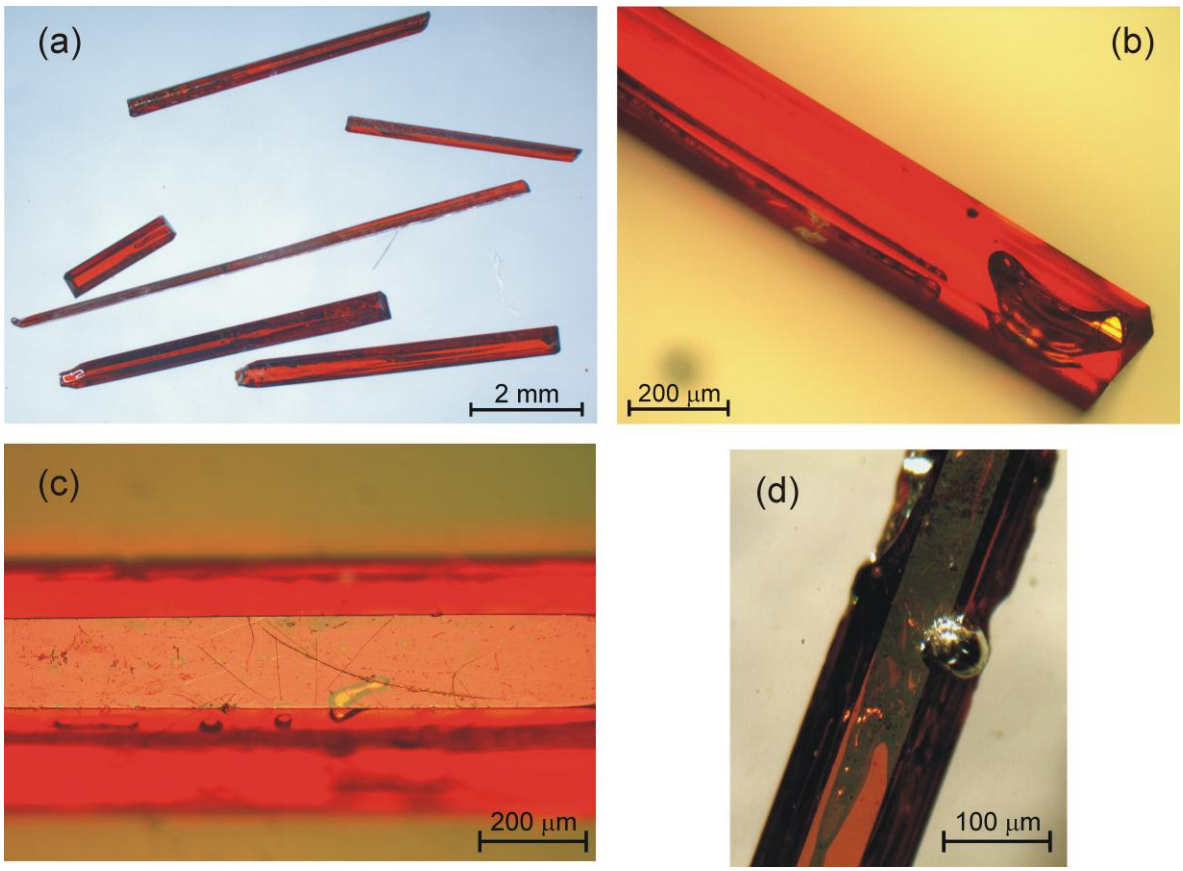

Figure 9.6: Single crystals of $ZnSiP_2$ obtained by Sn flux method (**a-c** (UA_MG95)**,** **d** (UA_MG99)). Smooth surfaces and sharp edges are visible as well as pronounced cavities (**b**, **c**) and sometimes Sn inclusions (**d**).

Table 9.3: Preparation of $ZnSiP_2$ crystals with Sn flux method at different experimental conditions.

Sample name	Starting material	mol.% $ZnSiP_2$ in Sn	Heat treatment	Sample mixing and furnace type	Ampoule ∅(mm) × *l*(cm)
UA_MG98	pre-reacted powder	3	24 h to 1100 °C, 2 d ann., 24 h to 600 °C, tin melt decanted	chamber furnace	20 × 13
UA_MG95	elements	6	½ h to 500 °C, 24 h to 1120 °C, 2 d ann., 60 h to, 680 °C 12 h to 400 °C tin melt decanted	chamber furnace	20 × 13
UA_MG99	elements	6	1 h to 500 °C, 24 h to 1120 °C, 2 d ann., 48 h to RT	tube furnace vibration applied during the heat treatment	14 × 13
UA_MG100	elements	6	1 h to 500 °C, 24 h to 1120 °C, 2 d ann., 48 h to RT	2 zone rocking furnace	14 × 13
UA_MG101	elements	6	1 h to 500 °C, 24 h to 1120 °C, 2 d ann., 48 h to RT	tube furnace	14 × 13
UA_MG103	elements	10	1h to 500 °C, 24 h to 1150 °C, 2d ann., 12 h to 1050 °C, 17 h to 950 °C, 20 h to 850 °C, 25 h to 750 °C, 50 h to 550 °C, tin melt decanted	tube furnace vibration stopped after high temperature annealing	14 × 13

9.2.2 Preparation of polycrystalline and single crystalline $CuAlS_2$

For the synthesis of polycrystalline $CuAlS_2$, stoichiometric mixture of the elements (in total 3 g) were placed in a glassy carbon crucible, sealed in a dried quartz glass ampoule ($\varnothing_{outer}$ = 14 mm, l = 13mm) under 300 mbar Ar pressure. The sample was heated for 40 °C / h to 1000 °C. Annealing 3 d at this temperature and subsequent cooling with 80 °C / h to room temperature resulted in polycrystalline single phase powder material (Fig. 9.7).

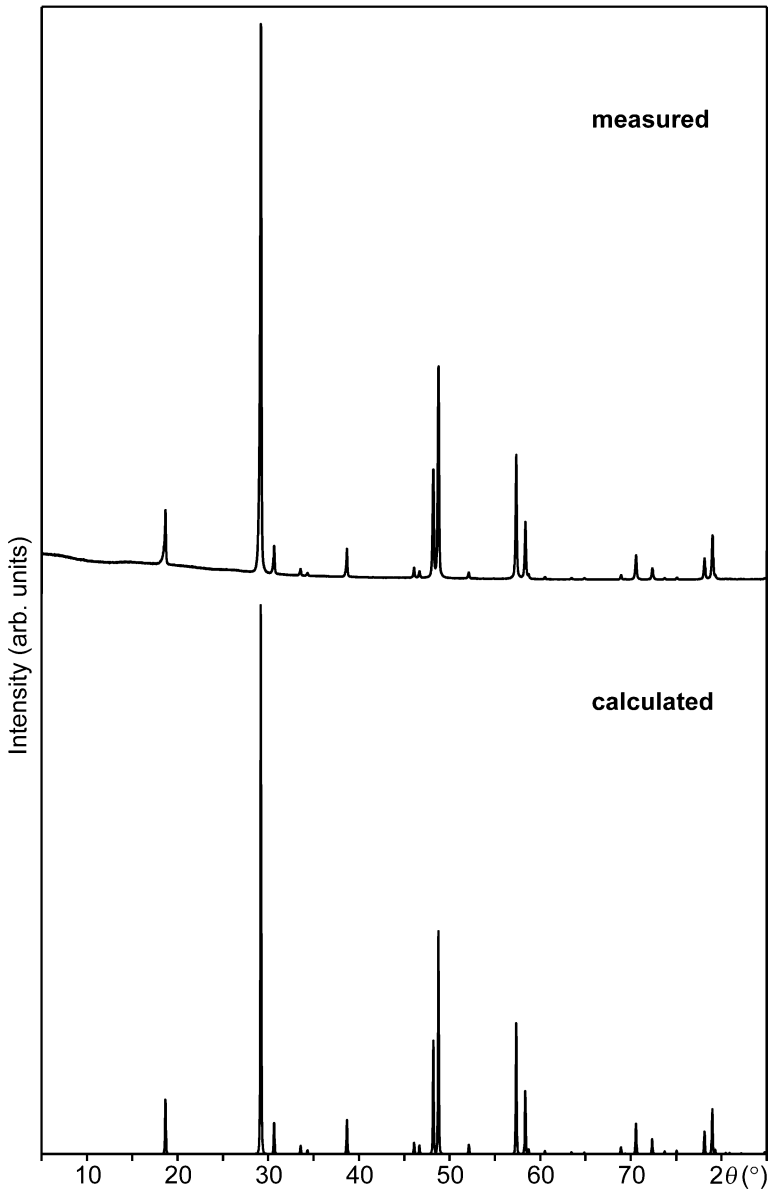

Figure 9.7: PXRD pattern of polycrystalline $CuAlS_2$ together with calculated one based on our single crystal X-ray analysis (Cu-$K\alpha_1$ radiation). The reflection intensities are in good agreement with the structure model derived from the single crystal diffraction data (see section 9.4). No additional phase was observed.

The single crystalline materials have been obtained via CVT reactions by use of pre-reacted polycrystalline $CuAlS_2$ as a starting material. A linear temperature gradient was applied to the ampoule in a two-zone furnace with the reaction conditions stated in Table 9.4. Around 30 mg I_2 was used as transport agent, which was filled inside a quartz capillary before sealing in a quartz ampoule. Well-shaped blue transparent single crystals were obtained after 4 d of vapor transport reaction (Fig. 9.8). In literature, the color of the $CuAlS_2$ crystals was related to the stoichiometry of the compound (determining the value of the band gap) or presence of impurities. Depending on the thickness green/black crystals of this phase was obtained by Honeyman *et al.*, which was reported to be slightly sulfur deficient.[286] No information about impurity phases was given. Colorless crystals were also grown by Bridenbaugh *et al.*[294] In blue crystals of $CuAlS_2$, Fe^{3+} impurities were identified by Guerrero *et al.* from magnetic susceptibility measurements with the concentration of around 300 ppm.[287] EDXS analysis performed on a single crystal from sample UA_MG128 revealed no detectable Fe contamination which may stem from very small amounts. The composition of a single was determined to be $Cu_{1.03}Al_{1.03}S_{1.94}$ which is slightly different from the ideal composition.

Table 9.4: Selected CVT experiments to grow $CuAlS_2$ single crystals from pre-reacted powder.

Sample name	Synthesis conditions	Lattice parameters (Å)
UA_MG117	800 °C → 700 °C, 2 d 1 g $CuAlS_2$, 30mg I_2 ∅ =20 mm, *l* = 13 cm	5.3341(2) 10.4396(6)
UA_MG127	790 °C → 710 °C, 3 d 1.5 g $CuAlS_2$, 30mg I_2 ∅ =14 mm, *l* = 13 cm	5.3341(2) 10.4402(6)
UA_MG128	820 °C → 670 °C, 3 d 1.5 g $CuAlS_2$, 30mg I_2 ∅ =14 mm, *l* = 13 cm	5.3342(1) 10.4396(3)

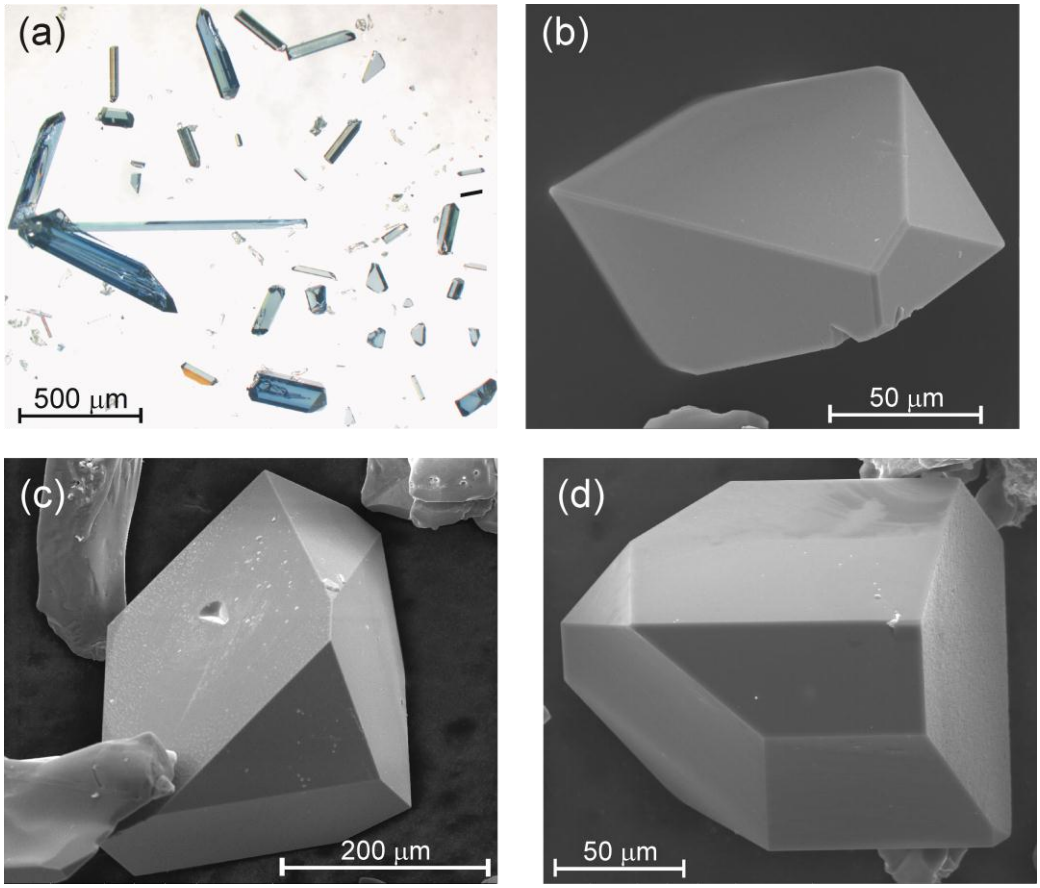

Figure 9.8: Single crystals of $CuAlS_2$ obtained by CVT reactions. (**a**) Optical microscope images of $CuAlS_2$ crystals from the sample UA_MG127. The SEM images labeled as (**b**), (**c**) and (**d**) belong to the samples UA_MG117, UA_MG127 and UA_MG128, respectively.

9.3 Preparation of $ZnSiP_2$ single crystals for static charge density analysis and analysis under external electric field

For single crystal X-ray analysis, either crystals were collected from the reaction products or small crystals were cut from as-grown single crystals which are too big (on the order of few mm) for that investigation. The cutting was carried out by use of a wire-saw as described in section 3.2. After cutting, crystals nearly in cube shape with the edge length of around 50 μm were obtained (Fig. 9.9). Some crystals were treated with conc. HF for around 20-30 sec. to smooth away the surface imperfections introduced during the cutting processes. Some others were post annealed at 950 °C in sealed quartz capillaries (∅ = 0.5 mm) several days to release the stress came along the same process.

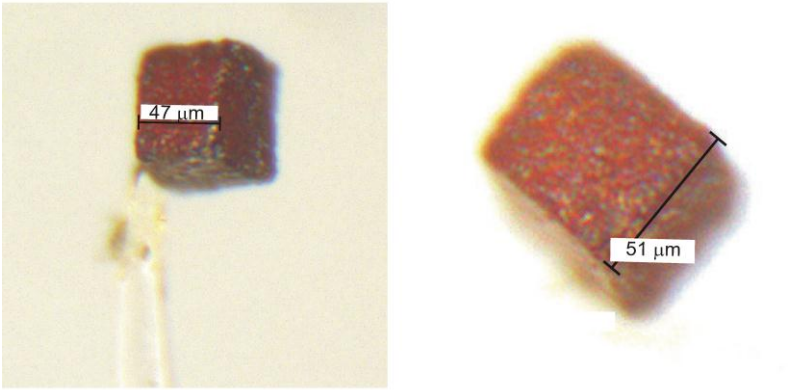

Figure 9.9: Single crystals of $ZnSiP_2$ (UA_MG02e) obtained after cutting with wire saw.

After reasonably large single crystals were obtained via CVT reactions, quality of a selected crystal was checked by X-ray diffraction and proved to be single domain. For charge density analysis under external electric field, a trapezoidal crystal with (111) faces was cut using a wire saw followed by grinding with silicon carbide paper (800 µm) and Glycerol as lubricant (Fig. 9.10). The trapezoidal faces were given by the shape of the as-grown crystal and not modified. Finally the crystal was placed in a vacuum chamber for gold sputter coating by Cressington 108 Auto Sputtercoater whereby the current was adjusted to 30 mA for 120 s to produce a gold layer of few nm thicknesses.

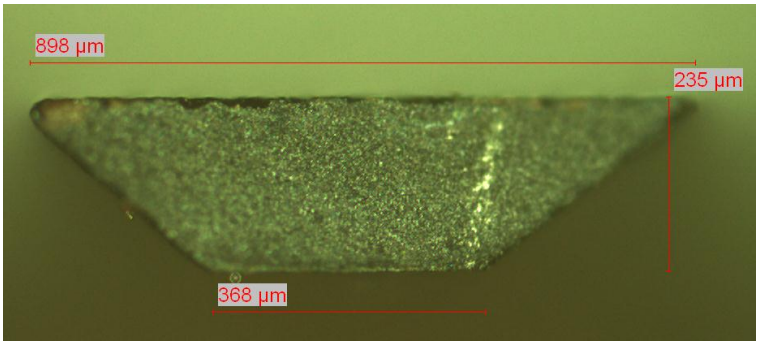

Figure 9.10: View of a $ZnSiP_2$ crystal after shaping for field-dependent measurements.

9.4 Crystal structure

Generally, complex crystal structures can be derived from simple structures by adding as well as substituting atoms or through distortion. These complex structures are called as derivative structures. There exists a special class of derivative structures in which the major difference from the simple structure is formation of a larger unit cell referred as super structures.[295] In this sense, the symmetry of the derivative structure is a subgroup of the space group of the basic structure.[296] The crystal structure of chalcopyrite, $CuFeS_2$, is derived from the sphalerite, ZnS, by substitution of the Zn sites by Cu and Fe. The crystal structure of sphalerite or zinc blende is closely related to the diamond structure. The crystal structure of diamond consists of two interpenetrating face centered cubic (fcc) Bravais lattices in which one displaced from the other by one quarter the length of the body diagonal (Fig. 9.11). Alternatively diamond structure may be visualized as a face-centered cubic lattice with additional atoms occupying half of the tetrahedral holes. All the atoms in a diamond structure are tetrahedrally coordinated. Like the diamond lattice, zinc blende structure consists of the two interpenetrating fcc lattices. Differently, in zinc blende each of the two interpenetrating fcc lattices consists of one type of atoms only *e.g.* Zn or S for ZnS (II–VI compound) or Ga or P for GaP (III–V compound). This crystal structure can be also described as face centered cubic lattice of Zn atoms in which half of the tetrahedral sites are filled with S atoms. I–III–VI_2 and II–IV–V_2 compounds, for simplicity will be denoted as ABC_2, crystallizing in chalcopyrite structure can be regarded as an ordered distribution of the three constituents on the sites of the cubic diamond structure but with a small distortion introduced by the loss of symmetry. Hence, the anions occupy one fcc sublattice of the diamond structure whereas the cations share the sites of the other one. Alternatively, I–III–VI_2 and II–IV–V_2 compounds can be considered as the ternary analogs of the binary II–VI and III–V compounds, respectively. These ternary compounds can be derived from the binary phases in a way that Group II or Group III cations in binary compounds are substituted with an equal number of Group I and III, or Group II and IV atoms, respectively. This replacement of the atoms in ordered manner lead to doubling of zinc blende unit cell along tetragonal *c*-axis of chalcopyrites ($c/a \approx 2$). If the cations *A* and *B* are distributed randomly, the cubic zinc blende structure would result. In this sense, the chalcopyrite structure would be regarded as a superstructure of the zinc blende structure. The derivation of ternary compounds starting from the group IV elements is illustrated in Fig. 9.11.

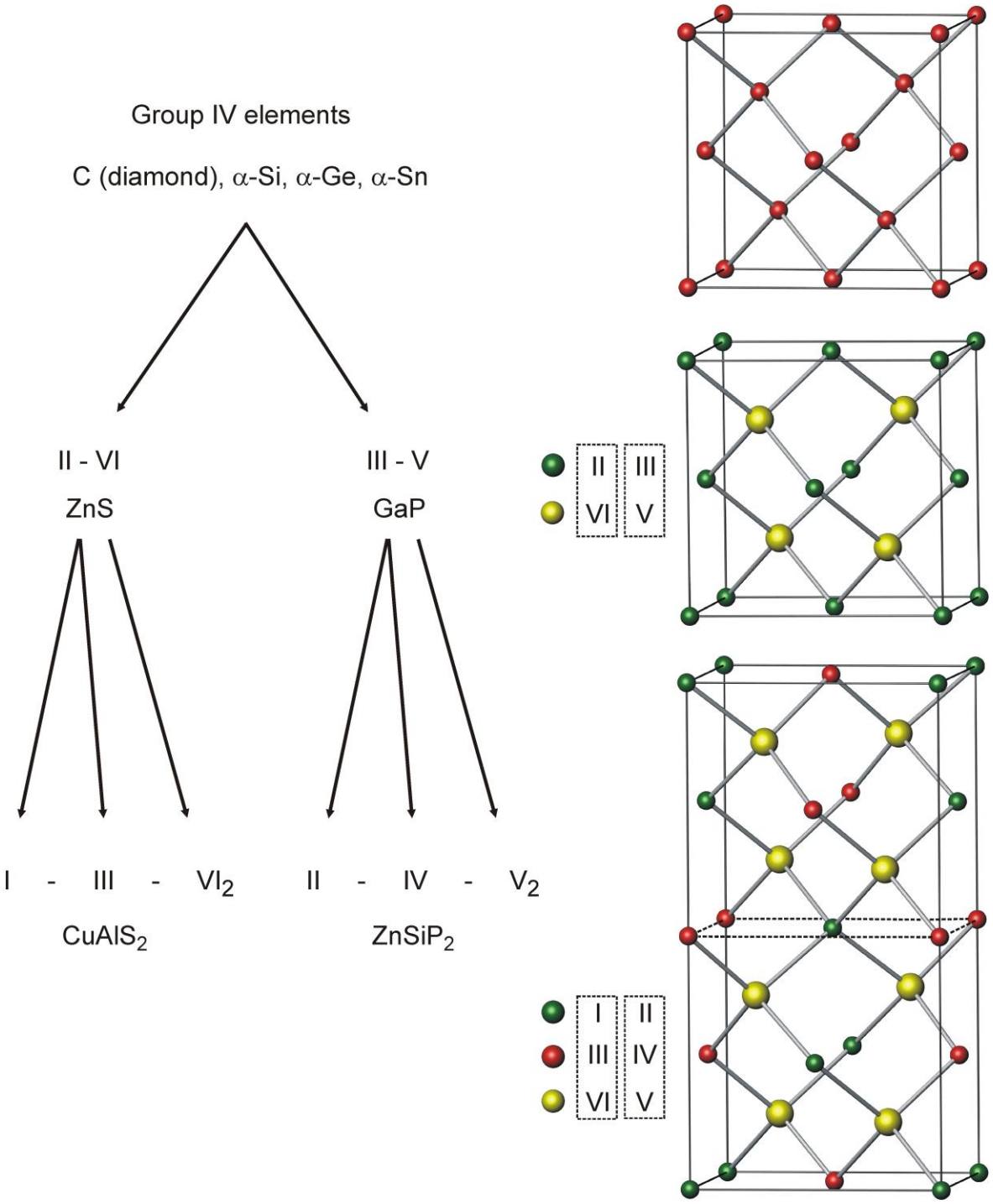

Figure 9.11: Schematic illustration of the formation of I–III–VI_2 and II–IV–V_2 compounds starting from group IV elements (**left**). Diamond (**top**), zinc blende (**middle**) and chalcopyrite (**bottom**) structures are shown on the right side of the figure. Tetragonal chalcopyrite structure corresponds to two cubic zinc blende unit cells of the binary analogs (illustrated with dashed lines) but distorted along the *c*-axis.

The ternary chalcopyrites ABC_2 crystallize in non-centrosymetric space group $I\bar{4}2d$ (no. 122) with four formula units per unit cell. In the crystal structure of ABC_2, each *A* and *B* atom is tetrahedrally coordinated to four *C* atoms, whereas each *C* atom is tetrahedrally coordinated to two *A* and two *B* atoms in an ordered way (Fig. 9.11). The point symmetry of the *A* and *B* sites is S_4 and the symmetry of the *C* site is lower as C_2. The atomic positions of chalcopyrite ABC_2 in standard settings are as follows: 4*A* atoms in site 4*a* (0, 0, 0), 4*B* atoms in site 4*b* (0, 0, 1/2) and 8*C* atoms in site 8*d* (*x*, ¼, 1/8). The free parameter *x* defining the position of the *C* atoms relative to *A* and *B* atoms is equal to ¼ for zinc blende structure leading to $c/a = 2$. However for chalcopyrites, the value of *x* deviates from 'ideal' value of ¼ due to the difference in electronegativity and / or different covalent radii of the cations *A* and *B*. Therefore, c/a ratio is no longer equal to 2. The quantity $2 - c/a$ is a measure of the tetragonal distortion in terms of the lattice constants which point to contraction or elongation along the *c*-axis. In general, chalcopyrite compounds are compressed along the tetragonal *c*-axis resulting in $c/a < 2$.[297] For this case, the free parameter *x* is greater than ¼ indicating the motion of the *C* atoms towards the *B* atoms and away from the *A* atoms. Some exceptions from this trend have been reported for *e.g.* $CuInS_2$ or $CuInSe_2$ with $c/a > 2$,[298, 299] indicating that the anion *C* is slightly displaced from the ideal position towards the cation *A* with higher charge state along with the smaller ionic radius.

The detailed investigation on $ZnSiP_2$ and $CdSiP_2$ showed that the Group IV atom Si forms almost perfect tetrahedra with Group V atom P which is the predominant structural feature of these materials.[278, 300] This is considered due to the strong tendency of Si atoms towards sp^3-hybridizaton. Considering a regular tetrahedron of *C* atoms around *B* atom, the parameter *x* is predicted to be no longer an independent variable but is directly related to the c/a ratio by following equation:[300]

$$x_{calc} = \frac{1}{2} - \left(\frac{c^2}{32a^2} - \frac{1}{16}\right)^{\frac{1}{2}} \tag{9.2}$$

From the calculated value of *x* by using Eq. 9.2, it is possible to calculate the interatomic distances d_{A-C} and d_{B-C} in terms of *a* and *c*:[300]

$$d_{A-C} = \left(a^2x^2 + \frac{4a^2 + c^2}{64}\right)^{\frac{1}{2}} \tag{9.3}$$

$$d_{B-C} = \left(a^2\left(\frac{1}{2} - x\right)^2 + \frac{4a^2 + c^2}{64}\right)^{\frac{1}{2}} \tag{9.4}$$

From these equations, the lattice parameter c can be related to d_{B-C} by,

$$c = \frac{8}{\sqrt{3}} d_{B-C} \tag{9.5}$$

The predicted values of x based on Eq. 9.2 for II–IV–V_2 chalcopyrites compare well with most of the experimental values such as for $ZnSiP_2$ (x_{calc} = 0.2671, x_{meas} = 0.2691), $ZnGeP_2$ (x_{calc} = 0.2573, x_{meas} = 0.2582) and $ZnSiAs_2$ (x_{calc} = 0.2646, x_{meas} = 0.2658).[272, 278, 299, 300] The difference between measured and calculated values of x, $\Delta x = x_{meas} - x_{calc}$, is called sublattice distortion and is in most cases less than 0.02 Å, but positive for II–IV–V_2 chalcopyrites. However, Δx is sometimes as large as 0.09 Å and negative for I–III–VI_2 chalcopyrites.[299] These results may point for crystal structure of II–IV–V_2 compounds that tetrahedra formed by *A* and *C* atoms are distorted to form a regular tetrahedron formed by *B* and *C* atoms which leads overall tetragonal distortion along the *c*-axis. Whereas, the tetrahedral arrangement around *B* atoms in the crystal structure of some I–III–VI_2 compounds, *e.g.*, $AgGaS_2$, $CuGaS_2$, or $CuInS_2$,[272] is less perfect as suggested due to the stronger bonding of the *C* atom with its two nearest neighbors of *A* atoms presumably because of short-range bonding with the d electrons of *e.g.* Ag or Cu.[301]

One of the major goals in this project was to grow larger single crystals of different chalcopyrite compounds, but also to perform an experimental charge density analysis of the material itself, *i.e.* without external electric field on small single crystals. The data collection, reduction, and refinement procedures for charge density analysis require considerable expertise. Severe systematic errors, *e.g.* extinction and thermal diffuse scattering, can be revealed during data reduction and refinement which are generally difficult to handle. Additionally, it is required to measure single crystals with the highest possible resolution meaning that extending the data collection to as high scattering angles as possible. All these aspects can be realized by lowering the wavelength of the primary radiation and using low temperature X-ray diffraction technique.

For crystal structure analysis, small single crystals were selected (Fig. 9.12) or cut (Fig. 9.9) whenever growth parameters had been changed significantly and investigated by single crystal diffraction methods according to section 3.3. In order to identify single crystals suitable for a data collection up to high resolution, screening of selected crystals was very rigorous. All crystals which showed even faint hints of satellites, twinning, or broadening of reflections were abandoned. Table 9.5 shows a compilation of $ZnSiP_2$ samples for which high-resolution data sets were collected and further analyzed. Besides UA_MG80aa all data were collected applying Ag-*K*α radiation on a Weissenberg-type diffractometer with imaging plate detector. For a comparison, data set UA_MG80aa was

collected on a four-circle goniometer with CCD-detector and Mo-*K*α radiation. The crystal structure refinements were achieved by employing a full-matrix least-squares procedure with SHELXL-97 program integrated in WinGX software package. Details concerning the data collection and structure refinements of $ZnSiP_2$ and $CuAlS_2$ are given in Table 11.24. Atomic coordinates, displacement parameters (in $Å^2$) and site occupancies are tabulated in Table 11.25-11.26.

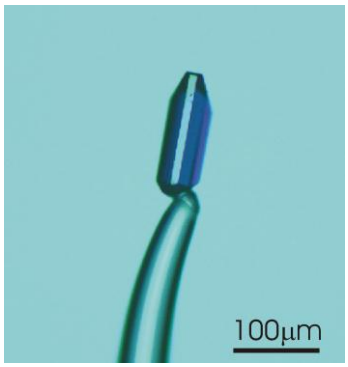

Figure 9.12: Selected and mounted single crystal of $CuAlS_2$ (UA_MG128) for single crystal X-ray diffraction analysis.

Table 9.5: $ZnSiP_2$ single crystals for which high-resolution data sets were collected.

Sample name	Synthesis methods	$\sin\theta/\lambda$ ($Å^{-1}$)	$2\theta_{max}$ (°)	no. of reflections collected	no. of reflections unique	R_{int} (%)	R_{σ} (%)
UA_MG02e	CVT	1.66	138	14438	2439	2.27	2.56
UA_MG02k	CVT	1.38	102	2706	1260	2.89	4.49
UA_MG02m	CVT	1.66	138	9639	2892	3.33	3.80
UA_MG80aa	CVT	0.80	69	969	301	3.42	5.98
UA_MG80ap	CVT	1.56	122	8722	2425	2.59	3.20
UA_MG89	CVT	1.25	89	5921	1257	2.38	2.72
UA_MG103c	Flux	1.56	122	8722	2426	3.58	4.02

As discussed previously, in contrast to other related chalcopyrites, there should be no disordering at high temperatures for $ZnSiP_2$. According to our thermal analysis based on DSC, there is no indication of any kind of phase transition up to 1340 °C. However, severe problems were found with respect to crystal and data quality. Despite extensive efforts in variation of crystal growth conditions and crystal handling, this problem remained rather unchanged. Whenever crystals seemed suitable, a high-resolution data set was collected up

to $\sin\theta/\lambda$ around 1.7Å^{-1} (Fig. 9.13, Table 9.5). Despite the considerable variation in growth conditions crystal size and crystal shape the results are very consistent but unsatisfactory.

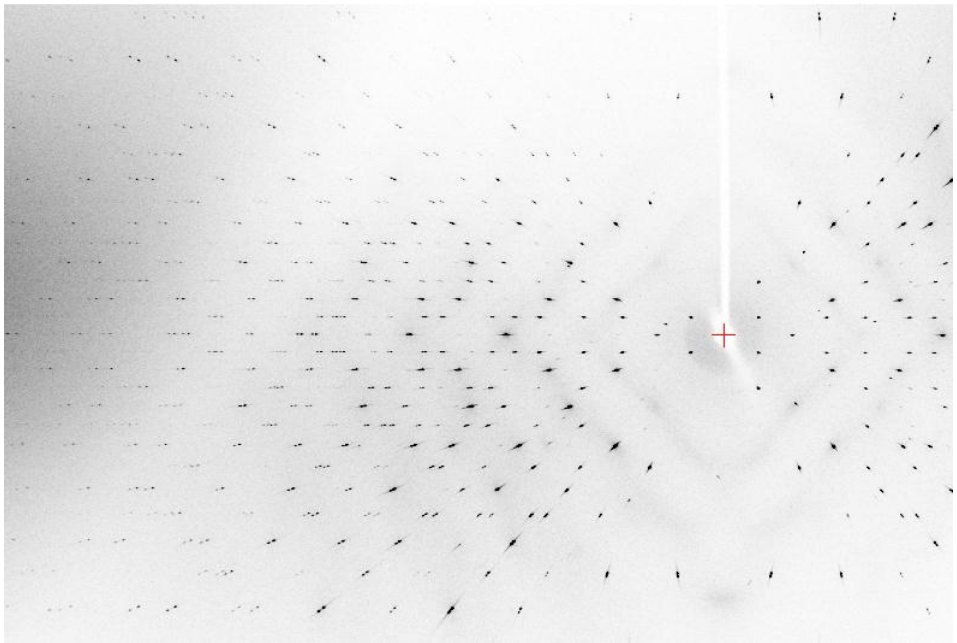

Figure 9.13: X-ray diffraction image of a large single crystal of $ZnSiP_2$ taken with Ag-$K\alpha$ radiation. Diffraction limit on the left is about $2\theta = 150°$.

The quality of the single crystal data after merging can be evaluated by mainly two reliability factors, R_{int} and R_σ called as merging residual values. The value of R_{int} is a measure of the consistency of intensity measurements for symmetry related reflections and R_σ value provides a measure of accuracy of the data and the data reduction process. Irrespective of the crystal system, the merging R-factors should be as close as possible to zero (typically 0.5 – 2 %) to perform charge density analysis. Considering this criterion, the tabulated R_{int} and R_σ values for selected single crystals of $ZnSiP_2$ and $CuAlS_2$ are relatively high (Table 9.5-11.24). From the single crystal data analysis, no trend with respect to particular classes of reflections for typical indications of twinning (no case as F_o^2 is much greater than F_c^2 for most disagreeable reflections) was observed as also reflected in Flack parameter which is close to 0 within standard deviations (Table 11.24). Refinements of the well known structural model did not provide any insight into this “data problem”, but very consistently revealed additional peculiarities. There are always quite large contributions from extinction (Table 11.24). Although small inhomogeneities have been observed for single crystals under optical microscope as well as the composition determined by EDXS analysis show small deviation from ideal stoichiometry, site occupancies do not significantly deviate from unity based on single crystal analyses. Even mixed occupancies at A and B atom sites, which might be possible due to the similar environments, are not

detectable. Accordingly, the differences in displacement parameters remain unchanged. Neither very careful inspections of the data nor the refinement of various twin models did provide any further conclusion. Finally, anharmonic refinement of the atoms did not improve the model either. These unexpected results are very consistent with a large variety of data sets. Even collecting data for a particular crystal of $ZnSiP_2$ from sample UA_MG80aa on another instrument with goniometer geometry, X-ray source and wavelength as well as detector being quite different, the refined model with all peculiarities mentioned was very well reproduced. Detailed inspection of the reciprocal space did not reveal any significant intensity for systematically absent reflections nor for any other additional reflections for investigated crystals. Diffuse scattering seemed more pronounced for crystals which had been cut using a wire saw, but looked improved after etching. In the end, very similar results were obtained for crystals from two different families of chalcopyrites (I–III–VI_2 and II–IV–V_2) which may point to a fact that these are inherent properties of this particular class of materials. All these results have hampered so far a reasonable static charge density analysis of both $ZnSiP_2$ and $CuAlS_2$. Due to this fact, although $ZnSiP_2$ single crystals were prepared, a further investigation of the response of crystals to an external electric field was not carried out.

The TEM investigations performed on natural chalcopyrite crystals $CuFeS_2$ as well as $ZnSiP_2$ single crystals revealed the existence of lattice defects such as dislocation loops, dislocation walls, stacking faults, *etc.*[302, 303] These aspects may affect the quality of the prepared single crystals. In addition, a careful inspection of grown single crystals by use of HRTEM may provide valuable information in terms of presence of any of these lattice defects.

Considering the crystal structures of $ZnSiP_2$, for all investigated data sets the displacement parameters of Zn are considerably larger than the ones for Si and P atoms (Table 11.25). No significant change is observed when site occupancies are refined. That is even more significant for $CuAlS_2$ in which the displacement parameters of Cu atoms are almost two times bigger than those of Al and S atoms (Table 11.26). It seems that it is a common feature for compounds crystallizing in chalcopyrite structure that the atomic displacement parameters of atom *A* are larger compared to those of *B* and *C* atoms. The lattice parameters, *c*/*a* ratio, calculated and experimental values of *x* parameter as well as the distances $d_{A–C}$ and $d_{B–C}$ for single crystals of UA_MG02 ($ZnSiP_2$) and UA_MG128 ($CuAlS_2$) are tabulated in Table 9.6. The lattice parameters of all investigated $ZnSiP_2$ samples are not significantly different taking into account the standard deviations (Table 9.2 and 9.6), and the values are in agreement with the reported ones.[278, 304-306] The *c*/*a* ratio for all samples is close to 1.933(1) pointing to a structural contraction along the *c* axis. The lattice parameters of all investigated $CuAlS_2$ samples are almost the same within standard

deviations (Table 9.4 and 9.6). The tetragonal distortion is less pronounced for $CuAlS_2$ in which the *c*/*a* ratio is around 1.957(1). The calculated values of *x* parameter for $ZnSiP_2$ and $CuAlS_2$ are 0.2670 and 0.2608, respectively, which are very close to the ones obtained from the single crystal analyses. The interatomic distances for $ZnSiP_2$ were found to be *d*(Zn – P) = 2.3776(1) Å and *d*(Si – P) = 2.2505(1) Å. The distances for $CuAlS_2$ were obtained with the values *d*(Cu – S) = 2.3327(1) Å and *d*(Al – S) = 2.2554(1) Å. The calculated interatomic distances are in agreement with the experimental values in which the difference in extreme case is about 0.01Å.

Table 9.6: Lattice parameters, experimental and calculated values of *x* as well as the interatomic distances. The calculated values are shown in parenthesis below the experimental ones (*x* values are obtained based on Eq. 9.2 and interatomic distances are derived from Eq. 9.3 and Eq. 9.4).

ABC_2	*a* (Å)	*c* (Å)	*c* / *a*	*x*	d_{A-C} (Å)	d_{B-C} (Å)
$ZnSiP_2$	5.3995(1)	10.4386(3)	1.9333(1)	0.27017(2) (0.2670)	2.3776(1) (2.3670)	2.2505(1) (2.2600)
$CuAlS_2$	5.3342(1)	10.4396(3)	1.9571(1)	0.26247(3) (0.2608)	2.3327(1) (2.3275)	2.2554(1) (2.2602)

The tetrahedral bond angles determined from the single crystal X-ray analysis of $ZnSiP_2$ and $CuAlS_2$ are given in Table 11.27. As discussed above for ABC_2, all *A* and *B* atoms are coordinated to four *C* atoms, while all *C* atoms are coordinated to two *A* and two *B* atoms. The environment of Si atoms in $ZnSiP_2$ is close to the regular tetrahedron with bond angles changing from 109.6 º to 109.1 º. On the other hand Zn and P atoms form distorted tetrahedra with bond angles varying from 104.3 º to 113.4 º. For $CuAlS_2$, the environment of Al is even closer to regular tetrahedron with 109.6 º and 109.3 º and the deviation of angles for Cu and S atoms from ideal tetrahedron are slightly less compared to Zn and P environments varying from 106.2 º to 112 º. The results demonstrate that the tetragonal distortion is indeed due to four-fold Zn or Cu atoms rather than Si or Al atoms in $ZnSiP_2$ and $CuAlS_2$.

9.5 NMR investigation of $ZnSiP_2$

^{29}Si as well as ^{31}P NMR experiments on polycrystalline and single crystals of $ZnSiP_2$ were performed in collaboration with Prof. Dr. Frank Haarmann according to section 3.3 ^{29}Si MAS NMR experiment on isotope-enriched polycrystalline $ZnSiP_2$ shows a single narrow signal when a rotation frequency of ν_{rot} = 10 kHz was applied. The isotropic signal shift of –1.1 ppm is in the range of diamagnetic non-conducting compounds (–350 ppm $\leq \delta \leq$ 50

ppm).[244] The full width at half maximum of FWHM = 250 Hz indicates a well ordered compound and excludes the presence of significant atomic disorder (Fig. 9.14). ^{31}P NMR experiments without sample rotation result in a broad signal with the characteristic line shape of chemical shift anisotropy (CSA) (Fig. 9.15a). Slow rotation of the sample using a rotation frequency of ν_{rot} = 1.1 kHz result in a typical MAS CSA signal (Fig. 9.15b). The isotropic shift (δ_{iso}) of the signal was confirmed in a series of MAS experiments with different rotation frequencies. The spectral parameters were determined by a least-squares fit of the slow spinning experiment (Table 9.7). Anisotropy (Δ) and the asymmetry parameter (η) of the signal are in agreement with the low site symmetry of the P atoms. The isotropic shift of the ^{31}P signal is negative and inside of the expected range of –400 ppm $\leq \delta \leq$ 600 ppm for diamagnetic, non-conducting materials.[244] The FWHM of about 105 Hz indicates no significant contribution of atomic disorder in agreement with the results of the ^{29}Si MAS experiments.

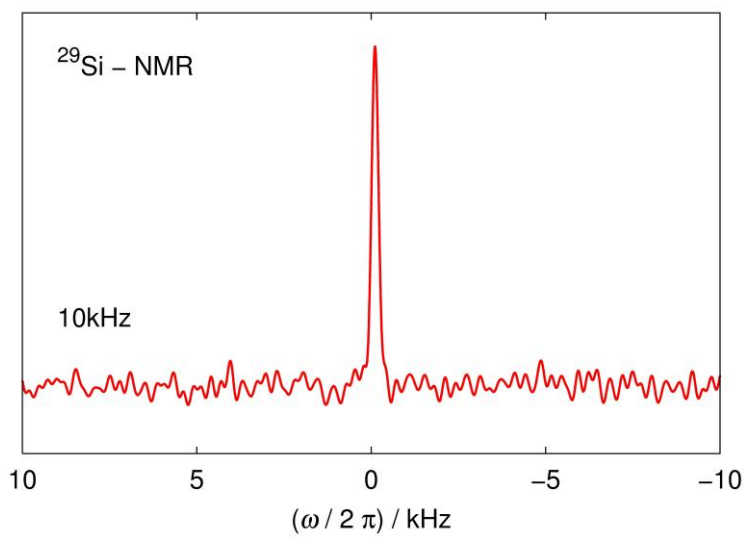

Figure 9.14: ^{29}Si MAS NMR signal of enriched $ZnSiP_2$ using a rotation frequency of ν_{rot} = 10 kHz.

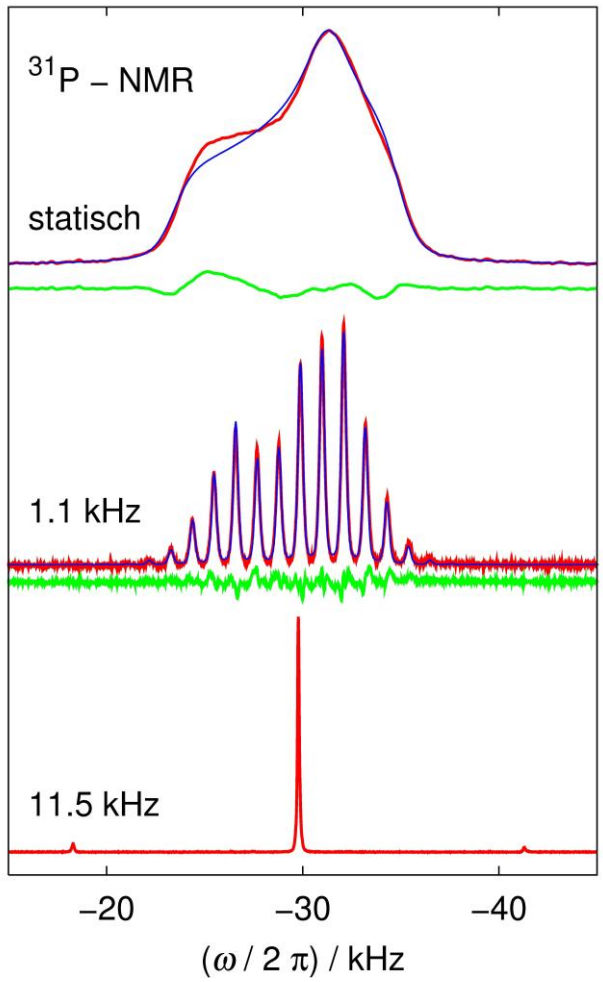

Figure 9.15: ^{31}P NMR signals of $ZnSiP_2$. (**top**) Static experiment: experimental data are represented by red lines and the simulated signal contribution with blue lines. The simulation is based on the spectral parameters obtained by least-squares fitting of the MAS signal using ν_{rot} = 1.1 kHz (**middle**). Blue lines represent the simulated signal contributions and red lines the experimental results. The difference between the simulated and experimental signals is shown at the bottom in green. The simulations of the signals are based on the parameters from Table 9.11. (**bottom**) Fast rotation MAS experiment using ν_{rot} = 11.5 kHz.

Table 9.7: Spectral parameters of the ^{31}P NMR signals of $ZnSiP_2$ determined by least-squares analysis.[141] δ_{iso} corresponds to the isotropic shift, Δ to the anisotropy parameter and η to the asymmetry parameter.

Atom	δ_{iso} / ppm	Δ / ppm	η
P	–147.61	29.49	0.609

9.6 Conclusions

Single phase polycrystalline materials as well as single crystals of chalcopyrites $ZnSiP_2$ and $CuAlS_2$ were successfully prepared. Although optical microscopy inspection of the crystals indicates in most cases good crystal quality, the investigated ones were not adequate for charge density analysis as indicated by high internal *R*-values for collected data sets with relatively high diffraction limit. Rather wide variation of crystal growth conditions did not provide any significant improvements in crystal quality of both $ZnSiP_2$ and $CuAlS_2$. There is no indication in thermal analyses for a potential order-disorder transition for $ZnSiP_2$. ^{31}P as well as ^{29}Si NMR experiments did not reveal any hint towards local disorder which may stem from the mixed occupancy of Zn and Si sites having similar local environments. Based on these results, so far a reasonable static charge density analysis of both $ZnSiP_2$ and $CuAlS_2$ could not be achieved and further investigation of the response of crystals to an external electric field was not proceeded with.

Chapter 10

Summary and Outlook

Single phase bulk polycrystalline samples of $Ba_8Ge_{43}\square_3$ were prepared by steel-quenching technique and investigated to identify the vacancy ordering along with the relationship between the composition, the crystal structure and the physical properties. Other preparation routes resulted with the partial decomposition of $Ba_8Ge_{43}\square_3$ into secondary phases *e.g.* Ba_6Ge_{25}, α-Ge and $BaGe_5$. DSC results confirmed the stability of $Ba_8Ge_{43}\square_3$ within limited temperature range 770 – 810 °C. Single crystal X-ray diffraction experiments enabled a thorough study of the crystal structure of steel-quenched and annealed samples. Within some basic crystallographic considerations, a model of the vacancy ordering is proposed enabling a possible explanation for the presence of three vacancies per formula unit in $Ba_8Ge_{43}\square_3$. The electrical properties reflect a metallic-like regime of conduction turning into a semiconductor-like behavior near room temperature. Two crossovers from electronic- to hole-like transport characterize the complex temperature dependence of the thermopower. Thermal transport measurements reveal a crystal-like behavior of the lattice thermal conductivity that exhibits low values up to high temperatures. Additional information on the phonon spectrum of $Ba_8Ge_{43}\square_3$ is provided by analysis of the temperature dependence of the specific heat. Within the framework of the Debye model, Ba2 atoms in the 24-atom cages show Einstein-like modes. All these results revealed the complex transport behavior of $Ba_8Ge_{43}\square_3$ and constitute a first step toward a unified picture of the subtle relationship between its structural and electronic properties. The study on parent compound $Ba_8Ge_{43}\square_3$ may serve as a basis to investigate the concentration and distribution of vacancies along with the physical properties in the related ternary clathrates $Ba_8TM_xGe_{46-x-y}\square_y$ (*TM* = transition metals) which are considered as appropriate thermoelectric materials.

After the synthesis of single phase $Ba_8Ge_{43}\square_3$, $BaGe_5$ could be synthesized via decomposition of $Ba_8Ge_{43}\square_3$ at temperatures between 350 ºC and 520 ºC. The results of thermal analyses indicate that $BaGe_5$ is an equilibrium phase decomposing at a peritectoid temperature of around 535 ºC to Ba_6Ge_{25} and α-Ge. Upon annealing, $Ba_8Ge_{43}\square_3$ completely transforms into $BaGe_5$ and α-Ge at 520 ºC within 1 h and at 400 ºC within 12 h. Towards lower temperatures, the transformation takes place in longer time period *e.g.* at 350 ºC in 40 d. Elongation of $BaGe_5$ grains was observed after long time annealing process. Within the experimental accuracy, a homogeneity range of $BaGe_5$ could not be detected as samples obtained from different preparation conditions show similar compositions and

lattice parameters. $BaGe_5$ crystallizes in a new structure type, clathrate *oP*60 (space group *Pmna*, *Z* = 10). The crystal structure contains characteristic layers of dodecahedra Ge_{20}, which are condensed via common pentagons and hexagons. The layers are linked by $(3b)Ge^-$ anions, which alternatively occupy closely adjacent split positions. The Ba atoms are either located in the pentagon dodecahedra or they are assembled in channels or cavities. $BaGe_5$ structure type can be considered as intermediate between those of the clathrate *cP*124 Ba_6Ge_{25} and the clathrate-I $Ba_8Ge_{43}\square_3$: the infinite channels are reminiscent to those of Ba_6Ge_{25}, while the arrangement of pentagons and hexagons resembles the polyhedral cages in the clathrate-I $Ba_8Ge_{43}\square_3$. The Rietveld refinements of X-ray synchrotron data revealed no resolvable variations in the structural parameters depending on the preparation conditions. From PXRD and SAED measurements at room temperature, there is no hint for an ordering of $(3b)Ge^-$ anions. Variations in the microstructure and possibly the crystal structure on annealing have direct consequences on the transport properties for which significant differences arise for short-time annealing treatments. These differences are lessened by applying longer annealing times regardless of the annealing temperatures applied. Transport property measurements indicated a semiconducting behavior which is expected from the Zintl count $[Ba^{2+}]_{10}[(3b)Ge^-]_{20}[(4b)Ge^0]$ and electronic band structure calculations. Even though a low thermal conductivity emerges from the complex crystal structure, the high electrical resistivity values prevent to achieve high *ZT* values ($ZT_{max} \approx 0.2$ at 550 K). This might be overcome by ternary variants of this structure type thereby optimizing their thermoelectric efficiency.

Complete characterization of $Ba_8Ge_{43}\square_3$ and $BaGe_5$ allowed a detailed investigation of ternary clathrate $Ba_8Ni_x\square_yGe_{46-x-y}$ in which Ni can substitute the Ge atoms and/or fill the vacancies. Type-I clathrate with framework vacancies $Ba_8Ni_x\square_yGe_{46-x-y}$ constitutes two existence fields depending on Ni content: compounds with low Ni content, $0 < x \leq 1$, are considered as solution of Ni in the binary $Ba_8Ge_{43}\square_3$ and compounds with higher Ni content, $1 < x \leq 4.2$, crystallize in the space group $Pm\bar{3}n$ for which the chemical composition derives from a hypothetic compound "$Ba_8Ge_{42}\square_4$". The change in the Ni content is associated with the respective change in lattice parameters, but also confirmed by microprobe analyses. Compounds towards lower Ni content show a lower stability range ΔT, whereas compounds with high Ni content are stable at temperatures lower than 700 °C. Ni atoms in $Ba_8Ni_{0.6}Ge_{42.6}\square_{2.8}$ are found in 24*c* and/or 24*d* sites in which a decisive assessment is not possible due to similar X-ray scattering power of Ni and Ge atoms. Although XRD experiments do not provide any hint for the Ni site, total energy calculations suggest that it is energetically favorable to fill the vacancies at the 24*c* site rather than to replace the Ge atoms at the 24*d* site. Crystal structure of Bridgman-grown single crystal $Ba_8Ni_{3.5}Ge_{42.1}\square_{0.4}$ is characterized by an accumulation of all Ni atoms and all

vacancies at the 6*c* site leading to a distortion of the framework. The clathrate in the system Ba – Ni – Ge offers an opportunity to probe the evolution of the peculiar properties of the parent clathrate $Ba_8Ge_{43}\square_3$ upon substituting the Ge atoms or filling the vacancies with Ni atoms. Susceptibility measurements show a temperature independent diamagnetism for all investigated compositions. Thermopower data reveal a smooth evolution from a nearly-compensated semimetallic state for $Ba_8Ge_{43}\square_3$ towards a narrow-band-gap semiconducting state for $x = 4$. Variation from metal-like to semiconductor-like as well as a crossover from *n*- to *p*-type behavior is confirmed for the polycrystalline samples with nominal compositions $3.8 \leq x \leq 4.2$. The maximum *ZT* values for polycrystalline samples reach ≈ 0.2 at 500 and 650 K for $x = 2$ and 3.8, respectively. Single crystalline $Ba_8Ni_{3.5}Ge_{42.1}\square_{0.4}$ is an *n*-type metal with estimated $ZT \approx 0.21$ at 680 K which is slightly higher than that of the polycrystalline material ($ZT \approx 0.14$ at 680 K). The dependence of the thermopower on the charge carrier concentration suggests that there is further room for *ZT* improvement in type-I clathrates in this system.

Type-I clathrate $Ba_{8-\delta}Ni_x\square_ySi_{46-x-y}$ was synthesized and the homogeneity range was revealed by combined microprobe analyses and PXRD data. The homogeneity range of the clathrate-I phase $Ba_8Ni_x\square_ySi_{46-x-y}$ was determined to be $2.4 \leq x \leq 3.8$ and $0 \leq y \leq 0.9$ at 1000 °C. This experimental result is in agreement with the heat of formation calculations. Primary crystallization fields and isothermal section at 1000°C of the system $BaSi_2$ – NiSi – α-Si were established based on combined microstructure, thermal analysis and X-ray diffraction. Clathrate in this system crystallizes in the space group $Pm\bar{3}n$. Single crystal X-ray diffraction together with microprobe analyses indicate the presence of framework vacancies for clathrate compositions with higher Ni content which has been overlooked for many other Si-based clathrates. Within the homogeneity range, the lattice parameter decreases as the Ni content increases. The atomic interactions in the $Ba_8Ni_x\square_ySi_{46-x-y}$ system are studied within the ELI-ED approach revealing two-electron two-center type Si-Si and two-center banana-type Ni–Si bonds. Ni K-edge X-ray absorption spectroscopy measurements indicate electronic state close to elemental Ni in clathrate compositions which is in agreement with magnetic susceptibility data signifying that the Ni atoms have a non-magnetic state in clathrate samples. Low-temperature electrical resistivity measurements show the samples with compositions $Ba_{7.9}Ni_{1.4}Si_{44.6}$ and $Ba_{7.9}Ni_{1.6}Si_{44.4}$ are superconducting with T_c at around 6.0 K and 5.5 K, respectively. First-principles calculations revealed a non-rigid variation in the electronic band structure and strong variations in $N(E_F)$ with Ni content. These theoretical results are in line with experimental findings. The thermopower data indicate that both charge carriers, holes and electrons, are involved in the electrical conduction. All these results highlight the sensitivity of the electronic properties to the Ni content suggesting that these properties may not be confined

to the Ni-substitution but may be observed in other ternary Si-based type-I clathrates. The metallic nature of clathrate samples prevents achieving high *ZT* values in the temperature range investigated. Further adjustment of the carrier concentration through another partial substitution such as Ga or Au may be worthwhile to consider and may help further assess the thermoelectric potential of Si-based type-I clathrates.

During the investigations of the Ba – Ni – Si system, it was realized that the phase analysis of Ba_3Si_4 was not performed and the Si–Si bond lengths in the Si_4^{6-} anion was reported unexpectedly short and different (2.29 Å – 2.34 Å).[25] Hence, the Ba_3Si_4 phase was reinvestigated and synthesized from the elements as a single phase. No homogeneity range has been found. Ba_3Si_4 decomposes peritectically at 1034(5) °C to $BaSi_2$ and melt. The butterfly-shaped Si_4^{6-} Zintl anion in the crystal structure of Ba_3Si_4 (space group $P4_2/mnm$) shows only slightly different Si–Si bond lengths of d(Si–Si) = 2.4183(6) Å (1×) and 2.4254(3) Å (4×) and resolved the apparent discrepancy with the already published results. The compound is diamagnetic and show characteristic of a bad metal in terms of electrical transport. The temperature dependence of the isotropic signal shift and the spin-lattice relaxation times in ^{29}Si NMR confirms the metallic behavior. The experimental results are in accordance with the calculated electronic band structure, which indicates a metal with a low density of states at the Fermi level. Topological analysis of the ELF yields two bond attractors which are off the direct connection line between the Si atoms and three lone-pair attractors in the valence region. The reaction of solid Ba_3Si_4 with gaseous HCl led to the oxidation of the Si_4^{6-} Zintl anion and yielded nanoporous silicon.

Single phase polycrystalline materials as well as single crystals of chalcopyrites $ZnSiP_2$ and $CuAlS_2$ were prepared to make static charge density analysis as well as to investigate charge distribution changes by external electric field. Despite the fact that optical microscopy inspection of the specimens indicates in most cases homogenous appearance, the data quality of the selected crystals was not satisfactory to perform experimental charge density analysis. Rather wide variation of crystal growth conditions did not provide any significant improvements in crystal quality of both $ZnSiP_2$ and $CuAlS_2$. ^{31}P as well as ^{29}Si NMR experiments did not reveal any hint towards local disorder which might be realized due to mixed occupancy of Zn and Si sites having similar local environments. Clearly further analysis of the crystal structure as well as micro structure is needed even more as such unusual behaviors seems not uncommon with quite “simple” compounds. Along this line, single crystal X-ray analyses at low temperatures as well as HRTEM analyses are on progress to unveil the aspects regarding to insufficient crystal qualities of the investigated chalcopyrites.

Chapter 11

Appendix – Figures

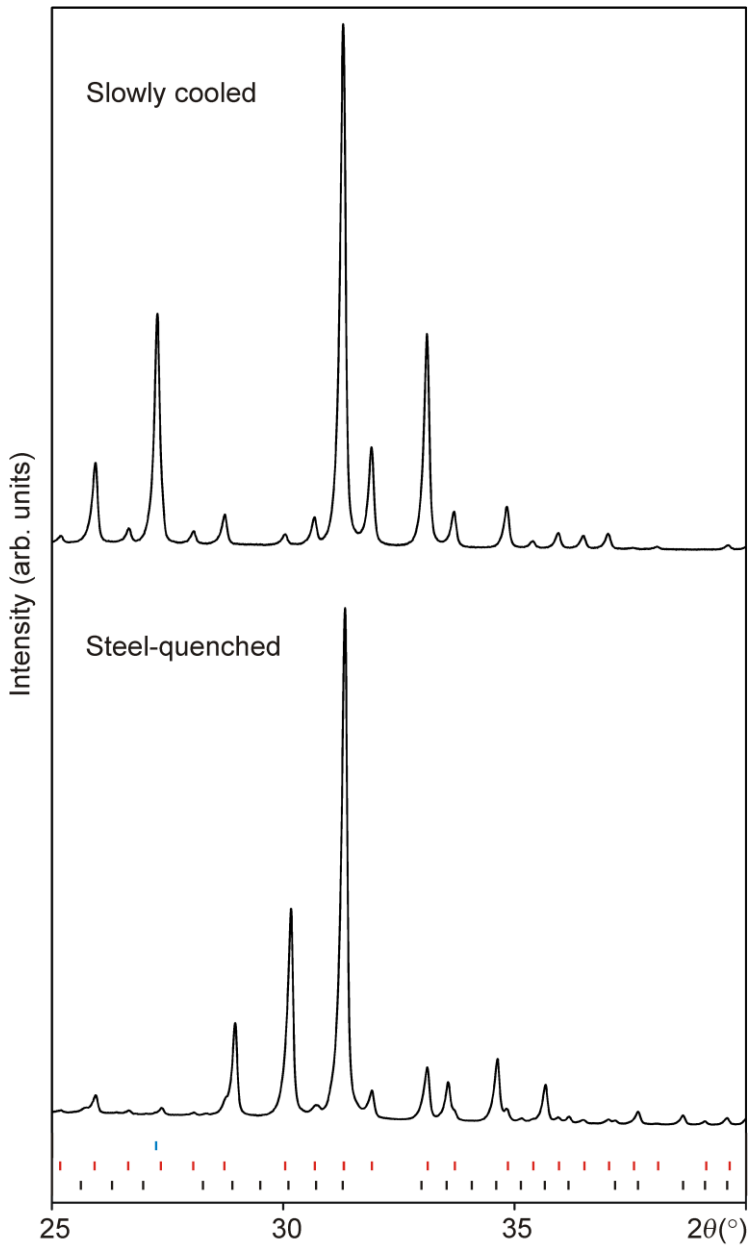

Figure 11.1: PXRD patterns of $Ba_{16.67}Ge_{83.33}$ ($BaGe_5$) after steel-quenching in Ar atmosphere (**bottom**) and after slowly cooling (12 h) to room temperature (**top**) (Cu-$K\alpha_1$ radiation). The ticks mark the calculated reflection positions of $Ba_8Ge_{43}\square_3$ (black), Ba_6Ge_{25} (red), and α-Ge (blue). By slow cooling, formation of only Ba_6Ge_{25} and α-Ge is observed, whereas after steel-quenching the sample consists of $Ba_8Ge_{43}\square_3$ and Ba_6Ge_{25}.

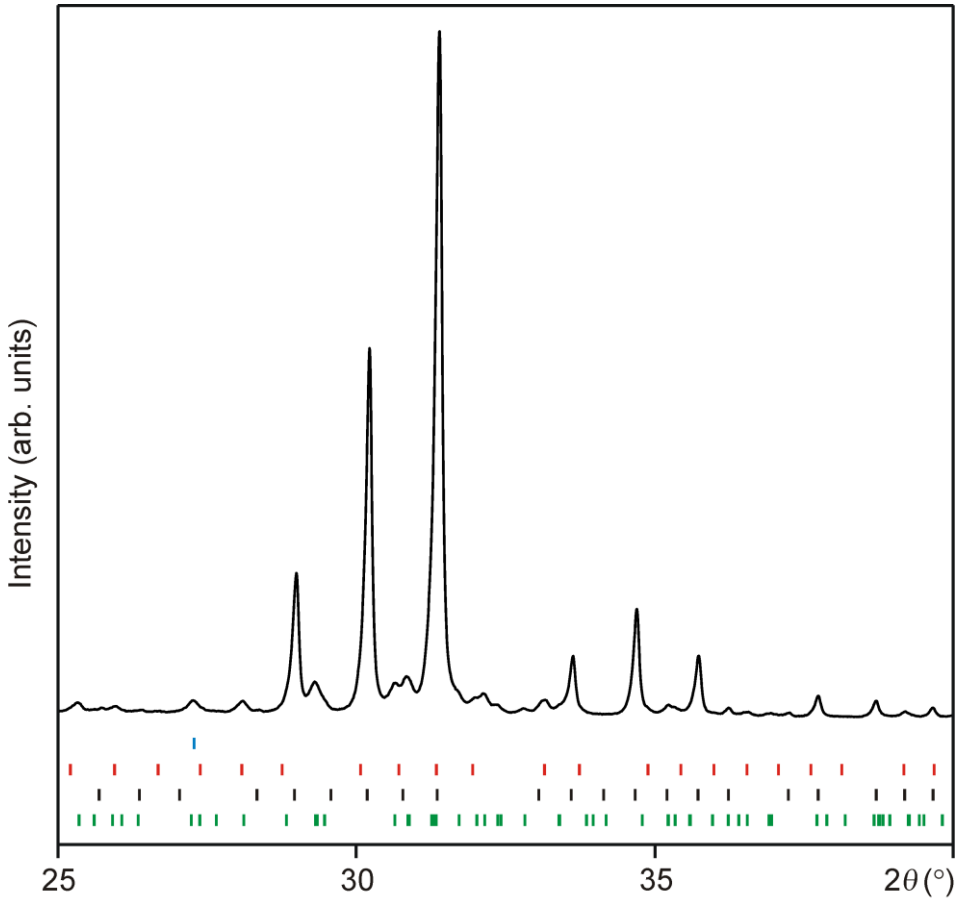

Figure 11.2: PXRD pattern of the sample $Ba_{16.67}Ge_{83.33}$ ($BaGe_5$) after cooling the stoichiometric melt in 2-3 min to room temperature (Cu-$K\alpha_1$ radiation). The ticks mark the calculated reflection positions of $BaGe_5$ (green), $Ba_8Ge_{43}\square_3$ (black), Ba_6Ge_{25} (red), and α-Ge (blue). In this sample, $BaGe_5$ presents besides $Ba_8Ge_{43}\square_3$, Ba_6Ge_{25} and α-Ge.

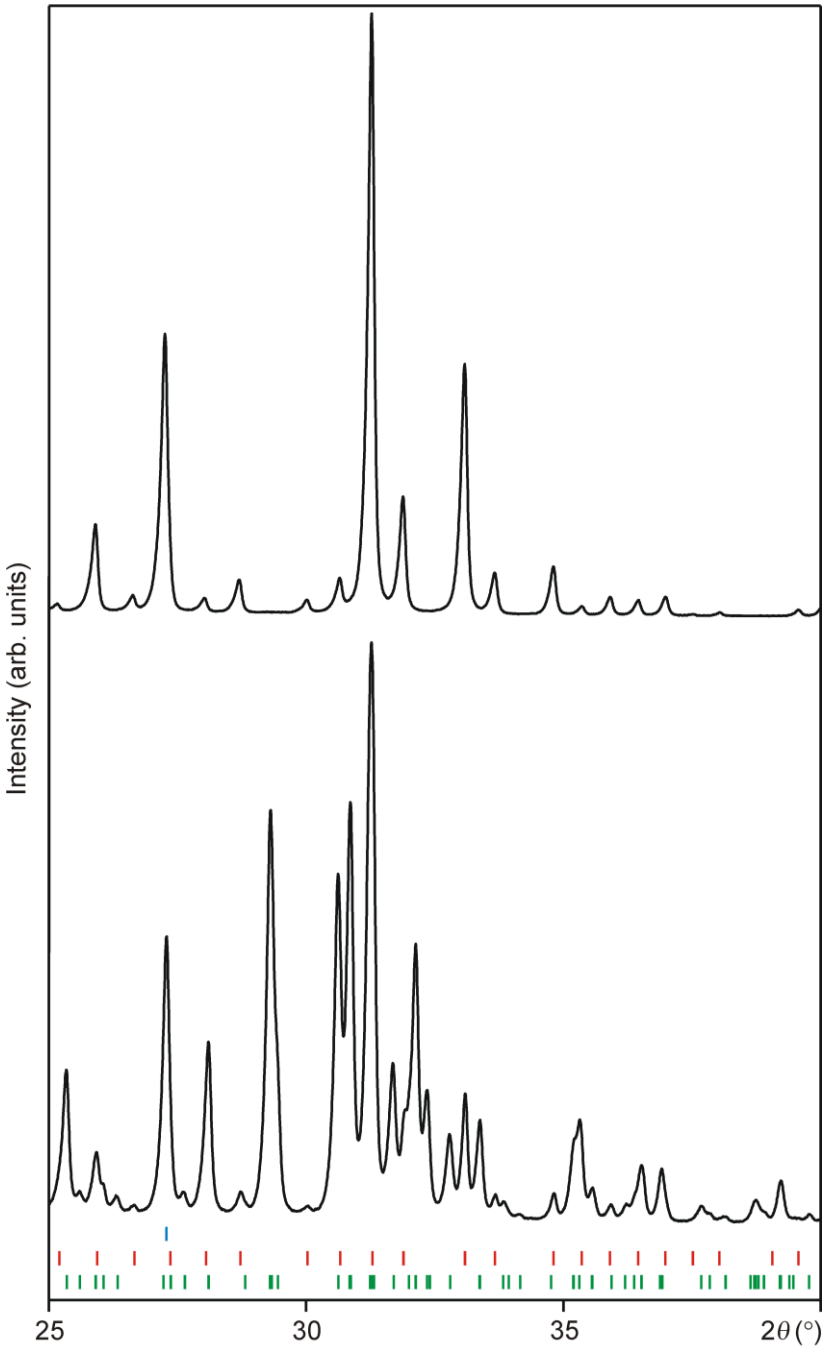

Figure 11.3: PXRD patterns of the sample $BaGe_5$ after annealing for 1 week at 575 °C (**top**) and 550 °C (**bottom**) (Cu-$K\alpha_1$ radiation). The ticks mark the calculated reflection positions of $BaGe_5$ (green), Ba_6Ge_{25} (red), and α-Ge (blue). Initial sample partially decomposed after heat treatment at 550 °C to α-Ge and Ba_6Ge_{25}. A complete decomposition to Ba_6Ge_{25}, and α-Ge was observed within 1 week at 575 °C.

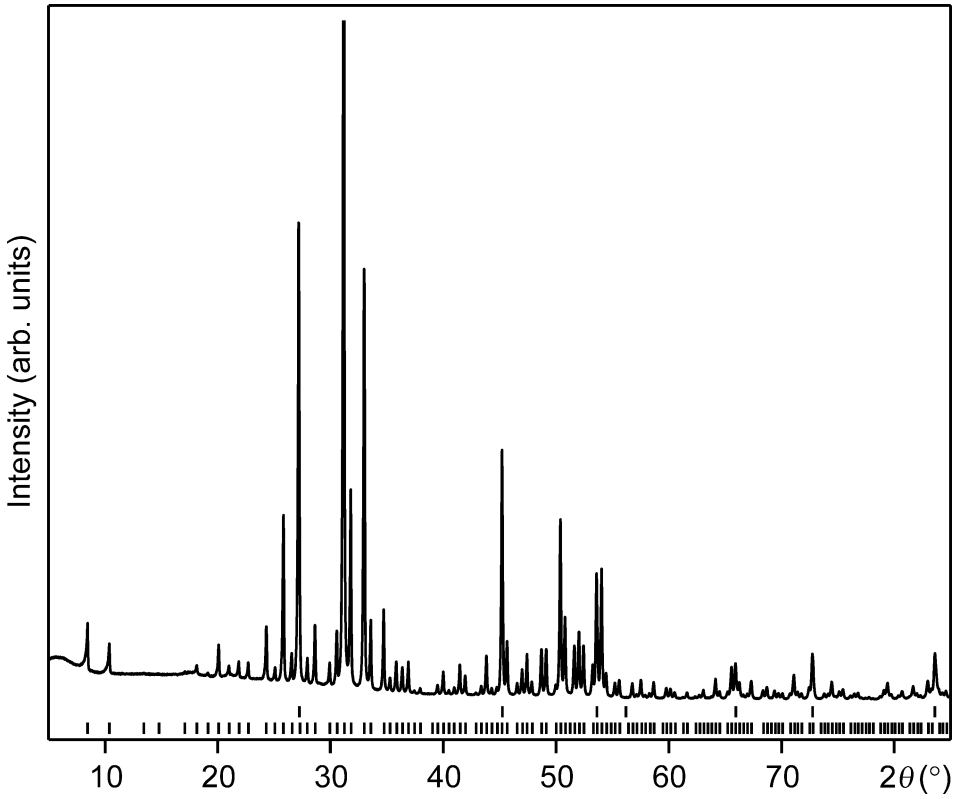

Figure 11.4: PXRD pattern of the $BaGe_5$ sample after thermal analysis with DSC (dT/dt = 5 ºC /min, Cu-$K\alpha_1$ radiation). Upper and lower ticks mark the calculated reflection positions of α-Ge and Ba_6Ge_{25}, respectively. The sample decomposes after heat treatment to α-Ge and Ba_6Ge_{25}.

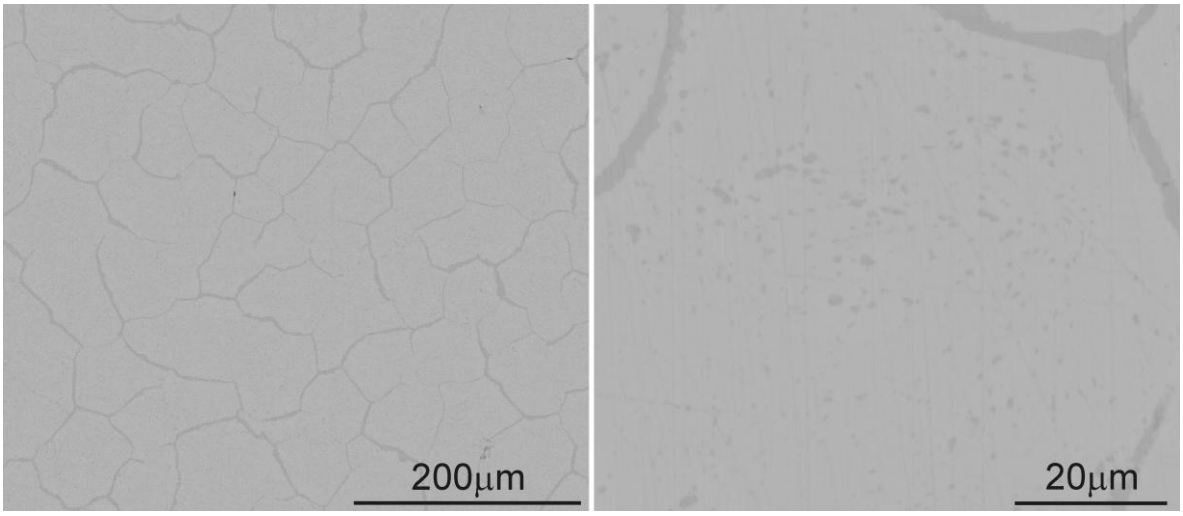

Figure 11.5: SEM images (BSE contrast) of the sample obtained via decomposition of $Ba_8Ge_{43}\square_3$ at 550 °C in 1 week ($BaGe_5$ is shown in light grey areas and α-Ge in dark grey areas). α-Ge precipitates at the grain boundaries and in point-like morphology within the grains of $BaGe_5$ at this temperature.

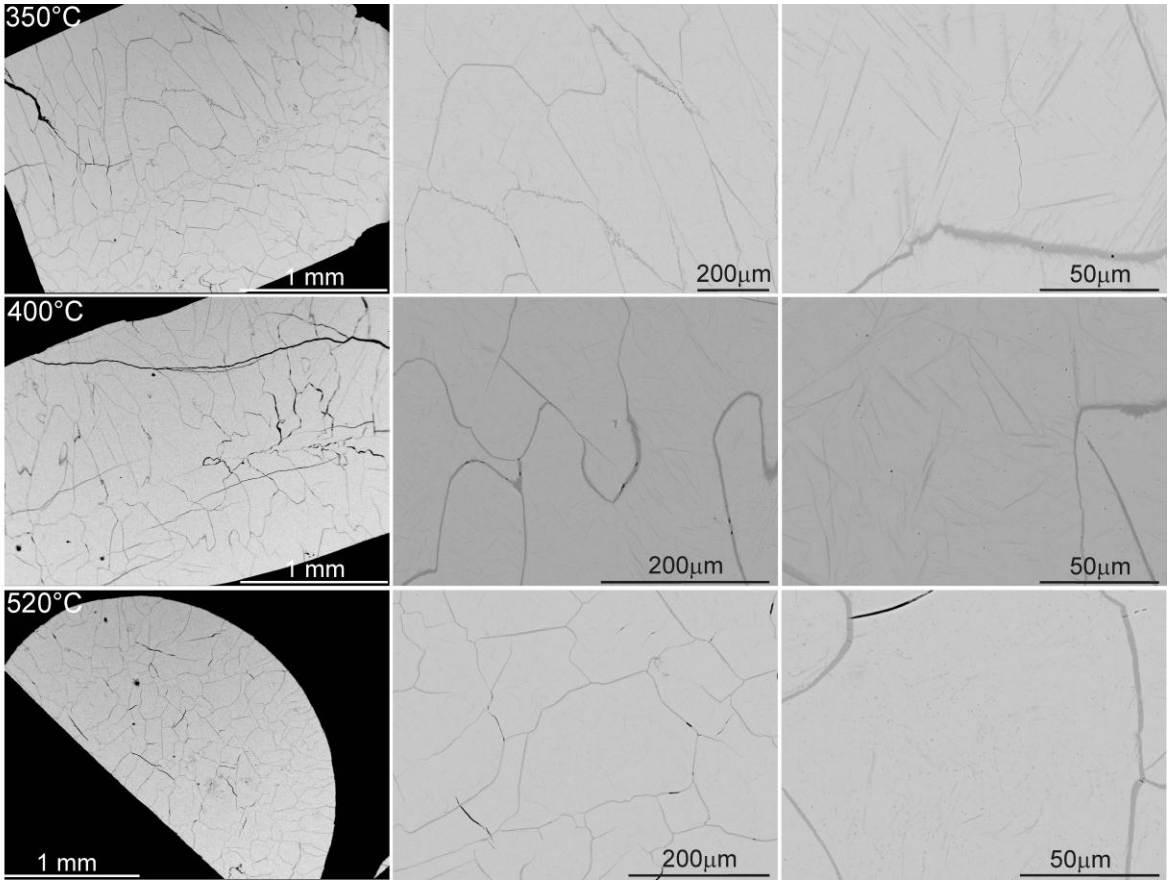

Figure 11.6: SEM images (BSE contrast) of the samples obtained via decomposition of $Ba_8Ge_{43}\square_3$ at 350 ºC in 40 d (**top**), at 400 ºC in 30 d (**middle**) and at 520 °C in 30 d (**bottom**). The figures show formation of large $BaGe_5$ grains (light grey areas) and the precipitation of α-Ge within and at the boundaries of $BaGe_5$ grains (dark grey areas).

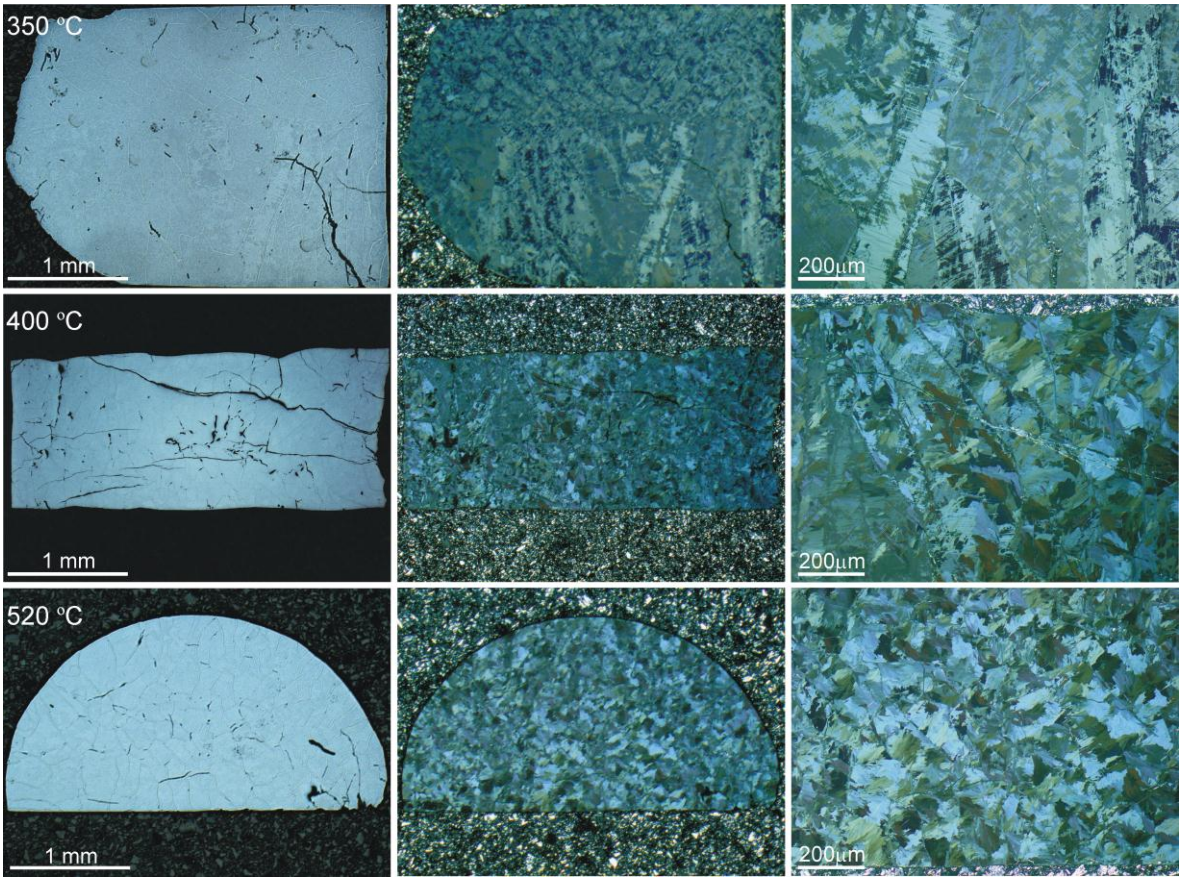

Figure 11.7: Bright field (**left**) and polarized light (**middle** and **right**) images of samples formed via decomposition of $Ba_8Ge_{43}\square_3$ at 350 ºC in 40 d (**top**), at 400 ºC in 30 d (**middle**) and at 520 ºC in 30 d (**bottom**).

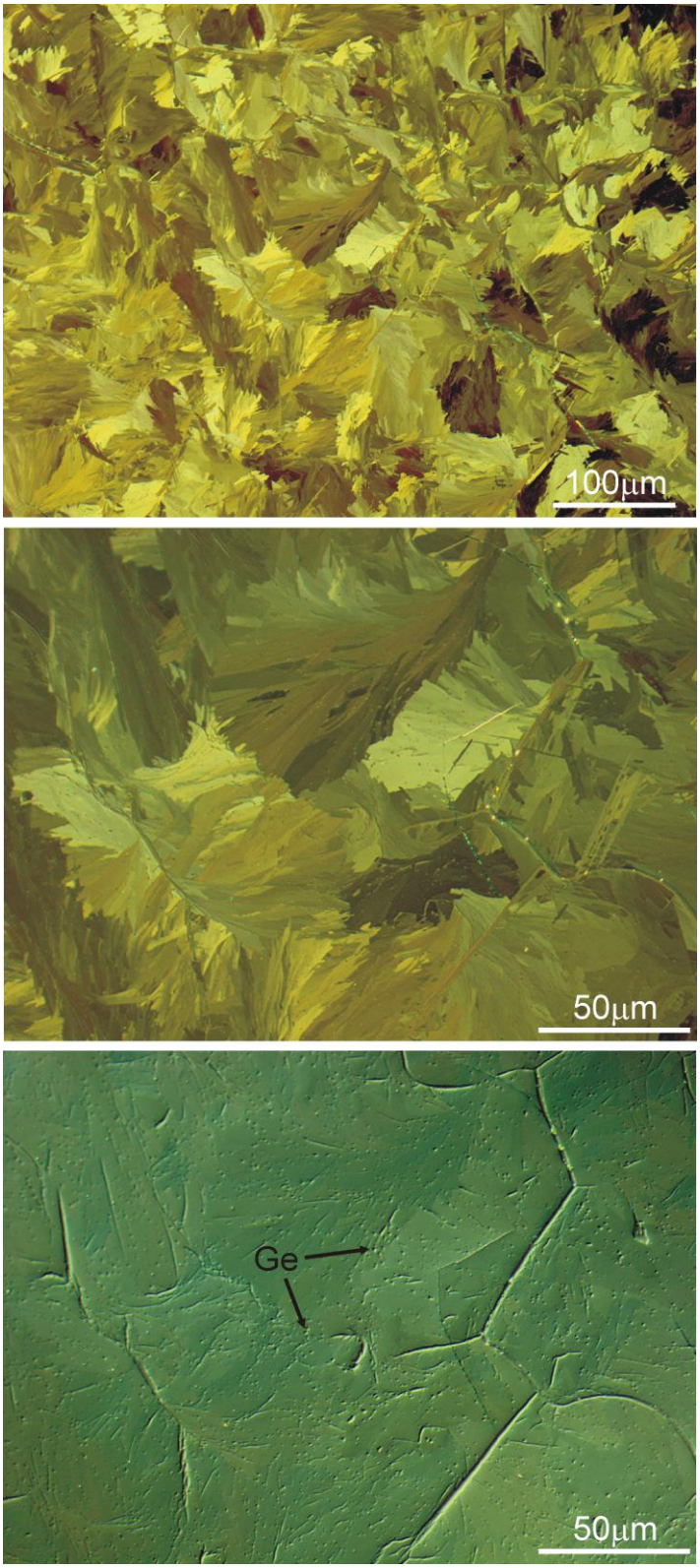

Figure 11.8: After annealing $Ba_8Ge_{43}\square_3$ at 520 °C for 10 d, a completely transformed microstructure containing mostly $BaGe_5$ phase and some amounts of α-Ge appears in polarised light microscope like paint brush painting (**top** and **middle**). Precipitation of point-like a-Ge particles is visible from the bright field image (**bottom**).

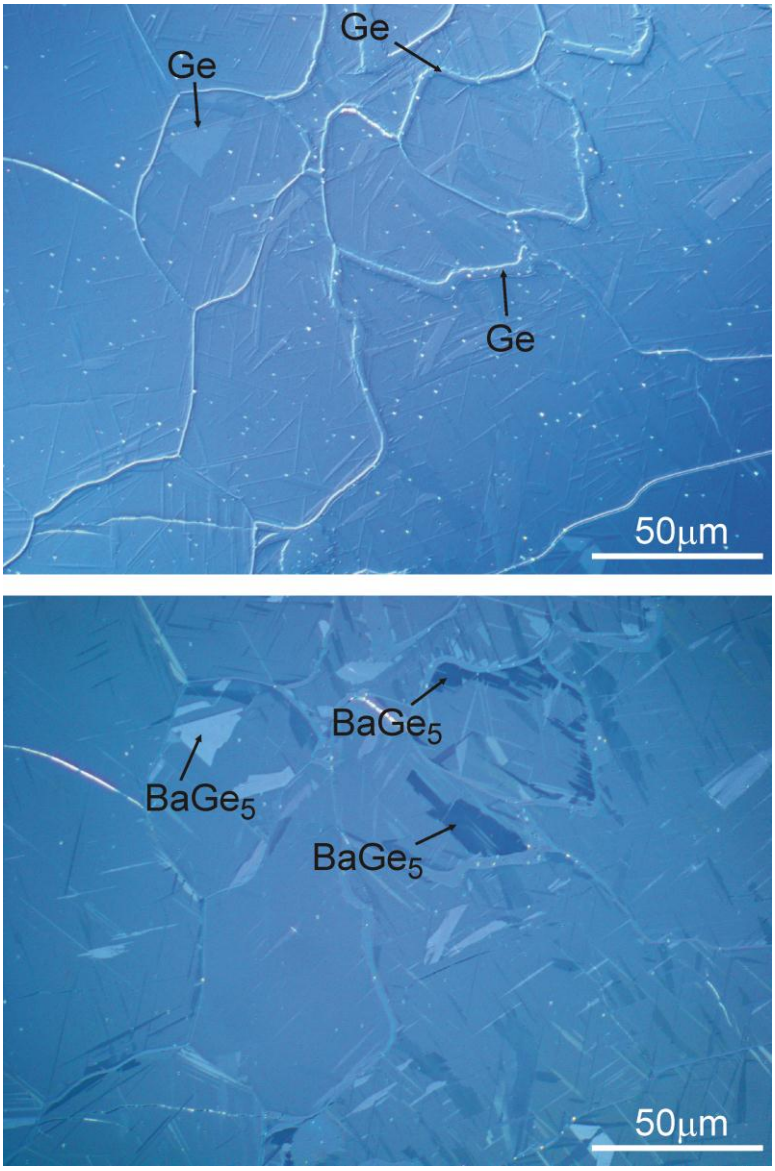

Figure 11.9: The bright field (**top**) and the polarized light (**bottom**) microscopy images of the sample obtained after annealing $Ba_8Ge_{43}\square_3$ at 400 °C for 1.5 h. The polarized light image shows that $BaGe_5$ grains grow at the surfaces of α-Ge precipitates.

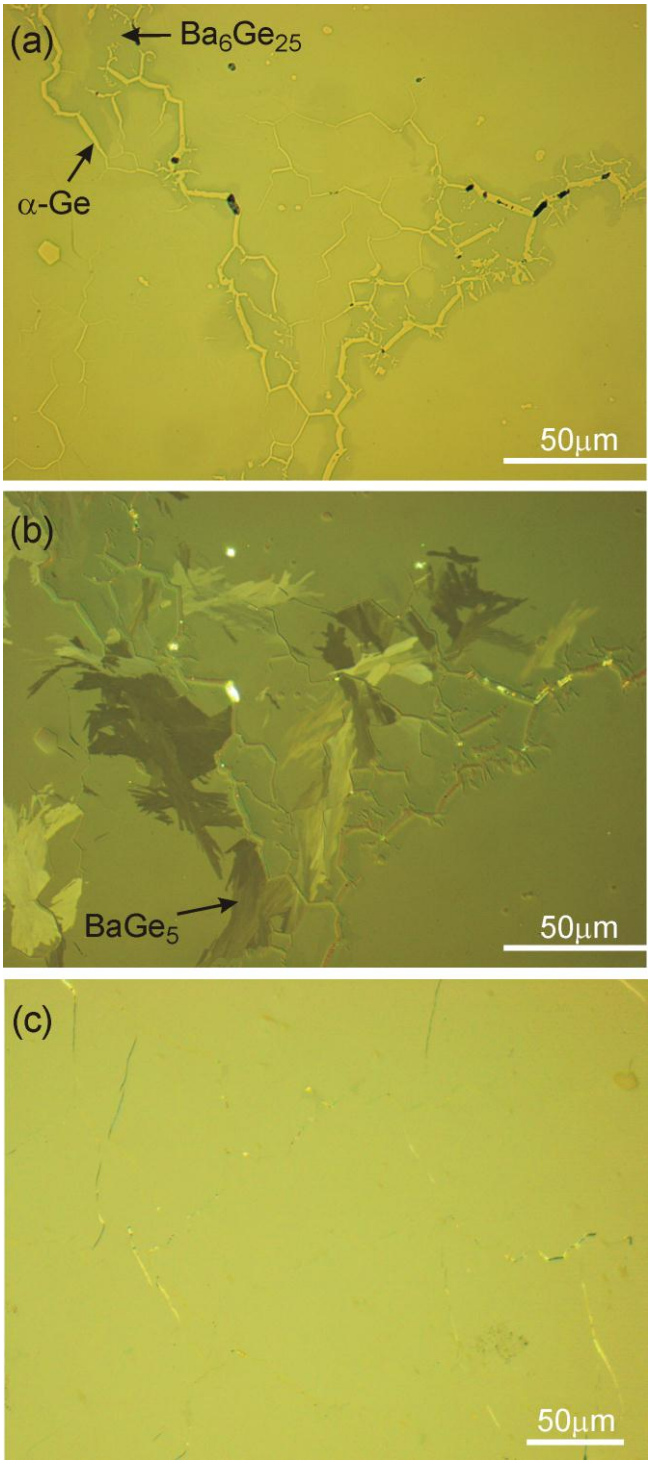

Figure 11.10: The microstructures of $BaGe_5$ sample after annealing at 790 °C for 3 d (**a**: bright field, **b**: polarized light image) gives hint about the nucleation of $BaGe_5$ grains. After further annealing at 790 °C for 2 weeks, $Ba_8Ge_{43}\square_3$ phase was obtained without secondary phases as $BaGe_5$, Ba_6Ge_{25} and α-Ge (**c**).

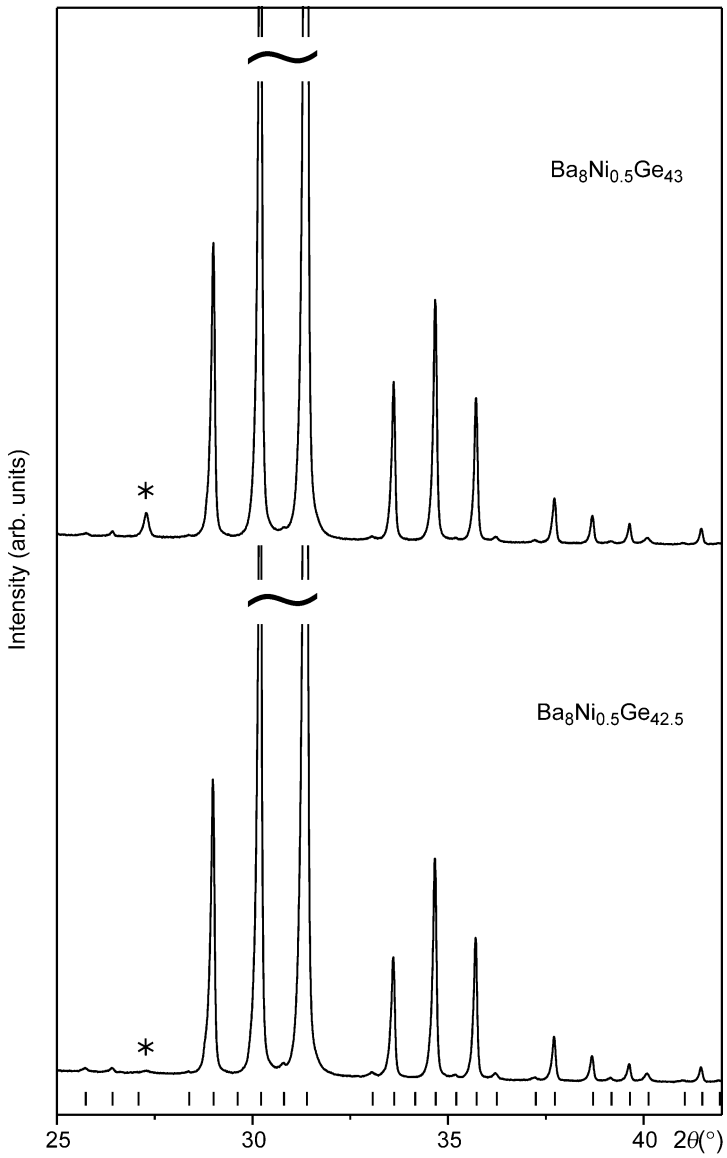

Figure 11.11: PXRD patterns of the samples with nominal compositions $Ba_8Ni_{0.5}Ge_{42.5}$ (**bottom**) and $Ba_8Ni_{0.5}Ge_{43}$ (**top**) (Cu-$K\alpha_1$ radiation). The reflection from α-Ge is shown with asterisk. The ticks mark the calculated reflection positions based on our single crystal data.

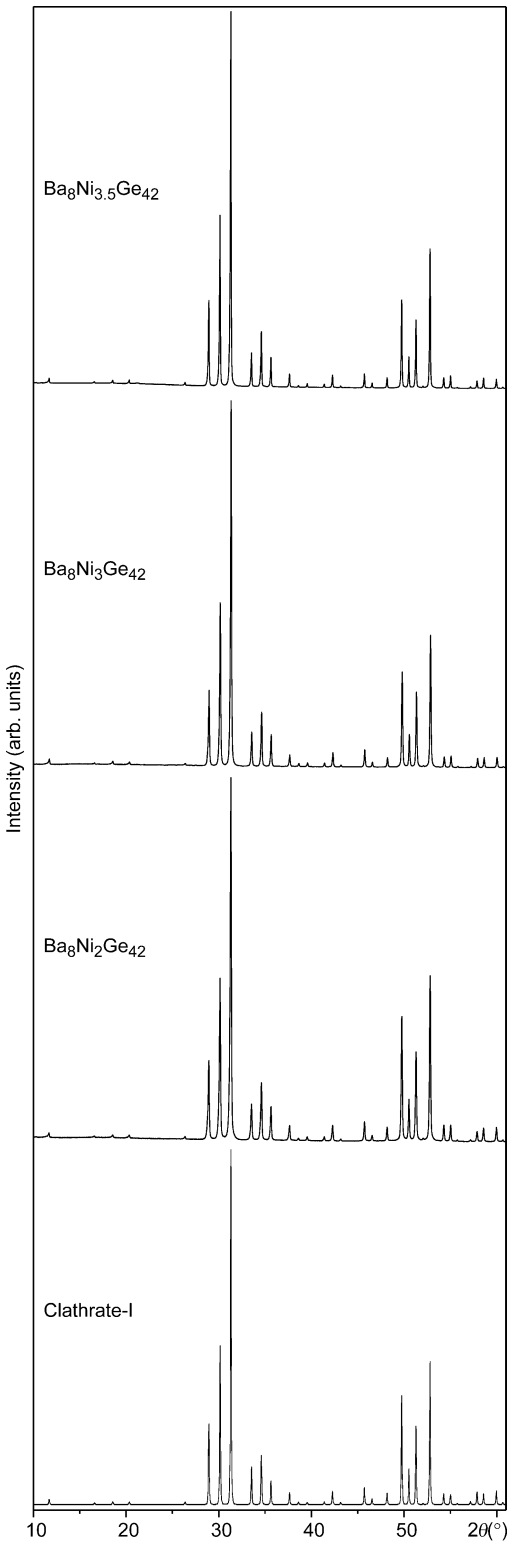

Figure 11.12: Experimental PXRD patterns of clathrate-I compounds with nominal compositions $Ba_8Ni_2Ge_{42}$, $Ba_8Ni_3Ge_{42}$ and $Ba_8Ni_{3.5}Ge_{42}$ (Cu-$K\alpha_1$ radiation). The theoretical powder pattern of this phase is shown at the bottom which is calculated based on the single crystal investigation.

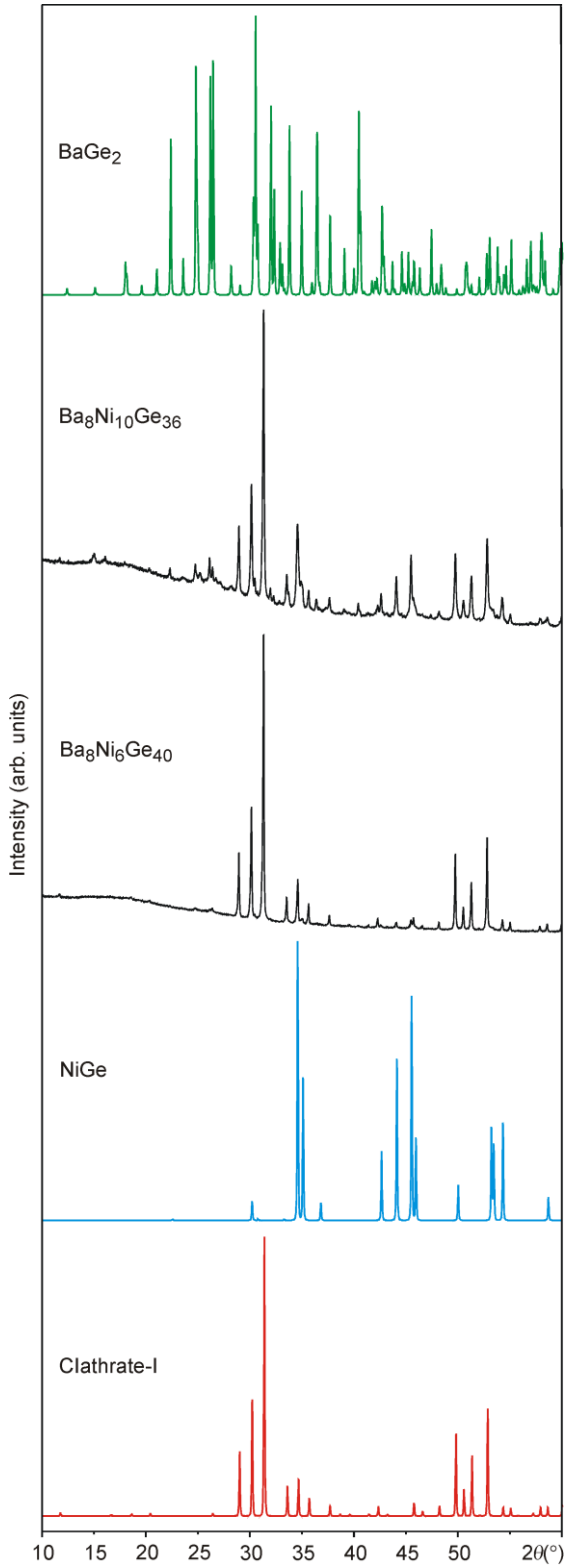

Figure 11.13: PXRD patterns of samples with nominal compositions $Ba_8Ni_6Ge_{40}$ and $Ba_8Ni_{10}Ge_{36}$ after annealing at 700 °C for 4 days (Cu-$K\alpha_1$ radiation). Theoretical powder patterns of clathrate-I phase, NiGe and $BaGe_2$ are shown. Samples prepared with high Ni content show increasing amount of NiGe and $BaGe_2$ as secondary phases.

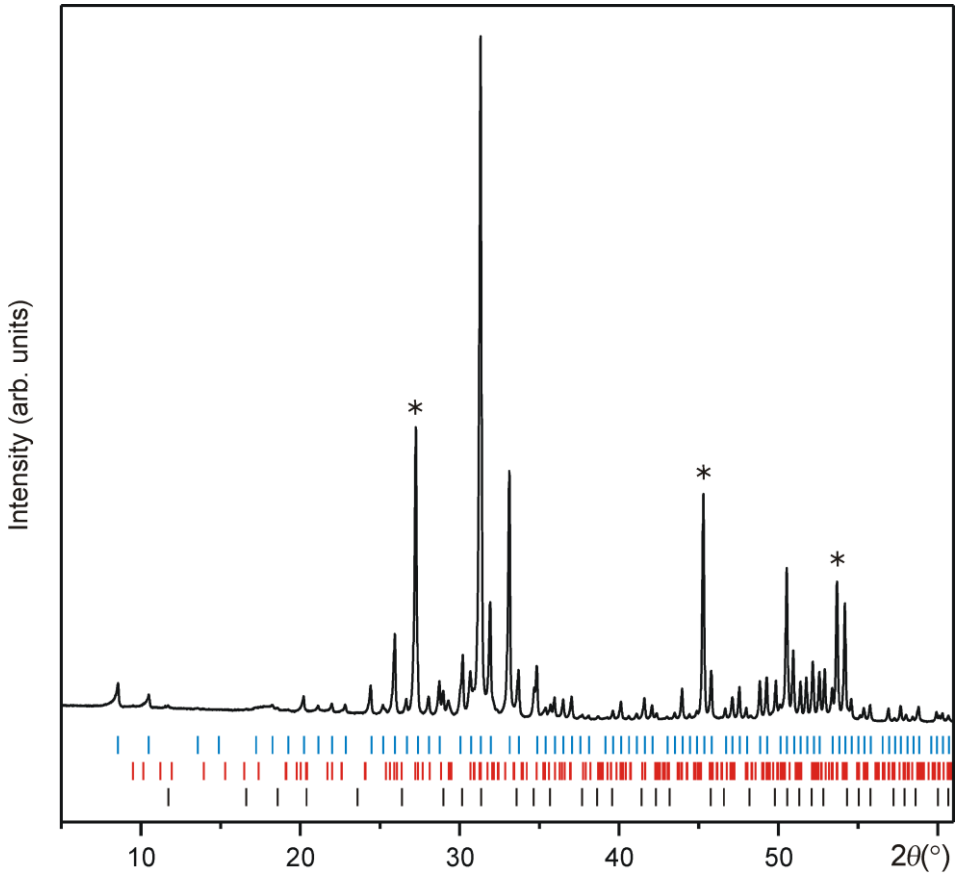

Figure 11.14: PXRD pattern (Cu-$K\alpha_1$ radiation) of the sample with nominal composition $Ba_8Ni_{0.5}Ge_{42.5}$ crystallized from the melt with 5 K/min cooling rate (DSC). The end product consists of mainly Ba_6Ge_{25} (blue ticks) and α-Ge (marked with asterisk) but clathrate-I phase (black ticks) and $BaGe_5$ (red ticks) were also observed.

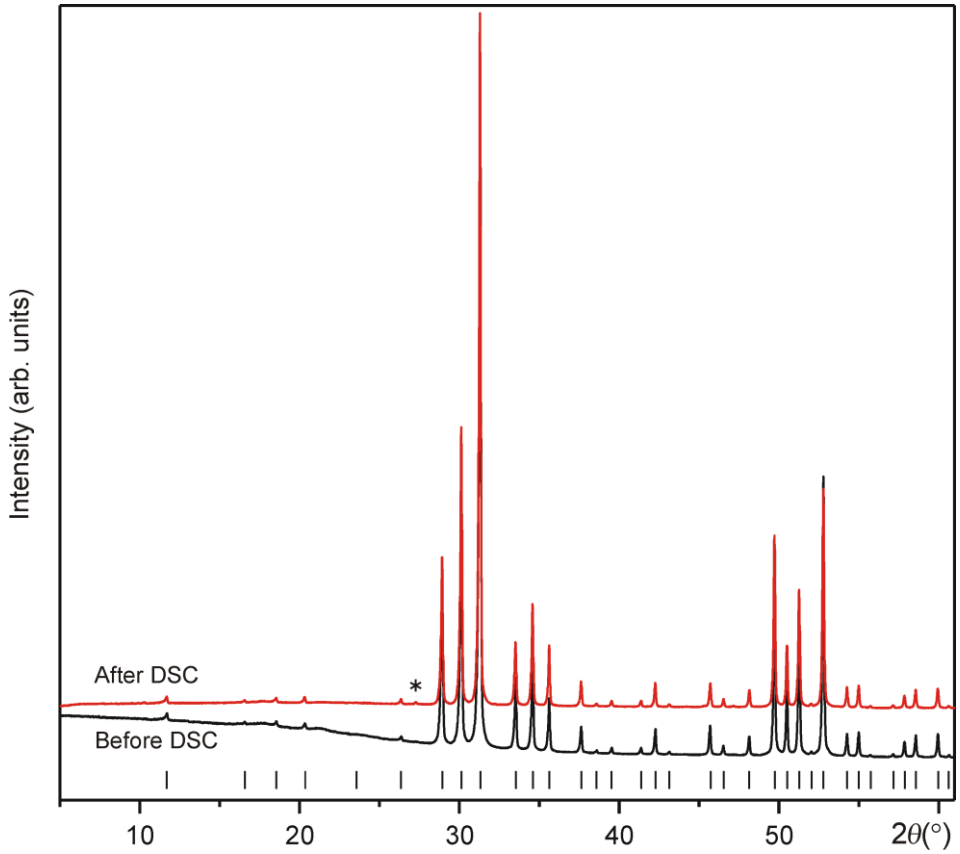

Figure 11.15: PXRD pattern of the sample with nominal composition $Ba_8Ni_{3.5}Ge_{42}$ before (black) and after DSC experiment (red; λ = Cu-$K\alpha_1$). The end product is almost single phase (except for very small inclusion of α-Ge as marked with asterisk) clathrate-I compound.

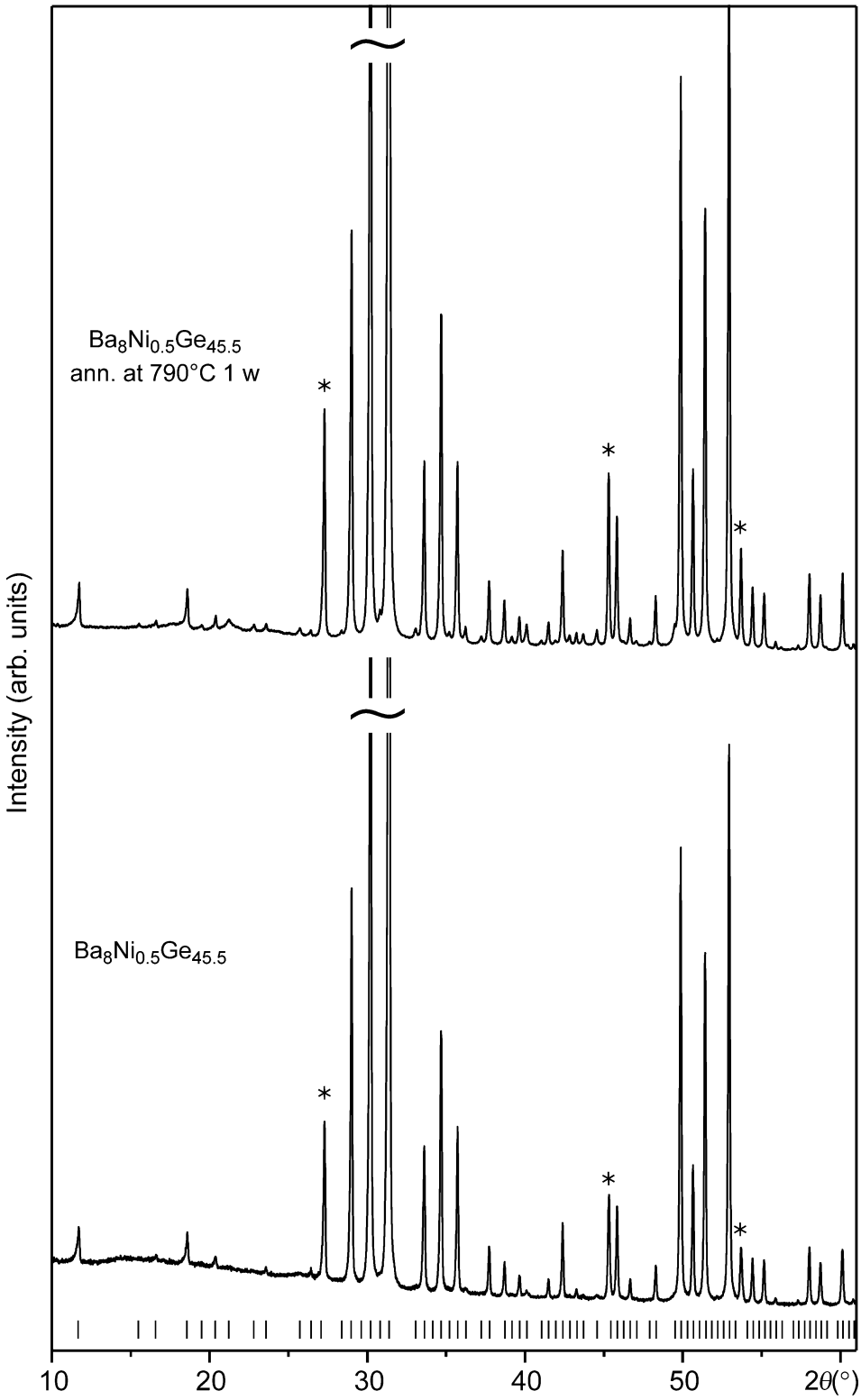

Figure 11.16: PXRD patterns of samples with the nominal composition $Ba_8Ni_{0.5}Ge_{45.5}$ after steel-quenching (**bottom**) and after annealing at 790 °C for 1 week (**top**; Cu-$K\alpha_1$ radiation). The reflections due to α-Ge impurities are marked with asterisks.

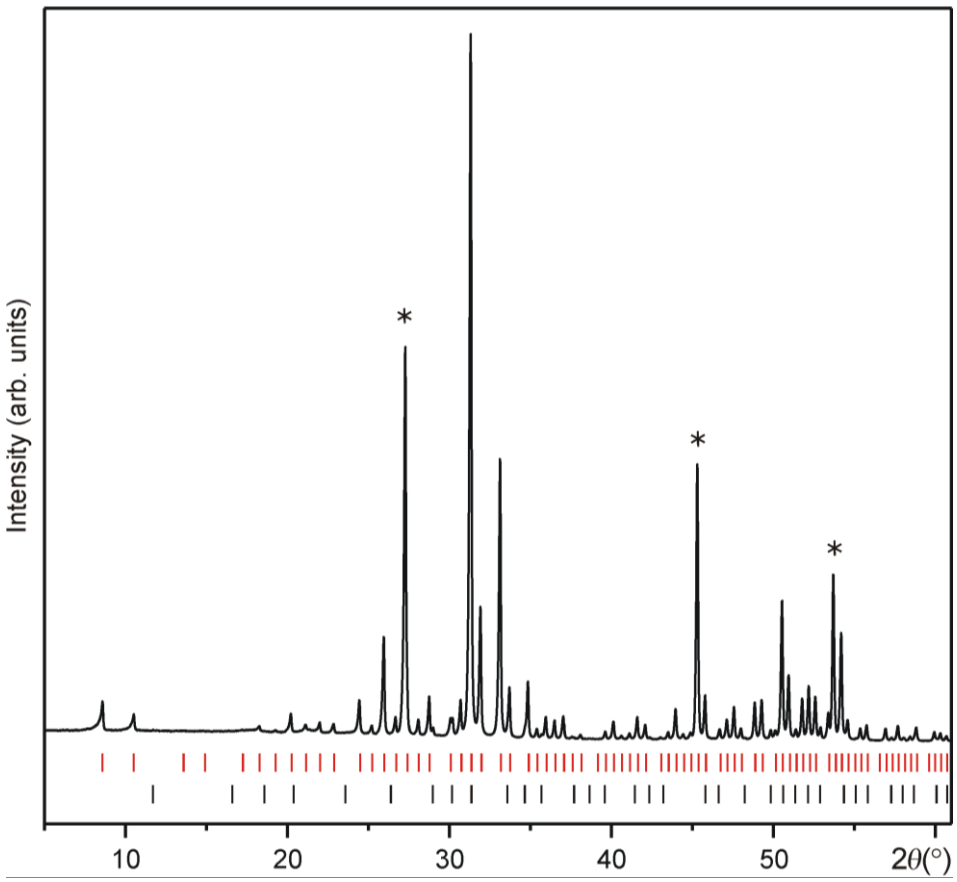

Figure 11.17: PXRD pattern of the sample with nominal composition $Ba_8Ni_{0.5}Ge_{45.5}$ after annealing at 700 °C for 1 week (Cu-$K\alpha_1$ radiation). The ticks mark the calculated reflection positions of clathrate-I phase (black) and Ba_6Ge_{25} (red). The reflections of α-Ge are marked with asterisks.

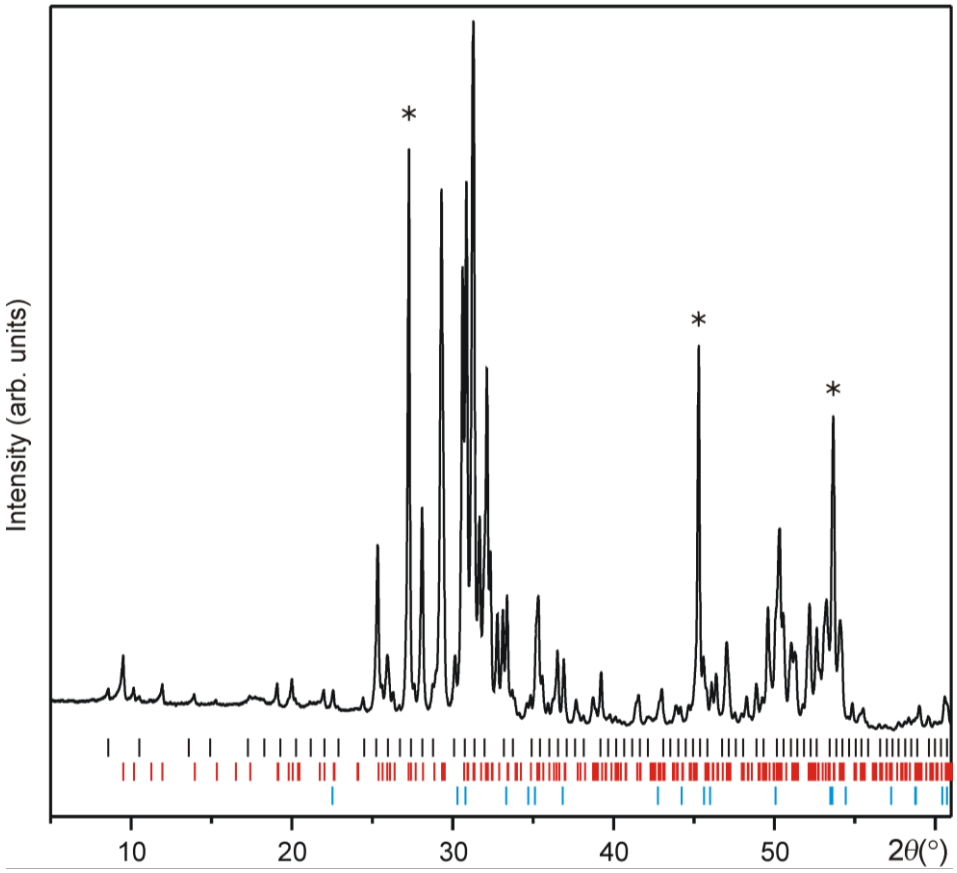

Figure 11.18: PXRD pattern of the sample with nominal composition $Ba_8Ni_{0.5}Ge_{45.5}$ after annealing at 500 °C for 1 week (Cu-$K\alpha_1$ radiation). The ticks mark the calculated reflection positions of Ba_6Ge_{25} (black), $BaGe_5$ (red) and NiGe (blue). The reflections of α-Ge are indicated with asterisks.

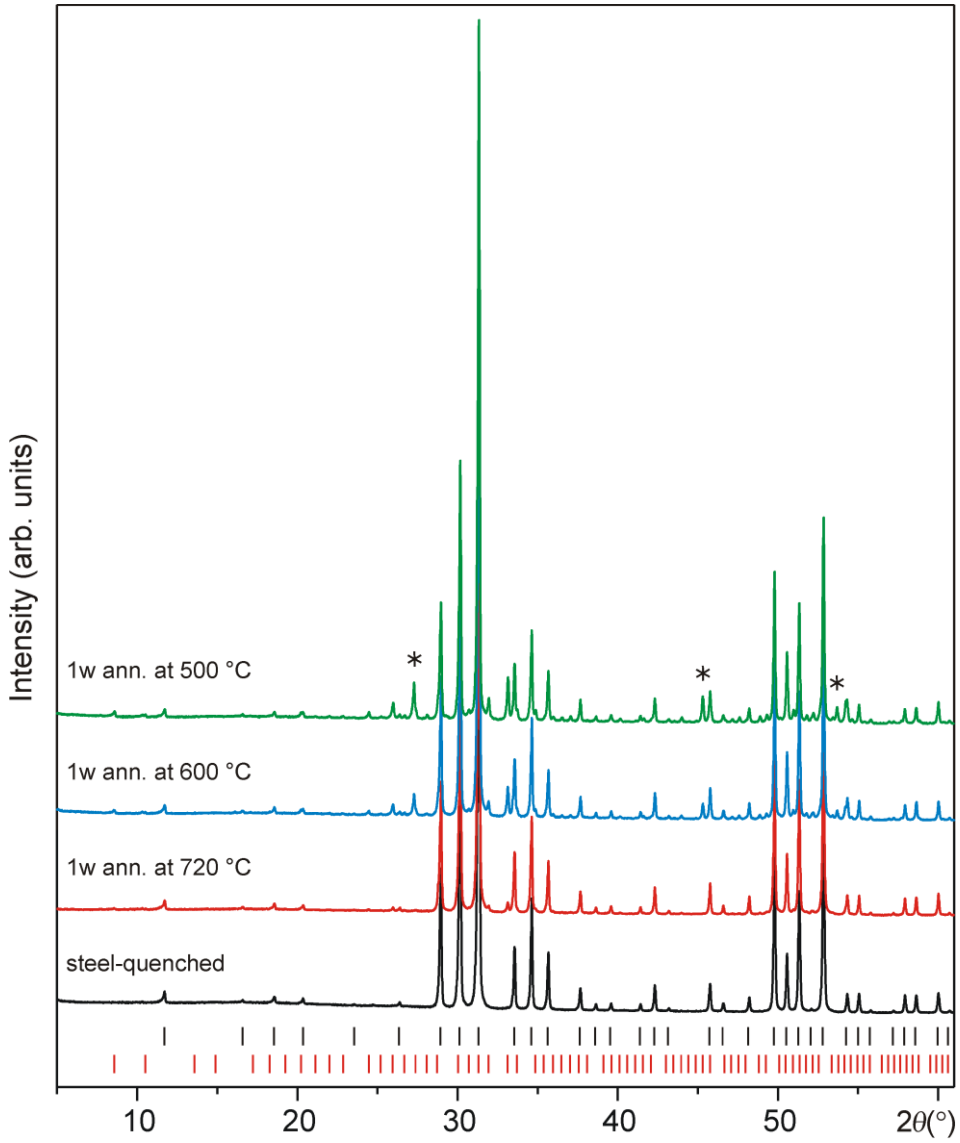

Figure 11.19: PXRD patterns of the samples with nominal composition $Ba_8Ni_2Ge_{42}$ after steel-quenching (black), and after annealing at 720 °C (red), 600 °C (blue) and 500 °C (green) for 1 week (Cu-$K\alpha_1$ radiation). The ticks mark the calculated reflection positions of clathrate phase and Ba_6Ge_{25} (red). The reflections of α-Ge are marked with asterisks.

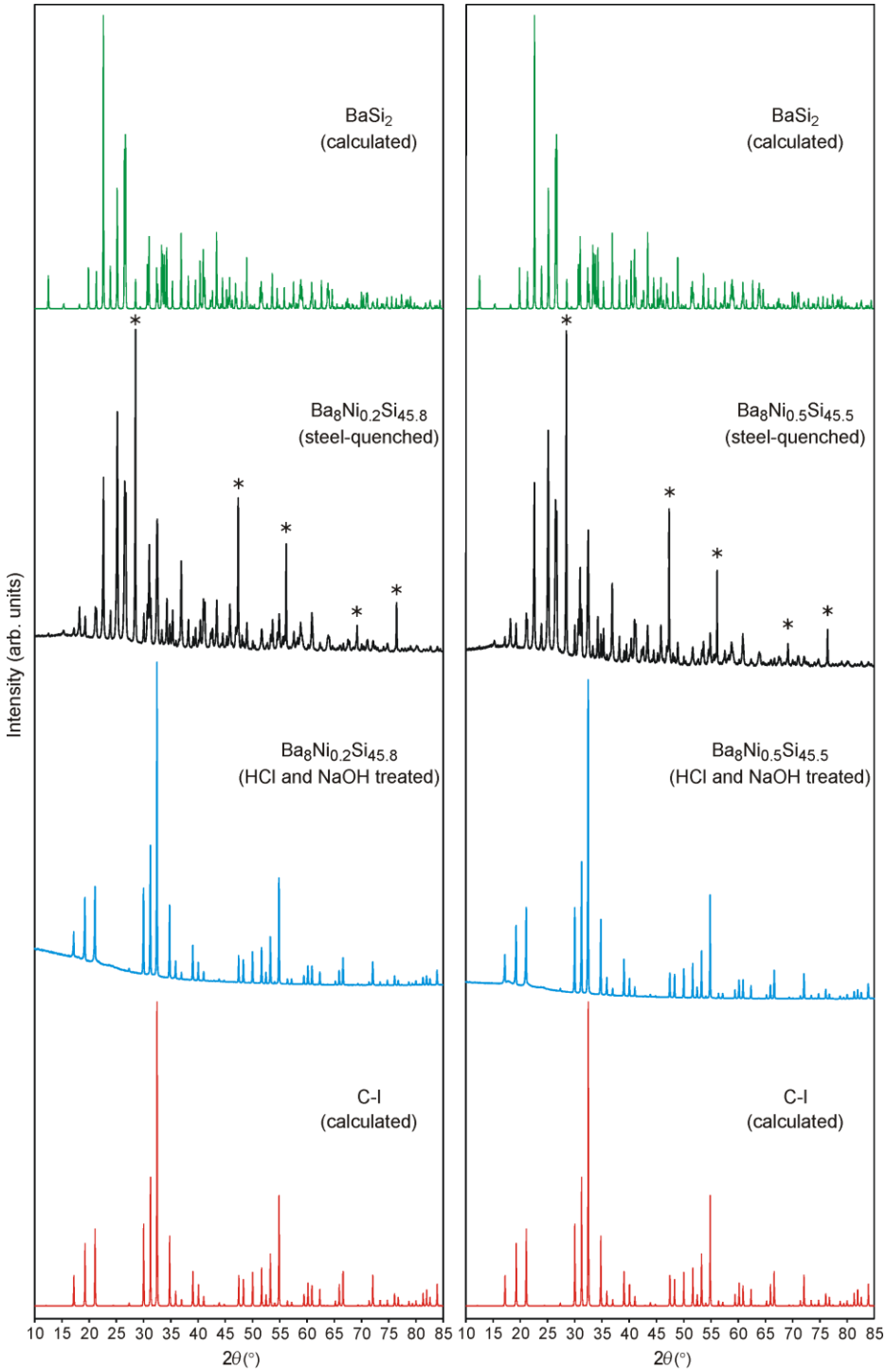

Figure 11.20: PXRD patterns (Cu-$K\alpha_1$ radiation) of the samples with nominal compositions $Ba_8Ni_{0.2}Si_{45.8}$ (left) and $Ba_8Ni_{0.5}Si_{45.5}$ (right) after steel-quenching (black) and after treatment with dilute HCl and NaOH (blue). Theoretical patterns of clathrate-I ($Ba_8Ni_{3.7}Si_{41.4}\square_{0.9}$) and $BaSi_2$ are shown for comparison and α-Si reflections are indicated with asterisks. After treatment with HCl and then with NaOH, single phase clathrates were obtained.

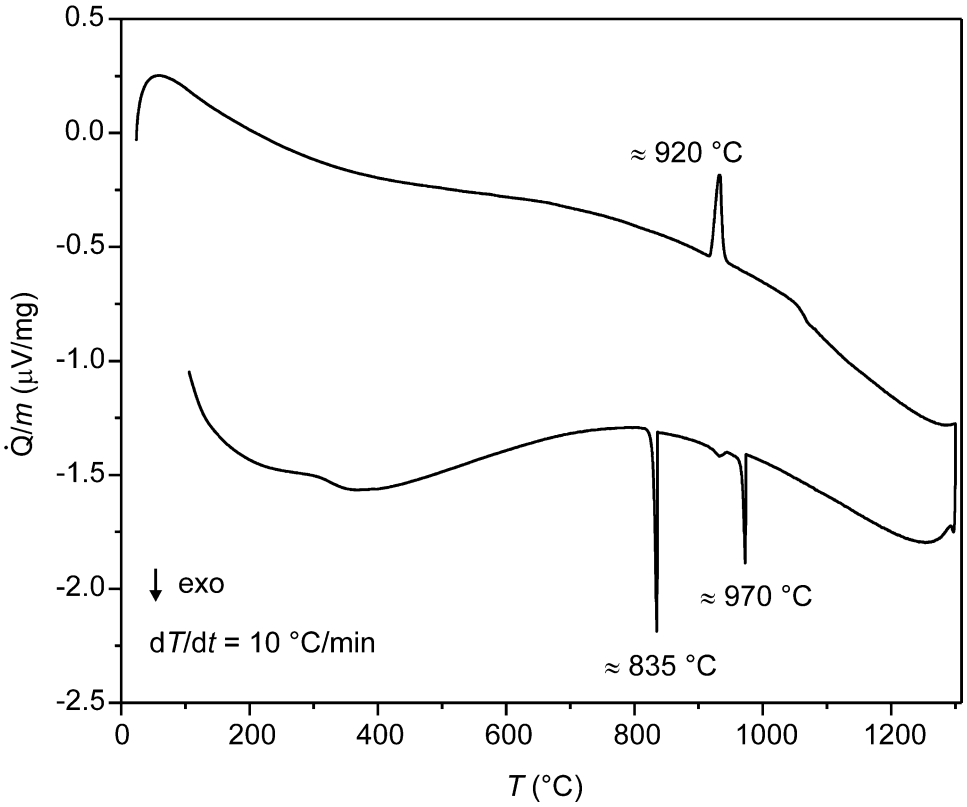

Figure 11.21: Thermal behavior of the sample with the nominal composition $BaNiSi_3$ melting at the eutectic temperature (920 °C, onset) of the quasi-binary system $BaSi_2$ – NiSi. The peaks on cooling at around 970 °C may correspond to the primary formation of $BaSi_2$ or the cotectic formation of $BaSi_2$ and NiSi. The peak at 835 °C may indicate the eutectic crystallization.

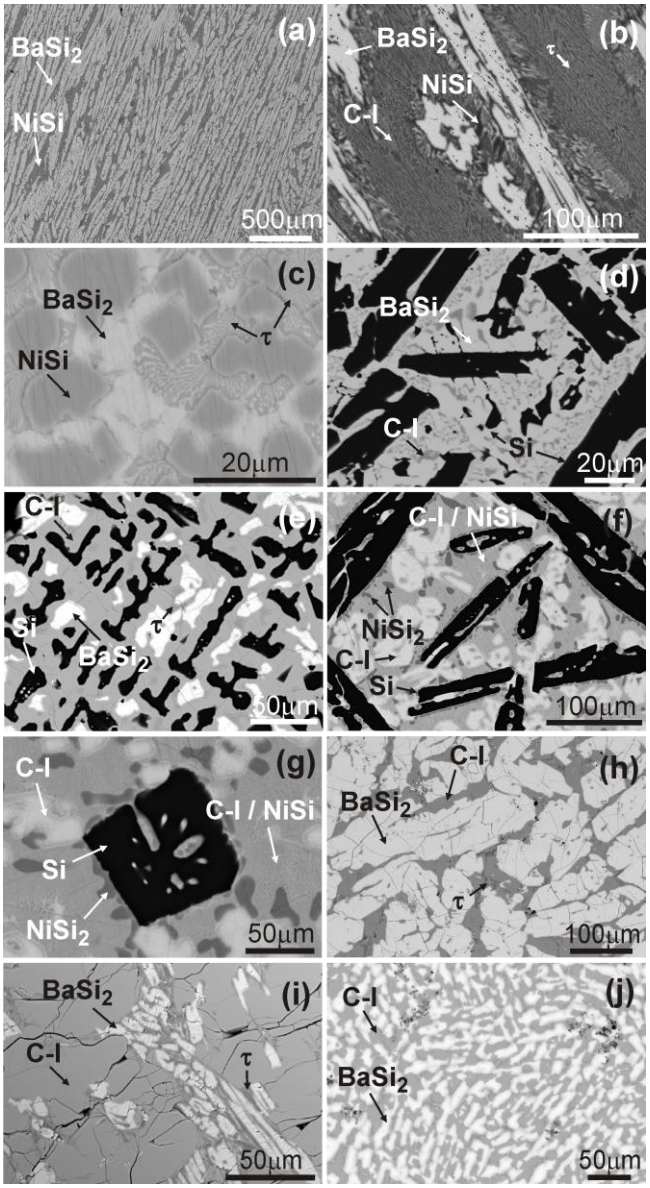

Figure 11.22: SEM images (BSE contrast) of the samples obtained by fast cooling from the melt in the system $BaSi_2$ – NiSi – α-Si. The nominal compositions of the samples are: $Ba_{20}Ni_{20}Si_{60}$ (sample 1, **a**), $Ba_{12}Ni_{30}Si_{58}$ (sample 2, **b**), $Ba_5Ni_{40}Si_{55}$ (sample 3, **c**), $Ba_8Ni_{0.5}Si_{45.5}$ (sample 4, **d**), $Ba_8Ni_4Si_{42}$ (sample 7, **e**), $Ba_5Ni_{20}Si_{75}$ (sample 8, **f**), $Ba_5Ni_{30}Si_{65}$ (sample 9, **g**), $Ba_{25}Ni_5Si_{70}$ (sample 10, **h**), $Ba_8Ni_6Si_{40}$ (sample 11, **i**), and $Ba_{20}Ni_{10}Si_{70}$ (sample 13, **j**). Sample numbers are given according to Fig. 7.2 and observed phases are marked.

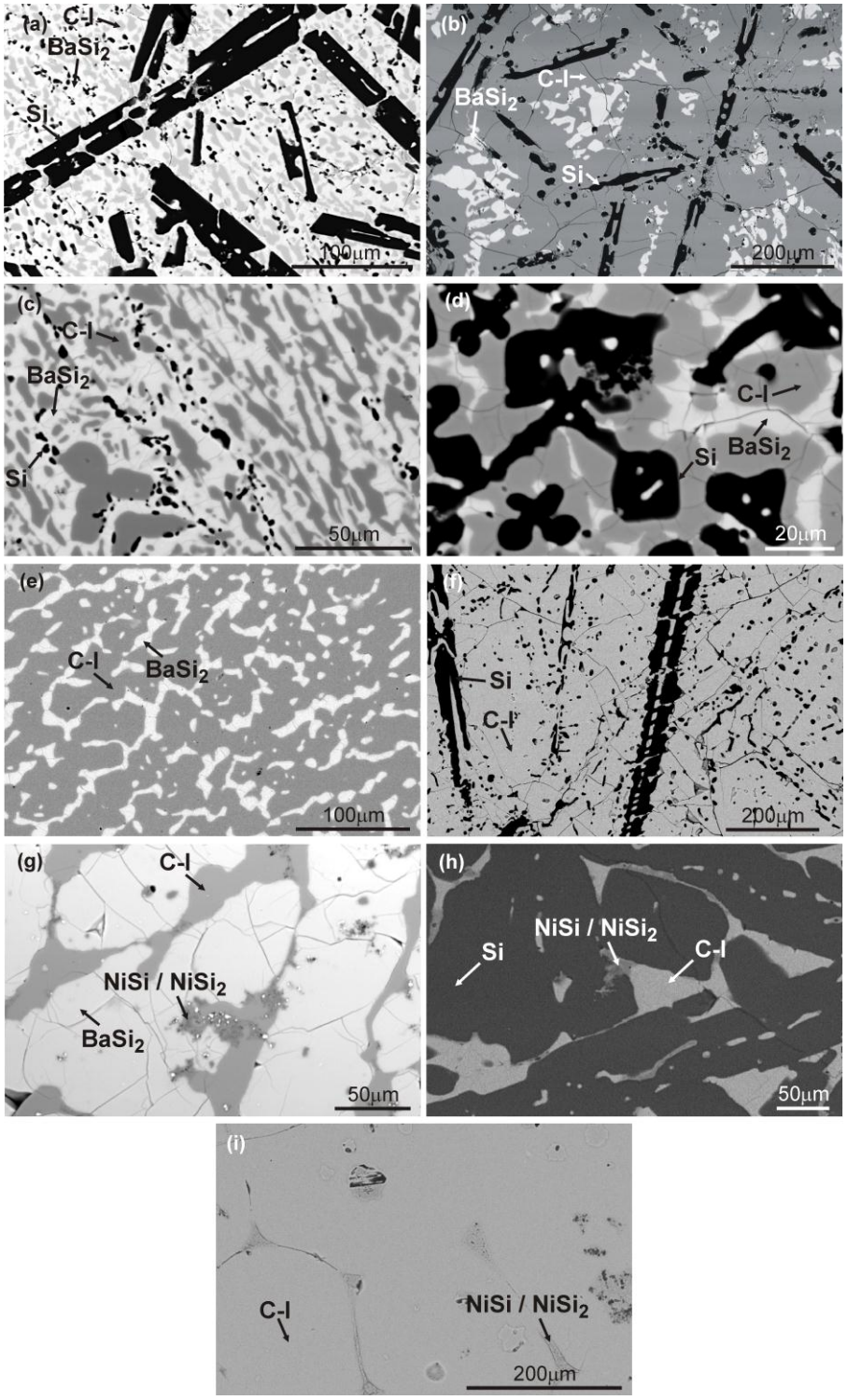

Figure 11.23: Microstructure (SEM, BSE contrast) of the samples investigated for isothermal section of the system $BaSi_2$ – NiSi – α-Si at 1000 °C. The nominal compositions of the investigated samples are: $Ba_8Ni_{0.5}Si_{45.5}$ (sample 1, **a**), $Ba_8Ni_2Si_{44}$ (sample 2, **b**), $Ba_{22.5}Ni_{2.5}Si_{75}$ (sample 3, **c**), $Ba_{10}Ni_2Si_{88}$ (sample 4, **d**), $Ba_{18}Ni_5Si_{77}$ (sample 5, **e**), $Ba_{13}Ni_5Si_{82}$ (sample 6, **f**), $Ba_{25}Ni_5Si_{70}$ (sample 7, **g**), $Ba_{2.5}Ni_{2.5}Si_{95}$ (sample 8, **h**), and $Ba_8Ni_4Si_{42}$ (sample 9, **i**). For details please see the text.

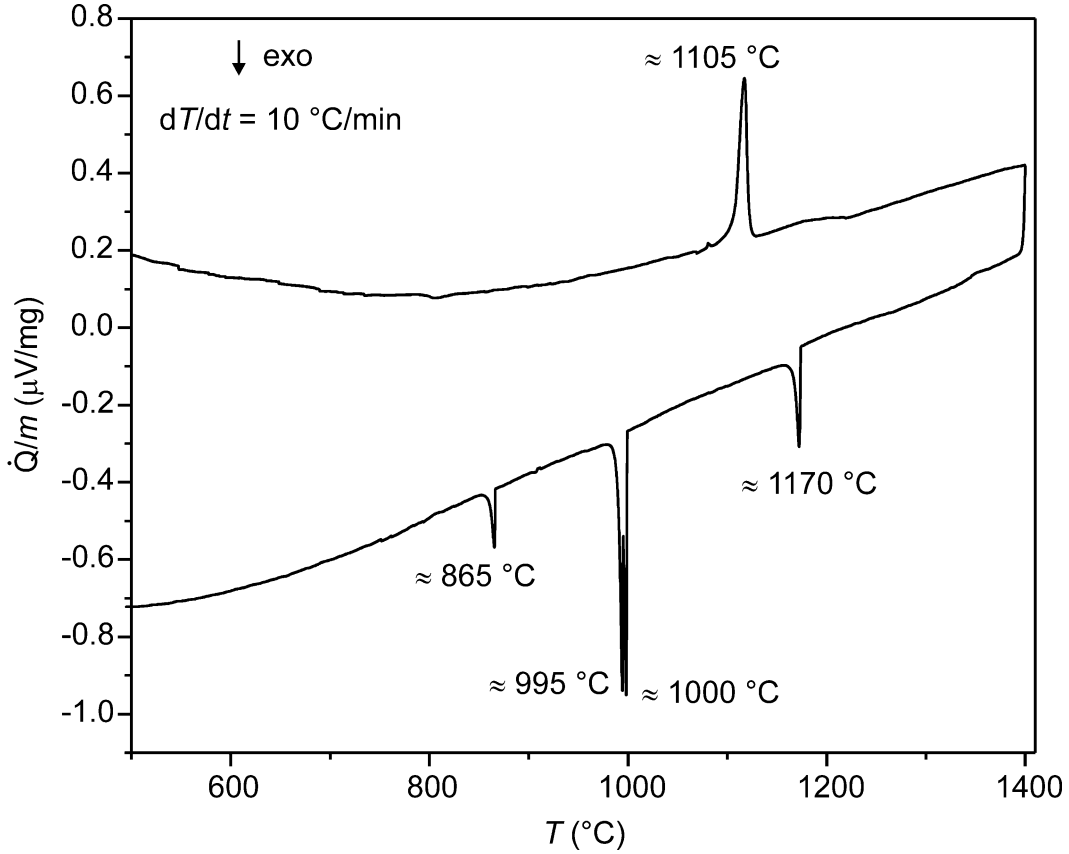

Figure 11.24: Heat-flux DSC measurement of the sample $Ba_8Ni_{3.5}Si_{42.5}$ prepared by annealing at 1000 °C. The peritectic temperature at this composition was estimated to be 1105 °C from the heating curve. This temperature was found to be almost invariant for the clathrate samples with other compositions. Complete melting of the sample is indicated by the broad endothermic effect following the peritectic reaction. In agreement with the microstructure analysis, the exothermic peak on cooling at 1170 °C corresponds to the primary crystallization of α-Si, and the peak at 1000 °C to the crystallization of the clathrate phase. The peaks at 995 °C and 865 °C may indicate a cotectic formation of $BaSi_2$ and clathrate-I phase and ternary eutectic, respectively.

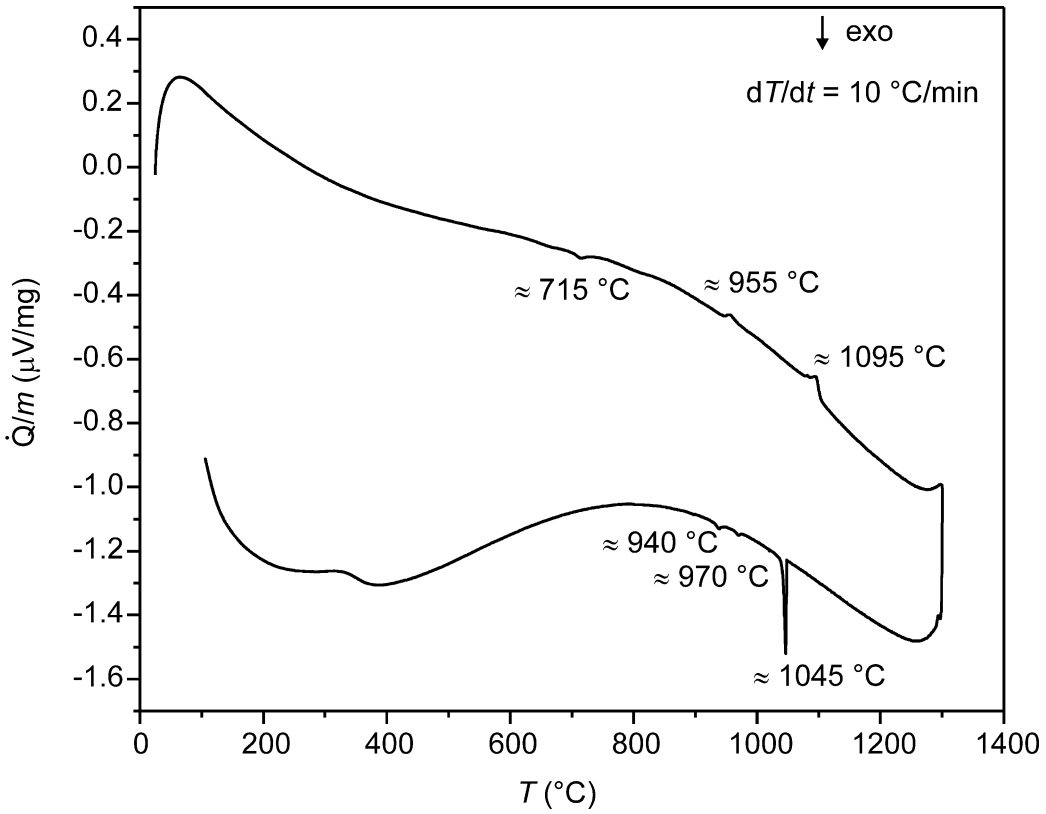

Figure 11.25: Heat-flux DSC measurement of the clathrate $Ba_{7.9(1)}Ni_{1.6(1)}Si_{44.4(1)}$ obtained after steel-quenching followed by HCl and NaOH treatment. The exothermic effect at around 715 °C on heating indicates that the clathrate phase is metastable at this composition. The endothermic effect at around 1095 °C on heating is in agreement with the observed peritectic reaction temperatures of the annealed clathrate-I samples. The main exothermic peak at 1045 °C on cooling may indicate the crystallization of the clathrate-I phase or α-Si from the melt.

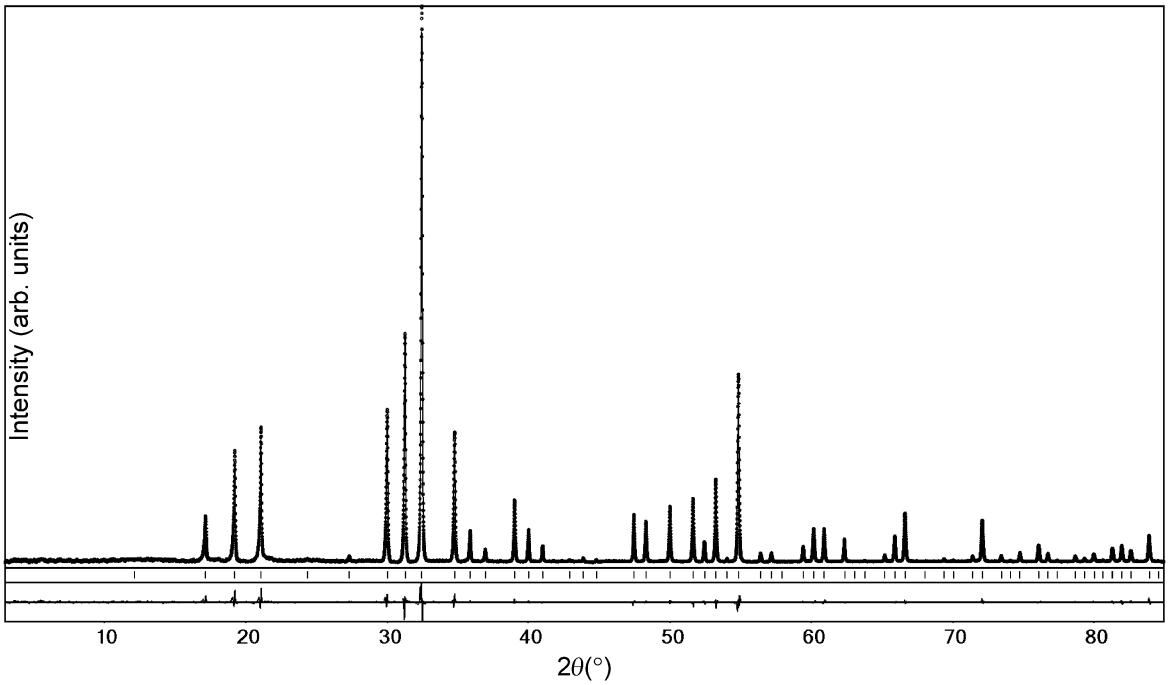

Figure 11.26: PXRD pattern (Cu-$K\alpha_1$ radiation) of the sample with composition $Ba_{7.9(1)}Ni_{1.4(1)}Si_{44.6(1)}$ (dotted line). The calculated profile after Rietveld refinement (solid line) and difference curve (below) are shown. The ticks mark the calculated reflection positions of the clathrate-I phase.

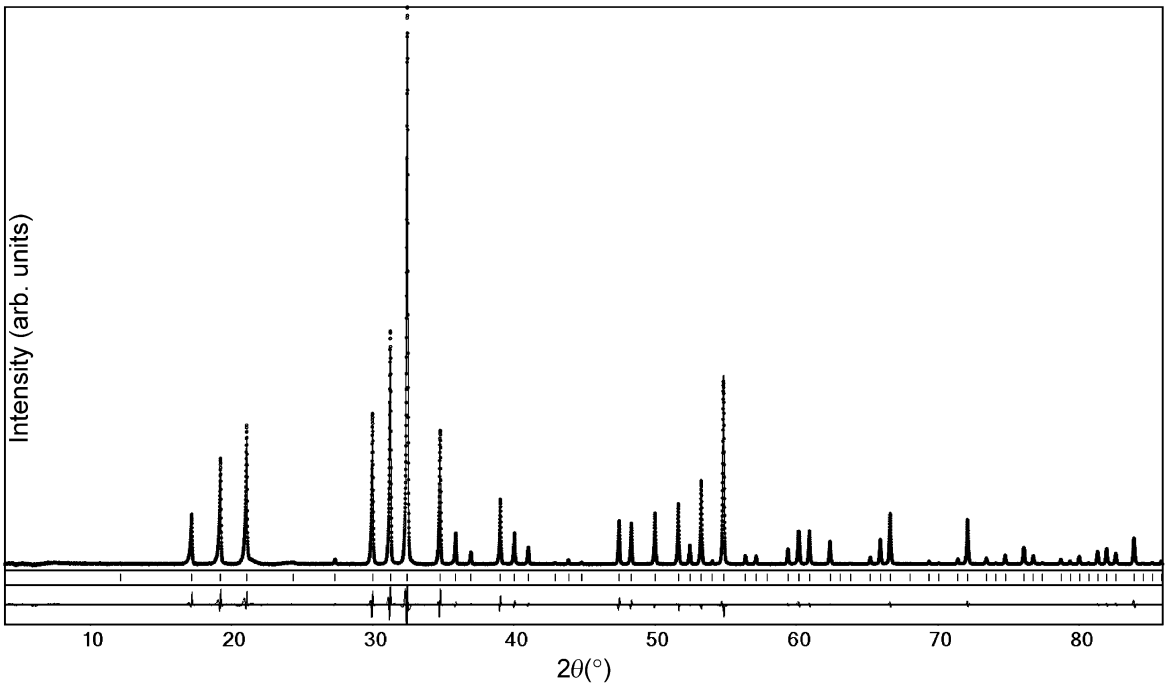

Figure 11.27: PXRD pattern (Cu-$K\alpha_1$ radiation) of the sample with composition $Ba_{7.9(1)}Ni_{1.6(1)}Si_{44.4(1)}$ (dotted line). The calculated profile after Rietveld refinement (solid line) and difference curve (below) are shown. The ticks mark the calculated reflection positions of the clathrate-I phase.

Chapter 11

Appendix – Tables

Table 11.1: Crystallographic data for $Ba_8Ge_{43}\square_3$. Lattice parameter of $Ba_8Ge_{43}\square_3$ samples were determined based on PXRD data.

	Quenched	**Annealed**
Formula; molar mass (g mol^{-1})	Ba_8Ge_{43}; 4220.85	Ba_8Ge_{43}; 4220.85
Crystal system; space group	Cubic; $Ia\bar{3}d$ (no. 230)	Cubic; $Ia\bar{3}d$ (no. 230)
***a* (Å)**	21.3079(2)	21.3069(3)
Number of reflections (XRPD)	112	112
Unit cell volume (Å^3)	9674.4(2)	9673.0(4)
***Z*; ρ_{calc} (g cm^{-3})**	8; 5.794	8; 5.795
Diffractometer	RIGAKU Spider	RIGAKU Spider
λ (Å); monochromator	0.56087; multilayer-optics	0.56087; multilayer-optics
Crystal size (µm^3)	40 60 100	20 80 120
***T* (K)**	295	295
2θ range (°)	3.7 to 30.15	2.8 to 34.2
Indexes ranges	$-38 \le h \le 21$, $-38 \le k \le 38$, $-37 \le l \le 34$	$-24 \le h \le 41$, $-27 \le k \le 42$, $-32 \le l \le 41$
μ (mm^{-1})	17.144	17.144
***F*(000) (e)**	14592	14592
Absorption correction	Multi-scan	Multi-scan
Reflections collected; unique	42422; 2430 [$R_{int} = 0.03$]	50827; 3407 [$R_{int} = 0.05$]
Refined parameters	54	50
Refinement method	Full-matrix least-squares on *F*	Full-matrix least-squares on *F*
$R(F)$, $R(F^2)$ [I > 4σ(I)]	0.030, 0.021	0.067, 0.061
Goodness-of-fit on *F*	1.02	1.01

Table 11.2: Atomic coordinates, displacement parameters (in Å^2) and site occupancies for quenched $Ba_8Ge_{43}\square_3$.

Atom	**Site**	***x***	***y***	***z***	U_{eq}	***Occ.***
Ba1	16*a*	0	0	0	0.01082(4)	1.0
Ba2	48*g*	0.125	0.24755(2)	0.00245(2)	0.02867(8)	1.0
Ge11	24*d*	0.375	0	0.25	0.01266(2)	0.94(1)
Ge12	24*c*	0.125	0	0.25	0.012(2)*	0.06(1)
Ge21	32*e*	0.09149(2)	*x*	*x*	0.01237(7)	1.0
Ge22	96*h*	0.15546(2)	0.34015(2)	0.15900(2)	0.01199(1)	1.0
Ge311	96*h*	0.09666(3)	0.24949(3)	0.30634(3)	0.01219(1)	0.94(1)
Ge312	96*h*	0.0821(4)	0.2488(5)	0.3168(5)	0.013(2)*	0.06(1)
Ge321	96*h*	0.00093(3)	0.16674(4)	0.06541(3)	0.01591(1)	0.94(1)
Ge322	96*h*	0.0010(6)	0.1535(5)	0.0552(5)	0.015(2)	0.06(1)

Atom	U_{11}	U_{22}	U_{33}	U_{12}	U_{13}	U_{23}
Ba1	0.01082(7)	U_{11}	U_{11}	0.00017(1)	U_{12}	U_{12}
Ba2	0.0195(2)	0.03326(1)	U_{22}	−0.00185(1)	U_{12}	−0.0027(2)
Ge11	0.0137(3)	0.0121(2)	U_{22}	0	0	0
Ge21	0.01237(1)	0.01237(1)	U_{11}	−0.00163(1)	U_{12}	U_{12}
Ge22	0.0122(2)	0.0121(2)	0.0117(2)	0.00191(1)	−0.00130(1)	0.00165(1)
Ge311	0.0113(2)	0.0125(2)	0.0127(2)	0.0003(2)	0.0010(2)	0.0003(2)
Ge321	0.0144(2)	0.0163(3)	0.0170(3)	−0.0005(2)	0.0005(2)	0.0023(2)

*U_{iso}.

U_{eq} is defined as one third of the trace of the orthogonalized U_{ij} tensor, which is exp $(-2\pi^2 [h^2a^{*2}U_{11} + ... + 2\, h\, k\, a^*\, b^*\, U_{12}])$.

Table 11.3: Atomic coordinates, displacement parameters (in Å^2) and site occupancies for annealed $Ba_8Ge_{43}\square_3$.

Atom	**Site**	***x***	***y***	***z***	U_{eq}	***Occ.***
Ba1	16*a*	0	0	0	0.01207(6)	1.0
Ba2	48*g*	0.125	0.24773(3)	0.00227(3)	0.03088(1)	1.0
Ge11	24*d*	0.375	0	0.25	0.0135(2)	0.91(1)
Ge12	24*c*	0.125	0	0.25	0.012(2)*	0.09(1)
Ge21	32*e*	0.09150(3)	*x*	*x*	0.01339(1)	1.0
Ge22	96*h*	0.15562(3)	0.34021(3)	0.15895(3)	0.01340(1)	1.0
Ge311	96*h*	0.09661(4)	0.24951(4)	0.30637(4)	0.0130(2)	0.91(1)
Ge312	96*h*	0.0814(5)	0.2490(6)	0.3170(5)	0.017(2)*	0.09(1)
Ge321	96*h*	0.00091(5)	0.16668(5)	0.06536(5)	0.0170(2)	0.91(1)
Ge322	96*h*	0.0004(6)	0.1528(5)	0.0554(5)	0.016(2)	0.09(1)

Atom	U_{11}	U_{22}	U_{33}	U_{12}	U_{13}	U_{23}
Ba1	0.01207(1)	U_{11}	U_{11}	0.00034(1)	U_{12}	U_{12}
Ba2	0.0210(3)	0.0358(2)	U_{22}	−0.0016(2)	U_{12}	−0.0030(3)
Ge11	0.0141(5)	0.0132(3)	U_{22}	0	0	0
Ge21	0.0134(2)	0.01237(1)	U_{11}	−0.0018(2)	U_{12}	U_{12}
Ge22	0.0133(2)	0.0134(3)	0.0135(3)	0.0023(2)	−0.0014(2)	0.0018(2)
Ge311	0.0120(3)	0.0133(3)	0.0137(3)	-0.0000(3)	0.0006(3)	0.0004(2)
Ge321	0.0156(3)	0.0171(4)	0.0184(4)	−0.0003(3)	0.0007(3)	0.0025(3)

*U_{iso}.

U_{eq} is defined as one third of the trace of the orthogonalized U_{ij} tensor, which is exp $(-2\pi^2 [h^2 a^{*2} U_{11} + ... + 2\, h\, k\, a^*\, b^*\, U_{12}])$.

Table 11.4: Interatomic distances in $Ba_8Ge_{43}\square_3$ with multiplicity *n*.

Atoms		*n*	*d* (Å) (quenched)	*d* (Å) (annealed)
Ba1	– Ge21	2 ×	3.3766(4)	3.3768(6)
	– Ge22	6 ×	3.3923(4)	3.3914(6)
	– Ge322	6 ×	3.48(1)	3.46(1)
	– Ge311	6 ×	3.4809(6)	3.482(1)
	– Ge321	6 ×	3.8165(7)	3.815(1)
	– Ge312	6 ×	3.85(1)	3.87(1)
Ba2	– Ge321	2 ×	3.4284(8)	3.432(1)
	– Ge312	2 ×	3.466(9)	3.46(1)
	– Ge322	2 ×	3.50(1)	3.52(1)
	– Ge321	2 ×	3.5122(8)	3.511(1)
	– Ge311	2 ×	3.5546(7)	3.555(1)
	– Ge312	2 ×	3.557(9)	3.54(1)
	– Ge322	2 ×	3.59(1)	3.59(1)
	– Ge311	2 ×	3.6306(7)	3.626(1)
	– Ge12	2 ×	3.7304(3)	3.7328(5)
	– Ge11	2 ×	3.8041(3)	3.8012(5)
	– Ge21	2 ×	3.8946(6)	3.899(1)
	– Ge11	2 ×	3.8041(3)	3.930(1)
	– Ge22	2 ×	3.9285(6)	3.9285(6)
	– Ge22	2 ×	3.9296(6)	3.931(1)
	– Ge321	2 ×	3.9819(8)	3.986(1)
	– Ge312	2 ×	4.06(1)	4.06(1)
	– Ge22	2 ×	4.0932(6)	4.085(1)
Ge11	– Ge312	4 ×	2.14(1)	2.13(1)
	– Ge311	4 ×	2.5264(6)	2.5250(9)
Ge12	– Ge321	4 ×	2.1818(6)	2.183(1)
	– Ge322	4 ×	2.54(1)	2.55(1)
Ge21	– Ge322	3 ×	2.46(1)	2.46(1)
	– Ge21	1 ×	2.4736(6)	2.4726(9)
	– Ge321	3 ×	2.5697(9)	2.569(1)
Ge22	– Ge322	1 ×	2.44(1)	2.42(1)
	– Ge22	1 ×	2.4439(6)	2.4449(9)
	– Ge311	1 ×	2.5055(8)	2.504(1)
	– Ge311	1 ×	2.5095(8)	2.507(1)
	– Ge321	1 ×	2.5358(9)	2.538(1)
	– Ge312	1 ×	2.63(1)	2.63(1)
	– Ge312	1 ×	2.64(1)	2.64(1)
Ge311	– Ge322	1 ×	2.38(1)	2.38(1)
	– Ge22	1 ×	2.5055(8)	2.504(1)
	– Ge22	1 ×	2.5095(8)	2.507(1)
	– Ge11	1 ×	2.5264(6)	2.5250(9)
	– Ge321	1 ×	2.6099(9)	2.609(1)
Ge312	– Ge11	1 ×	2.14(1)	2.13(1)
	– Ge322	1 ×	2.62(1)	2.63(2)
	– Ge22	1 ×	2.63(1)	2.63(1)
	– Ge22	1 ×	2.64(1)	2.64(1)
	– Ge321	1 ×	2.82(1)	2.82(1)
Ge321	– Ge12	1 ×	2.1818(8)	2.183(1)
	– Ge22	1 ×	2.5358(8)	2.538(1)
	– Ge21	1 ×	2.5696(9)	2.569(1)
	– Ge311	1 ×	2.6099(9)	2.609(1)
	– Ge312	1 ×	2.82(1)	2.82(1)
Ge322	– Ge311	1 ×	2.38(1)	2.38(1)
	– Ge22	1 ×	2.44(1)	2.42(1)
	– Ge21	1 ×	2.46(1)	2.46(1)
	– Ge12	1 ×	2.54(1)	2.55(1)
	– Ge312	1 ×	2.62(1)	2.63(1)

Table 11.5: Bond angles in the framework of steel-quenched $Ba_8Ge_{43}\square_3$.

Atoms	Angle (°)	Atoms	Angle (°)
Ge312 – Ge11 – Ge312	109.5(4)	Ge322 – Ge311 – Ge22	109.2(3)
Ge312 – Ge11 – Ge312	109.3(4)	Ge322 – Ge311 – Ge22	106.5(3)
Ge312 – Ge11 – Ge311	109.9(3)	Ge22 – Ge311 – Ge22	104.10(3)
Ge312 – Ge11 – Ge311	109.3(3)	Ge322 – Ge311 – Ge11	125.3(3)
Ge312 – Ge11 – Ge311	109.2(3)	Ge22 – Ge311 – Ge11	104.28(2)
Ge311 – Ge11 – Ge311	109.59(2)	Ge22 – Ge311 – Ge11	105.59(3)
Ge311 – Ge11 – Ge311	109.23(2)	Ge22 – Ge311 – Ge321	112.61(3)
		Ge22 – Ge311 – Ge321	109.9(3)
		Ge11 – Ge311 – Ge321	119.11(3)
Ge321 – Ge12 – Ge321	108.82(3)	Ge11 – Ge312 – Ge322	132.1(5)
Ge321 – Ge12 – Ge321	108.90(3)	Ge11 – Ge312 – Ge22	114.1(4)
Ge321 – Ge12 – Ge321	110.70(3)	Ge322 – Ge312 – Ge22	96.7(4)
Ge321 – Ge12 – Ge322	108.5(3)	Ge11 – Ge312 – Ge22	112.0(4)
Ge321 – Ge12 – Ge322	109.1(3)	Ge322 – Ge312 – Ge22	98.5(4)
Ge321 – Ge12 – Ge322	110.8(3)	Ge22 – Ge312 – Ge22	97.5(3)
Ge322 – Ge12 – Ge322	108.2(4)	Ge22 – Ge312 – Ge321	100.7(4)
Ge322 – Ge12 – Ge322	109.3(4)	Ge22 – Ge312 – Ge321	102.58(2)
Ge322 – Ge12 – Ge322	110.9(4)		
Ge322 – Ge21 – Ge322	110.1(4)	Ge12 – Ge321 – Ge22	111.18(3)
Ge322 – Ge21 – Ge21	108.9(3)	Ge12 – Ge321 – Ge21	112.85(3)
Ge322 – Ge21 – Ge321	111.6(3)	Ge22 – Ge321 – Ge21	98.61(3)
Ge322 – Ge21 – Ge321	115.4(3)	Ge12 – Ge321 – Ge311	131.87(3)
Ge21 – Ge21 – Ge321	101.43(2)	Ge22 – Ge321 – Ge311	98.32(3)
Ge321 – Ge21 – Ge321	116.17(3)	Ge21 – Ge321 – Ge311	98.61(3)
Ge322 – Ge21 – Ge321	115.4(3)	Ge12 – Ge321 – Ge312	125.1(2)
Ge21 – Ge21 – Ge321	101.43(2)	Ge22 – Ge321 – Ge312	102.8(2)
		Ge21 – Ge321 – Ge312	102.8(2)
Ge322 – Ge22 – Ge22	110.2(3)	Ge311 – Ge322 – Ge22	108.0(4)
Ge322 – Ge22 – Ge311	110.6(3)	Ge311 – Ge322 – Ge21	108.5(4)
Ge22 – Ge22 – Ge311	109.90(2)	Ge22 – Ge322 – Ge21	104.4(4)
Ge322 – Ge22 – Ge311	110.4(3)	Ge311 – Ge322 – Ge12	126.0(5)
Ge22 – Ge22 – Ge311	107.71(2)	Ge22 – Ge322 – Ge12	103.2(4)
Ge311 – Ge22 – Ge311	107.87(3)	Ge21 – Ge322 – Ge12	104.9(4)
Ge22 – Ge22 – Ge321	102.58(2)	Ge22 – Ge322 – Ge312	111.9(5)
Ge311 – Ge22 – Ge321	116.17(3)	Ge21 – Ge322 – Ge312	111.9(5)
Ge311 – Ge22 – Ge321	112.24(3)	Ge12 – Ge322 – Ge312	119.1(3)
Ge322 – Ge22 – Ge312	115.8(3)		
Ge22 – Ge22 – Ge312	99.7(2)		
Ge311 – Ge22 – Ge312	110.0(2)		
Ge321 – Ge22 – Ge312	116.7(2)		
Ge322 – Ge22 – Ge312	112.5(3)		
Ge22 – Ge22 – Ge312	102.2(2)		
Ge311 – Ge22 – Ge312	113.3(2)		
Ge321 – Ge22 – Ge312	1172(2)		
Ge312 – Ge22 – Ge312	114.5(3)		

Table 11.6: Crystallographic data for $BaGe_5$.

	400 °C	**520 °C**
Formula; molar mass (g mol^{-1})	$BaGe_5$; 500.37	
Crystal system; space group	Orthorhombic; *Pmna* (no.53)	
***a, b, c* (Å)**	10.7265(8), 9.2839(5), 14.791(1)	10.7246(9), 9.2860(8), 14.797(1)
Unit cell volume (Å^3)	1472.9(3)	1474.1(4)
Z; ρ_{calc} (g cm^{-3})	10; 5.640	10; 5.635
Diffractometer	Nine-crystal multi-analyzer stage	
λ (Å); monochromator	0.35415; Si 111 crystal	
***T* (K)**	Room temperature	
θ range (°)	0 to 11.3	
μ (mm^{-1})	16.60	
***F*(000) (e)**	2160	
Reflections in measured range	1064	
Refined parameters	38	
Refinement method	Full-profile Rietveld	
R_i; R_p; R_{wp}	0.066; 0.107; 0.086	0.063; 0.113; 0.090

Table 11.7: Atomic coordinates, displacement parameters (in Å^2) and site occupancies for $BaGe_5$ (top: for sample obtained at 400 ºC, bottom: for sample obtained at 520 ºC sample).

Atom	**Site**	***x***	***y***	***z***	U_{iso}	***Occ.***
Ba1	2*a*	0	0	0	0.0120(9)	1.0
Ba2	*4g*	1/4	0.4237(3)	1/4	0.0215(8)	1.0
Ba3	4*h*	0	0.2048(3)	0.6324(2)	0.0374(9)	1.0
Ge1	4*h*	0	0.3641(4)	0.1102(3)	0.008(1)	1.0
Ge2	4*h*	0	0.2136(4)	0.3807(3)	0.006(1)	1.0
Ge3	4*h*	0	0.1451(4)	0.2147(3)	0.008(1)	1.0
Ge4	4*h*	0	0.4668(9)	0.4091(5)	0.010(3)	0.5
Ge5	8*i*	0.3377(4)	0.5073(8)	0.0310(3)	0.005(2)	0.5
Ge6	8*i*	0.3049(3)	0.0939(3)	0.0608(2)	0.0073(8)	1.0
Ge7	8*i*	0.1194(3)	0.7216(3)	0.1550(2)	0.0090(8)	1.0
Ge8	8*i*	0.1807(3)	0.3084(3)	0.0060(2)	0.0074(8)	1.0
Ge9	8*i*	0.3181(3)	0.0205(3)	0.6850(2)	0.0063(8)	1.0
Atom	**Site**	***x***	***y***	***z***	U_{iso}	***Occ.***
Ba1	2*a*	0	0	0	0.0122(9)	1.0
Ba2	*4g*	1/4	0.4233(3)	1/4	0.0238(8)	1.0
Ba3	4*h*	0	0.2046(3)	0.6317(2)	0.0339(9)	1.0
Ge1	4*h*	0	0.3643(4)	0.1106(3)	0.006(1)	1.0
Ge2	4*h*	0	0.2149(4)	0.3802(3)	0.007(1)	1.0
Ge3	4*h*	0	0.1459(4)	0.2148(3)	0.007(1)	1.0
Ge4	4*h*	0	0.4669(8)	0.4085(5)	0.010(2)	0.5
Ge5	8*i*	0.3365(4)	0.5075(7)	0.0310(3)	0.006(1)	0.5
Ge6	8*i*	0.3058(2)	0.0937(3)	0.0609(2)	0.0070(7)	1.0
Ge7	8*i*	0.1196(3)	0.7219(3)	0.1551(2)	0.0078(7)	1.0
Ge8	8*i*	0.1807(3)	0.3085(3)	0.0056(2)	0.0070(6)	1.0
Ge9	8*i*	0.3183(2)	0.0201(3)	0.6846(2)	0.0062(7)	1.0

The positions Ge4 and Ge5 are alternatively occupied and were fixed to 0.5 at the final stage of the refinement. Free refinement of the occupancies led to the values 0.510(5) for Ge4 and 0.500(3) for Ge5 for the sample obtained at 400 ºC and 0.518(5) for Ge4 and 0.499(3) for Ge5 for the sample obtained at 520 ºC.

Table 11.8: The interatomic distances for Ba–Ge and Ge–Ge atoms in the crystal structure of $BaGe_5$ obtained at 400 ºC in 10 d.

Atoms		*n**	*d* (Å)
Ba1	– Ge9	4 ×	3.366(3)
	– Ge3	2 ×	3.449(4)
	– Ge8	4 ×	3.459(3)
	– Ge6	4 ×	3.502(3)
	– Ge7	4 ×	3.685(3)
	– Ge1	2 ×	3.753(4)
Ba2	– Ge7	2 ×	3.403(3)
	– Ge1	2 ×	3.431(3)
	– Ge5	1 ×	3.462(5)
	– Ge4	1 ×	3.590(5)
	– Ge3	2 ×	3.762(3)
	– Ge8	2 ×	3.837(3)
	– Ge2	2 ×	3.838(3)
Ba3	– Ge4	0.5×	3.111(8)
	– Ge7	2 ×	3.462(4)
	– Ge5	1 ×	3.526(7)
	– Ge6	2 ×	3.632(3)
	– Ge6	2 ×	3.689(4)
	– Ge2	1 ×	3.724(5)
	– Ge9	2 ×	3.745(3)
	– Ge2	1 ×	3.889(4)
	– Ge9	2 ×	3.895(3)

Atoms		*n**	*d* (Å)
Ge1	– Ge8	2×	2.530(4)
	– Ge3	1×	2.554(5)
Ge2	– Ge4	0.5×	2.387(9)
	– Ge6	2×	2.522(3)
	– Ge3	1×	2.537(6)
Ge3	– Ge9	2×	2.523(4)
	– Ge2	1×	2.537(6)
	– Ge1	1×	2.554(5)
Ge4	– Ge2	1×	2.387(9)
	– Ge5	2×	2.518(7)
Ge5	– Ge8	1×	2.462(7)
	– Ge4	1×	2.518(7)
	– Ge8	1×	2.526(7)
Ge6	– Ge9	1×	2.498(4)
	– Ge6	1×	2.506(4)
	– Ge2	1×	2.522(3)
	– Ge8	1×	2.529(4)
Ge7	– Ge8	1×	2.487(4)
	– Ge9	1×	2.526(4)
	– Ge7	1×	2.562(4)
Ge8	– Ge5	0.5×	2.462(7)
	– Ge7	1×	2.487(4)
	– Ge5	0.5×	2.526(7)
	– Ge6	1×	2.529(4)
	– Ge1	1×	2.530(4)
Ge9	– Ge9	1×	2.414(4)
	– Ge6	1×	2.498(4)
	– Ge3	1×	2.523(4)
	– Ge7	1×	2.526(4)

***** Number of interatomic distances per unit cell.

Table 11.9: Crystallographic data for $Ba_8Ni_{0.6}Ge_{42.6}\square_{2.8}$. The lattice parameter is determined based on the PXRD data.

Molar mass (g mol^{-1})	4227.02
Crystal system; space group	Cubic; $Ia\bar{3}d$ (no. 230)
***a* (Å)**	21.3140(2)
Number of reflections (PXRD)	106
Unit cell volume (Å^3)	9682.7(3)
Z; ρ_{calc} **(g cm^{-3})**	8; 5.796
Diffractometer	RIGAKU Spider
λ **(Å); monochromator**	0.56087; multilayer-optics
Crystal size (µm^3)	45 × 70 × 145
***T* (K)**	295(2)
$2\theta_{max}$ **(°); (sinθ/λ)$_{max}$**	79.16; 1.136
μ **(mm^{-1})**	17.969
***F*(000) (e)**	14620
Absorption correction	Multi-scan
Reflections collected; unique	51737; 1757 [R_{int} = 0.02]
Refined parameters	49
Refinement method	Full-matrix least-squares on F
R_F; $R_{F^2}[I > 4\sigma(I)]$	0.028; 0.022
Goodness-of-fit on *F*	1.01

Table 11.10: Atomic coordinates, site occupancies and displacement parameters (in Å^2) of $Ba_8Ni_{0.6}Ge_{42.6}\square_{2.8}$. Ni atoms are considered to occupy 24*c* and/or 24*d* sites together with Ge atoms.

Atom	**Site**	***x***	***y***	***z***	U_{eq}	***Occ.***
Ba1	16*a*	0	0	0	0.01125(4)	1.0
Ba2	48*g*	0.125	0.24796(3)	-*y* + 1/4	0.0311(1)	1.0
Ge11 / Ni11	24*d*	0.375	0	1/4	0.0111(2)	0.85(1)
Ge12 / Ni12	24*c*	0.125	0	1/4	0.0106(12)*	0.18(1)
Ge21	32*e*	0.09146(3)	*x*	*x*	0.01255(10)	1.0
Ge22	96*h*	0.15594(3)	0.34040(3)	0.15886(3)	0.0124(2)	1.0
Ge311	96*h*	0.09616(3)	0.24956(4)	0.30667(3)	0.0128(1)	0.89(1)
Ge312	96*h*	0.0824(2)	0.2494(3)	0.3176(3)	0.0128(10)*	0.11(1)
Ge321	96*h*	0.00077(4)	0.16705(4)	0.06580(4)	0.0156(2)	0.79(1)
Ge322	96*h*	0.0008(2)	0.1557(1)	0.0572(1)	0.0126(5)*	0.21(1)

Atom	U_{11}	U_{22}	U_{33}	U_{12}	U_{13}	U_{23}
Ba1	0.01125(7)	U_{11}	U_{11}	0.0001(1)	U_{12}	U_{12}
Ba2	0.0208(2)	0.0362(2)	U_{22}	−0.0014(2)	U_{12}	−0.0031(3)
Ge11/Ni11	0.0123(5)	0.0105(3)	U_{22}	0	0	0
Ge21/Ni12	0.0126(2)	U_{11}	U_{11}	−0.0020(2)	U_{12}	U_{12}
Ge22	0.0128(2)	0.0127(2)	0.0117(2)	0.0024(2)	0.0013(2)	0.0015(2)
Ge311	0.0126(2)	0.0124(2)	0.0136(2)	0.0001(2)	-0.0001(2)	0.0004(2)
Ge321	0.0151(2)	0.0153(3)	0.0164(3)	−0.0003(2)	0.0003(2)	0.0003(2)

*U_{iso}.

U_{eq} is defined as one third of the trace of the orthogonalized U_{ij} tensor, which is exp $(-2\pi^2 [h^2 a^{*2} U_{11} + ... + 2\, h\, k\, a^*\, b^*\, U_{12}])$.

Table 11.11: Crystallographic data for $Ba_8Ni_{3.5}Ge_{42.1}\square_{0.4}$.[22] The lattice parameter was determined based on PXRD data.

Molar mass (gmol^{-1})	4360.92
Crystal system; space group	Cubic; $Pm\bar{3}n$ (no. 223)
***a* (Å)**	10.6798(2)
Unit cell volume (Å^3)	1218.12(7)
Z; ρ_{calc} (g cm^{-3}); ρ_{exp} (g cm^{-3})	1; 5.932; 5.93(6)
Diffractometer	RIGAKU Spider
λ (Å); monochromator	0.56087; multilayer-optics
Crystal size (µm^3)	15 × 40 × 185
***T* (K)**	295(2)
$2\theta_{max}$ (°); $(\sin\theta/\lambda)_{max}$	88.97; 1.249
μ (mm^{-1})	17.415
***F*(000) (e)**	1893
Absorption correction	Multi-scan
Reflections collected; unique	19334; 1409 [R_{int} = 0.03]
Refined parameters	34
Refinement method	Full-matrix least-squares on F
Residuals [$I > 4\sigma(I)$]	R_1 = 0.039; wR_2 = 0.021
Residuals (all data)	R_1 = 0.053; wR_2 = 0.024
Goodness-of-fit on *F*	1.01
Extinction coefficient	0.0036(1)

Table 11.12: Atomic coordinates, site occupancies and displacement parameters (in Å^2) of $Ba_8Ni_{3.5}Ge_{42.1}\square_{0.4}$.[22] Vacancies are only considered at position 6*c* and the overall occupancy of Ge31 + Ge32 + Ge33 is regarded to be around 1.

Atom	**Site**	***x***	***y***	***z***	U_{eq}	***Occ.***
Ba1	2*a*	0	0	0	0.01132(6)	1.0
Ba2	24*k*	0.2409(3)	0.5155(3)	0	0.0271(8)	0.25
Ni1	6*c*	1/4	0	1/2	0.0104(2)	0.583*
Ge1	6*c*	1/4	0	1/2	0.0104(2)	0.346(6)
Ge2	16*i*	0.18363(3)	*x*	*x*	0.00998(4)	1.0
Ge31	24*k*	0	0.30757(1)	0.10980(1)	0.0084(2)	0.317(3)
Ge32	24*k*	0	0.32013(8)	0.12612(1)	0.0120(2)	0.583*
Ge33	24*k*	0	0.3282(13)	0.1415(10)	0.0139(14)	0.096(2)

Atom	U_{11}	U_{22}	U_{33}	U_{12}	U_{13}	U_{23}
Ba1	0.01132(1)	U_{11}	U_{11}	0	0	0
Ba2	0.0097(10)	0.0255(13)	0.046(2)	0.0040(6)	0	0
Ni1	0.0137(4)	0.0088(3)	U_{22}	0	0	0
Ge1	0.0137(4)	0.0088(3)	U_{22}	0	0	0
Ge2	0.00998(7)	U_{11}	U_{11}	-0.00138(6)	U_{12}	U_{12}
Ge31	0.0102(4)	0.0059(3)	0.0092(5)	0	0	-0.009(3)
Ge32	0.0100(2)	0.0120(3)	0.0139(5)	0	0	0.0008(3)
Ge33	0.014(2)	0.019(3)	0.009(2)	0	0	-0.005(2)

* fixed according to WDXS result.

U_{eq} is defined as one third of the trace of the orthogonalized U_{ij} tensor, which is exp $(-2\pi^2 [h^2 a^{*2} U_{11} + ... + 2\, h\, k\, a^*\, b^*\, U_{12}])$.

Table11.13: Interatomic distances of $Ba_8Ni_{3.5}Ge_{42.1}\square_{0.4}$ with their multiplicity *n*. The sites Ge31, Ge32 and Ge33 represent alternatively occupied split positions of the site Ge3.

Atoms		*n*	*d* (Å)	Atoms		*n*	*d* (Å)
Ba1	– Ge2	8 ×	3.3968(3)	Ni/Ge1	– Ge32	4 ×	2.170(13)
	– Ge31	12 ×	3.488(2)		– Ge31	4 ×	2.333(2)
	– Ge32	12 ×	3.675(2)		– Ge33	4 ×	2.543(2)
	– Ge33	12 ×	3.817(14)				
Ba2	– Ge32	2 ×	3.394(4)	Ge2	– Ge2	1 ×	2.4553(4)
	– Ge31	2 ×	3.401(4)		– Ge31	3 ×	2.494(1)
	– Ge33	2 ×	3.419(9)		– Ge32	3 ×	2.520(1)
	– Ge32	2 ×	3.570(3)		– Ge33	3 ×	2.536(9)
	– Ge32	2 ×	3.576(4)				
	– Ge33	2 ×	3.582(9)	Ge31	– Ge31	1 ×	2.345(2)
	– Ge31	2 ×	3.591(3)		– Ge2	2 ×	2.494(1)
	– Ge33	2 ×	3.592(10)		– Ge32	1 ×	2.523(2)
	– Ge31	2 ×	3.595(4)		– Ni/Ge1	1 ×	2.543(2)
	– Ge32	2 ×	3.692(3)		– Ge33	1 ×	2.693(11)
	– Ge31	2 ×	3.697(3)				
	– Ni1/Ge1	2 ×	3.712(3)	Ge32	– Ni/Ge1	1 ×	2.333(2)
	– Ge33	2 ×	3.719(9)		– Ge2	2 ×	2.520(1)
	– Ni1/Ge1	1 ×	3.732(4)		– Ge31	1 ×	2.523(2)
	– Ge33	1 ×	3.780(11)		– Ge32	1 ×	2.694(2)
	– Ge2	2 ×	3.814(3)		– Ge33	1 ×	2.859(11)
	– Ge33	2 ×	3.903(11				
	– Ge2	2 ×	3.910(2)	Ge33	– Ni/Ge1	1 ×	2.170(13)
	– Ge32	1 ×	3.920(4)		– Ge2	2 ×	2.536(9)
	– Ni1/Ge1	1 ×	3.961(4)		– Ge31	1 ×	2.693(9)
	– Ge32	2 ×	4.049(1)		– Ge32	1 ×	2.859(11)
	– Ge33	1 ×	4.065(4)		– Ge33	1 ×	3.022(15)
	– Ge2	2 ×	4.073(2)				
	– Ge2	2 ×	4.096(3)				
	– Ge33	1 ×	4.101(11				
	– Ge31	2 ×	4.203(2)				
	– Ge32	1 ×	4.243(4)				
	– Ge31	1 ×	4.391(4)				

Table 11.14: Crystallographic data for $Ba_8Ni_{2.6}Si_{43.3}\square_{0.1}$, $Ba_8Ni_{3.2}Si_{42.4}\square_{0.4}$, and $Ba_8Ni_{3.7}Si_{41.4}\square_{0.9}$.

	$Ba_8Ni_{2.6}Si_{43.3}\square_{0.1}$	$Ba_8Ni_{3.2}Si_{42.4}\square_{0.4}$	$Ba_8Ni_{3.7}Si_{41.4}\square_{0.9}$
Molar mass (gmol^{-1})	2470.13	2477.25	2478.51
Crystal system; space group	Cubic; $Pm\bar{3}n$ (no. 223)	Cubic; $Pm\bar{3}n$ (no. 223)	Cubic; $Pm\bar{3}n$ (no.223)
***a* (Å)**	10.2982(1)	10.2922(1)	10.2906(1)
Number of reflections (PXRD)	66	64	61
Unit cell volume (Å^3)	1092.15(3)	1090.25(3)	1089.74(3)
Z; ρ_{calc}(g cm^{-3})	1; 3.752	1; 3.776	1; 3.779
Diffractometer	RIGAKU Spider	RIGAKU Spider	RIGAKU Spider
λ (Å); monochromator	0.56087; multilayer-optics	0.56087; multilayer-optics	0.56087; multilayer-optics
Crystal size (µm^3)	20 × 35 × 55	10 × 10 × 40	20 × 30 × 50
***T* (K)**	295	295	295
2θ range (°)	3.82 to 34.97	3.12 to 30.11	3.12 to 30.65
Indexes ranges	$-21 \le h \le 15$, $-16 \le k \le 12$, $-18 \le l \le 13$	$-3 \le h \le 15$, $-17 \le k \le 17$, $-17 \le l \le 18$	$-18 \le h \le 17$, $-18 \le k \le 15$, $-16 \le l \le 18$
μ (mm^{-1})	4.90	5.01	5.14
***F*(000) (e)**	1128	1131	1132
Absorption correction	Multi-scan	Multi-scan	Multi-scan
Reflections collected; unique	11916; 720 [R_{int} =0 .04]	6635; 503 [R_{int} =0 .04]	12195; 560 [R_{int} = 0.03]
Refined parameters	25	33	36
Refinement method	Full-matrix least-squares on *F*	Full-matrix least-squares on *F*	Full-matrix least-squares on *F*
$R(F)$; $R(F^2)$ [$I > 4\sigma(I)$]	0.030; 0.021	0.023; 0.019	0.021; 0.022

Table 11.15: Atomic coordinates, displacement parameters (in Å^2) and site occupancies for $Ba_8Ni_{2.6}Si_{43.3}\square_{0.1}$ (top), $Ba_8Ni_{3.2}Si_{42.4}\square_{0.4}$ (middle), and $Ba_8Ni_{3.7}Si_{41.4}\square_{0.9}$ (bottom).

Atom	**Site**	***x***	***y***	***z***	U_{eq}	***Occ.***
Ba1	2*a*	0	0	0	0.00949(5)	1.0
Ba2	24*k*	0.2474(8)	0.5163(3)	0	0.0159(5)	0.25
Ni1/Si1	6*c*	1/4	0	1/2	0.0086(2)	0.433/0.55(1)
Si2	16*i*	0.18461(6)	*x*	*x*	0.00814(8)	1.0
Si31	24*k*	0	0.3087(2)	0.1164(2)	0.0089(3)	0.567(4)
Si32	24*k*	0	0.3148(2)	0.1279(2)	0.0097(4)	0.433

Atom	U_{11}	U_{22}	U_{33}	U_{12}	U_{13}	U_{23}
Ba1	0.00949(8)	U_{11}	U_{11}	0	0	0
Ba2	0.0122(5)	0.0145(6)	0.0211(10)	0.0040(6)	0	0
Ni1/Si1	0.0097(4)	0.0080(3)	U_{22}	0	0	0
Si2	0.0081(1)	U_{11}	U_{11}	-0.0008(1)	U_{12}	U_{12}
Si31	0.0095(5)	0.0068(5)	0.0106(5)	0	0	0.0012(4)
Si32	0.0066(6)	0.0128(7)	0.0098(7)	0	0	0.0020(6)

Atom	**Site**	***x***	***y***	***z***	U_{eq}	***Occ.***
Ba1	2*a*	0	0	0	0.00899(5)	1.0
Ba2	24*k*	0.24105(7)	0.51441(7)	0	0.0151(5)	0.25
Ni1/Si1	6*c*	1/4	0	1/2	0.0073(2)	0.533 / 0.404(7)
Si2	16*i*	0.18434(5)	*x*	*x*	0.00796(8)	1.0
Si31	24*k*	0	0.3067(2)	0.1122(2)	0.0063(4)	0.405(3)
Si32	24*k*	0	0.3151(2)	0.1281(2)	0.0074(3)	0.533
Si33	24*k*	0	0.3278(13)	0.1325(13)	0.009(2)*	0.063(3)

Atom	U_{11}	U_{22}	U_{33}	U_{12}	U_{13}	U_{23}
Ba1	0.00899(9)	U_{11}	U_{11}	0	0	0
Ba2	0.0019(2)	0.0118(10)	0.0315(10)	0.0027(5)	0	0
Ni1/Si1	0.0079(5)	0.0069(3)	U_{22}	0	0	0
Si2	0.0080(1)	U_{11}	U_{11}	-0.0006(2)	U_{12}	U_{12}
Si31	0.0082(7)	0.0069(7)	0.0037(7)	0	0	-0.0025(6)
Si32	0.0073(5)	0.0066(5)	0.0082(5)	0	0	-0.0001(4)

Atom	**Site**	***x***	***y***	***z***	U_{eq}	***Occ.***
Ba1	2*a*	0	0	0	0.01052(5)	1.0
Ba2	24*k*	0.24311(9)	0.51155(9)	0	0.0214(8)	0.25
Ni1/Si1	6*c*	1/4	0	1/2	0.0088(2)	0.617 / 0.231(8)
Si2	16*i*	0.18434(5)	*x*	*x*	0.00981(7)	1.0
Si31	24*k*	0	0.3072(3)	0.1094(3)	0.0076(6)	0.232(3)
Si32	24*k*	0	0.3122(1)	0.1231(1)	0.0099(3)	0.617
Si33	24*k*	0	0.3216(5)	0.1343(5)	0.0080(9)	0.152(4)

Atom	U_{11}	U_{22}	U_{33}	U_{12}	U_{13}	U_{23}
Ba1	0.01052(8)	U_{11}	U_{11}	0	0	0
Ba2	0.0085(2)	0.019(2)	0.037(2)	-0.0008(7)	0	0
Ni1/Si1	0.0090(3)	0.0082(2)	U_{22}	0	0	0
Si2	0.0098(1)	U_{11}	U_{11}	-0.0006(1)	U_{12}	U_{12}
Si31	0.0048(9)	0.0095(11)	0.0086(10)	0	0	-0.0006(8)
Si32	0.0119(4)	0.0089(4)	0.0089(4)	0	0	0.0016(3)
Si33	0.0040(2)	0.008(2)	0.012(2)	0	0	-0.0027(14)

*U_{iso}.

Table 11.16: Interatomic distances with multiplicity *n* for the single crystal of $Ba_8Ni_{2.6}Si_{43.3}\square_{0.1}$. The sites Si31 and Si32 represent alternatively occupied positions of the site Si3.

Atoms		*n*	*d* / Å	Atoms		*n*	*d* / Å
Ba1	– Si2	8 ×	3.2929(6)	Ni1	– Si32	4 ×	2.284(2)
	– Si31	12 ×	3.399(2)	Si1	– Si31	4 ×	2.402(2)
	– Si32	12 ×	3.500(2)				
Ba2	– Si31	2 ×	3.343(6)	Si2	– Si2	1 ×	2.3327(8)
	– Si32	2 ×	3.354(6)		– Si31	3 ×	2.396(1)
	– Si31	2 ×	3.421(6)		– Si32	3 ×	2.399(2)
	– Si32	2 ×	3.423(6)				
	– Si31	2 ×	3.536(6)	Si31	– Si2	2 ×	2.396(1)
	– Si31	2 ×	3.537(6)		– Si31	1 ×	2.398(2)
	– Si32	2 ×	3.541(6)		– Si1	1 ×	2.402(2)
	– Ni1/Si1	1 ×	3.543(6)		– Si32	1 ×	2.517(3)
	– Si32	2 ×	3.551(6)				
	– Ni1/Si1	2 ×	3.627(6)	Si32	– Ni1	1 ×	2.284(2)
	– Si2	2 ×	3.676(3)		– Si2	2 ×	2.399(2)
	– Si32	1 ×	3.728(4)		– Si31	1 ×	2.517(3)
	– Si2	2 ×	3.747(2)		– Si32	1 ×	2.635(3)
	– Ni1/Si1	1 ×	3.780(6)				
	– Si31	1 ×	3.834(4)				
	– Si32	2 ×	3.889(3)				
	– Si2	2 ×	3.914(2)				
	– Si2	2 ×	3.963(3)				
	– Si31	2 ×	3.996(2)				
	– Si32	1 ×	4.060(4)				
	– Si31	1 ×	4.167(4)				

Table 11.17: Interatomic distances with multiplicity *n* for the single crystal of $Ba_8Ni_{3.2}Si_{42.4}\square_{0.4}$. The sites Si31, Si32 and Si33 represent alternatively occupied positions of the site Si3.

Atoms		*n*	*d* / Å	Atoms		*n*	*d* / Å
Ba1	– Si2	8 ×	3.2862(6)	□	– Si33	4 ×	2.146(13)
	– Si31	12 ×	3.361(2)	Ni1	– Si32	4 ×	2.279(2)
	– Si32	12 ×	3.502(2)	Si1	– Si31	4 ×	2.443(2)
	– Si33	12 ×	3.639(13)				
Ba2	– Si33	2 ×	3.264(9)	Si2	– Si2	1 ×	2.3409(8)
	– Si31	2 ×	3.298(2)		– Si31	3 ×	2.395(1)
	– Si32	2 ×	3.312(1)		– Si32	3 ×	2.397(1)
	– Si33	2 ×	3.421(9)		– Si33	3 ×	2.463(8)
	– Si33	2 ×	3.424(8)				
	– Si31	2 ×	3.473(2)	Si31	– Si31	1 ×	2.311(3)
	– Si31	2 ×	3.475(1)		– Si2	2 ×	2.395(1)
	– Si32	2 ×	3.477(1)		– Si1	1 ×	2.443(2)
	– Si32	2 ×	3.479(1)		– Si32	1 ×	2.476(2)
	– Si33	2 ×	3,540(9)		– Si33	1 ×	2.528(13)
	– Si31	2 ×	3.572(1)				
	– Ni1/Si1	2 ×	3,5774(5)	Si32	– Ni1	1 ×	2.279(2)
	– Si32	2 ×	3.588(1)		– Si2	2 ×	2.397(1)
	– Ni1/Si1	1 ×	3.6031(8)		– Si31	1 ×	2.476(2)
	– Si2	2 ×	3.68151(9)		– Si32	1 ×	2.638(2)
	– Si33	1 ×	3.742(13)		– Si33	1 ×	2.685(13)
	– Si32	1 ×	3.757(2)				
	– Si2	2 ×	3.7687(7)	Si33	– □	1 ×	2.146(13)
	– Ni1/Si1	1 ×	3.8091(8)		– Si2	2 ×	2.463(8)
	– Si33	2 ×	3.851(13)		– Si31	1 ×	2.528(13)
	– Si32	2 ×	3.874(2)		– Si32	1 ×	2.685(13)
	– Si31	1 ×	3.901(2)		– Si33	1 ×	2.73(2)
	– Si2	2 ×	3.9152(7)				
	– Si2	2 ×	3.9346(9)				
	– Si31	2 ×	4.024(2)				
	– Si33	1 ×	4.031(13)				
	– Si32	1 ×	4.048(2)				
	– Si31	1 ×	4.194(2)				

Table 11.18: Interatomic distances with multiplicity *n* for the single crystal of $Ba_8Ni_{3.7}Si_{41.4}\square_{0.9}$. The sites Si31, Si32 and Si33 represent alternatively occupied positions of the site Si3.

Atoms		*n*	*d* / Å	Atoms		*n*	*d* / Å
Ba1	– Si2	8 ×	3.2857(5)	□	– Si33	4 ×	2.188(5)
	– Si31	12 ×	3.356(3)	Ni1	– Si32	4 ×	2.332(1)
	– Si32	12 ×	3.454(1)	Si1	– Si31	4 ×	2.455(3)
	– Si33	12 ×	3.587(5)				
Ba2	– Si31	2 ×	3.318(2)	Si2	– Si2	1 ×	2.3405(7)
	– Si33	2 ×	3.334(3)		– Si32	3 ×	2.3935(9)
	– Si32	2 ×	3.339(1)		– Si31	3 ×	2.406(2)
	– Si31	2 ×	3.455(2)		– Si33	3 ×	2.420(3)
	– Si31	2 ×	3.457(2)				
	– Si33	2 ×	3.457(3)	Si31	– Si31	1 ×	2.253(4)
	– Si33	2 ×	3.463(3)		– Si32	1 ×	2.394(3)
	– Si32	2 ×	3.470(1)		– Si2	2 ×	2.406(2)
	– Si33	2 ×	3.474(1)		– Si1	1 ×	2.455(3)
	– Si31	2 ×	3.532(2)		– Si33	1 ×	2.513(6)
	– Si33	2 ×	3,551(3)				
	– Si32	2 ×	3.555(1)	Si32	– Ni1	1 ×	2.332(1)
	– Ni1/Si1	2 ×	3.5905(7)		– Si2	2 ×	2.3935(9)
	– Ni1/Si1	1 ×	3.607(1)		– Si31	1 ×	2.394(3)
	– Si2	2 ×	3.709(1)		– Si32	1 ×	2.534(2)
	– Si33	1 ×	3.732(5)		– Si33	1 ×	2.651(5)
	– Ni1/Si1	1 ×	3.773(1)				
	– Si2	2 ×	3.7776(7)	Si33	– □	1 ×	2.188(5)
	– Si33	2 ×	3.823(5)		– Si2	2 ×	2.420(3)
	– Si32	1 ×	3.826(2)		– Si31	1 ×	2.513(6)
	– Si2	2 ×	3.8952(7)		– Si32	1 ×	2.651(5)
	– Si2	2 ×	3.912(1)		– Si33	1 ×	2.765(7)
	– Si32	2 ×	3.922(1)				
	– Si31	1 ×	3.955(3)				
	– Si33	1 ×	3.965(5)				
	– Si31	2 ×	4.054(3)				
	– Si32	1 ×	4.060(2)				
	– Si31	1 ×	4.190(3)				

Table 11.19: Atomic coordinates, displacement parameters (in Å^2) and site occupancies for $Ba_{7.88(2)}Ni_{1.39(3)}Si_{44.61(3)}$.

Atom	**Site**	***x***	***y***	***z***	U_{eq}	***Occ.***
Ba1	2*a*	0	0	0	0.0115(6)	0.938(3)
Ba2	24*k*	0.248(2)	0.5164(7)	0	0.0139(11)	¼
Ni1/Si1	6*c*	¼	0	½	0.0101(10)	0.231(5)/0.769(5)
Si2	16*i*	0.1850(1)	*x*	*x*	0.0103(7)	1
Si3	24*k*	0	0.3093(2)	0.1213(2)	0.0114(5)	1

Table 11.20: Atomic coordinates, displacement parameters (in Å^2) and site occupancies for $Ba_{7.90(2)}Ni_{1.60(4)}Si_{44.40(4)}$.

Atom	**Site**	***x***	***y***	***z***	U_{eq}	***Occ.***
Ba1	2*a*	0	0	0	0.0127(7)	0.951(3)
Ba2	24*k*	0.2533(9)	0.5168(3)	0	0.0175(14)	¼
Ni1/Si1	6*c*	¼	0	½	0.0123(11)	0.267(7)/0.733(7)
Si2	16*i*	0.1847(1)	*x*	*x*	0.0128(7)	1
Si3	24*k*	0	0.3098(2)	0.1219(2)	0.0137(6)	1

Table 11.21: Crystallographic data of Ba_3Si_4.

Formula; molar mass (g mol^{-1})	Ba_3Si_4; 524.323
Crystal system; space group	Tetragonal; $P4_2/mnm$ (no. 136)
a; c (Å)	8.5233(3); 11.8322(6)
Unit cell volume (Å^3)	859.57(6)
Z; ρ_{calc} (g cm^{-3})	4; 4.052
Diffractometer	RIGAKU Spider
λ(Å); monochromator	0.56087; multilayer-optics
Crystal size (µm^3)	$40 \times 50 \times 70$
T (K)	295
θ range (°)	2.67 to 40.00
Indexes ranges	$-19 \leq h \leq 13$, $-18 \leq k \leq 10$, $-26 \leq l \leq 20$
μ (mm^{-1})	7.424
F(000) (e)	896
Absorption correction	Multi-scan
Reflections collected; independent	24327; 2931 [R_{int} = 0.017]
Refinement method	Full-matrix least-squares on F^2
Refined parameters	24
Residuals [$I > 2\sigma(I)$]	$R1$ = 0.015, $wR2$ = 0.023
Residuals (all data)	$R1$ = 0.021, $wR2$ = 0.024
Goodness-of-fit on F^2	1.212
Extinction coefficient	0.00471(12)
Largest diff. peak and hole (eÅ^{-3})	1.372 and −0.973

Table 11.22: Atomic coordinates and displacement parameters (in Å^2) for Ba_3Si_4.

Atom	**Site**	***x***	***y***	***z***	U_{eq}
Ba(1)	4*f*	0.33515(1)	*x*	0	0.01466(2)
Ba(2)	4*e*	0	0	0.16963(1)	0.01031(1)
Ba(3)	4*d*	0	½	1/4	0.01212(1)
Si(1)	8*i*	0.90055(3)	0.30007(3)	0	0.01134(4)
Si(2)	8*j*	0.20077(3)	*x*	0.35403(3)	0.01359(5)
Atom	U_{11}	U_{22}	U_{33}	$U_{23} = U_{13}$	U_{12}
Ba(1)	0.01296(2)	U_{11}	0.01805(3)	0	–0.00047(2)
Ba(2)	0.01111(2)	U_{11}	0.00871(2)	0	0.00067(2)
Ba(3)	0.01186(2)	U_{11}	0.01264(3)	0	0
Si(1)	0.01005(9)	0.01263(10)	0.01135(9)	0	–0.00111(8)
Si(2)	0.01303(6)	U_{11}	0.01472(11)	−0.00326(6)	0.00064(8)

U_{eq} is defined as one third of the trace of the orthogonalized U_{ij} tensor, which is exp $(-2\pi^2 [h^2 a^{*2} U_{11} + ... + 2\, h\, k\, a^* b^*\, U_{12}])$.

Table 11.23: Interatomic distances for Ba_3Si_4 with multiplicity *n*.

Atoms		*n*	*d* / Å
Ba(1)	– Si(2)	4 ×	3.5761(3)
	– Si(1)	2 ×	3.7017(3)
	– Si(1)	2 ×	3.7163(3)
Ba(2)	– Si(2)	2 ×	3.2584(3)
	– Si(1)	4 ×	3.3598(3)
	– Si(2)	2 ×	3.6177(3)
Ba(3)	– Si(2)	4 ×	3.3088(2)
	– Si(1)	4 ×	3.5174(2)
Si(1)	– Si(1)	1 ×	2.4183(6)
	– Si(2)	2 ×	2.4254(3)
	– Ba(2)	2 ×	3.3598(3)
	– Ba(3)	2 ×	3.5174(2)
	– Ba(1)	1 ×	3.7017(3)
	– Ba(1)	1 ×	3.7163(3)
Si(2)	– Si(1)	2 ×	2.4254(3)
	– Ba(2)	2 ×	3.2584(3)
	– Ba(3)	2 ×	3.3088(2)
	– Ba(1)	2 ×	3.5761(3)

Table 11.24: Crystallographic data for single crystals of $ZnSiP_2$ (UA_MG02e) and $CuAlS_2$ (UA_MG128). Lattice parameters are calculated based on the PXRD data.

	$ZnSiP_2$	**$CuAlS_2$**
Formula; molar mass (g mol^{-1})	$ZnSiP_2$; 155.436	$CuAlS_2$; 154.67
Crystal system; space group	Tetragonal; $I\bar{4}2d$ (no. 122)	Tetragonal; $I\bar{4}2d$ (no. 122)
a; c (Å)	5.3995(1); 10.4386(3)	5.3342(1); 10.4396(3)
Number of reflections (PXRD)	37	37
Unit cell volume (Å^3)	304.333(12)	297.045(12)
Z; ρ_{calc} (g cm^{-3})	4; 3.392	4; 3.458
Diffractometer	RIGAKU Spider	RIGAKU Spider
λ (Å); monochromator	0.56087; multilayer-optics	0.56087; multilayer-optics
Crystal size (µm^3)	45×50×55	40×80×140
T (K)	295	295
2θ –range (°)	3.3 to 69.2	5.3 to 69.4
Indexes ranges	$-17 \le h \le 17$, $-17 \le k \le 10$, $-25 \le l \le 27$	$-5 \le h \le 17$, $-12 \le k \le 14$, $-31 \le l \le 22$
μ (mm^{-1})	4.782	4.525
F(000) (e)	296	296
Absorption correction	Multi-scan	Multi-scan
Reflections collected; unique	14438; 2439 [R_{int} = 2.27]	5115; 2212 [R_{int} = 2.21]
Refined parameters	11	11
Refinement method	Full-matrix least-squares on F^2	Full-matrix least-squares on F^2
$R1$; $wR2$ ($I > 2\sigma(I)$)	0.021; 0.036	0.04; 0.06
$R1$; $wR2$ (all data)	0.035; 0.047	0.069; 0.060
Goodness-of-fit on F^2	1.34	1.04
Extiction coefficient	0.098(3)	0.133(5)
Flack parameter	-0.002(4)	-0.007(10)
Largest diff. peak and hole	2.31 and -2.23	1.03 and -1.79

Table 11.25: Atomic coordinates and displacement parameters (in Å^2) for $ZnSiP_2$.

Atom	**Site**	***x***	***y***	***z***	U_{eq}	***Occ.***
Zn	4*a*	0	0	0	0.00883(2)	1.0
Si	4*b*	0	0	1/2	0.00579(2)	1.0
P	8*d*	0.27017(2)	1/4	1/8	0.00620(2)	1.0

Atom	U_{11}	U_{22}	U_{33}	U_{23}	U_{13}	U_{12}
Zn	0.00862(2)	U_{11}	0.00924(4)	0	0	0
Si	0.00595(3)	U_{11}	0.00549(7)	0	0	0
P	0.00613(3)	0.00621(3)	0.00625(6)	0.00060(2)	0	0

Table 11.26: Atomic coordinates and displacement parameters (in Å^2) for $CuAlS_2$.

Atom	**Site**	***x***	***y***	***z***	U_{eq}	***Occ.***
Cu	4*a*	0	0	0	0.01570(4)	1.0
Al	4*b*	0	0	1/2	0.00747(5)	1.0
S	8*d*	0.26247(3)	1/4	1/8	0.00767(3)	1.0

Atom	U_{11}	U_{22}	U_{33}	U_{23}	U_{13}	U_{12}
Cu	0.01539(5)	U_{11}	0.01632(6)	0	0	0
Al	0.00760(6)	U_{11}	0.00721(9)	0	0	0
S	0.00722(5)	0.00778(5)	0.00800(5)	0.00100(4)	0	0

U_{eq} is defined as one third of the trace of the orthogonalized U_{ij} tensor, which is exp $(-2\pi^2 [h^2 a^{*2} U_{11} + ... + 2\, h\, k\, a^*\, b^*\, U_{12}])$.

Table 11.27: Bond angles in the crystal structures of $ZnSiP_2$ and $CuAlS_2$ with multiplicity *n*.

$ZnSiP_2$					$CuAlS_2$				
Atoms			***n***	**Angle (°)**	**Atoms**			***n***	**Angle (°)**
P	Zn	P	4 ×	107.529(1)	S	Cu	S	4 ×	108.237(2)
			2 ×	113.429(3)				2 ×	113.969(4)
P	Si	P	4 ×	109.643(2)	S	Al	S	4 ×	109.559(2)
			2 ×	109.128(3)				2 ×	109.259(2)
Si	P	Si	1 ×	113.071(5)	Al	S	Al	1 ×	111.641(7)
Si	P	Zn	2 ×	108.420(1)	Al	S	Cu	2 ×	108.835(1)
			2 ×	111.142(2)				2 ×	110.581(2)
Zn	P	Zn	1 ×	104.305(5)	Cu	S	Cu	1 ×	106.232(7)

References

1. D. M. Rowe, *Thermoelectrics Handbook : Macro to Nano*, CRC ; London : Taylor & Francis [distributor], Boca Raton, Fla., 2006.
2. G. S. Nolas, G. A. Slack and S. B. Schujman, *Semiconductors and Semimetals*, Academic Press, San Diego, CA, 2001.
3. G. J. Snyder and E. S. Toberer, *Nat. Mater.*, 2008, **7**, 105-114.
4. M. Christensen, S. Johnsen and B. B. Iversen, *Dalton Trans.*, 2010, **39**, 978-992.
5. Y. Mudryk, P. Rogl, C. Paul, S. Berger, E. Bauer, G. Hilscher, C. Godart and H. Noël, *J. Phys.: Condens. Matter*, 2002, **14**, 7991.
6. S. Yamanaka, *Dalton Trans.*, 2010, **39**, 1901-1915.
7. H. Kleinke, *Chem. Mater.*, 2010, **22**, 604-611.
8. A. Saramat, G. Svensson, A. E. C. Palmqvist, C. Stiewe, E. Mueller, D. Platzek, S. G. K. Williams, D. M. Rowe, J. D. Bryan and G. D. Stucky, *J. Appl. Phys.*, 2006, **99**, 023708.
9. X. Shi, J. Yang, S. Q. Bai, J. H. Yang, H. Wang, M. F. Chi, J. R. Salvador, W. Q. Zhang, L. D. Chen and W. Wong-Ng, *Adv. Funct. Mater.*, 2010, **20**, 755-763.
10. H. Zhang, H. Borrmann, N. Oeschler, C. Candolfi, W. Schnelle, M. Schmidt, U. Burkhardt, M. Baitinger, J. T. Zhao and Y. Grin, *Inorg. Chem.*, 2011, **50**, 1250-1257.
11. V. L. Kuznetsov, L. A. Kuznetsova, A. E. Kaliazin and D. M. Rowe, *J. Appl. Phys.*, 2000, **87**, 7871-7875.
12. W. Carrillo-Cabrera, S. Budnyk, Y. Prots and Y. Grin, *Z. Anorg. Allg. Chem.*, 2004, **630**, 2267-2276.
13. N. L. Okamoto, M. W. Oh, T. Nishii, K. Tanaka and H. Inui, *J. Appl. Phys.*, 2006, **99**, 033513.
14. N. L. Okamoto, K. Tanaka and H. Inui, *Acta Mater.*, 2006, **54**, 173-178.
15. U. Aydemir, C. Candolfi, H. Borrmann, M. Baitinger, A. Ormeci, W. Carrillo-Cabrera, C. Chubilleau, B. Lenoir, A. Dauscher, N. Oeschler, F. Steglich and Y. Grin, *Dalton Trans.*, 2010, **39**, 1078-1088.
16. C. Candolfi, U. Aydemir, M. Baitinger, N. Oeschler, F. Steglich and Y. Grin, *J. Electron. Mater.*, 2010, **39**, 2039-2042.
17. U. Aydemir, L. Akselrud, W. Carrillo-Cabrera, C. Candolfi, N. Oeschler, M. Baitinger, F. Steglich and Y. Grin, *J. Am. Chem. Soc.*, 2010, **132**, 10984-10985.
18. C. Candolfi, U. Aydemir, A. Ormeci, W. Carrillo-Cabrera, U. Burkhardt, M. Baitinger, N. Oeschler, F. Steglich and Y. Grin, *J. Appl. Phys.*, 2011, **110**, 043715.
19. W. Carrillo-Cabrera, H. Borrmann, S. Paschen, M. Baenitz, F. Steglich and Y. Grin, *J. Solid State Chem.*, 2005, **178**, 715-728.

20. W. Carrillo-Cabrera, J. Curda, H. G. von Schnering, S. Paschen and Y. Grin, *Z. Kristallogr. NCS*, 2000, **215**, 207-208.
21. H. Fukuoka, Iwai, K., Yamanaka,S., Abe,H.,Yoza, K., Haming, L., *J. Solid State Chem.*, 2000, **151**, 117-121.
22. L. T. K. Nguyen, U. Aydemir, M. Baitinger, E. Bauer, H. Borrmann, U. Burkhardt, J. Custers, A. Haghighirad, R. Hofler, K. D. Luther, F. Ritter, W. Assmus, Y. Grin and S. Paschen, *Dalton Trans.*, 2010, **39**, 1071-1077.
23. L. T. K. Nguyen, U. Aydemir, M. Baitinger, J. Custers, A. Haghighirad, R. Hofler, K. D. Luther, F. Ritter, Y. Grin, W. Assmus and S. Paschen, *J. Electron. Mater.*, 2010, **39**, 1386-1389.
24. C. Candolfi, U. Aydemir, A. Ormeci, M. Baitinger, N. Oeschler, F. Steglich and Y. Grin, *Phys. Rev. B*, 2011, **83**, 205102.
25. Eisenman.B, K. H. Janzon, H. Schäfer and A. Weiss, *Z. Naturforsch. Pt. B.*, 1969, **24**, 457-458.
26. U. Aydemir, A. Ormeci, H. Borrmann, B. Bohme, F. Zurcher, B. Uslu, T. Goebel, W. Schnelle, P. Simon, W. Carrillo-Cabrera, F. Haarmann, M. Baitinger, R. Nesper, H. G. von Schnering and Y. Grin, *Z. Anorg. Allg. Chem.*, 2008, **634**, 1651-1661.
27. A. F. Wells, *Structural Inorganic Chemistry*, Clarendon, Oxford, 1984.
28. H. M. Powell, *J. Chem. Soc.*, 1948, 61-73.
29. H. Davy, *Philos. Trans. R. Soc. London*, 1811, **101**, 155-162.
30. M. Faraday, *Quarterly J. Sci.*, 1823, **15**, 71-74.
31. W. F. Claussen, *J. Chem. Phys.*, 1951, **19**, 1425-1426.
32. L. Pauling and R. E. Marsh, *P. Natl. Acad. Sci. USA*, 1952, **38**, 112-118.
33. O. G. M. von Stackelberg, J. Pietuchovsky, O. Witscher, H. Fruhbuss, and W. Meinhold, *Fortschr. Mineral.*, 1947, **26**, 122.
34. K. A. Kovnir and A. V. Shevelkov, *Russ. Chem. Rev.*, 2004, **73**, 923-938.
35. C. Cros, M. Pouchard and Hagenmul.P, *Compt. Rend. Hebd. Seances Acad. Sci.*, 1965, **260**, 4764-4767.
36. J. S. Kasper, Hagenmul.P, M. Pouchard and C. Cros, *Science*, 1965, **150**, 1713-1714.
37. C. Cros, M. Pouchard, Hagenmul.P and J. S. Kasper, *Bull. Soc. Chim. Fr.*, 1968, 2737-2742.
38. J. Gallmeier, H. Schäfer and A. Weiss, *Z. Naturforsch. Pt. B.*, 1969, **B 24**, 665-667.
39. G. A. Jeffrey, *Hydrate Inclusion Compounds*, Academic Press, New York, 1984.
40. T. C. W. Mak and G. D. Zhou, *Crystallography in Modern Chemistry*, New York, 1992.
41. A. Muller, H. Reuter and S. Dillinger, *Angew. Chem. Int. Edit.*, 1995, **34**, 2328-2361.
42. S. M. Kauzlarich, *Chemistry, Structure, and Bonding of Zintl Phases and Ions*, VCH, New York ; Cambridge, 1996.

43. H. G. von Schnering and H. Menke, *Angew. Chem. Int. Edit.*, 1972, **11**, 43-44.
44. H. Menke and H. G. von Schnerin, *Z. Anorg. Allg. Chem.*, 1973, **395**, 223-238.
45. M. M. Shatruk, K. A. Kovnir, A. V. Shevelkov, I. A. Presniakov and B. A. Popovkin, *Inorg. Chem.*, 1999, **38**, 3455-3457.
46. M. M. Shatruk, K. A. Kovnir, M. Lindsjo, I. A. Presniakov, L. A. Kloo and A. V. Shevelkov, *J. Solid State Chem.*, 2001, **161**, 233-242.
47. S. Bobev and S. C. Sevov, *J. Solid State Chem.*, 2000, **153**, 92-105.
48. G. S. Nolas, T. J. R. Weakley and J. L. Cohn, *Chem. Mater.*, 1999, **11**, 2470-2473.
49. S. J. Kim, S. Q. Hu, C. Uher, T. Hogan, B. Q. Huang, J. D. Corbett and M. G. Kanatzidis, *J. Solid State Chem.*, 2000, **153**, 321-329.
50. B. C. Chakoumakos, B. C. Sales and D. G. Mandrus, *J. Alloys Compd.*, 2001, **322**, 127-134.
51. S. Paschen, V. Pacheco, A. Bentien, A. Sanchez, W. Carrillo-Cabrera, M. Baenitz, B. B. Iversen, Y. Grin and F. Steglich, *Physica B*, 2003, **328**, 39-43.
52. S. Paschen, W. Carrillo-Cabrera, A. Bentien, V. H. Tran, M. Baenitz, Y. Grin and F. Steglich, *Phys. Rev. B*, 2001, **64**, 214404.
53. B. C. Chakoumakos, B. C. Sales, D. G. Mandrus and G. S. Nolas, *J. Alloys Compd.*, 2000, **296**, 80-86.
54. A. Bentien, A. E. C. Palmqvist, J. D. Bryan, S. Latturner, G. D. Stucky, L. Furenlid and B. B. Iversen, *Angew. Chem. Int. Edit.*, 2000, **39**, 3613-3616.
55. N. P. Blake, D. Bryan, S. Latturner, L. Mollnitz, G. D. Stucky and H. Metiu, *J. Chem. Phys.*, 2001, **114**, 10063-10074.
56. W. Jung, J. Loerincz, R. Ramlau, H. Borrmann, Y. Prots, F. Haarniann, W. Schnelle, U. Burkhardt, M. Baitinger and Y. Grin, *Angew. Chem. Int. Edit.*, 2007, **46**, 6725-6728.
57. H. G. von Schnering, *Nova Acta Leopold.*, 1985, **59**, 168 -182.
58. H. G. von Schnering, J. Llanos, K. Peters, M. Baitinger, Y. Grin and R. Nesper, *Z. Kristallogr. NCS*, 2011, **226**, 9-10.
59. F. Dubois and T. F. Fassler, *J. Am. Chem. Soc.*, 2005, **127**, 3264-3265.
60. A. Kaltzoglou, S. D. Hoffmann and T. F. Fassler, *Eur. J. Inorg. Chem.*, 2007, 4162-4167.
61. W. P. Cordier G., *J. Less-Common Met.*, 1991, **169**, 291-302.
62. S. Bobev and S. C. Sevov, *J. Am. Chem. Soc.*, 1999, **121**, 3795-3796.
63. R. Kröner, K. Peters, H. G. von Schnering and R. Nesper, *Z. Kristallogr. NCS*, 1998, **213**, 664.
64. J. Gryko, P. F. McMillan, R. F. Marzke, G. K. Ramachandran, D. Patton, S. K. Deb and O. F. Sankey, *Phys. Rev. B*, 2000, **62**, R7707-R7710.
65. A. Ammar, C. Cros, M. Pouchard, N. Jaussaud, J. M. Bassat, G. Villeneuve, M. Duttine, M. Menetrier and E. Reny, *Solid State Sci.*, 2004, **6**, 393-400.

66. A. M. Guloy, R. Ramlau, Z. J. Tang, W. Schnelle, M. Baitinger and Y. Grin, *Nature*, 2006, **443**, 320-323.
67. M. Beekman, M. Baitinger, H. Borrmann, W. Schnelle, K. Meier, G. S. Nolas and Y. Grin, *J. Am. Chem. Soc.*, 2009, **131**, 9642-9643.
68. S. Bobev and S. C. Sevov, *J. Am. Chem. Soc.*, 2001, **123**, 3389-3390.
69. J. V. Zaikina, K. A. Kovnir, F. Haarmann, W. Schnelle, U. Burkhardt, H. Borrmann, U. Schwarz, Y. Grin and A. V. Shevelkov, *Chem.-Eur. J.*, 2008, **14**, 5414-5422.
70. J. L. Atwood, J. E. D. Davies and D. D. MacNicol, *Inclusion Compounds*, Academic Press, London ; Orlando, 1984.
71. B. Eisenmann, H. Schäfer and R. Zagler, *J. Less-Common Met.*, 1986, **118**, 43-55.
72. Y. Li, J. Gao, N. Chen, Y. Liu, Z. P. Luo, R. H. Zhang, X. Q. Ma and G. H. Cao, *Physica B*, 2008, **403**, 1140-1141.
73. S. Srinath, J. Gass, D. J. Rebar, G. T. Woods, H. Srikanth and G. S. Nolas, *J. Appl. Phys.*, 2006, **99**, 08K902.
74. H. G. von Schnering, R. Kroner, W. Carrillo-Cabrera, K. Peters and R. Nesper, *Z. Kristallogr. NCS*, 1998, **213**, 665-666.
75. H. G. von Schnering, A. Zurn, J. H. Chang, M. Baitinger and Y. Grin, *Z. Anorg. Allg. Chem.*, 2007, **633**, 1147-1153.
76. H. Fukuoka, K. Ueno and S. Yamanaka, *J. Organomet. Chem.*, 2000, **611**, 543-546.
77. T. F. Fassler and C. Kronseder, *Z. Anorg. Allg. Chem.*, 1998, **624**, 561-568.
78. F. C. Frank and J. S. Kasper, *Acta Crystallogr*, 1959, **12**, 483-499.
79. M. O'Keeffe, G. B. Adams and O. F. Sankey, *Philos. Mag. Lett.*, 1998, **78**, 21-28.
80. S. Bobev and S. C. Sevov, *Inorg. Chem.*, 2000, **39**, 5930-5937.
81. X. Zhang, Y. B. Park, T. Hogan, J. L. Schindler, C. R. Kannewurf, S. Seong, T. Albright and M. G. Kanatzidis, *J. Am. Chem. Soc.*, 1995, **117**, 10300-10310.
82. R. Patschke, X. Zhang, D. Singh, J. Schindler, C. R. Kannewurf, N. Lowhorn, T. Tritt, G. S. Nolas and M. G. Kanatzidis, *Chem. Mater.*, 2001, **13**, 613-621.
83. S. Bobev and S. C. Sevov, *J. Am. Chem. Soc.*, 2002, **124**, 3359-3365.
84. N. Jaussaud, M. Pouchard, G. Goglio, C. Cros, A. Ammar, F. Weill and P. Gravereau, *Solid State Sci.*, 2003, **5**, 1193-1200.
85. H. Schäfer, B. Eisenman and W. Müller, *Angew. Chem. Int. Edit.*, 1973, **12**, 694-712.
86. H. G. von Schnering, *Angew. Chem. Int. Edit.*, 1981, **20**, 33-51.
87. E. Zintl and W. Dullenkopf, *Z. Phys. Chem. Abt. B*, 1932, **16**, 183-194.
88. W. Klemm, *P. Chem. Soc. London*, 1958, 329-341.
89. R. Kröner, K. Peters, H. G. von Schnering and R. Nesper, *Z. Kristallogr. NCS*, 1998, **213**, 667-668.
90. A. Bentien, E. Nishibori, S. Paschen and B. B. Iversen, *Phys. Rev. B*, 2005, **71**, 144107.

91. M. Christensen, N. Lock, J. Overgaard and B. B. Iversen, *J. Am. Chem. Soc.*, 2006, **128**, 15657-15665.
92. X. W. Hou, Y. F. Zhou, L. Wang, W. B. Zhang, W. Q. Zhang and L. D. Chen, *J. Alloys Compd.*, 2009, **482**, 544-547.
93. G. S. Nolas, J. M. Ward, J. Gryko, L. Qiu and M. A. White, *Phys. Rev. B*, 2001, **64**, 153201.
94. A. Wosylus, I. Veremchuk, W. Schnelle, M. Baitinger, U. Schwarz and Y. Grin, *Chem.-Eur. J.*, 2009, **15**, 5901-5903.
95. J. Llanos, Dissertation, Universität Stuttgart, 1984.
96. H. G. von Schnering, R. Kroner, M. Baitinger, K. Peters, R. Nesper and Y. Grin, *Z. Kristallogr. NCS*, 2000, **215**, 205-206.
97. C. Cros, M. Pouchard and P. Hagenmuller, *J. Solid State Chem.*, 1970, **2**, 570-581.
98. A. Grytsiv, N. Melnychenko-Koblyuk, N. Nasir, P. Rogl, A. Saccone and H. Schmid, *Int. J. Mater. Res.*, 2009, **100**, 189-202.
99. T. K. Kawaguchi T. , Yasukawa M., *Appl. Phys. Lett.*, 2000, **77**, 3438-3440.
100. S. Johnsen, A. Bentien, G. K. H. Madsen, M. Nygren and B. B. Iversen, *Phys. Rev. B*, 2007, **76**, 245126.
101. H. Zhang, J.-T. Zhao, M.-B. Tang, Z.-Y. Man, H.-H. Chen and X.-X. Yang, *J. Phys. Chem. Solids*, 2009, **70**, 312-315.
102. N. Melnychenko-Koblyuk, A. Grytsiv, P. Rogl, M. Rotter, E. Bauer, G. Durand, H. Kaldarar, R. Lackner, H. Michor, E. Royanian, M. Koza and G. Giester, *Phys. Rev. B*, 2007, **76**, 144118.
103. N. Melnychenko-Koblyuk, A. Grytsiv, P. Rogl, M. Rotter, R. Lackner, E. Bauer, L. Fornasari, F. Marabelli and G. Giester, *Phys. Rev. B*, 2007, **76**, 195124.
104. N. Melnychenko-Koblyuk, A. Grytsiv, P. Rogl, H. Schmid and G. Giester, *J. Solid State Chem.*, 2009, **182**, 1754-1760.
105. I. Zeiringer, M. Chen, I. Bednar, E. Royanian, E. Bauer, R. Podloucky, A. Grytsiv, P. Rogl and H. Effenberger, *Acta Mater.*, 2011, **59**, 2368-2384.
106. I. Zeiringer, N. Melnychenko-Koblyuk, A. Grytsiv, E. Bauer, G. Giester and P. Rogl, *J. Phase Equilib. Diff.*, 2011, **32**, 115-127.
107. E. Alleno, G. Maillet, O. Rouleau, E. Leroy, C. Godart, W. Carrillo-Cabrera, P. Simon and Y. Grin, *Chem. Mater.*, 2009, **21**, 1485-1493.
108. N. Melnychenko-Koblyuk, A. Grytsiv, L. Fornasari, H. Kaldarar, H. Michor, F. Rohrbacher, M. Koza, E. Royanian, E. Bauer, P. Rogl, M. Rotter, H. Schmid, F. Marabelli, A. Devishvili, M. Doerr and G. Giester, *J. Phys.: Condens. Matter*, 2007, **19**, 216223.
109. B. Kuhl, A. Czybulka and H.-U. Schuster, *Z. Anorg. Allg. Chem.*, 1995, **621**, 1-6.
110. A. Kaltzoglou, S. Ponou and T. F. Fässler, *Eur. J. Inorg. Chem.*, 2008, **2008**, 4507-4510.

111. P. Rogl, *Proceedings of the 24th International Conference on Thermoelectrics*, 2005, **IEEE**, 443.
112. R. Nesper, in *Silicon Chemistry*, eds. P. Jutzi and U. Schubert, Wiley-VCH, Weinheim; Cambridge, 2007, ch. 13, pp. 171-180.
113. R. Nesper and H. G. von Schnering, *TMPM Tschermaks Min. Petr. Mitt.*, 1983, **32**, 195-208.
114. H. Kawaji, H. Horie, S. Yamanaka and M. Ishikawa, *Phys. Rev. Lett.*, 1995, **74**, 1427-1429.
115. S. Yamanaka, E. Enishi, H. Fukuoka and M. Yasukawa, *Inorg. Chem.*, 2000, **39**, 56-58.
116. M. H. Phan, G. T. Woods, A. Chaturvedi, S. Stefanoski, G. S. Nolas and H. Srikanth, *Appl. Phys. Lett.*, 2008, **93**, 252505.
117. G. S. Nolas, T. J. R. Weakley, J. L. Cohn and R. Sharma, *Phys. Rev. B*, 2000, **61**, 3845-3850.
118. T. M. Tritt, *Recent Trends in Thermoelectric Materials Research I*, Academic Press, San Diego, Calif. ; London, 2001.
119. D. M. Rowe, *CRC Handbook of Thermoelectrics*, CRC Press, Boca Raton, Fl. ; London, 1995.
120. C. J. L. Nolas G. S., Slack G.A., Schujman S.B., *Appl. Phys. Lett.*, 1998, **73**, 178-180.
121. J. L. Cohn, Nolas, G.S., Fessatidis, V., Metcal, T.H., Slack, G.A., *Phys. Rev. Lett.*, 1999, **73**, 779-782.
122. J. D. Bryan, N. P. Blake, H. Metiu, G. D. Stucky, B. B. Iversen, D. R. Poulsen and A. Bentien, *J. Appl. Phys.*, 2002, **92**, 7281.
123. A. Bentien, Christensen, M., Bryan,J. D., Sanchez,A.,Paschen, S.,Steglich, F., Stucky,G.D., Iversen, B. B., *Phys. Rev. B*, 2004, **69**, 045107.
124. H. Anno, M. Hokazono, M. Kawamura, J. Nagao and K. Matsubara, *Proceedings of the 21st International Conference on Thermoelectrics*, 2002, 77-80.
125. M. Christensen, F. Juranyi and B. B. Iversen, *Physica B*, 2006, **385**, 505-507.
126. S. K. Deng, X. F. Tang and Q. J. Zhang, *J. Appl. Phys.*, 2007, **102**, 043702
127. S. K. Deng, X. F. Tang, P. Li and Q. J. Zhang, *J. Appl. Phys.*, 2008, **103**, 073503.
128. H. Anno, M. Hokazono, H. Takakura and K. Matsubara, *Proceedings of the 24th International Conference on Thermoelectrics*, 2005, 102 - 105
129. E. S. Toberer, M. Christensen, B. B. Iversen and G. J. Snyder, *Phys. Rev. B*, 2008, **77**, 075203.
130. S. Deng, Y. Saiga, K. Kajisa and T. Takabatake, *J. Appl. Phys.*, 2011, **109**, 103704.
131. STOE WinXPOW, Stoe & Cie GmbH, Darmstadt, 2.08 edn., 2003.
132. ICSD database, Fachinformationszentrum (FIZ) Karlsruhe 2009/01 edn., 2009.
133. L. G. Akselrud, P. Y. Zavalii, Y. Grin, V. K. Pecharsky, B. Baumgartner and E. Wölfel, *Mater. Sci. Forum*, 1993, **335**, 133-136.

134. H. M. Rietveld, *J. Appl. Crystallogr.*, 1969, **2**, 65-71.
135. ATOMS, Shape Software Kingsport, TN, 6.3.1 edn., 2006.
136. G. M. Sheldrick, *Acta Crystallogr. A*, 2008, **64**, 112-122.
137. L. J. Farrugia, *J. Appl. Crystallogr.*, 1999, **32**, 837-838.
138. M. Newville, *J. Synchrotron Radiat.*, 2001, **8**, 96-100.
139. M. Newville, *J. Synchrotron Radiat.*, 2001, **8**, 322-324.
140. B. Ravel and M. Newville, *J. Synchrotron Radiat.*, 2005, **12**, 537-541.
141. M. Bak, J. T. Rasmussen and N. C. Nielsen, *J. Magn. Reson.*, 2000, **147**, 296-330.
142. R. Turton, *The Physics of Solids*, New York : Oxford University Press, Oxford, 2000.
143. D. Jiles, *Introduction to the Electronic Properties of Materials*, Nelson Thornes, Cheltenham, 2001.
144. H. Eschrig, *Optimized LCAO Method and the Electronic Structure of Extended Systems*, Springer, Berlin, 1989.
145. K. Koepernik and H. Eschrig, *Phys. Rev. B*, 1999, **59**, 1743-1757.
146. G. Krier, O. Jepsen, A. Burkhardt and O. K. Andersen, Tight Binding LMTO-ASA Program, Max-Planck-Institut für Festkörperforschung, Stuttgart, 4.7 edn., 1999.
147. P. Hohenberg and W. Kohn, *Phys. Rev. B*, 1964, **136**, B864.
148. W. Kohn and L. J. Sham, *Phys. Rev.*, 1965, **140**, A1133-A1138.
149. J. P. Perdew and Y. Wang, *Phys. Rev. B*, 1992, **45**, 13244-13249.
150. U. V. Barth and L. Hedin, *J. Phys. C : Solid State Phys.*, 1972, **5**, 1629-1642.
151. O. K. Andersen, *Phys. Rev. B*, 1975, **12**, 3060-3083.
152. M. Kohout, *Int. J. Quantum Chem.*, 2004, **97**, 651-658.
153. M. Kohout, K. Pernal, F. R. Wagner and Y. Grin, *Theor. Chem. Acc.*, 2004, **112**, 453-459.
154. M. Kohout, K. Pernal, F. R. Wagner and Y. Grin, *Theor. Chem. Acc.*, 2005, **113**, 287-293.
155. M. Kohout, F. R. Wagner and Y. Grin, *Theor. Chem. Acc.*, 2008, **119**, 413-420.
156. F. R. Wagner, V. Bezugly, M. Kohout and Y. Grin, *Chem.-Eur. J.*, 2007, **13**, 5724-5741.
157. A. D. Becke and K. E. Edgecombe, *J. Chem. Phys.*, 1990, **92**, 5397-5403.
158. A. Ormeci, H. Rosner, F. R. Wagner, M. Kohout and Y. Grin, *J. Phys. Chem. A*, 2006, **110**, 1100-1105.
159. M. Kohout, E. R. Wagner and Y. Grin, *Int. J. Quantum Chem.*, 2006, **106**, 1499-1507.
160. M. Kohout, Program Basin, Max-Planck-Institut für Chemische Physik fester Stoffe, Dresden, 4.3 edn., 2008.
161. R. F. W. Bader, *Atoms in Molecules : A Quantum Theory*, Clarendon Press, Oxford, 1990.

162. W. Carrillo-Cabrera, J. Curda, K. Peters, S. Paschen, M. Baenitz, Y. Grin and H. G. von Schnering, *Z. Kristallogr. NCS*, 2000, **215**, 321-322.
163. H. Fukuoka, J. Kiyoto and S. Yamanaka, *J. Solid State Chem.*, 2003, **175**, 237-244.
164. T. K. Herrmann F.W., Kawaguchi T.,Kuroshima S. ,Zhou O., *Phys. Rev. B*, 1999, **60**, 13245-13248.
165. M. Pani and A. Palenzona, *J. Alloys Compd.*, 2008, **462**, L9-L11.
166. H. Okamoto, *J. Phase Equilib. Diff.*, 2009, **30**, 114-114.
167. J. J. Dong and O. F. Sankey, *J. Phys.: Condens. Matter*, 1999, **11**, 6129-6145.
168. J. J. Zhao, A. Buldum, J. P. Lu and C. Y. Fong, *Phys. Rev. B*, 1999, **60**, 14177-14181.
169. A. Weiss and H. Witte, *Magneto-Chemie Grundlagen und Anwendungen*, Verlag Chemie, Weinheim/Bergstr, 1973.
170. O. Madelung, U. Rössler and M. Schulz, *Group III Condensed Matter*, Landolt-Börnstein V41A1b, Springer-Verlag, Berlin, 2002.
171. A. P. Ramirez, R. C. Haddon, O. Zhou, R. M. Fleming, J. Zhang, S. M. Mcclure and R. E. Smalley, *Science*, 1994, **265**, 84-86.
172. R. C. Haddon, *Nature*, 1995, **378**, 249-255.
173. C. Candolfi, A. Ormeci, U. Aydemir, M. Baitinger, N. Oeschler, Y. Grin and F. Steglich, *Phys. Rev. B*, 2011, **84**, 205118.
174. C. Candolfi, A. Ormeci, U. Aydemir, M. Baitinger, N. Oeschler, Y. Grin and F. Steglich, *Phys. Rev. B*, 2011, **84**.
175. Y. Li, Y. Liu, N. Chen, G. H. Cao, Z. S. Feng and J. H. Ross, *Phys. Lett. A*, 2005, **345**, 398-408.
176. K. Tanigaki, T. Shimizu, K. M. Itoh, J. Teraoka, Y. Moritomo and S. Yamanaka, *Nat. Mater.*, 2003, **2**, 653-655.
177. M. A. Avila, K. Suekuni, K. Umeo, H. Fukuoka and T. Takabatake, *Phys. Rev. B*, 2006, **74**, 125109.
178. K. Suekuni, M. A. Avila, K. Umeo and T. Takabatake, *Phys. Rev. B*, 2007, **75**, 195210.
179. H. Shimizu, T. Iitaka, T. Fukushima, T. Kume, S. Sasaki, N. Sata, Y. Ohishi, H. Fukuoka and S. Yamanaka, *J. Appl. Phys.*, 2007, **101**, 063549.
180. C. B. C. Sales B. C. , Jin R. , Thompson J. R., Mandrus D., *Phys. Rev. B*, 2001, **63**, 245113.
181. W. Carrillo-Cabrera, in *Instrumentation and Methodology*, Microscopy Conference MC2009, Graz, Austria, 2009, Vol. 1, pp. 275–276.
182. A. Bentien, S. Johnsen and B. B. Iversen, *Phys. Rev. B*, 2006, **73**, 094301.
183. L. T. K. Nguyen, Dissertation, Technischen Univiesität Wien, 2010.
184. C. Hébert, B. Bartova, M. Cantoni, U. Aydemir and M. Baitinger, in *EMC 2008 14th European Microscopy Congress 1–5 September 2008, Aachen, Germany*, eds. S. Richter and A. Schwedt, Springer Berlin Heidelberg, 2008, pp. 531-532.

185. H. Pfisterer and K. Schubert, *Z. Metallkd.*, 1950, **41**, 358-367.
186. J. Emsley, *The Elements*, Clarendon, 1991.
187. E. Du Trémolet de Lacheisserie, D. Gignoux and M. Schlenker, *Magnetism*, Kluwer Academic Publishers, Boston ; [London], 2002.
188. U. Aydemir, C. Candolfi, A. Ormeci, Y. Oztan, M. Baitinger, N. Oeschler, F. Steglich and Y. Grin, *Phys. Rev. B*, 2011, **84**, 195137.
189. S. Stefanoski, J. Martin and G. S. Nolas, *J. Phys.: Condens. Matter*, 2010, **22**, 485404.
190. S. Yamanaka, H. Horie, H. Nakano and M. Ishikawa, *Fullerene Sci. Technol.*, 1995, **3**, 21-28.
191. Y. Li, R. H. Zhang, Y. Liu, N. Chen, Z. P. Luo, X. Q. Ma, G. H. Cao, Z. S. Feng, C. R. Hu and J. H. Ross, *Phys. Rev. B*, 2007, **75**, 054513.
192. N. Kamakura, T. Nakano, Y. Ikemoto, M. Usuda, H. Fukuoka, S. Yamanaka, S. Shin and K. Kobayashi, *Phys. Rev. B*, 2005, **72**, 014511.
193. N. Jaussaud, P. Gravereau, S. Pechev, B. Chevalier, M. Ménétrier, P. Dordor, R. Decourt, G. Goglio, C. Cros and M. Pouchard, *C. R. Chim.*, 2005, **8**, 39-46.
194. H. Fukuoka, Kiyoto, J., Yamanaka, S., *Inorg. Chem.*, 2003, **42**, 2933-2937.
195. P. Toulemonde, C. Adessi, X. Blase, A. San Miguel and J. L. Tholence, *Phys. Rev. B*, 2005, **71**, 094504.
196. Y. Liang, B. Böhme, M. Reibold, W. Schnelle, U. Schwarz, M. Baitinger, H. Lichte and Y. Grin, *Inorg. Chem.*, 2011, **50**, 4523-4528.
197. T. B. Massalski, *Binary Alloy Phase Diagrams Second Edition*, ASM International, Materials Park, Ohio, 1990, pp 613-615.
198. T. B. Massalski and H. Okamoto, *Binary Alloy Phase Diagrams*, ASM International, Materials Park, Ohio, 1990, pp 2859-2861.
199. D. W. Davidson, *Can. J. Chem.*, 1971, **49**, 1224-1242.
200. B. Böhme, U. Aydemir, A. Ormeci, W. Schnelle, M. Baitinger and Y. Grin, *Sci. Technol. Adv. Mat.*, 2007, **8**, 410-415.
201. M. Baitinger, H. G. von Schnering, J. H. Chang, K. Peters and Y. Grin, *Z. Kristallogr. NCS*, 2007, **222**, 87-88.
202. W. Wopersnow and K. Schubert, *Z. Metallkd.*, 1976, **67**, 807-810.
203. S. Ackerbauer, N. Krendelsberger, F. Weitzer, K. Hiebl and J. C. Schuster, *Intermetallics*, 2009, **17**, 414-420.
204. A. N. Mansour and C. A. Melendres, *J. Phys. Chem. A*, 1998, **102**, 65-81.
205. M. Crespin, P. Levitz and L. Gatineau, *J Chem. Soc. Farad. T 2*, 1983, **79**, 1181-1194.
206. K. Moriguchi, M. Yonemura, A. Shintani and S. Yamanaka, *Phys. Rev. B*, 2000, **61**, 9859-9862.
207. J. S. Tse, T. Iitaka, T. Kume, H. Shimizu, K. Parlinski, H. Fukuoka and S. Yamanaka, *Phys. Rev. B*, 2005, **72**, 155441.

208. R. Lortz, R. Viennois, A. Petrovic, Y. Wang, P. Toulemonde, C. Meingast, M. M. Koza, H. Mutka, A. Bossak and A. S. Miguel, *Phys. Rev. B*, 2008, **77**, 224507.
209. W. L. McMillan, *Phys. Rev.*, 1968, **167**, 331.
210. D. Connétable, V. Timoshevskii, B. Masenelli, J. Beille, J. Marcus, B. Barbara, A. M. Saitta, G. M. Rignanese, P. Mélinon, S. Yamanaka and X. Blase, *Phys. Rev. Lett.*, 2003, **91**, 247001.
211. Y. Noat, T. Cren, P. Toulemonde, A. San Miguel, F. Debontridder, V. Dubost and D. Roditchev, *Phys. Rev. B*, 2010, **81**, 104522.
212. H. Lueken, *Magnetochemie*, Teubner, Stuttgart, 1999.
213. D. T. Morelli, T. Caillat, J. P. Fleurial, A. Borshchevsky, J. Vandersande, B. Chen and C. Uher, *Phys. Rev. B*, 1995, **51**, 9622.
214. D. Mandrus, V. Keppens, B. C. Sales and J. L. Sarrao, *Phys. Rev. B*, 1998, **58**, 3712.
215. E. Gruneisen, *Ann Phys-Berlin*, 1933, **16**, 530-540.
216. N. Melnychenko-Koblyuk, A. Grytsiv, P. Rogl, E. Bauer, R. Lackner, E. Royanian, M. Rotter and G. Giester, *J. Phys. Soc. Japan*, 2008, **77**, 54-60.
217. S. Paschen, V. H. Tran, M. Baenitz, W. Carrillo-Cabrera, Y. Grin and F. Steglich, *Phys. Rev. B*, 2002, **65**, 134435.
218. R. Nesper, *Prog. Solid State Chem.*, 1990, **20**, 1-45.
219. H. Schäfer, B. Eisenmann and W. Müller, *Angew. Chem.*, 1973, **85**, 742-760.
220. B. Böhme, A. Guloy, Z. J. Tang, W. Schnelle, U. Burkhardt, M. Baitinger and Y. Grin, *J. Am. Chem. Soc.*, 2007, **129**, 5348-5349.
221. I. Obinata, Y. Takeuchi, K. Kurihara and M. Watanabe, *Nippon Kinzoku Gakkaishi*, 1964, **28**, 568.
222. A. Widera and H. Schäfer, *Z. Naturforsch.* , 1976, **31b**, 1434-1435.
223. G. Bruzzone and E. Franceschi, *J. Less-Common Met.*, 1978, **57**, 201-208.
224. K. H. Janzon, H. Schäfer and A. Weiss, *Z. Naturforsch.* , 1966, **21b**, 287.
225. R. Nesper and F. Zürcher, *Z. Kristallogr. NCS*, 1999, **214**, 20.
226. F. Merlo and M. L. Fornasini, *J. Less-Common Met.*, 1967, **13**, 603-610.
227. A. Currao, J. Čurda and R. Nesper, *Z. Anorg. Allg. Chem.*, 1996, **622**, 85-94.
228. H. Schäfer, K. H. Janzon and A. Weiss, *Angew. Chem*, 1963, **75**, 451-452.
229. K. H. Janzon, H. Schäfer and A. Weiss, *Z. Anorg. Allg. Chem.*, 1970, **372**, 87-99.
230. H. Fukuoka, Ueno, K., Yamanaka, S., *J. Organomet. Chem.*, 2000, **611**, 543-546.
231. T. Goebel, P. Jeglič and F. Haarmann, presented in part at the 11th European Conference on Solid State Chemistry, Caen, 2007.
232. NIST Database: https://srmors.nist.gov.
233. H. G. von Schnering, M. Schwarz, J.-H. Chang, K. Peters, E. M. Peters and R. Nesper, *Z. Kristallogr. NCS*, 2005, **220**, 525.
234. M. Baitinger, K. Peters, M. Somer, W. Carrillo-Cabrera, Y. Grin, R. Kniep and H. G. von Schnering, *Z. Kristallogr. NCS*, 1999, **214**, 455-456.

235. U. Aydemir, *unpublished results*.
236. P. Engel, T. Matsumoto, G. Steinmann and H. Wondratschek, eds., *The Non-characteristic Orbits of the Space Groups*, Oldenbourg Verlag, München, 1984.
237. W. Carrillo-Cabrera, N. Caroca-Canales and H. G. von Schnering, *Z. Anorg. Allg. Chem.*, 1994, **620**, 247-257.
238. L. Pauling, *The Nature of the Chemical Bond and the Structure of Molecules and Crystals: An Introduction to Modern Structural Chemistry.*, Ithaca, New York, 1960.
239. R. T. Sanderson, *Polar Covalence*, Academic Press, New York, 1983.
240. A. Savin, O. Jepsen, J. Flad, O. K. Andersen, H. Preuss and H. G. von Schnering, *Angew. Chem. Int. Ed.*, 1992, **31**, 185-187.
241. D. B. Chestnut, *Chem. Phys.*, 2001, **271**, 9-16.
242. M. Kohout and A. Savin, *Int. Jour. Quan. Chem.* , 1996, **60**, 875-882.
243. N. W. Ashcroft and N. D. Mermin, *Solid State Physics*, W. B. Saunders Co., Philadelphia, 1976.
244. J. Mason, *Multinuclear NMR*, Kluwer Academic/Plenum Publishers, New York 1987.
245. A. Abragam, *Principles of Nuclear Magnetism*, Oxford University Press, New York 1961.
246. C. P. Slichter, *Principles of Magnetic Resonance*, Springer-Verlag, New York 1990.
247. H. Selbach, O. Kanert and D. Wolf, *Phys. Rev. B*, 1979, **19**, 4435.
248. D. Mayeri, B. L. Phillips, M. P. Augustine and S. M. Kauzlarich, *Chem. Mater.*, 2001, **13**, 765-770.
249. F. Haarmann, D. Gruner, V. Bezugly, H. Rosner and Y. Grin, *Z. Anorg. Allg. Chem.*, 2006, **632**, 1423-1431.
250. G. S. Armatas and M. G. Kanatzidis, *Science*, 2006, **313**, 817-820.
251. A. Smits and W. de Lange, *J. Chem. Soc.*, 1928, 2944-2952.
252. H. Oppermann and D. Q. Huong, *Z. Anorg. Allg. Chem.*, 1995, **621**, 665-670.
253. P. F. McMillan, J. Gryko, C. Bull, R. Arledge, A. J. Kenyon and B. A. Cressey, *J. Solid-State Chem.*, 2005, **178**, 937-949.
254. X. Zhang, D. Neiner, S. Wang, A. Louie and S. M. Kauzlarich, *Nanotechnology* 2007, **18**, 095601.
255. G. U. Kulkarni, R. S. Gopalan and C. N. R. Rao, *J. Mol. Struc-Theochem*, 2000, **500**, 339-362.
256. M. A. Spackman, *Annu. Rep. Prog. Chem., Sect. C: Phys. Chem.*, 1998, **94**, 177-207.
257. V. G. Tsirel'son and R. P. Ozerov, *Electron Density and Bonding in Crystals : Principles, Theory, and X-ray Diffraction Experiments in Solid State Physics and Chemistry*, Institute of Physics Pub., Bristol, 1996.

258. T. S. Koritsanszky and P. Coppens, *Chem. Rev.*, 2001, **101**, 1583-1627.
259. P. Coppens, *X-ray Charge Densities and Chemical Bonding*, Oxford University Press, Oxford, 1997.
260. J. P. Walter and M. L. Cohen, *Phys. Rev. B*, 1971, **4**, 1877.
261. J. Davaasambuu, A. Daniel, J. Stahn and U. Pietsch, *J. Phys. Chem. Solids*, 2001, **62**, 2147-2152.
262. U. Pietsch, *Phys. Status Solidi B*, 1985, **128**, 439-451.
263. N. K. Hansen and P. Coppens, *Acta Crystallogr. A*, 1978, **34**, 909-921.
264. T. Koritsanszky, S. Howard, T. Richter, Z. Su, P. R. Mallinson and N. K. Hansen, *XD-A Computer Program Package for Multipole Refinement and Analysis of electron Densities from Diffraction Data*, Free University of Berlin, Germany, 1995.
265. A. ElHaouzi, N. K. Hansen, C. LeHenaff and J. Protas, *Acta Crystallogr. A*, 1996, **52**, 291-301.
266. O. Schmidt, S. Gorfman and U. Pietsch, *Cryst. Res. Technol.*, 2008, **43**, 1126-1132.
267. B. R. Pamplin, T. Kiyosawa and K. Masumoto, *Prog. Cryst. Growth Charact. Mater.*, 1979, **1**, 331-387.
268. H. Hahn, G. Frank, W. Klingler, A. D. Meyer and G. Storger, *Z. Anorg. Allg. Chem.*, 1953, **271**, 153-170.
269. C. H. L. Goodman, *Nature*, 1957, **179**, 828-829.
270. E. Buehler and J. H. Wernick, *J. Cryst. Growth*, 1971, **8**, 324-332.
271. J. S. Shah, *Prog. Cryst. Growth Charact. Mater.*, 1980, **3**, 333-389.
272. J. L. Shay and J. H. Wernick, *Ternary Chalcopyrite Semiconductors : Growth, Electronic Properties and Applications*, Pergamon, Oxford, 1975.
273. H. Schäfer, *Z. Anorg. Allg. Chem.*, 1973, **400**, 242-252.
274. M. Schmidt, *Chemical Transport*, in Scientific Report 2001-2002, MPI-CPfS, Dresden, 2003.
275. M. G. Kanatzidis, R. Pottgen and W. Jeitschko, *Angew. Chem. Int. Edit.*, 2005, **44**, 6996-7023.
276. A. J. Spring-Thorpe and B. R. Pamplin, *J. Cryst. Growth*, 1968, **3-4**, 313-316.
277. S. A. Mughal, A. J. Payne and B. Ray, *J. Mater. Sci.*, 1969, **4**, 895-901.
278. S. C. Abrahams and J. L. Bernstein, *J. Chem. Phys.*, 1970, **52**, 5607-5613.
279. S. A. Mughal and B. Ray, *J. Cryst. Growth*, 1974, **21**, 146-148.
280. S. A. Mughal and B. Ray, *J. Mater. Sci.*, 1973, **8**, 1523-1526.
281. T. Shirakawa, K. Okamura and J. Nakai, *Phys. Lett. A*, 1979, **73**, 442-444.
282. H. Baum and K. Winkler, *Kristall und Technik*, 1978, **13**, 645-655.
283. R. H. Plovnick and W. E. Thatcher, *Mater. Res. Bull.*, 1977, **12**, 219-225.
284. X. C. He, H. S. Shen, P. Wu, K. Dwight and A. Wold, *Mater. Res. Bull.*, 1988, **23**, 799-803.
285. N. Yamamoto, H. Kubo and T. Miyauchi, *Jpn. J. Appl. Phys.*, 1975, **14**, 299-300.

286. W. N. Honeyman, *J. Phys. Chem. Solids*, 1969, **30**, 1935-1940.
287. E. Guerrero, V. Sagredo and J. Shah, *J. Electron. Mater.*, 1981, **10**, 987-998.
288. V. P. Zhuze, V. M. Sergeeva and E. L. Shtrum, *Sov. Phys.-Tech. Phys.*, 1958, **3**, 1925-1938.
289. G. Krabbes, W. Bieger, K.-H. Sommer and T. Söhnel, Program TRAGMIN, IFW Dresden, TU Dresden, Institut für Anorganische Chemie, Dresden, 1995.
290. G. Eriksson, *Acta Chem. Scand.*, 1971, **25**, 2651-2658.
291. I. Barin, *Thermochemical Data of Pure Substances*, VCH, Weinheim, 1989.
292. H. J. Deiseroth and H. Pfeifer, *Z. Kristallogr.*, 1991, **196**, 197-205.
293. C. Reiner, H. J. Deiseroth and M. Schlosser, *Z. Anorg. Allg. Chem.*, 2002, **628**, 249-257.
294. P. Bridenbaugh and B. Tell, *Mater. Res. Bull.*, 1975, **10**, 1127-1130.
295. D. J. Vaughan, *Sulfide Mineralogy and Geochemistry*, Mineralogical Society of America, Chantilly, Va., 2006.
296. M. J. Buerger, *J. Chem. Phys.*, 1947, **15**, 1-16.
297. U. Kaufmann and J. Schneider, in *Festkörperprobleme 14*, ed. H. Queisser, Springer Berlin / Heidelberg, 1974, vol. 14, pp. 229-260.
298. H. W. Spiess, U. Haeberlen, G. Brandt, A. Räuber and J. Schneider, *Phys. Stat. Sol. (b)*, 1974, **62**, 183-192.
299. S. C. Abrahams and J. L. Bernstein, *J. Chem. Phys.*, 1973, **59**, 5415-5422.
300. S. C. Abrahams and J. L. Bernstein, *J. Chem. Phys.*, 1971, **55**, 796-803.
301. M. Robbins, J. C. Phillips and V. G. Lambrech Jr., *J. Phys. Chem. Solids*, 1973, **34**, 1205-1209.
302. L. E. Murr and S. L. Lerner, *J. Mater. Sci.*, 1977, **12**, 1349-1354.
303. M. Pasemann and P. Klimanek, *Kristall und Technik*, 1973, **8**, 1141-1151.
304. H.-S. Shen, G. Q. Yao, R. Kershaw, K. Dwight and A. Wold, *J. Solid State Chem.*, 1987, **71**, 176-181.
305. A. A. Vaipolin, E. O. Osmanov and D. N. Tret'yakov, *Inorg. Mater.*, 1967, **3**, 231-236.
306. A. Miller, R. Humphreys, G. and B. Chapman, *J. Phys. Colloques*, 1975, **36**, C3-31 - C3-34.

Curriculum Vitae

Personal Data

Name and Surname	Umut Aydemir
Date of Birth	November 15th, 1981
Place of Birth	Erzincan, Turkey
Marital Status	Single

Academic Qualifications

July 2006 – Present	Dr. rer. nat. candidate in Chemistry, Max Planck Institute for Chemical Physics of Solids (MPI-CPfS), Dresden
Sept. 2004 – June 2006	M.S. in Materials Science and Engineering (MASE), Koç University, Istanbul
Sept. 1998 – June 2004	B.S. in Chemistry and Physics (Double Major), Koç University, Istanbul
Sept. 1995 – June 1998	High School, Maltepe High School, Istanbul

Scholorships and Awards

2006	Top Ranking Student in MASE Graduates (GPA: 3.94/4.0)
2004	Full 2-Year Vehbi Koç Scholarship for M.S. Studies
2004	Top Ranking Student in Chemistry Graduates (GPA: 3.42/4.0)
1998	Full 5-Year Vehbi Koç Scholarship for B.S. Studies

Work Experience

2004 - 2006	Research and Teaching Assistant at the Faculty of Materials Science and Engineering, Koç University, Istanbul
2002 - 2005	Summer Internships, MPI-CPfS, Dresden
2000 - 2004	Research Assistant at the Inorganic Chemistry Research Lab., Koç University, Istanbul

Publications

Journal Articles

17. Synthesis, Crystal Structure and Physical Properties of the Type-I Clathrate $Ba_{8-\delta}Ni_x\square_ySi_{46-x-y}$.
U. Aydemir, C. Candolfi, A. Ormeci, H. Borrmann, U. Burkhardt, Y. Oztan, N. Oeschler, M. Baitinger, F. Steglich, Yu. Grin, *Inorg. Chem.* 2012, **51**, 4730.

16. High temperature thermoelectric properties of the type-I clathrate $Ba_8Au_xSi_{46-x}$.
C. Candolfi, U. Aydemir, M. Baitinger, N. Oeschler, F. Steglich, Yu. Grin, *J. Appl. Phys.* 2012, **111**, 043706.

15. Low-temperature thermoelectric, galvanomagnetic, and thermodynamic properties of the type-I clathrate $Ba_8Au_xSi_{46-x}$.
U. Aydemir C. Candolfi, A. Ormeci, Y. Oztan, M. Baitinger, N. Oeschler, F. Steglich, Yu. Grin, *Phys. Rev. B*, 2011, **84**, 195137.

14. Multiband conduction in the type-I clathrate $Ba_8Ge_{43}\square_3$.
C. Candolfi, A. Ormeci, U. Aydemir, M. Baitinger, N. Oeschler, F. Steglich, Yu. Grin, *Phys. Rev. B*, 2011, **84**, 205118.

13. Transport properties of the clathrate $BaGe_5$.
C. Candolfi, U. Aydemir, A. Ormeci, W. Carrillo-Cabrera, U. Burkhardt, M. Baitinger, N. Oeschler, F. Steglich, and Yu. Grin, *J. Appl. Phys.*, 2011, **110**, 043715.

12. Vibrational Spectra and Quantum Chemical Calculations of the Pure and Mixed Cluster Anions $[Si_xGe_{4-x}]^{4-}$ and $[Ge_xSn_{4-x}]^{4-}$ (x = 0-4) in Compounds with Potassium and Cesium.
A. Ormeci, U. Aydemir, M. Somer, *Z. Anorg. Allg. Chem.*, 2011, **637**, 907.

11. Syntheses, Crystal Structures, Magnetic Properties, and Vibrational Spectra of Nitridoborate-Halide Compounds $Sr_2[BN_2]Br$ and $Eu_2[BN_2]X$ (X = Br, I) with Isolated $[BN_2]^{3-}$ Units.
I. Kokal, U. Aydemir, Yu. Prots, W. Schnelle, L. Akselrud, P. Höhn, M. Somer, *Z. Kristallogr.*, 2011**, 226,** 633.

10. Low-temperature magnetic, galvanomagnetic, and thermoelectric properties of the type-I clathrates $Ba_8Ni_xSi_{46-x}$.
C. Candolfi, U. Aydemir, A. Ormeci, M. Baitinger, N. Oeschler, F. Steglich, Yu. Grin, *Phys. Rev. B*, 2011, **83**, 205102.

9. α- and β-$Na_2[BH_4][NH_2]$: Two modifications of a complex hydride in the system $NaNH_2$–$NaBH_4$; syntheses, crystal structures, thermal analyses, mass and vibrational spectra.
M. Somer, S. Acar, C. Koz, I. Kokal, P. Höhn, R. Cardoso-Gil, U. Aydemir, L. Akselrud, *J. Alloys Compd.*, 2010, **491**, 98.

8. $BaGe_5$: A New Type of Intermetallic Clathrate.
U. Aydemir, L. Akselrud, W. Carrillo-Cabrera, C. Candolfi, N. Oeschler, M. Baitinger, F. Steglich, Yu. Grin, *J. Am. Chem. Soc.*, 2010, **132**, 10984.

7. Atomic ordering and thermoelectric properties of the n-type clathrate $Ba_8Ni_{3.5}Ge_{42.1}\square_{0.4}$.
L. T. K. Nguyen, U. Aydemir, M. Baitinger, E. Bauer, H. Borrmann, U. Burkhardt, J. Custers, A. Haghighirad, R. Hofler, K. D. Luther, F. Ritter, W. Assmus, Yu. Grin, S. Paschen, *Dalton Trans.*, 2010, **39**, 1071.

6. Crystal structure and transport properties of $Ba_8Ge_{43}\square_3$.
U. Aydemir, C. Candolfi, H. Borrmann, M. Baitinger, A. Ormeci, W. Carrillo-Cabrera, C. Chubilleau, B. Lenoir, A. Dauscher, N. Oeschler, F. Steglich, Yu. Grin, *Dalton Trans.*, 2010, **39**, 1078.

5. The Metallic Zintl Phase Ba_3Si_4 – Synthesis, Crystal Structure, Chemical Bonding, and Physical Properties.
U. Aydemir, A. Ormeci, H. Borrmann, B. Bohme, F. Zurcher, B. Uslu, T. Goebel, W. Schnelle, P. Simon, W. Carrillo-Cabrera, F. Haarmann, M. Baitinger, R. Nesper, H. G. von Schnering, Yu. Grin, *Z. Anorg. Allg. Chem.*, 2008, **634**, 1651.

4. Cs_4Ge_9·*en*: A Novel Compound with $[Ge_9]^{4-}$ Clusters – Synthesis, Crystal Structure and Vibrational Spectra.
W. Carrillo-Cabrera, U. Aydemir, M. Somer, A. Kircali, T. F. Fässler, S. D. Hoffmann, *Anorg. Allg. Chem.*, 2007, **633**, 1575.

3. Synthesis of the intermetallic clathrate $Na_2Ba_6Si_{46}$ by oxidation of Na_2BaSi_4 with HCl.
B. Böhme, U. Aydemir, A. Ormeci, W. Schnelle, M. Baitinger, Yu. Grin, *Sci. Technol. Adv. Mat.*, 2007, **8**, 410.

2. Crystal structure of tetrapotassium diarsenidozincate, K_4ZnAs_2.
Y. Prots, U. Aydemir, S. S. Ozturk, M. Somer, *Z Kristallogr. NCS*, 2007, **222**, 163.

1. Vibrational spectra of cluster anions. 2 [1] Vibrational spectra of compounds with the cluster anions $[E_4]^{4-}$: M_4E_4 (M = K, Rb, Cs; E = Ge, Sn) and beta-Na_4Sn_4.
M. Somer, U. Aydemir, M. Baitinger, H. G. von Schnering, *Z. Anorg. Allg. Chem.*, 2006, **632**, 1281.

Refereed Conference Proceedings

3. Thermoelectric Properties of the Clathrate I $Ba_8Ge_{43}\square_3$.
C. Candolfi, U. Aydemir, M. Baitinger, N. Oeschler, F. Steglich and Yu. Grin, *J. Electron. Mater.*, 2010, **39**, 2039-2042.

2. Physical Properties of Single-Crystalline $Ba_8Ni_{3.5}Ge_{42.1}\square_{0.4}$.
L. T. K. Nguyen, U. Aydemir, M. Baitinger, J. Custers, A. Haghighirad, R. Hofler, K. D. Luther, F. Ritter, Yu. Grin, W. Assmus and S. Paschen, *J. Electron. Mater.*, 2010, **39**, 1386-1389.

1. Characterization of Ge-based clathrates oxidized in air by means of TEM and SEM.
C. Hébert, B. Bartova, M. Cantoni, U. Aydemir and M. Baitinger, in *EMC 2008 14th European Microscopy Congress 1–5 September 2008, Aachen, Germany*, eds. S. Richter and A. Schwedt, Springer Berlin Heidelberg, 2008, pp. 531-532.

Scientific Reports

2. New Developments in Clathrate Research.
M. Baitinger, L. Akselrud, U. Aydemir, et. al., Scientific Report 2009-2010, MPI-CPfS, Dresden, Germany.

1. Intermetallic Clathrates Revisited.
M. Baitinger, U. Aydemir, B. Bohme, et. al., Scientific Report 2006-2008, MPI-CPfS, Dresden, Germany.

Oral and Poster Presentations

12. U. Aydemir, C. Candolfi, A. Ormeci, L. Akselrud, M. Baitinger, Yu. Grin, "Thermoelectric Properties of the Clathrate $BaGe_5$**",** *2012 MRS Spring Meeting*, April 9 – 13, **2012**, San Francisco, California, USA (**Poster**).

11. U. Aydemir, "$BaGe_5$: A new type of intermetallic clathrate", *Baltic Boat Conference*, June 18 – 21, **2010**, Baltic Sea (**Oral**).

10. U. Aydemir, H. Borrmann, C. Hébert, L. T. K. Nguyen, U. Burkhardt, M. Baitinger, Yu. Grin, "Existence Region of Type-I Clatrates in the System Ba – Ni – Ge", *25th European Crystallographic Meeting*, August 16 – 21, **2009**, Istanbul, Turkey (**Poster**).

9. U. Aydemir, N. T. K. Lien, J. Custers, R. Höfler, F. Widder, H. Borrmann, W. Schnelle, C. Hebert, B. Lenoir, C. Candolfi,, E. Alleno, C. Godart, M. Baitinger, S. Bühler-Paschen, Yu. Grin, "Synthesis and transport properties of the type-I clathrates $Ba_8Ni_{3.8+x}Ge_{42.2-x}$ (x = 0, 0.2, 0.4)", *28th International / 7th European Conference on Thermoelectrics*, July 26 – 30, **2009**, Freiburg, Germany (**Poster**).

8. U. Aydemir, H. Borrmann, "Synthesis and crystal growth of $ZnSiP_2$ and FeSi for experimental charge density analyses", *DFG Meeting: Proposal colloquium SPP 1178*, February 4 – 5, 2009, Kloster Banz, Germany (**Poster**).

7. U. Aydemir, "X-ray Powder Diffraction", *Sigma 5 Common PhD Seminer: X-Ray Methods in Solids*, July 17, **2008**, Dresden, Germany (**Oral**).

6. U. Aydemir, S. Leoni, H. Borrmann, W. Schnelle, U. Burkhardt, Y. Prots, M. Baitinger, "TaNiSi: A preparation route to refractory compounds", *Advanced Processing for Novel Functional Materials – APNFM 2008*, January 23 – 25, **2008**, Dresden, Germany (**Poster**)

5. U. Aydemir, "General overview about the CMA project $Ba_8(Ni_xGe_y\square_z)Ge_{40}$ ($x + y + z$ = 6)", *CMA Meeting*, November 18 – 19, **2007**, TU WIEN, Austria (**Oral**).

4. U. Aydemir, A. Ormeci, H. Borrmann, W. Schnelle, B. Böhme, P. Simon, W. Carrillo-Cabrera, M. Baitinger and Yu. Grin, "Synthesis, Characterization and Reactivity of the

Metallic Zintl Phase Ba_3Si_4", *11th European Conference on Solid State Chemistry*, September 11 – 13, **2007**, Caen, France (**Poster**).

3. U. Aydemir, "Sample Preparation and Phase Range Investigations on $Ba_8Ni_xGe_{46-x}$ clathrates", *CMA Meeting*, October 23 – 25, **2006**, TUWIEN Vienna, Austria (**Oral**).

2. U. Aydemir, M. Baitinger, Yu. Grin., "Investigation of the Ternary Clathrates of $Ba_8(Ni_xGe_y\square_z)Ge_{40}$ ($x + y + z = 6$)", *20th National Chemistry Congress*, September 4 – 8, **2006**, Kayseri, Turkey (**Poster**)

1. U. Aydemir, "Ni substituted Ge clathrates", *Baltic Boat Conference*, May **2006** Stockholm, Sweden (**Oral**).

Presented by Colleagues

8. M. Ikeda, U. Aydemir, M. Baitinger, R. Cardoso, J. Custers, R. Höfler, L.T.K. Nguyen, F. Widder, Yu. Grin, and S. Paschen," Transport properties of type-I clathrate compounds", *1st International Conference on Complex Metallic Alloys and their Complexity*, October 4 – 7, **2009**, Nancy, France (**Poster**).

7. L. T. K. Nguyen, U. Aydemir, M. Baitinger, J. Custers, A. Haghighirad, R. Höfler, K. D. Luther, F. Ritter, Yu. Grin, W. Assmus, and S. Paschen, "Physical Properties of Single Crystalline Clathrate I $Ba_8Ni_{3.5}Ge_{42}\square_{0.5}$", *28th International / 7th European Conference on Thermoelectrics*, July 26 – 30, **2009**, Freiburg, Germany (**Poster**).

6. M. Baitinger, U. Aydemir, H. Borrmann, C. Candolfi, W. Carrillo-Cabrera, N.T.K. Lien, N. Oeschler, I. Veremchuk, S. Bühler-Paschen, Yu. Grin, "Point defects and physical properties of clathrates", *28th International / 7th European Conference on Thermoelectrics*, July 26 – 30, **2009**, Freiburg, Germany (**Poster**).

5. R. Höfler, T.K.L. Nguyen, U. Aydemir, J. Custers, M. Baitinger, Yu. Grin, W. Assmus, S. Paschen, "Resistivity and Hall Measurements on the Clathrate-System $Ba_8Ni_4Ge_{42}$", *ARW Workshop on Correlated Thermoelectrics: Properties and Applications of Thermoelectric Materials*, September 20 – 26, **2008,** Hvar, Croatia (**Poster**).

4. C. Hébert, B. Bartova, M. Cantoni, U. Aydemir, and M. Baitinger, Characterization of Ge-based clathrates oxidized in air by means of TEM and SEM, *14th European Microscopy Congress*, September 1 – 5, **2008**, Aachen, Germany (**Oral**).

3. M. Sakaliyska, U. Aydemir, S. Scudino, M. Baitinger, K. B. Surreddi, Yu. Grin, J. Eckert, "Mechanical Milling of $Ba_8Ni_xGe_{46-x}$ Clathrates", *Advanced Processing for Novel Functional Materials – APNFM 2008*, January 23 – 25, **2008**, Dresden, Germany (**Oral**).

2. S Acar, I. Kokal, M. Somer, P. Höhn, U. Aydemir, R. Cardoso-Gil and L. Akselrud, "$Na_2[BH_4][NH_2]$: A Novel complex hydride in $NaNH_2$-$NaBH_4$ system; Syntheses, Crystal structures, Thermal Analyses, Mass and Vibrational Spectra", *11th European Conference on Solid State Chemistry*, W49, September 11 – 13, **2007**, Caen, France (**Poster**).

1. I. Kokal, M. Somer, U. Aydemir, W. Carrillo-Cabrera, Y. Prots, W. Schnelle, "$Li_{0.42}Eu_3[B_3N_6]$: Synthesis, Crystal Structure, Vibrational Spectroscopy and Magnetic Properties", *11th European Conference on Solid State Chemistry*, W39, September 11 – 13, **2007**, Caen, France (**Poster**).

Schools and Workshops Attended

9. Workshop on WinCSD Program Package for Crystallographic Calculations, August 24 – 25, **2011**, MPI-CPfS, Dresden, Germany.

8. Workshop on JANA 2006 - Program for Structure Analysis of Crystals Periodic in Three or More Dimensions from Diffraction Data -, September 22 – 24, **2010**, MPI-CPfS, Dresden, Germany.

7. Workshop on Electron Localizability and Chemical Bonding, March 29th – April 1st, **2009**, MPI-CPfS, Dresden, Germany.

6. Complex Metallic Alloys: Surfaces and Coatings, 3rd European School in Materials Science, May 26 – 31, **2008**, Ljubljana, Slovenia.

5. Workshop on XD2006 program package: Advanced Methods in X-ray Charge Density Analysis: Extracting Properties from a Multipole Refinement, September 3 – 6, **2007**, Martina Franca, Italy.

4. Properties and Application of Complex Metallic Alloys: 2nd European School in Materials Science, May 21 – 26, **2007**, Ljubljana, Slovenia.

3. The 11th BCA/CCG Intensive Teaching School in X-ray Structure Analysis, March 24th – April 2nd, **2007**, Trevelyan College, University of Durham, UK.

2. The Second Bilateral Workshop on Solid State and Materials Chemistry, July 17 – 19, **2006**, MPI-CPfS, Dresden, Germany.

1. Workshop of the AK Computational Crystallography of the DGK Electron Density – Theory and Applications, February 19 – 21, **2006**, Aachen, Germany.

Versicherung

Hiermit versichere ich, dass ich die vorliegende Arbeit ohne unzulässige Hilfe Dritter und ohne Benutzung anderer als der angegebenen Hilfsmittel angefertigt habe; die aus fremden Quellen direkt oder indirekt übernommenen Gedanken sind als solche kenntlich gemacht. Die Arbeit wurde bisher weder im Inland noch im Ausland in gleicher oder ähnlicher Formeiner anderen Prüfungsbehörde vorgelegt.

Die vorliegende Dissertation wurde unter Betreuung durch Herrn Prof. Juri Grin am Max-Planck-Institut für Chemische Physik fester Stoffe in Dresden angefertigt.

Es haben keine früheren erfolglosen Promotionsverfahren stattgefunden.

Ich erkenne die Promotionsordnung der Fakultät Mathematik und Naturwissenschaften der Technische Universität Dresden vom 17. Juli 2008 in vollem Umfang an.

Dresden, den

(Umut Aydemir)